frontiers | Research Topics

Monitoring, early warning and mitigation of natural and engineered slopes – volume II

Edited by
Wen Nie, Haijun Qiu and Afshin Asadi

Published in
Frontiers in Earth Science

ISSN 1664-8714
ISBN 978-2-8325-2358-2
DOI 10.3389/978-2-8325-2358-2

About Frontiers

Frontiers is more than just an open access publisher of scholarly articles: it is a pioneering approach to the world of academia, radically improving the way scholarly research is managed. The grand vision of Frontiers is a world where all people have an equal opportunity to seek, share and generate knowledge. Frontiers provides immediate and permanent online open access to all its publications, but this alone is not enough to realize our grand goals.

Frontiers journal series

The Frontiers journal series is a multi-tier and interdisciplinary set of open-access, online journals, promising a paradigm shift from the current review, selection and dissemination processes in academic publishing. All Frontiers journals are driven by researchers for researchers; therefore, they constitute a service to the scholarly community. At the same time, the *Frontiers journal series* operates on a revolutionary invention, the tiered publishing system, initially addressing specific communities of scholars, and gradually climbing up to broader public understanding, thus serving the interests of the lay society, too.

Dedication to quality

Each Frontiers article is a landmark of the highest quality, thanks to genuinely collaborative interactions between authors and review editors, who include some of the world's best academicians. Research must be certified by peers before entering a stream of knowledge that may eventually reach the public - and shape society; therefore, Frontiers only applies the most rigorous and unbiased reviews. Frontiers revolutionizes research publishing by freely delivering the most outstanding research, evaluated with no bias from both the academic and social point of view. By applying the most advanced information technologies, Frontiers is catapulting scholarly publishing into a new generation.

What are Frontiers Research Topics?

Frontiers Research Topics are very popular trademarks of the *Frontiers journals series*: they are collections of at least ten articles, all centered on a particular subject. With their unique mix of varied contributions from Original Research to Review Articles, Frontiers Research Topics unify the most influential researchers, the latest key findings and historical advances in a hot research area.

Find out more on how to host your own Frontiers Research Topic or contribute to one as an author by contacting the Frontiers editorial office: frontiersin.org/about/contact

Monitoring, early warning and mitigation of natural and engineered slopes – volume II

Topic editors

Wen Nie — Jiangxi University of Science and Technology, China

Haijun Qiu — Northwest University, China

Afshin Asadi — Wilton Joubert Consulting Engineers, New Zealand

Citation

Nie, W., Qiu, H., Asadi, A., eds. (2023). *Monitoring, early warning and mitigation of natural and engineered slopes – volume II*. Lausanne: Frontiers Media SA.

doi: 10.3389/978-2-8325-2358-2

Table of contents

frontiers | Frontiers in Earth Science

TYPE Editorial
PUBLISHED 21 April 2023
DOI 10.3389/feart.2023.1200777

OPEN ACCESS

EDITED AND REVIEWED BY
Yi Xue,
Xi'an University of Technology, China

*CORRESPONDENCE
Wen Nie,
wen.nie@vip.tom.com

RECEIVED 05 April 2023
ACCEPTED 13 April 2023
PUBLISHED 21 April 2023

CITATION
Qiu H, Nie W and Asadi A (2023), Editorial: Monitoring, early warning and mitigation of natural and engineered slopes—Volume II.
Front. Earth Sci. 11:1200777.
doi: 10.3389/feart.2023.1200777

Editorial: Monitoring, early warning and mitigation of natural and engineered slopes—Volume II

Haijun Qiu[1], Wen Nie[2]* and Afshin Asadi[3]

[1]College of Urban and Environmental Sciences, Northwest University, Xi'an, China, [2]Jiangxi University of Science and Technology, Ganzhou, China, [3]International College of Auckland (ICA), Auckland, New Zealand

KEYWORDS

natural and engineering slope, slope failure mechanism, slope monitoring, risk assessment, ecology and land use

Editorial on the Research Topic
Monitoring, early warning and mitigation of natural and engineered slopes—Volume II

Introduction

Natural and engineered slopes are widely distributed all over the world (He et al., 2021; Qiu et al., 2022). Due to natural factors or human activity, many slopes are becoming unstable and showing a very high exposure to landslides (Zhou et al., 2022; Pei et al., 2023). Thus, it is necessary to monitor these unstable slopes and conduct early warning accordingly (Zhu et al., 2021; Yang et al., 2022). Recently, with the development of science and technology and the theory of multidisciplinary interaction, they provide new opportunities for the research on early detection, dynamic monitoring and risk reduction of unstable slopes (Liu et al., 2022; Wang et al., 2022). However, efficient detection, low-cost monitoring, accurate early warning, and reliable risk assessment still require further breakthroughs (Qu et al., 2021; Ma et al., 2023). Volume I of this Research Topic received 14 manuscripts last year (Nie et al., 2023). Now Volume II brings together 16 papers designed to present the latest research advances and methods for monitoring, early warning and mitigation of natural and engineered slopes.

Slope hazards mechanism and reduction technology

The stability prediction of soil-rock slopes with complex physical and mechanical properties is an important topic in the field of geological engineering. To study the stability of mine slope under deep bench blasting vibration, Su et al. analyzed mechanical parameters of a mine slope under uniaxial and triaxial instruments by field vibration monitoring and numerical simulation methods. The results show that the overall displacement of the slope is small under the action of dynamic blasting load, and the change of displacement decreases with the decrease of the vibration wave.

Fu et al. predicted the stability of soil-rock slope by machine learning algorithm coupled with intelligent optimization algorithm-weighted mean of vectors algorithm (INFO).

Dynamic process and formation mechanisms of landslides are essential to hazard assessment, three different related researches proposed this issue. Yang et al. studied the characteristics and formation mechanism of a debris flow that occurred in Zhangjiayuan gully through field investigation and remote sensing interpretation. Dai et al. used the Xigou debris flow in the Three Gorges Reservoir Region (TGRR) as a case study, the development characteristics and initiation pattern of which were analyzed based on field investigation. Song et al. made a critical area identification and dynamic process simulation for landslide hazard chain formation in the upstream Jinsha River. In another study, the impact pressure and flow velocity in the flow field were measured synchronously using the impact detection system and a particle image velocimetry system in a water channel and the effects of the turbulence structure on the impact process of flash flood were investigated (Gu et al.).

Wang et al. studied the hydrological effects of macropore flow and proposed a mechanistic model of the formation of shallow landslides by introducing the macropore coefficient of granite residual soil. The study results showed that the macropores of vegetation roots had a significant effect by increasing the permeability of granite residual soil. The accuracy of data-driven model is closely affected by the quality of negative samples, Ye et al. proposed a method combining a self-organizing-map (SOM) and a one-class SVM (SOM-OCSVM) to generate more reasonable non-landslide samples. The aforementioned results prove that the proposed method can enhance the performance of ML models to produce more reliable LSM.

In addition, two studies on actual engineering projects are of interest, as they provide experience and techniques from field investigations. Liu et al. studied the development characteristics, distribution, and communication law of ground fissures along the highway using the comprehensive investigation method and technology. The Daofu landslide, Xianshui River Earthquake Zone is a typical landslide directly threatening the road below and forming a debris flow channel. Zhang et al. combined traditional methods (drilling and field investigation) with two geophysical techniques, multichannel analysis of surface waves (MASW) and electrical resistivity tomography (ERT) to effectively determine the electrical characteristics, velocity characteristics and spatial structure of the landslide. Their study indicates the use of MASW and ERT can quickly and effectively characterize the subsurface of landslides to assess landslide risk and prevent debris flow hazards.

The ecology and land use of the disaster area

The effects of geohazards on the ecological environment and ecological spatial pattern have received wide attention from scholars. In this issue, three studies focus on ecological, environmental and land use change in areas affected by geological hazards. Yang et al. explored the land-use evaluation and utilization advice on a debris flow disaster deposit area-The upstream Fujiang River. The author believes that the agriculture scenario can be used in the high soil fertility area, and the potential construction scenario is best suited for infrastructure because of its low soil fertility. Vegetation coverage is an important indicator for evaluating regional environmental. Liu et al. found the vegetation coverage in the Ganjiang River Basin showed a fluctuating increasing trend 2000–2020, and an increasing trend with increasing elevation, the result show that the anti-sustainability effect of vegetation change was stronger than that of sustainability, and weak anti-sustainability was dominant. The findings could provide a scientific basis for the management of regional ecosystems. Sui et al. utilized a quantitative analysis of the ecological recoverability of Jiuzhaigou in cases of artificial restoration and spontaneous restoration under different types of geohazards. Results showed that forests play a vital role in maintaining and controlling habitat quality; artificial restoration can significantly ameliorate the impact of geohazards on the scenic area. The above studies show that geological hazards have a negative effect on local ecosystems, there is a need to quantify this effect, moreover, human restoration contributes to ecosystem recovery.

Engineering properties and microcosmic mechanism of landslide materials

The other two studies focus on the engineering properties and microcosmic mechanism of different materials. In the first study, Liu et al. explored the mechanical effect of clay under acidic and basic conditions, they thought that the cohesive force and internal friction angle of clay decreases under acidic conditions, whereas in basic conditions the opposite is true. In this study of Cui et al., the engineering properties of remolded diatomite and the effects of cement on the compression characteristic, strength properties and microstructures of cement-stabilized diatomite were investigated. Results show that compared with undisturbed diatomite, the compressibility of the remolded diatomite increases while the strength characteristics decrease. Xu et al. considered the key physical factors of Yunan laterite by laboratory tests, and the dielectric constant model was finally proposed to evaluate the natural water state of the laterite. The results show that the relative dielectric constant of laterite increases gradually with the increasing volumetric water content, dry density and temperature respectively. Their findings provide new prevention and control ideas for soil landslides.

Perspectives

The new volume of this Research Topic is dedicated to the use of modern technologies, data-based approaches and techniques incorporating multiple disciplines for monitoring, warning and mitigation of natural and engineered slopes. However, under the influence of extreme weather and the construction of large-scale

projects, slope failure needs new attention. On this basis, it provides reference for mitigating damage from the following aspects. I) Multi-scale and multi-disciplinary integration to analyze the physical mechanism and dynamic process inside the slope; II) Early warning and analysis of slope instability based on big data information and field refined detection system; III) Innovate green, efficient and sustainable slope post-disaster restoration projects.

Author contributions

Three authors co-organized the album, with WN on Slope hazards mechanism and reduction technology, HQ on ecology and land use of the disaster area, and AA on Engineering properties and microcosmic mechanism of landslide materials.

Conflict of interest

The authors declare that the research was conducted in the absence of any commercial or financial relationships that could be construed as a potential conflict of interest.

Publisher's note

All claims expressed in this article are solely those of the authors and do not necessarily represent those of their affiliated organizations, or those of the publisher, the editors and the reviewers. Any product that may be evaluated in this article, or claim that may be made by its manufacturer, is not guaranteed or endorsed by the publisher.

References

He, J., Qiu, H., Qu, F., Hu, S., Yang, D., Shen, Y., et al. (2021). Prediction of spatiotemporal stability and rainfall threshold of shallow landslides using the TRIGRS and Scoops3D models. *CATENA* 197, 104999. doi:10.1016/j.catena.2020.104999

Liu, Z., Qiu, H., Zhu, Y., Liu, Y., Yang, D., Ma, S., et al. (2022). Efficient identification and monitoring of landslides by time-series InSAR combining single- and multi-look phases. *Remote Sens.* 14, 1026. doi:10.3390/rs14041026

Ma, S., Qiu, H., Zhu, Y., Yang, D., Tang, B., Wang, D., et al. (2023). Topographic changes, surface deformation and movement process before, during and after a rotational landslide. *Remote Sens.* 15, 662. doi:10.3390/rs15030662

Nie, W., Qiu, H., and Asadi, A. (2023). Editorial: Monitoring, early warning, and mitigation of natural and engineered slopes. *Front. Earth Sci.* 10, 1041180. doi:10.3389/feart.2022.1041180

Pei, Y., Qiu, H., Yang, D., Liu, Z., Ma, S., Li, J., et al. (2023). Increasing landslide activity in the Taxkorgan River Basin (eastern Pamirs Plateau, China) driven by climate change. *CATENA* 223, 106911. doi:10.1016/j.catena.2023.106911

Qiu, H., Zhu, Y., Zhou, W., Sun, H., He, J., and Liu, Z. (2022). Influence of DEM resolution on landslide simulation performance based on the Scoops3D model. *Geomatics, Nat. Hazards Risk* 13 (1), 1663–1681. doi:10.1080/19475705.2022.2097451

Qu, F., Qiu, H., Sun, H., and Tang, M. (2021). Post-failure landslide change detection and analysis using optical satellite Sentinel-2 images. *Landslides* 18, 447–455. doi:10.1007/s10346-020-01498-0

Wang, L., Qiu, H., Zhou, W., Zhu, Y., Liu, Z., Ma, S., et al. (2022). The post-failure spatiotemporal deformation of certain translational landslides may follow the pre-failure pattern. *Remote Sens.* 14, 2333. doi:10.3390/rs14102333

Yang, D., Qiu, H., Ma, S., Liu, Z., Du, C., Zhu, Y., et al. (2022). Slow surface subsidence and its impact on shallow loess landslides in a coal mining area. *CATENA* 209, 105830. doi:10.1016/j.catena.2021.105830

Zhou, W., Qiu, H., Wang, L., Pei, Y., Tang, B., Ma, S., et al. (2022). Combining rainfall-induced shallow landslides and subsequent debris flows for hazard chain prediction. *CATENA* 213, 106199. doi:10.1016/j.catena.2022.106199

Zhu, Y., Qiu, H., Yang, D., Liu, Z., Ma, S., Pei, Y., et al. (2021). Pre- and post-failure spatiotemporal evolution of loess landslides: A case study of the jiangou landslide in ledu, China. *Landslides* 18 (10), 3475–3484. doi:10.1007/s10346-021-01714-5

frontiers | Frontiers in Earth Science

TYPE Original Research
PUBLISHED 16 August 2022
DOI 10.3389/feart.2022.991776

OPEN ACCESS

EDITED BY
Haijun Qiu,
Northwest University, China

REVIEWED BY
Wu Pengfei,
Taiyuan University of Technology, China
Xingqian Xu,
Yunnan agriculture university, China

*CORRESPONDENCE
Jian Liu,
5102135@163.com

SPECIALTY SECTION
This article was submitted to Geohazards and Georisks, a section of the journal Frontiers in Earth Science

RECEIVED 12 July 2022
ACCEPTED 19 July 2022
PUBLISHED 16 August 2022

CITATION
Liu J, Guan Y, Shao Z and Wang H (2022), Mechanical effect of clay under the acid-base action: A case study on montmorillonite and illite.
Front. Earth Sci. 10:991776.
doi: 10.3389/feart.2022.991776

Mechanical effect of clay under the acid-base action: A case study on montmorillonite and illite

Jian Liu[1,2]*, Yurong Guan[1], Zhenbao Shao[1] and Huihao Wang[1]

[1]School of Geosciences and Engineering, Hebei University of Engineering, Handan, China, [2]Institute of Mountain Hazards and Environment, CAS, Chengdu, China

To study the mechanical effect of clay under acidic and basic conditions, typical clay minerals, montmorillonite and illite, were taken as the main research objects in this study. The variation law and mechanism of the cohesive force and internal friction angle were studied by immersing the remoulded soil in HNO_3 solution with pH = 3 and NaOH (alkaline waste liquid) with pH = 13.5, respectively. It was found that, under acidic conditions, a corrosion reaction between clay minerals and nitric acid occurred. Except for the medium-term, the cohesion generally shows a decreasing trend, and the internal friction angle has little change. Under alkaline conditions, the cohesion of montmorillonite-quartz sand remoulded soil decreased briefly in the early immersion stage of and increased in the middle and late stages. The internal friction angle increases steadily with the extension of immersion time. The cohesion of illite-quartz sand remoulded soil also decreased first and then increased, while the internal friction angle changed little. X-ray diffraction analysis shows that montmorillonite and illite will corrode under acidic conditions, and no new material will be generated, resulting in a decrease in soil cohesion. Under alkaline conditions, montmorillonite was seriously depleted, resulting in the formation of zeolite minerals (zeolite X, garronite) and new cement hydrated calcium silicate CSH (xonotlite). Strong alkali reacts with illite to generate sodium metaaluminate ($NaAlO_2$) and liquid cement Na_2SiO_3 (sodium silicate). The formation of new cements is the main reason for the increase in cohesion under acid-base conditions, and chemical corrosion and ion exchange cause a decrease in cohesion.

KEYWORDS

water-soil chemical interaction, acid-base action, montmorillonite, illite, mechanical effect

1 Introduction

Water is the key factor in soil landslides. Statistics show that water is the main inducing factor for more than 90% of landslide events (Yan et al., 2013; Xu and Liu, 2019; Zhu and Zhang, 2019). The chemical interaction between water and soil plays an important role in the breeding process of soil landslides. Especially in recent years,

environmental problems such as acid rain and alkaline waste discharge caused by the rapid development of industry and agriculture have occurred frequently. These chemically active aqueous solutions contact the soil, which will inevitably have a water–soil chemical interaction and a profound impact on the mechanical properties of the soil.

The influence of soil–water chemistry on soil mechanical properties is long-term and complex. As early as the 1980s, Gu (1981; 1984; 1984; 1988) carried out related research on the uneven settlement of an alkali recovery workshop in a paper mill in Fujian and the erosion hole of a wall foundation in a glucose workshop in Shanghai. Through field sampling, immersion tests and indoor analysis and identification, it was confirmed that the decrease in soil strength caused by acid and alkali waste liquid erosion was the main reason for the above events. Subsequently, the soil–water chemical mechanical effect quickly attracted the attention of researchers, and a series of related experimental studies were carried out to explore the trends of changes in the properties of soil under different aqueous chemical environments. For example, Tiwari et al., 2005 studied the effect of pore water salinity on the residual shear strength of soil and found that high concentrations of sodium chloride and calcium chloride aqueous solution had an obvious weakening effect on the strength of soil. Zhao et al. (2007; 2009; 2011) analysed the mineral composition and structure of the sliding surface and studied the influence of soil shear strength variation on landslide formation under acid rain through laboratory tests. Wang et al. (2010) took the subgrade of the Wuhan-Guangzhou high-speed railway as the test background, tested water samples and soil samples at different mileages, analysed the influence of solution chemical properties on the shear strength parameters of soil, and found that ion mass concentration had a strong correlation with cohesion. Gratchev and Towhata (2010; 2013) studied the effect of acid solution on undisturbed soil. The cement calcium carbonate ($CaCO_3$) in the soil corroded in acid, resulting in a decrease in soil cohesion and an increase in compressibility. Yu et al. (2019) also used different concentrations of NaCl solution to soak clay remoulded soil samples and obtained similar results. He et al. (2020) explored the influence of water–soil chemical processes on the stability of loess slope landslides under the action of acid rain. The leaching test showed that, under acidic conditions, H^+ promoted the corrosion of carbonate rocks and made the soil stability worse. In addition, some researchers conducted a series of studies on slope stability under the effect of rainfall by obtaining landslide deformation data and established a coupling model of soil–water interactions and landslide deformation, which provided a basis for predicting natural disasters such as landslides induced by rainfall infiltration (Ma et al., 2021; Liu et al., 2022; Yang et al., 2022; Zhou et al., 2022). In summary, although previous studies have carried out a great deal of work on the influence of water–soil chemical interactions on soil strength, it is difficult to clarify the mechanism of the water–soil chemical mechanical effect due to the complexity of the soil mineral composition. As the main secondary mineral, clay minerals have complex physical and chemical interactions with water, which have a great influence on the mechanical properties of soil. However, few people have carried out systematic studies on the mechanical effect and mechanism of clay under water–soil chemical interactions.

Cohesion and internal friction angle are important indicators for evaluating the stability of soil slopes. To explore the water–soil chemical mechanical effect of clay, in this paper, the typical clay minerals montmorillonite and illite were taken as the cement to make up montmorillonite-quartz sand remoulded soil and illite-quartz sand remoulded soil. The variation laws and mechanisms of cohesion and internal friction angle of soil under the action of acid rain and alkaline waste liquid were systematically studied, which not only provide a theoretical basis for revealing the breeding mechanism of soil landslides but also have important practical significance for the early warning and prevention of soil landslides.

2 Materials and methods

2.1 Test materials

In this study, the basic parameters of montmorillonite and illite samples are selected as shown in Table 1. The purity of the montmorillonite sample was 97%, and the chemical formula was $Ca_{0.2}(Al,Mg)_2SiO_{10}(OH)_{2.4}H_2O$, belonging to calcium montmorillonite. Due to the difficulty in the purification of illite, the purity of illite samples used in this study was low, 88.46%. In addition to illite, the samples also contained impurities such as quartz and mica. By X-ray diffraction (XRD) analysis, the chemical formula of illite in the sample was $(K,H_3O)Al_2Si_3AlO_{10}(OH)_2$, which is a potassium-based illite. The average particle size of the quartz sand used in the experiment is approximately 192.59 μm, the silicon content is more than 99.5%, and the hardness is 7.8, which meets the experimental requirements.

In terms of aqueous solution, concentrated nitric acid (mass fraction: 66.5%) and NaOH (mass fraction: 96%) of analytical purity were used in this study. HNO_3 solution with pH = 3 and NaOH solution with pH = 13.5 were prepared to simulate acid rain and alkaline waste liquid, respectively. The mechanical parameters of the remoulded soil and the physical-chemical parameters of the solution under the action of acid and alkali were studied through immersion tests.

2.2 Experimental design

In this study, the density of the remoulded soil is 2.0 g/cm^3 (clay ρ = 1.8–2.0 g/cm^3 (Gong et al., 1996)), and the clay mineral content is 10% (when the clay mineral content reaches 5%, the strength of the soil can be significantly affected (Yong et al., 1984), and 10% content should be sufficient to reflect its

TABLE 1 Basic parameters of clay mineral samples.

Clay Mineral	Mineral Chemical Formula	Sample Purity (%)	Mean Diameter /μm	Density /g cm^{-3}
Montmorillonite	$Ca_{0.2}(Al,Mg)_2SiO_{10}(OH)_2.4H_2O$	97	21.31	2.3
Illite	$(K,H_3O)Al_2Si_3AlO_{10}(OH)_2$	88.46	45	2.79

mechanical effect). The preparation process of the remoulded soil was as follows: clay minerals (montmorillonite or illite) and quartz sand were fully mixed on the test bench first, a certain amount of chemical solution (HNO_3 solution at pH = 3 or NaOH solution at pH = 13.5) was added, and the mixture was fully mixed again. After reaching the control moisture content (17.65%) throughout the sample, 120 g of wet soil sample was weighed and compacted in the 60 cm^3 cutting ring (Φ61.8 × 20 mm). Five remoulded soil samples were placed in a 2 L large-calibre beaker with a cutting ring (five remoulded soil samples were Group 1). The soil samples were separated by permeable stone, injected with 1.8 L of the corresponding chemical solution and sealed with fresh-keeping film. The soil samples were placed in a biochemical incubator at constant temperature (20°C) for a certain time (1, 3, 5, 10 days, 15 days). The pH and conductivity of the solution were measured, and the direct shear test (fast shear) was immediately performed on the remoulded soil samples to measure the cohesion and internal friction angle.

3 Results

3.1 Variations in the solution parameters and mechanical parameters of montmorillonite-quartz sand remoulded soil

3.1.1 Variations in HNO_3 solution parameters and cohesion of montmorillonite-quartz sand remoulded soil

Acid rain is a serious environmental problem caused by fossil fuel combustion and automobile exhaust emissions. In recent years, with the adjustment of energy resources and the development of transportation, the type of acid rain has gradually changed from the sulfuric acid type to the mixed type and nitric acid type, and the acidity has shown an increasing trend (Zhang et al., 2010; Qiao et al., 2017). The pH of acid rain in some areas is even less than 3, and the minimum is approximately 2.8 (Sun et al., 1994). To explore the influence of acid rain on the mechanical properties of clay exposed to environmental pollution, HNO_3 solution with pH = 3 was selected for the immersion test in this study. The variations under acidic conditions are shown in Figure 1.

Under acidic conditions, the pH values were 3.51, 3.7, 3.73, 4.73 and 5.51 after soaking for 1, 3, 5, 10 and 15 days, respectively; the variation values of conductivity were -190, -242.9, -258, -307.7 and -305.5 μS/cm, respectively. With the extension of soaking time, the pH of the soaking solution showed an increasing trend and finally reached a nearly neutral value. The conductivity EC showed an overall decrease, and gradually slowed down in the later stage. Quartz sand was resistant to corrosion, and only montmorillonite could react with nitric acid, which consumed H^+ in the solution and generated corresponding nitrates. At the same concentration, the conductivity of salt solution was usually weaker than the one of corresponding strong acid. So, with the reaction, the conductivity gradually decreased and finally stabilized, indicating that the reaction reached equilibrium.

It can be seen from Figure 1C the cohesion of montmorillonite remoulded soil under acid conditions shows a trend of first decreasing, then increasing and then decreasing. When soaked for 10ays–15 days, the cohesion decreased from 33.84 kPa to 22.31 kPa, which was lower than the cohesion value at the initial stage of soaking. Overall, except for the middle point (10 days), the cohesion decreased generally. However, after many repeated tests, the phenomenon of cohesion increase in the middle stage always exists and cannot be ignored.

3.1.2 Variations in NaOH solution parameters and cohesion of montmorillonite-quartz sand remoulded soil

The alkaline waste liquid produced in the process of industrial production in China is mostly discharged from paper mills, with pH as high as 12.94 (Gu, 1988) and strong alkalinity. In addition, the pH value of highly alkaline pore water formed during the operation of the nuclear waste repository is usually greater than 13, up to 13.5 (Ramirez, 2002), and the solutes are mainly NaOH and KOH (Berner, 1992). Direct contact between these alkaline waste liquids and soil will also cause changes in soil mechanical properties. In this study, NaOH solution with pH = 13.5 was used for the immersion test. The variations in the solution parameters and cohesion of montmorillonite-quartz sand remoulded soil are shown in Figure 2.

Under alkaline conditions, the pH and conductivity of the solution showed an overall decreasing trend, indicating that montmorillonite reacted with a strong alkali and consumed OH^- in the solution. At the initial stage of the reaction, the pH and electrical conductivity decreased significantly. From

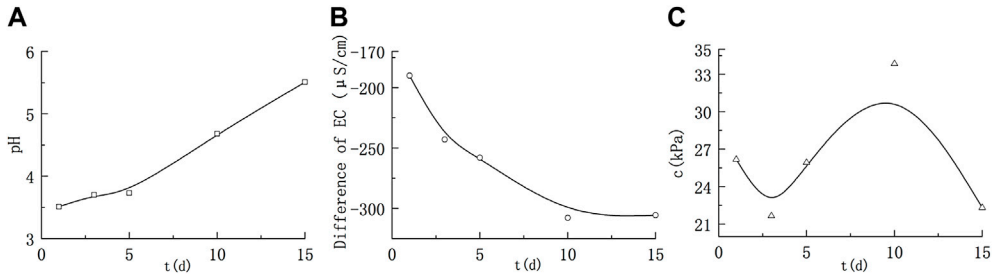

FIGURE 1
Variations in the solution parameters and cohesion of montmorillonite remoulded soil under acidic conditions. **(A)** Variation of pH; **(B)** Variation of electrical conductivity; **(C)** Variation of cohesion.

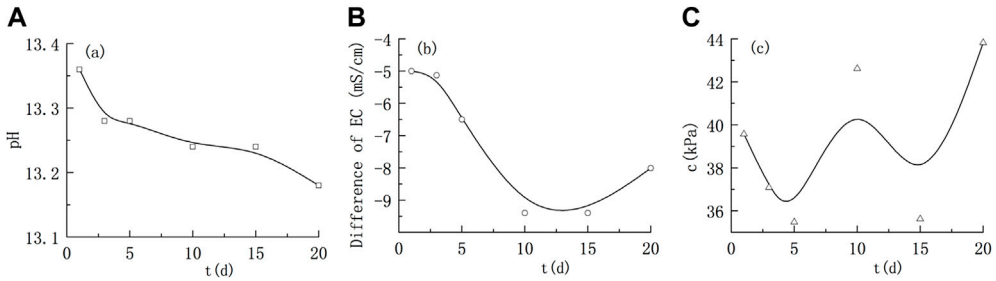

FIGURE 2
Variations in the solution parameters and cohesion of montmorillonite remoulded soil under alkaline conditions. **(A)** Variation of pH; **(B)** Characteristics of electrical conductivity; **(C)** Variation of cohesion.

1 d to 5 days, the pH and electrical conductivity changed from 13.36 and -5.0 mS/cm to 13.28 and -6.55 mS/cm, respectively. After 10 days, the pH decreased slowly, while the electrical conductivity rebounded. Finally, the pH value was 13.18, and the electrical conductivity changed to 8.01 mS/cm after 20 days.

Figure 2C shows that, under alkaline conditions, the cohesive force of montmorillonite-quartz sand remoulded soil showed an overall trend of first decreasing and then increasing. The cohesive force decreased briefly in the early stage of immersion (1 d–5 days), although the cohesive force fluctuated in the middle and late stages of immersion, it generally showed an increasing trend.

3.2 Variations in solution parameters and mechanical parameters of illite-quartz sand remoulded soil

3.2.1 Variations in hno_3 solution parameters and cohesion of illite-quartz sand remoulded soil

The physical and chemical parameters and cohesion value under acidic conditions are shown in Figure 3. Under acidic conditions, the pH showed an increasing trend, while the conductivity EC decreased, indicating that the chemical reaction between illite and strong acid HNO_3 consumed H^+ in the solution and generated the corresponding nitrate. Under the same concentration conditions, the salt conductivity is usually weaker than the corresponding strong acid conductivity, so the overall conductivity decreased. At the same time, of the above changes in pH and conductivity, the cohesion value showed the characteristics of first decreasing, then increasing and then decreasing. Under acidic conditions, the cohesion of illite remoulded soil increased in the middle stage, which was similar to that of montmorillonite remoulded soil. In general, except for the middle stage of immersion, the cohesion showed a decline.

3.2.2 Variations in naoh solution parameters and cohesion of iillite-quartz sand remoulded soil

Under alkaline conditions (Figure 4), the pH was generally decreased, indicating that illite reacted with the strong alkali and consumed OH^-. However, with the progress of the reaction, the pH rebounded slowly. After 10 days of reaction, the pH range was stable at 12.81–12.83, indicating that alkaline substances were

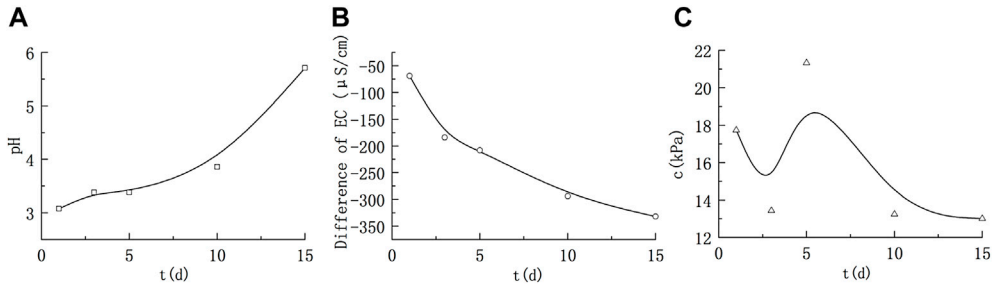

FIGURE 3
Variations in the solution parameters and cohesion of illite remoulded soil under acidic conditions. **(A)** Variation of pH; **(B)** Variation of electrical conductivity; **(C)** Variation of cohesion.

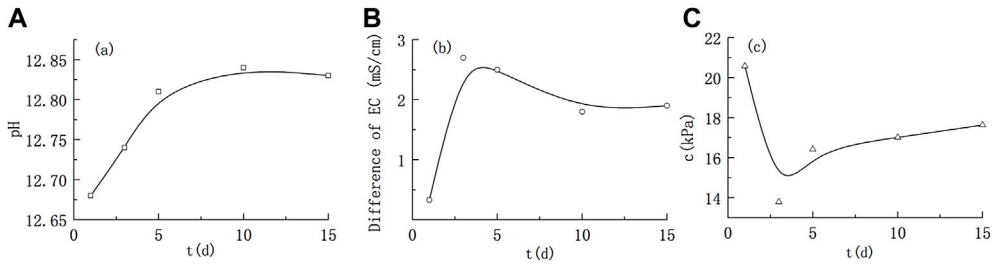

FIGURE 4
Variations in the solution parameters and cohesion of illite remoulded soil under alkaline conditions. **(A)** Variation of pH; **(B)** Variation of electrical conductivity; **(C)** Variation of cohesion.

generated in the reaction, and the pH gradually increased with the increase in alkaline substances. The overall electrical conductivity showed an increasing trend, indicating that the reaction generated soluble substances with strong conductivity, which increased the ion concentration of solution, such as K^+ between illite layers.

The cohesion of illite-quartz sand remoulded soil showed a trend of decreasing first and then increasing. On the 5th day of reaction, the cohesion entered a stage of slow increase, and the later change gradually stabilized, with the range of cohesion values ranging from 16.42 to 17.63 kPa.

3.3 Variation characteristics of the internal friction angle under acid-base conditions

The change in the internal friction angle of montmorillonite-quartz sand remoulded soil and illite-quartz sand remoulded soil under acid and alkali conditions is shown in Table 2. Whether under acidic or alkaline conditions, the internal friction angle of illite-quartz sand remoulded soil showed little change. For montmorillonite-quartz sand remoulded soil, the internal friction angle remained basically unchanged under acidic conditions, while the internal friction angle increased steadily as the immersion time was prolonged under alkaline conditions.

On the basis of the aforementioned changes in cohesion and internal friction angle, considering that the vertical pressure provided by the soil landslide is small (the thickness of the soil landslide is mainly concentrated in the two intervals of 0–5 m and 5–10 m (Qiu et al., 2012), and the density of the landslide soil is 2.0 g/cm^3 (Gong, 1996), the vertical pressure values at thicknesses of 5 m and 10 m are only approximately 0.1 MPa and 0.2 MPa, respectively), the shear strength of illite-rich soil under acid and alkali action is consistent with the change in cohesion. For montmorillonite-rich soil, the change in shear strength is consistent with the change in cohesion under acidic conditions, and the shear strength increases overall under alkaline conditions.

4 Mechanism analysis of cohesion change

Cement is an important source of soil cohesion. In this study, the cement of the remoulded soil is mainly clay

TABLE 2 Variations in the internal friction angle of clay mineral remoulded soil under acid-base conditions.

Soak Condition		Internal Friction angle (°)	
		pH = 3 HNO_3	pH = 13.5 NaOH
Montmorillonite	1d	38.58	35.12
	3d	36.01	33.73
	5d	37.02	40.03
	10d	35.30	41.71
	15d	37.72	43.07
Illite	1d	34.32	31.60
	3d	34.22	35.33
	5d	35.48	34.88
	10d	36.51	38.19
	15d	35.85	33.73

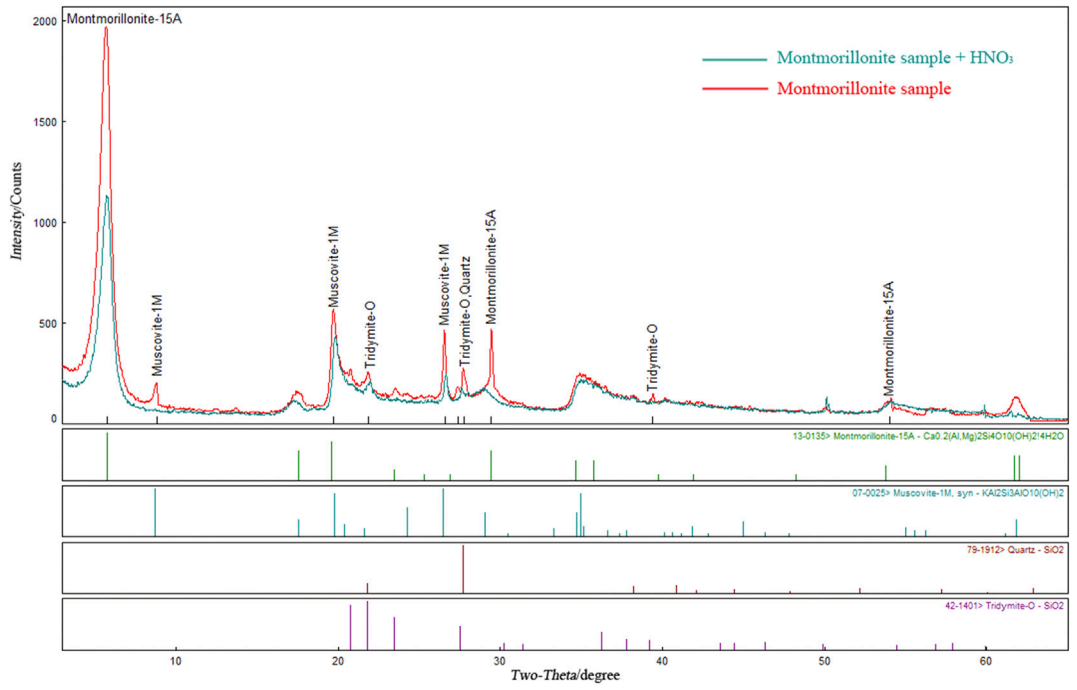

FIGURE 5
Comparison of XRD results of montmorillonite samples before and after immersion in HNO_3 solution.

minerals. Under the action of acid and alkali, the chemical reaction between clay minerals and solution is an important reason for the change in cohesive force of remoulded soil. Therefore, based on the X-ray diffraction (XRD) analysis of the mineral composition changes of montmorillonite and illite samples before and after immersion, this study studied the change mechanism of remoulded soil cohesion under different water–soil chemical interactions, combined with the changes of solution parameters.

4.1 Variation mechanism of cohesion of montmorillonite-quartz sand remoulded soil under acid-base action

4.1.1 Variation mechanism of cohesion of montmorillonite-quartz sand remoulded soil under acidic conditions

The XRD patterns of montmorillonite soaked in pH = 3 HNO_3 and the original samples were superimposed and

analysed. The results are shown in Figure 5. The intensity of the characteristic peaks of montmorillonite minerals changed. The intensity of the characteristic peaks with a diffraction angle of 5.7° decreased greatly from 1990 to 1,204, while the diffraction angles were consistent, which were 5.71° and 5.79° before and after soaking, respectively. The characteristic peak intensity of montmorillonite minerals at approximately 29° also decreased from 495 to 201, and the corresponding angles before and after soaking were 29.47° and 29.06°, respectively, which were consistent. The intensity of the characteristic peaks of other components in the sample did not change significantly, nor did the characteristic peaks of new substances appear. This shows that only montmorillonite minerals have a large degree of loss, and no new substances are generated after the montmorillonite samples reacted with HNO_3. The chemical reactions in this process are shown in Eq. 4-1:

$$Ca_{0.2}(Al,Mg)Si_4O_{10}(OH)_2 \cdot 4H_2O + HNO_3 \rightarrow Ca(NO_3)_2 + Mg(NO_3)_2 + Al(NO_3)_3 + SiO_2 \downarrow + H_2O \quad (4\text{–}1)$$

Based on XRD pattern analysis, combined with the variations of solution parameters and cohesion under acid conditions described in the previous section, it is considered that HNO_3 will corrode and consume montmorillonite, resulting in the cementation being reduced in the sample, which was macroscopically manifested as a decrease in the cohesion of the remoulded soil. However, the increase in cohesion in the middle stage indicated that new cements were generated, which can provide greater cohesion for the soil, while no new material was found in the XRD pattern.

4.1.2 Variation mechanism of cohesion of montmorillonite-quartz sand remoulded soil under alkaline conditions

The XRD pattern of montmorillonite soaked in pH = 13.5 NaOH solution was superimposed with the original pattern of montmorillonite, and the results are shown in Figure 6. Compared with the XRD pattern of the original sample, the XRD pattern of the soaked samples changed significantly. The characteristic peak of montmorillonite minerals at approximately 5.7° shifted from 5.71° to 6.53°, and the intensity of the characteristic peak decreased sharply from 1990 to 519. The conversion from calcium montmorillonite ($Ca_{0.2}(Al,Mg)_2SiO_{10}(OH)_2.4H_2O$) to sodium montmorillonite ($Na_{0.3}(Al,Mg)_2Si_4O_{10}(OH)_2{\cdot}4H_2O$) indicates that Ca^{2+} in the montmorillonite structural layer was replaced by Na^+ in the NaOH solution. The characteristic peak intensity of montmorillonite minerals at approximately 29° decreased from 495 to 204, and the corresponding angles before and after soaking were 29.47° and 29.42°, respectively, which were consistent. In addition, there are new characteristic peaks in the XRD patterns of the soaked montmorillonite samples. Comparative interpretation of the diffraction card database (PDF2) demonstrates that these new substances are mainly zeolite minerals (zeolite X, garronite) and calcium silicate hydrate CSH (xonotlite). Among these, calcium silicate hydrate CSH is a common cement in industrial cement, which includes ionic compounds connected with each other by chemical bonds; its bond strength is much larger than the van der Waals force between the montmorillonite layers.

Combined with the XRD analysis results, the reaction process mainly includes the following steps:

1) Ion exchange shown in eqs. 4–2 and 4–3:

$$Montmorillonite - Ca^{2+} + 2Na^+ \Leftrightarrow Montmorillonite - 2Na^+ + Ca^{2+} \quad (4\text{–}2)$$

$$Ca^{2+} + 2OH^- = Ca(OH)_2 \quad (4\text{–}3)$$

2) The main components of montmorillonite minerals, silicon (SiO_2) and aluminium ($Al(OH)_3$), react with $Ca(OH)_2$ by the chemical reactions shown in Eqs 4–4 and 4–5:

$$Ca(OH)_2 + SiO_2 = CaSiO_3 + H_2O \quad (4\text{–}4)$$

$$Ca(OH)_2 + 2Al(OH)_3 = Ca(AlO_2)_2 + 4H_2O \quad (4\text{–}5)$$

3) The formation of zeolite minerals and hydrated calcium silicate CSH

Calcium silicate $CaSiO_3$ and calcium metaaluminate $Ca(AlO_2)_2$ further reacted to form aluminium-rich silicate mineral-zeolite minerals with higher Al/Si (atomic ratio of 0.5) than montmorillonite minerals (the Al/Si atomic ratios of zeolite X and garronite were 1.0 and 0.6, respectively). The residual Si atoms are retained in the form of cement hydrated calcium silicate CSH (xonotlite), which provides new and greater cohesion for the remoulded soil.

Combined with the variation in pH and EC, the change mechanism of the cohesive force of montmorillonite-quartz sand remoulded soil under alkaline conditions is analysed as follows:

1) At the beginning of the reaction, the strong alkali solution will corrode clay minerals so that the montmorillonite content in remoulded soil is greatly decreased, resulting in a decrease in cohesion. The montmorillonite denaturation (that is, from calcium montmorillonite to sodium montmorillonite) caused

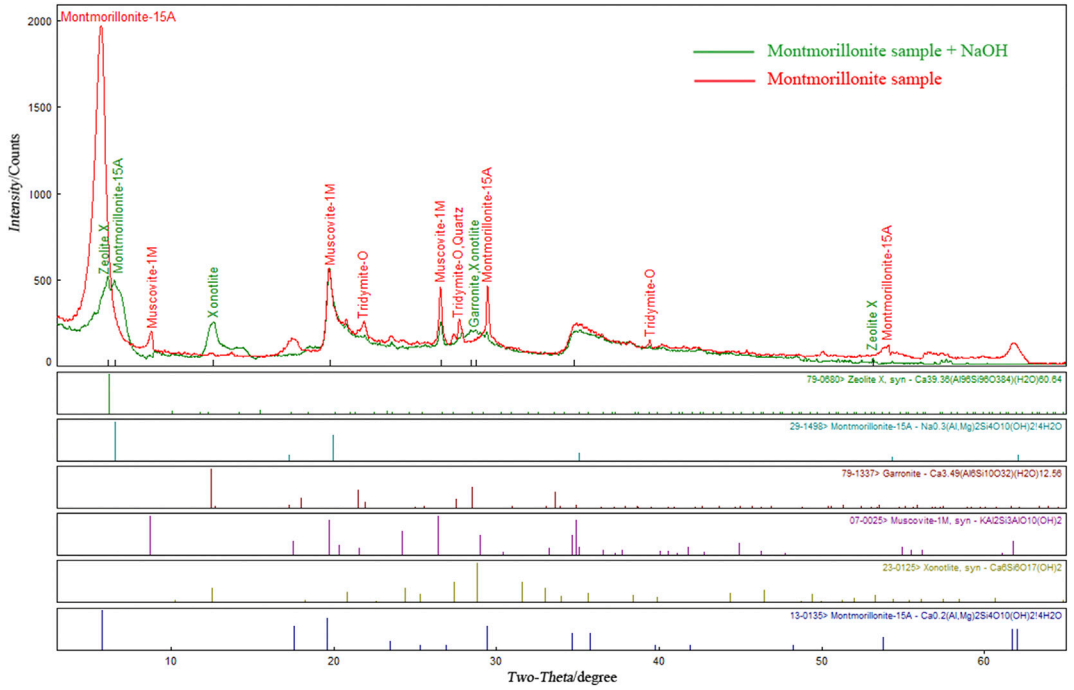

FIGURE 6
Comparison of XRD results of montmorillonite samples before and after immersion in NaOH solution.

by ion exchange also plays a certain role in promoting the process.

2) The strong alkali reacts with montmorillonite to form a new cement hydrated calcium silicate CSH. Since CSH is connected by chemical bonds, with the increase in CSH production, the cohesion of remoulded soil stops decreasing and increases.
3) The pH value remained essentially unchanged in the middle and late stages, indicating that the reaction between the strong alkali solution and montmorillonite was largely complete. This may be due to the attachment of calcium silicate hydrate CSH and zeolite minerals to the surface of the montmorillonite, which blocked the contact between the strong alkali solution and montmorillonite. However, this does not affect the ion exchange between the high-valence exchangeable cation Ca^{2+} between the montmorillonite layers and the low-valence Na+ in the solution, resulting in an increase in the thickness of the dielectric layer of montmorillonite minerals, a decrease in the force between layers, and ultimately a decrease in cohesion.
4) The solubility of $Ca(OH)_2$ is low. With the continuous exchange action, the concentration of $Ca(OH)_2$ in the soil solution reaches saturation and precipitates. Since the precipitation of $Ca(OH)_2$ involves ionic compounds, the cohesion rebounds in the later stage of immersion.

4.2 Variation mechanism of cohesion of lllite-quartz sand remoulded soil under acid-base action

4.2.1 Variation mechanism of cohesion of illite-quartz sand remoulded soil under acidic conditions

The illite samples soaked in pH = 3 HNO_3 for some period of time were tested by XRD, and the patterns were superimposed and analysed with the original illite. The results are shown in Figure 7.

Figure 7 shows that, after the sample was soaked in pH = 3 HNO_3, the intensity of the characteristic peaks of illite minerals at a diffraction angle of approximately 9° decreased significantly from 155.60×10^3 to 132.97×10^3, and the corresponding angles of the characteristic peaks before and after soaking were 8.9° and 8.98°, respectively, which were consistent. The characteristic peak intensity of illite minerals at approximately 17.8° also decreased from 61.56×10^3 to 50.63×10^3, and the corresponding angles before and after soaking were 17.78° and 17.86°, respectively, which were also consistent. There is no obvious change in the intensity of characteristic peaks of other components in the sample, and there is no formation of characteristic peaks of new substances. This indicates that only illite has a large degree of loss after interacting with HNO_3, and no new substance is

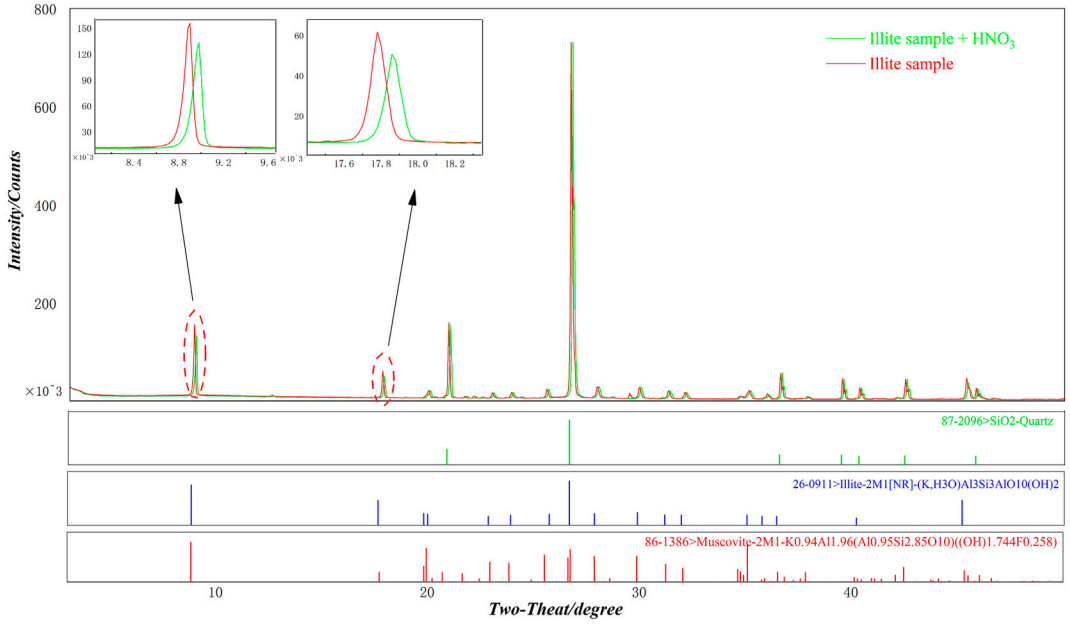

FIGURE 7
Comparison of XRD results of illite samples before and after immersion in HNO_3 solution.

generated. Combined with the chemical formula of illite, the chemical reaction involved in this process is as follows (4–6):

$$(K,H_3O)Al_2Si_3AlO_{10}(OH)_2 + HNO_3 \rightarrow KNO_3 + Al(NO_3)_3 + SiO_2 \downarrow + H_2O \quad (4\text{–}6)$$

Considering the changes in pH and conductivity EC of the acid solution, it can be considered that HNO_3 corroded illite, which reduced the content of illite in the sample and led to a decrease in cohesion of the remoulded soil. The cohesion increased firstly and then decreased after the first decline. This growth process suggests the presence of substances that provide greater cohesion, but the XRD pattern shows that no new substances were generated. The phenomenon of increased cohesion in the middle stage has appeared more than once in this study, and its mechanism is still unclear.

4.2.2 Variation mechanism of cohesion of illite-quartz sand remoulded soil under alkaline conditions

The XRD pattern of the illite sample soaked in pH = 13.5 NaOH solution was superimposed with that of the original illite sample, and the results are shown in Figure 8.

Compared with the original illite sample, the map of the illite sample soaked in strong alkali changed to a certain extent, mainly showing a decrease in the intensity of various mineral characteristic peaks, but no new material characteristic peaks were generated. Figure 8 shows that, after soaking in pH = 13.5 NaOH solution, the intensity of the characteristic peaks of illite minerals at diffraction angles of approximately 9° and 17.8° decreased to 151.77×10^3 and 58.26×10^3, and the corresponding angles of the characteristic peaks after soaking were 9.0° and 17.9°, respectively, which were consistent. In addition, the intensity of the characteristic peaks corresponding to quartz in the sample also changed significantly, the intensity of the characteristic peaks at a diffraction angle of approximately 27° decreased significantly from 731.41×10^3 to 659.10×10^3, and the corresponding angles of the characteristic peaks before and after soaking were 26.68° and 26.8°, respectively, which were consistent. The characteristic peak intensity of quartz at approximately 21° also decreased from 159.86×10^3 to 150.92×10^3, and the corresponding angles before and after soaking were 20.9° and 21.02°, respectively, which were also consistent.

This indicates that illite and quartz in the sample were both depleted after reaction with strong alkali, especially quartz, but no new solid material was generated. The chemical reaction of quartz and the main components of illite minerals (silica (SiO_2) and aluminium ($Al(OH)_3$)) with NaOH are shown in Eqs. 4–7 and 4–8:

$$2NaOH + SiO_2 = Na_2SiO_3 + H_2O \quad (4\text{–}7)$$

$$NaOH + Al(OH)_3 = NaAlO_2 + 2H_2O \quad (4\text{–}8)$$

Sodium silicate (Na_2SiO_3) and sodium metaaluminate ($NaAlO_2$) are strong alkaline and weak acid salts, respectively.

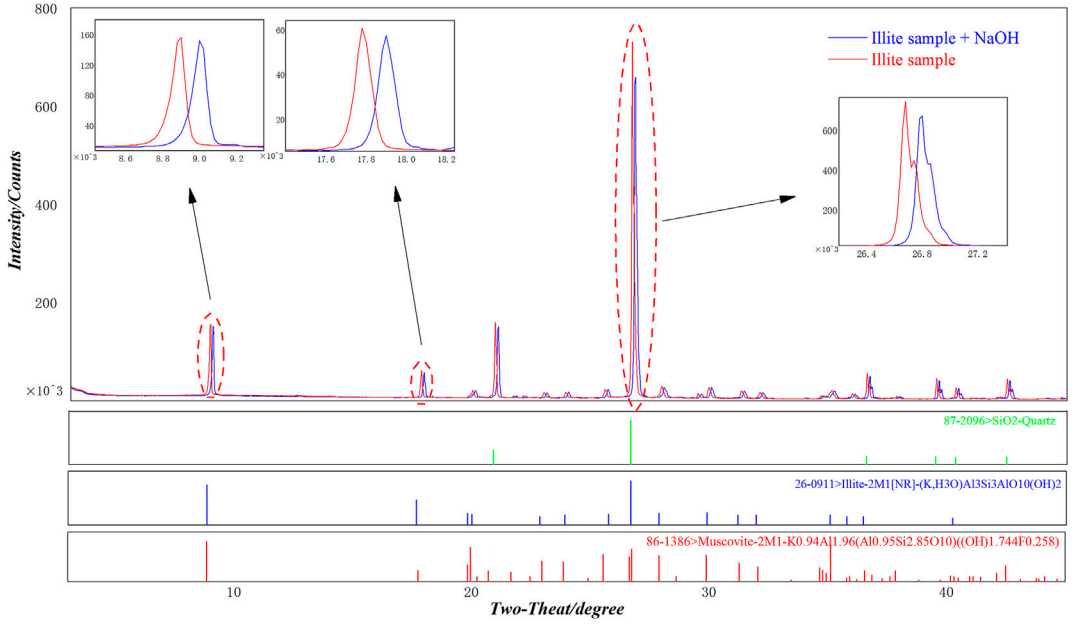

FIGURE 8
Comparison of XRD results of illite before and after immersion in NaOH solution.

During the reaction, the amount of production increases gradually, resulting in a slow recovery of pH. At the same time, since the above two products are soluble in water, they were not found in the XRD pattern of the samples after washing, filtering and drying. Combined with the above variations in pH and conductivity EC, it can be considered that NaOH corroded illite at the initial stage, which reduced the content of illite in the remoulded soil, so the cohesion fell. In addition, Na_2SiO_3 generated by the reaction of strong alkali with illite, also known as sodium silicate, has a certain degree of adhesion. As the amount of Na_2SiO_3 increased, the cohesion of the remodeled soil stopped decreasing and increased instead.

5 Conclusion and discussion

5.1 Conclusion

1) Under acidic conditions, for both montmorillonite-quartz sand remoulded soil and illite-quartz sand remoulded soil, as the reaction proceeded, the pH showed an increasing trend, the conductivity EC decreased overall, and cohesion showed the law of first decreasing, then increasing and then decreasing. On the whole, except for the medium immersion period, the cohesion decreased overall.
2) Under alkaline conditions, for montmorillonite-quartz sand remoulded soil, the cohesion decreased briefly in the early immersion stage and increased in the middle and late stages. The pH and EC showed a decreasing trend and gradually slowed down in the late stage. The cohesive force of illite-quartz sand remoulded soil first decreased and then increased. As the reaction proceeded, the pH value showed a slow upwards trend in the decreasing environment, and the conductivity EC increased overall.
3) Under the action of acid and alkali, the internal friction angle of illite-quartz sand remoulded soil has little overall change, and the change in soil shear strength is consistent with that of cohesion. For montmorillonite-quartz sand remoulded soil, the internal friction angle remains essentially unchanged under acidic conditions, and the change in shear strength is consistent with the change in cohesion. Under alkaline conditions, the internal friction angle increases steadily with the extension of soaking time, and the shear strength increases overall.
4) Under acidic conditions, montmorillonite and illite are corroded, and no new material is generated, resulting in a decrease in soil cohesion. The reason for the increase in cohesion in the middle stage is not clear. Under alkaline conditions, montmorillonite was corroded seriously, resulting in the formation of zeolite minerals (zeolite X, garronite) and new cement hydrated calcium silicate CSH (xonotlite). The strong alkali reacts with illite to form sodium metaaluminate ($NaAlO_2$) and liquid cement Na_2SiO_3 (sodium silicate). The formation of new cements is the main reason for the increase in cohesion under alkaline conditions, and chemical corrosion and ion exchange cause a decrease in cohesion.

Discussion

1) The different effects and mechanisms of acid-base effects on soil cohesion provide a new prevention and control idea for soil landslides. For example, a certain amount of alkali can be applied to greatly improve the cohesion of soil and promote the formation of the internal cementation of the soil slope. Chemical measures can also be combined with structural engineering measures, internal bonding and external anti-sliding, which not only maximize the effect of prevention and control but also avoid disasters caused by engineering failure when the engineering life is exhausted. On the other hand, in areas with severe acid rain, considering the long-term cumulative effects of acid rain on the attenuation of soil cohesion, it is necessary to improve the design parameters of soil slope protection engineering and use an acid rain drainage groove (avoiding contact between acid rain and soil) to reduce the negative impact of acid rain on the stability of the soil slope to realize the full use of protective engineering.
2) The cohesive force of soil is controlled by the amount of cement, and the reduction and generation of cement are restricted by soil–water chemical interactions, which, as a chemical reaction, must follow the chemical reaction kinetics and be controlled by the rate equation of the chemical reaction. Therefore, it is very necessary to carry out the quantitative model research of soil cohesion based on cement and the kinetics of water and soil chemical reaction, so as to realize the quantitative calculation of soil cohesion. This has important practical significance for the stability analysis of soil slopes and the prediction and early warning of soil landslides under the water–soil chemical interaction.

Data availability statement

The original contributions presented in the study are included in the article/Supplementary Material, further inquiries can be directed to the corresponding author.

Author contributions

JL is the first author and corresponding author, is responsible for directing the experiments and paper writing. YG is the second author and is responsible for the processing of experimental data. ZS is the third author and is responsible for the production of figures and tables. HW is the fourth author and is responsible for checking the structure of this paper.

Funding

This work was supported by the Natural Science Foundation of Hebei Province, China (Grant No. E2019402361, E2020402075), Natural Science Foundation of Shanxi Province, China (Grant No. 201901D211549), Hebei Provincial Key Research Projects, China (Grant No. 21374104D), Science and Technology Research Projects of Higher Education Institutions in Hebei Province, China (Grant No. ZD2021309), Postdoctoral Research Projects of Hebei Province, China (Grant No. B2020003010), Innovation Fund Project of Hebei University of Engineering (Grant No. BSJJ 1930, BSHJJ 1904).

Conflict of interest

The author declares that the research was conducted in the absence of any commercial or financial relationships that could be construed as a potential conflict of interest.

Publisher's note

References

Berner, U. (1992). Evolution of pore water chemistry during degradation of cement in a radioactive waste repository environment. *Waste Manag.* 12 (2), 201–219. doi:10.1016/0956-053X(92)90049-O

Gong, X. N. (1996). *Higher soil mechanics*. Hangzhou: Zhejiang University Press.

Gratchev, I., and Towhata, I. (2011). Compressibility of natural soils subjected to long-term acidic contamination. *Environ. Earth Sci.* 64 (1), 193–200. doi:10.1007/s12665-010.0838-2

Gratchev, I., and Towhata, I. (2013). Stress-strain characteristics of two natural soils subjected to long-term acidic contamination. *Soils Found.* 53 (3), 469–476. doi:10.1016/j.sandf.2013.04.008

Gu, J. W. (1981). Effect of waste alkali pollution on soil strength. *Shanghai Geol.* 03, 10–14.

Gu, J. W. (1984). Influence of acid-base waste water pollution on engineering properties of clay. *Shanghai Geol.* 02, 42.

Gu, J. W. (1988). The influence of acid-base waste liquid erosion on foundation soil on engineering quality. *J. Geotechnical Eng.* 04, 72–78.

He, C., Shi, T. T., Zeng, W., Lin, G. H., and Lian, Z. P. (2020). Study on the leaching test of the sliding zone soil of huangtupo riverside 1# landslide. *Saf. Environ. Eng.* 04, 53–60. doi:10.13578/j.cnki.issn.1671-1556.2020.04.008

Liu, Y., Qiu, H. J., Yang, D. D., Liu, Z. J., Ma, S. Y., Pei, Y. Q., et al. (2022). Deformation responses of landslides to seasonal rainfall based on InSAR and wavelet analysis. *Landslides* 19 (1), 199–210. doi:10.1007/s10346-021-01785-4

Ma, S., Qiu, H., Hu, S., Dongdong, I., and Liu, Z. J. (2021). Characteristics and geomorphology change detection analysis of the Jiangdingya landslide on July 12, 2018, China. *Landslides* 18 (1), 383–396. doi:10.1007/s10346-020-01530-3

Qiao, X., Du, J., Kota, S. H., Ying, Q., Xiao, W. Y., and Tang, Y. (2017). Wet deposition of sulfur and nitrogen in Jiuzhaigou National Nature Reserve, Sichuan, China during 2015-2016: Possible effects from regional emission reduction and

local tourist activities. *Environ. Pollut.* 233, 267–277. doi:10.1016/j.envpol.2017.08.041

Qiu, H. J. (2012). *Study on the regional landslide characteristic analysis and hazard assessment: A case study of ningqiang countyXi'an*. United States: Northwest University.

Ramirez, S., Cuevas, J., Vigil, R., and Leguey, S. (2002). Hydrothermal alteration of "La Serrata" bentonite (Almeria, Spain) by alkaline solutions. *Appl. Clay Sci.* 21 (5), 257–269. doi:10.1016/S0169-1317(02)00087-X

Sun, C. X., Zhang, J. H., Shu, L. C., and Chen, Y. M. (1994). The influence of acid rain and acid mist on clean insulators' AC flashover performance. *High. Volt. Appar.* 26 (2), 14–18.

Tiwari, B., Tuladhar, G. R., and Marui, H. (2005). Variation in residual shear strength of the soil with the salinity of pore fluid. *J. Geotech. Geoenviron. Eng.* 131, 1456. doi:10.1061/(asce)1090-0241(2005)131:12(1445)

Wang, J., Cao, P., Zhao, Y. L., and Chai, H. B. (2010). Influence of chemical action of water-soil on soil shear strength. *J. Central South Univ. Sci. Technol.* 41 (1), 245–250.

Xu, H., and Liu, H. Z. (2019). Multi-scale rainfall characteristics of rainfall-induced landslides. *Mt. Res.* 037 (6), 858–867. doi:10.16089/j.cnki.1008-2786.000476

Yan, R. M., Teng, W. F., and Yan, R. X. (2013). Research on shear strength properties and microstructure of sliding soil in landslides under water-soil interaction. *Yangtze River* 44 (22), 82–55. doi:10.16232/j.cnki.1001-4179.2013.22.002

Yang, D. D., Qiu, H. J., Ma, S. Y., Liu, Z. J., Du, C., Zhu, Y. R., et al. (2022). Slow surface subsidence and its impact on shallow loess landslides in a coal mining area. *Catena* 209, 105830. doi:10.1016/j.catena.2021.105830

Yong, R. N., Sadana, M. L., and Gohl, W. B. (1984). "Compositional control on swelling behaviour of an expansive soil," in Proceedings of the fifth international conference on expansive soils, Australia, 21-23 May 1984. (Vermont: ARRB Group Limited).

Yu, H. H., and Sun, D. A. (2019). Shear strength of weakly expansive soils in differernt solution. *Chin. J. Undergr. Space Eng.* 15 (2), 423–427.

Zhang, X. M., Chai, F. H., Wang, S. L., Sun, X. Z., and Han, M. (2010). Research progress of acid precipitation in China. *Res. Environ. Sci.* 3 (5), 527–532. doi:10.13198/j.res.2010.05.3.zhangxm.005

Zhao, Y., Cui, P., Hu, L. B., and Hueckel, T. (2007). "First north American landslide conference, landslides and society: Integrated science," in Evolution of shear strength of clayey soils in a landslide due to acid rain: a case study in the area of Three Gorges, China. Landslide Conference, June 3-8, 200 7 (Colorado USA: Vail), 1656–1666.

Zhao, Y., Cui, P., and Hu, L. B. (2009). Relation between evolution of clay shear strength and landslide induced by acid rain: Taking landslides in Three Gorges reservoir area for example. *Chin. J. Rock Mech. Eng.* 28 (3), 576–582. doi:10.3321/j.issn:1000-6915.2009.03.017

Zhao, Y., Cui, P., Hu, L. B., and Tomasz, H. (2011). Multi-scale chemo-mechanical analysis of the slip surface of landslides in the Three Gorges, China. *Sci. China Technol. Sci.* 54 (7), 1757–1765. doi:10.1007/s11431-011-4370-8

Zhou, W. Q., Qiu, H. J., Wang, L. Y., Pei, Y. Q., Tang, B. Z., Ma, S. Y., et al. (2022). Combining rainfall-induced shallow landslides and subsequent debris flows for hazard chain prediction. *Catena* 213, 106199. doi:10.1016/j.catena.2022.106199

Zhu, X. X., and Zhang, L. (2019). Characteristics of rainfall-induced loess landslides and threshold rainfall in Lanzhou. *Chin. J. Geol. Hazard Control.*4, 24–31. doi:10.16031/j.cnki.issn.1003-8035.2019.04.04

frontiers | Frontiers in Earth Science

TYPE Original Research
PUBLISHED 17 August 2022
DOI 10.3389/feart.2022.989488

OPEN ACCESS

EDITED BY
Haijun Qiu,
Northwest University, China

REVIEWED BY
Jiangcheng Huang,
Yunnan University Kunming, China
Jun Wang,
Guangzhou Institute of Geography, China

*CORRESPONDENCE
Shun Yang,
yangshun09@foxmail.com

SPECIALTY SECTION
This article was submitted to Geohazards and Georisks, a section of the journal Frontiers in Earth Science

RECEIVED 08 July 2022
ACCEPTED 22 July 2022
PUBLISHED 17 August 2022

CITATION
Yang S, Pan H, She T, Jiao J, Tian Y and Chen K (2022), Land-use evaluation and utilization advice research on debris flow disaster deposit area.
Front. Earth Sci. 10:989488.
doi: 10.3389/feart.2022.989488

Land-use evaluation and utilization advice research on debris flow disaster deposit area

Shun Yang[1,2]*, Huali Pan[3], Tao She[4], Jiaxuan Jiao[1,2], You Tian[4] and Kun Chen[1,2]

[1]School of Emergency Management, Xihua University, Chengdu, China, [2]Sichuan College of Emergency Management, Chengdu, China, [3]Institute of Mountain Hazards and Environment, Chinese Academy of Sciences (CAS), Chengdu, China, [4]Institute of Exploration Technology, Chinese Academy of Geological Sciences (CAGS), Chengdu, China

The upstream Fujiang River are famous for their high mountains and narrow canyons, which results in a conflict of interest between local residents and land use. To make good use of precious land resources is a meaningful work for local people and government. Therefore, field surveys and theoretical analysis were carried out in the upstream Fujiang River to explore the land-use evaluation and utilization advice. Firstly, we analyzed the factors which affect the land use of debris flow depositional area. Secondly, we chose the factors of soil fertility quality, soil particle conservation, and the geological engineering condition to set up the land-use evaluation method. Thirdly, through index classification, we give the planting type, land-use type, construction type respectively, according to grading and assignment value for each factor, we built the debris flow disaster-prone land utilization mode *R* by using an analytical hierarchy process method. Lastly, taking Huangjiaba village as an example, based on the debris flow disaster land-use evaluation method and debris flow hazard evaluation, we identified four land-use scenarios. The results show that the value of the four scenarios is between 1.00 and 4.00, the four scenarios utilization advices are given based on each *R*-value and Huangjiaba natural condition. It also obtained that the developmental tendencies of the debris flow disaster areas appear to deposit recently, the frequency of debris-flow activity is evolving from high to stable, on making good use of debris flow deposit fan's usage is necessary to explore the disaster prone land and avoid disaster loss. Further studies need to systematically consider more factors to evaluate debris flow and disaster-prone land utilization, which can provide a reference for the rural space planning and revitalization for the local government.

KEYWORDS

debris flow, land use evaluation, disaster deposit area, scenario, utilization advice

Introduction

Environmental Earth science constitutes the study of the natural world and its interaction with society (Siegert, 2016). Currently, land, as the carrier of all economic and social activities, appears increasingly scarce with ongoing socioeconomic development. Therefore, more attention has been paid to the remediation of disaster-destroyed land. Debris flows are widely distributed and a frequently occurring hazard in mountainous regions. Due, in part, to its high sand and clay content, huge areas of debris flow cause deposit fans to form before it runs into the main river (Gregoretti et al., 2016). It has been reported in over 70 countries in the world and often causes severe economic losses and human casualties, seriously retarding social and economic development (Imaizumi et al., 2006; Cui et al., 2009; Tecca and Genevois, 2009; Tiranti and Deangeli, 2015; Gregoretti et al., 2016; Hu et al., 2016). Presently, the relationship between the economic supply and social demand for land will further deepen the uncoordinated tension, in particular, the productive capacity of currently available land resources in ecologically fragile areas is likely to decrease, while the possibility of increases in quality or quantity is limited (Cui et al., 2011; He et al., 2018; He et al., 2020).

Currently, several kinds of "hard to use land" have been developed and utilized, such as desert land (Cao et al., 2018), mining wasteland (Liu et al., 2016), Loess land (Wang et al., 2022).) and karst land (Chen et al., 2017). Meanwhile, China faces the problem of accelerating urbanization in mountainous areas and needs to explore the use of new land, which requires further investigation and planning to achieve the rational allocation of new land resources (Liu, 2018). It is noteworthy that rational allocation refers to the land use type and the selection of suitable land types, for instance, flat and safe areas are developed into building land and cultivated land, and steep slope areas are developed into forest or grassland (Liu et al., 2022). In Lhasa River Basin, land suitable for settlement or living is experiencing a shortage of resources, alluvial fans have the potential to alleviate the problem, survey results showed that alluvial fans are important land resources in LRB and may have huge utilization potential (Chen et al., 2021). Abundant debris-flow deposits on land are widely distributed in mountainous areas. Currently, those areas have mainly been developed for crop cultivation, rural village construction, and tourism (Okunishi and Suwa, 2001; Sancho et al., 2008). To some extent, it is necessary for locals in mountainous regions to use those widely-distributed debris flow and disaster-prone landscapes for agricultural and house building because they are the only available lands that are essentially flat. Through statistical and field surveys, those areas appear gently flat and have abundant water supplies, which are the superior land source in mountainous areas, due to their high quality of heat and water condition. These areas offer promising development prospects. Therefore, making good use of debris flow depositional land represents the key method to develop the local economy and change the ecological environment, it can also balance the relationship between human needs and debris flow control.

Previous literature has found that the debris flow disaster-prone land research changed over time and began with a hazard risk evaluation and sedimentation events (Jakob and Hungr, 2005; He et al., 2016), then it shifted to natural protection and land use for damage reduction. Recently, it focused on land use and spatial planning, as He et al. (2018, 2019) analyzed land-use changes and their driving forces in the debris flow active area of Gansu and Yunnan province, China. Minimal attention has been paid to these areas compared to traditional land sources; thus, it is easy to neglect the function of debris flow disaster-prone fans in mountain development and engineering protection. Therefore, there is a need to improve the understanding of the debris flow depositional land. Generally, the debris flow waste fans are often distributed in the gully mouth, which is close to the main river and appears as relatively flat terrain. Therefore, those areas are a land type directly destroyed by debris flow and other geo-hazards (Qiu et al., 2022; Zhou et al., 2022). With field investigation and information queries, we found that local residents are usually undertaking agriculture, village, and road construction in those areas. In recent years, domestic and international scholars focused research related to debris flow deposits, which include the depositional characteristics, land-use classification and sedimentation processes, and the debris flow hazard zoning method (Ibe and Ebe, 2000; Liu et al., 2001; Okunishi and Suwa, 2001; Xu et al., 2001; Wang et al., 2018). Meanwhile, the debris flow disaster deposit area is the combination of a resource and disaster as its development has both positive and negative effects. To increase the economic benefits and decrease the hazardous impact, it is useful to undertake hazard zone research.

This research focuses on a small mountain watershed, exploring the evaluation of land resource utilization caused by debris flow disasters. The Fujaing River, central to this study, is a tributary of the Jialing River. Field survey and data analysis justified the urgency of summarizing the characteristics of the debris flow disaster-prone area in the Fujiang mountainous region. Generally, the debris flow deposit fans are the most important areas for local residents, a premise that has helped to attract much research attention from debris flow scholars. Along with the development of debris flow depositional land, it is helpful to change the ecological environment and support the local economy. Through field surveys and interviews with local residents, we find that many debris flow gullies from the upstream areas of the Fujiang River have frequently broken out as debris flows after the Wenchuan earthquake. Every gully could form debris flows during heavy rainfall in the rainy season, especially in the Nanba and old Beichuan districts. According to field surveys and debris flow statistics of the upstream Fujiang River, we found that the frequency of occurrence and scale of regional debris flows are gradually stabilizing. Thus, how to make good use of those areas, especially the potential debris flow, disaster-prone areas, is an extremely urgent and necessary topic of research. This research takes the upstream

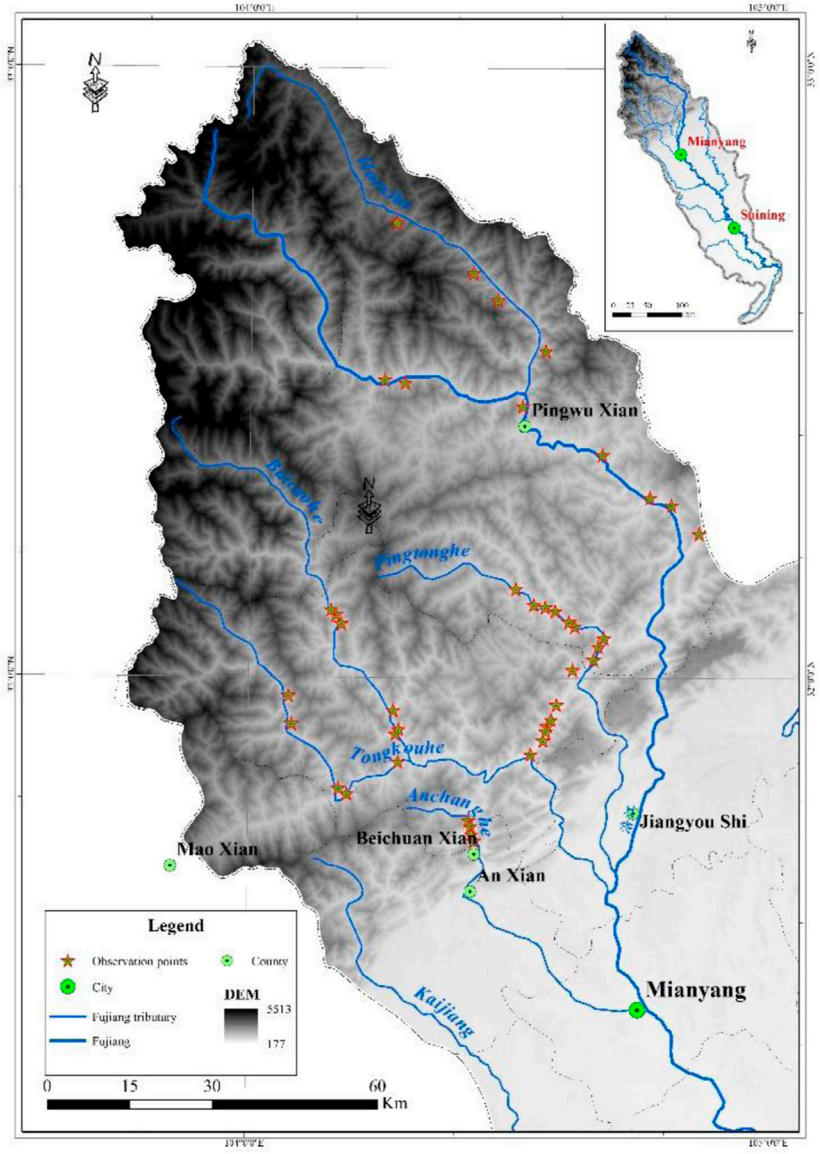

FIGURE 1
The field survey location of the Fujiang River upstream.

Fujiang River basin as an example based on the characteristics of regional debris flow depositional land to set up an evaluation method and then proposes advice for applying each land-use scenario.

The study area

The study area of the Fujiang River is almost 36,400 km^2 in size. Its main river length is 670 km and it originates from Xuebaoding Mountain, Pingwu County, Sichuan Province. The Fujiang River flows across Pingwu, Jiangyou, Mianyang, Santai, Shehong, Suining, Tongguan, and lastly merges with the Jialing River in the Hechuan district, Chongqing. Among its characteristics, the geomorphology of the upstream Fujiang River is a typical alpine valley region, and the Longmen Fault traverses across the entire watershed from Beichuan County to Nanba town. On both sides of the fault, the mountain surface is crushed and the landform undulates dramatically based on the complex geological structure and frequent geotectonic movement. Debris flow, landslides, and rock falls are the main potential geological hazards in this region. While the geomorphology of the downstream areas of the Fujiang River consists of small plains and hills, which appear to be within a relatively stable regional geological environment, only a few minor landslips and water source pollution episodes constitute the main

TABLE 1 The development tendency of debris flow disaster lands of Fujiang River upstream.

Field survey sample	Development tendency	
	Deposit	Cut-down
Number	33	9
Percent	78.6%	21.4%

hazard problems along the bank side. Figure 1 illustrates the watershed which helps to infer the character of the disaster area. Field investigation points are also shown.

Statistical analysis outlines the development tendency of the debris flow disaster area (see Table 1).

From Table 1, 9 investigation points appeared to show a cut-down tendency, which accounts for 21.4 percent, while the other 33 survey points show a deposit tendency, which accounts for 78.6 percent. Therefore, the debris flow deposits of the upstream Fujiang River are mainly characterized by deposition rather than cut-down, so far, which indicates that the debris flow occurrence transitions from a high susceptibility to a low susceptibility state, after the Wenchuan earthquake, indicative of a gradual stabilization.

Methods

Through literature review and sample lab tests, we learn that many factors affect the land use of debris flow depositional areas, such as the soil fertility quality, fine particle content, slope angle, engineering geological characteristics, and debris flow form condition, debris flow watershed, lithology, the height difference (Cui et al., 2008). The soil fertility quality factor can be assessed by soil nutrient index (organic content), total nitrogen, total phosphorus, and total potassium, the value can be attained by physical and chemical experiments. Additionally, fine particle content determines the soil texture, especially soil moisture, nutrient retention, and transport. The soil erosion ratio affects the debris flow depositional land-use type, which is the factor obtained from the numerous sample particle size analysis. Through engineering geological data references and *in situ* tests with proposed equipment in the debris flow depositional area, the bearing capacity of foundation soil can be obtained is between 100 and 260 kPa, which can be used to support a resident's homestead or a factory foundation, the index can be obtained by *in situ* tests and laboratory strength tests. Therefore, we choose soil fertility quality, soil particle conservation, and engineering geological condition as the main factors to evaluate the land use of debris flow deposit fans. Based on the connotations of each factor, we expand upon the classification of the three factors.

Soil fertility quality

Soil fertility is an important indicator that reflects the vegetative-supporting health of the soil. It represents the most essential characteristic of soil that distinguishes soil from parent material and other natural bodies. The soil nutrient classification standard mainly grades the contents of organic matter, total nitrogen, available nitrogen, available phosphorus, and available potassium, and each grade has different contents/proportions of different components. Organic materials are a key sign of soil fertility because of their abundance of botanical nutrients. According to the soil fertility evaluation model (Wang et al., 2003), using the single-factor analysis method, the soil organic matter content can be used as the land potential classification standard of debris flow deposit fans. According to the second national soil survey and related standards, the organic material content is divided into six levels. Based on the degree of soil fertility and properties of the particle distribution of debris flow depositional land, we can divide the four soil quality levels into good, quite well, ordinary, and bad according to its organic materials content. Through the grade of organic materials content, the soil quality is divided into four grades, and the planting type suggestion for the upstream Fujiang River can be seen in Table 2.

Fine particle content

Soil not only provides crops with nutrients, water, and air but the soil environment also affects the amount of nutrients and water absorbed by crops. Generally, debris flow deposits exhibit a wide gradation, especially from clay particles to large boulders, which are widely distributed in the depositional fans. Differing particle contents and concentrations profoundly affect the debris flow density, which determines the debris flow erosion capacity. Meanwhile, fine particle content determines the soil texture, especially affecting the soil moisture and nutrient retention and transport. The soil erosion ratio affects the debris flow depositional land-use type. Soil and water conservation is another key factor for a debris flow ravine. The fine particle content of debris flow depositional fans was determined by the loose solid materials in the source area, such as soil landslides and gully depositional materials. Nevertheless, the frequent floods in the gully also carried away large amounts of fine particulate matter. According to the classification of debris flow erosion ability, four levels represent the condition of the debris flow density determined by the fine particle content. Thus, the debris flow erosion capacity can be subdivided into four levels of soil conservation: good, quite well, ordinary, and bad. The water and soil erosion ratio can directly reflect upon the fine soil particle conservation. Therefore, based on the water and soil ratio and particle distribution, we obtain the soil conservation and land-use types given in Table 3.

TABLE 2 The soil fertility grading and planting type.

Soil fertility X1	Organic materials content (%)	Planting type
Good	>1.5	High quality cultivated land: modern agricultural planting base
Quite well	1.1–1.5	Ordinary arable land: suitable for crops
Ordinary	0.7–1.1	Forest land: trees as walnut
Bad	<0.7	Wood land: trees as shrubs

TABLE 3 The soil conservation classification and land use type.

Soil conservation X2	Soil erosion ratio (%)	Land-use type
Good	<25	Construction land
Quite well	26–50	Plantation
Ordinary	51–75	Forestation and transportation land
Bad	>75	Useless

Engineering geological characteristics

Whether a house is safe and stable is closely related to the quality of the foundations. Soil can be divided into many types, such as sand, clay, boulder, and fill. In mountainous areas, debris flow deposit fans often physically support the living and producing platforms for local residents, and the engineering geological characteristics of debris flow in disaster-prone areas can directly affect local residential construction and production. The bearing capacity of the foundation soil is one of the most important factors because it can indicate the soil strength for debris flow in disaster-prone land. According to the field survey data collected in the upstream Fujiang river, the bearing capacity of foundation soil is commonly between 100 and 260 kPa in mountainous areas; the characteristic values of bearing capacities for clay, silt, sand, medium sand, and coarse sand pebbles are 120, 150, 170, 260, and 350 kPa, respectively. Therefore, the land gets its classification and construction type suggestion based on the bearing capacity of the foundation soil grade, as seen in Table 4.

The debris flow land-use evaluation method

Considering the land utilization factors ahead, we obtain the three classification factors in Table 5. For their evaluation, we set the four classification values to 4, 3, 2, and 1, respectively.

The Analytic Hierarchy Process (AHP) is a decision analysis method that combines qualitative and quantitative methods. Using less quantitative information makes the thinking process of decision making less mathematical, to provide a simple decision-making method for multi-objective, multi-criteria, or complex decision issues without structural characteristics. When using the AHP to construct a system model, the process can be divided into four steps, setting up the hierarchy structure model, constructing a judgment matrix, conducting a hierarchical ranking, and testing for consistency. The debris flow land-use evaluation is the goal, and the soil fertility, soil conservation, and engineering geological characteristics represent the criteria for decision making. Therefore, to obtain the weight of the debris flow evaluation factors, matrix A is built as follows:

$$AW = n \cdot W \tag{1}$$

where A is the debris flow disaster land-use evaluation factor judgment matrix, W is the determined eigenvectors of matrix A, and n is an eigenvalue of A. Through an analytical hierarchy process, we obtain the sorting results, as seen in Table 6.

From Table 6, the weighting coefficients X_1, X_2, and X_3 are obtained, which are 0.63, 0.26, and 0.11, respectively. According to the verification of the maximum characteristic roots, we found it found that the three weighting coefficients are reasonable. Thus, the debris flow disaster utilization mode can be expressed by the following formula:.

$$R = 0.63X_1 + 0.26X_2 + 0.11X_3, \tag{2}$$

where R is the debris flow disaster-prone land-use evaluation value.

From Eq. 2 and its factors classification, we can obtain the three levels for the debris flow disaster potential land use. These

TABLE 4 The engineering geological characteristics and construction type.

Engineering geological characteristics X3	Bearing capacity of foundation soil (kPa)	Construction type
Good	>260	Critical infrastructure
Quite well	100–260	Residential construction
Ordinary	70–100	Affiliated facilities
Bad	<70	Useless

TABLE 5 The factors classification of land utilization.

Evaluation factors	Classification value			
	Good	Quite well	Ordinary	Bad
	4	3	2	1
Soil fertility X_1	>1.5	1.1–1.5	0.7–1.1	<0.7
Soil conservation X_2	<25	26–50	51–75	>75
Engineering geological characteristics X_3	>260	100–260	70–100	<70

TABLE 6 The land utilization factors sorting and weight reference value.

A	X_1	X_2	X_3	W	Sorting
X_1	1	3	5	0.63	1
X_2	1/3	1	5/3	0.26	2
X_3	1/5	3/5	1	0.11	3

λ =3.018, *CI*=0.009, *RI*=0.58, *CR*=0.015<0.10.

are low extent, medium extent, and high extent, respectively. Based on the evaluation factors, the interval evaluation values are 1.00–2.00, 2.00–3.00, and 3.00–4.00, accordingly.

Results

Land use scenario

Huangjiaba is a village along the Longmen Mountain Fault. Due to its flat depositional fans and proximity to the Jian River, many residents currently live here. In the upstream areas of Huangjiaba, steep gullies and drop ridges have developed, which provide powerful topographic conditions for the confluence and movement of debris flow. Meanwhile, numerous areas of rock fragmentation, collapse, and landslides develop and provide enough loose solid materials for debris flow. The symbiotic relationship between disasters and land resources determines the debris flow depositional land utilization. Taking the Huangjiaba village debris flows as an example, our method divides the area by hazard assessment first, probing the planting type by soil fertility. Then, together with engineering characteristics and other factors, we can get the potential land-use classification of the debris flow deposit-prone area.

Based on the debris flow disaster land-use evaluation method and the factor classification of potential soil use, we can learn that the entire Huangjiaba village debris flow disaster-prone areas are between 1.00 and 4.00, and each irregular district has a different R-value. Then, together with the current land-use type, we obtain the four land-use scenarios, R-values, and definition expressions as indicated in Table 7.

From Table 7, we see the four scenario values ranging from 1.00 to 4.00. Based on the scenario values and semi-quantitative analysis, it can be used to obtain the land-use scenario, as shown in Figure 2. Accordingly, the village scenario mainly focuses on the bearing capacity of the foundation. The irregular area overlaid by light blue includes the local, currently existing rural building area and future potential planning construction area. The agriculture scenario concentrates on the higher soil fertility quality, especially the flat areas, so the area covered by pale yellow generally indicates high soil fertility quality (such as organic matter), total phosphorus, and total nitrogen, and the flat area on the edge of the depositional fans, which are close to the Jian river. Soil and water conservation scenarios are mainly related to the debris flow hazard evaluation. The areas overlaid by light green are debris flow gullies on the depositional fans, especially the area moved by debris flow once in a 100-years return period. As for the potential construction scenario, those areas that show low soil fertility, but are relatively safe, are covered by pink color. In fact, the determination of boundaries is subject to many factors—such as rural homestead planning, soil

TABLE 7 Debris flow land use scenario introduction of Huangjiaba.

Land use scenario	Qualitative/semi-quantitative expression	Remarks	R value
Village scenario	Larger of the bearing capacity of the foundation, which is more than 100 kPa	Including existing local building area and potential construction area	1.00–2.00
Agriculture scenario	Higher soil fertility quality, the organic matter is larger than 1.5 percent	Relatively flat and the deposit slope angle is between 50 and 80 per thousandths	3.00–4.00
Soil and water conservation scenario	The area covered by a 100- year debris flow outbreak frequency	Planned prevention trees	2.00–3.00
Potential construction scenario	Bad soil fertility but relatively safe areas	Planned village road and pipeline et al	1.00–2.50

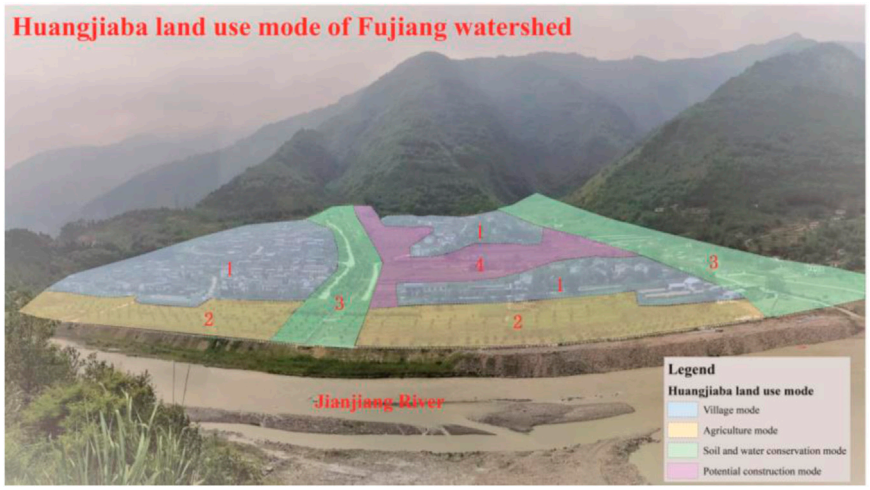

FIGURE 2
The diagram of Huangjiaba four land-use scenario.

fertility, debris flow path, and scale—so the four scenario boundaries in Figure 2 only show reference schematics.

The utilization advice for land use scenario

Through the land-use scenarios to be mentioned ahead, we offer suggestions for each scenario as follows.

Village scenario: The existing building area can maintain its original status or be reconstructed according to village space planning. Other potential construction areas can be planned on a reasonable basis, depending on the soil capacity of the foundation and hazard risk assessment. Moreover, due to the low debris flow disaster risk of damaged land and that the land-use scenario can be flexibly planned, these regions are mainly used as resettlement homesteads, see Figure 3A.

Agriculture scenario: Through sample tests, we conclude that the soil fertility at the fan edge is superior, but due to its proximity to the Jian River, there is a high flooding risk. Therefore, it is advisable to set the fan edge as the economic crop area. In addition, considering the local precipitation pattern, seasonal vegetables can be planted below the village road. On the other areas of the fan edge, one can plant high-value economic crops such as Ginkgo, tea trees, greenhouse vegetables, and flowers, as seen in Figure 3B.

Soil and water conservation scenario: These areas mainly consist of flood and debris flow movement areas. The characteristics of the flood and debris flow hazard zone of a small watershed suggest fast-growing trees and shrubs can be planted along the overflow side of the ditch to enhance the resistance to disasters, while economic trees such as walnuts and cherries can be planted near the channel side. We took the submerged area of 100-, 50-, and 20-years occurrence frequency as examples, correspondingly, the debris flow break-out frequencies are 1%, 2%, and 5%, respectively. In the area covered by 1%–5% frequencies, ornamental trees can be planted, such as Ginkgo; in the 2%–5% areas, shrubbery can be planted, such as tea trees, and village roads set. Areas covered by 5% frequency can be fixed as debris flow channels, see Figure 3C.

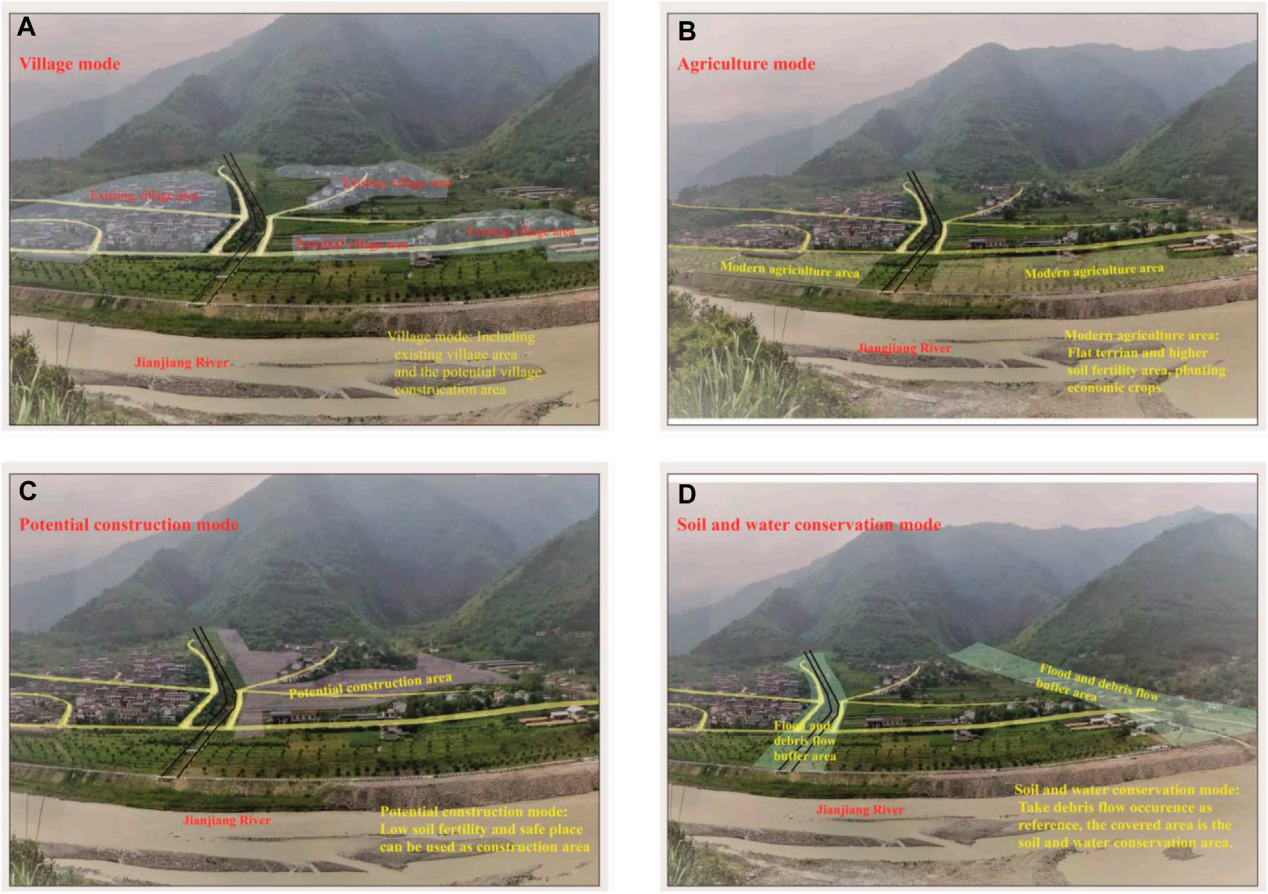

FIGURE 3
Huangjiaba debris flow disaster land-use scenario (**(A)** Village scenario **(B)** Agriculture scenario**(C)** Soil and water conservation scenario **(D)** Potential construction scenario).

Potential construction scenario: These areas are characterized by serious land and water erosion, mainly involving infrastructure, such as village roads, pipelines, factories, etc. We utilize the low soil fertility content and gently sloping terrain, especially if the slope angle is less than 10°, to build pig farms, chicken farms, sand mining factories, etc. These areas can also be created into water and soil conservation forests by a reasonable collocation of trees and shrubs, such as planting red leafy trees, Ginkgo biloba, flowers, shrubs, and other plants, as seen in Figure 3D.

Discussion

Characteristics of debris flow disaster-prone areas

Debris flow fan: Debris flow deposit areas mainly consist of loose solid materials transported from upstream areas. It is the most important living and producing location for residents. Through statistical analysis of the investigation points, we can characterize the integrity of the debris flow deposit fans, as seen in Figure 4.

From Figure 4, the integrity of debris flow deposit fans in the upstream Fujiang River is between 30 and 95%, with an average value of 58%. According to these statistics, there are four types of fan integrity in the upper Fujiang River, as seen in Table 8.

From Table 8, the low integrity of the debris flow disaster fan is found at only one point, which accounts for 2.4% of the 42 investigated points. Median integrity fans are found at 13 points, accounting for 31.7%, high integrity fans are found at 19 points, accounting for 46.3%, and extremely high integrity fans are found at nine points and account for 22% of all investigated points. Generally, the integrity type of the deposit fans is either high or median; therefore, these areas could be used for resident living and production places.

The distance from the river: The deposits of debris flows are mainly from the upper watershed and the gully sides, and the distance between the debris flow at the fan top and the main river

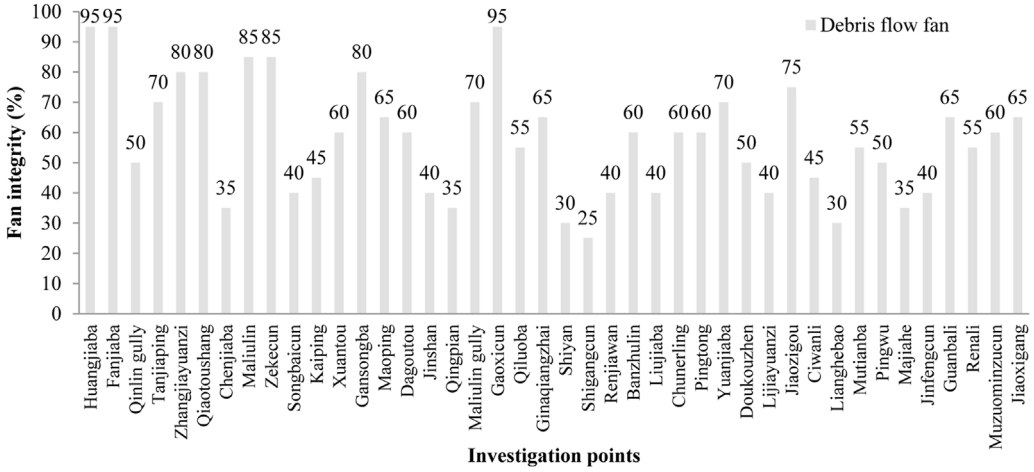

FIGURE 4
The disaster fans of the Fujiang River upstream.

TABLE 8 The fans integrity classification of the Fujiang River upstream.

Fan integrity	Low	Median	High	Extremely high
	<25%	25–50%	51–75%	>75%
Number	1	13	19	9
Percentage	2.4	31.7	46.3	22.0

could be a result of the activity intensity of the debris flow. Figure 5 shows the statistical analysis of the distance between the fan top and the main river.

As seen in Figure 5, the direct length from the debris flow gully mouth to the Fujiang River is between 100 and 350 m; some special fans even reach 700 m, such as those in disaster-prone land, which is determined by the watershed and debris flow activity intensity. For example, the distance value between Huangjiaba and Shiyan reached more than 700 m. Huangjiaba is located along the left bank of Jianjiang River, where the debris flow area is more than 10 km^2. The Longmen Mountain fault cuts across the upstream of the Huangjiaba debris flow source area. Due to frequent earthquake activities, the mountain surface has become widely crushed and abundant with loose solid materials as landslide bodies and rock falls are distributed along the gullies and on both sides. This area also gathered more than a thousand cubic meters of volume; this fact, together with stimulating heavy rainfall in the Longmen Mountain area during the rainy season, caused rainfall-type debris flow to frequently occur after the Wenchuan earthquake. According to statistical analysis, which lasted 5–8 years, the Huangjiaba debris flow event occurred 3 to 5 times each year, with increasingly uneven debris. The deposit fans formed and stabilized gradually, becoming the most important living and production place for local residents.

Planting characteristics: Due to its special location and complex geomorphology, only a few land types can be used for production and living in the upstream Fujiang River basin; thus, the debris flow deposit fans became the primary living place under proper water and sunlight conditions in those areas. Regarding the specification of land use in China, the Fujiang River watershed has many landforms classified as farmland, garden plots, woodland, grass plots, settlements, and unutilized land. However, the high mountainous areas of the upstream Fujiang River basin are useless for the garden plot and settlement land types. Therefore, considering the land uses of debris-flow deposits, they can be preliminarily divided into five types: farmland, woodland, grassland, unutilized land, and local settlement land.

According to the 42 investigated points, it can be statistically determined that the main land use of debris flow deposit fans in the upstream Fujiang River watershed are farmland, woodland, and local settlements (including road and factory use). Quantitatively, farmland accounts for 41.5% of the investigated points, woodland for 32.8%, local settlement for 12.1%, and other grasslands and unutilized land for 13.6%, see Figure 6.

Regarding farmland in the deposit fans, the steep slope generally lies upward of the deposit fan, and the gentle slope is on the downward side close to the main river. Crops such as corn and peanuts are often planted on steep land, some seasonal vegetables are cultivated along the gentle slope, and economic crops, such as Cypress and Bamboo, are planted on the sides of the field and along both banks of the gully. Some debris flow, disaster-prone areas that possess gentle slopes close to the Fujiang River have already been used for building land. The

FIGURE 5
The distance of investigation sites from the main river in the Fujiang River upstream.

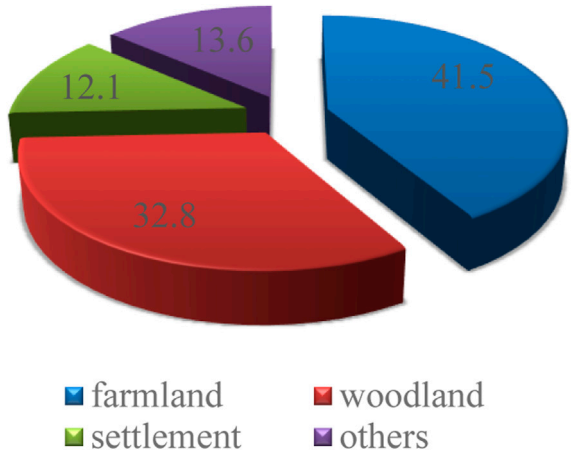

FIGURE 6
The debris flow disaster land-use type of Fujiang River upstream.

first choice of local inhabitants is to make good use of depositional land. Currently, the villages of local resettlements are distributed widely along the Fujiang River banks.

Susceptibility evaluation results: The basic characteristics of the actual debris flow watershed could be investigated and counted easily, including disaster type, loose solid materials reserves, hydrodynamic condition, gully geomorphology, land use, debris flow events, and the preliminary susceptibility evaluation, among others. Through qualitative judgments and semi-quantitative calculations, we can use this content to obtain the discriminant result of the 42 debris flow disaster-prone areas; among these, there are two high prone susceptibility sites, 28 medium prone sites, and 12 low prone sites, which account for 5, 67, and 29%, respectively. Therefore, it can be concluded that the debris flow, disaster-prone areas in the upstream Fujiang River primarily consist of medium and low susceptibility sites. Furthermore, the high prone sites only account for 5% of the total, which illustrates that post-earthquake debris flow activity has gradually changed from high susceptibility to low susceptibility to a certain extent.

Generally, current debris flow in the upstream Fujiang River is mainly shown according to its depositional characteristics. The integrity of the deposit fan is high, and the distance from the Fujiang River to the fan apex is between 100 and 350 m. The land-use types of debris flow depositional areas in the upstream Fujiang River consist of farming, foresting, and local settlements, which shows that the frequency of debris-flow activity in this region is indirectly evolving from high to stable.

Impact factors

This research chose three factors related to soil, organic materials, soil erosion ratio, and soil bearing capacity of the foundation to evaluate the land use of debris flow disaster-prone areas. This evaluation method can provide a beneficial reference for land utilization in debris flow deposit-prone areas.

Many factors can affect the evaluation results, such as soil structure, soil particle distribution, soil nutrients, and soil pH (Zhang et al., 2014). Geomorphology, hydrodynamic condition, and vegetation distribution are also relevant factors to debris flow disaster-prone land. On the one hand, the soil structure and soil nutrients can reflect the development of the debris flow deposit fan. On the other hand, the rush-out materials from every debris flow event would also change the soil characteristics, especially for those solid materials that came from the upper watershed (Massimo et al., 2015; Zhang et al., 2015). Moreover, a

TABLE 9 Development stages for debris flow deposit fan's usage (Tan, 2000).

Level	Initial stage	Development stage	Mature stage
Land use scenario	✓Forest, animal husbandry, arable land, farmland, fruits, and vegetables	✓Irrigation/drainage channel, electrical transmission, communication line utilization	✓Station setting, township-level town construction, and utilization development
	✓Aquaculture industry, economic forest land use	✓Highway, roads, oil (gas) pipeline, railway wiring, bridge, and culvert project utilization	✓Industrial and mining areas, county-level town construction, military facilities
	✓Work sheds, construction site utilization, temporary buildings, infrastructure	✓Tourism, leisure, residential, and tourism development use	✓Comprehensive construction and utilization of medium and large cities

few researchers have utilized a numerical comprehensive evaluation method to evaluate the fertility level of each plot; the contribution degree of individual fertility factors was calculated based on the correlation of soil fertility index. Evaluation methods frequently used by many researchers include the Fuzzy mathematical method, cluster analysis, and principal component analysis (Huang et al., 2010; Wu et al., 2010). Therefore, we need to systematically consider additional factors to evaluate debris flow disaster-prone land utilization in future studies.

Land use scenario

Debris flow deposit fans are among the most precious land resources in mountainous areas, especially in west China and other mountainous countries like Japan and some European countries. Meanwhile, the fan is the depositional place for the debris flow activity, representing the highest risk area for debris flow washing and flooding in the rainy season.

Considering the economic development of local governments, making good use of debris flow fans is a key factor in the near future. However, the utilization of debris flow depositional fans comes with hazard risks. To exploit and utilize debris flow in disaster-prone land and avoid disaster loss, it is necessary to discuss the stratified modes of the exploitation and utilization of the debris flow deposit fan. Through analysis of the social economy and hazard risk extent, Tan (2000) posed a viewpoint of the evolution of debris flow, disaster-prone land usage, which can be divided into three stages: initial condition, developmental, and mature (Tan, 2000), as shown in Table 9.

Table 9 clearly shows that in the initial stage, higher risk and poorer soil properties make the debris flow deposit area most suitable for forestry, grassland, agriculture, or other temporary land uses such as for buildings or infrastructure. During the development stage, because the disaster risk is smaller and the debris flow depositional area gradually stabilizes, debris flow deposit land can be used for roads, tourism, water conservancy, and other development. In the mature period, large- and medium-sized debris flow depositional areas can be used for urban and rural construction or some other use. The tentative model of land-use scenarios for the debris flow deposit fans is given in Tan (2000). Furthermore, sustainable rural development also requires exploring and establishing appropriate criteria for evaluation and investigation.

Local village revitalization practices need to consider both environmental protection and regional security. In addition, relevant regulations should be established to strengthen the planning and management of debris flow land use development, and appropriate regulators are needed to supervise and manage debris flow disaster land use (Löschner and Nordbeck, 2020; Zhou et al., 2020). In the meantime, for lands suitable for agricultural and aquaculture development, local government and agencies should strengthen professional knowledge training and reinforce relevant knowledge by offering technical support (He et al., 2020). Regarding the debris flow disaster-prone land utilization measures, local governments first need to require evaluations of the hazard. Different catchments need to be treated accordingly upon considering variations in soil fertility and other factors. In future work, we need to systematically consider more factors to evaluate debris flow disaster-prone land utilization.

Conclusion

This study has taken a debris flow deposit-prone area of the upstream Fujiang River as its research target, carried out a field investigation and interviews with residents.

To characterize the debris flow disaster-prone area background of the upstream Fujiang River, we first chose the soil fertility quality, soil particle conservation, and engineering condition from other factors. Then based on the grading of these three factors, we obtained the planting type based on soil fertility/quality, land-use type based on soil conservation, and construction type based on the engineering geological characteristics. According to the grading value of each factor, we obtained the debris flow disaster-prone land-use evaluation R-value based on the hierarchy analytic process method. The evaluation formula can obtain the debris flow disaster potential land use in the low, medium, and high extent levels; the interval evaluation values are 1.00–2.00, 2.00–3.00, and 3.00–4.00, respectively.

We obtained four land-use scenarios by the Huangjiaba debris flow disaster-prone area as an example. The value of the four scenarios are calculated between 1.00 and 4.00, regarding

each land-use scenario and R-value, we offer utilization advice for each land scenario. The village scenario needs to refer to the village space planning and risk assessment protocols, the agriculture scenario can be used in the high soil fertility area, the soil and water conservation scenario is affected by debris flow and floods, so fast-growing trees and shrubs can be planted along the overflow side of the ditch, and the potential construction scenario is best suited for infrastructure because of its low soil fertility, which can help in rural space planning for the local government in advance.

According to the 42 debris flow deposit fans along the Fujiang Riverbank. It show that the developmental tendencies of the debris flow disaster areas appear to deposit recently, the average distance from the gully outlet to the Fujiang River is between 100 and 350 m, which is affected by watershed and debris flow activity intensity. Further studies still need to systematically consider more factors to evaluate debris flow and disaster-prone land utilization, which can provide a reference for the rural space planning for the local government.

Data availability statement

The original contributions presented in the study are included in the article/supplementary material, further inquiries can be directed to the corresponding author.

Author contributions

SY carried out the field investigation, data analysis, and manuscript writing. HP involved in manuscript supervision. TS undertook the field survey, participated in the discussion and decision-making process. JJ was involved in writing reviewing, manuscript editing, and supervision. YT undertook the field survey and discussion in advance. KC was involved in supervision. All the authors participated and contributed to the final manuscript.

Funding

This research work was supported by the Talent Introduction Program of Xihua University (Grand No. Z211016), the National Natural Science Foundation of China (Grant No. 42077275) and China Geological Survey Project (Grand No. DD20160251).

Conflict of interest

The authors declare that the research was conducted in the absence of any commercial or financial relationships that could be construed as a potential conflict of interest.

Publisher's note

All claims expressed in this article are solely those of the authors and do not necessarily represent those of their affiliated organizations, or those of the publisher, the editors and the reviewers. Any product that may be evaluated in this article, or claim that may be made by its manufacturer, is not guaranteed or endorsed by the publisher.

References

Cao, S., Liu, Y., and Yu, Z. (2018). China's successes at combating desertification provide roadmap for other nations. *Environ. Sci. Policy Sustain. Dev.* 60 (2), 16–24. doi:10.1080/00139157.2018.1419002

Chen, T., Jiao, J., Chen, Y., Lin, H., Wang, H., and Bai, L. (2021). Distribution and land use characteristics of alluvial fans in the Lhasa River Basin, Tibet. *J. Geogr. Sci.* 31 (10), 1437–1452. doi:10.1007/s11442-021-1905-1

Chen, T., Peng, L., Liu, S., and Wang, Q. (2017). Land cover change in different altitudes of guizhou-guangxi karst mountain area, China: Patterns and drivers. *J. Mt. Sci.* 14 (9), 1873–1888. doi:10.1007/s11629-016-4202-1

Cui, P., Ge, Y., Zhuang, J., and Wang, D. (2009). Soil evolution features of debris flow waste-shoal land. *J. Mt. Sci.* 6, 181–188. doi:10.1007/s11629-009-1035-1

Cui, P., Hu, K., Zhuang, J., Yang, Y., and Zhang, J. (2011). Prediction of debris-flow danger area by combining hydrological and inundation simulation methods. *J. Mt. Sci.* 8, 1–9. doi:10.1007/s11629-011-2040-8

Cui, P., Wang, D., and Zhuang, J. (2008). Land exploitation and utilization on debris-flow fan. *Sci. Soil Water Conservation* 6 (1), 6–11. (in Chinese).

Gregoretti, C., Degetto, M., and Boreggio, M. (2016). GIS-based cell model for simulating debris flow runout on a fan. *J. Hydrology* 534, 326–340. doi:10.1016/j.jhydrol.2015.12.054

He, S., Wang, D., Chen, S., Zhang, S., and Chang, S. (2016). Natural consolidation characteristics of viscous debris flow deposition. *J. Mt. Sci.* 13 (10), 1723–1734. doi:10.1007/s11629-016-3850-5

He, S., Wang, D., Li, Y., Fang, Y., Lan, H., and Chen, W. (2019). Implementation of a landscape ecological use pattern model: Debris flow waste-shoal land use in the Yeyatang Basin, Yunnan Province, China. *Land Use Policy* 81, 483–492. doi:10.1016/j.landusepol.2018.11.024

He, S., Wang, D., Li, Y., and Zhao, P. (2018). Land use changes and their driving forces in a debris flow active area of Gansu Province, China. *Sustainability* 10 (8), 2759. doi:10.3390/su10082759

He, S., Wang, D., Zhao, P., Li, Y., Lan, H., Chen, W., et al. (2020). A review and prospects of debris flow waste-shoal land use in typical debris flow areas, China. *Land Use Policy* 99, 105064. doi:10.1016/j.landusepol.2020.105064

Hu, W., Dong, X., Xu, Q., Wang, G., Van Asch, T., and Hicher, P. (2016). Initiation processes for run-off generated debris flows in the Wenchuan earthquake area of China. *Geomorphology* 253, 468–477. doi:10.1016/j.geomorph.2015.10.024

Huang, T., Yue, X., Ge, X., and Wang, X. (2010). Evaluation of soil quality on gully region of loess plateau based on principal component analysis. *Agric. Res. Arid Areas* 28 (3), 141–147. (in Chinese).

Ibe, K., and Ebe, A. (2000). Impacts of debris-flow deposits on hydrogeochemical processes and the development of dryland salinity in the Cross-River catchment, SE, Nigeria. *Environ. Monit. Assess.* 64 (2), 449–456. doi:10.1023/A:1006352922219

Imaizumi, F., Sidle, R., Tsuchiya, S., and Ohsaka, O. (2006). Hydrogeomorphic processes in a steep debris flow initiation zone. *Geophys. Res. Lett.* 33 (10), L10404. doi:10.1029/2006GL026250

Jakob, M., and Hungr, O. (2005). "Introduction," in *Debris-flow hazards and related phenomena*. Editors M. Jakob and O. Hungr (Berlin, Heidelberg: Springer), 1–7. doi:10.1007/3-540-27129-51

Liu, H., Liu, Y., Bi, R., Xu, Y., and Wang, S. (2016). Reuse type judgment of mining wasteland based on land use competitiveness. *Trans. Chin. Soc. Agric. Eng.* 32 (10), 258–266. (in Chinese).

Liu, Y. (2018). Introduction to land use and rural sustainability in China. *Land Use Policy* 74, 1–4. doi:10.1016/j.landusepol.2018.01.032

Liu, Y., Wei, F., Li, H., and Ai, N. (2001). The influence of exploitation of debris flow waste-shoal land on environment of ravine basin-taking Jiangjia Ravine Basin in Yunan Province as an Example. *J. Catastrophology* 16 (2), 18–22. (in Chinese). doi:10.3969/j.issn.1000-811X.2001.02.004

Liu, Z., Qiu, H., Zhu, Y., Liu, Y., Yang, D., Ma, S., et al. (2022). Efficient identification and monitoring of landslides by time-series InSAR combining single- and multi-look phases. *Remote Sens.* 14, 1026. doi:10.3390/rs14041026

Löschner, L., and Nordbeck, R. (2020). Switzerland's transition from flood defence to flood-adapted land use–A policy coordination perspective. *Land Use Policy* 95, 103873. doi:10.1016/j.landusepol.2019.02.032

Massimo, D., Carlo, G., and Martino, B. (2015). Comparative analysis of the differences between using Lidar and contour-based DEMs for hydrological modeling of runoff generating debris flows in the dolomites. *Front. Earth Sci.* 3, 21. doi:10.3389/feart.2015.00021

Okunishi, K., and Suwa, H. (2001). Assessment of debris-flow hazards of alluvial fans. *Nat. Hazards (Dordr).* 23 (2), 259–269. doi:10.1023/A:1011162516211

Qiu, H., Zhu, Y., Zhou, W., Sun, H., He, J., and Liu, Z. (2022). Influence of DEM resolution on landslide simulation performance based on the Scoops3D model. *Geomatics, Nat. Hazards Risk* 13 (1), 1663–1681. doi:10.1080/19475705.2022.2097451

Sancho, C., Peña, J. L., Rivelli, F., Rhodes, E., and Muñoz, A. (2008). Geomorphological evolution of the Tilcara alluvial fan (Jujuy Province, NW Argentina): Tectonic implications and palaeoenvironmental considerations. *J. S. Am. Earth Sci.* 26 (1), 68–77. doi:10.1016/j.jsames.2008.03.005

Siegert, M. (2016). Environmental sciences in the twenty-first century. *Front. Environ. Sci.* 4, 16. doi:10.3389/fenvs.2016.00016

Tan, W. (2000). Debris flow fan types and land-use models. *Geogr. Territ. Res.* 16 (1), 71–75. (in Chinese). doi:10.3969/j.issn.1672-0504.2000.01.016

Tecca, P., and Genevois, R. (2009). Field observations of the june 30, 2001 debris flow at acquabona (dolomites, Italy). *Landslides* 6 (1), 39–45. doi:10.1007/s10346-009-0145-8

Tiranti, D., and Deangeli, C. (2015). Modeling of debris flow depositional patterns according to the catchment and sediment source area characteristics. *Front. Earth Sci. (Lausanne).* 3, 8. doi:10.3389/feart.2015.00008

Wang, D., Cui, P., Zhu, B., and Wei, F. (2003). Soil fertility properties of debris flow waste-shoal land in Jiangjia Gully of Yunnan province. *Bull. Soil Water Conservation* 23 (6), 7–11. (in Chinese). doi:10.3969/j.issn.1000-288X.2003.06.002

Wang, J., Yang, S., Ou, G., Gong, Q., and Yuan, S. (2018). Debris flow hazard assessment by combining numerical simulation and land utilization. *Bull. Eng. Geol. Environ.* 77 (1), 13–27. doi:10.1007/s10064-017-1006-7

Wang, L., Qiu, H., Zhou, W., Zhu, Y., Liu, Z., Ma, S., et al. (2022). The post-failure spatiotemporal deformation of certain translational landslides may follow the pre-failure pattern. *Remote Sens.* 14, 2333. doi:10.3390/rs14102333

Wu, Y., Tian, X., Nan, X., Chi, W., Yan, X., and Zhu, R. (2010). Evaluation of soil quality under conservation tillage via factor and cluster analyses. *Chin. J. Eco-Agriculture* 18 (2), 223–228. (in Chinese). doi:10.3724/sp.j.1011.2010.00223

Xu, S., Li, C., and Wang, M. (2001). Xiaojiang debris flow and its bottomland exploitation in Yunnan, Southwest China. *Earth Sci. Front.* 8 (2), 296–300. (in Chinese). doi:10.3321/j.issn:1005-2321.2001.02.012

Zhang, G., Deng, H., Du, K., Lin, Y., Ma, R., and Wang, D. (2014). Comprehensive estimation of soil fertility in different land use types of debris flow waste-shoal land. *J. Fujian Coll. For.* 34 (3), 214–219. (in Chinese). doi:10.3969/j.issn.1001-389X.2014.03.005

Zhang, S., Wang, D., Mei, Y., Chang, S., and Wang, H. (2015). Effects of land use types on soil properties in a small watershed of debris flow activity region. *J. Soil Water Conserv.* 29, 258–262. (in Chinese). doi:10.13870/j.cnki.stbcxb.2015.01.049

Zhou, W., Qiu, H., Wang, L., Pei, Y., Tang, B., Ma, S., et al. (2022). Combining rainfall-induced shallow landslides and subsequent debris flows for hazard chain prediction. *CATENA* 213, 106199. doi:10.1016/j.catena.2022.106199

Zhou, Y., Li, X., and Liu, Y. (2020). Rural land system reforms in China: History, issues, measures and prospects. *Land Use Policy* 91, 104330. doi:10.1016/j.landusepol.2019.104330

frontiers | Frontiers in Earth Science

TYPE Original Research
PUBLISHED 25 August 2022
DOI 10.3389/feart.2022.971387

OPEN ACCESS

EDITED BY
Wen Nie,
Jiangxi University of Science and Technology, China

REVIEWED BY
Ping Liu,
Lanzhou University, China
Qiang Sun,
Xi'an University of Science and Technology, China

*CORRESPONDENCE
Su Li Cui,
cuisl@nwu.edu.cn

SPECIALTY SECTION
This article was submitted to Geohazards and Georisks, a section of the journal Frontiers in Earth Science

RECEIVED 17 June 2022
ACCEPTED 25 July 2022
PUBLISHED 25 August 2022

CITATION
Cui SL, Tao ZP, Zhang Y, Su H and Jia Y (2022), Engineering properties and microcosmic mechanism of cement stabilized diatomite.
Front. Earth Sci. 10:971387.
doi: 10.3389/feart.2022.971387

Engineering properties and microcosmic mechanism of cement stabilized diatomite

Su Li Cui[1]*, Zhi Peng Tao[2], Yang Zhang[1], Hang Su[1] and Yang Jia[1]

[1]State Key Laboratory of Continental Dynamics, Geological Department of Northwest University, Xi'an, China, [2]Engineering Department, Xi'an Aerospace Construction Supervision Limited Company, Xi'an, China

In this study, the engineering properties of remolded diatomite and the effects of cement on the compression characteristic, strength properties and microstructures of cement-stabilized diatomite were investigated. Samples were prepared and stabilized with different cement content ratios, ranging from 0% to 15% by dry mass. Results show that compared with undisturbed diatomite, the compressibility of the remolded diatomite increases while the strength characteristics decrease. With the increase of cement content, the compressibility of cement-stabilized diatomite is significantly reduced and the strength characteristics are improved. Adding cement to diatomite changes the structure of pure diatomite and forms more tiny pores between cement and diatomite, while curing reduces the porosity ratio of samples and enhance the strength of cement-stabilized diatomite, especially for diatomite with higher cement content. The physical-chemical reactions including hydrolysis and hydration between cement and diatomite increase the content of sodium aluminosilicate, calcium aluminosilicate and other minerals in the soil.

KEYWORDS

diatomite, cement, cure time, engineering properties, microcosmic mechanism

Introduction

Diatomite is a kind of biochemical deposition formed by diatom after its death during the accumulation period of 10,000–20,000 years. It belongs to the siliceous rocks, and its chemical composition is mainly SiO_2, which can be expressed by $SiO_2 \cdot nH_2O$.It is mostly deposited in Miocene and Pliocene age (Harben, 2002), China is one of the countries with the most extensive distribution of diatomite in the world and diatomite were found in 18 provinces (Cui, 2008). Diatomite was usually studied as a material for industrial applications in building, bleaching, filtering, and so on (Stoemer and Smoll, 2001; Fragoulis et al., 2005; Van Garderen et al., 2011). In recent decade, with the continuous development of foundation engineering, civil engineering construction is developing towards various complex geological conditions (Yang et al., 2022; Ma et al., 2021; Zhou et al., 2022; Liu et al., 2022; Qiu et al., 2022; Wang et al., 2022). In the construction of railways and highways, diatomite areas are often encountered along the route and the engineering characteristics of diatomite is also beginning to attract researchers' attention (Koizumi et al., 2009; Calvo et al., 2012).

Some scholars have studied the engineering properties and strength characteristics of diatomite, Day (1995) indicated that although diatomite has lower density and higher water content, it has lower compressibility and higher shear strength due to its good biting force and surface roughness of the original soil, the similar results also have been obtained by Tateishi (1997). (Hong et al., 2004a) studied the mechanical properties of natural diatomite in oita prefecture, Japan, providing that before the consolidation pressure reaches the consolidation yield stress, the compression curve is horizontal, but when the consolidation pressure reaches the yield stress, the compressibility will increase sharply, indicating that the original diatomite has a strong structure. The macro-and micro properties also have been investigated by Hong et al. (2006). Zhang et al. (2013) made study the mineralogical compositions, physical property, mechanical and engineering properties of diatomite in Tengchong region of Yunnan Province, Southwest China, results indicated that diatomite is a kind of strong structural soil, both the composition and the structure of diatomite could lead to its different mechanical and engineering properties.

Although the undisturbed diatomite has high structural strength, its mechanical strength will change after its structure is destroyed because of the extremely absorbent clay minerals it contains. However, in many projects, such as the construction of roads and railways, a large amount of backfill will be used, which will inevitably disturb and reshape the local soil, therefore, it is necessary to study the mechanical behavior of reconstructed diatomite.

Meanwhile, in the treatment of soil with poor geotechnical performance, a widespread used technique is to add modifier to improve the engineering properties, and the most commonly used modifier is cement, it has been used for many special soils. Sariosseiri and Muhunthan (2009) investigated the treatment effect of cement on geotechnical properties of Washington State soils; indicating that both the strength characteristics and workability are improved and the cement content should not be higher than 10%. Lemaire et al. (2013) studied the microstructure and macroscopic mechanical properties of plastic silt treated with combined cement and lime, found that the mechanical strength of soil has been significantly improved due to the change of microstructure of treated soil. Ho et al. (2017) investigated the effects of water content, carbonation, and pozzolanic reaction on the strength development of cement-treated soils under the drying condition. And the strength development of sand, sand-loam, and sand-bentonite mixtures treated with cement, founded that carbonation could have both positive and negative impacts on strength development of cement-treated soils were also studied (Ho et al., 2018). Moreover, some scholars have also studied other engineering properties of cement-treated soil, such as the resistance to liquefaction of loess treated with cement (Qian, 2016), the consolidation properties of compacted lateritic soil treated with cement (Mengue et al., 2017), the dynamic response of expansive soil treated with cement (Cai et al., 2020), and the hydraulic conductivity and strength of marine clay treated with foamed cement (Wu et al., 2019). However, the engineering properties of cement treated diatomite have not been studied.

Therefore, in this study, based on geotechnical tests and microstructure tests, the engineering properties, mineral content change and microstructure evolution of remoulded diatomite and cement-treated diatomite were investigated. The influence of cement content and curing period on these properties were obtained and analyzed.

Marerials and methods

Materials

The diatomite used in this investigation is obtained from the City of Shengzhou in Zhejiang province in China. It is grey white and collected at a depth between 3.0 and 5.0 m. The main mineral of diatomite is SiO_2, followed by $CaCO_3$, a small amount of Al_2O_3, Fe_2O_3, CaO, etc., and a certain amount of organic matter, the details of mineral component and the clay mineral composition are shown in Table 1. Table 2 lists the basic physicochemical properties of diatomite in terms. The particle size distribution curve of diatomite is shown in Figure 1, in which fine soil accounts for 98.24%, and part of coarse-grained soil has a particle size less than 0.25 mm.

The cement was 42.5# ordinary Portland cement supplied by Jingyang Cement Company (Shanxi province, China). It is an off-white soil, thin powder with a natural moisture content of 0.60% and a relative density of 2.58.

TABLE 1 Main chemical and clay mineral compositions of diatomite.

Mineral	Content/%
SiO_2	84.43
$CaCO_3$	5.27
Al_2O_3	2.34
Fe_2O_3	1.03
CaO	0.72
MgO	0.69
Loss on ignition	3.56
Other substance	1.96
Illite/Montmorillonite mixed layer (S/I)	47.29
Effective montmorillonite	23.88
Illite (I)	7.69
Kaolinite (K)	14.63

TABLE 2 Basic physicochemical properties of diatomite.

Property	Value
Specific gravity/g/cm^3	2.51
Specific surface area/m^2/g	249.32
Nature water content/%	49.5
Natural density/g/cm^3	1.65
Nature void ratio	1.26
Nature compressibility	0.27
Liquid limit/%	82.3
Plastic limit/%	40.6
Maximum density/g/cm^3	1.15
Optimum water content/%	38.4

Methods

Cement content ratio (C_c) is defined as the ratio of the dry mass of cement to the dry mass of the diatomite-cement mixture. For the sample preparation, the diatomite has an air-dried water content of 32.4%, diatomite is carefully mixed with cement of different content ratios (0%, 3%, 6%, 9%, and 15%) and distilled water to produce mixtures to the natural water content uniformly.

Samples were prepared by statically compacting in a confining ring with an inner diameter of 61.8 mm and a height of 20 mm (for swelling pressure and direct shear test) and a confining ring with an inner diameter of 50 mm and height of 100 mm (for unconfined compressive strength test). The static compaction speed was 5 kN/s and the maximal load was 20 MPa. The sample was pushed out of the apparatus 10 min after the height had reached the predetermined height. A rebound of less than 0.01 mm was observed in the height of the sample after the unloading stage was complete and this was deemed to be negligible. The density of the sample was 1.65 g/cm^3 determined according to the nature density for undisturbed diatomite (Table 1).

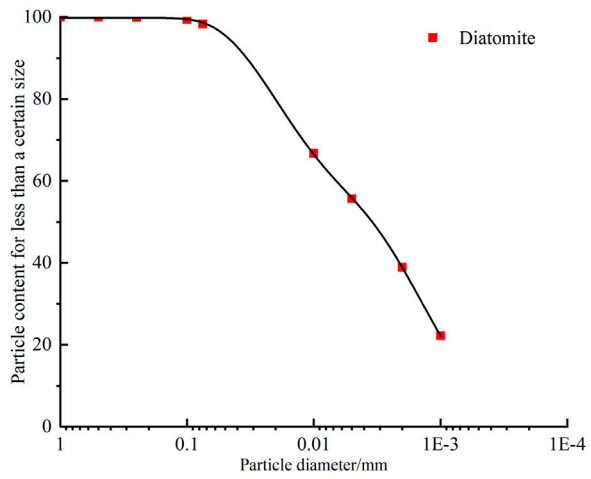

FIGURE 1
Particle size distribution curve.

Swelling pressure tests were performed in a swelling pressure testing apparatus. Direct shear test and unconfined compressive strength test were carried out respectively to determine the cohesion (c), internal friction angle (φ) and unconfined compressive strength (UCS). Direct shear takes the type of fast shear for this study, that is, the shear speed was defined as 0.8 mm/min. And the compression coefficient of soil sample was measured by uniaxial compression test on the consolidation instrument. In addition, in order to investigate the influence of curing age on mechanical behavior of cement-modified diatomite, the samples mixed with different cement ratios were cured for 1 day, 7 days, 14 days and 28 days respectively. Then the direct shear test and unconfined compressive strength test were carried out.

To further investigate the microstructure changes of diatomite stabilized by cement, X-Ray diffraction (XRD), Mercury intrusion porosimetry (MIP) and scanning electron microscope (SEM) were used. MIP used in this study is to determine the pore size distribution in porous materials based on the unique relationship between intrusion pressure and equivalent pore diameter. as proposed by Washburn (1921): $D=-(4\gamma\cos\theta)/P$. In this test, θ was 140° and γ was 0.480 N/m, the measured pore sizes ranged from 0.005 μm to 340 μm.

Results

Engineering properties of remolded and undisturbed diatomite

The engineering properties of remolded and undisturbed diatomite are shown in Table 3. Compared with undisturbed diatomite, it can be seen the compression coefficient of the remolded diatomite is increased by 51.2%; while the values of cohesion, internal friction angle and *UCS* (Unconfined Compressive Strength) are reduced by 52.95%, 56.88% and 57.14% respectively. These results indicate that the remolded soil sample destroys the original structure of the undisturbed soil, although the remolded soil has the same initial conditions as the undisturbed soil, its compressibility is increased and strength characteristic is reduced due to the lack of good engineering performance provided by the soil structure. It is worth mentioning that the value of the maximal swelling pressure is very low and basically unchanged, which is attributed to the high porosity of diatomite, most of the expansion is consumed in the reduction of pore volume,

TABLE 3 Engineering properties of remolded and undisturbed diatomite.

Soil type	Maximal swelling pressure/kPa	Compression coefficient $a_{1\text{-}2}$/MPa	Cohesion/kPa	Internal friction angle/°	*UCS*/MPa
Undisturbed diatomite	21.57	0.41	142.6	21.8	0.98
Remolded diatomite	20.68	0.62	67.1	9.4	0.42

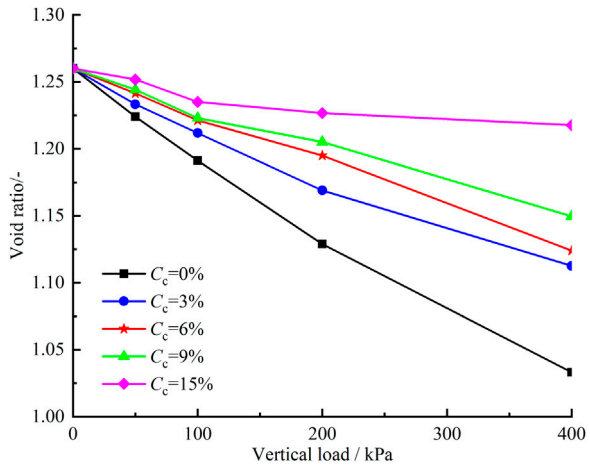

FIGURE 2
e-p curves of cement modified diatomite.

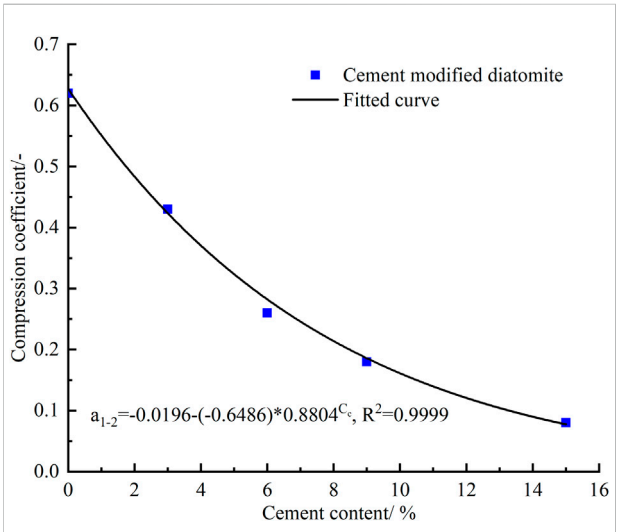

FIGURE 3
Compression coefficient vs. cement content.

which is called "internal expansion" (Zhang et al., 2013), so it cannot form a very high expansion force. Meanwhile, the results also indicate that the damage of soil structure has little effect on the soil expansibility.

Effect of cement content on compressibility of diatomite

Unidirectional compression tests were carried out on diatomite samples with different proportions of cement, and the results are shown in Figure 2, it can be seen that with the increase of cement content, the falling gradient of *e*-p curves of the samples slows down significantly. For remolded pure diatomite sample, with the increase of the load, the compressive deformation of the sample continues to increase, and the void ratio decreases from the initial 1.260 to 1.033 under the loading of 400 kPa, decreasing by 0.227 kPa; when the cement content is 3%, it decreases by 0.147 kPa, which is only 64.8% of pure diatomite. And when the cement content is 15%, the void ratio is 1.128 under the loading of 400 kPa, decreasing by 0.042, which is only 18.5% of pure diatomite sample.

Compressibility coefficients of 100–200 kPa, $a_{1\text{-}2}$(MPa), were calculated, which is a parameter used to judge the compressibility of the sample, and the relationship between $a_{1\text{-}2}$ and cement content is listed in Figure 3. Result shows that $a_{1\text{-}2}$ decreases exponentially with the increase of cement content, and the fitting formula is as follows: $a_{1\text{-}2}$=−0.0196−(−0.6486)*0.8804^{Cc}, R^2=0.9842.

The void ratio of pure diatomite sample is 0.62, and the void ratios of 3% and 15% cement samples are 0.43 and 0.08 respectively. According to the specification, soil with $a_{1\text{-}2}$≥0.5 MPa is defined as high compressibility soil, soil with 0.1 MPa≤$a_{1\text{-}2}$<0.5 MPa is defined as medium compressibility soil, and soil with $a_{1\text{-}2}$<0.1 MPa is defined as low compressibility soil. Therefore, the sample of remolded pure diatomite belongs to high compressibility soil. The sample with 3% cement is reduced to medium compressibility soil, and when the cement content is 15%, it is directly reduced to low compressibility soil. It shows that adding cement to diatomite can significantly reduce the compressibility of soil. It's worth noting that when the cement content is 3%, the value of $a_{1\text{-}2}$ is close to that of undisturbed diatomite (0.41 MPa).

Effect of cement content on strength properties of diatomite

Direct shear tests were conducted on cement-stabilized diatomite and the shear strength parameters were obtained. Figure 4 shows the typical shear stress-shear deformation

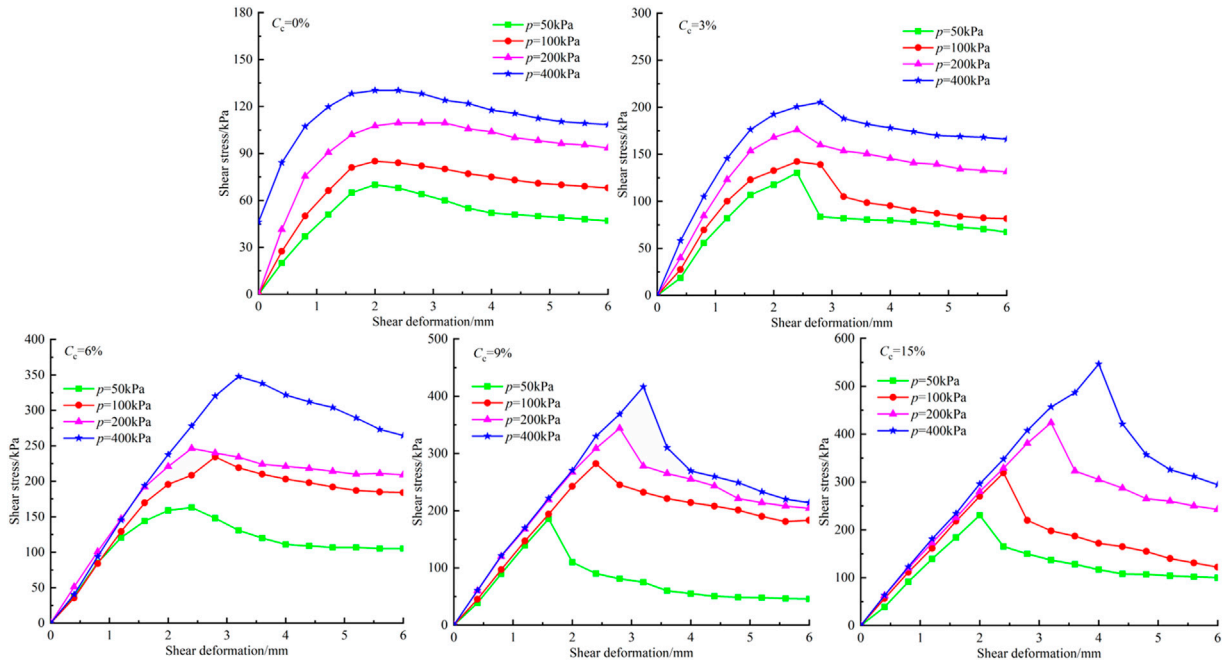

FIGURE 4
Shear stress-shear deformation.

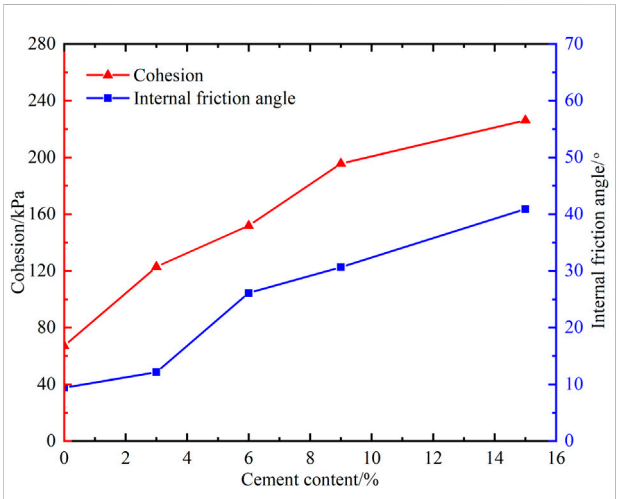

FIGURE 5
Shear strength parameters vs. cement content.

curves for the samples of diatomite with different cement contents, results display that shear strength is enhanced as cement content increases. It's worth noting that with the increase of cement content, the stress-deformation relationship of samples gradually changes from strain hardening to strain softening, when the cement content is 6%, the stress-strain curve shows a very obvious peak strength. These indicate that adding cement to diatomite makes the soil harder and more brittle, which means that the shear behavior is like that of rock and the soil is harder.

The change of cohesion (c) and internal friction angle (φ) with cement content are shown in Figure 5, it shows that with the increase of cement content, both cohesion and internal friction angle increase. Moreover, when the cement content is 6%, the shear strength parameters are close to that of the undisturbed diatomite samples, indicating that cement has an obvious effect on improving the shear strength of diatomite. However, the strength growth rate is not invariable, with the increase of cement content, the increasing effect of cement on soil strength gradually decreases.

Figure 6 shows the result of Unconfined Compressive Strength test, it can be seen after adding cement to diatomite, the soil gradually transforms from strain hardening type to strain softening type.

Figure 7 shows the relationship between *UCS* value and cement content. The *UCS* value increases exponentially with the increase of cement content, similar to the shear strength parameter, when the cement content is 6%, the *UCS* value of the sample exceeds that of undisturbed diatomite, meaning that adding cement significantly improves the strength of soil.

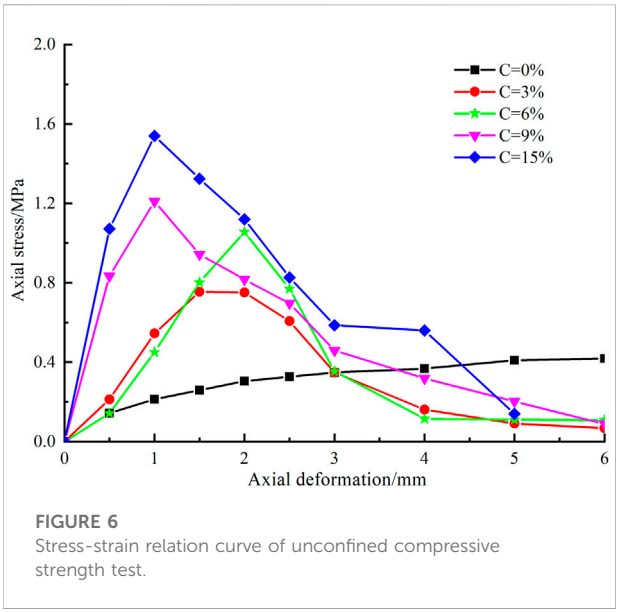

FIGURE 6
Stress-strain relation curve of unconfined compressive strength test.

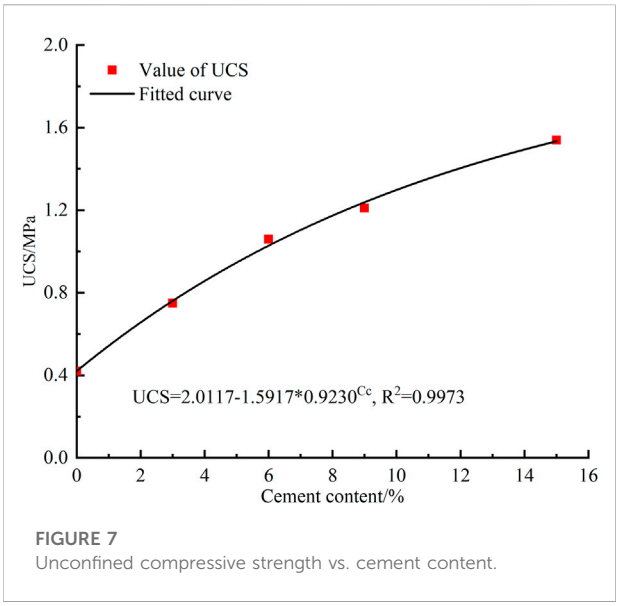

FIGURE 7
Unconfined compressive strength vs. cement content.

Influence of curing period on strength characteristics of cement-stabilized diatomite

In order to clarify the influence of curing period on strength characteristics of cement-modified diatomite, samples with different cement content were cured for 0 days, 7 days, 14 days and 28 days separately, and then direct shear test and Unconfined Compressive Strength tests were conducted on them.

The variation of shear strength parameters with curing period are shown in Figure 8. Curing has almost no effect on pure diatomite. The effect of curing on cohesion and internal friction angle is quite different. For internal friction angle (Figure 8A), the values are increased with the increase of curing time, but the increase rate are different, the value of the sample with 3% cement content increases significantly, while these values of samples with other cement content increase slowly. For cohesion (Figure 8B), curing can significantly improve the value of cohesion, and the strength improvement is mainly reflected in the early curing stage, which has reached more than 85% of the stable value within 14 days. When curing period is more than 14 days, the value of cohesion increases slowly. In addition, results indicate that the value of cohesion of sample with 3% cement content increases from 122.9 kPa to 194.1 kPa after curing for 28 days; While these two values are 226.2 kPa and 648.7 kPa respectively for sample with 15% cement content, which is 5.93 times than that of the sample with 3% cement content, indicating that the curing effect on the sample with higher cement content is more significant.

The UCS value of diatomite with various cement content after different curing period are determined and presented in Figure 9. Results indicate that the value of sample without cement has almost no change with curing time. While the value of other samples with different proportions of cement are increased with curing period and gradually stabilized. And there is little difference in the increase rate of samples with different the cement content.

Microscopic mechanism study

Figure 10 displays the cumulative pore volume curves and the pore size distribution curves of samples with various cements content and samples with 15% cements content after various curing period. It can be seen from Figure 10A, the total pore number of the sample increases with the increase of cement content, but the value of sample with 15% and 9% cement content is almost the same, and from Figure 10C, it can be concluded that the main increased pore size range is 0.01–10 um. While the total pore number of the sample decreases with the growth cure time (Figure 10B), and reduction in pore size is concentrated in 0.1–0.01 μm (Figure 10D).

Meanwhile, the results of both cumulative pore volume curves and pore size distribution curves show that most of the pores in the sample are less than 10um. Furthermore, the results of SEM (Figure 11) also provide sufficient evidence for the phenomenon, indicating that the diameter of diatom remains are mostly less than 10 μm (Figure 11A), and adding cement to diatomite changes the structure of soil and increases the number of pores with diameters ranging from 0.01 um to 0.4 um, (Figure 11B), which are classified as inter-granular pores according to the pore classification proposed by Shear et al. (1993).

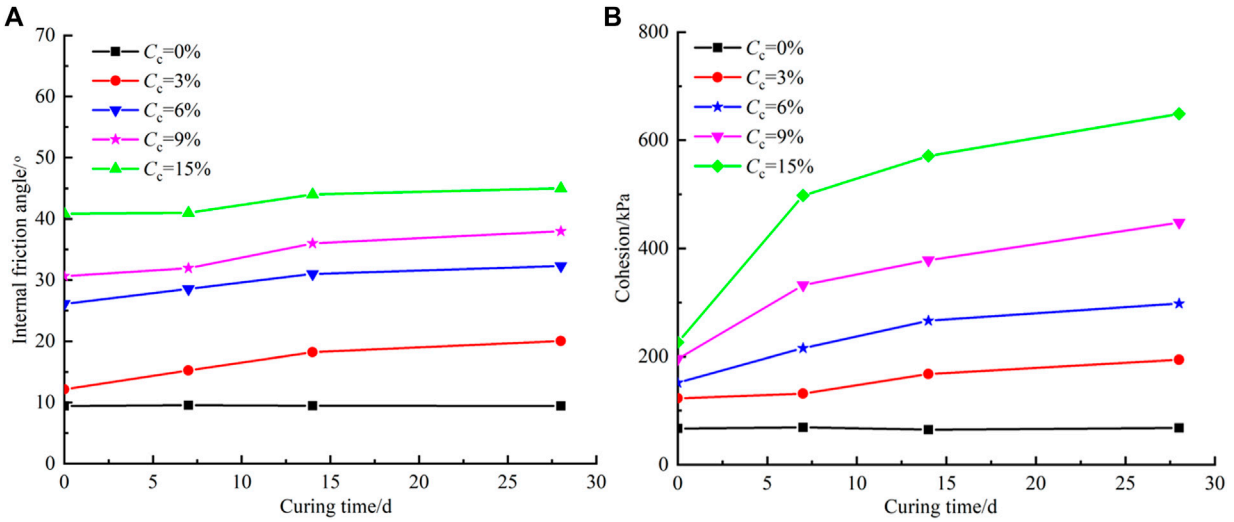

FIGURE 8
Shear strength parameters vs. cure time.

Discussion

The above research results show that adding cement to diatomite can significantly reduce its compressibility and increases its strength. For adding cement can change the structure of pure diatomite and form more tiny pores between cement and diatomite, and the number of pores stabilizes when the cement content reaches 9%, then with the increase of cement content, the total porosity is basically unchanged, but the number of micropores has been increased.

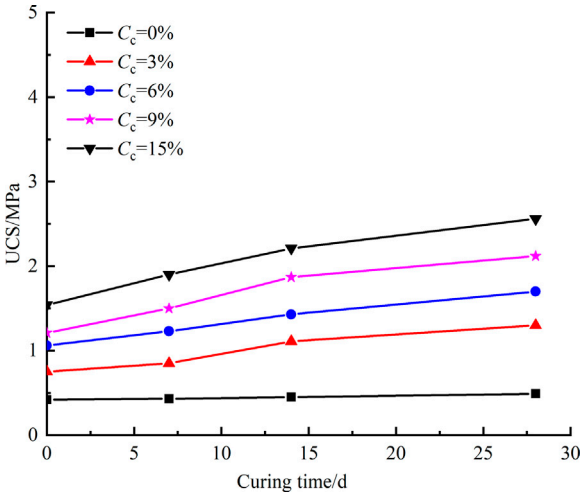

FIGURE 9
Unconfined Compressive Strength vs. cure time.

However, curing can reduce the number of pores, with the growth of cure period, the total pore number of sample decreases (Figure 10B), and at the curing age of 7 days, the void ratio of the sample is 0.59, which is lower than that of pure diatomite (Figure 10A). the missing pores are mainly in the range of 0.01–0.1 um in diameter, and the number of pores with diameters of 0.1um–0.4 um also decreases (Figure 10D). These results also can be verified by SEM (Figure 11C), When the curing period is 28 days, the tiny pores in the sample of cement-modified diatomite are significantly reduced and the sample presents a condensed structure, which is more dense than that of pure diatomite.

Cement can improve soil properties through a series of physical-chemical reactions including hydrolysis and hydration. The main composition of cement is silicate, including tricalcium silicate ($3CaO{\cdot}SiO_2$), dicalcium silicate ($2CaO{\cdot}SiO_2$), tricalcium aluminate ($3CaOAl_2O_3$), etc. When diatomite is mixed with cement and water, the hydration reaction occurs rapidly, forming hydrates such as hydrated calcium silicate ($xCaOSiO_2{\cdot}nH_2O$) and calcium hydroxide ($Ca(OH)_2$). Then $Ca(HO)_2$ diffuses to the surface of diatomite particles and gradually eroded the active CaO, Al_2O_3 and Fe_2O_3 to generate hydrated calcium silicate ($xCaOAl_2O_3nH_2O$), hydrated calcium aluminate ($xCaOAl_2O_3yCaO_3nH_2O$) and hydrated calcium ferrite ($xCaOFe_2O_3nH_2O$).

It can be seen from the XRD spectrums of diatomite and 15% cement-stabilized diatomite with curing period of 0 and 28 days (Figure 12), after the addition of 15% cement, calcite content as well as sodium aluminosilicate and calcium aluminosilicate minerals increased significantly. At the curing period of 28 days, the contents of odium aluminosilicate and calcium aluminosilicate minerals in diatomite with cement content of 15% are increased, indicating that with the growth of curing

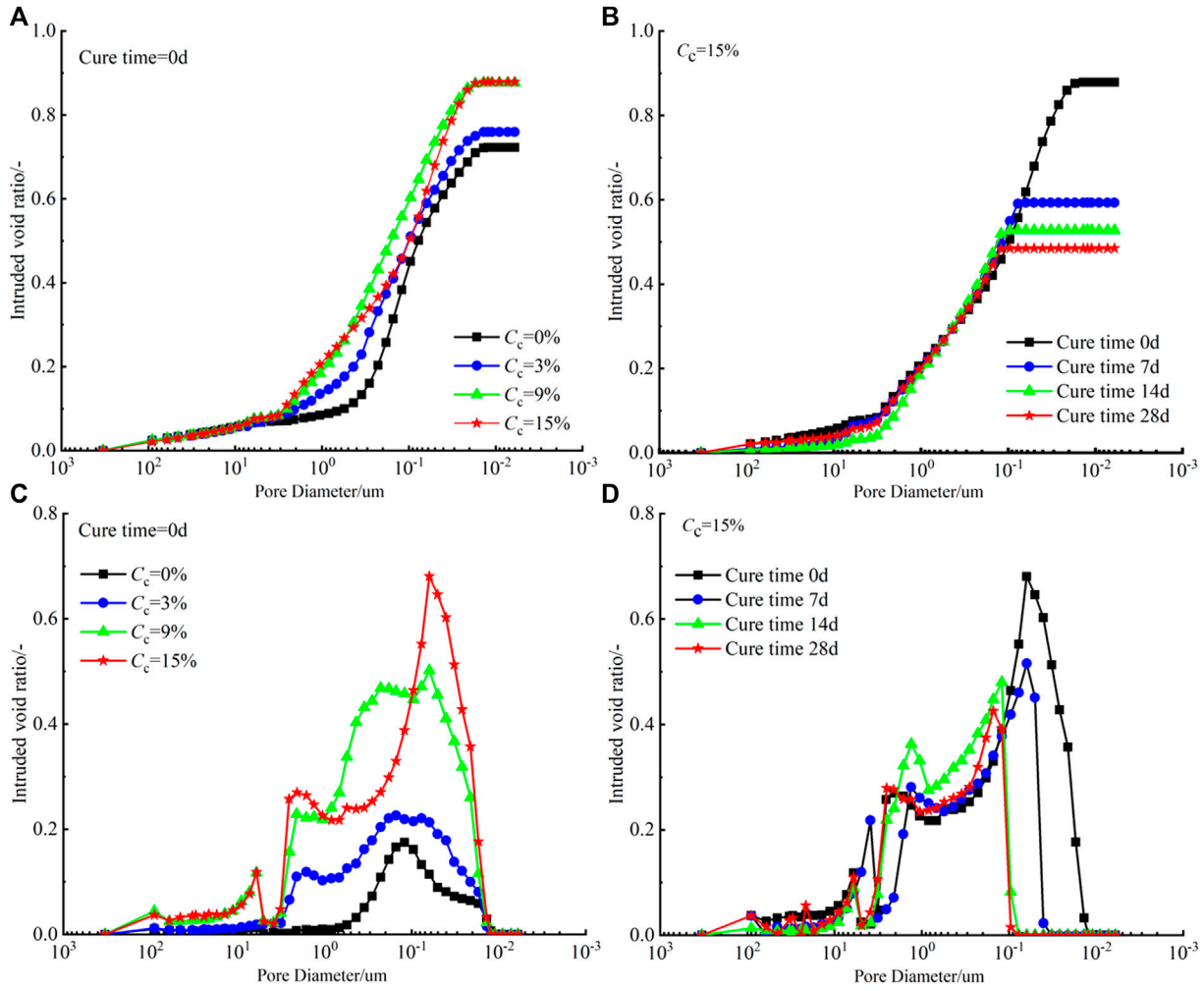

FIGURE 10
Cumulative and pore size distribution curves of cement modified diatomite.

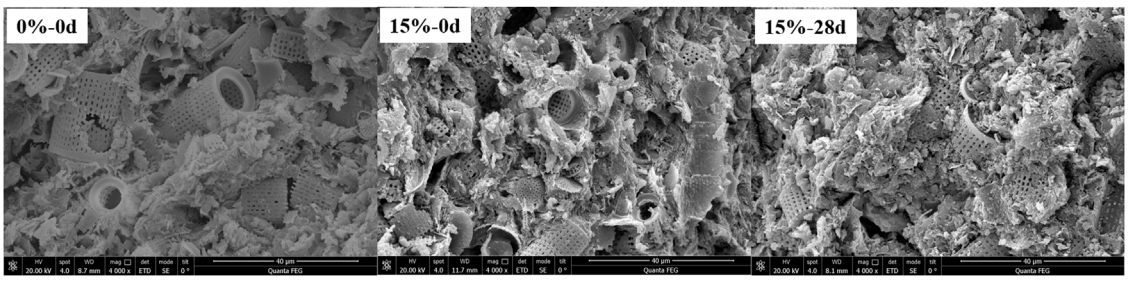

FIGURE 11
SEM of cement modified diatomite.

period, hydration reactions in cement-stabilized diatomite soils develop continuously and more hydrates are generated. These hydrates connect to the particles and filled the void and continues to harden to form the skeleton of cement stone with high strength, while the aggregate of soil is similar to the concrete, which increases the strength of diatomite.

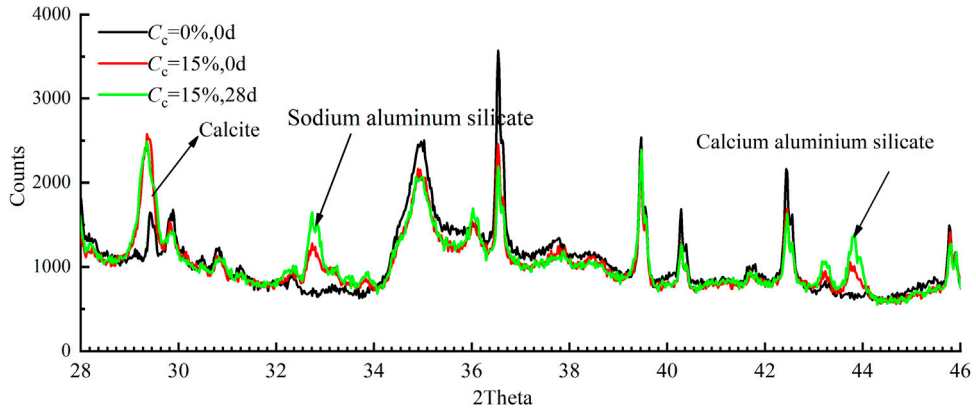

FIGURE 12
XRD spectrums of cement modified diatomite.

Conclusion

The microstructure of remolded diatomite is changed, and thus its engineering properties is affected. The purpose of this paper is to find out the changes of engineering properties of remolded diatomite compared with undisturbed diatomite, study the engineering properties and microstructure of cement modified diatomite by adding different proportions of cement into diatomite. The following conclusions are drawn from the present study.

1 Compared with undisturbed diatomite, the compression coefficient of remolded diatomite is increased by 51.2%; while the values of cohesion, internal friction angle and UCS are reduced by 52.94%, 56.74% and 57.14% respectively; the value of the maximal expansion force is very low and basically unchanged.
2 Adding cement to diatomite makes the pore ratio no longer decrease obviously with the increase of load, and makes the stress-strain curve of samples gradually change from strain hardening to strain softening. With the increase of cement content, both cohesion and internal friction angle increase, and the value of *UCS* increases exponentially while compression coefficient $a_{1\text{-}2}$ decreases exponentially.
3 Curing can improve the internal friction angle of cement stabilized diatomite, but the effect is not very obvious, only the sample with cement content of 3% has a relatively obvious improvement. However, the values of cohesion and *UCS* are significantly improved with the increase of curing time, and the strength improvement is mainly reflected in the early curing stage, the curing effect on the sample with higher cement content is more significant.
4 Adding cement to diatomite changes the structure of pure diatomite, forms more tiny pores between cement and diatomite and increases the total pore number of the sample; while with the increase of curing period, the total pore number of sample decreases.
5 Adding cement to diatomite increases the amount of calcite content, sodium aluminosilicate and calcium aluminosilicate minerals, and curing also increases the contents of odium aluminosilicate and calcium aluminosilicate minerals in diatomite with 15% cement content.

Data availability statement

The original contributions presented in the study are included in the article/supplementary material, further inquiries can be directed to the corresponding author.

Author contributions

SC, ZT, and YZ contributed to conception and design of the study. ZT, YZ, HS, and YJ performed the experiments and statistical analysis. SC performed the theoretical analysis, ZT wrote the first draft of the manuscript. YZ, HS, and YJ wrote sections of the manuscript. All authors contributed to manuscript revision, read, and approved the submitted version.

Funding

Stabilization Support program by Department of Geology, Northwestern University.

Conflict of interest

ZT was employed by the Xi'an Aerospace Construction Supervision Limited Company.

The remaining authors declare that the research was conducted in the absence of any commercial or financial relationships that could be construed as a potential conflict of interest.

Publisher's note

References

Cai, Y., Xu, L., Liu, W., Shang, Y., Su, N., and Feng, D. (2020). Field Test Study on the dynamic response of the cement-improved expansive soil subgrade of a heavy-haul railway. *Soil Dyn. Earthq. Eng.* 128, 105878. doi:10.1016/j.soildyn.2019.105878

Calvo, J. P., Triantaphyllou, M. V., Regueiro, M., and Stamatakis, M. G. (2012). Alternating diatomaceous and volcaniclastic deposits in milos island, Greece. A contribution to the upper pliocene-lower pleistocene stratigraphy of the aegean sea. *Palaeogeogr. Palaeoclimatol. Palaeoecol.* 321-322, 24–40. doi:10.1016/j.palaeo.2012.01.013

Cui, S. L., Zhang, H. Y., and Zhang, M. (2012). Swelling characteristics of compacted GMZ bentonite–sand mixtures as a buffer/backfill material in China. *Eng. Geol.* 141-142, 65–73. doi:10.1016/j.enggeo.2012.05.004

Cui, S., Xie, W., Wang, J., and Huang, S. (2019b). Engineering properties of collapsible loess stabilized by cement kiln dust. *Soil Mech. Found. Eng.* 56 (5), 328–335. doi:10.1007/s11204-019-09610-w

Cui, Y. (2008). *China non-metallic industry*. Beijing: Geological Publishing House, 138–142.

CuiWang, S, J., Huang, S., and Xie, W. (2019a). Coupled effects of saline solutions and temperature on the swelling deformation property of GMZ bentonite-sand mixtures. *Soils Found.* 59 (5), 1417–1427. doi:10.1016/j.sandf.2019.06.006

Day, R. B. (1995). Engineering properties of diatomaceous fill. *J. Geotech. Engrg.* 121, 908–910. doi:10.1061/(asce)0733-9410(1995)121:12(908)

Fragoulis, D., Stamatakis, M. G., Papageorgiou, D., and Chaniotakis, E. (2005). The physical and mechanical properties of composite cements manufactured with calcareous and clayey Greek diatomite mixtures. *Cem. Concr. Compos.* 27, 205–209. doi:10.1016/j.cemconcomp.2004.02.008

Harben, P. W. (2002). "Diatomite. The industrial minerals handbook," in *A guide to markets, specifications and prices*. 4th Ed. (Surrey UK: IMI, Publication), 118–122.

Ho, L. S., Nakarai, K., Duc, M., Kouby, A. L., Maachi, A., and Sasaki, T. (2018). Analysis of strength development in cement-treated soils under different curing conditions through microstructural and chemical investigations. *Constr. Build. Mat.* 166, 634–646. doi:10.1016/j.conbuildmat.2018.01.112

Ho, L. S., Nakarai, K., Ogawa, Y., Sasaki, T., and Morioka, M. (2017). Strength development of cement-treated soils: Effects of water content, carbonation, and pozzolanic reaction under drying curing condition. *Constr. Build. Mat.* 134, 703–712. doi:10.1016/j.conbuildmat.2016.12.065

Hong, Z. S., Tateishi, Y., and Deng, Y. F. (2004a). Relationship between entrance pore distribution and stress level of natural sedimentary diatomaceous soil. *Rock Soil Mech.* 25, 1023–1026. (in Chinese with English abstract). doi:10.1007/BF02911033

Hong, Z. S., Yoshitaka, T., and Han, J. (2006). Experimental study of macro-and micro-behavior of natural diatomite. *J. Geotech. Geoenviron. Eng.* 132 (5), 603–610. doi:10.1061/(asce)1090-0241(2006)132:5(603)

Koizumi, I., Sato, M., and Matoba, Y. (2009). Age and significance of Miocene diatoms and diatomaceous sediments from northeast Japan. *Palaeogeogr. Palaeoclimatol. Palaeoecol.* 272 (1-2), 85–98. doi:10.1016/j.palaeo.2008.11.007

Lemaire, K., Demeele, D., Bonnet, S., and Legret, M. (2013). Effects of lime and cement treatment on the physicochemical, microstructural and mechanical characteristics of a plastic silt. *Eng. Geol.* 166, 255–261. doi:10.1016/j.enggeo.2013.09.012

Liu, Ya, Qiu, Haijun, Yang, Dongdong, Liu, Zijing, Ma, Shuyue, Pei, Pei Yanqian, et al. (2022). Deformation responses of landslides to seasonal rainfall based on InSAR and wavelet analysis. *Landslides* 19, 199–210. doi:10.1007/s10346-021-01785-4

Ma, Shuyue, Qiu, Haijun, Hu, Sheng, Yang, Dongdong, and Liu, Zijing (2021). Characteristics and geomorphology change detection analysis of the Jiangdingya landslide on July 12, 2018, China. *Landslides* 18, 383–396. doi:10.1007/s10346-020-01530-3

Mengue, E., Mroueh, H., Lancelot, L., and Eko, R. M. (2017). Physicochemical and consolidation properties of compacted lateritic soil treated with cement. *Soils Found.* 57 (1), 60–79. doi:10.1016/j.sandf.2017.01.005

Qian, W. (2016). Liquefaction behavior and mechanism of the cement-stabilized loess. *Chin. J. Geotechnical Eng.* 11, 2129–2134. doi:10.1061/(ASCE)GT.1943-5606.0002638

Qiu, H., Zhu, Y., Zhou, W., Sun, H., He, J., and Liu, Z. (2022). Influence of DEM resolution on landslide simulation performance based on the Scoops3D model. *Geomatics, Natural Hazards and Risk.* 13 (1), 1663–1681.

Sariosseiri, F., and Muhunthan, B. (2009). Effect of cement treatment on geotechnical properties of some Washington State soils. *Eng. Geol.* 104, 119–125. doi:10.1016/j.enggeo.2008.09.003

Shear, M. K., Cooper, A. M., Klerman, G. L., Busch, F. N., and Shapiro, T. (1993). A psychodynamic model of panic disorder. *Am. J. Psychiatry* 150, 859–866. doi:10.1176/ajp.150.6.859

Stoemer, F., and Smoll, J. P. (2001). *The diatoms: Applications for the environmental and earth science*. Cambridge: Cambridge University Press, 482.

Tateishi, Y. (1997). *Geotechnical properties of diatom earth and stability of surface layer for the cut slope*. spain: Doctoral Thesis Saga University.

Van Garderen, N., Frank, J. C., Matheus, M., Bergmann, C. P., and Graule, T. (2011). Investigation of clay content and sintering temperature on attrition resistance of highly porous diatomite based material. *Appl. Clay Sci.* 52, 115–121. doi:10.1016/j.clay.2011.02.008

Washburn, E. W. (1921). Note on a method of determining the distribution of pore sizes in a porous material. *Proc. Natl. Acad. Sci. U. S. A.* 7 (4), 115–116. doi:10.1073/pnas.7.4.115

Wang, L., Qiu, H., Zhou, W., Zhu, Y., Liu, Z., Ma, S., et al. (2022). The post-failure spatiotemporal deformation of certain translational landslides may follow the pre-failure pattern. *Remote Sensing* 14, 2333.

Wu, J., Deng, Y., Zheng, X., Cui, Y., Zhao, Z., Chen, Y., et al. (2019). Hydraulic conductivity and strength of foamed cement-stabilized marine clay. *Constr. Build. Mat.* 222, 688–698. doi:10.1016/j.conbuildmat.2019.06.164

Yang, Dongdong, Qiu, Haijun, Ma, Shuyue, Liu, Zijing, Du, Chi, Zhu, Yaru, et al. (2022). Slow surface subsidence and its impact on shallow loess landslides in a coal mining area. *CATENA* 209, 105830. doi:10.1016/j.catena.2021.105830

Zhang, Y. S., Guo, C., Yao, X., Qu, Y., and Zhou, N. (2013). Engineering geological characterization of clayey diatomaceous Earth deposits encountered in highway projects in the Tengchong region, Yunnan, China. *Eng. Geol.* 167, 95–104. doi:10.1016/j.enggeo.2013.10.009

Zhou, Wenqi, Qiu, Haijun, Wang, Luyao, Pei, Yanqian, Tang, Bingzhe, Ma, Shuyue, et al. (2022). Combining rainfall-induced shallow landslides and subsequent debris flows for hazard chain prediction. *CATENA* 213, 106199. doi:10.1016/j.catena.2022.106199

frontiers | Frontiers in Earth Science

TYPE Original Research
PUBLISHED 07 September 2022
DOI 10.3389/feart.2022.990012

OPEN ACCESS

EDITED BY
Wen Nie,
Jiangxi University of Science and Technology, China

REVIEWED BY
Shui-Hua Jiang,
Nanchang University, China
Danqing Song,
Tsinghua University, China

*CORRESPONDENCE
Hengyu Su,
Suhygzmd@163.com

SPECIALTY SECTION
This article was submitted to Geohazards and Georisks, a section of the journal Frontiers in Earth Science

RECEIVED 09 July 2022
ACCEPTED 17 August 2022
PUBLISHED 07 September 2022

CITATION
Su H and Ma S (2022), Study on the stability of high and steep slopes under deep bench blasting vibration in open-pit mines.
Front. Earth Sci. 10:990012.
doi: 10.3389/feart.2022.990012

Study on the stability of high and steep slopes under deep bench blasting vibration in open-pit mines

Hengyu Su[1]* and Shu Ma[2,3]

[1]School of Architectural Engineering, Guizhou University for Nationalities, Guiyang, China, [2]Guizhou Energy Industry Research Institute Co, Ltd, Guiyang, China, [3]School of Safety Engineering, China University of Mining and Technology, Xuzhou, China

In order to study the stability of the high and steep slope of an open-pit mine under deep bench blasting vibration, a mine in Inner Mongolia is taken as the engineering background, and the mechanical parameters of rock samples were determined based on uniaxial and triaxial instruments. The stability of the high and steep slope of the open-pit mine under static and dynamic loads was analyzed by using field vibration monitoring and numerical simulation methods. The results show that the vibration range of the vibration wave is -1.25–1.25 cm/s, and the vibration wave shows a gradual attenuation trend. The Sadovsky regression equation was used to analyze and fit the monitoring data and the corresponding regression equations in each direction were obtained. Under static action, the safety factor of the high and steep slope is 1.20, and the displacement of the sliding zone passing through the slope is small, so the slope stability is good. Under the action of dynamic blasting load, the overall displacement of the slope is small, and the change of displacement decreases with the decrease of the vibration wave.

KEYWORDS

blast vibration, field monitoring, high and steep slopes, numerical simulation, stability

1 Introduction

Metal mineral resources are the basis for human survival and development. With the continuous progress of the industry, more and more metal minerals have been mined, among which metal open-pit mining accounts for a large proportion (Song et al., 2021a). Taking China as an example, the proportion of open-pit mining in metal mining is as high as 90% (Yang et al., 2011; Wang et al., 2013; Lv et al., 2019). With the continuous development and utilization of shallow surface resources, deep open-pit mining has become the trend of open-pit mining development in the world. In the process of deep mining, with the increase of mining depth, the safety and stability of the slope are getting worse and worse. However, for deep-pit mines, increasing slope angle and implementing fine blasting are important means to reduce mining costs and improve economic benefits. Blasting production has been used in mine production as a relatively mature production method and a relatively wide range of production processes. However, the vibration effect

generated by the blasting operation has a certain impact on the stability of the slope. Therefore, it is of great theoretical and practical significance to carry out research on the stability of high and steep slopes in deep concave open-pit mines under the action of blasting vibration to prevent and control geological disasters caused by high slopes and improve the economic benefits of mines (Du et al., 2020; Song et al., 2021b).

In recent years, scholars at home and abroad have conducted numerous studies on slope stability under the action of blasting. Chong et al. (2018) established a numerical model of the slope with a smooth step using FLAC3D, analyzed the vibration response law of the slope under the action of blasting vibration, and formulated the safety threshold of blasting vibration. Ming et al. (2012) established a slope vibration model under the action of blasting seismic waves and obtained the slope dynamic response under the action of different blasting frequencies using modal analysis and harmonic response analysis. Hoang et al. (2021) studied three intelligent hybrid models based on different nature-inspired optimization algorithms and deep neural networks to predict GV and proposed a deep neural network model based on deep learning techniques. Ke et al. (2021) proposed an intelligent prediction model for GVI based on the hybridization of self-encoder neural network and support vector machine regression (SVR). A total of nine input variables were used to estimate GVI: borehole diameter, step height, borehole length, batching, spacing, hardness factor, powder factor, the maximum explosive charge per extension, and monitoring distance. Sun et al. (2021) proposed a Bayesian method for predicting blast damage on highly rocky slopes using vibration and acoustic data and established the relationship between blast damage and intrinsic frequency of rock mass for the first time. Xuan-Nam et al. (2021) proposed a cuckoo search optimization model based on an artificial neural network based on 118 blasting events collected from a quarry in Vietnam. Bazzi et al. (2020) investigated the effect of blasting vibration on slope stability using the finite element analysis method. Pit slopes containing faults were examined under the action of seismic loads caused by successive blasts of different intensities. Wu et al. (2020) took the high and steep slope of the Daye iron ore mine as an example and used shaking table tests, the limit equilibrium theory, and the least squares method to better evaluate the stability of slopes under repeated blasting vibrations in fracture zones. Based on the limit equilibrium theory and shaking table test data, the stability of slopes under different. Yin et al. (2018) analyzed the energy distribution of blast vibration signals by peak mass velocity (PPV), frequency characteristics, and time-frequency processing method using different rock blast vibration signals monitored at a blasting site.

In the past, domestic and foreign scholars used theoretical research, physical test, numerical simulation, mathematical model, and other research methods to study the slope stability under blasting vibration, but there are few studies on the stability of high and steep slopes in open-pit mines under blasting. With the development of blasting technology and the increase in mining depth, most mines enter the deep mining stage. The exposed area of the slope becomes larger, the slope stability is poor, and the blasting vibration plays a major role in the slope instability. Therefore, the analysis of the influence of deep bench blasting vibration on the stability of high and steep slopes in open-pit mines has become an urgent problem to be solved in deep mining blasting. Taking the high and steep slope of a mine in Inner Mongolia as the engineering background, this work studies the stability of the high and steep slope under blasting vibration by using the methods of physical test, field monitoring, and numerical simulation, to ensure the safe production efficiency of the mine and the life and property safety of the staff in the quarry and provide some reference for similar projects.

2 Project overview

This high steep-sided metal open-pit mine is located in the central region of Inner Mongolia and is a Cenozoic Tertiary outcrop located at the northern edge of the Inner Mongolia geotechnical axis. The strata in the area are strongly wrinkled and metamorphosed and fractures are developed. The type of engineering geological exploration in the mine area is type II, category II: medium engineering geological conditions, with hard and semi-hard metamorphic rocks as the main block rock deposits. The topography and geomorphology are simple, the terrain is conducive to natural drainage, and the lithology of the strata is relatively single. There are no large tectonic fracture zones in the mine area, the fractures are filled by fault breccias, and the contact fracture zones and weathering zones are not developed, so the geological structure is simple. The rock structure is mainly blocky, with high rock strength and an open mining area, and the stability of the slope becomes more complicated with the increase of mining depth. The mine's east quarry is nearly elliptical in shape, with an east-west length of 1.43 km and a width of 1.06 km, covering an area of 3.213 km^2. The east quarry has been mined for more than 50 years, with an overall slope of 43°–39°, a design end slope depth of 1,230 m, and a final average slope height of 372 m. The geographic location and geomorphology of the mine are shown in Figure 1.

3 Determination of mechanical parameters

The rock and ore specimens were collected from the field and processed into suitable specimens at a later stage, mainly for rock gravity density, uniaxial compression deformation, tensile strength, rock shear resistance at variable angles, and rock structural surface straight shear tests. The field collection area

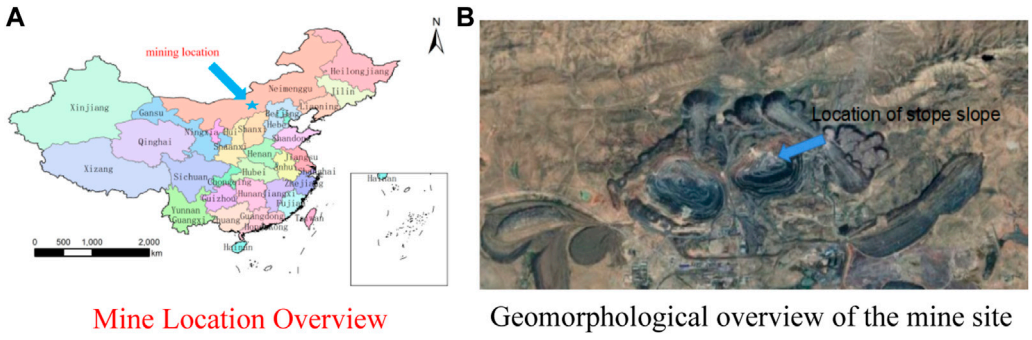

FIGURE 1
Schematic diagram of the location of the mine.

FIGURE 2
Field acquisition.

is reasonably distributed in all levels of steps as far as possible under safety conditions. The collected rock samples include slate, dolomite, and iron ore, in addition to some weak structural interview samples. Pictures of the field collection are shown in Figure 2. The rock samples collected from the mine site were processed to meet the test requirements by using a TY-450 sawing machine with high processing accuracy and other types of stone grinding machines according to the relevant regulations to meet the experimental requirements. Figure 3 1) shows the large sample of mineral rock to be processed and Figure 3 2) shows the sample under processing. The specimen specifications are as follows: uniaxial compressive and bi-directional strain test: 50mm×50mm×100mm; triaxial shear test: Φ50×100. No artificial fissures were allowed to appear during the specimen preparation. According to the accuracy of specimen production, the error of specimen edge length should be less than 0.03 cm, and the parallel error of the upper and lower opposing surfaces of the specimen must be less

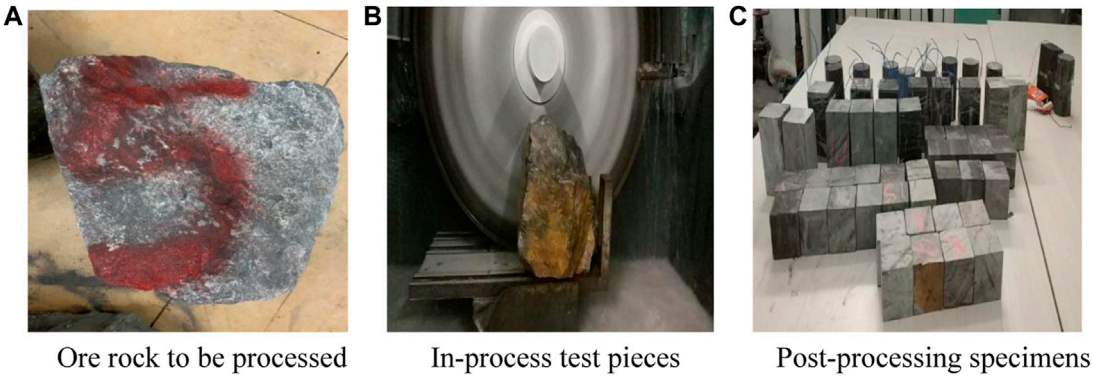

FIGURE 3
Machining process of the test piece.

TABLE 1 Statistical table of apparent density measurement results of mineral rocks.

Statistical item	Sample size, N	Average, X	Standard deviation, S	Coefficient of variation, δ	Correction coefficient	Standard value, xa
		(kg/m^3)		δ=S/X		(kg/m^3)
Iron ore	6	37.1	0.09	0.02	0.980	36.4
Dolomite	6	29.8	0.06	0.02	0.983	29.3
Mica rock	6	30.1	0.05	0.02	0.986	29.7
Feldspar–slate	6	29.3	0.07	0.02	0.980	28.7

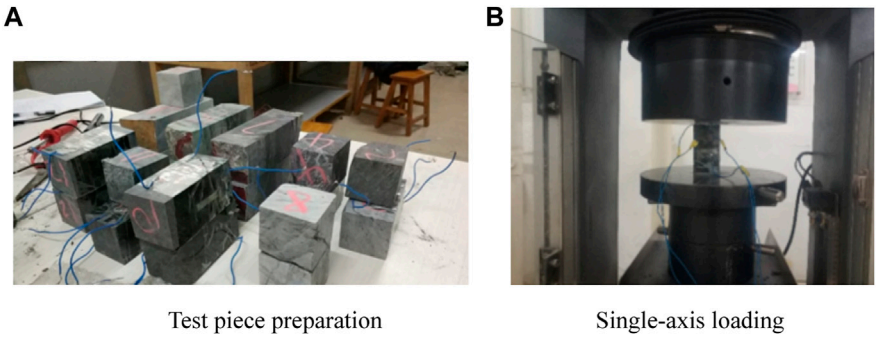

FIGURE 4
Uniaxial compressive test procedure for mineral rock specimens.

than 0.05 mm; the adjacent two sides of the specimen should be less than 0.25° perpendicular to each other; the same is true for the perpendicularity of the specimen end face and axis, and the processing accuracy of all specimens reached the specified standard.

The density determination test focused on determining the apparent density of the ore and rock and the sample used was the sample for determining the uniaxial shear strength, which was carried out before the determination of uniaxial shear strength and its deformation parameters (Sugiyama et al., 2021; Zingano et al., 2021; Anderson et al., 2022). The results of the measurements are presented in Table 1, and according to the test results, the density of iron ore is 3.64 g/cm^3, the density of dolomite is 2.93 g/cm^3, the density of mica rock is 2.97 g/cm^3, and the density of feldspar–slate is 2.87 g/cm^3.

The uniaxial compressive strength experiment uses the apparatus including a WANCE-106 type electronic universal testing machine and digital static strain gauge. The principle of determination is by the ratio of the maximum load to the loaded area when the specimen is compressed by longitudinal load only and damage occurs without restriction around; the value is numerically made the uniaxial compressive strength of the specimen. Longitudinal and transverse resistance strain gauges were applied to each specimen, as shown in Figure 4A. During the experiment, the loading speed was set to 0.5 MPa/s, and the maximum load from the beginning of the experiment to the time of damage to the specimen was recorded, as shown in Figure 4B. The experimental results are shown in Table 2. According to the uniaxial compressive strength test, the uniaxial compressive strength, elastic modulus, and Poisson's ratio of iron ore were 185.57 MPa, 7.4×104 MPa, and 0.24, respectively; the uniaxial compressive strength, elastic modulus, and Poisson's ratio of dolomite were 120.96 MPa, 7.34×104 MPa, and 0.22, respectively. The uniaxial compressive strength, elastic modulus, and Poisson's ratio of mica rock were 50.64 MPa, 5.49×104 MPa, and 0.22, respectively; the uniaxial compressive strength, elastic modulus, and Poisson's ratio of feldspar–slate were 128.61 MPa, 9.56×104 MPa, and 0.25, respectively.

In order to make the test conditions close to the three-way stress state that the rock is subjected to, the equipment used in this experiment is a triaxial press. The specimens were subjected to a lateral envelope pressure of $\sigma_2 = \sigma_3$, and the triaxial press was loaded at a rate of 0.5–1.0 MPa/s loading σ_1 until complete shear failure of the specimens occurred. The shear damage of the rock specimen was consistent with the Moore strength criterion, and the angle between the damaged section and the maximum principal stress plane of the specimen was (45-φ/2)°. In this

TABLE 2 Test results of compressive strength of mineral rock specimens.

Statistical item		Sample size, *N*	Mean, X (MPa)	Standard deviation, S	Coefficient of variation, δ	Correction coefficient	Standard value, xa
					$\delta=S/X$		(MPa)
Iron ore	σ	30	187.35	5.62	0.03	0.991	185.57
	E		7.53	0.4	0.05	0.983	7.40
	μ		0.25	0.02	0.08	0.975	0.24
Dolomite	σ	30	122.2	3.93	0.03	0.990	120.96
	E		7.48	0.45	0.06	0.981	7.34
	μ		0.23	0.03	0.13	0.959	0.22
Mica rock	σ	30	51.89	3.95	0.08	0.976	50.64
	E		5.67	0.57	0.10	0.968	5.49
	μ		0.23	0.03	0.13	0.959	0.22
Feldspar slate	σ	30	131.86	10.26	0.08	0.975	128.61
	E		9.83	0.85	0.09	0.973	9.56
	μ		0.26	0.03	0.12	0.964	0.25

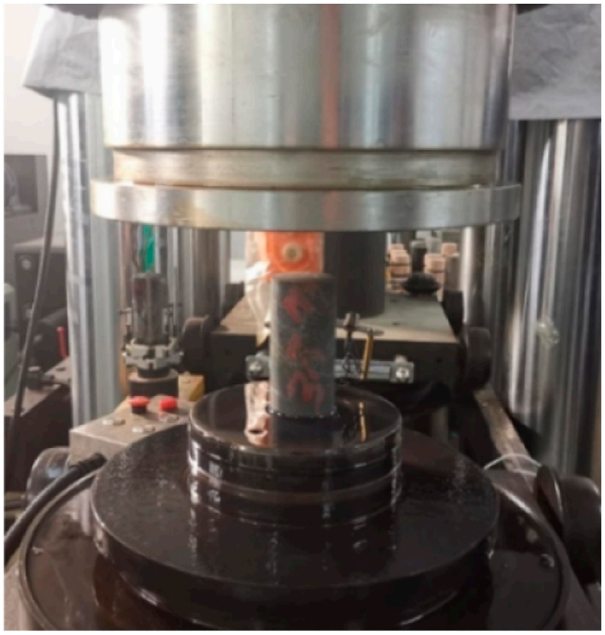

FIGURE 5
Triaxial shear test of mineral rock specimens.

experiment, the SAJS-2000 rock triaxial straight shear testing machine was used for the test and its experimental procedure is shown in Figure 5, and the triaxial shear strength results are shown in Table 3. According to the rock triaxial shear test, the cohesion and internal friction angle of dolomite were 17.61 MPa and 47.24°, respectively; the cohesion and internal friction angle of the feldspar–slate were 16.98 MPa and 44.31°, respectively.

4 On-site blast vibration monitoring

The blast vibration monitoring system is generally composed as shown in Figure 6, in which the most critical is the placement and selection of the pickups and vibrometers. The two together determine the accuracy of blasting seismic wave pickup and the reliability of the pickup date. The TC-4850 blasting monitoring system of Chengdu Zhongke measurement and control is used for this blasting slope monitoring (Afanasev and Makhmudov, 2021; Leng et al., 2021). The device is compact in size and easy to carry. With versatility, it can be matched with velocity and acceleration sensors to complete different testing requirements. The instrument has an adaptive range and can preview the value, frequency, and waveform information immediately after sampling, without the support of an external computer.

In the open-pit mine blasting monitoring, the monitoring results and the results processed by the attenuation formula and other analytical applications have a significant impact on the selection of measurement points. Based on the geological engineering of the slope of the open pit, the selection of measurement points is based on the following principles: in general, blast vibration monitoring points are to be arranged in the back of the measured blast area, to determine and evaluate the impact of blast vibration on the slope; according to the location of the blast area, selected different step heights and the same engineering geological state for the deployment of points, different step heights and geological conditions on the propagation of blast vibration waves also have a great impact. In the range near the blast area that is blasting seismic effects of the range of more measurement points, to determine the range of blasting vibration attenuation and propagation law; blasting

TABLE 3 Triaxial shear strength of rock specimens.

Statistical item		Sample size, N	Mean, X	Standard deviation, S	Coefficient of variation, δ	Correction factor	Standard value, xa
					$\delta=S/X$		
Dolomite	C	3	21.58	2.64	0.12	0.816	17.61
	φ		50.26	2.12	0.04	0.940	47.24
Feldspar slate	C	3	19.98	1.98	0.10	0.850	16.98
	φ		46.30	1.32	0.03	0.957	44.31

C is the bonding force, MPa; φ is the rock internal friction angle, °.

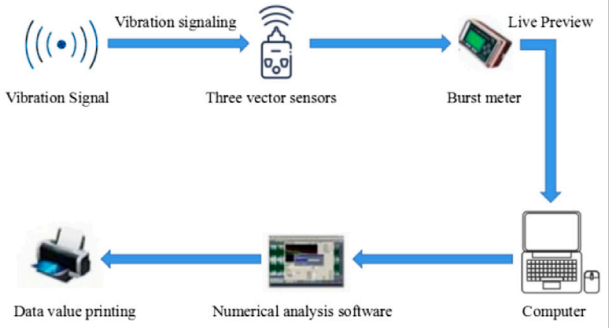

FIGURE 6
Blasting vibration monitoring system.

FIGURE 7
Blasting vibration measurement point arrangement.

measurement points are generally chosen to be laid out in a corresponding representative point and roughly linear with the blast center. The distance and location of the measurement points from the blast area are measured and calibrated with two southern industrial GPS data collectors GIStar710, and the blast vibration measurement points are shown in Figure 7. The blasting vibration monitoring of the high steep slope open-pit mine lasted for nearly 7 months, during which vibration monitoring was conducted for pre-cracking blasting and step blasting against the boundary, respectively. Before each blasting ban, the blasting area was surveyed, the location of the measurement points was set, the required parameters of the vibration measurement instrument were set, the mode was set to be triggered after the commissioning was completed, and the location of the measurement points was recorded. The management of the guard was obeyed, the monitoring instrument was retrieved after the blasting was completed, and the relevant data were exported in time for analysis and processing. Surface mine blasting vibration test by the sensor picks up a vibration; the recorder will be a large number of vibration data processing into a waveform time course curve with speed as the vertical axis and selected time as the horizontal axis. This curve is often called the random signal waveform of the vibration parameters. The waveform mainly reflects the blast vibration rate as the relevant information embodied, eliminating other irrelevant and redundant data, and it is used to reveal the decay law of blast vibration propagation; part of the data acquisition waveform diagram is shown in Figure 8.

Based on the regression analysis test data of slope vibration by boundary blasting, the Sadowski regression analysis was conducted on the measured vibration data using the one-dimensional linear regression method. An accurate analysis of the regression results was carried out, and the regression analysis results are shown in Table 4: K is the topographic coefficient, α is the blasting vibration decay coefficient, and r is the correlation coefficient. V is the particle vibration velocity, cm/s; Q is the maximum loading amount for one period, kg; R is the horizontal distance between the measuring point of step arrangement and the center of explosion area, m. The higher the absolute value of the correlation coefficient r is close to 1, the higher the correlation

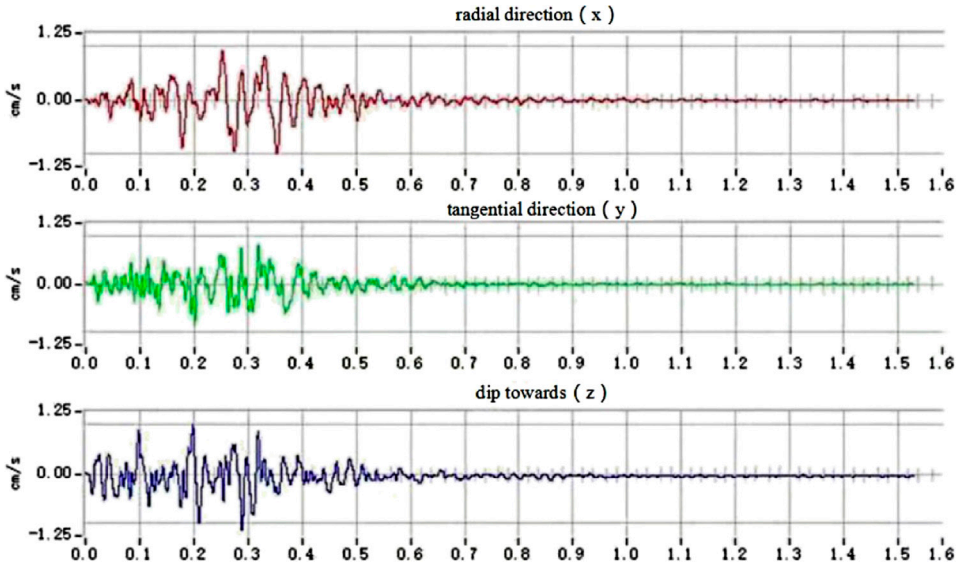

FIGURE 8
Blast vibration monitoring waveform.

TABLE 4 Results of regression analysis of measured vibration speed.

Direction	K	α	r	Resulting functional relationship
Horizontal radial	191.25	1.60	0.810	$V = 191.25(\frac{\sqrt[3]{Q}}{R})^{1.60}$
Horizontal tangential direction	105.68	1.57	0.912	$V = 105.68(\frac{\sqrt[3]{Q}}{R})^{1.57}$
Dip toward	212.55	1.66	0.856	$V = 212.55(\frac{\sqrt[3]{Q}}{R})^{1.66}$

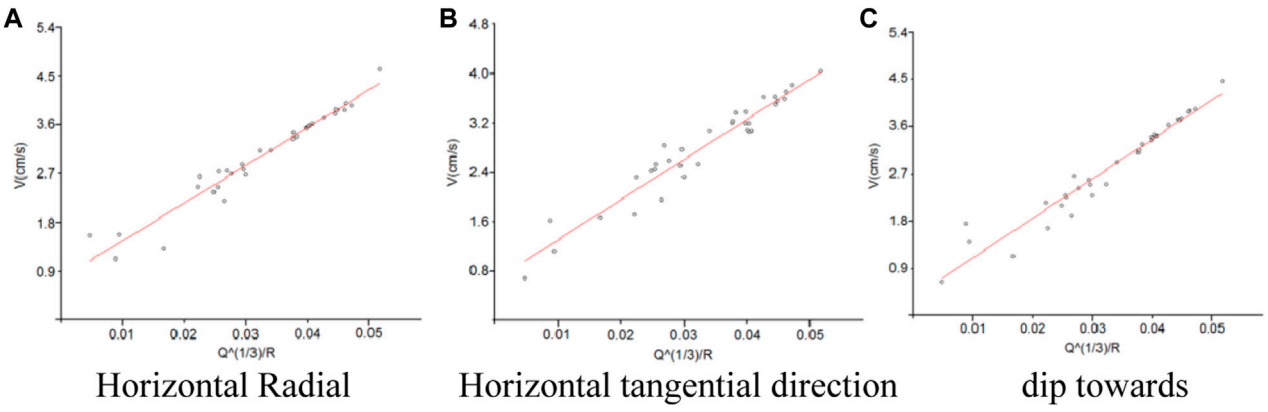

FIGURE 9
Regression curve of measured vibration speed of pre-cracking blasting.

TABLE 5 Results of regression analysis of measured vibration speed.

Direction	*K*	*α*	*r*	Resulting functional relationship
Horizontal radial	166.33	1.31	0.890	$V = 166.33(\frac{\sqrt[3]{Q}}{R})^{1.31}$
Horizontal tangential direction	259.81	1.87	0.865	$V = 259.81(\frac{\sqrt[3]{Q}}{R})^{1.87}$
Dip toward	240.47	1.61	0.832	$V = 240.47(\frac{\sqrt[3]{Q}}{R})^{1.61}$

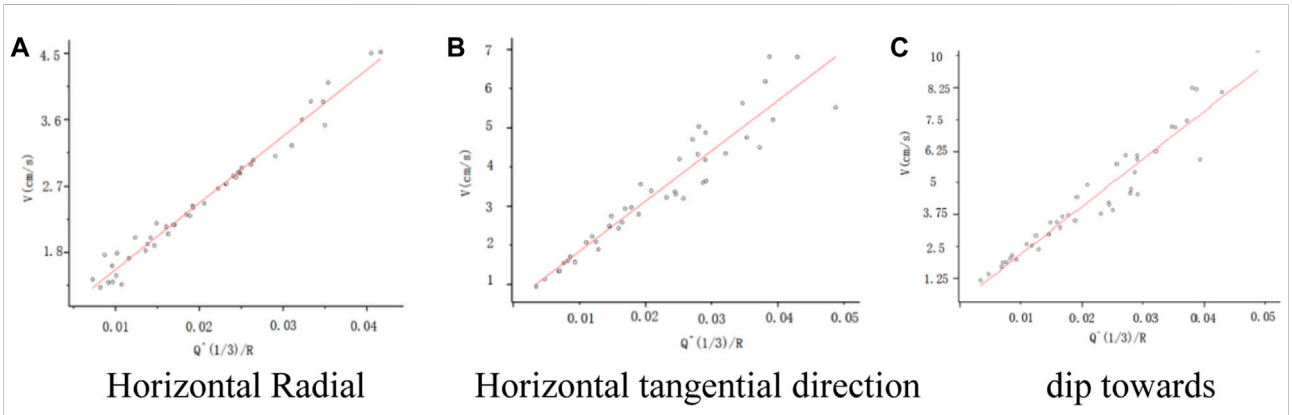

FIGURE 10
Regression curve of measured vibration velocity of step blasting.

is, and it is generally considered that the value of r is highly correlated when it is greater than 0.8. The regression curve of measured vibration velocity of pre-cracking blasting is shown in Figure 9. Based on the regression analysis test data of slope vibration of step blasting, the Sadowski regression analysis of measured vibration data was carried out by using the one-dimensional linear regression method through the formula, and the accuracy analysis was carried out by using the regression results. Regression analysis results are shown in Table 4, and the regression curve of measured vibration speed of pre-cracking blasting is shown in Figure 9. Regression analysis results are shown in Table 5, and the regression curves of the measured vibration velocity of pre-cracking blasting are shown in Figure 10. The correlation coefficient R is a close degree of evaluating the linear relationship, which measures the similarity between the regression analysis value and the real value. The value of R is greater than 0.8 and the closer it is to 1, the higher the degree of linear correlation. Combined with Figures 9–10 and tables 4–5, the correlation coefficient of velocity fitting results in three directions is greater than 0.8, which indicates that the vibration propagation formula has good applicability to the attenuation law of slope vibration under geological conditions. With the increase of blasting center distance, the vibration velocity of slope particles decreases continuously, and the influence of blasting center distance on blasting vibration velocity is much greater than that of elevation, indicating that the vibration measurement results have a certain reference value.

5 Numerical simulations

5.1 Strength discounting method and numerical modeling

The slope strength discount method refers to the slope with discounted slope anti-slip force that is shear strength just less than or equal to the shear force, and its slope reaches the critical damage state. The safety factor is the ratio of the discounted shear strength to the original shear strength at the critical damage strength. The calculation guideline of the strength reduction method is to apply Eqs. 1,2 to the slope rock strength: the bond force c and the friction angle are adjusted accordingly so that the slope model shows critical damage, and the safety factor Fs, which is the discount factor of the slope, is obtained at this time.

$$cF = c/F_{trial}, \quad (1)$$

$$\phi_F = \tan^{-1}\left((\tan\phi)F_{trial}\right). \quad (2)$$

In the formula, c is the bonding force, ϕ is the frictional force, $\mathbf{F_{trial}}$ is the discount factor, and c_F and ϕF are the discounted calculated bond force and friction angle, respectively.

In the calculation of strength reduction, there are two ways to judge the slope instability caused by strength reduction. One is that the plastic zone of the slope model is penetrated, and the other is that the calculation solution of the model is not convergent. 1) The coalescence of the plastic zone: with the decrease of slope strength, its shear capacity is continuously destroyed. Then the shear strain is produced and the plastic failure occurs. The shear strain extends from one free surface to another free surface until it is fully communicated, that is, the plastic zone is penetrating. At this time, it can be determined that the slope has been unstable. 2) The non-convergence of the solution: when the slope failure occurs, the instability part changes from static to dynamic, and the landslide also appears as unlimited displacement. In the numerical simulation, the judgment based on this phenomenon is that the ratio of displacement to the strain of the plastic failure surface with sliding displacement is not constant. At this time, the calculation program cannot find a solution that satisfies the equilibrium convergence for the static and stress–strain criteria at the same time and the slope failure is determined at this time. In the case of the natural slope only considering the self-weight effect, the safety system of the slope is calculated to find out the possible slip surface when the slope is damaged. At the same time, it also provides a basis for analyzing the influence of vibration on the slope under the following blasting dynamic loading conditions.

Numerical analysis software FLAC3D will be used to model the middle part of the south gang of the slope of this open-pit mine. The measured slope height of the south gang part of the slope is 372 m, and the final slope angle is 45°–47°. Most of the sloping rock is composed of slate, with some dolomite outcrops. The rock quality is good and there is no significant influence on the structural weakness. After years of mining, nearly 21 steps have been formed in the middle of the north gang, including three sweeping platforms, from the bottom to the upper boundary of the mine, in order of 1348 m horizontal sweeping platform, 1488 m horizontal sweeping platform, and 1544 m sweeping platform. The width of the sweeping platform is 30m, the width of the safety platform is 10 m, and the side slope angle is 75°; in the stage from 1348 m level to 1544 m level, the safety platform height is changed to 14 m and the side slope angle is still 75°; in the stage from 1544 m level to 1544 m level at the top of the slope, the platform height is 14 m and the side slope angle is 70°. The modeling uses AutoCAD to draw the slope model and then uses Rhino modeling software for 3D extrusion and mesh division. Based on the abovementioned information, the numerical analysis model is established. The Mohr–Coulomb model is selected for this slope model. The boundary constraints

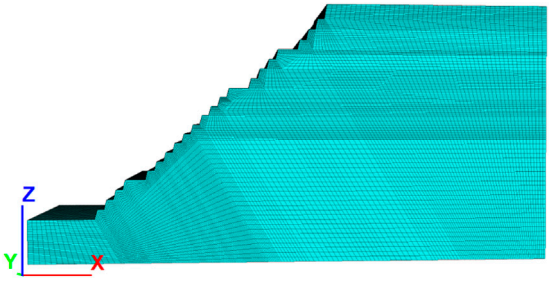

FIGURE 11
Side slope model.

of the model are set as follows: along the X-direction, the left and right boundaries are constrained, and displacement is allowed in the remaining two directions; along the Y-direction, the front and rear boundaries are constrained, and displacement is allowed in the remaining directions; along the Z-direction, displacement is restricted at the bottom of the model, and free displacement is allowed at the top of the slope. The final slope model is 800 m long, 200 m wide, and 372 m high, as shown in Figure 11.

5.2 Analysis of results

5.2.1 Static stability analysis of high and steep slopes

The destabilization of the high and steep slopes of the open-pit with damage phenomena such as sliding is associated with the creep rupture result of the shear slip zone formed by the shear force on the rock body with time steps, which in turn leads to the damage of the potential breakage zone with reduced strength unable to support the vertical gravity of its upper rock body. The slope stress and displacement clouds of this open-pit mine under self-weight conditions are shown in Figure 12. According to Figures 12 1) (b), it can be seen that the stress of the high steep slope under the influence of its gravity only appears at the maximum value at the foot of the slope, where the maximum horizontal stress is 8.7188e+04 MPa and the maximum vertical stress is 3.8691e+04 M Pa. According to the theoretical analysis, the gravity load calculation formula, where it is constant for the homogeneous continuous rock mass, the gravity load is proportional to the rock mass. Therefore, the gravity load is proportional to the height h of the rock mass, which is most influenced by the gravity load of the overlying rock layer, and the largest part of the high and steep slope is also pressurized at the foot of the slope. In the analysis of the safety of the numerically simulated slope, the slope displacement can be used as a parametric index to judge the stability of the slope. The magnitude of displacement at each node of the slope can measure whether the slope has been damaged there. As shown

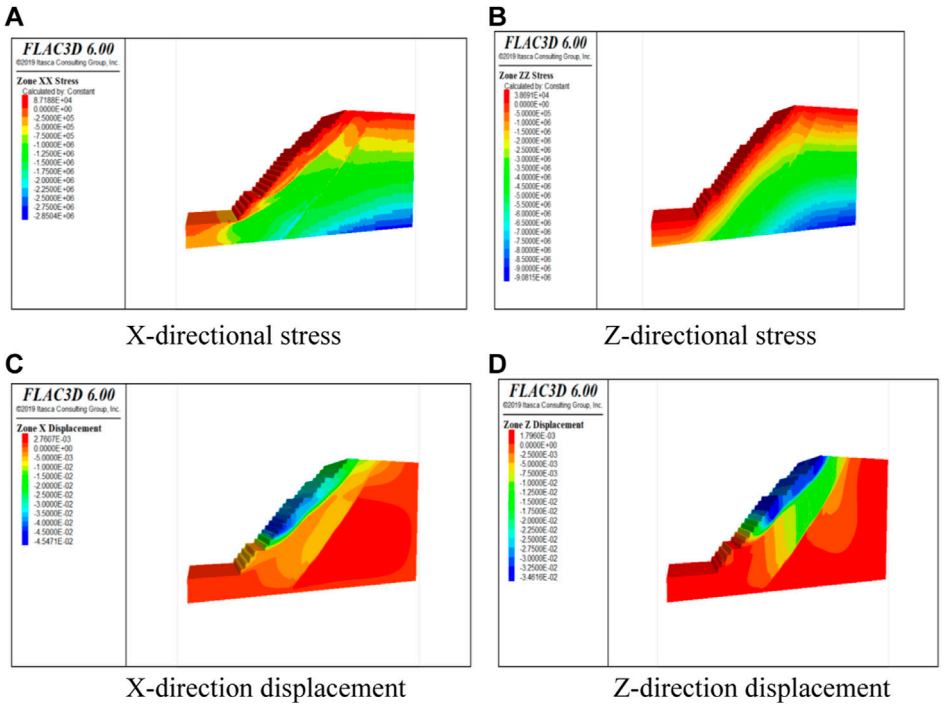

FIGURE 12
Stress and displacement clouds in *x* and *z* directions under self-weight conditions.

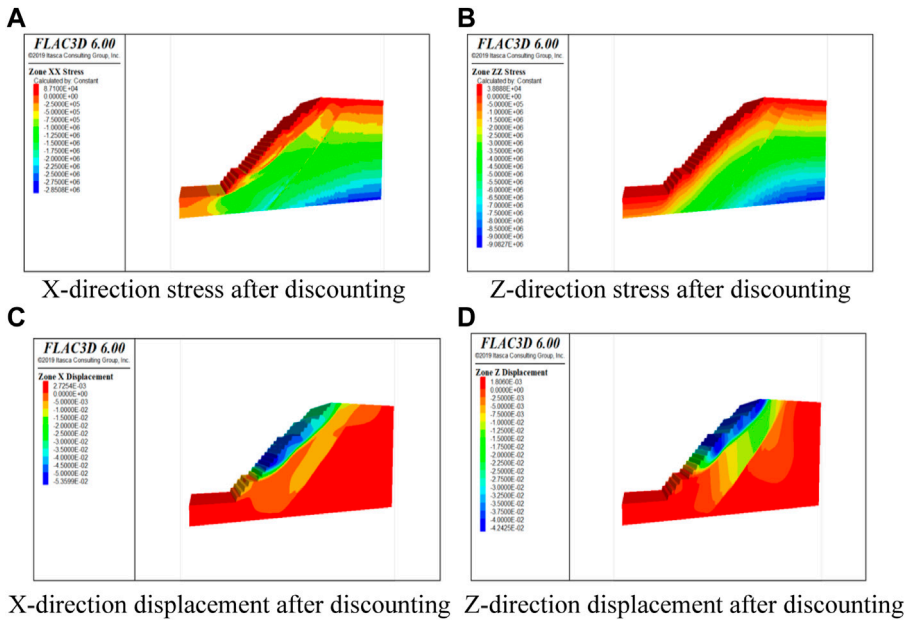

FIGURE 13
Stress and displacement clouds after strength discounting.

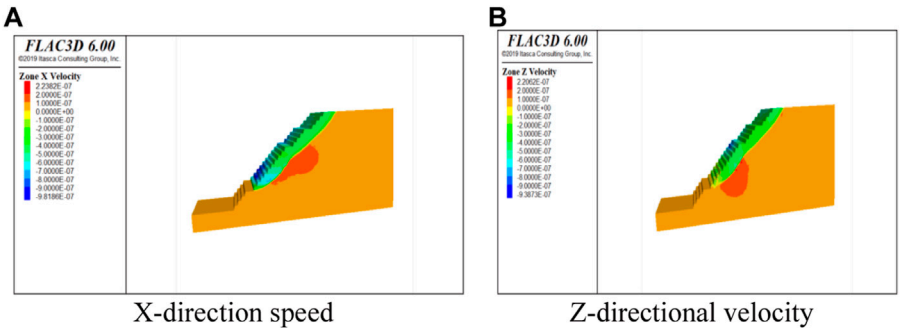

FIGURE 14
Velocity clouds in *x* and *z* directions after discounting slope strength.

in Figures 12C, D, the horizontal displacement cloud and vertical displacement cloud of the high and steep slope under self-weight, the largest negative displacement appears at the upper step of the bottom clearing platform, and the maximum displacement is -4.5471e-02 m. This is because the simulated amount of rock at this place is dolomite, whose mechanical strength is lower than the rest of the slate rock on the slope; the maximum horizontal positive displacement of the slope appears inside the slope with the value of 2.7607e-03 m, which is due to the gravitational settlement of the overlying rock slope. By observing the vertical displacement cloud, it can be concluded that the maximum negative displacement appears at the excavation of the slope, and the displacement located at the deep part of the slope is a small positive value, which is due to the settlement effect of the overlying rock on the slope under the self-weight of the slope. The result is consistent with the objective settlement law.

In the actual project, it is necessary to consider that the slope deformation of the open pit is mainly shear deformation and there is tensile damage, so the tensile strength should be discounted accordingly when discounting. In this study, the strength reduction factor is 1.2, and the stress and displacement clouds after the corresponding strength reduction are shown in Figure 13. The stress of the slope at the bottom is the maximum, the maximum horizontal stress is 8.7100e+04 MPa, and the maximum vertical stress is 3.8888e+04 MPa. The maximum stress appears on the step of the slope, which is in line with the theoretical logic. The maximum displacement of the slope occurs at the step appearing at the upper part of the bottom clearing platform, which is in line with the objective law that the dolomite strength conforms to the slate strength. In the horizontal displacement diagram, the side slope steps along the top of the steps to the weak structural surface have appeared as displacement partition interface, that is, there is an obvious abrupt change in displacement. In the vertical displacement map, there is also an obvious sliding fault surface, and there is an abrupt change of displacement. Therefore, it can be concluded that the sliding

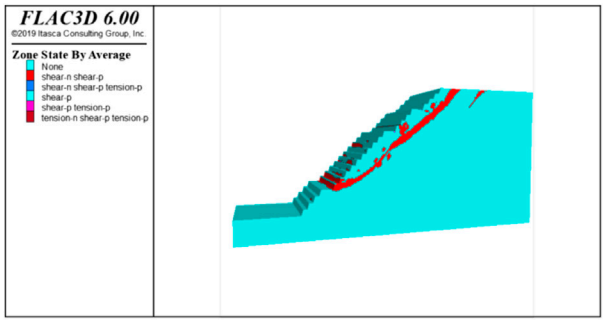

FIGURE 15
Distribution nephogram of the plastic zone after slope strength reduction.

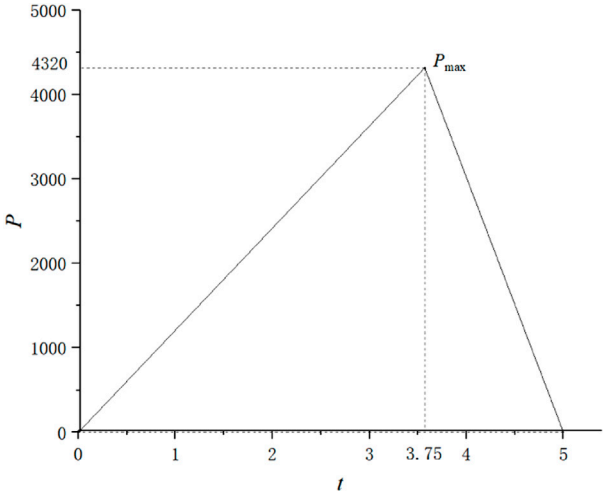

FIGURE 16
Equivalent triangular load diagram of blasting.

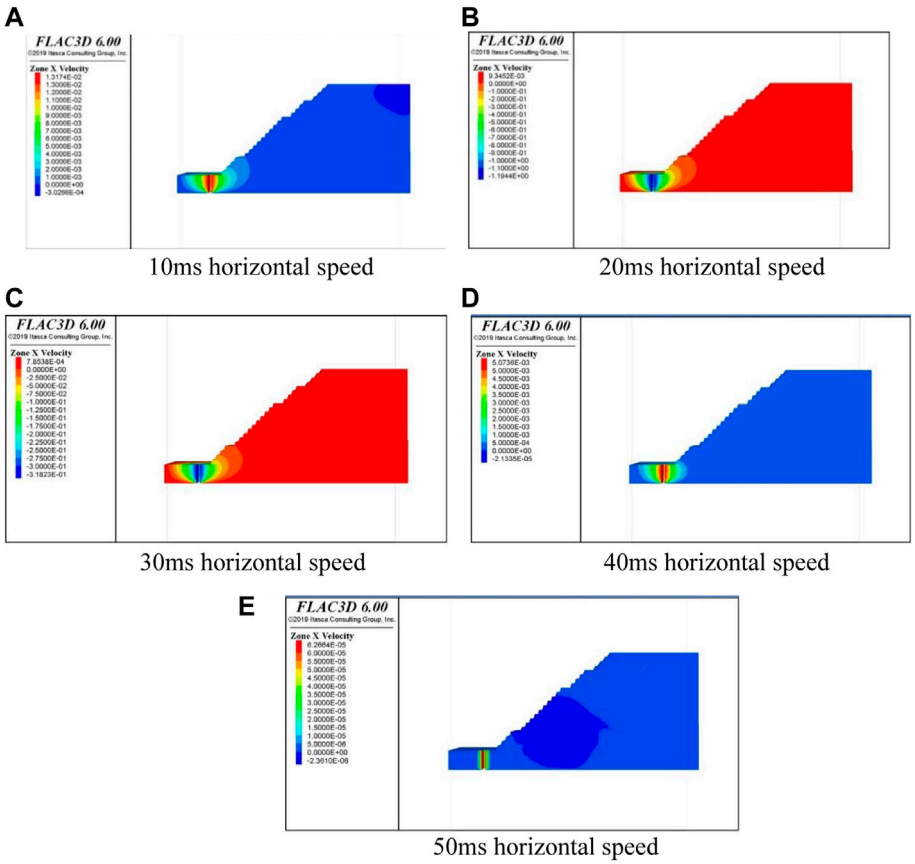

FIGURE 17
Horizontal displacement cloud map.

damage has occurred at this time. In addition to the stress displacement cloud, the velocity cloud can also be used as a way to determine whether the slope is unstable or not. The velocity cloud is similar to the displacement cloud as shown in Figure 14. A continuous velocity equivalence zone can be seen in the velocity cloud, and the position of the potential sliding surface is consistent with the position of the sliding surface in the displacement cloud, which is verified.

The plastic zone of the potential sliding surface is the standard of instability. When the generalized plastic strain or equivalent plastic strain passes through the top of the slope, it is used as a sign of slope failure. According to the change and distribution of some physical quantities, such as the generalized shear strain in the numerical calculation domain. When the plastic region in the domain is completely connected, the judge of the slope failure degree also needs to see whether the slope body produces infinite plastic deformation and displacement. The calculation of finite element software is judged by observing the plastic strain diagram of the plastic zone.

Figure 15 is the plastic zone distribution map of the slope after reduction. According to the distribution nephogram of the plastic zone, whether the failure surface is penetrated or not can be directly observed, which is also an important measure of slope failure. Combined with Figure 15 and the plastic zone penetration criterion, it can be seen that from the top free surface of the slope to the free surface of the first cleaning platform, the tensile failure occurs at the top of the slope and a continuous surface appears in the plastic zone and gradually forms a sliding surface.

5.2.2 Dynamic stability analysis of high and steep slopes

The overall propagation velocity should be attenuated when the breaking vibration load is loaded on the high and steep slope model, so it is necessary to construct damping for the slope model. For simulating the impact process in the propagation of blasting vibration in engineering reality, the commonly used triangular impulse load waveform is proposed to be used. When the triangular load is loaded, the peak value of the load needs to be determined to simulate the blast impact, and the loading action time of the dynamic load also needs to be considered. There are two nodes of this load, that is, the dynamic load value

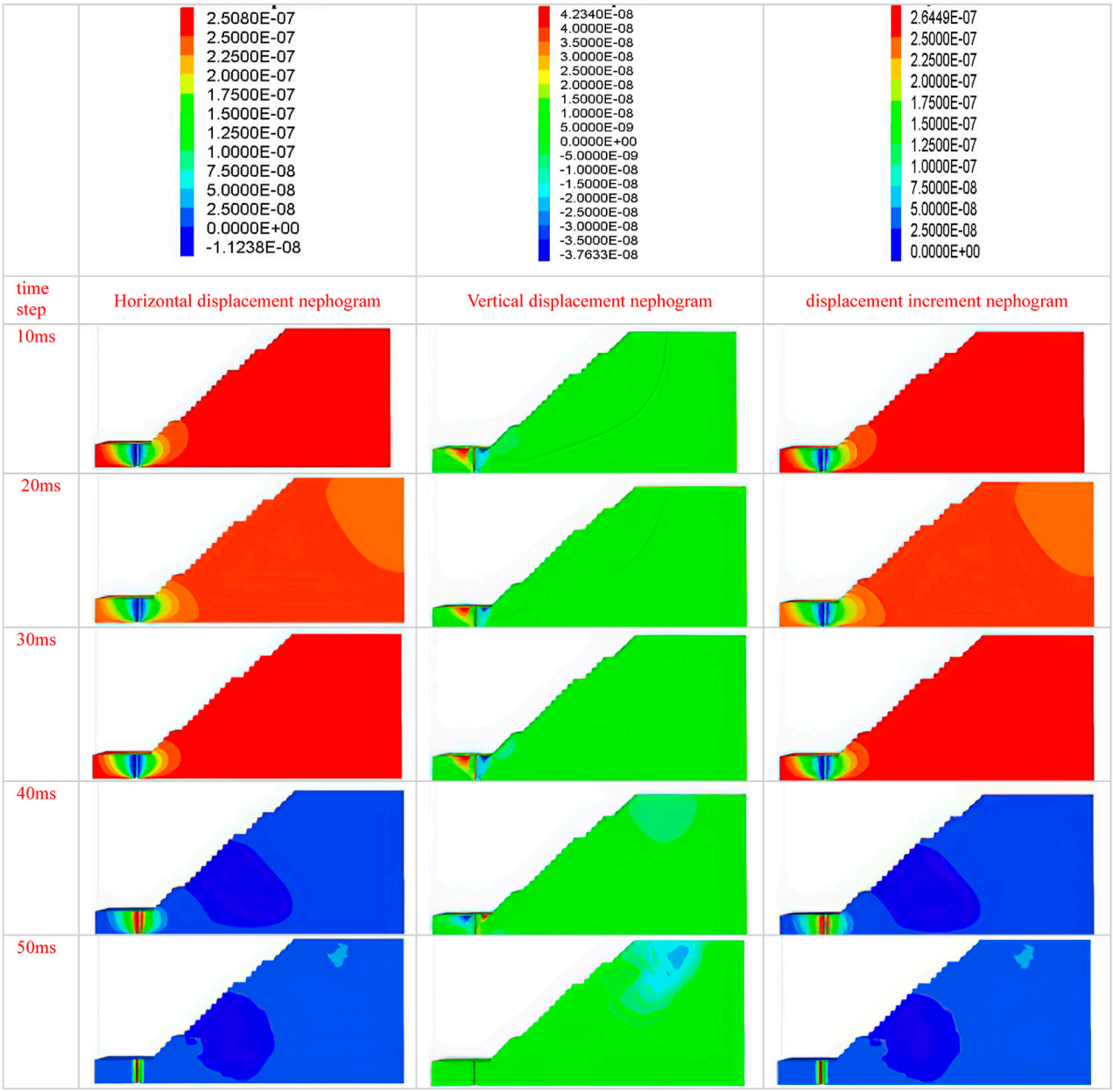

FIGURE 18
Horizontal displacement, vertical displacement, and displacement incremental cloud map 5.

undergoes two loading parts, rising and falling. According to the literature, the formula for the peak stress P_{max} of the blast dynamic load is shown as follows.

$$P_{max} = \frac{\rho_e D^2}{2(\gamma+1)}\left[\frac{d_c}{d_b}\right]^{2\gamma}\left(\frac{I_c}{I_b}\right)^{\gamma} n. \quad (3)$$

Pmax is the peak blast vibration load pressure, pa. ρ_e is the density of the field explosive or emulsion explosive,1300 kg/m^3, and D is the detonation velocity of the explosive used, The value is 4000 m/s. γ is the isentropic index of the explosive and the value depends on ρ_e. According to the relevant literature, γ=3; D_c and D_b are charge diameter and hole diameter respectively, mm; l_c and l_b are the lengths of the bore, m; n is the magnification of uncoupled charge. Values of 8–11 and n=11. The relevant literature shows (Sugiyama et al., 2021; Zingano et al., 2021; Anderson et al., 2022) an explosive shock wave produced by an explosive. The action time is only 10^{-6} s

to 10^{-1} s, and the burst wave pressure action time is about 10^{-3} s ~ 10^{-1}s. The equivalent triangular load for blasting is shown in Figure 16.

The blasting equivalent triangular load built, shown in Figure 16, is loaded on the slope after discounting; 10 ms, 20 ms, 30 ms, 40 ms, and 50 ms time steps under the model horizontal direction of the velocity are shown in Figure 17. According to Figure 17, the horizontal velocity cloud under different time intervals can be seen, the velocity in the gun hole near the center shows a regular waveform transmission, indicating that the blast wave generated by the blast is also from the center to the surrounding dispersion, and as the horizontal velocity decreases, the blast wave also decreases. Also, as the horizontal velocity decreases, the blast waveform gradually decreases. In addition, the blast waveform is irregular or asymmetric diffusion trend at the periphery of the hole, the main reasons for this phenomenon are the following two aspects: first, the model is not a symmetrical structure on the left and right of the hole, which leads to different blast responses, that is, different velocity propagation patterns; second, the blast center is different from the boundary on both sides, and the left side of the simplified gun hole near the boundary is set as a static boundary, to prevent the boundary on both of the abovementioned cases, which will cause the difference of dynamic response of the slope.

After loading the blast equivalent triangular load, the response of the slope to the vibration load under different time intervals is calculated for the dynamic load of the high and steep slope model, that is, the horizontal displacement clouds, vertical displacement clouds, and displacement increment clouds of this model at 10 ms, 20 ms, 30 ms, 40 ms, and 50 ms time intervals are studied, as shown in Figure 18. As can be seen from Figure 18, the horizontal displacement and displacement increment cloud show that the maximum value of both appears at the 1290 m level, that is, at the foot of the slope, and the vertical displacement on the cloud shows that its maximum value is easy to appear at the position of the waist and the top of the slope and coincides with the place where the slope is easy to slide after the discount of static load strength. The maximum horizontal displacement is 2.5e-7m, the maximum vertical displacement is 4.23e-8m, and the maximum displacement increment is 2.64e-7m, and the displacement changes gradually decrease with the weakening of the vibration wave.

6 Conclusion

In this study, the high and steep slope of an open-pit mine in Inner Mongolia is taken as the engineering research background. After the preliminary field survey, the physical and mechanical properties of the ore and rock indoor test and the long-term production blasting vibration monitoring, the monitoring data are analyzed by regression analysis. Then the results of processing and analysis are combined with FLAC3D to establish a numerical model, respectively, based on the static weight and blasting dynamic load under two kinds of slope stability studied, and the conclusions are as follows:

1) The vibration frequency of pre-splitting bench blasting in the quarry is mainly between 10 and 50 Hz, the vibration velocity of the mass point is 8–12 cm/s, and the allowable vibration velocity of pre-splitting bench blasting is 10 cm/s. The pre-splitting blasting of the quarry adopts a single-ring detonation limited charge and radial decoupling charge, and the bench blasting adopts hole-by-hole detonation. The energy of blasting seismic waves is small and the overall trend of blasting vibration velocity is still attenuation law. Pre-cracking blasting in the quarry takes a single-ring detonation charge limit and radial uncoupled charge, step blasting using hole-by-hole detonation, blasting seismic wave energy is small, so the blast vibration speed on the slope of the elevation amplification effect is not obvious, and the overall trend is still the decay law of the blast vibration speed.
2) The blast vibration decay law equations for the horizontal radial, horizontal tangential, and vertical directions of pre-cracking blasting in the east quarry are $V = 191.25(\frac{\sqrt[3]{Q}}{R})^{1.60}$, $V = 105.68(\frac{\sqrt[3]{Q}}{R})^{1.57}$, and $V = 212.55(\frac{\sqrt[3]{Q}}{R})^{1.66}$. The decay law formula of vibration velocity in the horizontal radial, horizontal tangential, and vertical directions of step blasting are $V = 166.33(\frac{\sqrt[3]{Q}}{R})^{1.31}$, 、 $V = 259.81(\frac{\sqrt[3]{Q}}{R})^{1.87}$, and $V = 240.47(\frac{\sqrt[3]{Q}}{R})^{1.61}$. Slope horizontal radial, horizontal tangential, and vertical blasting vibration velocity arrangements are not fixed, with the blasting single sound amount and blast source distance different.
3) A potential slip surface appears after the strength reduction of the slope, and the size of the surface and the arc of the slip band will continue to increase with time. After calculation, the safety factor of the high and steep slope is about 1.2, and the displacement of the sliding zone passing through the slope is small. Therefore, it is concluded that the slope has good stability in the current state. Under blasting triangular load, the maximum horizontal displacement of the slope is 2.5e-7m and the maximum vertical displacement is 4.23e-8m. With the attenuation of seismic waves, the displacement decreases gradually, and the overall displacement of the slope is small. Considering that the slope has high rock mechanical strength and good rock integrity, the blasting center position has a certain distance from the slope position.

Data availability statement

The raw data supporting the conclusions of this article will be made available by the authors without undue reservation.

Author contributions

HS was responsible for writing the article. SM was responsible for data statistics and visualization.

Funding

This project was funded by Qian Jiaohe KY 108, Qiankehe LH 7387, and the Geological Research Project of Guizhou Geological and Mineral Exploration and Development Bureau No.16.

Conflict of interest

Author SM was employed by Guizhou Energy Industry Research Institute Co, Ltd.

The remaining author declares that the research was conducted in the absence of any commercial or financial relationships that could be construed as a potential conflict of interest.

Publisher's note

References

Afanasev, P. I., and Makhmudov, K. F. (2021). Assessment of the parameters of a shock wave on the wall of an explosion cavity with the refraction of a detonation wave of emulsion explosives. *Appl. Sci. (Basel).* 11 (9), 3976. doi:10.3390/app11093976

Anderson, I., Ma, J., Wu, X., and Stow, D. (2022). Determining reservoir intervals in the Bowland Shale using petrophysics and rock physics models[J]. *Geophys. J. Int.* 228 (1), 39–65. doi:10.1093/gji/ggab334

Bazzi, H., Noferesti, H., and Farhadian, H. (2020). Modelling the effect of blast-induced vibrations on the stability of a faulted mine slope[J]. *J. South. Afr. Inst. Min. Metallurgy* 120 (10), 591–597. doi:10.17159/2411-9717/1066/2020

Chong, M., Zhan, H., and Yao, W. (2018). Stability and safety criterion of slopes containing soft inclusions under the action of blasting vibration[J]. *Blast Impact* 38 (3), 563. doi:10.11883/bzycj-2016-0275

Du, H., Song, D., Chen, Z., and Guo, Z. (2020). Experimental study of the influence of structural planes on the mechanical properties of sandstone specimens under cyclic dynamic disturbance. *Energy Sci. Eng.* 8, 4043–4063. doi:10.1002/ese3.794

Hoang, N., Xuan-Nam, B., Quang-Hieu, T., Nguyen, D. A., Hoa, L. T. T., Le, Q. T., et al. (2021). Predicting blast-induced ground vibration in open-pit mines using different nature-inspired optimization algorithms and deep neural network. *Nat. Resour. Res.* 30, 4695–4717. doi:10.1007/s11053-021-09896-4

Ke, B., Nguyen, H., Bui, X., and Costache, R. (2021). Estimation of ground vibration intensity induced by mine blasting using a state-of-the-art hybrid autoencoder neural network and Support vector regression model. *Nat. Resour. Res.* 30 (5), 3853–3864. doi:10.1007/s11053-021-09890-w

Leng, Z., Sun, J., Lu, W., Xie, X., Jia, Y., Zhou, G., et al. (2021). Mechanism of the in-hole detonation wave interactions in dual initiation with electronic detonators in bench blasting operation. *Comput. Geotechnics* 129, 103873. doi:10.1016/j.compgeo.2020.103873

Lv, J., Han, Y., Nan, C., and Bai, R. (2019). Study on the overburden and surface deformation damage law of end gang compression coal shaft mining in Haidaigou open pit mine[J]. *J. Min. Saf. Eng.* 36 (3), 535

Ming, F., Zhu, C., and Li, D. Q. (2012). Effect of blasting vibration frequency on slope stability[J]. *J. Central South Univ. Nat. Sci. Ed.* 43 (11), 4439

Song, D., Liu, X., Huang, J., Zhang, Y., and Nkwenti, B. N. (2021). Seismic cumulative failure effects on a reservoir bank slope with a complex geological structure considering plastic deformation characteristics using shaking table tests. *Eng. Geol.* 286, 106085. doi:10.1016/j.enggeo.2021.106085

Song, D., Liu, X., Li, B., and Bastos, J. J. V. (2021). Assessing the influence of a rapid water drawdown on the seismic response characteristics of a reservoir rock slope using time-frequency analysis. *Acta Geotech.* 16, 1281–1302. doi:10.1007/s11440-020-01094-5

Sugiyama, Y., Homae, T., Matsumura, T., and Wakabayashi, K. (2021). Numerical study on the effect of the initiation process of cylindrical high explosives on the blast-wave behavior. *Shock Waves* 31 (5), 427–438. doi:10.1007/s00193-021-01021-x

Sun, P., Lu, W., Hu, H., Zhang, Y., Chen, M., and Yan, P. (2021). A bayesian approach to predict blast-induced damage of high rock slope using vibration and sonic data. *Sensors* 21 (7), 2473. doi:10.3390/s21072473

Wang, G., Yang, Y., Zhang, H., and Zhang, Z. X. (2013). Failure characteristics and its influencing factors of talus-derived rock mass during open-pit mining. *Trans. Nonferrous Metals Soc. China* 23 (2), 462–471. doi:10.1016/s1003-6326(13)62486-3

Wu, T., Zhou, C., Jiang, N., Xia, Y., Bin, Z., et al. (2020). Study on the mechanical cumulative damage model of slope fault fracture zone under the cumulative effect of blasting vibration[J]. *Period. Polytechnica-Civil Eng.* 64 (3), 845. doi:10.3311/PPci.16030

Xuan-Nam, B., Hoang, N., and Quang-Hieu, T. (2021). Predicting ground vibrations due to mine blasting using a novel artificial neural network-based cuckoo search optimization[J]. *Nat. Resour. Res.* 30 (3), 2663–2685. doi:10.1007/s11053-021-09823-7

Yang, T. H., Zhang, F. C., Yu, Q. L., Cai, M. F., and Li, H. Z. (2011). Current status and development trend of research on stability of high and steep slopes in open pit mines[J]. *Geotechnics* 32 (5), 1437. doi:10.16285/j.rsm.2011.05.031

Yin, Z., Hu, Z., Wei, Z., Zhao, G. M., Ma, H. F., huo, Z., et al. (2018). Assessment of blasting-induced ground vibration in an open-pit mine under different rock properties[J]. *Adv. Civ. Eng.* 2018 (6), 1–10. doi:10.1155/2018/4603687

Zingano, A. C., Salvadoretti, P., Rocha, R. U., and Costa, J. F. C. L. (2021). Estimating uniaxial compressive strength, density and porosity of rocks from the p-wave velocity measurements *in-situ* and in the laboratory. *Rem. Int. Eng. J.* 74 (4), 521–528. doi:10.1590/0370-44672021740022

frontiers | Frontiers in Earth Science

TYPE Original Research
PUBLISHED 07 November 2022
DOI 10.3389/feart.2022.1035692

OPEN ACCESS

EDITED BY
Haijun Qiu,
Northwest University, China

REVIEWED BY
Feng Liu,
Tianjin University, China
Xinlan Liang,
Sichuan Agricultural University, China

*CORRESPONDENCE
Xin Qu,
xqu1987@163.com
Cheng Li,
licheng_730@163.com

SPECIALTY SECTION
This article was submitted to Geohazards and Georisks, a section of the journal Frontiers in Earth Science

RECEIVED 03 September 2022
ACCEPTED 20 October 2022
PUBLISHED 07 November 2022

CITATION
Xu X, Wang H, Qu X, Li C, Cai B and Peng G (2022), Study on the dielectric properties and dielectric constant model of laterite.
Front. Earth Sci. 10:1035692.
doi: 10.3389/feart.2022.1035692

Study on the dielectric properties and dielectric constant model of laterite

Xingqian Xu[1], Haijun Wang[1], Xin Qu[2]*, Cheng Li[3]*, Bo Cai[1] and Guangcan Peng[1]

[1]College of Water Conservancy, Yunnan Agricultural University, Kunming, China, [2]School of Civil and Construction Engineering, Anyang Institute of Technology, Anyang, China, [3]School of Architectural Engineering, Kaili University, Kaili, Guizhou, China

The soil dielectric constant model reflects the relationship between the volumetric water content and the dielectric constant. The ground penetrating radar (GPR) could quickly, precisely and non-destructively obtain the water state of the soil layers. A reasonable and reliable dielectric constant model is of great significance for predicting, monitoring and exploring water migration in soils. Taking Yunnan laterite as an example, this study comprehensively considered the key physical factors (dry density, water content, temperature) of the *in situ* laterite dielectric properties. The dielectric properties and the influencing factors of laterite has been discussed with the laboratory tests by reshaping laterite, and the dielectric constant model was finally proposed to evaluate the natural water state of the laterite. The results show that the relative dielectric constant of laterite increases gradually with the increasing volumetric water content, dry density and temperature respectively. The water content is the most important influencing factor, secondly followed by temperature and dry density. The dielectric constant model of laterite was built based on the influence of dry density and temperature on the relationship between the relative dielectric constant and volumetric water content. The proposed multivariate model has a good prediction effect on the water content of laterite, and the prediction effects compared with other existing models are as follows: Multivariate model, Zhao model, Malicki model, Zhou model, Topp model, Liao mode and Herkelrath model. This model could be applied to evaluate the plastic limit index and the liquid limit index using the relative dielectric constant, and then finally estimate the soft and hard state grades of laterite. This study could provide a reference for the construction of laterite dielectric constant models in different regions, and a convenient way for the estimation of the laterite water content state and engineering categories.

KEYWORDS

laterite, relative dielectric constant, dielectric properties, volumetric water content, model

1 Introduction

Laterite is widely distributed in the Yunnan-Guizhou plateau, eastern Sichuan, Hunan and Guangxi and other regions in China as a kind of special clay soil. It is a maroon highly plastic soil formed by intense weathering and lateritizaton of carbonate rocks. Laterite has special physical and mechanical properties such as high water content, high void ratio, high strength and low compressibility, etc. (Sun et al., 2014). The dry and wet climate in laterite region is obvious, the changes of surface water and groundwater are relatively complicated, and the soil dielectric constant mainly depends on the moisture content (Chen et al., 2012; Hu et al., 2021; Wang et al., 2022). Ground penetrating radar (GPR), time domain reflectometry (TDR) and frequency domain reflectometry (FDR) techniques based on soil dielectric properties were widely applied to estimate surface soil water content (Luo et al., 2019; Liu et al., 2022). In practical engineering applications, the soil dielectric constant could be quickly and accurately measured by the above nondestructive techniques to indirectly predict the spatial and temporal distribution of surface soil moisture (Wu et al., 2019; Qiu et al., 2022). Therefore, the laterite dielectric constant model has very important applications in the irrigation automatic control of regional agricultural, protection of soil ecological environment, geological disasters monitoring, evaluation of soil and water conservation, etc.

The dielectric constant of soil is a physical quantity used to characterize the soil dielectric properties or polarizability. It is always expressed as a relative dielectric constant, this is, the ratio of the real part of the dielectric constant to the vacuum dielectric constant. There are many factors affecting the dielectric properties of soil, especially water content is known as the decisive factor. In recent years, domestic and foreign scholars have deeply studied on the dielectric properties of soil with fruitful results. They found that the dielectric properties were not only affected by water content, but also affected by soil type, composition, texture, bulk density, temperature, dry density, porosity, saturation, humidity and test frequency (Chen et al., 2012; Liao et al., 2016; Christian et al., 2017; Lv et al., 2018; Dong et al., 2020; Xiao et al., 2020; Pan et al., 2021). However, the existing studies have built different dielectric constant models for the different soil types. The dielectric constant models of the same soil type was different due to different influencing factors. Thus, how to determine the key influencing factors of soil dielectric constant and to build a reliable soil dielectric constant model deserves further discussion.

At present, the soil dielectric constant models according to different influencing factors and applicable conditions are mainly divided into three categories: empirical models, volume mixing models, and diffusion models. As far as empirical models concerned, the empirical relationships of "dielectric constant-volume moisture content" for sandy soil, fluvo-aquic soil, aeolian sandy soil, paddy soil, loess, silty clay, cohesive soil and reconstructed soil were studied widely (Topp et al., 1980; Herkelrath et al., 1991; Malicki et al., 1996; Zhu et al., 2011; Zhao et al., 2016; Liao et al., 2019; Zhou et al., 2022; Mu et al., 2022). With respect to the mixing models, they were proposed after weighted average of volume fraction and dielectric constant of soil solid, liquid and gas phases. These models were widely applied in concrete, frozen soil and other engineering fields. The representative models included linear models, root mean square models and Rayleigh models (Roth and Schulin, 1990; Taoufik et al., 2012; Gou et al., 2018; Meng and Meng, 2018; Jin and Mohammod, 2019; Savin and Muzalevskiy, 2020; Fomin and Muzalevskiy, 2021; Xu et al., 2022). In terms of diffusion models, the soil was regarded as a homogeneous four-phase mixture according to the effective medium theory, and the relationships between the volume fraction of each single phase and dielectric constant were proposed. These models could describe the microscopic effects of continuous and dispersed phases using depolarization factors (Deloor, 1968; Dobson et al., 1985; Blonquist et al., 2006; Lv et al., 2016; Xu et al., 2019).

The existing soil dielectric constant models mainly established the relationships between the water content and the dielectric constant. The soil dielectric constant could be tested by non-destructive electromagnetic techniques to inverse the soil moisture content. In particular, the soil dielectric constant models were applied to evaluate the soil water content, compactness, hardness, structures, and related quality indicators (Liao et al., 2016; Liu et al., 2016; Kabir et al., 2020; Zhou et al., 2022). However, the sensitivity analysis of the influencing factors of dielectric properties and the laterite dielectric constant models for laterite were rarely reported. It limited the model applications in the fields of environmental geotechnology, agricultural soil ecological monitoring and soil remediation.

In this study, the basic physical and mechanical indexes of laterite were determined by *in-situ* sampling. The laboratory tests of the laterite dielectric properties has been done with water content, temperature and dry density as variables. The sensitivity of influencing factors were analyzed by regression statistics, and then the laterite multivariate model has been proposed finally. The existing empirical models was comprehensively simulated and compared for the water state of laterite, and the prediction accuracy of each model was evaluated respectively. In contrast, the multivariate model has higher accuracy for laterite water content prediction, and it could provide a reliable reference way for the division of soft and hard grades.

2 Materials and methods

2.1 Experiment materials

The laterite was taken from Yunnan Province in China, and the samples were maroon and hard plastic state after removing the disturbed soil. The samples were naturally air-dried, crushed

TABLE 1 The basic physical properties of laterite.

Maximum dry density (g.cm^{-3})	Optimal water content (%)	Liquid limit (%)	Plastic limit (%)	Specific gravity (G_S)	Natural water content (%)	Natural density (g.cm^{-3})
1.43	29.1	53.2	28.9	2.73	22.3	1.75

and passed through a 2 mm mesh sieve, and then put into an oven at 105°C for 24 h, and the dried soil samples were stored into plastic boxes finally. According to "Standard for Soil Test Method" (GB/T50123-2019), routine soil tests had been done to give the specific gravity, moisture content, density and consistency limit of laterite. The basic physical parameters were in Table 1.

2.2 Experiment scheme

The soil column samples with a diameter of 61.8 mm and a height of 20 mm were prepared by the same volume mass method. The dielectric constant of samples with different water content and dry density were tested on the condition of different temperatures. A total of 108 groups of soil samples were prepared in the test, and three groups of parallel tests were used. The test results were averaged, and a total of 216 data were obtained. The specific experiment scheme as follows: ① The dry density was 1.15, 1.20, 1.25, 1.30, 1.35, and 1.40 g/cm^3;② The mass water content around the optimal water content was 19%, 22%, 25%, 28%, 31%, and 34%; ③ The temperature was controlled at 5°C, 10°C, 15°C, 20°C, 25°C, and 30°C; ④ The soil column samples were made according to the above water content and dry density, and the relative dielectric constants were measured under different temperature conditions.

2.3 Experiment procedure

The specific experiment procedure as follows:① The dry soil mass corresponding to different dry densities was separately weighed using the same volume mass method; ② The soil column samples with different mass water content were prepared separately, and left for 12 h to make the moisture evenly distributed; ③ The soil column samples with diameter of 61.8 mm and height of 20 mm were made by compaction tests; ④ The prepared test samples were sealed with plastic wrap and placed in an incubator for 8 h, and then the dielectric constants were measured under different temperatures using the VC4090A LCR digital bridge; ⑤ The soil column samples after the test were dried to measure the actual water content compared with the predesigned, and the average of mass water content was converted to volumetric water content.

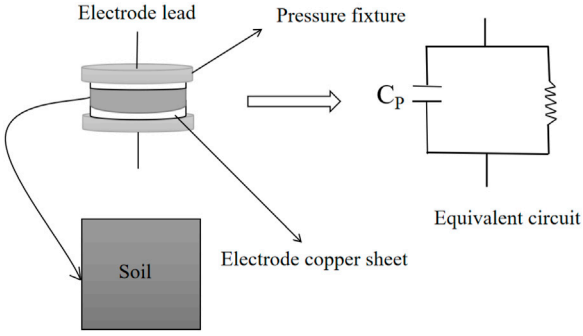

FIGURE 1
Principle of parallel plate capacitance test.

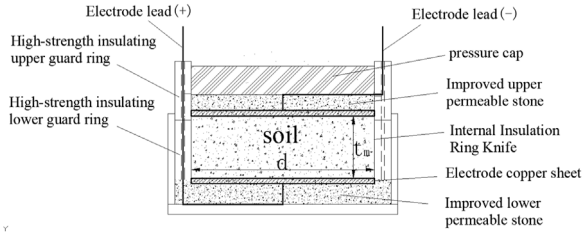

FIGURE 2
Improved parallel plate electrode device.

2.4 Experiment principle

The improved parallel plate electrode device was used to measure the relative dielectric constant of soil samples. The capacitance of soil samples was measured with parallel plate capacitance method to give the relative dielectric constant. The test principle and device were separately shown in Figure 1 and Figure 2. The VC4090A LCR digital bridge was connected with the parallel plate electrode wires. The copper electrodes with a diameter of 62 mm were closely contacted with the top and bottom of the samples, and the same pressure was applied. The capacitance of the samples has been tested with the same frequency and voltage. The relative dielectric constants were calculated by Eq. 1 as follows:

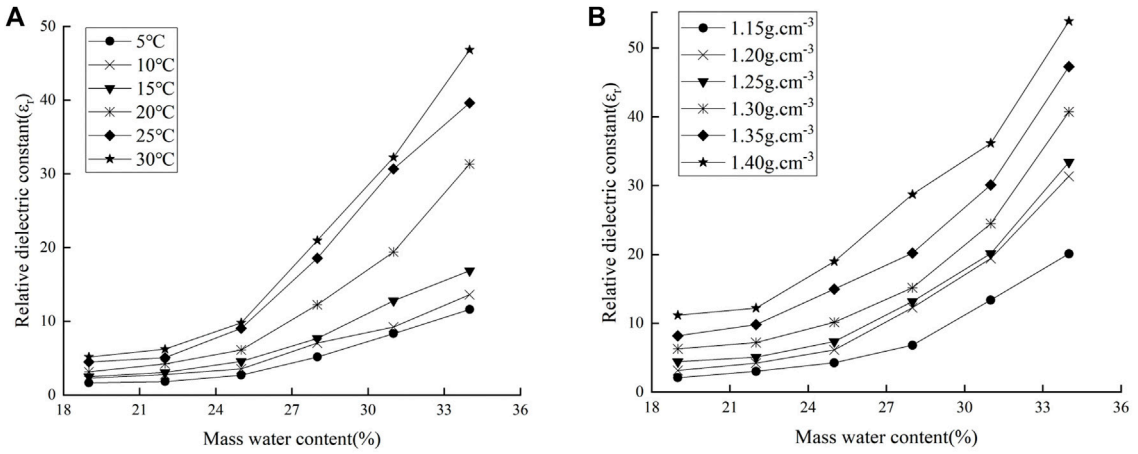

FIGURE 3
Relationship between water content and relative dielectric constant of laterite [**(A)** ρd = 1.20 g cm^{-3}; **(B)** T = 20°C].

$$\varepsilon_r = \frac{t_m \times C_p}{A \times \varepsilon_0} = \frac{t_m \times C_p}{\pi \times \left(\frac{d}{2}\right)^2 \times \varepsilon_0} = \frac{4 \times t_m \times C_p}{\pi \times \varepsilon_0 \times d^2} \quad (1)$$

Here, ε_r is the relative dielectric constant; $\varepsilon_0 = 8.85 \times 10^{-12}(F/m)$; A is the effective area of soil sample; t_m is the thickness of the soil sample; d is the diameter of the soil sample; C_P is the capacitance.

3 Results and discussion

3.1 Influencing factors of laterite dielectric properties

3.1.1 Water content

In the three phases of soil, the proportion of water not only affects the physical properties, but also plays a decisive role in the soil dielectric properties. To investigate the effect of water content on the dielectric properties of laterite, the dry density of 1.20 g cm^{-3} and the temperature of 20°C were controlled respectively. The relationships between relative dielectric constant and water content at different temperatures were shown in Figure 3A. The relationships between the relative dielectric constant and water content under different dry densities were shown in Figure 3B. It could be seen that the variations of relative dielectric constant with water content were more significant on the condition of different dry densities and temperatures.

As shown in Figure 3, the relative dielectric constant gradually increases with the increasing water content. When the water content was low, the soil particles constituted the basic skeleton of the soil, and the relative dielectric constant was relatively less affected by the soil itself. With the gradual increase of water content, the polarization of free water increases in the soil, and the relative dielectric constant increases significantly. At the same time, the free water on the soil surface increases with the increasing temperature and dry density, and the Brownian motion and the polarization ability of free water intensifies, so the relative dielectric constant changes more obviously.

3.1.2 Dry density

The compaction of soil particles has the important effect on the dielectric properties. The spacing among soil particles variate with the increasing dry density to affect the polarization of the electric field on the particles surface. When the temperature was 15°C, the relationships between relative dielectric constant and dry density under different water content was shown in Figure 4A. When the water content was 28%, the relationships between the relative dielectric constant with dry density under different temperatures was shown in Figure 4B. The variations of dielectric constant with dry density was more obvious under the same water content conditions.As shown in Figure 4, the relative dielectric constant increases with the increasing dry density, and it is basically proportional to the dry density. Because the laterite itself has strong water absorption, so it has large pores and low relative dielectric constant when dry density is low. The contact area among soil particles increases with the increasing dry density, but the water volume remains constants, so that the thickness of the water film and the relative dielectric constant increases uniformly. The relative dielectric constant gradually increases under the same dry density when the pore water affected by the increasing water content. Meanwhile, the relative dielectric constant also gradually increases with the increasing activity of water molecules from the increasing temperature.

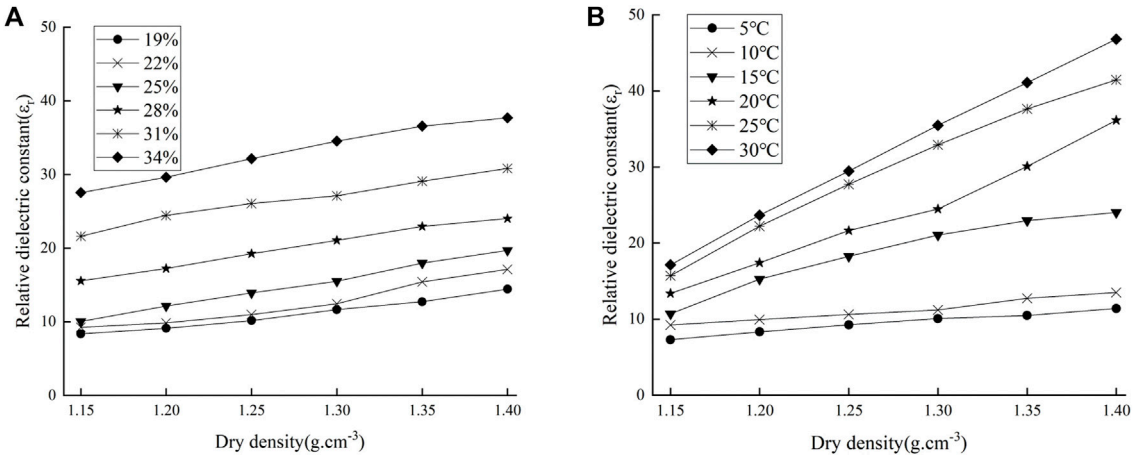

FIGURE 4
The relationship between dry density and relative dielectric constant of laterite [**(A)** T = 15°C; **(B)** ω = 28%].

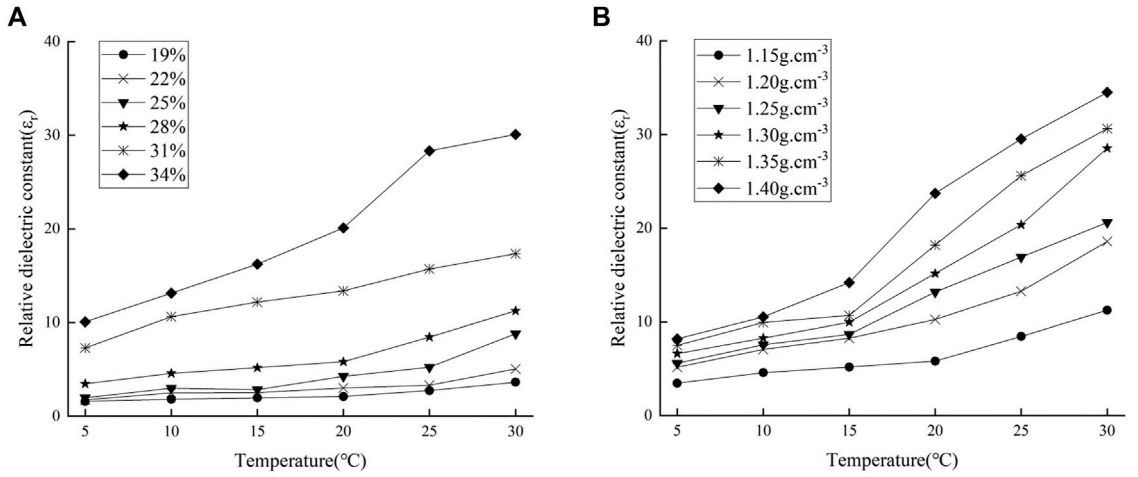

FIGURE 5
The relationship between temperature and relative dielectric constant of laterite [**(A)** ρd = 1.15 g cm^{-3}; **(B)** ω = 28%].

3.1.3 Temperature

Temperature is an important factor affecting the dielectric properties of soil. The thermal movement of water molecules intensifies to affect the density, viscosity and polarizability of water in the soil with the increasing temperatures. To investigate the influence of temperature on the relative dielectric constant, the dry density of 1.15 g cm^{-3} and the water content of 28% were controlled respectively. The relationships between the relative dielectric constant and temperature under different water content were shown in Figure 5A. The relationships between the relative dielectric constant and temperatures under different dry densities were shown in Figure 5B.

As shown in Figure 5, the relative dielectric constant shows a gradually increasing trend with the temperatures, and the polarization ability of pore water in the soil were accelerated. The relative dielectric constant in Figure 5A continued to increase on the condition of dry density 1.15 g cm^{-3}, especially when the water content was greater than 28%. It could be seen that the relative dielectric constant in Figure 5B gradually increased with the increasing temperature, especially when the temperature was greater than 15°C. The reason was that the

TABLE 2 Results of multiple regression statistical analysis.

Parameter	Unstandardized coefficients		Standard coefficient	Correlation coefficient	t value	*p* value	Collinearity statistics	
	B	Standard error	Beta				Tolerance	VIF
(constant)	−104.820	7.366			−14.230	0.000**		
Water content	1.667	0.098	0.608	0.622	16.998	0.000**	0.999	1.001
Dry density	47.257	5.389	0.314	0.334	8.770	0.000**	0.999	1.001
Temperature	0.936	0.068	0.493	0.498	13.792	0.000**	1.000	1.000

(Notes: B represents the regression coefficient; Beta represents the standardized partial regression coefficient, the larger the absolute value, the higher the degree of influence; t represents the significance test of the regression coefficient; *p* represents the significance level, and "*" represents $p < 0.05$ (significant correlation), "**" means $p < 0.01$ (very significant correlation); VIF means variance inflation factor, when tolerance >0.2 and VIF < 5, there is no multicollinearity).

thickness and the active of water film on soil surface was simultaneously enhanced in the soil.

3.1.4 Sensitivity analysis

The significant correlation analysis between the relative dielectric constant and the influencing factors was the basis of the dielectric constant model construction. Based on the least squares method, the partial variance was minimized, and the relative dielectric constant was taken as the target factor (dependent variable). The water content, dry density and temperature were used as various factors (independent variables). The results of multiple regression statistical analysis were shown in Table 2.

As seen from Table 2, the relative dielectric constant was significantly correlated with water content, dry density and temperature ($p < 0.01$), the tolerances were between 0.999 and 1.000, and the VIF values were between 1.000 and 1.001. It showed that the collinearity between the independent variables was very weak, and the key regression factors of the dielectric properties were water content, dry density and temperature. The greater the absolute value of the standardized partial regression coefficient (Beta), the greater the influence of independent variable on the target factor. It concluded that the influence of water content on the relative dielectric constant was the largest, followed by temperature, and dry density was the smallest.

3.2 Construction of laterite dielectric constant model

3.2.1 Model building method

Currently, the most representative empirical relationship between soil dielectric constant and volumetric water content is the Topp model (Topp et al., 1980), and the general expression is:

$$\theta_v = a + b\varepsilon_r + c\varepsilon_r^2 = d\varepsilon_r^3 \tag{2}$$

Here, θ_v is the volume water content, ε_r is the relative dielectric constant, and *a, b, c*, and *d* are the fitting parameters. Herkelrath et al. (1991) gives a linear relationship between the volumetric water content (θ_v), the square root of the relative dielectric constant ($\sqrt{\varepsilon_r}$) is given by:

$$\sqrt{\varepsilon_r} = \alpha\theta_v + \beta \tag{3}$$

In Eq. 3, α and β are related to soil dry density and temperature. Considering the influence of various soil types and dry density (ρ_d), Malicki et al. (1996) revised the relationship between θ_v and $\sqrt{\varepsilon_r}$, and further improved the empirical relationship as follows:

$$\theta_v = \frac{\sqrt{\varepsilon_r} + a + b\rho_d + c\rho_d^2}{d + e\rho_d} \tag{4}$$

It effectively improves the prediction accuracy of soil water content, but Eq. 4 is complex with relatively poor engineering applicability. Subsequently, Siddiqui and Drnevich (1995) established a more simplified empirical formula:

$$\sqrt{\varepsilon_r}\frac{\rho_d}{\rho_d} = a + bw \tag{5}$$

where *w* is the mass water content, and ρ_w is the density of water. Zhao et al. (2016) calibrated the water content of sand, silt soil and cohesive sand in the field considering the soil dry density, the relationship between *w* and $\sqrt{\varepsilon_r}$ is:

$$\text{Correction equation: } w = \frac{A + \sqrt{\varepsilon_r}}{B + C\sqrt{\varepsilon_r}} \tag{6}$$

In Eq. 6, *A, B*, and *C* are undetermined parameters, which are related to the dry density. Based on the simulation analysis on the field (Zhao et al., 2016), the following relationship was obtained:

$$\theta_v = \frac{\left[\left(\alpha\frac{\rho_d}{\rho_w} + \beta\right) + \sqrt{\varepsilon_r}\right]\frac{\rho_d}{\rho_w}}{\left(\gamma\frac{\rho_d}{\rho_w} + \eta\right) + \left(\mu\frac{\rho_d}{\rho_w} + \phi\right)\sqrt{\varepsilon_r}} \tag{7}$$

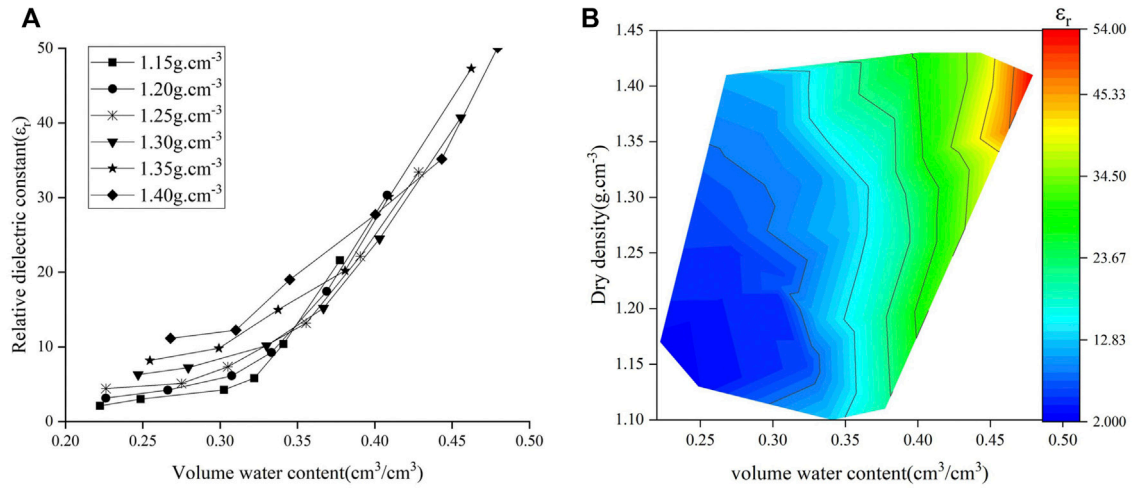

FIGURE 6
Relationship between water content, dry density and relative dielectric constant of laterite (T = 20°C). **(A)** The relationship between volume water content and relative dielectric constant of laterite (T = 20°C); **(B)** The relationship between volume water content, dry density and relative dielectric constant of laterite (T = 20°C).

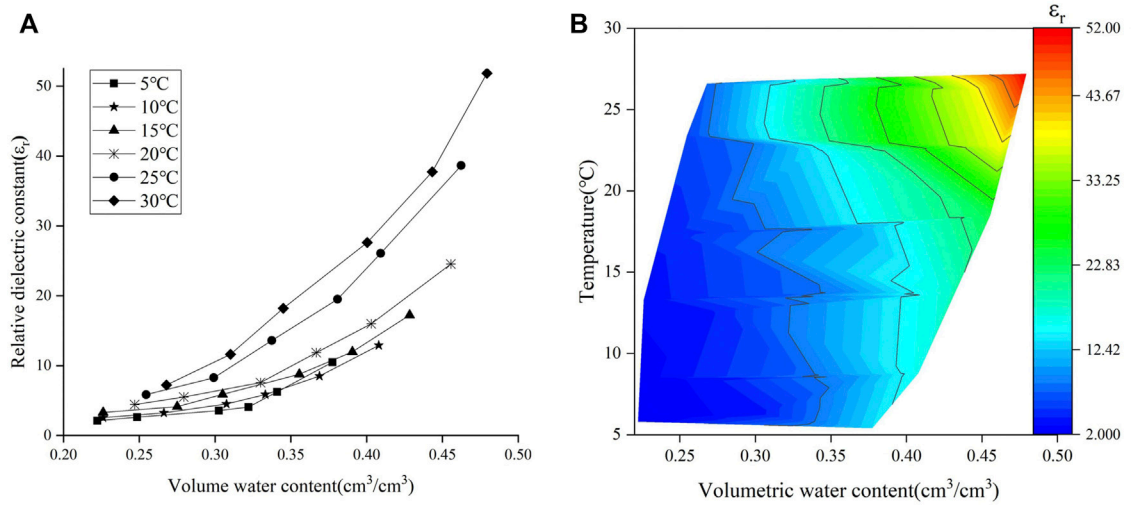

FIGURE 7
Relationship between water content, temperature and relative dielectric constant of laterite (ρ_d = 1.25 g cm^{-3}). **(A)** The relationship between volume water content and relative dielectric constant of laterite (ρ_d = 1.25 g cm^{-3}); **(B)** The relationship between volume water content, temperature and relative dielectric constant of laterite (ρ_d = 1.25 g cm^{-3}).

Liao et al. (2016) established an empirical model of soil dielectric constant for loess with different sand contents:

$$\theta_v = a\lg\frac{\varepsilon_r}{b} \tag{8}$$

Zhou et al. (2022) obtained a linear relationship between θ_v and $\sqrt{\varepsilon_r}$ on the basis of Eq. 5, it was given as follows:

$$\theta_v = \frac{\sqrt{\varepsilon_r}}{b} - \frac{a}{b}\frac{\rho_d}{\rho_w} \tag{9}$$

In summary, it was beneficial for improving the accuracy of dielectric constant model considering the influence of dry density on dielectric properties. Based on the sensitivity analysis of influencing factors, the water content is the main factor,

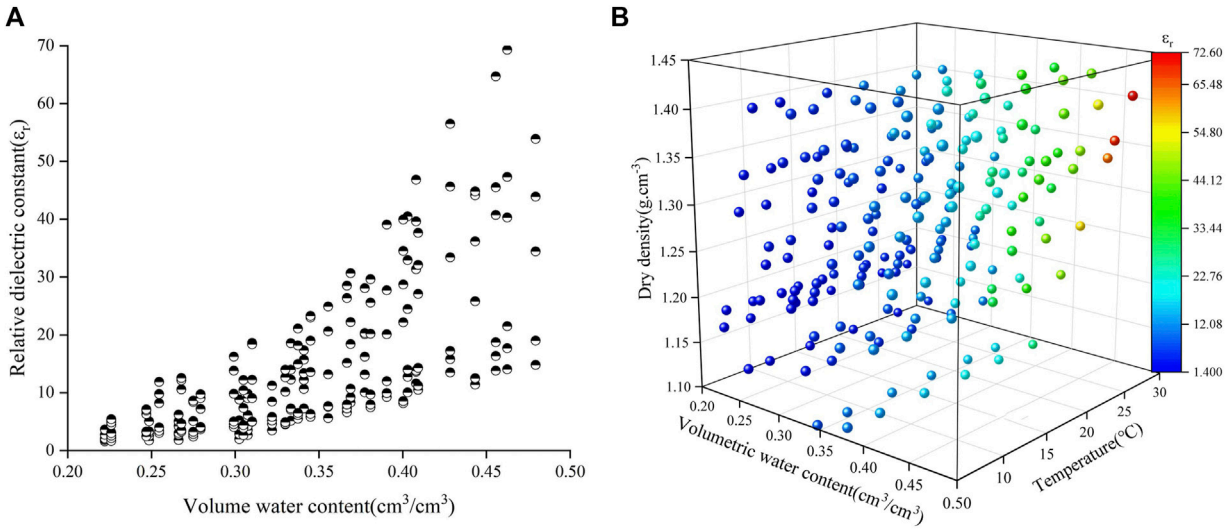

FIGURE 8
Relationship between dry density, water content, temperature and relative dielectric constant of laterite. **(A)** The relationship between volume water content and relative dielectric constant of laterite; **(B)** The relationship between volume water content, temperature, dry density and relative dielectric constant of laterite.

followed by temperature, and the dry density has the least impact. Therefore, the influence of temperature and dry density as the key factors should be considered when the relationship of "relative dielectric constant-volume water content" was built for laterite.

3.2.2 Model building analysis

The influence of dry density and temperature is the basis of laterite dielectric constant model. To investigate the influence of both factors on the relationship between relative dielectric constant and volumetric water content, the experimental data were analyzed. The relative dielectric constants increased with the increasing volumetric water content under the different dry densities shown in Figure 6 when the temperature was 20°C. Meanwhile, the relative dielectric constants increased with the increasing volumetric water content under the different temperatures shown in Figure 7 when the dry density was 1.25 g cm^{-3}. The relationship between the relative dielectric constant and volumetric water content shown in Figure 8 has been obtained on the conditions of the temperature range of 5°C–30°C, the dry density range of 1.15–1.40 g cm^{-3} and the water content range of 19%–34%.

As shown in Figure 6, the experimental and numerical results are highly consistent, and the relative dielectric constant increases with the increasing dry density and volumetric water content. The reason was that the dry density gradually increased with the decreasing pores and the increasing particles contact area in the soil, so that the free water was squeezed into the soil surface result in the increase of dielectric constant. As shown in

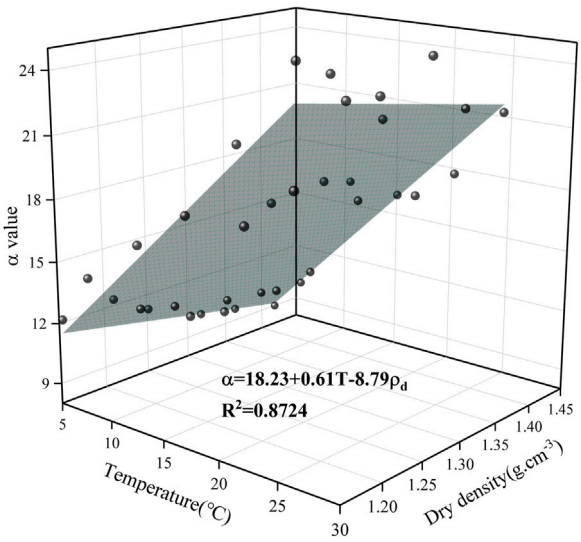

FIGURE 9
The relationship between α value and dry density and temperature.

Figure 7, the experimental results agree well with the numerical results, and the relative dielectric constant increases with both the temperature and volumetric water content. The reason was that the increasing temperature accelerated the Brownian motion of free water in soil for the electric field variations. As shown in Figure 8, it shows that the relative dielectric constant has significant correlation with volumetric water content, dry density and temperature. Therefore, the influence of dry

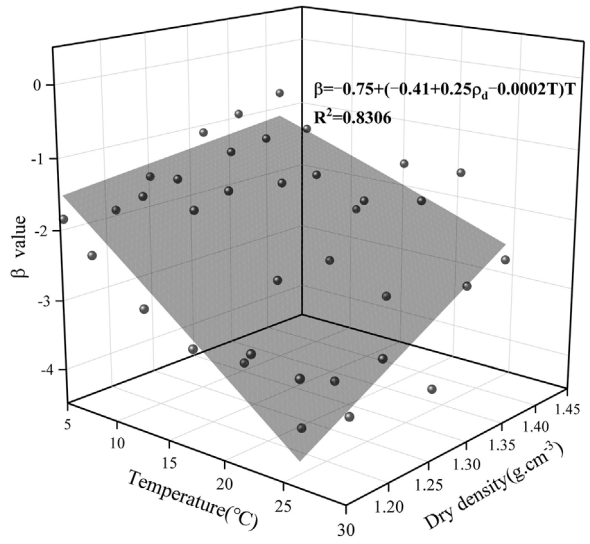

FIGURE 10
The relationship between β value and dry density and temperature.

density and temperature could not be ignored when the dielectric constant model of laterite was built.

Based on the above analysis, this study proposed the influence of dry density and temperature on the parameters of Herkelrath model for laterite. The relative dielectric constant and volumetric water content of laterite were brought into the Herkelrath model to get the parameters α and β in Eq. 3. The α and β have been fitted with the temperature and dry density shown in Figure 9 and Figure 10, respectively.

$$\boldsymbol{\alpha = a + bT + c\rho_d} \tag{10}$$

$$\boldsymbol{\beta = d + (e + f\rho_d + gT)T} \tag{11}$$

Here, α and β are the correction parameter; *a, b, c, d, e, f, g* are the fitting parameters, ρ_d is the dry density, T is the temperature.

As seen from the fitting results in Figure 9 and Figure 10, α and β values are significantly correlated with the temperature and dry density. The Eqs 10, 11 were brought into Eq. 3 to correct the parameters, and finally the multivariate model of laterite dielectric constant was as follows:

$$\boldsymbol{\theta_v = \frac{\sqrt{\varepsilon_r} - d - (e + f\rho_d + gT)T}{a + b\rho_d + cT}} \tag{12}$$

3.3 Simulation verification of laterite dielectric constant model

3.3.1 Simulation comparison verification

The comparison analysis of the existing empirical models and the multivariate model were applied together on the prediction of laterite water content, and this is an effective way to verify the reliability of the multivariate model. A total of 216 groups testing data of volumetric water content and relative dielectric constant were brought into Eqs 2, 3, 4, 7, 8, 9, 12 on the condition of the temperature 5°C–30°C and the dry density 1.15–1.40 g cm^{-3}. The fitting results of each model and the correlation R were in Table 3.

The simulating results of single variable models in Figure 11 and the bivariate variable models in Figure 12 were compared with the test data respectively, and the multivariate variable models was shown in Figure 13. The specific expressions of all the models including the Topp model, Herkelrath model, Malicki model, Liao model, Zhao model, and Zhou model for laterite were shown in Table 3. The multivariate model compared with the other models has the best accuracy for the relationship between the volume water content and the relative dielectric constant for laterite.

TABLE 3 Expressions of seven empirical models for laterite.

Model	Model expressions	R value	
Topp model	$\boldsymbol{\theta_v = 0.232 + 0.013\varepsilon_r - 0.00031\varepsilon_r^2 + 0.0000025\varepsilon_r^3}$	0.79089	(13)
Herkelrath model	$\boldsymbol{\theta_v = 0.219 + 0.035\sqrt{\varepsilon_r}}$	0.77509	(14)
Malicki model	$\boldsymbol{\theta_v = \frac{\sqrt{\varepsilon_r} - 5.482 + 13.851\rho_d - 5.425\rho_d^2}{33.018\rho_d - 12.237}}$	0.80436	(15)
Liao model	$\boldsymbol{\theta_v = 0.144\lg\frac{\varepsilon_r}{0.044}}$	0.78703	(16)
Zhao model	$\boldsymbol{\theta_v = \frac{[(3.335\frac{\rho_d}{\rho_w} - 3.773) + \sqrt{\varepsilon_r}]\frac{\rho_d}{\rho_w}}{(20.467\frac{\rho_d}{\rho_w} - 19.389) + (0.015\frac{\rho_d}{\rho_w} + 145.364)\sqrt{\varepsilon_r}}}$	0.81303	(17)
Zhou model	$\boldsymbol{\theta_v = \frac{\sqrt{\varepsilon_r}}{27.614} + 0.156\frac{\rho_d}{\rho_w}}$	0.80182	(18)
Multivariate model	$\boldsymbol{\theta_v = \frac{\sqrt{\varepsilon_r} + 0.861 + (0.376 - 0.173\rho_d - 0.0015T)T}{16.094 - 6.066\rho_d + 0.65T}}$	0.97546	(19)

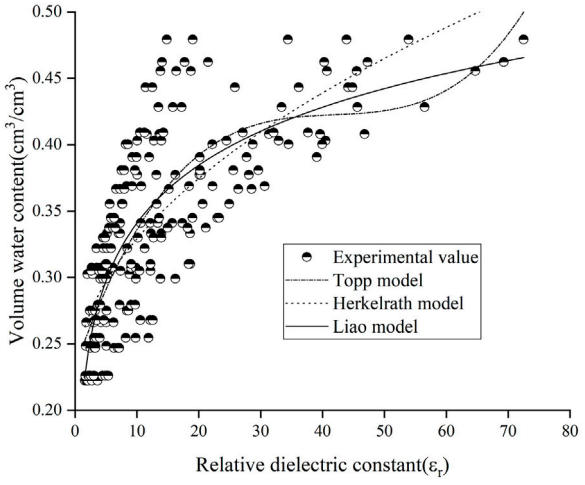

FIGURE 11
Comparative analysis of single variable simulation for latertite.

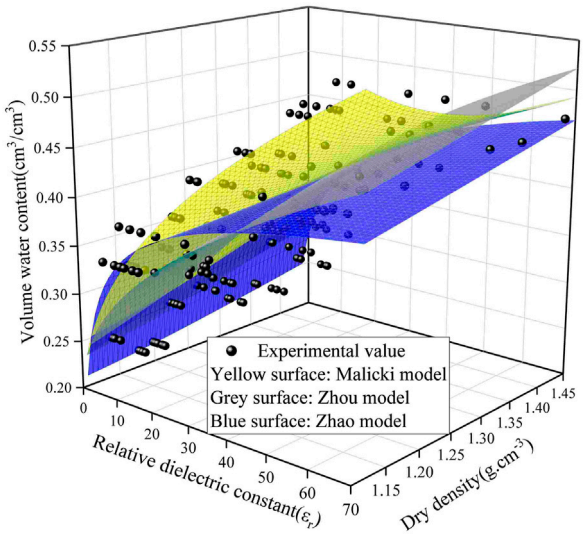

FIGURE 12
Comparative analysis of bivariate simulation for latertite.

3.3.2 Evaluation of simulation comparison verification

The root mean square error (*RMSE*) was used to accurately evaluate the predicting effect of each model on the water content as follows:

$$RMSE = \sqrt{\frac{\sum(\theta_v - \theta_g)^2}{n}} \tag{20}$$

Where θ_v is the calculated value of the volume water content, θ_g is the measured value of the volume water content, and n is the testing numbers. The *RMSE* was smaller, and the better the model predicted the water content. The testing relative dielectric constant, temperature and dry density were brought into above seven models to predict the volumetric water content. Finally, the calculated value and the measured value of volume water content were brought into Eq. 20 to give the root mean square error in Table 4.

The root mean square error of the multivariate model was the smallest in Table 4. The prediction effects of seven models on the laterite water content were as follows: Multivariate model, Zhao model, Malicki model, Zhou model, Topp model, Liao model, and Herkelrath model. This study has built the multivariate model for laterite considering the influence of temperature and dry density on the dielectric properties *in situ* field. The multivariate model effectively improved the prediction accuracy of the laterite water content.

3.3.3 Evaluation of the natural water content of laterite

The cohesive soil has different physical states and engineering properties with the changes of soil water content. The water content state of cohesive soil could be quickly detected using ground penetrating radar if the dielectric constant model were precise and reliable enough. The surface average temperature of Yunnan laterite was 14.4°C, the average dry density was 1.23 g cm^{-3}, and the density of water was 1.00 g cm^{-3} (Wu et al., 2017; Gao and Zhang, 2021). The liquid limit of laterite was 53.2%, and the plastic limit was 30.1%. To explore a more convenient way for the evaluation of natural water content of laterite, and the relative dielectric constant should be tried to apply in the prediction of the plastic limit index as follows:

$$w = \frac{\theta_v \times \rho_w}{\rho_d} \tag{21}$$

$$I_P = W_L - W_P \tag{22}$$

$$I_L = \frac{W - W_P}{W_L - W_P} \tag{23}$$

The volumetric water content could be converted to the plastic limit index and liquid limit index using Eqs 21–23:

$$I_P = W_L - W_P = \frac{(\theta_{vL} - \theta_{vP}) \times \rho_w}{\rho_d} \tag{24}$$

$$I_L = \frac{W - W_P}{W_L - W_P} = \frac{\theta_v - \theta_{vP}}{\theta_{vL} - \theta_{vP}} \tag{25}$$

Finally, the laterite dielectric constant model Eq. 19 was brought into Eqs 24, 25, the relationship between the plastic limit index, liquid limit index and dielectric constant could be expressed as:

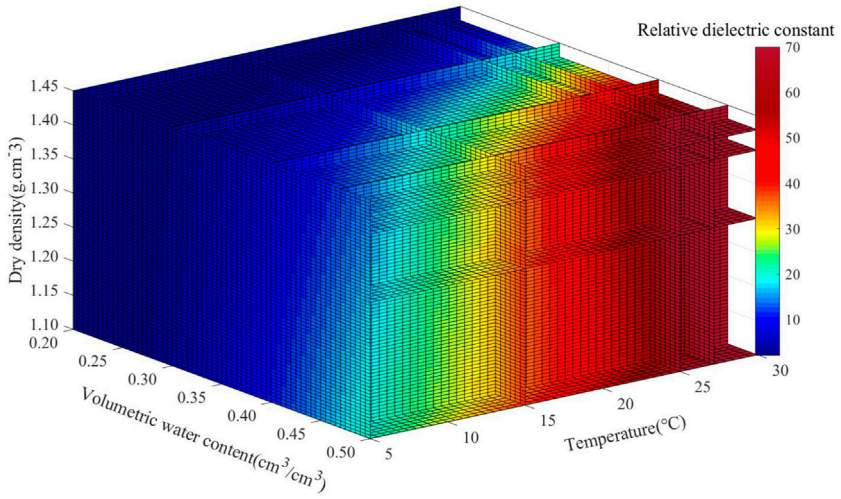

FIGURE 13
Multivariate simulation analysis for laterite.

TABLE 4 Root mean square error of seven models.

Topp model	Herkelrath model	Malicki model	Liao model	Zhou model	Zhao model	Multivariate model
0.04345	0.04468	0.04238	0.04456	0.04327	0.04178	0.02175

TABLE 5 Classification of natural water content state of laterite with the relative dielectric constant.

Soil state	Hard	Hard plastic	Plastic	Soft plastic	Flow
Liquid index (I_L)	$I_L \leq 0$	$0 < I_L \leq 0.25$	$0.25 < I_L \leq 0.75$	$0.75 < I_L \leq 1.00$	$I_L \geq 1.00$
Water ratio (α_w)	$\alpha_w \leq 0.55$	$0.55 < \alpha_w \leq 0.70$	$0.70 < \alpha_w \leq 0.85$	$0.85 < \alpha_w \leq 1.00$	$\alpha_w \geq 1.00$
Natural water content (w)	$w \leq 0.293$	$0.293 < w \leq 0.372$	$0.372 < w \leq 0.452$	$0.452 < w \leq 0.532$	$w \geq 0.532$
relative dielectric constant (ε_r)	$\varepsilon_r \leq 13$	$13 < \varepsilon_r \leq 28$	$28 < \varepsilon_r \leq 55$	$55 < \varepsilon_r \leq 76$	$\varepsilon_r \geq 78$

$$I_P = \frac{\left(\sqrt{\varepsilon_{rL}} - \sqrt{\varepsilon_{rP}}\right) \times \rho_w}{(a - b\rho_d + cT) \times \rho_d} \tag{26}$$

$$\boldsymbol{I_L} = \frac{\sqrt{\boldsymbol{\varepsilon_r}} - \sqrt{\boldsymbol{\varepsilon_{rP}}}}{\sqrt{\boldsymbol{\varepsilon_{rL}}} - \sqrt{\boldsymbol{\varepsilon_{rP}}}} \tag{27}$$

Where w is the natural water content, θ_v is the volume water content, ρ_w is the density of water, ρ_d is the dry density, w_L is the liquid limit, w_P is the plastic limit, I_L is the liquid limit index, I_P is the plastic limit index, ε_r is the relative dielectric constant, ε_{rL} and ε_{rP} are the relative dielectric constants corresponding to the liquid limit and the plastic limit, respectively.

As the average temperature of Yunnan laterite is 14.4°C and the average dry density is 1.23 g cm^{-3}, and the laterites $\sqrt{\varepsilon_{rL}} = 8.74$, $\sqrt{\varepsilon_{rP}} = 4.2$, $I_P = 20.5$ corresponding to the liquid limit 55.6% and the plastic limit 30.1%. It could be judged that the laterite in our tests was cohesive soil ($I_P \geq 17$). Based on Eq. 27, the liquid limit $I_L \approx 1$ and $I_L \approx 0$ was respectively close to the relative dielectric constant of the liquid limit and the plastic limit for laterite. The water ration was defined $\alpha_\omega = \frac{w}{w_L}$, and it was listed to classify the natural water state of the cohesive from the "Engineering Geology Handbook" (Chang, 2018). The corresponding relationships between the relative dielectric constant and the liquid limit index has been calculated with Eq. 19 on the condition of different natural water content for laterite in Table 5. It could be seen that the water content state evaluation of laterite has a good consistency between the liquid limit index and the relative dielectric constant. The proposed multivariate model was

feasible for the application in the engineering categories of laterite.

4 Conclusion

(1) The relative dielectric constant of laterite gradually increases with the increasing water content, dry density and temperature respectively, and the main influencing factors of the laterite dielectric properties was water content, followed by temperature, and finally dry density from the multiple linear regression analysis.

(2) The influence of dry density and temperature could not be ignored for the construction of dielectric constant model of laterite according to the analysis of existing models and the testing results. The laterite dielectric constant model considering the joint effects of dry density and temperature has been proposed on the basis of Herkelrath model.

(3) The comparison and verification of the test data with the existing models shows that the multivariate model has the best fitting accuracy on the relationship "relative dielectric constant-volume water content" of laterite. The root mean square error was used to evaluate the prediction accuracy of each model for the laterite water content as follows: Multivariate model, Zhao model, Malicki model, Zhou model, Topp model, Liao model, and Herkelrath model.

(4) The relationships between the relative dielectric constant, plastic limit index and liquid limit index of laterite were derived based on the multivariate model, and this model could be used to classify the natural water content state of laterite. The multivariate model could provide a convenient way for the rapid, nondestructive and accurate quantitative prediction of the surface water content state, and further evaluate the soft and hard grades and engineering categories of laterite (Hu et al., 2021).

Data availability statement

The original contributions presented in the study are included in the article/supplementary material, further inquiries can be directed to the corresponding authors.

Author contributions

XX: Conceptualization, investigation, writing—original draft, writing—review and editing. HW: Data acquisition and analysis, investigation and editing. XQ: Methodology, funding acquisition. CL: Formal analysis, supervision. BC: Testing samples preparations. GP: Data acquisition, investigation. All authors have read and agreed to the published version of the manuscript.

Funding

This study has been financially supported by National Natural Science Foundation of China (Grant No. 41867040), Qiandongnan Science and Technology plan project [(2022) No. 51], National Natural Science Foundation of China (Grant No. 42107195), Fundamental Research Program of Yunnan Province (202101AT070271); Yunnan Province High level Talents Training Support Program "Young Topnotch Talent" Special Project (XX).

Acknowledgments

We are grateful for the comments of the reviewers, which greatly improved the quality of this study.

Conflict of interest

The authors declare that the research was conducted in the absence of any commercial or financial relationships that could be construed as a potential conflict of interest.

Publisher's note

References

Blonquist, J., Jones, S., Lebron, I., and Robinson, D. A. (2006). Microstructural and phase configurational effects determining water content: Dielectric relationships of aggregated porous media. *Water Resour. Res.* 42 (5), 387–403. doi:10.1029/2005WR004418

Chang, S. B. (2018). *Engineering Geology Handbook*. Beijing: China Construction Industry Press.

Chen, Q., Zeng, J., Li, Z., Zhou, J., Tian, B., and Zhou, J. (2012). Relationship model of soil moisture and dielectric constant monitored with remote sensing. *Trans. Chin. Soc. Agric. Eng.* 28 (12), 171–175. doi:10.3969/j.issn.1002-6819.2012.12.028

Christian, N. K., Liu, H., Takahashi, K., Shimada, M., Watanabe, M., Khuut, T., et al. (2017). *In-situ* measurement of soil permittivity at various depths for the calibration and validation of low-frequency SAR soil moisture models by using GPR. *Remote Sens.* 9 (6), 580. doi:10.3390/rs9060580

Deloor, G. P. (1968). Dielectric properties of heterogeneous mixtures containing water. *J. Microw. Power* 3 (2), 67–73. doi:10.1080/00222739.1968.11688670

Dobson, M. C., Ulaby, F. T., Hallikainen, M. T., and El-rayes, M. (1985). Microwave dielectric behavior of wet soil-Part II: Dielectric mixing models. *IEEE Trans. Geosci. Remote Sens.* 23 (1), 35–46. doi:10.1109/tgrs.1985.289498

Dong, L., Wang, W., and Wu, Y. (2020). Dielectric properties of saline soil and an improved dielectric model. *Remote Sens. Technol. Appl.* 35 (4), 786–796. doi:10.11873/j.issn.1004-0323.2020.4.0786

Fomin, S., and Muzalevskiy, K. (2021). A dielectric model for frozen mineral soils at a frequency of 435MHz. *Remote Sens. Lett.* 212 (9), 944–950. doi:10.1080/2150704x.2021.1947537

Gao, H., and Zhang, J. (2021). Statistical regularity of physical and mechanical indexes of secondary red clay in Chenggong district, kunming. *Coal Geol. Explor.* 49 (5), 174–181. doi:10.3969/j.issn.1001-1986.2021.05.019

Guo, Y., Xu, S., and Shan, W. (2018). Development of a frozen soil dielectric constant model and determination of dielectric constant variation during the soil freezing process. *Cold Regions Sci. Technol.* 151, 28–33. doi:10.1016/j.coldregions.2018.03.006

Herkelrath, W. N., Hamburg, S. P., and Murphy, F. (1991). Automatic real time monitoring of soil moisture in a remote field area with time domain reflectometry. *Water Resour. Res.* 27 (5), 857–864. doi:10.1029/91WR00311

Hu, J. D., Li, L., Iderawumi, A. M., Feng, Y., Li, B., and Wei, W. (2021). Research progress of soil water content measurements using dielectric properties. *Henan Agric. Univ. Newsp.* 55 (4), 603–611. doi:10.16445/j.cnki.1000-2340.20210618.002

Jin, X., and Mohammod, A. (2019). Simple empirical formulas to estimate the dielectric constant and conductivity of concrete. *Microw. Opt. Technol. Lett.* 61 (2), 386–390. doi:10.1002/mop.31577

Kabir, H., Khan, M., Brodie, G., Gupta, D., Pang, A., Jacob, M. V., et al. (2020). Measurement and modelling of soil dielectric properties as a function of soil class and moisture content. *J. Microw. Power Electromagn. Energy* 54 (2), 3–18. doi:10.1080/08327823.2020.1714103

Liao, H., Sun, J., Zan, Y., Zhu, Q., and Gu, F. (2016). Dielectric constant model for soil and its application in engineering. *Chin. J. Geotechnical Eng.* 38 (S2), 36–41. doi:10.11779/CJGE2016S2006

Liao, H., Dong, H., Ning, C., Zhang, J., and Sun, J. (2019). A new logarithmic dielectric constant model of soils. *JGS. Spec. Publ.* 7 (2), 281–286. doi:10.3208/jgssp.v07.044

Liu, N., Li, X., Guo, B., and Min, X. (2016). Compaction evaluation of reclamation soil in coal mining district based on modified dielectric constant model. *J. Soil Water Conservation* 30 (04), 318–322. doi:10.13870/j.cnki.stbcxb.2016.04.053

Liu, Z., Qiu, H., Zhu, Y., Liu, Y., Yang, D., Ma, S., et al. (2022). Efficient identification and monitoring of landslides by time-series InSAR combining single- and multi-look phases. *Remote Sens.* 14, 1026. doi:10.3390/rs14041026

Luo, G., Cao, Y., Bai, Z., Kuang, X., Wang, S., and Song, L. (2019). Representation and inversion of reconstructed soil volumetric water content in loess open pit mining area. *J. Ecol. Rural Environ.* 35 (4), 529–537. doi:10.19741/j.issn.1673-4831.2018.0506

Lv, H., Jiang, W., Zhao, Y., and Zeng, Z. (2016). Relationship between volumetric water content and effective dielectric permittivity of Nanning expansive soil. *Rock Soil Mech.* 37 (08), 2145–2150. doi:10.16285/j.rsm.2016.08.003

Lv, G., Yang, J., Li, N., Hu, D., Zhang, Y., and Zhao, F. (2018). Dielectric characteristics of unsaturated loess and the safety detection of the road subgrade Based on GPR. *J. Sensors* 2018 (01), 1–8. doi:10.1155/2018/5185460

Malicki, M., Plagge, R., and Roth, C. (1996). Improving the calibration of dielectric TDR soil moisture determination taking into account the solid soil. *Eur. J. Soil Sci.* 47 (3), 357–366. doi:10.1111/j.1365-2389.1996.tb01409.x

Meng, M., and Meng, X. (2018). Effect of temperature and frequency on dielectric model of cement concrete. *Bull. Chin. Ceram. Soc.* 37 (05), 1758–1764. doi:10.16552/j.cnki.issn1001-1625.2018.05.045

Mu, Q., zheng, J., Yu, Y., Meng, L., and Liu, F. (2022). *In-situ* discrimination of collapsible loess through the time-domain reflectometry (TDR). *Chin. J. Geotechnical Eng.* 44 (06), 1115–1123. doi:10.11779/CJGE202206016

Pan, X., Han, Y., Chun, K., Zhang, J., Ma, D., and Gao, H. (2021). On the laboratory calibration of dielectric permittivity models for agricultural soils: Effect of systematic porosity variation. *Vadose zone J.* 20 (1), 1–14. doi:10.1002/vzj2.20096

Qiu, H., Zhu, Y., Zhou, W., Sun, H., He, J., and Liu, Z. (2022). Influence of DEM resolution on landslide simulation performance based on the Scoops 3D model. *Geomat. Nat. Hazards Risk* 13 (1), 1663–1681. doi:10.1080/19475705.2022.2097451

Roth, K., Schulin, R., Fluhler, H., and Attinger, W. (1990). Calibration of time domain reflectometry for water content measurement using a composite dielectric approach. *Water Resour. Res.* 26 (10), 2267–2273. doi:10.1029/wr026i010p02267

Savin, I., and Muzalevskiy, K. (2020). Dielectric model for thawed organic soils at frequency of 435 MHz. *IEEE Geosci. Remote Sens. Lett.* 18 (2), 218–221. doi:10.1109/LGRS.2020.2975027

Siddiqui, S., and Drnevich, V. (1995). *A new method of measuring density and moisture content of soil using the technique of time domain reflectometry*. West Lafayette: Joint Highway Research Project, Purdue University.

Sun, D., Liu, W., and Lu, H. (2014). Soil-water characteristic curve of guilin lateritic clay. *Geomechanics* 35 (12), 3345–3351. doi:10.16285/j.rsm.2014.12.038

Taoufik, B., Jamal, E., Broone, F., and Ballivy, G. (2012). Modelling dielectric-constant values of concrete: An aid to shielding effectivenes prediction and ground-penetrating radar wave technique interpretation. *J. Phys.* 45 (40), 1–12. doi:10.1088/0022-3727/45/40/405401

Topp, G., Davis, J., and Annan, A. (1980). Electromagnetic determination of soil water content: Measurements in coaxial transmission lines. *Water Resour. Res.* 16 (3), 574–582. doi:10.1029/WR016i003p00574

Wang, L., Qiu, H., Zhou, W., Zhu, Y., Liu, Z., Ma, S., et al. (2022). The post-failure spatiotemporal deformation of certain translational landslides may follow the pre-failure pattern. *Remote Sens.* 14, 2333. doi:10.3390/rs14102333

Wu, J., Gao, X., Han, Z., and Xu, Y. (2017). Analysis of the change of comfort index over Yunnan Province based on effective temperature. *Adv. Earth Sci.* 32 (2), 174–186. doi:10.11867/j.issn.1001-8166.2017.02.0174

Wu, Z., Du, W., Nie, J., and Cui, F. (2019). Detection of cohesive soil water content based on early signal amplitude envelope of ground penetrating radar. *Chin. J. Agric. Eng.* 35 (22), 115–121. doi:10.11975/j.issn.1002-6819.2019.22.013

Xiao, J., Yang, W., Gao, X., and Li, Z. (2020). Analysis and modeling of the complex dielectric constant of bound water with application in soil microwave remote sensing. *Remote Sens.* 12 (21), 3544–1030. doi:10.3390/rs12213544

Xu, J., Zhao, Z., Wang, Y., Wang, L., and Shao, M. (2019). Soil dielectric measurement based on bilinear theory. *J. Agric. Mach.* 50 (12), 322–331. doi:10.6041/j.issn.1000-1298.2019.12.037

Xu, X., Zhang, W., and Wang, Y. (2022). Measuring and modeling the dielectric constant of soil during freezing and thawing processes: An application on silty clay. *Acta Geotech.* 2 (2), 1–20. doi:10.1007/s11440-022-01487-8

Zhao, Y., Ling, D., Wang, Y., Huang, B., and Wang, H. (2016). Study on a calibration equation for soil water content in field tests using time domain reflectometry. *J. Zhejiang Univ. Sci.* 17 (03), 240–252. doi:10.1631/jzus.A1500065

Zhou, J., Li, Y., Zang, Y., Mao, H., Wang, M., and Wang, L. (2022). A method for determination of soil gravimetric water content and dry density rapidly based on frequency domain reflectometry. *J. Hohai Univ.* 5 (12), 1–12. https://kns.cnki.net/kcms/detail/32.1117.tv.20220425.1147.010.html.

Zhu, A., Ji, L., and Zhang, J. (2011). Empirical relationship between soil dielectric constant and volumetric water content in various soils. *Acta Pedol. Sin.* 48 (02), 263–268.

frontiers | Frontiers in Earth Science

TYPE Original Research
PUBLISHED 09 January 2023
DOI 10.3389/feart.2022.994593

OPEN ACCESS

EDITED BY
Haijun Qiu,
Northwest University, China

REVIEWED BY
Chao Ma,
Beijing Forestry University, China
Lingzhi Xiang,
Chongqing Jiaotong University, China

*CORRESPONDENCE
Weimin Yang,
snon_72@163.com

SPECIALTY SECTION
This article was submitted to Geohazards and Georisks, a section of the journal Frontiers in Earth Science

RECEIVED 15 July 2022
ACCEPTED 26 September 2022
PUBLISHED 09 January 2023

CITATION
Yang W, Wan F, Ma S, Qu J, Zhang C and Tang H (2023), Hazard assessment and formation mechanism of debris flow outbursts in a small watershed of the Linxia Basin.
Front. Earth Sci. 10:994593.
doi: 10.3389/feart.2022.994593

Hazard assessment and formation mechanism of debris flow outbursts in a small watershed of the Linxia Basin

Weimin Yang[1,2,3]*, Feipeng Wan[1,2,4], Siqi Ma[1,2,3], Jingkai Qu[1,4], Chunshan Zhang[1,2,3] and Haibing Tang[1,2,4]

[1]Institute of Geomechanics, Chinese Academy of Geological Sciences, Beijing, China, [2]Key Laboratory of Active Tectonics and Geological Safety, Ministry of Natural Resources, Beijing, China, [3]Research Center of Neotectonism and Crustal Stability, China Geological Survey, Beijing, China, [4]School of Earth Sciences and Resources, China University of Geosciences, Beijing, China

The Linxia Basin is located in the transition zone between the Qinghai–Tibet Plateau and the Loess Plateau in China. Collapse–landslide–debris flow geological disasters are particularly prevalent in this region. Taking a debris flow that occurred in Zhangjiayuan gully, Dongxiang County, as an example, the characteristics and formation mechanism were studied through field investigation and remote sensing interpretation methods. The hazard zoning and influence range of the debris flow were analysed under different precipitation conditions using numerical simulations. The results show that the debris flow in Zhangjiayuan gully experienced medium-to small-scale, rapid and catastrophic viscous mud flows, with activity frequencies ranging from medium to low. Because large numbers of landslides, collapses and overland flows developed on the gully bank slope, material sources for debris flows were abundant but were supplied intermittently. Induced by heavy rainfall, the landslides on the bank slipped into the gully, and then the landslide mass blocked the channel and formed a weir dam. As water converged in the gully, the dam body softened to mud, seepage deformation occurred, and the dam then burst to form a debris flow. This disaster mode represents a kind of rainfall-type landslide–blockage–debris flow disaster chain. Under varying conditions in which heavy rainfall occurs once every 10 years or once every 50 years, debris flows may break out in Zhangjiayuan gully, and the Zheda highway and the associated tunnels located below the gully are in medium–high debris flow danger zones. When a debris flow rushes out of the gully mouth and cannot be discharged in time, it accumulates and buries the highway and tunnels. Therefore, attention should be given to preventing such small-scale sudden debris flow disasters and strengthening the early warning capacity of debris flow prevention to ensure the safe operation of highway.

KEYWORDS

debris flow, hazarda assessment, formation mechanism, small watershed, western gully of zhangjiayuan

1 Introduction

Debris flows are one of the geomorphic agents carrying large amounts of solid material. Because of sudden initiation and complicated formation processes, debris flows have strong destructive power to cause casualties (Peng et al., 2004; Zhang et al., 2016). The Linxia Basin in Gansu Province China is located at the transitional region between the Tibetan Plateau and the Loess Plateau, where debris flows are highly developed (Li and Zeng 1982). Debris flows in this region often accompany with catastrophic disasters, as exemplified by some cases on 20 July 1964, 7 July 1965 and 21 July 2013 (Qu et al., 2018). In fact, debris flows in the region mainly depend on the rainfall condition, as the material resources is unlimited and mainly from the loess deposits (Zhang and Tang 1994; Liu et al., 2001). However, detailed information about local debris flow event is few, and it is worth us to explore the characteristics and risk potential in rainstorm with varied recurrence period.

Debris flows in Linxia Basin are commonly small scale and low frequency (Wang, 1995; Ma et al., 2006). Due to the concealment, unclear genetic mechanisms and insufficient hazard estimation, local debris flow has been rarely documented. Though the annual precipitation in Linxia Basin is far less than other regions, occasional rainstorm occur in rainy season (Liu et al., 2001; Qu et al., 2018). In the eastern part of the Tibetan Plateau, local debris flows can be triggered not by rainstorm, but a combination of heavy rainfall and earthquakes (Hu and Zhong, 2002; Wei et al., 2002; Su et al., 2004; Tang et al., 2011a; Liu et al., 2011; Ni et al., 2011; Guo et al., 2014; Xu et al., 2017). With the global climate warming and increasing seismic events, extreme weather in Linxia Basin and its surrounding areas may occur in future. Recently, some extreme events that never occur before have been documented. On 21 July 2013, a heavy rain in Hedong, Gansu Province, poured hourly rainfall up to 82.3 mm. From August 17 to 30, 2017, a continuous rainfall lasted 15 days and covered the hilly area from Lanzhou to Jingyuan. From September to October 2021, the southeast part of Gansu province suffered heavy rainfall and caused tremendous landslides. It can be speculated that extreme events could promote the debris flows possibility because slope failures in Linxia Basin are more prone to occur than other mountain regions in eastern marginal boundary of the Tibetan Plateau.

Quantitative evaluation provides an effective way to reduce disaster losses (Pasutoa and Soldati 2004). Many hazard assessment methods have been proposed, such as the analytic hierarchy process, fuzzy comprehensive evaluation, logistic regression model, deterministic distribution model, and geographic information system (Delmonaco et al., 2003; Huggel et al., 2003; Paudel et al., 2020). Numerical simulations analysis can better simulate the movement process and movement characteristics (Chau and Lo 2004; Song et al., 2018; Monia et al., 2020), and determine the runout and deposition of debris flows (Magirl et al., 2010). Among them, FLO-2D is commonly used to analyse the risk potential of mud flow or flood (O'Brien et al., 2009; Bertolo and Wieczorek 2005; Zhang et al., 2014; Liang et al., 2016). Such method can provide the potential inundation areas under given rainstorm with varied recurrence period, which is helpful for risk zoning according to the predicted flow depth, maximum velocity and flow mass (Hungr, 1995; Erena et al., 2018; Chang et al., 2019a; Liu et al., 2020; Wu et al., 2022). In Linxia Basin where debris flows are rarely documented, it is important to delineate the potential inundation areas considering the rainstorm recurrence period. Furthermore, detailed description of debris flows there are also important for risk assessment and hazard mitigation.

The early identification and genetic mechanism of debris flows in the Linxia basin are few, and potential risk evaluation is also rarely reported. On 24 April 2021, a severe mud flow event occurred in the Zhangjiayuan watershed, Dongxiang County, Linxia Hui Autonomous Prefecture, Gansu Province, China. This case provided a valuable chance to know about the characteristics and formation condition of mud flow. In this work, the rainfall triggering condition, material sources and deposits were clearly documented according to the timely investigation by the research team of Institute of Geomechanics, Chinese Academy of Geological Sciences. Then, the potential hazard of mud flows at two rainfall probabilities were numerically assessed by FLO-2D and the hazard zoning were divided by the flow depth and momentum. The results will contribute to comprehend the formation mechanics of mud flow in Loess Plateau, China, and its nearby surroundings, which also provide a reference for hazard mitigation and forecasting for debris flows.

2 Environmental and geological settings

The study area is located in north-western part of Dongxiang County, Linxia Hui Autonomous Prefecture, Gansu Province. As the study area is on the transitional region between the Tibet- and Loess-Plateau (Figure 1A), the tableland area is heavily incised. Tectonically, the Linxia Basin is between the Qilian Mountain and the Qinling orogenic belt (Figure 1B). Upper Pleistocene Malan loess mainly exposed in the study area. In Zhangjiayuan watershed, Neogene rocks expose at the gully bottom and at the valley bottom, and the brick-red-sandy mudstone is nearly horizontal. The Malan loess, which is more than 50 m thick, drapes on the Neogene deposits. The Zhangjiayuan watershed is a fan-shaped watershed located on the tableland of Yellow River. The area of the watershed is 1.36 km^2, and the mean channel gradient is 130‰. The main channel, which has a total length of 1.78 km, drains into the Liujiaxia Reservoir. Within the Zhangjiayuan watershed, the highest elevation is 2020 m, and the relative relief of watershed is 251 m (Figure 1C). The watershed outlet is approximately 30 m over the Liujiaxia Reservoir. In the

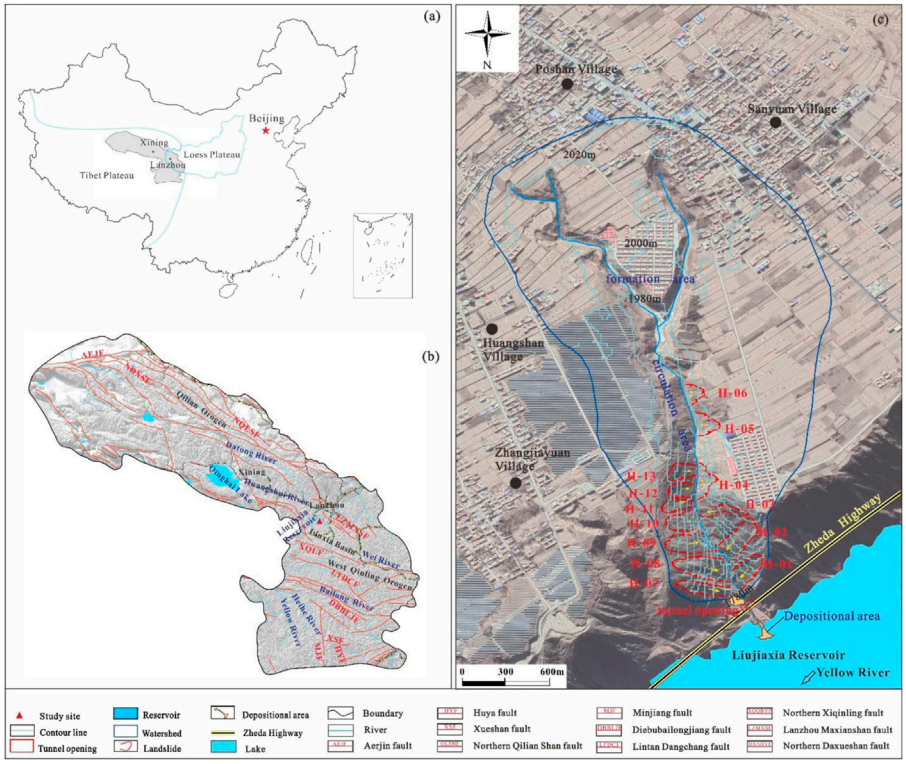

FIGURE 1
Simplified topography and geological setting of the Zhangjiayuan watershed **(A)** location of the study area in the transitional regions of Tibet Plateau and Loess Plateau, **(B)** geological setting of the study area and **(C)** simplified topography of the study area.

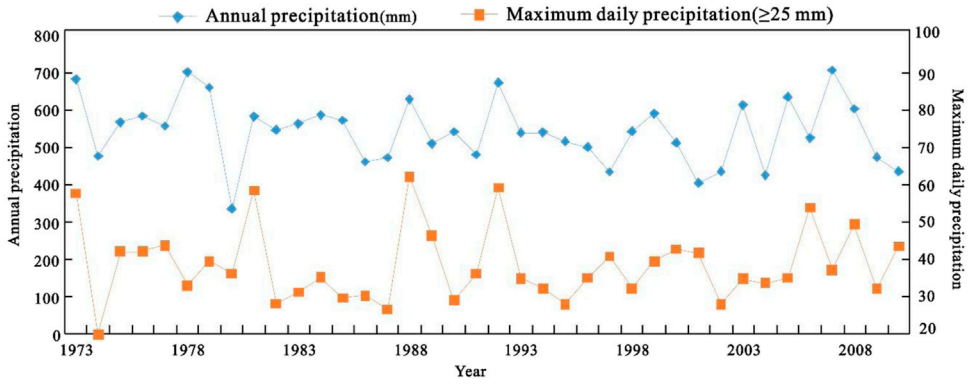

FIGURE 2
Climatic conditions of the study area according to the meteorological station at Dongxiang County.

transport section, the channel is 1.21 km long and is incised to V-shape.

This area is located in temperate semiarid climate zone with most rain fallen between July and September. The annual precipitation ranges from 336.5 mm (in 1980) to 707.5 mm (in 2007). According to the meteorological records from 1986 to 2005, the annual mean temperature was 5.6°C and annual mean precipitation was 530 mm. However, the average

annual temperature and monthly average temperature of Zhangjiayuan watershed were slightly higher than those of the whole county. Within the study area, the rainy years have a general recurrence pattern of 5–6 years, and the dry years have a recurrence of 8 to 10 years (Figure 2). The maximum daily precipitation was high up to 62.7 mm, and the maximum hourly rainfall was 45.0 mm. In the past 50 years, there were 5 events with daily precipitation >50 mm, and approximately one heavy rainfall event (>50 mm) occurred in 10 years interval.

3 Data and methods

3.1 Data collection

In this work, field investigation and remote sensing image interpretation combine to examine the material resources. Laboratory tests, inspecting the mudflow properties, provide the physical parameters to numerical simulation work of delineating potential inundation areas. The morphological and geometric parameters of the gully, the landslides developed on the bank, and the flow marks of debris flow were measured by hand-held laser rangefinder during field investigation. The distribution of landslides and depositional area is finely interpreted by remote sensing images (Liu et al., 2022b; Qiu et al., 2022). The physical parameters of the debris flow deposits are analysed in laboratory tests.

Debris flow samplings were taken at the depositional area of Zhangjiayuan watershed. During investigation, road departments and debris flow control personnel were interviewed to determine the flow pattern of debris flows. The samples were adjusted to the fluid state at the time of the debris flow outbreak, and the bulk density was calculated after weighing. The consistency limit of the deposits was measured by a liquid–plastic combine tester in the laboratory. Grains >0.05 mm were sorted by sieve analysis, and grains <0.05 mm were treated by hydrometer analysis.

3.2 Setting the simulation conditions and characterization parameters of the debris flow

According to meteorological records from the China National Meteorological Administration and local meteorological bureaus, the maximum daily precipitation of the study area was 62.7 mm on 18 August 1970. During 2011 and 2021, the maximum daily rainfall reached 55.7 mm. Therefore, the maximum 50-year precipitation (probability p =2%) was set to 62.7 mm and the maximum 10-year precipitation (probability p =10%) was set to 55.7 mm.

The parameters of the debris flow calculation were set based on field investigations and lab tests, by referring to existing research results and the FLO-2D user manual. Referencing the FLO-2D manual and previous researches (Zhang et al., 2014; Hou et al., 2021), the laminar flow arrest coefficient (K) was set to 2280 as the debris flows in Zhangjiayuan watershed are typically mud flows. The viscosity coefficient (η) and yield stress (τ_y) mainly depend on the volume concentration of sediments, which is solved by obtaining the correlation between η and τ_y (Hou et al., 2021; Wu et al., 2022). Wang et al. (2003) proposed a unified relationship among the sand ratio–volume concentration–rheological parameters. The calculated experimental parameters, namely, α_1, α_2, β_1, and β_2, were set to 0.000247, 0.03, 15.48, and 14.42, respectively. According to the above relationship, mud depth and other characteristics of the debris flow, the Manning roughness coefficient (n_c) of channel and slope were calculated to be 0.30 and 0.35, respectively.

Due to the reactivation of the H-08 landslide, the sliding body blocked the channel and formed a barrier dam. The upstream side of the landslide dam was determined as the water catchment point (Figure 1C and Figure 3A). According to the clear water flow line and amplification coefficient $BF = 1/(1 - C_v) = 1.862$ (where C_v is volumetric concentration of the solid phase within debris flow) extracted from rainfall-runoff simulations, the flow process curves of debris flow at catchment point can be obtained with probabilities of 10% and 2%, respectively (Figures 3B,C).

4 Results

4.1 Description of the debris flow event

The debris flow in Zhangjiayuan watershed occurred in the early morning of 24 April 2021, following the rainstorm started in the night of 23 April 2021. There were no meteorological stations near the study area, as it is about 33 km away from the urban area of Linxia County. However, the local inhabitants near the study area told that April this year was sufficient in precipitation, whereas it was not so previously. Owing to increasing extreme weather events in recent years, the rainy seasons occur earlier or later, and heavy rainfall may occur in April or even October subsequent years. In the study area, the rainy season of 2021 started at the end of March (Figure 4). Four heavy precipitation events occurred till the end of April, including the events from March 31 to April 4, April 7 to April 12, April 18 to April 20 and April 23 to April 25. The rainfall totals were 15.4 mm on April 2 and 11.5 mm on April 23, indicating that the rainfall process was long duration.

According to the field investigation and the information from Transport Department of Gansu Province, the debris flow volume was approximately 9, 000 m^3, with approximately 2, 000 m^3 in tunnel and 7, 000 m^3 in channel. Majority of sediments deposited at the tunnel mouth and on the Zheda highway, thus caused damage to the west entrance of Tunnel No. 408 and to the east entrance of Tunnel No. 409. The length of the

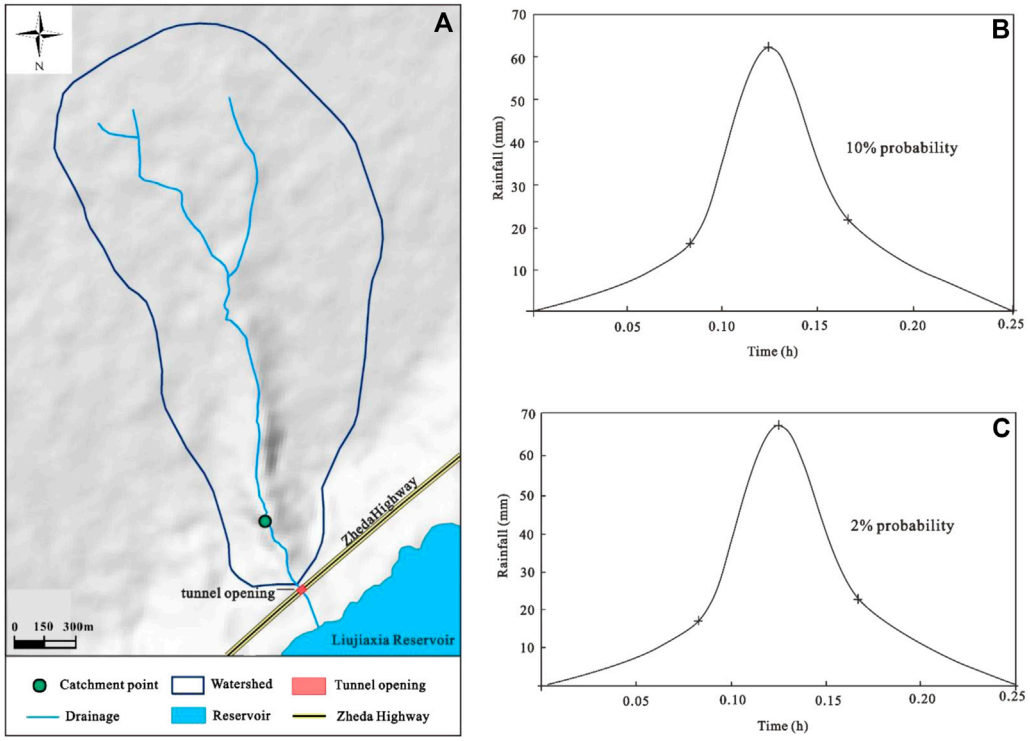

FIGURE 3
Catchment point setting and flow process curve of the analysed debris flow.

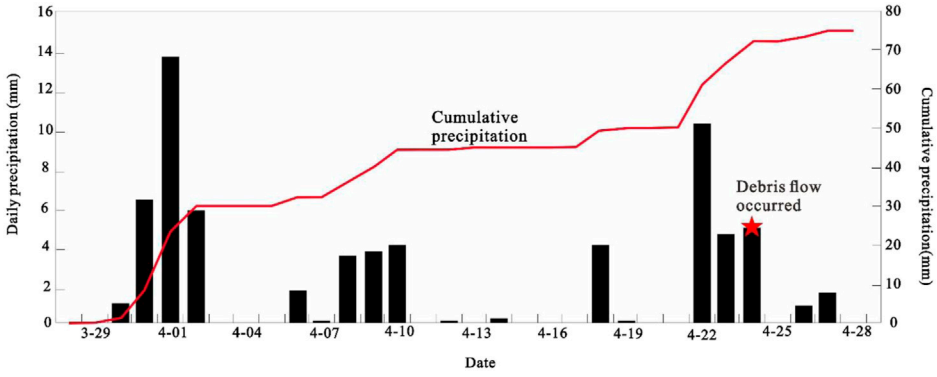

FIGURE 4
Precipitation variations in Ningxia County from 29 March 2021, to 29 April 2021.

depositional area in Tunnel No. 408 was 146 m, and the highest mud level was 3.5 m (Figure 5A); however, this length was 25 m in Tunnel No. 409, with a mud level of 3.3 m. Importantly, the debris flow travelled across the road and delivered sediments on the right bank of the Liujiaxia Reservoir (Figure 5B). The depositional fan was 90 m in length, 58 m in width, 1–3 m in thickness, with diffusion angle 120° and magnitude of 2, 500 m^3.

In accordance with particle component analysis and physical property measurement, the debris flow density is 18.0 kN/m^3. The liquid and plastic limit are 25.7% and 18.4%, respectively.

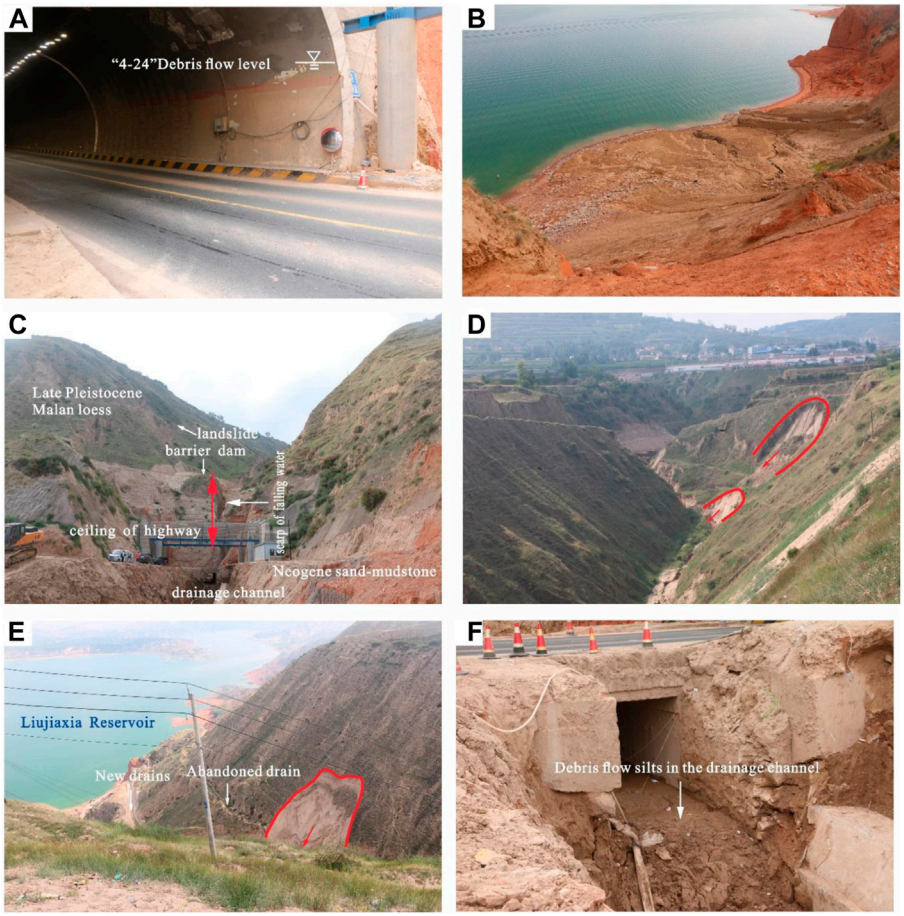

FIGURE 5
Debris flow characteristics and treatment engineering measures applied in Zhangjiayuan gully **(A)** Mud level at the west entrance of Tunnel 408 lens: NE; General view of the circulation area and debris flow outlet: SEE; **(B)** Debris flow depositional area lens: NE; **(C)**. Landslides that occurred on the left bank of the gully upstream (H-06) lens: S; **(D)** Landslide on the right bank in the transportation area lens: NE; **(E)** Culvert under the highway lens: SE; **(F)** Retaining wall upstream of the culvert lens: SE.

TABLE 1 Results of the grain analysis performed on samples obtained from the Zhangjiayuan gully debris flow.

Sand particles			Silt particles		Clay particles
Coarse-grained	Medium-grained	Fine-grained			
2–0.5/mm	0.5–0.25/mm	0.25–0.05/mm	0.05–0.01/mm	0.01–0.005/mm	<0.005/mm
0	0.3%	16.4%	58.9%	10.1%	14.3%

The debris flow deposits are mainly composed of fine sand and silt–clay particles (Table 1), and the fine sand accounts for 16.4%, silt 69.0% and clay 14.3%. This indicates that the material sources are mainly from Epipleistocene Malan loess on the gully bank. Therefore, debris flows in Zhangjiayuan watershed belongs to viscous-mud flow.

4.2 Material sources

The primary material sources of the debris flow are mainly from slope-surface erosion and loess mass movements. As the slope top is relatively flat, the amount of slope erosion is far less than Collapse-landslide mass. On basis of landslide detailed

TABLE 2 Statistics of the geometric characteristic parameters of landslides on the Zhangjiayuan gully bank.

Landslide number	Length (m)	Width (m)	Average thickness (m)	Slip (°)	Volume (×10⁴ m³)
H-01	125	80	2	40	1.0
H-02	155	77	2	40	1.2
H-03	164	30	1.5	90	0.4
H-04	57	120	1.5	80	0.5
H-05	65	100	1.5	80	0.5
H-06	48	75	1.5	80	0.3
H-07	180	65	4	290	2.3
H-08	155	115	4	270	3.6
H-09	117	77	2	260	0.9
H-10	89	75	2	270	0.7
H-11	105	52	1.5	260	0.4
H-12	83	63	1.5	260	0.4
H-13	95	58	2	260	0.6

Note: The geometric parameters of landslides in the table were obtained from high-resolution remote sensing image interpretations, and those of new landslides were obtained from field surveys and mapping.

interpretation (Liu et al., 2022a and, Liu et al., 2022b) and field investigation, small collapses, landslides and overland flows mainly developed on the left and right banks of the middle and lower reaches (Figures 5C,D,E), especially within the 500 m channel downstream of the gully mouth. A group of landslides developed (Figure 1 and Table 2) on the right bank of the transportation area in the middle–lower reaches, which consisted of 7 landslides with volumes of 0.4–2.3 $\times 10^4$ m^3. Six small landslides occurred on the left bank, with volumes of 0.3–1.6$\times 10^4$ m^3. These 13 landslides were all small-scale and were mainly composed of Pleistocene loess and locally sourced Neogene sands and mudstones. The bed underneath comprise of Pleistocene loess, and Neogene sandstone–mudstone slide beds are exposed near the gully mouth (Figure 5A).

On 23 April 2021, a new landslide No.H-06 (Figure 5D) occurred on the left bank. It has a length 48 m, width 75 m, thicknesses 1–2 m and volume about 3000 m^3. On the right bank, two new landslides occurred. The first one developed from the lower part of old landslide No.H-08 (Figure 5E), with length 85 m, width 65 m, thickness 1–2 m, and volume 5000 m^3. The Landslide No. H-13 was 95 m in length, 58 m in width, 2 m in thickness and approximately 6000 m^3 in volume. Based on *in situ* investigations (Table 2), the total and dynamic material storage were calculated, including sediments from landslide (V_1) and slope erosion (V_2). The total landslide recharge amount can be obtained from the accumulative volume of each landslide, i.e., 1.26 × 10^5 m^3. On the basis of the watershed distribution area (F_{total}), landslide distribution area (F_{slide}) and loose soil layer thickness (h), the slope supply can be determined by multiplying the product of the slope-type provenance distribution area ($F_{total} - F_{slide}$) by the average thickness of the soil layer, i.e., 6.25 × 10^6 m^3. Therefore, the total material storage can be: calculated as $V_{total} = V_1 + V_2 = 6.375 \times 10^6 m^3$.

Referring to appendix I of the Chinese Geological and Mineral Industry standard (DZ/T 0220–2006 Debris flow disaster prevention engineering investigation code) and Appendix F.1 of the geological disaster hazard assessment "Procedure of Gansu Province local standard DB62/T-2009" (in Chinese), the rainfall-flood method was adopted herein to calculate the maximum debris flow outflow amount at a given time:

$$W = 0.278 \times Q_C \times T \quad (1)$$

$$Q_C = (1 + \psi) \times Q_p \times D \quad (2)$$

$$\psi = (\gamma_c - 1)/(\gamma_h - \gamma_c) \quad (3)$$

where W is the maximum mass of a single debris flow outrush (m^3); Q_C is the debris flow discharge (m^3/s); T is the debris flow duration (s), with a value of 900 s; ψ is the sediment coefficient; D is the gross blockage factor, with a value of 2.3; γ_C is the debris flow bulk density (kN/m^3), with a value of 18 kN/m^3; and γ_H is the solid particle weight (kN/m^3), with a value of 26 kN/m^3.

Based on the data of the Chinese National Meteorological Administration, the maximum daily precipitation in the Linxia from June 2011 to June 2021 was 55.7 mm (15 August 2016). According to the 10 years recurrence rain event, the maximum debris flow discharge in Zhangjiayuan gully was calculated to be 61.2 m^3/s, and the maximum outflow of a debris flow could reach 1.53 × 10^4 m^3. The above information reveals that the probability of daily precipitation greater than 50 mm is approximately once every 10 years for the rainy- and dry water-year periods in Dongxiang County. Thus, the one-time maximum outburst amount calculated using the 10-year probability occurrence can be considered the dynamic source reserve of Zhangjiayuan gully debris flows.

The field investigation and material interpretation show that the material sources of debris flow in Zhangjiyuan watershed are mainly

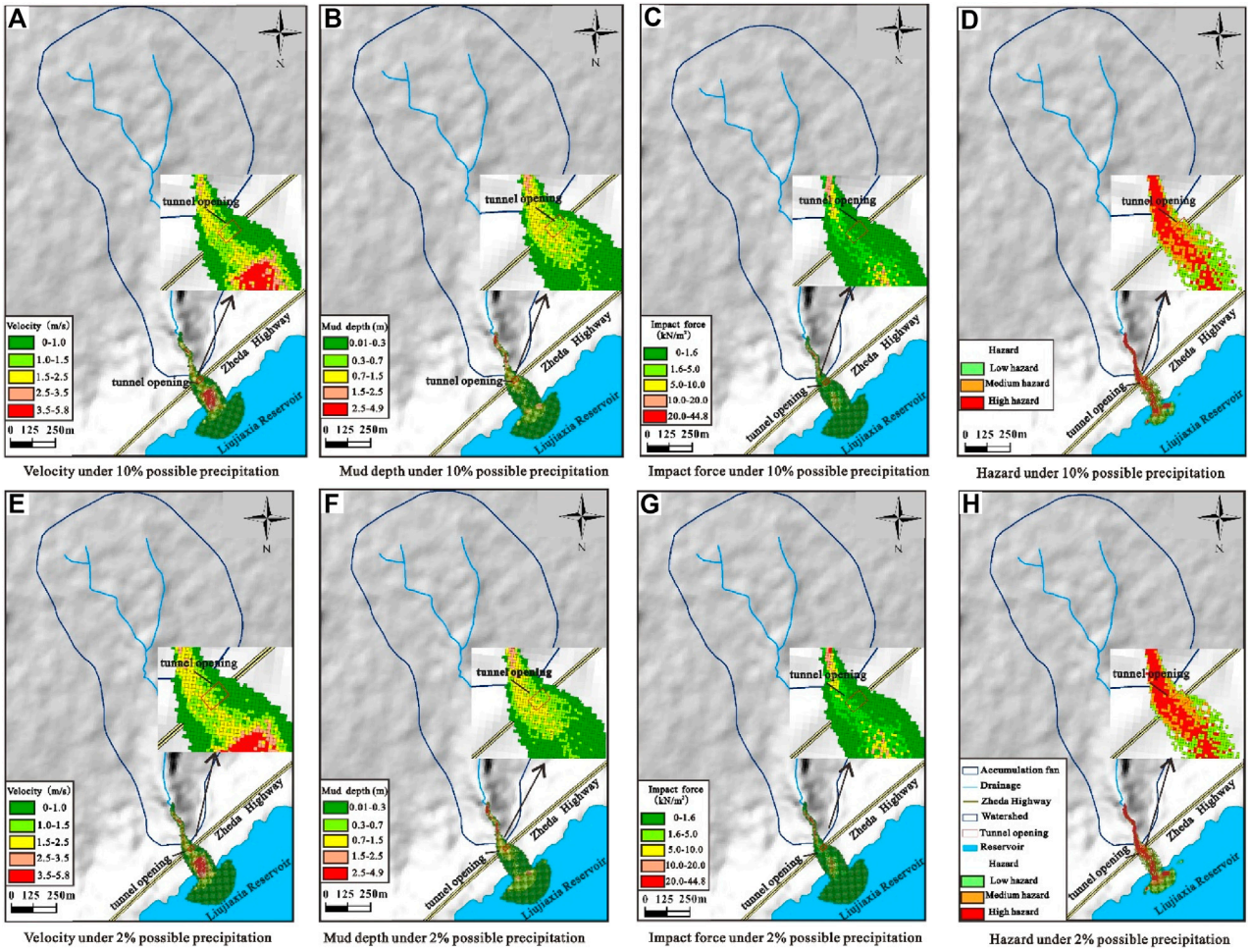

FIGURE 6
Simulation results of debris flow movement characteristics and danger ranges based on FLO-2D under two precipitation conditions.

from the landslides and collapses along gully bank, and the overland flow erosion on the hilly slope. As known to all, the occurrence of mass movements in Loess Plateau, China, closely relates to the annual rainy season precipitation and rainfall duration (Palladino et al., 2018; Ma et al., 2021; Zhou et al., 2022). The material supply from collapse–landslide–overland flow mass is more in rainy years and less in dry years, which leads to the great difference in the size of the provenance dynamic storage provided each year. Therefore, the material source of debris flow in the gully is abundant, but has the characteristics of intermittent supply.

4.3 Hazard simulation results of the analysed debris flow

Figure 6 and Table 4 show the simulation results of the debris flow movement process in Zhangjiayuan gully for precipitation conditions with different probabilities (p =10% and p =2%). Except for the hazard index, the classification of the other indexes was automatically generated by the calculation results.

With reference to the research of Tang et al. (1994), Li et al. (2021), Hou et al. (2021), and the Swiss Disaster Degree Classification (Garcia et al., 2004), the hazard zoning of Zhangjiayuan gully debris flows was carried out on the basis of the velocity (Vc), mud depth (Hc), and other indexes. The area within the hazard range was divided into high-, medium-, and low-hazard zones (Table 3).

According to Figures 6A–D and Table 4, the maximum flow velocity of a debris flow could reach 5.8 m/s in the case of heavy rainfall over 10 years. The zone with flow velocities greater than 3.5 m/s was distributed in the middle of the accumulation body, covering an area of 3750 m^2, and the zone with flow velocities less than 1 m/s covered an area of 45,975 m^2. The maximum mud depth of the debris flow was 4.8 m, and the area with mud depths

TABLE 3 Standards of debris flow hazard zoning.

Hazard	Accumulation mud depth/m	Logical relationship	Product of the mud depth accumulation and flow velocity
High	Hc≥1.5	OR	Hc×Vc≥2.5
Medium	0.5<Hc<1.5	AND	0.5<Hc×Vc<2.5
Low	0.01≤Hc≤0.5	AND	0.1≤Hc×Vc≤0.5

TABLE 4 Simulation and hazard classification results of debris flows in Zhangjiayuan gully under two precipitation conditions.

Parameter	Index size and classification	Area (p=10%) (m^2)	Area (p=2%) (m^2)
Velocity Vc/m/s	Vc<1	45975	37350
	1≤Vc<1.5	9175	9675
	1.5≤Vc<2.5	7450	8275
	2.5≤Vc<3.5	3075	3275
	Vc≥3.5	3750	4050
Mud depth Hc/m	Hc<0.3	46150	46425
	0.3≤Hc<0.7	14350	17975
	0.7≤Hc<1.5	6250	6350
	1.5≤Hc<2.5	1875	2050
	Hc≥2.5	800	1000
Impact force δ/kN/m^2	δ<1.6	54450	57800
	1.6≤δ<5.0	8125	8775
	5.0≤δ<10.0	3150	3475
	10.0≤δ<20.0	1475	1625
	δ>20.0	200	425
Hazard	Low	15325	17700
	Medium	5625	6625
	High	10825	12175

greater than 2.5 m was located at the bottom of the circulation area with an area of 800 m^2. The maximum impact force of the debris flow was 44.8 kN/m^2, and an impact force greater than 20 kN/m^2 acted on the bottom of the circulation area; the area with impact forces greater than 10 kN/m^2 was only 1675 m^2. The high-hazard debris flow area was located from the starting site of the debris flows to the inside channel of the Liujiaxia Reservoir bank, covering an area of 10825 m^2. The middle hazard area was located in the middle of the inlet of the Liujiaxia Reservoir and the gully mouth to the northern Zheda highway. The low-hazard area was located outside the accumulation body of the north Zheda highway.

In the case of a 50-year heavy rainfall event (Figures 6E–H and Table 4), the maximum flow velocity of the debris flow was still 5.8 m/s, and the area of flow velocities greater than 3.5 m/s was 4050 m^2. The maximum mud depth of the debris flow was 4.9 m, and the area with mud depths greater than 2.5 m was 1000 m^2. The maximum impact force of the debris flow was 50.6 kN/m^2, and the area with impact forces greater than 10.0 kN/m^2 was only 2050 m^2. The high-hazard area of the debris flow was distributed inside the channel from the starting site of the debris flow to the entrance of the Liujiaxia Reservoir, with a distribution area of 12,175 m^2, while the medium–low hazard area was basically the same as that obtained under the once-in-a-decade condition.

The simulation results show that debris flows erupt in Zhangjiayuan gully when it encounters heavy rainfall once every 10 years or extreme rainfall once every 50 years. Controlled by the gully morphology and debris flow properties in the circulation area, the debris flows in Zhangjiayuan gully reach their maximum velocity in the middle of the accumulation area, and the strongest impact force of the debris flows is applied to the area from the downstream region of the circulation area to the lower part of the gully mouth. When a debris flow rushes out of the gully, the debris flow begins to accumulate. In the case of a 10-year rainfall event, the mud silting height of the road and tunnel mouth is 1.27 m, the silting width of the east tunnel is 49 m, and that of the west tunnel is 21 m. In the case of a 50-year rainfall event, the maximum silting depth in the tunnel is 1.41 m, the silting width of the east tunnel is 53 m, and that of the west tunnel is 25 m. Under these two precipitation conditions, the tunnels are in the medium–high hazard zone of debris flows, and the silting hazard in the east tunnel is much higher than that in the west. If heavy rainfall occurs once in one hundred years, a large-scale debris flow would occur in the small watershed of Zhangjiayuan gully and may silt and scour the road and tunnel or even destroy the road or tunnel opening.

Based on the above results, three types of hazard-affected objects can be identified: tunnel; pavement and subgrade; and culverts (Figure 5F). Therefore, the susceptibility of the debris flow should be discussed. The susceptibility (C) indicates the resistance degree of the hazard-affected object against debris flow damage. Values for this variable ranges between 0 and 1, where larger susceptibility values indicate a more vulnerable hazard-affected object (Cui and Zou, 2016). According to the studies of Cui et al. (2016) and Li et al. (2021), the C value is mainly affected by two factors: structure susceptibility (C_1) and siltation susceptibility (C_2). Because the Zhangjiayuan debris flow is mud, the C_1 value is too small to be ignored. C_2 is calculated by:

$$C_2 = Hc/h \quad (4)$$

where Hc is the mud depth and h is the clearance of the culvert or tunnel. If $Hc/h \geq 1$, C_2 equals 1 because the culvert is completely silted. Similarly, the C_2 value for the buried tunnel and pavement and subgrade is set to 1. However, vehicles and pedestrians are not considered.

The geometric information of the culvert or tunnel was obtained during field investigation. The length × width × height dimensions of the culvert are 10 × 3 × 3 m, and the tunnel section is a semicircular arch with a size of 9 × 10 m.

The hazard zoning results of the Zhangjiayuan debris flow show that for 10-year and 50-year rainfall events, the mud depths of the road and tunnel under the gully mouth are 1.27 m and 1.41 m, respectively, and both the highway and tunnel are in the high hazard zone (Figures 6D,H). However, due to the large bulk density of the debris flow and the slow discharge of the culvert, the tunnel and culvert were buried on 24 April 2021, and the mud depths of the west opening of Tunnel 408 and the east opening of Tunnel 409 were 3.5 m and 3.3 m, respectively. In terms of Eq. 4, C_2 is equal to 1, which indicates that the siltation susceptibility of the culvert, tunnel or pavement and subgrade is high.

5 Discussion

5.1 Differences in debris flows between the Linxia Basin and the eastern Tibetan Plateau

Differentiating from the viscous debris flows in the eastern Tibetan Plateau, the debris flows in the Linxia Basin are mostly viscous mud flows, as the source materials are derived from the Quaternary loess. Due to the dry climate and uneven rainfall, debris flows generally occur at low frequencies and they are currently in a declining period. The solid sources of debris flows are abundant, and mainly provided by gully bottom erosion and lateral erosion. Most debris flows occur at medium-to high-frequencies and have medium–large magnitudes. Debris flows in the area are triggered by heavy rainfall (Liu et al., 2011; Tie et al., 2013; Chang et al., 2019b) or by both strong earthquakes and heavy rainfall (Cui et al., 2010; Tang et al., 2011b; Ni et al., 2011; Xu et al., 2017). The rainfall thresholds that induce debris flows are generally 25 mm/h~60 mm/h. In the eastern part of the Qinghai–Tibet Plateau, the types of debris flows are mainly gullies or valleys, with bulk densities of 1.3–2.3 kN/m^3. Due to large precipitation in the area and the uneven distribution of rainfall in various watersheds, heavy or extreme rainfall frequently occurs, and debris flows mainly occur at medium-to high-frequency, similar to the currently in flourishing or developing period. Multiple disaster modes, including ravine rainstorm debris flows, collapse–landslide–debris flow disaster chains, and even high-position collapse landslide debris flows have been observed.

5.2 Genetic mechanism of the analysed debris flow

The debris flows in Zhangjiayuan gully mainly form and develop as follows.

Thirteen landslides were identified on the middle and lower banks of the circulation area (Figure 1; Table 2), with channel blockage and poor drainage conditions. These landslides are mainly loess landslides, but some of the landslides on the left bank of the gully cut into the moderately to intensely weathered Neogene sandstone–mudstone zone (Figure 4A). The landslides of the right bank mainly slip along the unloading fissure plane and are mostly shallow landslides. Most of these landslides occurred before 2021. The H-01, H-07 and H-08 landslides, which developed on both banks of the gully mouth, rushed into the gully. Small portions of these landslide masses eroded away by subsequent water flows, but most of the residual parts still

accumulated in the gully, resulting in water crossing the section of the gully (Figure 4A) in the narrow outlet of the debris flow; the gully discharge was not smooth.

Due to continuous long-term rainfall, the water content of rock–soil in the basin increases, and the bank surface can be eroded to form overland flows. Alternatively, the reduction in slope stability may lead to the occurrence of landslides and collapses (Yang et al., 2022), such as the new H-06 landslide on the left bank, the revival of the H-08 and H-12 landslides on the right bank, and the landslide body blocking the gully to form a barrier dam after sliding into the gully (Wang et al., 2022). When this region subsequently encountered heavy rainfall, the water gathered and formed a barrier lake.

After rainwater converges, the deposits and landslide rock–soil mass accumulated in the channel soften and undergo argillization, resulting in dam bursting and the formation of a debris flow induced by short-term heavy rainfall. From the end of March to the end of April 2021, four heavy rainfall events (Figure 5) occurred in the region of Dongxiang, Yongjing and Linxia Counties, including two daily rainfall events exceeding 10 mm. This heavy rainfall led to the rapid increase in the water content and weight of the accumulated rock–soil mass. When the water content of the deposit exceeded the liquid limit, the soil mass was in the critical plastic flow state, implying that the slurry-making process had been completed. Another rainstorm occurred on the evening of April 23. The water promptly gathered in front of the dam, the water level surged, and the hydrostatic pressure and earth pressure increased (Wu et al., 2013). As the rainwater flowed downstream, the dynamic water pressure also increased. Under the action of the high-water level in the upstream dam, as well as the permeation pressure and fluid self-gravity associated with the debris flow, the shear fractures in the front edge of the landslide accumulation zone were internally eroded, extended and finally connected, and fissure fillings were quickly washed away to form a water inrush channel. When the vertical penetration was more than the effective weight of the soil mass of the dam, parts of the barrier dam experienced soil flow deformation, resulting in the bursting of the dam and the initiation of a debris flow (Zhou et al., 2022). It is worth pointing out that the long-term rainfall ensured sufficient time for rainwater to infiltrate into the rock–soil mass; this was the premise for softening and argillation of the channel accumulation and collapse-landslide bodies. However, the top of the gully is a plateau tableland, the amount of surface runoff converging into the channel is relatively small, and the fluid of the debris flow was not washed away promptly in the gestation process.

The bulk densities of the debris flows in Zhangjiayuan gully are high. After a debris flow starts, the fluid scours and erodes the channel and slope foot, resulting in the collapse of the bank foot and the lower part of old landslides, thereby increasing the severity and viscosity of the debris flow and enhancing the destructive power of fluid shear.

The circulation area downstream of Zhangjiayuan gully has been blocked by the loose solid materials of landslide bodies for a long time, and the discharge mouth is narrow, thus constituting a bottleneck of debris flow movement. A scarp of falling water is present between the outlet and the road surface below, with a height difference of 14.0 m. The initiation process of a debris flow is similar to the karst water and mud inrush phenomenon that occurs during tunnel excavation (Li et al., 2017), consisting of three parts: the disaster source, debris flow channel and barrier dam. The disaster source is the channel accumulation of the upper dam, the collapse and sliding accumulation body, and the converging water body. The debris flow channels are equivalent to the karst water inrush channels, that is, the migration path of the debris flows. The barrier dam is the eventual barrier that blocks water before the debris flow starts. When the analysed debris flow rushed out of the gully to the Zheda highway, the fluid could not be discharged in a timely manner to the Liujiaxia Reservoir due to the small cross-section (bottleneck) of the culvert under the highway, and the debris flow instead rushed into the tunnels on both sides of the highway until the road was silted and blocked.

6 Conclusion

The goal of this study was to analyse hazards and genetic mechanisms of a debris flow in a small watershed, which was induced by rainfall in the transition zone between the Qinghai-Tibet Plateau and the Loess Plateau. The study area is of loess ridge landform, with vertical and horizontal gullies. The bank slope of the gully is prone to collapse and landslide, and the debris flow sources are abundant. When encountering heavy rainfall or continuous rainfall for a long time, debris flows are prone to outburst in this type of small watershed. As the material sources were mainly loess and the underlying Neogene mudstone weathering material, which were intermittently supplied by previous collapses and landslides on the bank; thus, this kind of debris flow had the characteristics of a the medium-small scale, a medium-low activity frequency, and a viscous mud flow.

The four heavy rainfall events from the end of March to the end of April 2021, and the rainstorm from April 23 to the early morning of April 24 led to the outbreak of the debris flow in Zhangjiayuan gully. This event occurred because the bank slope collapse-landslide-overland flow sequence was induced by long-term rainfall and multiple heavy rainfall processes. The disaster bodies blocked the channel and formed a barrier dam. The water flow converged in front of the dam. The infiltration of water caused the channel deposits to soften and muddy, and led to the seepage deformation of the dam body prior to the debris flow outburst. The disaster formation mode was the rainfall-type landslide-blockage-debris flow disaster chain mechanism.

Under the condition of heavy rainfall once every 10 years or once every 50 years, debris flows will occur in Zhangjiayuan gully. After a debris flow starts, the maximum flow velocity is reached in the middle of the accumulation area, and the strongest impact forces are applied to the area from the downstream region of the circulation area to the lower part of the gully mouth. The Zhida highway and tunnel under the mouth of the gully are in the medium–high hazard zone of debris flow. If a debris flow rushing out of the gully mouth cannot be discharged in time, it will begin to accumulate and bury the highway and tunnel. Although the scale of the debris flow in this small watershed is not large, the debris flows in this region have strong concealment and sudden outbreak characteristics, which may cause a substantial catastrophe. Attention should be given to preventing such 'small disaster, big catastrophe' events to ensure the safe operation of highways and tunnels in a timely manner.

Data availability statement

The original contributions presented in the study are included in the article/Supplementary Material, further inquiries can be directed to the corresponding author.

Author contributions

WY, writing; FW, data analysis; SM, data analysis; JQ, programming; CZ, guidance, and HT programming.

Funding

This research is supported by the Second Tibetan Plateau Scientific Expedition and Research Program (2019QZKK0902).

Acknowledgments

The authors would like to thank the editor and two anonymous reviewers for their very helpful comments, which gave us the opportunity to address several issues that were initially overlooked.

Conflict of interest

The authors declare that the research was conducted in the absence of any commercial or financial relationships that could be construed as a potential conflict of interest.

Publisher's note

References

Bertolo, L. P., and Wieczorek, G. F. (2005). Calibration of numerical models for small debris flows in Yosemite Valley, California, USA. *Nat. Hazards Earth Syst. Sci.* 5 (6), 993–1001.

Chang, M., Dou, X. Y., and Tang, C. (2019a). Hazard assessment of typical debris flow induced by rainfall intensity. *Earth Sci.* 44 (8), 2794–2802. doi:10.3799/dqkx.2017.547

Chang, M., Liu, Y., Zhou, C., and Che, H. (2019b). Hazard assessment of a catastrophic mine waste debris flow of Hou Gully, Shimian, China. *Eng. Geol.* 275, 105733. doi:10.1016/j.enggeo.2020.105733

Chau, K. T., and Lo, K. H. (2004). Hazard assessment of debris flows for Leung King Estate of Hong Kong by incorporating GIS with numerical simulations. *Nat. Hazards Earth Syst. Sci.* 4 (4), 103–116. doi:10.5194/nhess-4-103-2004

Cui, P., Zhuang, J. Q., and Chen, X. C. (2010). Characteristics and countermeasures of debris flow in Wenchuan area after the earthquake. *J. Sichuan Univ. Sci. Ed.* 42 (5), 10–19. doi:10.15961/j.jsuese.2010.05.004

Cui, P., Zou, Q., Xiang, L. Z., and Zeng, C. (2016). Risk assessment of simultaneous debris flows in mountain townships. *Prog. Phys. Geogr.* 37 (4), 516–542. doi:10.1177/0309.1333.1349.1445

Cui, P., and Zou, Q. (2016). Theory and method of risk assessment and risk management of debris flows and flash floods. *Prog. Geogr.* 35 (2), 137–147. doi:10.18306/dlkxjz.2016.02.001

Delmonaco, G., Leoni, G., Margottini, C., Puglisi, C., and Spizzichino, D. (2003). Large scale debris-flow hazard assessment: A geotechnical approach and gis modelling. *Nat. Hazards Earth Syst. Sci.* 3 (3), 443–455. doi:10.5194/nhess-3-443-2003

Erena, S. H., Worku, H., and De Paola, F. (2018). Flood hazard mapping using FLO-2D and local management strategies of Dire Dawa city, Ethiopia[J]. *J. Hydrology Regional Stud.* 19, 224–239. doi:10.1016/j.ejrh.2018.09.005

Garcia, R., Rodriguez, J. J., and O'Brien, J. S. (2004). "Hazard zone delineation for urbanized alluvial fans," in Proceedings of the ASCE World Water and Environmental Resources Congress - Arid Lands Symposium, Salt Lake City, Utah.

Guo, F. Y., Meng, X. M., and Yin, N. W. (2014). formation mechanism and risk assessment of debris flow of "5.10" in eryang gully of minxian county, Gansu province. *J. Lanzhou Univ. Nat. Sci.* 50 (5), 628–632. doi:10.13885/j.issn.0455-2059.2014.05.008

Hou, S. S., Cao, P., and Liang, C. (2021). Debris flow hazard assessment of the Eryang River watershed based on numerical simulation. *Hydrogeology Eng. Geol.* 48 (2), 143–151. doi:10.1088/1755-1315/861/6/062002

Hu, X. W., and Zhong, P. L. (2002). Debris flow gully distribution and its nonlinear property of evolution in Jiangjiagou area, Yunnan province. *Resour. Environ. Yangtze Basin* 11 (1), 94–97. doi:10.3969/j.issn.1004-8227.2002.01.021

Huggel, C., Kaab, A., Haeberli, W., and Krummenacher, B. (2003). Regional-scale GIS-models for assessment of hazards from glacier lake outbursts: Evaluation and application in the Swiss alps. *Nat. Hazards Earth Syst. Sci.* 3 (3), 647–662.

Hungr, O. (1995). A model for the runout analysis of rapid flow slides, debris flows, and avalanches. *Can. Geotech. J.* 32 (4), 610–623.

Li, H. L., and Zeng, S. W. (1982). *Lanzhou institute of glaciology and cryopedology, academia sinica, Traffic science institute of Gansu province, China, Debris flow in Gansu province*. Beijing: Publishing House of People's Transportation.

Li, S. C., Wang, K., and Li, L. P. (2017). Mechanical mechanism and development trend of water-inrush disasters in karst tunnels. *Chin. J. Theor. Appl. Mech.* 49 (1), 22–30. doi:10.6052/0459-1879-16-345

Li, Y., Su, L. J., Zou, Q., and Wei, X. l. (2021). Risk assessment of glacial debris flow on alpine highway under climate change: A case study of aierkuran gully along karakoram highway. *J. Mt. Sci.* 18 (6), 1458–1475. doi:10.1007/s11629-021-6689-3

Liang, H. X., Shang, M., and Xu, X. (2016). Research on the influence factors of flow and deposition of debris flow based on the FLO-2D simulation. *J. Eng. Geol.* 24 (2), 228–234. doi:10.13544/j.cnki.jeg.2016.02.008

Liu, C. Z., Miao, T. B., and Chen, H. Q., (2011). Basic feature and origin of the "8.8" mountain torrent-debris flow disaster happened in Zhouqu County, Gansu, China. *Geol. Bull. China* 30 (1), 141–150. doi:10.3969/j.issn.1671-2552.2011.01.015

Liu, J. J., Ma, C., and Li, C. Y. (2020). Fundamental problems and prospects in the study of deposition dynamics of viscous debris flow in the gully-river junction. *J. Geomechanics* 26 (4), 544–555. doi:10.12090/j.issn.1006-6616.2020.26.04.047

Liu, Y. L., Guan, H. P., and Li, J. L. (2001). Time-and-Space distribution and prevention of debris flow in Lanzhou district. *J. Lanzhou Railw. Univ. Nat. Sci.* 20 (1), 30–35. doi:10.3969/j.issn.1001-4373.2001.01.005

Liu, Y., Qiu, H. J., Yang, D. D., Liu, Z., Ma, S., Pei, Y., et al. (2022a). Deformation responses of landslides to seasonal rainfall based on InSAR and wavelet analysis. *Landslides* 19, 199–210.

Liu, Z. J., Qiu, H. J., Zhu, Y. R., Liu, Y., Yang, D., Ma, S., et al. (2022b). Efficient identification and monitoring of landslides by time-series InSAR combining single- and multi-look phases. *Remote Sens.* 14, 1026.

Ma, D. T., Cui, P., and Zhang, J. S., (2006). Mudflow hazards and prevention countermeasures on the loess plateau. *Res. soil water conservation* 13 (4), 19–21. doi:10.3969/j.issn.1005-3409.2006.04.007

Ma, S. Y., Qiu, H. J., Hu, S., Yang, D. D., and Liu, Z. (2021). Characteristics and geomorphology change detection analysis of the Jiangdingya landslide on July 12, 2018, China. *Landslides* 18, 383–396.

Magirl, C. S., Griffiths, P. G., and Webb, R. H. (2010). Analyzing debris flows with the statistically calibrated empirical model LAHARZ in southeastern Arizona, USA. *Geomorphology* 119 (1/2), 111–124.

Monia, C., Valeria, M., Vania, M., Sciarra, N., and Miccadei, E. (2020). Rockfall and Debris Flow Hazard Assessment in the SW Escarpment of Montagna del Morrone Ridge (Abruzzo, Central Italy). *Water* 12, 1206. doi:10.3390/w12041206

Ni, H. Y., Zheng, W. M., and Tang, Y. Q., (2011). Formation, characteristics and trend of the group debris flows occurred on August 13 in Qingping, Mianzhu County. *Hydrogeology Eng. Geol.* 38 (3), 133–138. doi:10.16030/j.cnki.issn.1000-3665.2011.03.006

O'Brien, J. S. (2009). *FLO-2D Reference manual version 2009[R]*. Arizona: FLO-2D software, Inc.

O'Brien, J. S., Julien, P., and Fullerton, W. (1993). Two-dimensional water flood and mudflow simulation. *J. Hydraul. Eng.* 119 (2), 244–261.

Palladino, M. R., Vieroc, A., Turconi, L., Brunetti, M., Peruccacci, S., Melillo, M., et al. (2018). Rainfall thresholds for the activation of shallow landslides in the Italian alps: The role of environmental conditioning factors. *Geomorphology* 303 (1), 53–67. doi:10.1016/j.geomorph.2017.11.009

Pasutoa, A., and Soldati, M. (2004). An integrated approach for hazard assessment and mitigation of debris flows in the Italian Dolomites. *Geomorphology* 61 (1), 59–70. doi:10.1016/j.geomorph.2003.11.006

Paudel, B., Fall, M., and Daneshfar, B. (2020). GIS based assessment of debris flow hazards in Kulekhani Watershed, Nepal. *Nat. Hazards (Dordr).* 101 (9), 143–172. doi:10.1007/s11069-020-03867-3

Peng, J. B., Ma, R. Y., and Lu, Q. Z., (2004). Geological hazards of uplift of Qinghai-Tibet plateau. *Adv. earth Sci.* 19 (3), 457–466. doi:10.3321/j.issn:1001-8166.2004.03.018

Qiu, H. J., Zhu, Y. R., Zhou, W. Q., Sun, H., He, J., and Liu, Z. (2022). Influence of DEM resolution on landslide simulation performance based on the Scoops3D model. *Geomatics, Nat. Hazards Risk* 13 (1), 1663–1681.

Qu, R., Li, Z. X., and He, Z. W., (2018). Characteristics and causes of low frequency debris flow induced by heavy rainfall in Dagou village, Tianshui city, Gansu province, China. *Mt. Res.* 36 (3), 488–495. doi:10.16089/j.cnki.1008-2786.000345

Song, B., Shen, J. H., and Li, J. Y., (2018). Application of RAMMS model on simulation of debris flow in the Basha Gully [J]. *J. Sediment Res.* 43 (1), 32–37. doi:10.16239/j.cnki.0468-155x.2018.01.006

Su, P. C., Liu, X. L., and Wang, Q. C., (2004). Debris flow characteristics and hazard evaluation in Qiongshan gully of Danba County of Sichuan. *J. Geol. Hazards Environ. Preserv.* 15 (1), 9–12. doi:10.3969/j.issn.1006-4362.2004.01.003

Tang, C., Li, W. L., and Ding, J., (2011). Field investigation and research on giant debris flow on August 14, 2010 in yinxiu town, epicenter of wenchuan earthquake. *Earth Science- J. China Univ. Geosciences* 36 (1), 172–180. doi:10.3799/dqkx.2011.018

Tang, C., Zhou, J. Q., and Zhu, J., (1994). A study on the risk zonging of debris flow on alluvial fans by applying technology of numerical sumulation. *J. Catastrophology* 9 (4), 7–13.

Tang, C., Zhu, J., Ding, J., Cui, X. F., Chen, L., and Zhang, J. S. (2011). Catastrophic debris flows triggered by a 14 August 2010 rainfall at the epicenter of the Wenchuan earthquake. *Landslides* 8 (4), 485–497.

Tie, Y. B., Zhou, H. F., and Ni, H. Y. (2013). Formation of low frequency debris flow induced by short-time heavy rainfall in mountain area of southwest, China—take Lengmu debris flow as an example, Baoxing, Sichuan province. *J. Catastrophology* (04), 110–113. doi:10.3969/j.issn.1000-811X.2013.04.020

Wang, L. Y., Qiu, H. J., Zhou, W. Q., Zhu, Y., and Liu, Z., (2022). The post-failure spatiotemporal deformation of certain translational landslides may follow the pre-failure pattern. *Remote Sens.* 14, 2333.

Wang, W. Y. (1995). Debris flow and its control countermeasures in loess hilly and gully region of eastern Qinghai Province[J]. *Chin. soil water conservation* 02 (1), 11–13.

Wang, Y. Y., Zhan, Q. D., and Han, W. L., (2003). Stress-strain properties of viscous debris flow and determination of volocity parameter[J]. *Chin. J. Geol. Hazard Control* 14 (1), 9–13. doi:10.3969/j.issn.1003-8035.2003.01.002

Wei, F. Q., Hu, K. H., and Cui, P., (2002). Characteristics and origing debirs flow of Jiangjiagou valiey blodking. *J. Soil Water Conservation* 16 (6), 71–75. doi:10.13870/j.cnki.stbcxb.2002.06.021

Wu, J. H., Zhang, C. S., and Yang, W. M., (2022). Risk assessment of debris flow in Zhujiagully watershed based on entropy weight coefficient of variation fusion algorithm and FLO-2D[J]. *J. Nat. disasters* 31 (1), 81–91. doi:10.13577/j.jnd.2022.0108

Wu, Y. H., Liu, K. F., and Chen, Y. C. (2013). Comparison between FLO-2D and Debris-2D on the application of assessment of granular debris flow hazards with case study. *J. Mt. Sci.* 10 (2), 293–304.

Xu, Q., Li, H. J., and He, Y. S., (2017). Quantitative evaluation of engineering treatments for prevention of debris flow at Wenjia gully. *J. Eng. Geol.* 25 (4), 1046–1056. doi:10.13544/j.cnki.jeg.2017.04.019

Yang, D., Qiu, H., Ma, S., Liu, Z., Du, C., and Zhu, Y. (2022). Slow surface subsidence and its impact on shallow loess landslides in a coal mining area[J]. *Catena* 209, 105830. doi:10.1016/j.catena.2021.105830

Zhang, L. F., and Tang, S. Q. (1994). Debris flow and its countermeasures in Gansu province. *J. Arid Land Resour. Environ.* 8 (4), 27–34. doi:10.13448/j.cnki.jalre.1994.04.004

Zhang, P., Ma, J. Z., and Shu, H. P., (2014). Numerical simulation of erosion and deposition debris flow based on FLO-2D Model. *J. Lanzhou Univ. Nat. Sci.* 50 (3), 363–368. doi:10.13885/j.issn.0455-2059.2014.03.011

Zhang, Y. S., Guo, C. B., and Yao, X., (2016). Research on the geohazard effect of active fault on the eastern Margin of the Tibetan plateau. *Acta Geosci. Sin.* 37 (3), 277–286. doi:10.3975/cagsb.2016.03.03

Zhou, W. Q., Qiu, H. J., Wang, L. Y., Pei, Y., Tang, B., and Ma, S., (2022). Combining rainfall-induced shallow landslides and subsequent debris flows for hazard chain prediction. *CATENA* 213, 106199. doi:10.1016/j.catena.2022.106199

frontiers | Frontiers in Earth Science

TYPE Original Research
PUBLISHED 10 January 2023
DOI 10.3389/feart.2022.1102802

OPEN ACCESS

EDITED BY
Haijun Qiu,
Northwest University, China

REVIEWED BY
Yu Wang,
University of Science and Technology Beijing, China
Yuanjun Jiang,
Institute of Mountain Hazards and Environment (CAS), China

*CORRESPONDENCE
Bo Zhang,
zhangbo_dzs@126.com

SPECIALTY SECTION
This article was submitted to Geohazards and Georisks, a section of the journal Frontiers in Earth Science

RECEIVED 19 November 2022
ACCEPTED 28 December 2022
PUBLISHED 10 January 2023

CITATION
Fu X, Zhang B, Wang L, Wei Y, Leng Y and Dang J (2023), Stability prediction for soil-rock mixture slopes based on a novel ensemble learning model.
Front. Earth Sci. 10:1102802.
doi: 10.3389/feart.2022.1102802

Stability prediction for soil-rock mixture slopes based on a novel ensemble learning model

Xiaodi Fu[1,2,3], Bo Zhang[1,2,3]*, Linjun Wang[1,2], Yong Wei[1,2,3], Yangyang Leng[4,5] and Jie Dang[4,5]

[1]School of Civil Engineering and Architecture, Guizhou Minzu University, Guiyang, China, [2]Key Laboratory of Karst Environmental Geological Hazard Prevention, Guiyang, China, [3]Key Laboratory of Urban Underground Space Development and Safety in Karst Areas, Guizhou Minzu University, Guiyang, China, [4]State Key Laboratory of Geohazards Prevention and Geoenvironment Protection, Chengdu University of Technology, Chengdu, China, [5]Guizhou Geological Environment Monitoring Institute, Guiyang, China

Soil-rock mixtures are geological materials with complex physical and mechanical properties. Therefore, the stability prediction of soil-rock mixture slopes using machine learning methods is an important topic in the field of geological engineering. This study uses the soil-rock mixture slopes investigated in detail as the dataset. An intelligent optimization algorithm-weighted mean of vectors algorithm (INFO) is coupled with a machine learning algorithm. One of the new ensemble learning models, which named IN-Voting, is coupled with INFO and voting model. Twelve single machine learning models and sixteen novel IN-Voting ensemble learning models are built to predict the stability of soil-rock mixture slopes. Then, the prediction accuracies of the above models are compared and evaluated using three evaluation metrics: coefficient of determination (R^2), mean square error (MSE), and mean absolute error (MAE). Finally, an IN-Voting ensemble learning model based on five weak learners is used as the final model for predicting the stability of soil-rock mixture slopes. This model is also used to analyze the importance of the input parameters. The results show that: 1) Among 12 single machine learning models for the stability prediction of soil-rock mixture slopes, MLP (Multilayer Perceptron) has the highest prediction accuracy. 2) The IN-Voting model has higher prediction accuracy than single machine learning models, with an accuracy of up to 0.9846) The structural factors affecting the stability of soil-rock mixture slopes in decreasing order are the rock content, bedrock inclination, slope height, and slope angle.

KEYWORDS

soil-rock mixture slope, machine learning, ensemble learning model, stability prediction, feature importance

1 Introduction

Soil-rock mixture slopes are mainly discontinuous, loose soil-rock mixture deposits composed of massive rocks and fine-grained soils with varying physical and mechanical properties (Xu and Zhang, 2021; Zhao et al., 2021). These slopes are widely distributed in areas such as the mountainous regions of southwest China, the Three Gorges Reservoir Region, and the Qinling Mountains (Cen et al., 2017; Gao et al., 2018). The soil-rock mixture slope has significant characteristics of non-uniformity and dual structure, and its stability can be affected by the rock content and grain size gradation (Dong et al., 2020; Xu and Zhang, 2021). Therefore, its stability evaluation is complicated, and slope instability can cause large economic and life losses (Liu et al., 2022; Wang et al., 2022). In July 2011, a landslide of soil-rock mixture occurred

in Lueyang County, Hanzhong City, southern Shaanxi Province, resulting in the death of 18 people (Liu et al., 2019). In July 2020, the instability of a soil-rock mixture slope in Wulong District, Chongqing, caused substantial economic losses (Zhou et al., 2021).

Scholars have conducted numerous studies on the stability evaluation of soil-rock mixture slopes. Xu et al. (2016) studied the properties of soil-rock mixtures by numerical simulation with discrete elements. Gao et al. (2018) used the strength parameters of the soil-rock mixture obtained from the direct shear test for evaluation. The damage characteristics of slopes and their stability were simulated using the finite element method (Yue et al., 2003; Chen et al., 2021). Zhao et al. (2021) obtained the stability coefficients of soil-rock mixture slopes using FLAC 3D and strength reduction methods, revealing the influence of rock content on the stability coefficients and damage modes. Peng et al. (2022) coupled discontinuous deformation analysis and smooth particle hydrodynamics to investigate the mechanical properties of soil-rock mixture slopes. Qiu et al. (2022) using the physical deterministic model—Scoops3D model to analyze landslide stability. Zhao et al. (2022) investigated the mechanism of large deformation damage of slopes using the material point method for soil-rock mixture slopes.

With the development of computer technology, many scholars have used machine learning methods for slope stability prediction. For example, some scholars used several single machine learning algorithms or ensemble learning algorithms to predict the stability of slopes. The best prediction model for such slopes could be obtained by comparing the prediction accuracy of each model. Ray et al. (2020) showed that an improved machine learning prediction model based on artificial neural networks was effective for the stability prediction of residual soil slopes. Lin et al. (2021) concluded that non-linear regression models outperformed linear models in predicting slope stability. Ramos-Bernal et al. (2021) revealed that the Adaboost classifier was more suitable for slope prediction modeling. By comparing a single machine learning model with an ensemble learning model, Pham et al. (2021) found that the slope stability prediction model based on the ensemble algorithm was more accurate. Cheng et al. (2022) and Shahzad et al. (2022) found that slope analysis models developed with support vector machines had the highest robustness. Feng et al. (2022) found that support vector machine models and random forest models had more reliable prediction results. Other scholars have further improved the accuracy of slope stability prediction by coupling an intelligent optimization algorithm with a single machine learning algorithm to build a prediction model. Xue (2016) showed that determining the optimal parameters of a least square support vector machine model based on an improved particle swarm algorithm could significantly improve the accuracy of slope stability prediction models. Qi and Tang, 2018 showed that using the firefly optimization algorithm to separately determine the hyperparameters of six machine learning algorithms was effective in improving the model prediction accuracy.

However, due to the complexity of soil-rock mixture slopes, the use of machine learning methods to predict their stability was rarely reported. Therefore, a novel ensemble learning model is proposed in this study to predict the stability of soil-rock mixture slopes, providing new ideas and references for related studies and engineering applications. First, a weighted mean of vectors algorithm (INFO) is used to determine the hyperparameter combinations of 12 single machine learning models. The weight distribution in the novel IN-Voting ensemble learning model is also investigated. In this way, a more accurate slope stability prediction model for soil-rock mixtures is established. Then, the data of mixed soil and rock slopes in Wanzhou District (Chongqing, China) are used for case analysis. Importance analysis of four input parameters (i.e., slope angle, bedrock inclination, slope height, and rock content) is performed using the Permutation Importance method based on the IN-Voting model. The influence degree of these parameters on the stability of the soil-rock mixture slope is obtained.

2 Basic principles of the algorithm

2.1 Intelligent optimization algorithm—INFO

INFO is a new intelligent optimization algorithm proposed by Ahmadianfar et al. (Ahmadianfar et al., 2022), which has the advantages of strong searching ability, fast speed, and less overfitting. The core idea of INFO lies in three stages.

2.1.1 Updating rule stage

$$z1_1^g = \begin{cases} x_1^g + \sigma^* MeanRule + randn^* \dfrac{x_{bs} - {x_{a1}}^g}{f(x_{bs}) - f({x_{a1}}^g) + 1}, rand < 0.5 \\ x_{bs} + \sigma^* MeanRule + randn^* \dfrac{x_a^g - {x_{a3}}^g}{f(x_{a2}^g) - f({x_{a3}}^g) + 1}, rand \geq 0.5 \end{cases}$$

$$z2_1^g = \begin{cases} x_{bs} + \sigma^* MeanRule + randn^* \dfrac{x_a^g - {x_b}^g}{f(x_{a1}^g) - f({x_{a2}}^g) + 1}, rand < 0.5 \\ x_{bt} + \sigma^* MeanRule + randn^* \dfrac{x_{a1}^g - {x_{a2}}^g}{f(x_{a1}^g) - f({x_{a2}}^g) + 1}, rand \geq 0.5 \end{cases} \tag{1}$$

where $z1_1^g$ and $z2_1^g$ are the new position vectors for the g-th iteration; σ is the vector scaling; *MeanRule* is the formula based on the mean rule; x_{bs} and x_{bt} are the best and better solutions among all vectors in the population; $a1 \neq a2 \neq a3 \neq 1$ *is* a different integer randomly selected from [1, NP], NP denotes the number of variable species; *randn* is a standard normally distributed random value.

2.1.2 Vector combining stage

$$u_1^g = \begin{cases} \begin{cases} z1_1^g + \mu^* \left| z1_1^g - z2_1^g \right|, & rand1 < 0.5 \quad and \quad rand2 < 0.5 \\ z1_2^g + \mu^* \left| z1_1^g - z2_1^g \right|, & rand1 < 0.5 \quad and \quad rand2 \geq 0.5 \end{cases} \\ x_1^g, \quad rand1 < 0.5 \end{cases} \tag{2}$$

where u_1^g is the new vector obtained by merging the vectors in the g-th generation; $\mu = 0.05 \times randn$.

2.1.3 Local search equation

$$u_1^g = \begin{cases} x_{bs} + randn^* (MeanRule + randn(x_{bs}^g - x_{a1}^g)), \\ \qquad rand1 < 0.5 \quad and \quad rand2 < 0.5 \\ x_{rnd} + randn^* (MeanRule + randn(v_1{}^* x_{bs} - v_2{}^* x_{rnd})), \\ \qquad rand1 < 0.5 \quad and \quad rand2 \geq 0.5 \end{cases} \tag{3}$$

where:

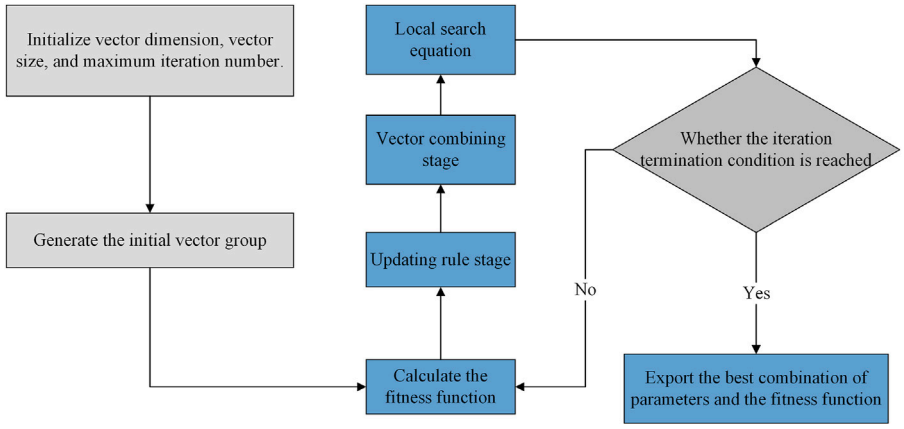

FIGURE 1
Flow chart of the INFO algorithm.

$$x_{rnd} = \phi^{*}x_{avg} + (1-\phi)^{*}\left(\phi^{*}x_{bt} + (1-\phi)^{*}x_{bs}\right) \quad (4)$$

$$x_{avg} = \frac{x_a + x_b + x_c}{3} \quad (5)$$

where ϕ denotes a random number of (0,1); x_{rnd} is a random solution obtained from x_{avg}, x_{bt}, and x_{bs}; v_1 and v_2 are two random numbers. If $rand < 5$, a new vector can be generated around x_{bs}^{g} with random values in [0,1].

This study mainly uses the INFO algorithm to determine hyperparameter combinations in single machine learning models and weight values among weak learners in Voting ensemble learning models.

For the practical application, the main flow of the algorithm (Figure 1) is as follows.

1) The maximum iteration number is 100, and the group number is 30. For a single machine learning model, the group dimension is the number of hyperparameters to be adjusted by the machine learning model. For the Voting ensemble learning model, the group dimension is the number of weight values to be adjusted.
2) A random group matching the upper and lower boundary vectors is initialized.
3) The coefficient of determination R^2 (Eq. (6)) is used as the fitness function of this algorithm.
4) The new vectors generated in the vector update phase are used to start the vector merge phase.
5) In the local search phase, whether the vector generated in the fourth step exceeds the upper and lower boundary of the group can be determined. By comparing the fitness function values of the old and new vectors, whether to perform the vector update and the change of the best fitness value are determined.
6) Steps 3–5 are repeated until the iteration termination condition is reached, then the results are exported.

2.2 Machine learning models

2.2.1 Adaptive boosting (ADBT) model

ADBT is an ensemble learning model that constructs strong learners by linear combinations of weak learners (Freund and Schapire, 1995). By using the performance in each training iteration to weight the attention created for subsequent training, ADBT assigns larger weights to data that are more difficult to predict and smaller weights to those less difficult to predict, thus improving the overall prediction accuracy of the model (Bui et al., 2019; Lee et al., 2022). In this study, the default learner of ADBT is used, and the three hyperparameters to be determined are the maximum iteration number (n_estimators), the learning rate (learning_rate), and the random seed (random_state).

2.2.2 Bayesian linear regression (BYS) model

Based on Bayesian conditional probability, BYS treats the parameters of the linear model as random variables and computes the posterior through the prior of the model parameters, thus completing the model construction and prediction (Gelman, 2015). The six hyperparameters to be determined in this study are the maximum iteration number (n_iter), the tolerance value (tol), the shape parameter of the Gamma distribution before the alpha parameter (alpha_1), the inverse scale parameter of the Gamma distribution before the alpha parameter (alpha_2), the shape parameter of the Gamma distribution before the lambda parameter (lambda_1), and the inverse scale parameter of the Gamma distribution before the lambda parameter (lambda_2).

2.2.3 ElasticNet regression (ELN) model

ELN combines the regularization methods of Lasso regression and Ridge regression. The L1 regularization and L2 regularization calculations are incorporated into the standard linear regression model conditions to form a new cost function (Zou and Hastie, 2005). The five hyperparameters to be determined for this model are the constant of the penalty term (Alpha), the mixing parameter (l1_ratio), the maximum iteration number (max_iter), the tolerance value (tol), and the random seed (random_state).

2.2.4 Extra-trees (ETR) model

ETR is a machine-learning model for bagging proposed by Geurts et al. (2006). Because the division points in ETR are random, the prediction results of this model require the combined action of multiple decision trees to achieve the best prediction (Ghatkar

et al., 2019). The five hyperparameters to be determined are the number of decision trees (n_estimators), the maximum iteration number (max_depth), the random seed (random_state), the minimum number of samples required to split the internal nodes (min_samples_split), and the minimum number of samples required for each node (min_samples_leaf).

2.2.5 Gradient boosting decision tree (GBDT) model

The GBDT model proposed by Friedman (Friedman, 2002) is an ensemble model based on multiple weak learners to obtain strong learning capabilities. In the regression problem, the negative gradient of the loss function is used to approximate the value of the current model as the residual of the boosted tree model, thus obtaining the best prediction results. GBDT has received much attention from scholars since its introduction (Wu and Lin, 2022). In this study, the five parameters to be determined are learning rate (learning_rate), maximum iteration of the weak learner (n_estimators), maximum depth of the decision tree (max_depth), subsample (subsample), and random seed (random_state).

2.2.6 Huber regression (HBR) model

In the HBR model, the loss function in the theoretical approach of linear regression is replaced with Huber loss (Sun et al., 2020). The four hyperparameters to be determined in this study are the number of outliers (Epsilon), the maximum iteration number (max_iter), the regularization parameter (alpha), and the tolerance value (tol).

2.2.7 K-nearest neighbor (KNN) model

The KNN model proposed by Cover and Hart, 1967 is theoretically mature, easy to understand, and highly accurate, which can be used to address classification and regression problems (Sevi and AuthorAnonymous, 2020). Since the selection of the K determines the accuracy of the model prediction (Deng, 2020), three hyperparameters need to be determined to improve the model prediction accuracy: k-value (n_neighbors), the threshold for the number of leaf nodes (leaf_size), and distance metric p).

2.2.8 Lasso (LAS) model

The LAS model is based on a standard linear regression model and L1 regularization (Leeuw, 2009). Compared to linear regression models, LAS models can handle high-dimensional data more quickly and efficiently. Therefore, many scholars considered using LAS models to build prediction models (Wagenaar et al., 2017). In this study, the three hyperparameters to be determined are the constant of the penalty term (Alpha), the maximum iteration number (max_iter), and the tolerance value (tol).

2.2.9 Multilayer Perceptron (MLP) model

The MLP model is constructed through full connectivity between input, hidden, and output layers. The main idea of the input layer is to accept multiple variables from the model and pass them into the hidden layer, where the number of neurons is the same as the type of input variables. The main idea of the hidden layer is to extend the data to a higher dimension, which improves the prediction accuracy of the model by increasing the complexity of the input variables. The main idea of the output layer is to output the final prediction of the model by accepting the last layer of the hidden layer (Almansi et al., 2022).

The seven hyperparameters to be determined in this study are: the regularization term parameter (Alpha), the initial learning rate (learning_rate_init), the index of the inverse scaling learning rate (power_t), the maximum iteration number (max_iter), the momentum of the gradient descent update (momentum), the proportion of the training data to be left as a validation set for early stops (validation_fraction), and the random number seed (random_state).

2.2.10 Random forest (RF) model

The RF model is composed of several unrelated regression trees, and the final output is jointly determined by each regression tree (Zhang et al., 2019). The model was proposed and developed by Ho et al. (Ho, 1998) and Breiman (2001). The five hyperparameters to be determined in this study are the number of decision trees (n_estimators), the minimum number of samples in each division (min_samples_split), the minimum number of samples in the leaf nodes: (min_samples_leaf), the random number seed (random_state), and the minimum weight required by the leaf nodes (min_weight_fraction _leaf).

2.2.11 Support vector machine (SVM) model

Cortes and Vapnik, 1995 proposed that support vector regression (SVR) in SVM models can be used for regression analysis (Kombo et al., 2020). The use of kernel tricks in SVM makes the model a good solution for analyzing non-linear data (Feng et al., 2022). The four hyperparameters to be determined in this study are the number of kernel functions (Degree), kernel coefficients (epsilon), kernel cache size (cache_size), and the maximum iteration number (max_iter).

2.2.12 Stochastic gradient descent (SGD) model

The SGD model is generated based on the gradient descent model (Bui et al., 2019). During the model operation, the dataset is randomly disrupted. Since a sample is randomly selected from the dataset at each iteration, the path used by the model to reach the minimum is usually noisier than that of a typical gradient descent model, but the training time can be significantly reduced. The five hyperparameters to be determined are the constant of the penalty term (Alpha), the elastic net mixing parameter (l1_ratio), the maximum iteration number (max_iter), the initial learning rate (eta0), the inverse scaling learning rate index (power_t), and the random number seed (random_state).

2.2.13 IN-voting model

Voting models are classified into two types: classification and regression. For common regression models, the prediction results of multiple weak learners are reprocessed through arithmetic mean fusion or geometric mean fusion, thus improving the prediction accuracy of the model.

In this study, a new ensemble learning model - IN-Voting is developed based on the regression model of traditional Voting. As shown in Figure 2, the flow of the IN-Voting model is as follows: Firstly, the data is pre-processed for soil-rock mixed slopes. The number of weak learners selected in the model is finally determined to be five based on the complexity of the IN-Voting ensemble learning model and the accuracy rate. Then, the INFO intelligent optimization algorithm improves the prediction accuracy of the model by assigning different weight values to the weak learner. Finally, the combined module in the new ensemble learning model of IN-Voting is used to complete the final building of the model and output the model prediction results.

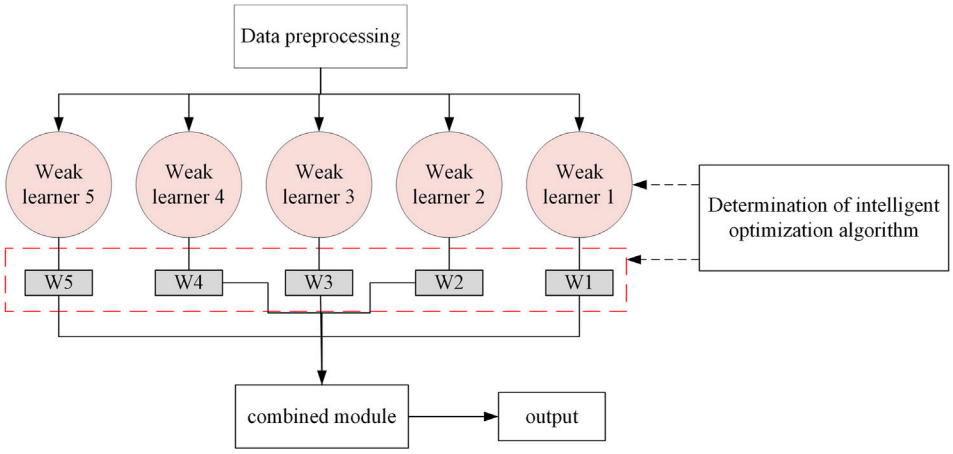

FIGURE 2
IN-Voting network structure (W in the figure indicates the weight value).

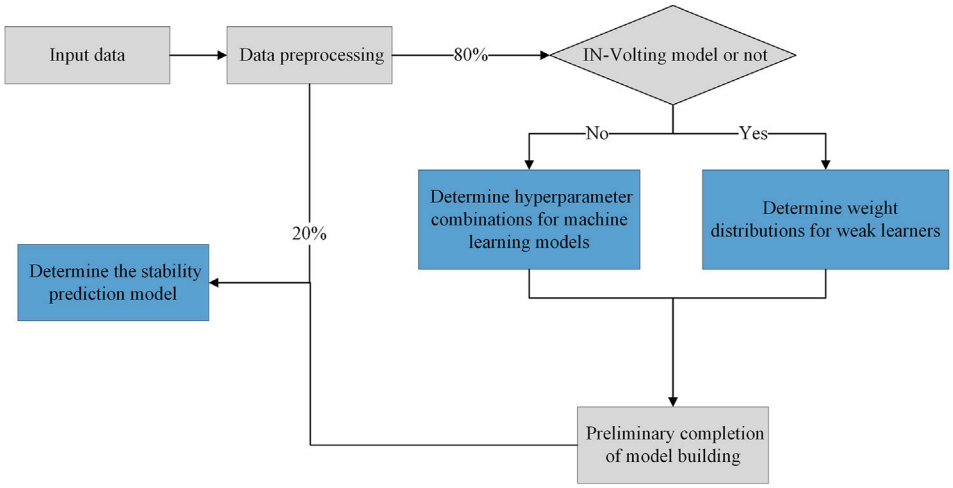

FIGURE 3
Stability prediction model for soil-rock mixture slopes.

2.3 Building process of the prediction model

The building process of the stability prediction model for soil-rock mixture slopes is shown in Figure 3, which is explained in detail below.

(1) The input parameters of the soil-rock mixture slopes (i.e., rock content, bedrock inclination, slope angle, and slope height) are standardized and normalized.
(2) To prevent overfitting of the model, 80% of the total data is classified into a training set for the initial establishment model, and 20% is classified into a test set for further validation.
(3) If the stability prediction model is based on a single machine learning model, the hyperparameters of each machine learning model are first determined using the INFO algorithm. In the case of the IN-Voting model, the INFO algorithm is required to determine the weight values of the weak learners.
(4) The training data are fed into the initial machine learning model, and the test set data are used to finalize the stability prediction model for soil-rock mixture slopes.

2.4 Evaluation indicators

For evaluating the prediction performance of the proposed model, the following three indicators are used: The coefficient of determination (R^2) that uses the mean value as the error base; the mean squared error (MSE) that reflects the difference degree between the estimated volume and the estimated volume; the mean absolute error (MAE) representing the absolute value of the deviation of all

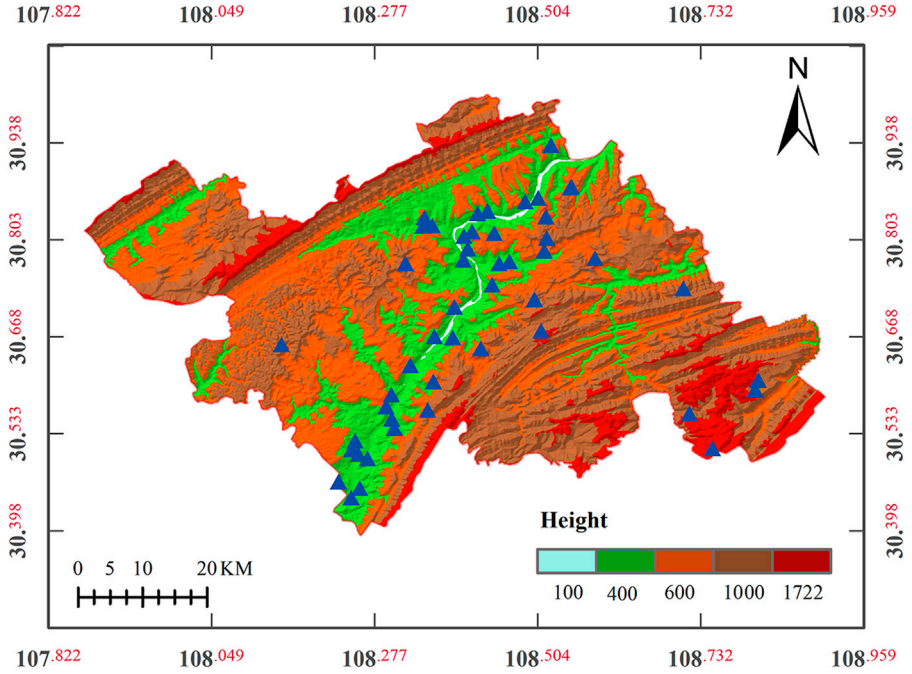

FIGURE 4
Locations of data points in Wanzhou District.

individual observations from the arithmetic mean. As the most important evaluation indicators in this study, the R^2 closer to one and smaller MSE and MAE values indicate higher prediction accuracy. The equations of the three indicators are as follows:

$$R^2(y,\hat{y}) = 1 - \frac{\sum_{i=0}^{n}(y-\hat{y})^2}{\sum_{i=0}^{n}(y-\bar{y})^2} \tag{6}$$

$$MSE(y,\hat{y}) = \frac{1}{n}\sum_{i=0}^{n}\left\|y_i - \hat{y}_i\right\|_2^2 \tag{7}$$

$$MAE(y,\hat{y}) = \frac{1}{n}\sum_{i=0}^{n}\left|y_i - \hat{y}_i\right| \tag{8}$$

where y_i denotes the true value of the ith sample; $\hat{y}_i$ is the predicted value of the ith sample; $\bar{y}$ denotes the mean value of $\{y_i\}_{i=1}^{n}$.

3 Sample analysis

The sample data were obtained from Wanzhou District (Chongqing, China), located in the Yangtze River valley zone of the northeast ridge and valley province of Chuandong. The terrain is high in the east and low in the west, with sufficient rainfall and strata containing rocky sand (Chen et al., 2021). A large number of slopes with mixed soil and rock are developed in this area, with frequent geological hazards. In this study, 49 soil-rock mixture slopes investigated in the previous study are used as the sample for analysis (Cheng, 2009), as shown in the blue-triangle points in Figure 4.

Soil-rock mixture slopes are distinguished from soil slopes and rock slopes. Its slope material is complex and has significant inhomogeneity. As a result, there are many factors affecting the stability of soil-rock mixture slopes, and it is difficult to obtain the parameters of such slopes. In slope stability analysis, the stability coefficient is correlated to the slip resistance and sliding force of the slope body. Therefore, the input parameters in this study are typical structural factors of soil-rock mixture slopes, including rock content, surface inclination, slope angle, and slope height.

In soil-rock mixtures, the rock content is a key parameter in determining the physical-mechanical properties and directly affects the weight, cohesion, and internal friction angle (Kalender et al., 2014). The rock contact, the rock content greatly contribute to the stability coefficient of soil-rock nixture slopes (Wang et al., 2022a; Wang et al., 2022b; Wang et al., 2022c). If there are multicollinearities among the input parameters in machine learning, the accuracy of the prediction model can be affected (Hitouri et al., 2022; Selamat et al., 2022; Xia et al., 2022). Therefore, this study uses rock content as an input parameter instead of weight, cohesion, and internal friction angle. The bedrock surface is the interface separating the soil and rock mixture from the underlying bedrock. Since the base overburden provides the soil-rock mixture slope with a typical binary structure, it is an important factor affecting the overall stability of the soil-rock mixture slopes. Slope angle and slope height are important geometric features significantly affecting the stability of slopes. With the increase of slope height and angle, the slope stability gradually decreases.

As shown in Figure 5, the slope angle ranges from 9°–15°, the base cover dip angle is 5°–13°, the slope height is in the range of 40 m–100 m, and the rock content ranges from 22%–60%. These data characteristics are consistent with the histogram (Figure 5) and the Gaussian curve.

In Figure 6, the single-peak curve distribution characterized by four input parameters and one output parameter reduces the difficulty of data analysis and improves the prediction accuracy of the model. The ten subplots at the lower triangle show the scatter distribution among the parameters. It can be seen that there is no multicollinearity among the four input parameters, which is consistent with the above analysis. The Pearson's r values in ten

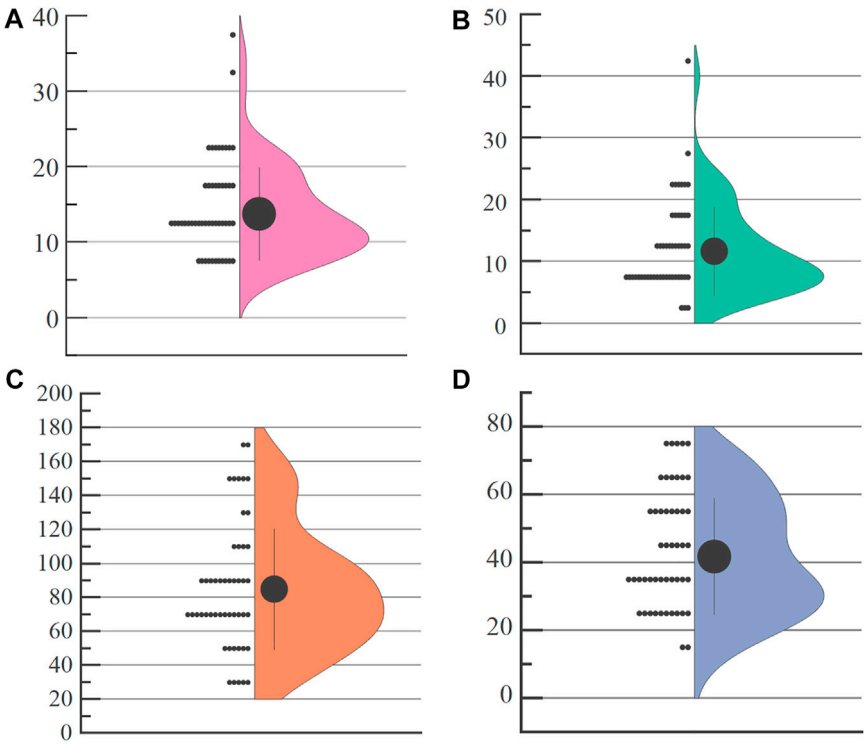

FIGURE 5
Analysis of input parameters **(A)** slope angle; **(B)** bedrock inclination; **(C)** slope height; **(D)** rock content.

subplots of the four input parameters have different correlations with the stability coefficients, Meanwhile slope angle, and slope height show a significant negative correlation with the stability coefficient. The rock content is positively correlated with the stability coefficient, with larger rock content indicating a greater stability coefficient.

4 Results

4.1 Single machine learning models

In this study, the prediction performance of 12 single machine learning models based on the INFO intelligent optimization algorithm is analyzed with R^2 as the main indicator and MSE and MAE as supplementary indicators, as shown in Figure 7. In Figure 7A, all models have R^2 values greater than 0.6. Twelve machine learning models can be divided into three sections: BYS, LAS, ELN, and HBR have R^2 values between 0.6 and 0.7, with the lowest prediction accuracy among the 12 machine learning models; The R^2 values of ADBT, KNN, SGD, and SVM models are in the range of 0.7–0.9, with the highest value of 0.8746 for the KNN model; The R^2 values of ETR, GBDT, MLP, and RFR models are greater than 0.90, with MLP having the highest R^2 value of 0.9681. As shown in Figure 7B, only ETR, GBDT, MLP, and RFR have MSE values less than 0.05, where ETR has the lowest MSE value of 0.043, followed by MLP. In Figure 7C, ETR, GBDT, MLP, and RFR have MAE values less than 0.005, with MLP having the lowest MAE of 0.0027.

According to the model evaluation criteria in this paper, the R^2 and MSE evaluation index values of MLP model are the best, which shows that compared with other models, the model has a very strong adaptive and self-learning function, so it has a higher prediction performance for a small number of samples.

4.2 Novel ensemble learning model—IN-voting

In this paper, five of the twelve single machine learning models are randomly selected to be rearranged as weak learners in IN-Voting. With the accuracy of model optimization and the optimization time of the IN-Voting model as the criteria, 16 results in Table 1 are obtained. In addition, the maximum R^2 among five weak learner combinations is used as the theoretical minimum value of the IN-Voting model, denoted as R2_stand. The INFO algorithm is then used to determine the weight values matched by the five weak learners in the IN-Voting model to maximize the prediction accuracy of 16 IN-Voting models and further improve the robustness and credibility of the ensemble model.

The evaluation indicators for the 16 ensemble IN-Voting learning models are shown in Figure 8. The left and right vertical coordinates in Figure 8A are the values of R^2 and R2_stand predicted by 16 ensemble IN-Voting learning models. Figures 8B,C show the values of MSE and MAE of the sixteen ensemble IN-Voting learning models. In Figure 8D, the left vertical coordinate indicates the degree of accuracy improvement (Difference value) for the sixteen IN-Voting models based on the five weak learners, and the right vertical coordinate is the optimization time taken by the INFO algorithm for each IN-Voting model. The Difference value is the difference between the R^2 and R2_stand of the sixteen ensemble IN-Voting learning models. By

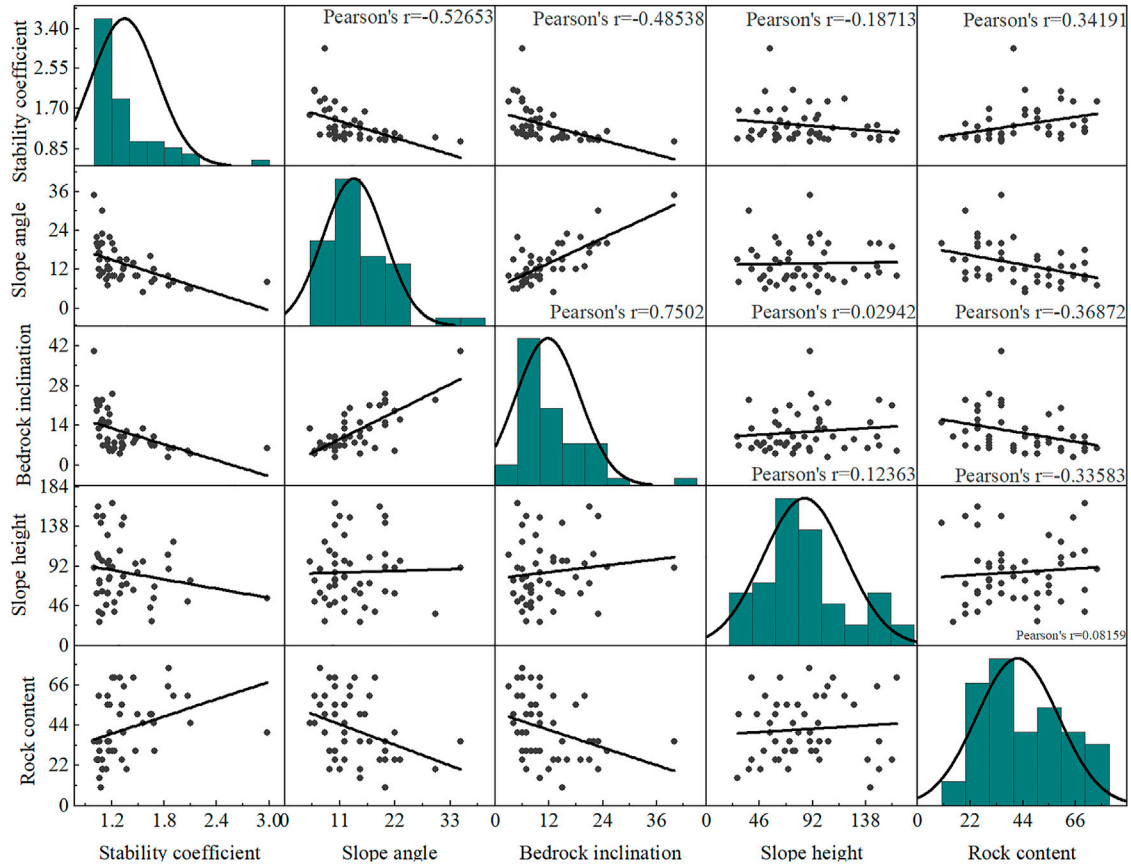

FIGURE 6
Correlation and statistical distribution of parameters related to soil-rock mixture slopes.

comparing Figure 8A with Figure 8D, the advantage of the IN-Voting model can be more significantly represented using the Difference value.

As can be seen in Figure 8A, the R^2 of all 16 groups of IN-Voting models is higher than the R2_stand value, indicating the high feasibility and robustness of the IN-Voting ensemble learning model. Especially in the M10—M16 groups, the MLP models with the highest prediction performance were included, and the R^2 index values were higher than 0.9681, with the highest R^2 of 0.9846 for the M16 group. In Figures 8B,C, the MSE and MAE values of the M2 group model are the highest, which are 0.0825 and 0.0099, respectively. The MSE values of the seven prediction models from M10 ~ M16 are all less than 04, with the M14 group having the lowest MSE value of 0.308. The MAE accuracy index values of these seven groups are less than or equal to 0.002, with M16 having the lowest value of 0.0013. In Figure 8D, the prediction accuracy of 16 ensemble IN-Voting learning models is improved to different degrees. M1 and M3 have the greatest improvement with Difference values of 0.0884 and 0.0712, respectively. In M10 ~ M16 with 0.9681 as the theoretical minimum of the IN-Voting model, the Difference values are all in the range of 0.01–0.016, with M16 improving the most with the Difference value of 0.0155. Among 16 IN-Voting models, M1, M2, M3, M8, and M9 have the shortest optimization time, and M6, M7, M15, and M16 have the longest optimization time. Therefore, the INFO algorithm is efficient in improving the prediction accuracy of the IN-Voting model.

Among the five evaluation indicators, R^2 and model optimization capability are the main indicators, and MSE, MAE, and optimization time are the supplementary indicators. It can be seen from Figure 8 that from M10 ~ M16, the model optimization times of M10 ~ M14 are relatively less, while these models have fewer overall improvements than the M16 group. Although the optimization time of M16 is relatively long, its R^2 and optimization performance are the highest among all prediction models.

The five indicators in Figure 8 are known, the ensemble IN-Voting learning model consisting of SGD, SVM, MLP, RFR, and GBDT is finally selected as the stability prediction model for soil-rock mixture slopes.

4.3 Importance ranking of input parameters for the stability prediction

Due to the complex mechanical properties and material properties of soil-rock mixtures, it is necessary to rank the structural factors (rock content, bedrock inclination, slope angle, and slope height) that affect the stability of soil-rock mixture slopes. Based on the ensemble IN-Voting learning model for the M16 group, this study uses the Permutation Importance method to obtain feature importance rankings.

The main idea of the Permutation Importance method is to randomly rearrange a column of the dataset in the trained model for prediction. The loss function is calculated using the predicted value and the true target value, and the difference due to random sequencing is obtained. In this way, the influence of each feature on the stability prediction is ranked, and the final importance ranking of the features is obtained. The calculation can be expressed as follows:

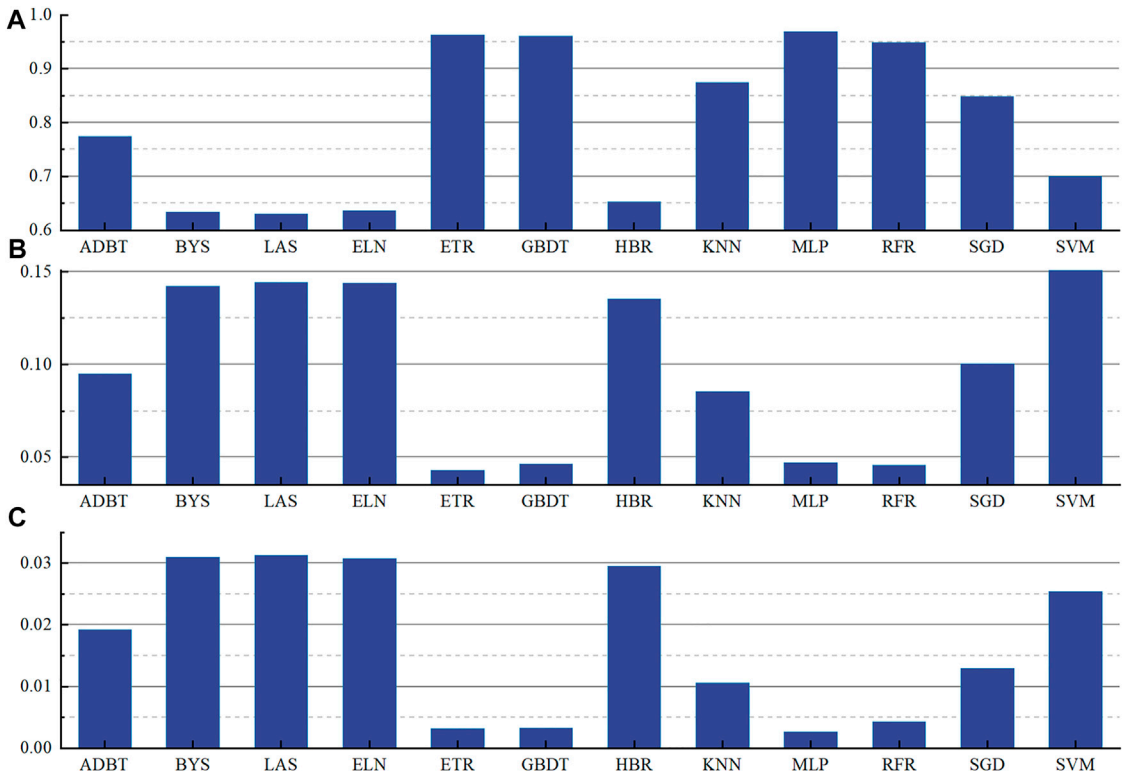

FIGURE 7
Values Model evaluation indicators under INFO algorithm optimization **(A)** R^2; **(B)** MSE; **(C)** MAE.

TABLE 1 Model combinations and their maximum R^2 values.

Model codes	Single learner					R2_stand
	Weak learner 1	Weak learner 2	Weak learner 3	Weak learner 4	Weak learner 5	
M1	ADBT	ELN	HBR	KNN	SGD	0.8746
M2	ADBT	ELN	HBR	KNN	SVM	0.8746
M3	ELN	HBR	KNN	SGD	SVM	0.8746
M4	ELN	HBR	KNN	SGD	RFR	0.949
M5	HBR	KNN	SGD	SVM	RFR	0.949
M6	ELN	HBR	KNN	SGD	GBDT	0.9608
M7	HBR	KNN	SGD	SVM	GBDT	0.9608
M8	ELN	HBR	KNN	SGD	ETR	0.9621
M9	HBR	KNN	SGD	SVM	ETR	0.9621
M10	ELN	HBR	KNN	SGD	MLP	0.9681
M11	HBR	KNN	SGD	SVM	MLP	0.9681
M12	KNN	SGD	SVM	MLP	RFR	0.9681
M13	KNN	SGD	SVM	MLP	ETR	0.9681
M14	SGD	SVM	MLP	RFR	ETR	0.9681
M15	SVM	MLP	RFR	ETR	GBDT	0.9681
M16	SGD	SVM	MLP	RFR	GBDT	0.9681

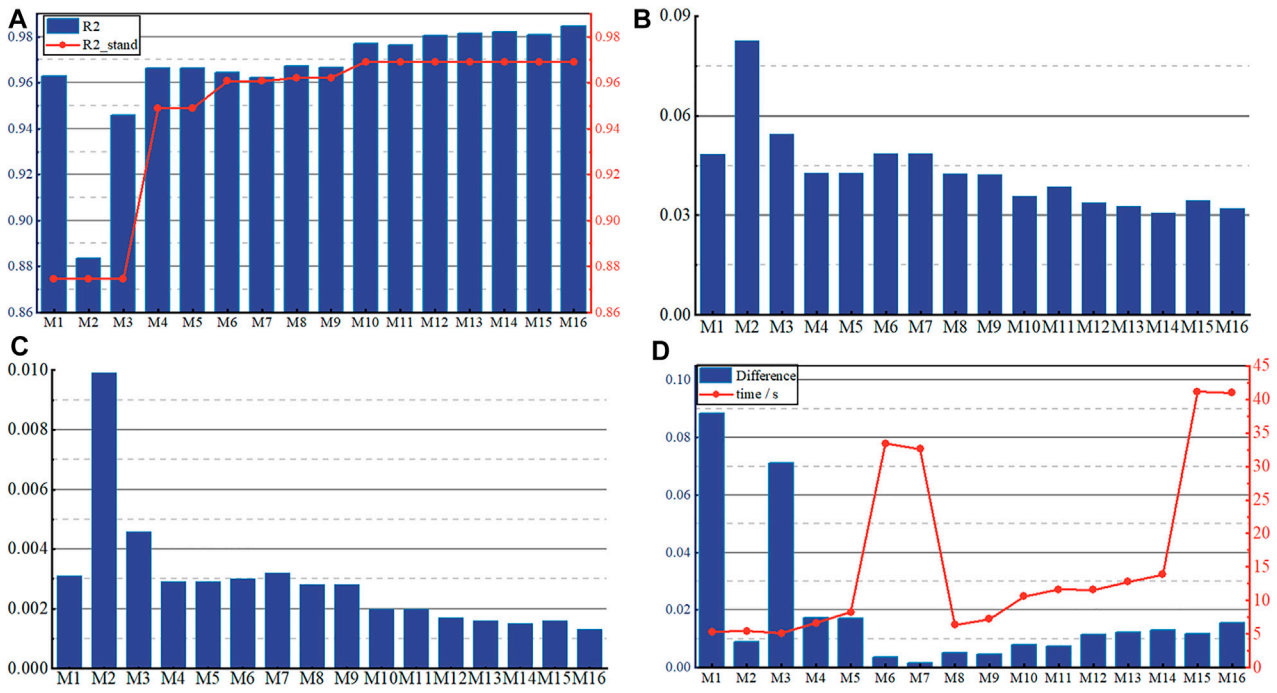

FIGURE 8
Indicators for the 16 IN-Voting models **(A)** R^2 and the distribution of maximum R^2 in each combination; **(B)** The distribution of MSE; **(C)** The distribution of MAE; **(D)** Difference values and optimization time.

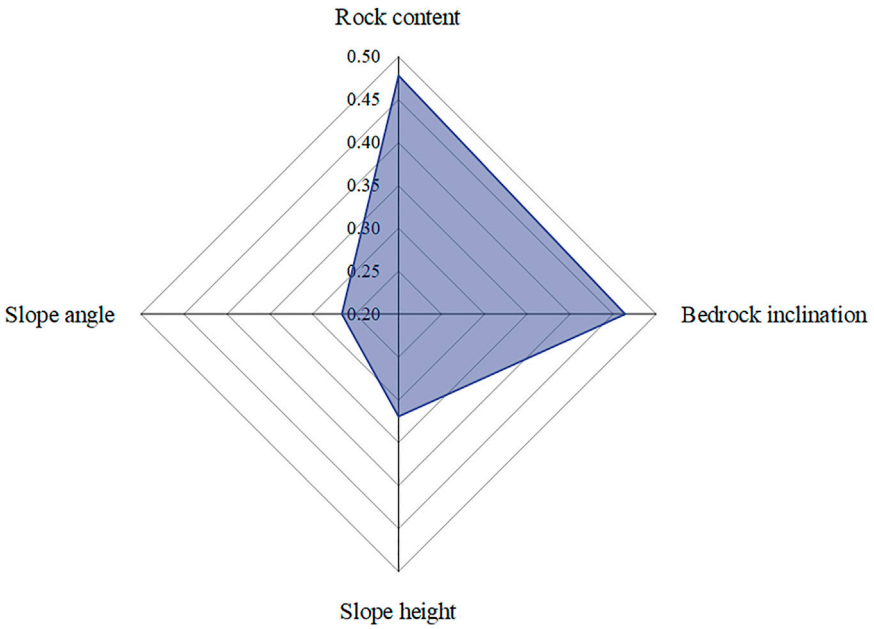

FIGURE 9
The Permutation Importance value of input parameters.

$$I_j = s - {}^{1}\Big/_{K}\sum_{m}^{K} s_{m,j} \tag{9}$$

where I_j denotes the importance score of randomly rearranged feature j; s denotes the performance score of the model in the dataset; m represents each iteration in K experiments.

Figure 9 shows the importance of four input parameters in descending order: rock content, bedrock inclination, slope height, and slope angle, which ordinate shows their specific values. Rock content is a structural factor of soil-rock mixture slopes, and its influence on slope stability widely varies (Yang et al., 2020). Therefore, for the engineering evaluation of soil-

rock mixture slopes, the rock content can be firstly considered, followed by the bedrock inclination.

5 Discussion

In this study, a novel modeling structure is developed by coupling the INFO algorithm and machine learning algorithm (including the single machine learning algorithm and ensemble learning algorithm) to form stability prediction models for soil-rock mixture slopes. The novel ensemble learning model developed shows the highest prediction accuracy.

Qi and Tang, 2018 concluded that the support vector machine model based on the firefly optimization algorithm had the highest prediction accuracy. Xue (2016) found that the least square support vector machine model based on the particle swarm algorithm could significantly improve the prediction accuracy. In this study, the INFO intelligent optimization algorithm is used to finalize the hyperparameters of a single machine learning algorithm. By comparing the prediction accuracy of the models, it is found that MLP presents more effective in predicting non-linear and small sample datasets. Among the novel ensemble learning models based on the INFO algorithm, the IN-Voting model consisting of five single machine learning algorithms (SGD, SVM, MLP, RFR, and GBDT) exhibits higher prediction accuracy than other models. On the one hand, the INFO intelligent optimization algorithm improves the model prediction performance more significantly in the Voting combination of five weak learners with low prediction accuracy. For example, the prediction accuracy of the M1 group is higher than that of the five weak learners. On the other hand, the INFO intelligent optimization algorithm can also improve the prediction accuracy by about 0.01 in the Voting combination with high prediction accuracy of the weak learner itself. Based on the R^2 values of single machine learning models and ensemble learning models under the INFO algorithm, the ensemble learning model has higher prediction accuracy (Pham et al., 2021).

In the new ensemble learning model, the complexity of the M16 is higher, resulting in a longer model optimization time. Therefore, in the stability prediction of soil-rock mixture slopes, the prediction accuracy of the model should be maximized with reduced model complexity. Moreover, the dual structure of soil-rock mixture slopes is complex, in which the distribution ratio of soil and rocks has a great influence on the prediction difficulty of slope stability (Dong et al., 2020; Xu and Zhang, 2021; Zhao et al., 2021). Therefore, in the prediction of slope stability, the soil content of 30%, 60%, and 90% can be divided into four intervals to study the characteristics of stability prediction.

6 Conclusion

In this study, two types of stability prediction models for soil-rock mixture slopes are developed through INFO, including 12 single machine learning models and 16 novel IN-Voting ensemble learning models with different combinations of weak learners. The stability coefficients of the two prediction models are examined in detail. Based on the three evaluation indicators, the novel IN-Voting ensemble learning model shows the best prediction performance. Finally, the importance analysis is performed for factors affecting slope stability, providing a new idea for stability prediction of soil-rock mixture slopes. The conclusions of this study are as follows.

(1) Among the 12 single stability prediction models, MLP has a highest prediction accuracy of 0.9681, which for non-linear data of Soil-rock mixture slopes. The MLP model plays an important role in the IN-Voting ensemble learning model.
(2) The 16 novel ensemble learning models are validated using data on mixed earth and rock slopes that have been investigated in detail. The results show that the R^2 of each IN-Voting model is higher than that of the five single weak learner models. In addition, the MSE and MAE are less than 0.01. The M16 group IN-Voting ensemble learning model has the highest prediction accuracy with R^2, MSE, and MAE of 0.9846, 0.0321, and 0.0013, respectively.
(3) The Permutation Importance method and the novel IN-Voting ensemble learning model developed by the M16 group are used to analyze the importance of factors affecting the stability of soil-rock mixture slopes. The four parameters in descending order are rock content, bedrock inclination, slope height, and slope angle. Therefore, in the engineering evaluation and treatment of soil-rock mixture slopes, the influence of the rock content rate and bedrock inclination should be emphasized.

Data availability statement

The raw data supporting the conclusions of this article will be made available by the authors, without undue reservation.

Author contributions

Conceptualization, BZ; methodology, XF; software, XF; investigation, JD; resources, YL; data curation, LW; writing-original draft preparation, YW; writing-review and editing, BZ.

Funding

This research is supported by the Guizhou Provincial Science and Technology Projects [Grant Nos. (2019)1169 and (2019)1173], Guizhou Education Department Foundation for Youth, China [Grant No. (2018)151], and Scientific Research Platform of Guizhou Minzu University [GZMUSYS (2021)01].

Conflict of interest

The authors declare that the research was conducted in the absence of any commercial or financial relationships that could be construed as a potential conflict of interest.

Publisher's note

References

Ahmadianfar, I., Heidari, A. A., Noshadian, S., Chen, H., and Gandomi, A. H. (2022). INFO: An efficient optimization algorithm based on weighted mean of vectors. *Expert Syst. Appl.* 195, 116516. doi:10.1016/j.eswa.2022.116516

Almansi, K. Y., Shariff, A. R. M., Kalantar, B., Abdullah, A. F., Ismail, S. N. S., and Ueda, N. (2022). Performance evaluation of hospital site suitability using multilayer Perceptron (MLP) and analytical hierarchy process (AHP) models in malacca, Malaysia. *Sustainability* 14, 3731. doi:10.3390/SU14073731

Breiman, L. (2001). Random forests. *Mach. Learn.* 45, 5–32. doi:10.1023/a:1010933404324

Bui, D. T., Shirzadi, A., Chapi, K., Shahabi, H., Pradhan, B., Pham, B. T., et al. (2019). A hybrid computational intelligence approach to groundwater spring potential mapping. *Water* 11, 2013. doi:10.3390/w11102013

Cen, D., Huang, D., and Ren, F. (2017). Shear deformation and strength of the interphase between the soil–rock mixture and the benched bedrock slope surface. *Acta Geotech.* 12, 391–413. doi:10.1007/s11440-016-0468-2

Chen, X., Shi, C., Ruan, H.-N., and Yang, W.-K. (2021). Numerical simulation for compressive and tensile behaviors of rock with virtual microcracks. *Arabian J. Geosciences* 14, 870. doi:10.1007/s12517-021-07163-7

Cheng, G. (2009). *Development of classification scheme on the stability of accumulative slopes and its application in three Gorges Reservoir area*. Beijing, China: Institute of Geology and Geophysics Chinese Academy of Sciences. [in chinese].

Cheng, J., Dai, X., Wang, Z., Li, J., Qu, G., Li, W., et al. (2022). Landslide susceptibility assessment model construction using typical machine learning for the three Gorges Reservoir area in China. *Remote Sens.* 14, 2257. doi:10.3390/rs14092257

Cortes, C., and Vapnik, V. (1995). Support-vector networks. *Mach. Learn.* 20, 273–297. doi:10.1023/A:1022627411411

Cover, T. M., and Hart, P. E. (1967). Nearest neighbor pattern classification. *IEEE Trans. Inf. Theory* 13, 21–27. doi:10.1109/tit.1967.1053964

Deng, B. (2020). Machine learning on density and elastic property of oxide glasses driven by large dataset. *J. Non-Crystalline Solids* 529, 119768. doi:10.1016/j.jnoncrysol.2019.119768

Dong, H., Peng, B., Gao, Q.-F., Hu, Y., and Jiang, X. (2020). Study of hidden factors affecting the mechanical behavior of soil–rock mixtures based on abstraction idea. *Acta Geotech.* 16, 595–611. doi:10.1007/s11440-020-01045-0

Feng, H., Miao, Z., and Hu, Q. (2022). Study on the uncertainty of machine learning model for earthquake-induced landslide susceptibility assessment. *Remote Sens.* 14, 2968. doi:10.3390/RS14132968

Freund, Y., and Schapire, R. E. (1995). A desicion-theoretic generalization of on-line learning and an application to boosting. *Lect. Notes Comput. Sci.* 904, 23–37. doi:10.1007/3-540-59119-2_166

Friedman, J. H. (2002). Stochastic gradient boosting. *Comput. Statistics Data Analysis* 38, 367–378. doi:10.1016/s0167-9473(01)00065-2

Gao, W.-W., Gao, W., Hu, R.-L., Xu, P.-F., and Xia, J.-G. (2018). Microtremor survey and stability analysis of a soil-rock mixture landslide: A case study in baidian town, China. *Landslides* 15, 1951–1961. doi:10.1007/s10346-018-1009-x

Gelman, A. (2015). Bayesian and frequentist regression methods. *Statistics Med.* 34, 1259–1260. doi:10.1002/sim.6427

Geurts, P., Ernst, D., and Wehenkel, L. (2006). Extremely randomized trees. *Mach. Learn.* 63, 3–42. doi:10.1007/s10994-006-6226-1

Ghatkar, J. G., Singh, R. K., and Shanmugam, P. (2019). Classification of algal bloom species from remote sensing data using an extreme gradient boosted decision tree model. *Int. J. Remote Sens.* 40, 9412–9438. doi:10.1080/01431161.2019.1633696

Hitouri, S., Varasano, A., Mohajane, M., Ijlil, S., Essahlaoui, N., Ali, S. A., et al. (2022). Hybrid machine learning approach for gully erosion mapping susceptibility at a watershed scale. *ISPRS Int. J. Geo-Information* 11, 401. doi:10.3390/ijgi11070401

Ho, T. K. (1998). The random subspace method for constructing decision forests. *IEEE Trans. Pattern Anal. Mach. Intell.* 20, 832–844. doi:10.1109/34.709601

Kalender, A., Sonmez, H., Medley, E., Tunusluoglu, C., and Kasapoglu, K. E. (2014). An approach to predicting the overall strengths of unwelded bimrocks and bimsoils. *Eng. Geol.* 183, 65–79. doi:10.1016/j.enggeo.2014.10.007

Kombo, O. H., Kumaran, S., Sheikh, Y. H., Bovim, A., and Jayavel, K. (2020). Long-term groundwater level prediction model based on hybrid KNN-RF technique. *Hydrology* 7, 59. doi:10.3390/hydrology7030059

Lee, S. J., Tseng, C. H., Yang, H. Y., Jin, X., Jiang, Q., Pu, B., et al. (2022). Random RotBoost: An ensemble classification method based on rotation forest and AdaBoost in random subsets and its application to clinical decision support. *Entropy (Basel)* 24, 617. doi:10.3390/e24050617

Leeuw, J. D. (2009). *Journal of statistical software*, Hoboken, NJ, USA: Wiley Interdisciplinary Reviews: Computational Statistics, 128–129. doi:10.1002/wics.10

Lin, S., Zheng, H., Han, C., Han, B., and Li, W. (2021). Evaluation and prediction of slope stability using machine learning approaches. *Front. Struct. Civ. Eng.* 15, 821–833. doi:10.1007/s11709-021-0742-8

Liu, L., Mao, X., Xiao, Y., Wu, Q., Tang, K., and Liu, F. (2019). Effect of rock particle content on the mechanical behavior of a soil-rock mixture (SRM) via large-scale direct shear test. *Adv. Civ. Eng.* 2019–16. doi:10.1155/2019/64526576452657

Liu, Z., Qiu, H., Zhu, Y., Liu, Y., Yang, D., Ma, S., et al. (2022). Efficient identification and monitoring of landslides by time-series InSAR combining single- and multi-look phases. *Remote Sens.* 14, 1026. doi:10.3390/rs14041026

Peng, C.-Y., Ren, Y.-F., Ye, Z.-H., Zhu, H.-Y., Liu, X.-Q., Chen, X.-T., et al. (2022). A comparative UHPLC-Q/TOF-MS-based metabolomics approach coupled with machine learning algorithms to differentiate Keemun black teas from narrow-geographic origins. *Food Res. Int.* 158, 111512. doi:10.1016/J.FOODRES.2022.111512

Pham, K., Kim, D., Park, S., and Choi, H. (2021). Ensemble learning-based classification models for slope stability analysis. *Catena* 196, 104886. doi:10.1016/j.catena.2020.104886

Qi, C., and Tang, X. (2018). Slope stability prediction using integrated metaheuristic and machine learning approaches: A comparative study. *Comput. Industrial Eng.* 118, 112–122. doi:10.1016/j.cie.2018.02.028

Qiu, H., Zhu, Y., Zhou, W., Sun, H., He, J., and Liu, Z. (2022). Influence of DEM resolution on landslide simulation performance based on the Scoops3D model. *Geomatics, Nat. Hazards Risk* 13, 1663–1681. doi:10.1080/19475705.2022.2097451

Ramos-Bernal, R. N., Vázquez-Jiménez, R., Cantú-Ramírez, C. A., Alarcón-Paredes, A., Alonso-Silverio, G. A., Bruzón, G., et al. (2021). Evaluation of conditioning factors of slope instability and continuous change maps in the generation of landslide inventory maps using machine learning (ML) algorithms. *Remote Sens.* 13, 4515. doi:10.3390/rs13224515

Ray, A., Kumar, V., Kumar, A., Rai, R., Khandelwal, M., and Singh, T. N. (2020). Stability prediction of Himalayan residual soil slope using artificial neural network. *Nat. Hazards* 103, 3523–3540. doi:10.1007/s11069-020-04141-2

Selamat, S. N., Majid, N. A., Taha, M. R., and Osman, A. (2022). Landslide susceptibility model using artificial neural network (ANN) approach in langat river basin, selangor, Malaysia. *Land* 11, 833. doi:10.3390/land11060833

Sevi, M., and İ, A. (2020). "COVID-19 detection using deep learning methods," in 2020 International Conference on Data Analytics for Business and Industry: Way Towards a Sustainable Economy (ICDABI)) (Sakheer, Bahrain, 1–6. doi:10.1109/ICDABI51230.2020.9325626

Shahzad, N., Ding, X., and Abbas, S. (2022). A comparative assessment of machine learning models for landslide susceptibility mapping in the rugged terrain of northern Pakistan. *Appl. Sci.* 12, 2280. doi:10.3390/app12052280

Sun, Q., Zhou, W. X., and Fan, J. (2020). Adaptive huber regression. *J. Am. Stat. Assoc.* 115, 254–265. doi:10.1080/01621459.2018.1543124

Wagenaar, D., Jong, J. D., and Bouwer, L. M. (2017). Multi-variable flood damage modelling with limited data using supervised learning approaches. *Nat. Hazards Earth Syst. Sci.* 17, 1683–1696. doi:10.5194/nhess-17-1683-2017

Wang, L., Qiu, H., Zhou, W., Zhu, Y., Liu, Z., Ma, S., et al. (2022). The post-failure spatiotemporal deformation of certain translational landslides may follow the pre-failure pattern. *Remote Sens.* 14, 2333. doi:10.3390/rs14102333

Wang, Y., Mao, T., Xia, Y., Li, X., and Yi, X. (2022b10701). Macro-meso fatigue failure of bimrocks with various block content subjected to multistage fatigue triaxial loads. *Int. J. Fatigue* 163, 107014. doi:10.1016/j.ijfatigue.2022.107014

Wang, Y., Su, Y., Xia, Y., Wang, H., and Yi, X. (2022a). On the effect of confining pressure on fatigue failure of block-in-matrix soils exposed to multistage cyclic triaxial loads. *Fatigue & Fract. Eng. Mater. Struct.* 45 (9), 2481–2498. doi:10.1111/ffe.13760

Wang, Y., Yi, X. F., Li, P., Cai, M. F., and Sun, T. (2022c). Macro-meso damage cracking and volumetric dilatancy of fault block-in-matrix rocks induced by freeze–thaw-multistage constant amplitude cyclic (F-T-MSCAC) loads. *Fatigue & Fract. Eng. Mater. Struct.* 45 (10), 2990–3008. doi:10.1111/ffe.13798

Wu, C.-Y., and Lin, S.-Y. (2022). Performance assessment of event-based ensemble landslide susceptibility models in shihmen watershed, taiwan. *Water* 14 (5), 717. doi:10.3390/w14050717

Xia, D., Tang, H., Sun, S., Tang, C., and Zhang, B. (2022). Landslide susceptibility mapping based on the germinal center optimization algorithm and support vector classification. *Remote Sens.* 14, 2707. doi:10.3390/rs14112707

Xu, W.-J., Hu, L.-M., and Gao, W. (2016). Random generation of the meso-structure of a soil-rock mixture and its application in the study of the mechanical behavior in a landslide dam. *Int. J. Rock Mech. Min. Sci.* 86, 166–178. doi:10.1016/j.ijrmms.2016.04.007

Xu, W.-J., and Zhang, H.-Y. (2021). Research on the effect of rock content and sample size on the strength behavior of soil-rock mixture. *Bull. Eng. Geol. Environ.* 80, 2715–2726. doi:10.1007/s10064-020-02050-z

Xue, X. (2016). Prediction of slope stability based on hybrid PSO and LSSVM. *J. Comput. Civ. Eng.* 31, 04016041. doi:10.1061/(asce)cp.1943-5487.0000607

Yang, Y., Sun, G., Zheng, H., and Yan, C. (2020). An improved numerical manifold method with multiple layers of mathematical cover systems for the stability analysis of soil-rock-mixture slopes. *Eng. Geol.* 264, 105373. doi:10.1016/j.enggeo.2019.105373

Yue, Z. Q., Chen, S., and Tham, L. G. (2003). Finite element modeling of geomaterials using digital image processing. *Comput. Geotechnics* 30, 375–397. doi:10.1016/s0266-352x(03)00015-6

Zhang, Y., Ge, T., Tian, W., and Liou, Y.-A. (2019). Debris flow susceptibility mapping using machine-learning techniques in shigatse area, China. *Remote Sens.* 11, 2801. doi:10.3390/rs11232801

Zhao, L., Huang, D., Zhang, S., Cheng, X., Luo, Y., and Deng, M. (2021). A new method for constructing finite difference model of soil-rock mixture slope and its stability analysis. *Int. J. Rock Mech. Min. Sci.* 138, 104605. doi:10.1016/j.ijrmms.2020.104605

Zhao, L., Qiao, N., Huang, D., Zuo, S., and Zhang, Z. (2022). Numerical investigation of the failure mechanisms of soil–rock mixture slopes by material point method. *Comput. Geotechnics* 150, 104898. doi:10.1016/j.compgeo.2022.104898

Zhou, C., Ai, D., Huang, W., Xu, H., Ma, L., Chen, L., et al. (2021). Emergency survey and stability analysis of a rainfall-induced soil-rock mixture landslide at chongqing city, China. *Front. Earth Sci.* 9, 774200. doi:10.3389/feart.2021.774200

Zou, H., and Hastie, T. (2005). Regularization and variable selection via the elastic net. *J. R. Stat. Soc. Ser. B Stat. Methodol.* 67, 301–320. doi:10.1111/j.1467-9868.2005.00503.x

frontiers | Frontiers in Earth Science

TYPE Original Research
PUBLISHED 11 January 2023
DOI 10.3389/feart.2022.1048427

OPEN ACCESS

EDITED BY
Haijun Qiu,
Northwest University, China

REVIEWED BY
Lincheng Jiang,
Xihua University, China
Ronghua Zhong,
Yunnan University, China

*CORRESPONDENCE
Jun Wang,
wangjun@gdas.ac.cn
Qinghua Gong,
gongqh@gdas.ac.cn

SPECIALTY SECTION
This article was submitted to Geohazards and Georisks, a section of the journal Frontiers in Earth Science

RECEIVED 19 September 2022
ACCEPTED 20 October 2022
PUBLISHED 11 January 2023

CITATION
Wang J, Gong Q, Yuan S and Chen J (2023), Combining soil macropore flow with formation mechanism to the development of shallow landslide warning threshold in South China. *Front. Earth Sci.* 10:1048427. doi: 10.3389/feart.2022.1048427

Combining soil macropore flow with formation mechanism to the development of shallow landslide warning threshold in South China

Jun Wang[1,2]*, Qinghua Gong[1,2]*, Shaoxiong Yuan[1,2] and Jun Chen[1,2]

[1]Guangdong Open Laboratory of Geospatial Information Technology and Application, Guangzhou Institute of Geography, Guangdong Academy of Sciences, Guangzhou, China, [2]Guangdong Geological Disaster Emergency Technology Research Center, Guangzhou, China

Because of the physical character of soil from granite weathering and the typhoon rains in South China, the model for early warnings of existing shallow landslides cannot be well applied in that area. This study developed a new shallow landslide model based on the effect of soil macropores for determining the rainfall threshold to post an early warning of the possibility of a shallow landslide in South China. We studied the hydrological effects of macropore flow and proposed a mechanistic model of the formation of shallow landslides by introducing the macropore coefficient of granite residual soil. The rainfall threshold of each slope unit was calculated by combining the hydrological model with the proposed shallow landslide model. Lastly, we tested the calculated result in the Maguihe watershed, Guangdong province, South China, which experienced a group of massive shallow landslides on 21 September 2010. The study results showed that the macropores of vegetation roots had a significant effect by increasing the permeability of granite residual soil. Coniferous forest land has the highest initial infiltration rate and stable infiltration rate, followed by shrub forest land, and then bare land. Statistical verification showed that the accurate prediction rate of the proposed model was 80.65%, which is adequate for early warning of shallow landslides in South China. We discuss the application conditions and parameter calibrations of the proposed model, and offer recommendations for future research.

KEYWORDS

shallow landslide, formation mechanism, soil macropore flow, rainfall threshold, granites weathering crust

Introduction

Shallow landslides induced by heavy rainfall are common phenomena around the world and are frequently accompanied by serious loss of life and property, particularly in mountainous and hilly areas (Asch et al., 2007; Beville et al., 2010; Chien et al., 2015; Palladino et al., 2018; Liu X. et al., 2022; Liu Z. J. et al., 2022). South China is located in a strong monsoon interaction zone. Under the influence of global climate change and intensifying human activities, landslide disasters have been increasing in frequency and people's lives and property in hilly and mountainous areas are facing huge threats (Dai et al., 1999; Gong, 2014; Gong et al., 2021; Shou and Chen, 2021). For example, on 21 September 2010, typhoon Fanapi caused a heavy rainstorm with a single-day rainfall of 814 mm. These conditions resulted in more than 2,000 shallow landslides in Gaozhou City, Guangdong Province, causing 73 deaths and direct economic losses of about 2.2 billion yuan (Wang and Xia, 2012). On 10 June 2019, thousands of shallow landslides occurred in Longchuan County, Heyuan City, Guangdong Province, causing the evacuation of 19,769 people and a direct economic loss exceeding 200 million yuan (Sohu news, 2019). History reminds us that engineering measures cannot always protect us against the forces of nature. Thus, an effective warning system based on well-calibrated rainfall readings is extremely important to mitigate the risks associated with shallow landslides caused by rainstorm in South China.

Currently, the commonly used approaches for analyzing shallow landslides are statistical or physical methods (Adams and Sidle, 1987; Kim et al., 2016; Palladino et al., 2018; Ran et al., 2018; Vandromme et al., 2020; Loche et al., 2022). The statistical method cannot address the physical mechanism or dynamic behavior of landslides and factors such as soil cohesion and friction angle have little correlation with landslide occurrence. The premise of this method for early warning of shallow landslides is to have long-term, relatively complete rainfall data (Florence et al., 2018; Bhardwaj et al., 2019; Gao et al., 2019; Hawas et al., 2019; Juliev et al., 2019; Mekonnen et al., 2022). However, in the mountainous and hilly areas of South China, landslide observation sites are scarce, the research foundation is weak, and relatively few historical records are available. Thus, the essential data such as the time of landslide occurrence and the corresponding accumulated rainfall are often lacking. In this case, the margin of error when using statistical methods to generate early warnings is relatively large. At present, most existing landslide warning systems in South China are based on this method, wherein a warning is issued when an observed value reaches a statistical threshold.

Physical and mechanical methods are based on rainfall infiltration, hydrological effects, and soil instability as a function of the slope to determine the rainfall threshold, or an analysis of the critical hydrological threshold of landslides by studying the movement mechanism and runoff process (Romano et al., 1998; Nguyen et al., 2014; Jiang et al., 2017; Liu et al., 2017; Wu et al., 2020; Qiu et al., 2022; Wang et al., 2022; Zhu et al., 2022). This is presently the most effective method for determining the risk of shallow landslides. With this approach, we can clearly describe the migration of precipitation on the surface and its infiltration into the ground, as well as observe and analyze changes in pore water pressure of soils that occur because of precipitation. In addition, specific changes in slope and the corresponding safety factor value can be calculated using the slope stability model (Wang et al., 2014; Fattah et al., 2017; Liang, 2022). Currently, the main physical models used to evaluate shallow landslides associated with rainfall are the Shallow Slope Stability model (SHALSTAB) (Pradhan and Kim, 2016; Kim, et al., 2019; Shou and Chen, 2021), the Stability Index MAPping model (SINMAP) (Michel et al., 2014; Edirisooriya et al., 2018), and the Transient Rainfall Infiltration and Grid-based Regional Slope Stability model (TRIGRS) (Alvioli and Baum, 2016; Marin et al., 2020; He et al., 2021). These physical models are mainly founded on the infinite slope method based on Mohr-Coulomb failure criteria to reveal landslide potential. The plane sliding model is representative of those methods in which it is assumed that slope instability can be extended indefinitely. Safety factors and the possible location of failure at the surface can be obtained using the limit equilibrium method. Therefore, this paper used the physical method to calculate the threshold for warning against shallow landslides induced by heavy rainfall in South China.

Because of the particular type of weathered granite soil in South China, the formation mechanism is quite different from that of the loess landslides in the northwest and the gravel landslides in the southwest. The surface layers of shallow landslides in South China consist mostly of strongly weathered granite and residual slope accumulation layers, with well-developed surface joints and fissures. Heavy rain can scour the pores, gradually enlarging them to form channels for surface infiltration, turning the precipitation into a preferential flow through large pores. A temporary groundwater level is formed in the loose layer with a larger hydraulic conductivity that causes floating drag and scouring of the rock and soil mass, and eventually leads to the large-scale occurrence of shallow landslides (Dai et al., 1999; Letto and Cella, 2016; Gong et al., 2017; Chen et al., 2022; Liao et al., 2022; Silva et al., 2022). At present, most relevant physical models assume that under conditions of no surface runoff, the mechanism of how macropore flow influences shallow landslides is still unclear. Most research has focused on conducting laboratory tests on soil macropore flow (Ilek et al., 2019; Muddle and Briggs, 2019; Kotlar et al., 2020; Tao et al., 2020; Jarvis and Larsbo, 2022); related studies evaluating the effect of macropore flow on shallow landslide stability are relatively rare, and no relevant physical model incorporating the soil macropore coefficient has been established so far.

Therefore, the overall objective of this study was to develop an innovative model of the mechanism of shallow landslides that takes into account the effect of soil macropore flow. We also

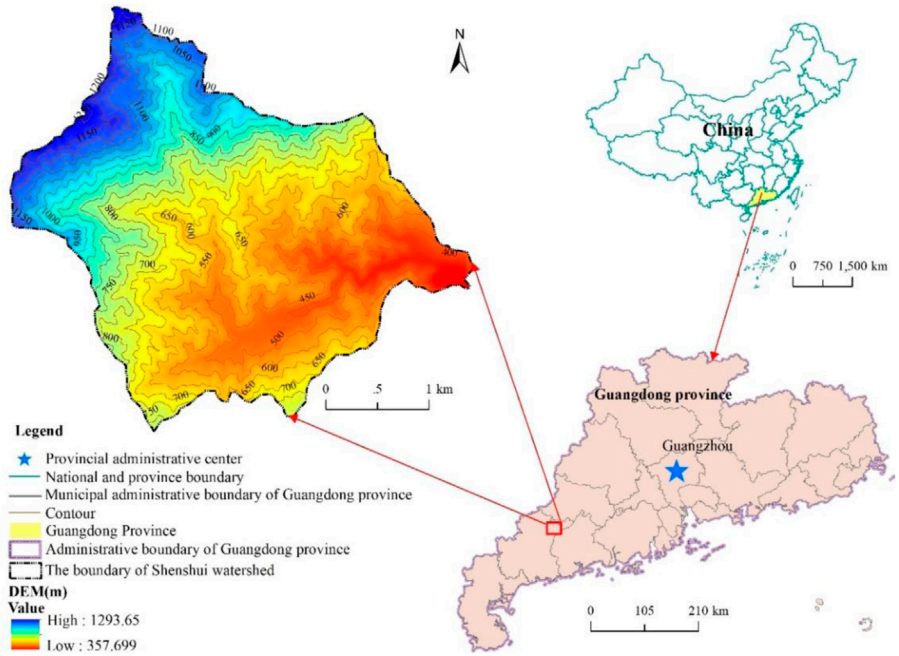

FIGURE 1
Location of the study area.

propose a method for determining the rainfall threshold for generating early warnings of shallow landslides in South China by combining the proposed physical model and the hydrological model. The specific objectives were 1) to analyze the effect of root macropores on soil permeability by field experiments using double-ring infiltration meters, 2) to develop a mechanistic model of shallow landslides including the effect of macropores, 3) to propose a method for determining the rainfall threshold for early warnings of shallow landslides based on the proposed model, and 4) to test the performance of the proposed method based on historical disaster data and from actual field data. To achieve these objectives, the Shenshui watershed, located in western Guangdong Province, South China, was selected as the study area. Because of the complex interaction of natural and artificial factors, this area has suffered repeatedly from shallow landslides from 2010 to 2021, causing serious loss of life and property. The study results provide a scientifically reliable theoretical basis for the mitigation of shallow landslides in South China.

Materials and methods

Study area

The Shenshui watershed, located in Magui town, Maoming City, Guangong Province, South China, was selected as the study area (Figure 1). The watershed area is approximately 9.52 km^2 with a maximum elevation of approximately 836 m, and the length of the main channel is nearly 4.71 km. The river bed gradient is relatively large, ranging from 0° to 58.34°. The range of a typical channel slope, accounting for 39.51% of the study area, is between 30° and 40°. The characteristic parameters of the debris flow gully watershed are listed in Table 1.

The study area is a subtropical monsoon region, with a climate strongly influenced by the South China Sea. The average annual temperature ranges from 21.3°C to 23.2°C (Wang and Xia, 2012). The average annual rainfall is 2160 mm, the maximum average annual rainfall is 3150 mm, and the maximum annual rainfall is 3175 mm as recorded by the Magui hydrological observation station (Liu 2011). Lithologically, the main exposed strata are mainly Late Proterozoic gneissic fine-grained and medium-grained monzonitic granite, Sinian feldspar quartz sandstone mixed with silty slate and phyllite, Jurassic metamorphic rock formations, and Quaternary clay silt and sandy gravel sandwiched in clay siltstone. The parent material of the natural soil is mainly granite, with gneiss and its weathered elements. The study area is subject to heavy rains from typhoons and other severe convective weather. Because of its peculiar natural and geographical conditions, the heavy rains frequently lead to collapses, shallow landslides, debris flows and other disasters. For example, on 21 September 2010, Magui town suffered from many collapses, landslides, and debris flows because of typhoon Fanapi (Figure 2), resulting

TABLE 1 Morphological characteristics of the study area.

Morphological factors	Value
Area (km^2)	9.52
Maximum altitude (m a.s.l.)	1293.65
Minimum altitude (m a.s.l.)	357.70
Elevation difference (m)	835.95
Main river channel length (km)	4.71
Average channel slope (°)	28.45
Range	23°26′53″–23°29′9″ N; 110°7′35″–110°10′17″ E

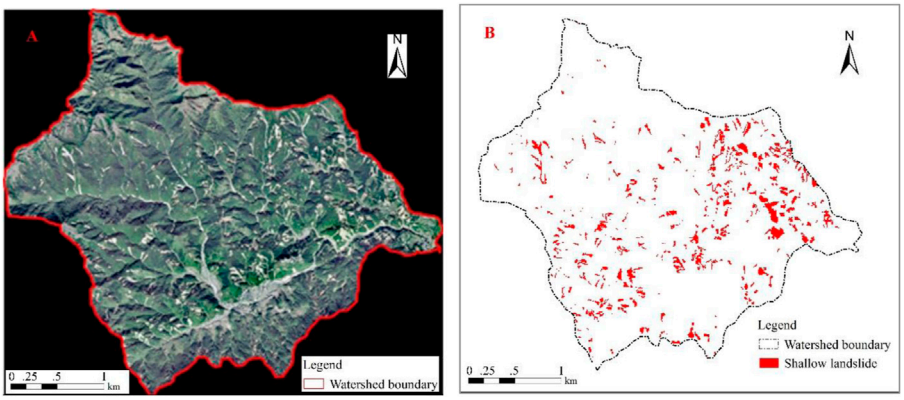

FIGURE 2
Distribution of shallow landslides in the Shenshui watershed induced by typhoon Fanapi. **(A)** Remote-sensing images after the event and **(B)** distribution of shallow landslides.

in the deaths of at least 73 people and damage to 8300 houses costing 2.2 billion yuan in economic losses (Wang and Xia, 2012), and having a serious impact on the environment and the lives of local residents. The shallow landslides occurred mostly at the top of the hill and halfway up the mountain, where loose solid materials were abundant. We determined the occurrence of shallow landslides induced by this event from the remote-sensing image data of the study area (Figure 2). It can be seen that the area of shallow landslides was nearly 0.60 km^2; therefore, the early warning of the risk of shallow landslides in this area was extremely important.

Field testing of effects of macropore flow on permeability enhancement

Numerous mass disaster events in South China, such as the Magui disaster on 21 September 2010 and the Longchuan disaster on 10 June 2019, show that mass shallow landslides are mainly concentrated on the mountains with well-developed vegetation. However, shallow landslides rarely occur in mountains with poor vegetation development. This is because the macropores of vegetation roots have a significant effect on increasing the permeability of granite residual soil. To discuss the effect of root macropores to the permeability of granite residual soil in South China, we measured the infiltration properties of granite residual soils under representative vegetation in South China using the double-loop method. Three cover types are used: coniferous forest, shrub forest and bare land. Every cover type conducted three groups of field tests. The field test of double-loop method was carried out according to the relevant specifications, mainly measuring the initial infiltration rate and stable infiltration rate of granite residual soils.

Mechanistic model of shallow landslides and the effect of macropores

According to the rainstorm infiltration mechanism of landslide formation, the surface runoff is taken as the node with two conditions being considered. With little surface runoff of rain, the groundwater infiltration and slope stability

coefficient are controlled by the amount of rainfall. In the second case, with surface runoff, the volume of groundwater infiltration depends on the presence of large soil pores, which causes the soil to become saturated; thus, rainfall infiltration is mainly affected by the hydraulic conductivity of the saturated soil. It is assumed that the landslide body is relatively impermeable, a temporarily confined aquifer is located below the slip surface, and groundwater flows and circulates in deep layers along the confined aquifer. In South China, the shallow landslides are mainly induced under the second case. Thus, this study focused on landslide stability under the condition of surface runoff during a heavy rainstorm.

Under the action of rain, the flotation force F_b acting on the landslide surface generated by the macropore flow is a non-negligible factor for rainstorm-induced landslides. The formula for calculation of F_b can be express as:

$$F_b = \rho_w g Z_w L \cos\theta \tag{1}$$

where F_b is the flotation force (N), ρ_w is the water density (kg/m^3), g is the gravitational acceleration (9.81 N/kg), Z_w is the depth of the aquifer from the surface (m), L is landslide surface length (m), and θ is the terrain gradient (°).

Innovatively considering the influence of macropore flow on landslide formation, the macropore coefficient (λ) is introduced here. The hydrostatic pressure F_t generated by the macropores is:

$$F_t = \lambda \rho_w g Z L \cos^2\theta \tag{2}$$

where F_t is the hydrostatic pressure generated by the macropores (N), λ is the macropore coefficient of the soil (%), and Z is the soil thickness (m).

When the seismic force is ignored and surface runoff occurs, the slope stability coefficient F_s can be obtained by considering the sliding body gravity, hydrostatic pressure, seepage pressure and floating force after formation of the temporary groundwater level:

$$F_s = \frac{CL + (\rho_s g Z L \cos^2\theta - \lambda \rho_w g Z_w L \cos^2\theta - \rho_w g Z_w L \cos\theta)\tan\varphi}{\rho_s g Z L \cos\theta \sin\theta + \rho_w g Z_w L \cos\theta \sin\theta} \tag{3}$$

where F_s is the slope stability coefficient, C is the cohesion of the soil (kPa), ρ_s is the density of soil (kg/m^3), and φ is the internal friction angle (°) of the soil.

Divide both the numerator and denominator of the above equation by $\rho_s g Z L$, as:

$$F_s = \frac{\frac{C}{\rho_s g Z} + \left(\cos^2\theta - \lambda \frac{\rho_w}{\rho_s}\frac{Z_w}{Z}\cos^2\theta - \frac{\rho_w}{\rho_s}\frac{Z_w}{Z}\cos\theta\right)\tan\varphi}{\cos\theta\sin\theta + \frac{\rho_w}{\rho_s}\frac{Z_w}{Z}\cos\theta\sin\theta} \tag{4}$$

Let $\gamma = \frac{\rho_w}{\rho_s}$ represent the density ratio of water to soil in the landslide area (dimensionless), and let $w = \frac{Z_w}{Z}$ be the saturation state of the slope soil, which is the saturation factor. The above formula can be further simplified as:

$$F_S = \frac{\frac{C}{Z\gamma_s} + (\cos^2\theta - \lambda\gamma w\cos^2\theta - \gamma w\cos\theta)\tan\varphi}{\cos\theta\sin\theta + \gamma w\cos\theta\sin\theta} = \frac{\frac{C}{Z\gamma_s} + \left(1 - \lambda\gamma w - \gamma w\frac{1}{\cos\theta}\right)\cos^2\theta\tan\varphi}{(1+\gamma w)\cos\theta\sin\theta} \tag{5}$$

Divide both the numerator and denominator of the above equation by $cos^2\theta$, and let $C' = \frac{C}{\rho_s g Z cos^2\theta}$ represent the effective soil cohesion, which is a variable associated with the soil cohesion (C). The above formula then becomes:

$$F_s = \frac{C' + \left(1 - \lambda\gamma w - \frac{\gamma w}{\cos\theta}\right)\tan\varphi}{(1+\gamma w)\tan\theta} \tag{6}$$

where w is the saturation state of the slope soil (dimensionless), which can be calculated by the following formula:

$$w = \frac{qa}{T\sin\theta} \tag{7}$$

where q is the effective rainfall (mm), a is the ratio of the rain collection area (the catchment area) to the drainage width (m), and T is the transmissibility ($T = KZ\cos\theta$, m^2/d), where K is the permeability coefficient (m/d or cm/s), and Z is the soil thickness (m). The F_s can be given as:

$$F_s = \frac{C' + \left(1 - \lambda\gamma\frac{qa}{T\sin\theta} - \frac{\gamma qa}{T\sin\theta\cos\theta}\right)\tan\varphi}{\left(1 + \gamma\frac{qa}{T\sin\theta}\right)\tan\theta} \tag{8}$$

Rainfall threshold of shallow landslides

When F_s >1, the slope is stable; when F_s =1, the slope is in a state of limit equilibrium; and when F_s <1, the slope is unstable. Considering the slope is in a state of limit equilibrium (F_s =1), Eq. 8 can further be simplified as:

$$q = \frac{T\sin\theta\left(C' + \tan\varphi - \tan\theta\right)}{a\gamma\left(\lambda\tan\varphi + \tan\theta + \tan\varphi/\cos\theta\right)} \tag{9}$$

The main reason for shallow landslides during heavy rainfall in South China is the rise in groundwater level, soil saturation and the reduction in effective shear strength caused by continuous heavy rainfall. The limit equilibrium theory can well express the coupling relationship between hydrology and geology. Therefore, according to the runoff characteristics and mechanical limit equilibrium of slopes in small watersheds, an early warning threshold model of shallow landslides occurring in groups can be established based on the hydrological-mechanical mechanism. The hydrological model of this study used the improved SCS model to simulate the relationship between rainfall and infiltration, and the established slope limit equilibrium formula to analyze the stability of the slope under heavy rainfall. The calculation unit used in this study is the slope unit. The small watershed digital elevation model (DEM) is used to realize the automatic

TABLE 2 Comparison of infiltration performance of three different vegetation coverage types.

The cover type	Initial infiltration rate (mm/min)			Stable infiltration rate (mm/min)		
	Plot 1	Plot 2	Plot 3	Plot 1	Plot 2	Plot 3
Coniferous forest	36.24	35.05	34.87	6.38	5.70	5.62
Shrub forest	22.82	22.75	25.02	2.91	3.08	3.05
Bare land	15.49	16.13	14.77	1.67	1.81	1.81

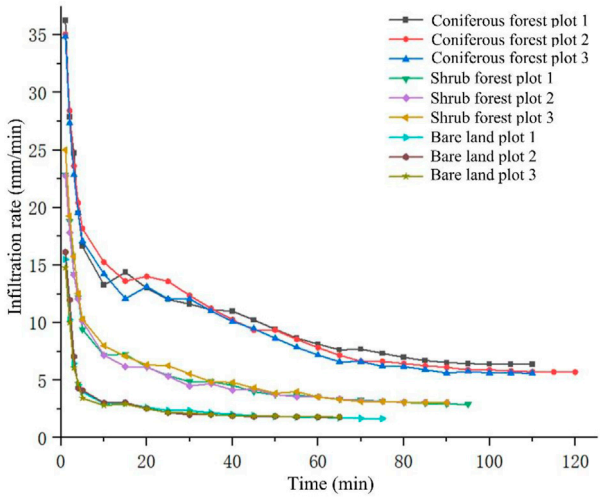

FIGURE 3
Infiltration process of different vegetation coverage in granite residual soil in South China.

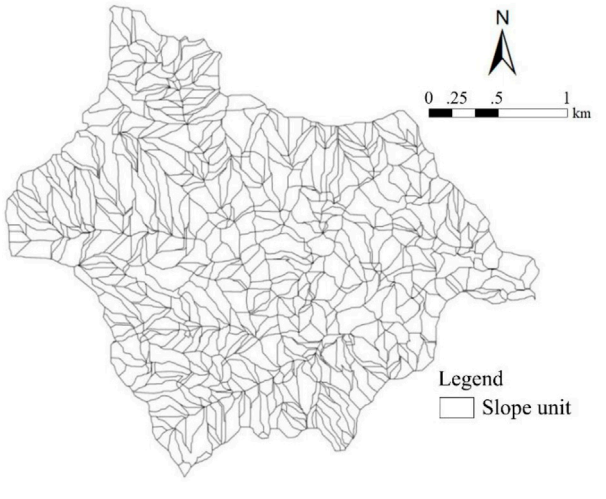

FIGURE 4
Divisions of the slope unit in the study area.

division of the slope unit, and each unit is coded and given element attribute information. On this basis, GIS spatial analysis is used to calculate the warning threshold of each division unit.

Results and discussion

Field test of the double-loop method

The test result of the initial infiltration rate and stable infiltration rate of granite residual soils in the three cover types are shown in Table 2. The processes of soil infiltration on different vegetation plots are shown in Figure 3.

It can be seen that although there are differences in the specific infiltration process on the different vegetation plots, the overall trend is the same. The soil infiltration rate was high in the initial stage, and decreased rapidly over a short period of time; then, the rate of decrease of infiltration slowed down, and the final infiltration rate approached a stable value.

In this paper, two infiltration indicators, initial infiltration rate and stable infiltration rate, were selected to analyze and evaluate the granite residual soil permeability in each plot (Table 2). It can be seen that the initial infiltration rate and the stable infiltration rate of coniferous forest land were the highest, followed by shrub forest land, and bare land. This is because the decomposing leaves form humus, and soil under the action of humus forms aggregates with a large pore structure. In addition, the coniferous forest soil is more transparent with many developed roots, root-soil gaps, rotted root channels and other large pores. The macropores of vegetation roots have a significant effect on increasing the permeability of granite residual soil. Therefore, a determination of the stability of a slope covered by vegetation must take into account the effect of macropore flow, which strongly influences slope stability; otherwise, the prediction of shallow landslides will be very different from the actual situation.

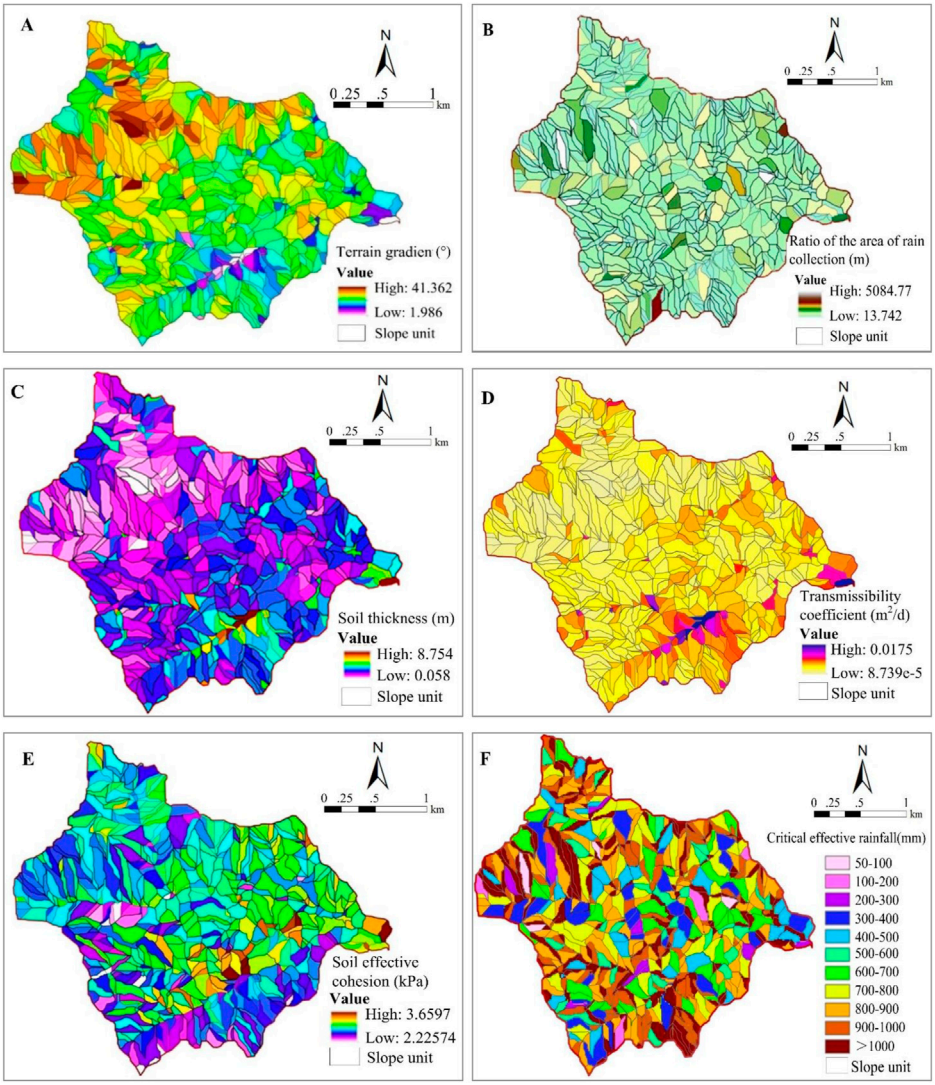

FIGURE 5
Calculated results of proposed model parameters and the critical effective rainfall of each slope unit in the study area. **(A)** Terrain gradient; **(B)** ratio of the area of rain collection; **(C)** soil thickness; **(D)** soil transmissibility coefficient; **(E)** soil effective cohesion; and **(F)** critical effect rainfall.

Calculated result of rainfall threshold of shallow landslides

Division of early warning unit

On the ArcGIS 10.5 platform, according to the digital elevation model (DEM) of the study area, the source-cutting method was adopted, and the ridge line and the valley line were used as the boundaries. The slope unit in the study area was divided into 624 slope subunits (Figure 4).

Results of model parameter calculations

In our proposed physical model of shallow landslides, the main parameters were terrain gradient (θ), the ratio of the area of rain collection (a), the soil transmissibility coefficient (T), the soil thickness (Z), the soil internal friction angle (φ), the soil effective cohesion (C'), the density ratio of water to soil in landslide (γ), and the soil macropore coefficient (λ).

1) Terrain gradient of the slope unit (θ)

Slope is the most influential element in the determination of the risk factor for shallow landslides. Using GIS software, we first calculated the slope of each grid, and then used the spatial statistics function to count the average slope of each slope unit. The result is shown in Figure 5A.

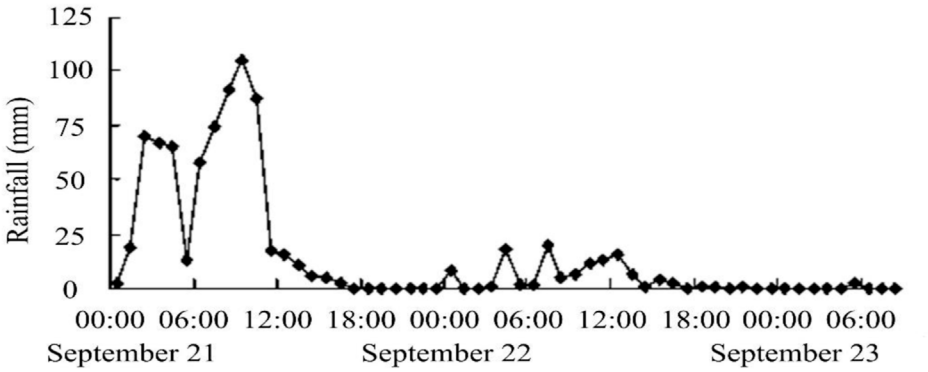

FIGURE 6
Precipitation levels associated with the landslide event of 21 September 2010.

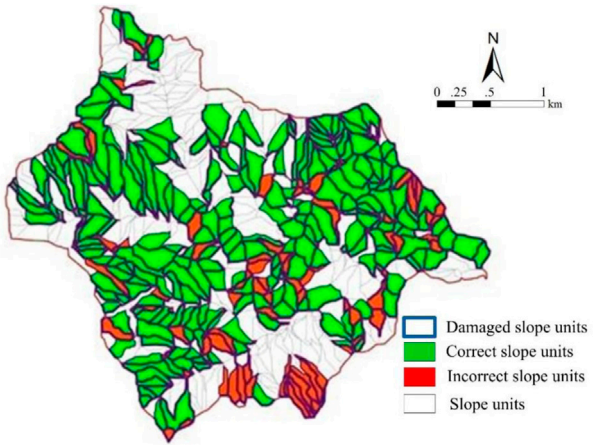

FIGURE 7
Comparison between the calculated results from the landslide early warning model and the actual occurrence.

2) The ratio of the area of rain collection (a)

The ratio of the area of rain collection was calculated as:

$$a = \frac{A}{b} \tag{10}$$

in which a is the ratio of the area of rain collection (m), A is the catchment area above the unit slope (m^2), which can be directly calculated in GIS software through the area operation function. B is the drainage width (m), which can be calculated in the GIS software by length. The results of calculating the ratios of the areas of rain collection are shown in Figure 5B.

3) The soil thickness (Z)

Soil thickness is one of the important factors affecting shallow landslides. In this study, in order to obtain the distribution of soil thickness in study area, field measurements of soil depth were made. The main measurements were soil thickness and surface slope. The measurement position of soil layer thickness was selected in the exposed section area, which was performed manually using an auger and tape measure. Based on the results of field measurements, a regression analysis was carried out on the relationship between slope and soil layer thickness, as:

$$Z = -2.864 \ln(\theta) + 10.719 \tag{11}$$

where Z is the soil thickness (m) and θ is the soil surface slope (°). Through DEM analysis, the average slope (θ) of each slope unit was obtained; then, the soil thickness (Z) was calculated by Eq. 11 (Figure 5C).

4) The soil transmissibility coefficient (T)

The soil transmissibility coefficient was calculated by the following equation:

$$T = KZ\cos\theta \tag{12}$$

where T is the soil transmissibility coefficient (m^2/d), K is the soil permeability coefficient (m/d or cm/s), Z is the soil thickness (m), and θ is the terrain gradient of the slope unit (°). The distribution of soil transmissibility coefficient is shown in Figure 5D.

5) The soil effective cohesion (C')

A slope is a unified system composed of its upper soil layer and covered vegetation, and the effective cohesion of the soil is the combination of soil cohesion and plant root cohesion. In this

TABLE 3 Method of obtaining the key parameters of the proposed physical model of shallow landslides.

Categories	Parameters	Parameters obtaining methods						
		Data collection	Investigation	Field observation	Remote sensing interpretation	Experimental analysis	Computational simulation	Weather forecast
Topographic parameter	Terrain gradient (θ)	●	●				●	
	Ratio of the area of rain collection (a)	●	●				●	
Geological parameter	Internal friction angle(φ)	●	●	●		●	●	
	Cohesion (C)	●	●	●		●	●	
	Soil thickness (Z)	●	●	●		●	●	
	Transmissibility coefficient (T)	●	●	●		●	●	
	density ratio of water to soil in landslide (dimensionless)	●	●	●		●		
	Soil macropore coefficient (λ)	●	●	●		●		
Vegetation parameter	Vegetation cover index ($NDVI$)	●	●		●		●	
Hydrological parameter	Preliminary soil moisture (AMC)	●	●	●	●		●	●
	SCS curve parameters (CN)	●	●	●	●		●	●
	Retention parameter (S)	●	●	●	●		●	●
	Initial infiltration (Ia)	●	●	●	●		●	●
Meteorological data	Precipitation (P)	●	●	●	●	●	●	●

10.3389/feart.2022.1048427

study, the effective cohesion of the soil as related to vegetation coverage was calculated by the following formula:

$$C' = C_{max}\frac{NDVI(x,y)+1}{2} \quad (13)$$

where C_{max} is the maximum value of soil cohesion (kPa), which was obtained through literature review and field surveys, $NDVI(x,y)$ is the vegetation cover index, which can be extracted from remote sensing images by the ENVI software. The calculated result of soil effective cohesion is shown in Figure 5E.

6) The density ratio of water to soil (γ) and the soil macropore coefficient (λ)

The density ratio of water to soil (γ) in the landslide area was a fixed value equal to the ratio of the density of water to the density of soil (dimensionless). In this study, the density ratio of water to soil was 0.378.

The soil macropore coefficient (λ) was obtained by field experiments on the soil (dimensionless). In this study, the soil macropore coefficient of the slope unit was between 0 and 0.04, with an average value of 0.025.

Lastly, according to Eq. 9 and the algebraic calculation of each factor in ArcGIS software, the critical effective rainfall amount triggering shallow landslides in each slope unit can be obtained (Figure 5F).

It can be seen that the terrain slope of the slope unit in the study area varied from 1.986° to 41.362°. The upstream slope of the small watershed was larger, and the slope of the valley and downstream areas was relatively gentle (Figure 5A). The ratio of the area of rain collection in the study area ranged from 13.742 to 5084.77 (Figure 5B). The thickness of granite residual soil in the Shenshui watershed was relative high, with a maximum value of 8.754 m (Figure 5C). The transmissibility coefficient was between 0.00008739 m^2/d and 0.0175 m^2/d (Figure 5D). The soil effective cohesion was relatively small, with a maximum value of 3.6597 kPa (Figure 5E). It can be seen that when the effective rainfall was greater than 50 mm, some slope units slided (Figure 5F). The greater the effective rainfall, the greater the number of unstable slope units and the larger the group of landslides occurring. We compared the actual measured rainfall with the critical rainfall, and obtained the unstable state of the slope unit under the actual rainfall, so as to carry out early warning and forecasting for each slope.

Verification of proposed model

On 21 September 2010, the residents of Magui town experienced many shallow landslides due to the strong rains associated with typhoon Fanapi. The total rainfall reached 829.7 mm (from 19 September, at 20:00 h, to 23 September, at 20:00 h). The time of heavy precipitation in Magui Town on 21 September occurred from 00:00 to 12:00, with two peaks of very heavy precipitation. One peak occurred at about 02:00 h and the precipitation was 74 mm/h. The other peak was at 11:00 h, and the peak precipitation reached 105.5 mm/h. The rainfall process of this event is shown in Figure 6.

By inputting the above precipitation process data into the improved hydrological SCS model, we were able to obtain the actual effective rainfall threshold triggering shallow landslides on each slope unit. Then, by comparison with the critical effective rainfall calculated by the physical model proposed in this study, the spatial distribution of unstable slope units calculated by the proposed theoretical model can be illustrated (Figure 7).

Figure 7 shows that within the scope of the disaster, there were 336 slope units on which shallow landslides occurred. According to the results of the proposed model calculations, landslides happened on 271 slope units, and the accuracy of the prediction rate was 80.65%. Thus, the model proposed in this study was successfully used for early warning of shallow landslides in the Magui River Basin.

Discussion

The key parameters of the proposed physical model for early warning of shallow landslides can be roughly divided into five categories, namely topographic parameters, geological parameters, hydrological parameters, vegetation cover parameters, and meteorological parameters. The key parameters and the methods for obtaining them are shown in Table 3.

The above model parameters are very important for the calculation of shallow landslide warning thresholds. Therefore, in specific applications, it is necessary to test and calibrate these parameters, to ensure that they are in agreement with the actual results, and only in that way can the predicted warning threshold be accurate. The proposed model can be used in those areas with soil composed of weathered granites and subject to typhoon rainstorms, such as South China. In the future, we will continue to test this model on other watersheds where shallow landslides have occurred, so as to increase its accuracy for use in other regions.

Conclusion

In this study, we developed a physical model of shallow landslides, influenced by the effect of soil macropore flow, and proposed a method for determining the rainfall threshold for early warnings of shallow landslides based on the hydrological model and the proposed physical model in South China. The conclusions are:

1) We measured the infiltration properties of granite residual soils under three representative vegetation covers in South China using the double-loop method. The initial infiltration

rate and the stable infiltration rate of coniferous forest land were highest, followed by shrub forest land, and bare land. The macropores of vegetation roots had a significant effect on increasing the permeability of granite residual soil; therefore, the type of vegetation coverage and the infiltration effect of macropores must be considered in determining the stability of a developed slope, otherwise the prediction of shallow landslides will be very different from the actual situation.

2) Considering the effect of macropore flow on shallow landslides, we introduced the macropore coefficient of soil into the shallow landslide mechanism model, and established a revised shallow landslide physical model of granite residual soil in South China.
3) We applied the proposed physical model to calculate the rainfall threshold for early warning of shallow landslides. The massive number of shallow landslides induced by the heavy rainfall on 21 September 2010 was used to verify the calculated results, and revealed a prediction accuracy of 80.65%. Thus, the model proposed in this study provided useful early warnings of the shallow landslides in the Magui River Basin.

Data availability statement

The raw data supporting the conclusion of this article will be made available by the authors, without undue reservation.

Author contributions

JW carried out the field investigation, data analysis, and manuscript writing. QG involved in manuscript supervision. SY undertook the field survey, participated in the discussion and decision-making process. JC was involved in writing reviewing, manuscript editing, and supervision. All the authors participated and contributed to the final manuscript.

Funding

This research work was supported by the National Natural Science Foundation of China (42101084; 41977413), Natural Science Foundation of Guangdong Province (2022A1515011898), Young S&T Talent Training Program of Guangdong Provincial Association for S&T (GDSTA), China (SKXRC202201), and 2022 National Park Construction Project, China (2021GJGY029).

Conflict of interest

The authors declare that the research was conducted in the absence of any commercial or financial relationships that could be construed as a potential conflict of interest.

Publisher's note

All claims expressed in this article are solely those of the authors and do not necessarily represent those of their affiliated organizations, or those of the publisher, the editors and the reviewers. Any product that may be evaluated in this article, or claim that may be made by its manufacturer, is not guaranteed or endorsed by the publisher.

References

Adams, P. W., and Sidle, R. C. (1987). Soil conditions in three recent landslides in Southeast Alaska. *For. Ecol. Manage.* 18 (2), 93–102. doi:10.1016/0378-1127(87)90136-8

Alvioli, M., and Baum, R. L. (2016). Parallelization of the TRIGRS model for rainfall-induced landslides using the message passing interface. *Environ. Model. Softw.* 81, 122–135. doi:10.1016/j.envsoft.2016.04.002

Asch, T., Beek, l., and Bogaard, T. A. (2007). Problems in predicting the mobility of slow moving landslides. *Eng. Geol.* 91 (1), 46–55. doi:10.1016/j.enggeo.2006.12.012

Beville, S. H., Mirus, B. B., Ebel, B. A., Mader, G. G., and Loague, K. (2010). Using simulated hydrologic response to revisit the 1973 Lerida Court landslide. *Environ. Earth Sci.* 61 (6), 1249–1257. doi:10.1007/s12665-010-0448-z

Bhardwaj, A., Wasson, R. J., Ziegler, A. D., Chow, W. T. L., and Sundriyal, Y. P. (2019). Characteristics of rain-induced landslides in the Indian himalaya: A case study of the mandakini catchment during the 2013 flood. *Geomorphology* 330, 100–115. doi:10.1016/j.geomorph.2019.01.010

Chen, P. J., Liu, X., Yu, S., Xu, J. H., Hong, B., Ma, J., et al. (2022). Stability assessment of the restored Benggang units in a weathered granite crust region of South China. *Ecol. Eng.* 182, 106709. doi:10.1016/j.ecoleng.2022.106709

Chien, L. K., Hsu, C. F., and Yin, L. C. (2015). Warning model for shallow landslides induced by extreme rainfall. *Water* 7, 4362–4384. doi:10.3390/w7084362

Dai, F. C., Lee, C. F., and Wang, S. J. (1999). Analysis of rainstorm-induced slide-debris flows on natural terrain of Lantau Island, Hong Kong. *Eng. Geol.* 51 (4), 279–290. doi:10.1016/S0013-7952(98)00047-7

Edirisooriya, K. V. D., Vitanage, N. S., Uluwaduge, P., and Senevirathna, E. M. T. K. (2018). Understanding disaster risk and mitigation special reference to Ratnapura District. *Procedia Eng.* 212, 1034–1039. doi:10.1016/j.proeng.2018.01.133

Fattah, M. Y., Al-Mosawi, M. J., and Al-Americ, A. F. I. (2017). Stresses and pore water pressure induced by machine foundation on saturated sand. *Ocean. Eng.* 16, 268–281. doi:10.1016/j.oceaneng.2017.09.055

Florence, W. Y., Frankie, K., and Lo, L. C. (2018). From landslide susceptibility to landslide frequency: A territory-wide study in Hong Kong. *Eng. Geol.* 242, 12–22. doi:10.1016/j.enggeo.2018.05.001

Gao, J., Zahng, Z., Wang, C. Z., Liu, J., and Zhang, L. (2019). Susceptibility assessment of landslides triggered by earthquakes in the Western Sichuan Plateau. *Catena* 175, 63–76. doi:10.1016/j.catena.2018.12.013

Gong, Q. H. (2014). DEM and GIS based analysis of topographic and geomorphologic factors of shallow landslide in red soil hilly region of South China. *Int. J. Earth Sci. Eng.* 7 (2), 393–399.

Gong, Q. H., Huang, G. Q., Zhang, D. L., and Xiong, H. X. (2017). On the application of the slope element unit method to the shallow landslide risk-prevention mapping with a case study sample of Songgang watershed. *J. Saf. Environ.* 17 (2), 615–620.

Gong, Q. H., Wang, J., Zhou, P., and Guo, M. (2021). A regional landslide stability analysis method under the combined impact of rainfall and vegetation roots in South China. *Adv. Civ. Eng.* 2021, 1–12. doi:10.1155/2021/5512281

Hawas, K., Muhammad, S., Muhammad, A., Bacha, M. A., Shah, S. U., and Calligaris, C. (2019). Landslide susceptibility assessment using Frequency Ratio, a case study of northern Pakistan. *Egypt. J. Remote Sens. Space Sci.* 22 (1), 11–24. doi:10.1016/j.ejrs.2018.03.004

He, J. Y., Qiu, H. J., Qu, F. H., Hu, S., Yang, D. D., Zhang, Y., et al. (2021). Prediction of spatiotemporal stability and rainfall threshold of shallow landslides using the TRIGRS and Scoops3D models. *CATENA* 197, 104999. doi:10.1016/j.catena.2020.104999

Ilek, A., Kucza, J., and Witek, W. (2019). Using undisturbed soil samples to study how rock fragments and soil macropores affect the hydraulic conductivity of forest stony soils: Some methodological aspects. *J. Hydrology* 570, 132–140. doi:10.1016/j.jhydrol.2018.12.067

Jarvis, N., and Larsbo, M. (2022). Macropores and macropore flow. *Reference Module Earth Syst. Environ. Sci* 2022, 1–8. doi:10.1016/B978-0-12-822974-3.00098-7

Jiang, S. H., Huang, J. S., Yao, C., and Yang, J. H. (2017). Quantitative risk assessment of slope failure in 2-D spatially variable soils by limit equilibrium method. *Appl. Math. Model.* 47, 710–725. doi:10.1016/j.apm.2017.03.048

Juliev, M., Mergili, M., Mondal, I., Nurtaev, B., Pulatov, A., and Hubl, J. (2019). Comparative analysis of statistical methods for landslide susceptibility mapping in the Bostanlik District, Uzbekistan. *Sci. Total Environ.* 653, 801–814. doi:10.1016/j.scitotenv.2018.10.431

Kim, M., An, H., Kim, J., Kim, S., Oh, H. J., and Song, Y. S. (2019). Assessment of sudden sediment source areas incurred by extreme rainfall in a mountainous environment: Approach using a subsurface hydrologic concept. *Quat. Int.* 519, 232–244. doi:10.1016/j.quaint.2018.10.031

Kim, M. S., Onda, Y., Uchida, T., and Kim, J. K. (2016). Effects of soil depth and subsurface flow along the subsurface topography on shallow landslide predictions at the site of a small granitic hillslope. *Geomorphology* 271, 40–54. doi:10.1016/j.geomorph.2016.07.031

Kotlar, A. M., Lier, Q. J., Andersen, H. E., Norgaard, T., and Iversen, B. V. (2020). Quantification of macropore flow in Danish soils using near-saturated hydraulic properties. *Geoderma* 375, 114479. doi:10.1016/j.geoderma.2020.114479

Letto, F., and Cella, P. F. (2016). Geotechnical and landslide aspects in weathered granitoid rock masses (Serre Massif, southern Calabria, Italy). *CATENA* 145, 301–315. doi:10.1016/j.catena.2016.06.027

Liang, W. L. (2022). Dynamics of pore water pressure at the soil–bedrock interface recorded during a rainfall-induced shallow landslide in a steep natural forested headwater catchment, Taiwan. *J. Hydrology* 587, 125003. doi:10.1016/j.jhydrol.2020.125003

Liao, D. L., Deng, Y. S., Duan, X. Q., Cai, C. Q., and Ding, S. W. (2022). Variations in weathering characteristics of soil profiles and response of the Atterberg limits in the granite hilly area of South China. *CATENA* 215, 106325. doi:10.1016/j.catena.2022.106325

Liu, C. Y., Ku, C. Y., Xiao, J. E., Huang, C. C., and Hsu, S. M. (2017). Numerical modeling of unsaturated layered soil for rainfall-induced shallow landslides. *J. Environ. Eng. Landsc. Manag.* 25 (4), 329–341. doi:10.3846/16486897.2017.1326925

Liu, J. H. (2011). *Analysis of heavy mountain flood on 21th, september, 2010 in Gaozhou caojiang river*. Guangdong Water Resources and Hydropower, 33–37.

Liu, X., Lan, H. X., Li, L. P., and Cui, P. (2022). An ecological indicator system for shallow landslide analysis. *CATENA* 214, 106211. doi:10.1016/j.catena.2022.106211

Liu, Z. J., Zhu, Y. R., Liu, Y., Yang, D. D., Ma, S. Y., Zhang, J. J., et al. (2022). Efficient identification and monitoring of landslides by time-series InSAR combining single- and multi-look phases. *Remote Sens.* 14, 1026. doi:10.3390/rs14041026

Loche, M., Alvioli, M., Marchesini, I., Bakka, H., and Lombardo, L. (2022). Landslide susceptibility maps of Italy: Lesson learnt from dealing with multiple landslide types and the uneven spatial distribution of the national inventory. *Earth-Science Rev.* 232, 104125. doi:10.1016/j.earscirev.2022.104125

Marin, R. J., García, E. F., and Aristizábal, E. (2020). Effect of basin morphometric parameters on physically-based rainfall thresholds for shallow landslides. *Eng. Geol.* 278, 105855. doi:10.1016/j.enggeo.2020.105855

Mekonnen, A. A., Raghuvanshi, T. K., Suryabhagavan, K. V., and Kassawmar, T. (2022). GIS-based landslide susceptibility zonation and risk assessment in complex landscape: A case of beshilo watershed, northern Ethiopia. *Environ. Challenges* 8, 100586. doi:10.1016/j.envc.2022.100586

Michel, G. P., Kobiyama, M., and Goerl, R. F. (2014). Comparative analysis of SHALSTAB and SINMAP for landslide susceptibility mapping in the Cunha River basin, southern Brazil. *J. Soils Sediments* 14 (7), 1266–1277. doi:10.1007/s11368-014-0886-4

Muddle, D. M., and Briggs, K. M. (2019). Macropore structure and permeability of clay fill samples from a historic clay fill earthwork. *Transp. Geotech.* 19, 96–109. doi:10.1016/j.trgeo.2019.02.003

Nguyen, M. N., Bui, T. Q., Yu, T., and Hirose, S. (2014). Isogeometric analysis for unsaturated flow problems. *Comput. Geotech.* 62, 257–267. doi:10.1016/j.compgeo.2014.08.003

Palladino, M. R., Viero, A., Turconi, L., Brunetti, M. T., Peruccacci, S., Melillo, M., et al. (2018). Rainfall thresholds for the activation of shallow landslides in the Italian alps: The role of environmental conditioning factors. *Geomorphology* 303, 53–67. doi:10.1016/j.geomorph.2017.11.009

Pradhan, A. M. S., and Kim, Y. T. (2016). Evaluation of a combined spatial multi-criteria evaluation model and deterministic model for landslide susceptibility mapping. *CATENA* 140, 125–139. doi:10.1016/j.catena.2016.01.022

Qiu, H., Zhu, Y., Zhou, W., Sun, H., He, J., and Liu, Z. (2022). Influence of DEM resolution on landslide simulation performance based on the Scoops3D model. *Geomat. Nat. Hazards Risk* 13 (1), 1663–1681. doi:10.1080/19475705.2022.2097451

Ran, Q. H., Hong, Y. Y., Li, W., and Gao, J. H. (2018). A modelling study of rainfall-induced shallow landslide mechanisms under different rainfall characteristics. *J. Hydrology* 563, 790–801. doi:10.1016/j.jhydrol.2018.06.040

Romano, N., Brunone, B., and Santini, A. (1998). Numerical analysis of one-dimensional unsaturated flow in layered soilsflow in layered soils. *Adv. Water Resour.* 21 (4), 315–324. doi:10.1016/S0309-1708(96)00059-0

Shou, K. J., and Chen, J. R. (2021). On the rainfall induced deep-seated and shallow landslide hazard in Taiwan. *Eng. Geol.* 288, 106156. doi:10.1016/j.enggeo.2021.106156

Silva, A. C. D., Resende, I., Costa, R. C. D., Uagoda, R. E. S., and Avelar, A. D. S. (2022). Geophysical for granitic joint patern and subsurface hydrology related to slope instability. *J. Appl. Geophys.* 199, 104607. doi:10.1016/j.jappgeo.2022.104607

Sohu New (2019). The 6.10 flood in Longchuan caused economic losses of about 80 million yuan and affected 28,000 people. AvaliableAt: https://www.sohu.com/a/319885598_669237.

Tao, Y., Zou, Z. Q., Guo, L., He, Y. B., Lin, L. R., Lin, H., et al. (2020). Linking soil macropores, subsurface flow and its hydrodynamic characteristics to the development of Benggang erosion. *J. Hydrology* 586, 124829. doi:10.1016/j.jhydrol.2020.124829

Vandromme, R., Thiery, Y., Sedan, S., and Sedan, O. (2020). ALICE (assessment of landslides induced by climatic events): A single tool to integrate shallow and deep landslides for susceptibility and hazard assessment. *Geomorphology* 367, 107307. doi:10.1016/j.geomorph.2020.107307

Wang, G. H., Zhang, D. X., Furuya, G., and Yang, J. (2014). Pore-pressure generation and fluidization in a loess landslide triggered by the 1920 haiyuan earthquake, China: A case study. *Eng. Geol.* 174, 36–45. doi:10.1016/j.enggeo.2014.03.006

Wang, L. Y., Qiu, H. J., Zhou, W. Q., Zhu, Y. R., Liu, Z. J., Ma, S. Y., et al. (2022). The post-failure spatiotemporal deformation of certain translational landslides may follow the pre-failure pattern. *Remote Sens.* 14, 2333. doi:10.3390/rs14102333

Wang, Y., and Xia, B. (2012). Eco-restoration strategies and measures for the soil and water conservation of typhoon-hit areas in Western Guangdong province: A case study of Magui town, Gaozhou city. *Sci. Soil Water Conservation* 10 (1), 88–93.

Wu, L. Z., Zhu, S. R., and Peng, J. B. (2020). Application of the Chebyshev spectral method to the simulation of groundwater flow and rainfall-induced landslides. *Appl. Math. Model.* 80, 408–425. doi:10.1016/j.apm.2019.11.043

Zhu, S. R., Wu, L. Z., and Peng, J. B. (2022). An improved Chebyshev semi-iterative method for simulating rainfall infiltration in unsaturated soils and its application to shallow landslides. *J. Hydrology* 590, 125157. doi:10.1016/j.jhydrol.2020.125157

frontiers | Frontiers in Earth Science

TYPE Original Research
PUBLISHED 12 January 2023
DOI 10.3389/feart.2022.1053461

OPEN ACCESS

EDITED BY
Haijun Qiu,
Northwest University, China

REVIEWED BY
Zongliu Huang,
Xihua University, China
Zhengshi Wang,
Northwest A&F University, China

*CORRESPONDENCE
Yu Lei,
leiyu@imde.ac.cn

SPECIALTY SECTION
This article was submitted to Geohazards and Georisks, a section of the journal Frontiers in Earth Science

RECEIVED 25 September 2022
ACCEPTED 31 October 2022
PUBLISHED 12 January 2023

CITATION
Gu H and Lei Y (2023), Experimental investigation of the effects of the turbulence on the impact force of flash flood.
Front. Earth Sci. 10:1053461.
doi: 10.3389/feart.2022.1053461

Experimental investigation of the effects of the turbulence on the impact force of flash flood

Haihua Gu[1] and Yu Lei[1,2]*

[1]Institute of Mountain Hazards and Environment, Chinese Academy of Sciences (CAS), Chengdu, China, [2]China-Pakistan Joint Research Center on Earth Sciences, CAS-HEC, Islamabad, Pakistan

Flash floods cause damage to engineering structures and buildings mainly due to their huge impact force. Scientific investigation of the impact process of flash floods has significant theoretical and engineering implications in ensuring the safety of flood-resistant structures and human life. In this experimental study, the impact pressure and flow velocity in the flow field were measured synchronously using the impact detection system and a particle image velocimetry system in a water channel and the effects of the turbulence structure on the impact process of flash flood were investigated. As shown by the experimental measurements, the large-scale coherent structure in the flow field reached six times the boundary layer thickness. The turbulence and impact force energy spectra were very similar in the low-frequency, large-scale wave band, indicating that the large-scale turbulence structure dominated the impact process. Both the mean and maximum impact pressures increased with the turbulence kinetic energy. An equation for impact force characterization that considers the effects of turbulence and thus was more accurate was given, providing a theoretical basis for the protection of engineering structures from the damage by flash floods.

KEYWORDS

flash flood, impact force, coherent structure, experimental study, turbulence kinetic energy

Introduction

Because of the complex natural environment, the frequency, intensity, and range of influence of disasters in the word have increased. These disasters include landslides, debris flows, flash floods and so on (Cui, 1999; Yang et al., 2015; Lei et al., 2018; Liu et al., 2022; Qiu et al., 2022; Wang et al., 2022). In the mountainous regions, the flash flood disasters are attracting a great deal of attention throughout the world (Zhang et al., 2019; Bazai et al., 2022). Flash floods are characterized by sporadic events, high flow velocity, strong transport capacity, with wide impacts and great destructive potential (Yang et al., 2015). Mountains account for approximately more than two thirds of China's territory, with rapid economic development and increasing anthropogenic activities, the occurrence of flash floods is rising in these areas. The flash floods have caused severe damage to railway bridges, buildings, and other engineering structures in these areas. For example, the Sichuan-Tibet Railway, the Sichuan-Tibet Road, the China-Pakistan Economic Corridor,

and other major engineering projects have been impacted by flash flood disasters at different degrees.

Flash flood disaster is also a common problem facing the world's countries and has received extensive attention from researchers (Yanmaz and Altinbilek, 1991; Kobayashi et al., 1988; Cui, 1999; Veerappadevaru et al., 2012; Lei et al., 2018). Field experiments, flume experiments and numerical methods have been carried out to detect the impact force of flash flood (Zanuttigh and Lamberti, 2006; Hu et al., 2011; Cui et al., 2015). At the macroscopic level, previous studies focused on the physical, destructive, and spatiotemporal characteristics, cause of formation, and early warning of flash flood disasters, providing scientific guidance on disaster prevention and mitigation.

On the other hand, there are many opportunities to observe turbulent flows in our surroundings, such as the flash flood or debris flow, or a strong wind. An important characteristic of turbulence is its ability to transport and mix fluid more effectively than a laminae flow, which were first demonstrated by the famous Reynolds' experiment by Osborne Reynolds (Reynolds, 1883). Since then, more and more researchers began to study the physical mechanism of turbulence aimed to developing tractable mathematical models that can accurately predict properties of turbulent flows, such as energy cascade and Kolmogorov hypotheses (Richardson, 1922; Kolmogorov, 1941). Moreover, an important focus of research on turbulence was inspired by the observation of coherent structures in turbulent boundary layers (Theodorsen, 1952; Kline et al., 1967; Townsend, 1976). Smits et al. (2011) identify four principal characteristic elements of turbulent structure: near-wall streaks, hairpin or horseshoe vortices, large-scale motions (LSMs) and very-large-scale motions (LSMs) (Theodorsen 1952; Kline et al., 1967; Kim and Adrian 1999; Wang and Zheng, 2016; Gu et al., 2019; Wang et al., 2020). Notably, the coherent structures have been evidenced in wall-bounded flows and demonstrated to play a crucial role in the turbulent kinetic energy (TKE), the momentum flux and the mass transport process (Baas and Sherman, 2005; Balakumar and Adrian, 2007; Dupont et al., 2013; Zheng et al., 2013; Wang et al., 2017). The studies on the coherent structures give an in-depth understanding of the flow phenomena and physical mechanisms in wall-bounded flows. Moreover, studies on large-scale turbulence structures have provided new approaches and perspectives to the examination of the impact process of flash floods.

However, the following aspects of the impart process of flash floods have remained unclear. The effects of the coherent turbulent structures on the impact process (whether the impact force is directly correlated with the coherent turbulent structure, and the quantitative effects of the turbulence characteristics on the impact force). In this experimental study, the turbulence characteristics of flash flood and the inherent physical mechanisms of the impact force were investigated, and an equational characterization of the impact force that considered the turbulence characteristics was established, with the aim of providing theoretical criteria for disaster prevention and mitigation engineering.

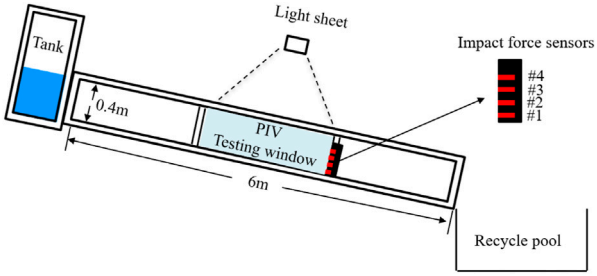

FIGURE 1
Schematic diagram of the experimental setup.

Experimental setup and data preprocessing

Experimental setup

The experimental setup consisted of a water channel measuring 4 m (length) × 0.2 m (width) × 0.4 m (height), its slope was set to 7° or 13° (a schematic diagram of the flume is shown in Figure 1). A material supply tank with a maximum volume of 1.3 m^3 was configured on top of the channel. A valve was configured at the water inlet to control the depth of flow in the channel. The flow velocity at the middle section of the channel (2 m from the water inlet) was measured using particle image velocimetry (PIV). Impact pressure sensors were configured at the end of the PIV measurement section to avoid interfering with the flow field, thereby enabling synchronous measurement of the flow field and impact force.

Turbulence intensity (TI) describes the rate at which the flow velocity varies with time and reflects the relative intensity of the velocity fluctuation. Turbulence intensity is defined as the ratio of the standard deviation of flow velocity (root mean square of fluctuating velocity) to the mean velocity (U). During the experiment, the turbulence intensity was varied by using grilles of two different grille blocking rate (30% and 50%) (just as show in Figure 2).

Two major parameters of the impact process of flash flood, flow velocity and impact force in the flow field, were measured using a high-speed PIV system and impact force sensors, respectively. The PIV system was used to record the flow morphology of flash floods and analyze their flow characteristics such as flow velocity, depth of flow, turbulence intensity, and the scale of coherent turbulent structure. The PIV system mainly consisted with: CCD, laser emitter, synchronizerand a computer. The glass spheres with a

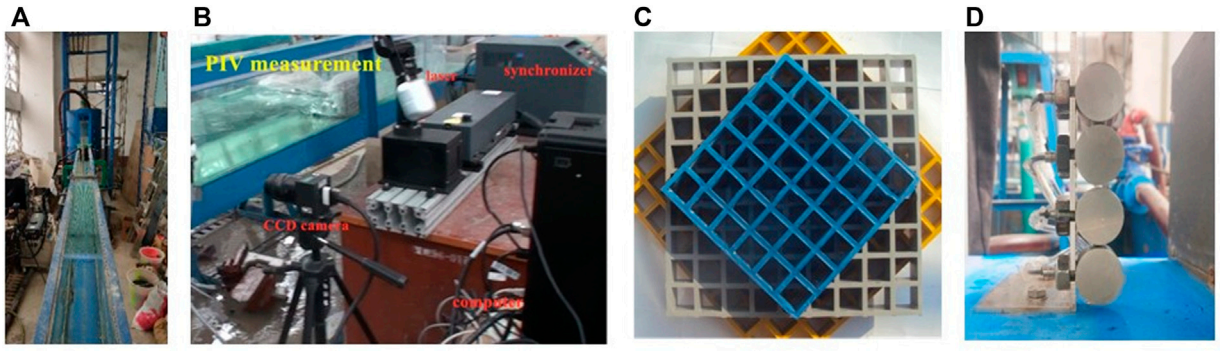

FIGURE 2
Experiment setups: **(A)** the flume; **(B)** PIV measurement; **(C)** grilles; **(D)** impact force sensor.

TABLE 1 List of work conditions and main parameters of the measurement.

Id	Set	Grille blocking rate	Flume slope (°)	Depth (cm)	Mean velocity (m/s) (h = 4.5 cm)	Meam pressure (kPa) (h = 4.5 cm)	Max pressure (kPa) (h = 4.5 cm)
S1	1	No grid	7	7.20	4.69	5.87	10.94
	2			7.30	4.55	6.50	11.80
	3			7.00	4.69	6.15	12.02
S2	1	30%		6.90	4.61	6.28	13.05
	2			7.20	4.53	6.90	12.81
	3			7.40	4.56	5.46	11.70
S3	1	50%		7.00	4.77	5.89	12.06
	2			6.80	5.02	5.98	12.08
	3			7.30	4.65	6.41	12.04
S4	1	No grid	13	6.70	4.93	6.18	13.61
	2			6.80	4.79	6.74	12.71
	3			7.00	4.93	6.48	12.64
S5	1	30%		6.60	4.85	7.57	13.97
	2			6.90	4.77	7.26	14.27
	3			7.20	4.80	6.75	12.30
S6	1	50%		6.80	5.02	6.92	13.53
	2			7.10	5.08	6.30	12.17
	3			6.80	4.89	6.75	12.66

medium diameter of 10 μm and a density of 1.05 gcm^{-3} were used as tracer particles during our experiment. The impact force sensor was of piezoresistive type and had a measurement range of 0–200 kPa. The diameter of the sensor was 20 mm and the precision of sensor was 0.02%. The data collection system had a sampling frequency of 1,000 Hz in this study. Four sensors were installed at four different heights (1.5, 4.5, 7.5, and 10.5 cm) from the bottom of the water channel and were referred to as sensors #1–#4, respectively (just as show in Figure 1). The impact force sensors were connected to the data collection system, which was then connected to the computer. Prior to the start of the experiment, the computer times of the PIV system and the impact force measurement system were synchronized, thereby realizing synchronized measurement of the flow field and impact force.

A total of 18 experiments were performed. Table 1 shows the major parameters for each of the experiments. Each experiment was repeated three times to minimize experimental error. The

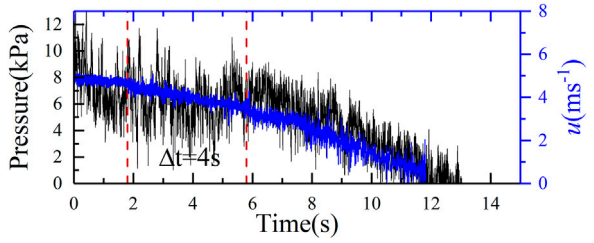

FIGURE 3
The streamwise velocity fluctuations from PIV measurement (blue line) and the impact force signal fluctuations from pressure sensor (black line) at 0.45 cm of s1-2.

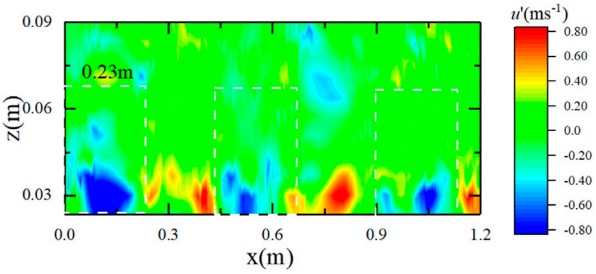

FIGURE 5
The contours of the streamwise velocity fluctuations of s1-2.

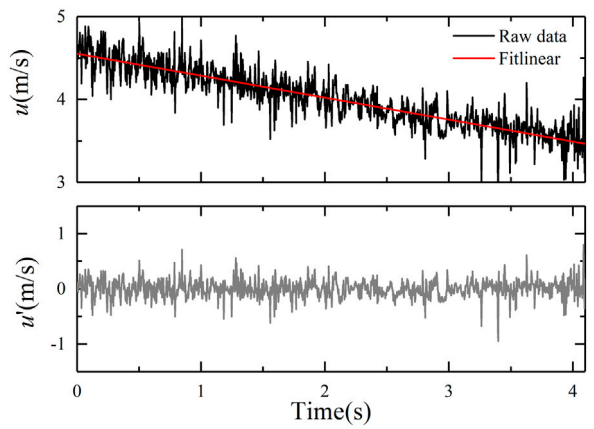

FIGURE 4
The de-trending process, the black line is the raw streamwise velocity fluctuations at 0.45 cm of s1-2, the red line is the linearly fit trend signal and the grey line is the de-trended signal.

mean velocity with the flume slope of 7° (for all 9 Set experiments) was calculated at 4.67 m/s and the corresponding standard deviation was 0.15 m/s. When the flume slope of 13°, the mean velocity was calculated at 4.89 m/s and the corresponding standard deviation was 0.10 m/s, which is litter bigger than the velocity with the flume slope of 7°.

Data preprocessing

The black line in Figure 3 shows the original impact pressure signal fluctuations obtained from experiment s1-2 (h = 4.5 cm). The maximum impact pressure was 11.80 kPa. The blue line in this figure shows the streamwise velocity fluctuations from PIV measurement. From Figure 3, the streamwise velocity (blue line) has an obviously decreasing trend during this time period (as shown by the red rectangle in Figure 3). The envelopes defined by the local maxima and local minima of impact pressure (black line) also have a decreasing trend although it is not obviously. This phenomenon may be caused by the pressure signal fluctuations cannot respond as quickly as the velocity signal fluctuations. In general, from a comparison with the streamwise velocity fluctuations of the flow obtained by the PIV system, the impact pressure signal fluctuations were correlated with the streamwise velocity fluctuation.

The subsequent analyses mainly focused on the mechanisms underlying the effects of the turbulence structure on the impact force. Such analyses require stable data. However, the streamwise velocity and impact pressure signals obtained from the experiments showed an evidently decreasing trend which were not suitable for our analyses. Therefore, to facilitate subsequent spectral analysis, some specific selection and pretreatment should be performed on the flow velocity fluctuation and impact pressure signals. Figure 4 shows an illustration of the treatment process (the streamwise velocity fluctuations at 0.45 cm of s1-2 for example). First, the impact pressure signals and velocity fluctuation were divided into 4-s segments (as shown by the red rectangle in Figure 3). Then, each segment of velocity fluctuation and impact force signal fluctuations was subjected to linear fitting, thereby obtaining the linearly fit trend of each segment of data (as shown by the red solid line in Figure 4). Finally, the trend component of the signals was subtracted from the original raw data, thereby obtaining the de-trended fluctuations in the impact pressure and velocity, the grey line in Figure 4.

The effects of the coherent turbulent structures on the impact process

Experimental and numerical studies have shown that a turbulence structure induces continuous losses in the streamwise velocity, resulting in the streamwise velocity in the structural space being lower than the mean horizontal convection

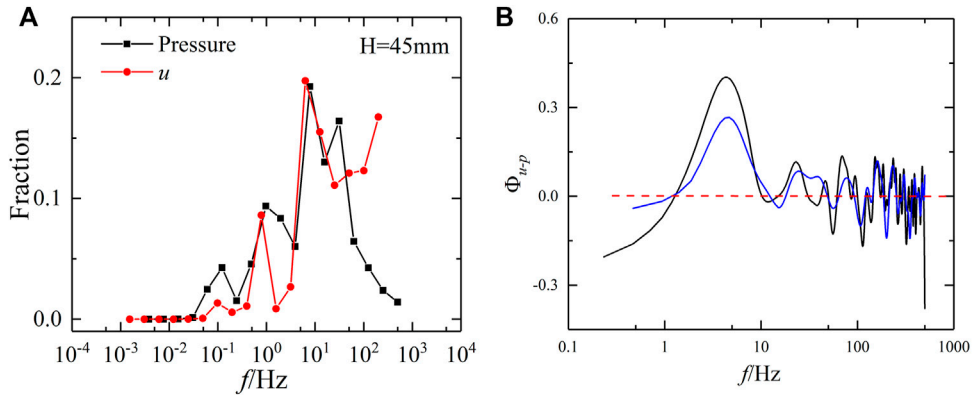

FIGURE 6
(A) The normalized energy spectra of the streamwise velocity *u* and the impart force *p* measured at 0.45 cm of s1-2. **(B)** The co-spectra for the streamwise velocity perturbations *u* and impart force *p* measured at 0.45 cm of s1-2.

velocity. For example, Hutchins and Marusic (2007) used streamwise velocity contours to represent turbulence structures and found the existence of a meandering morphology of the large-scale structure. Different from the method of Hutchins and Marusic (2007) of using the horizontal contours of streamwise velocity for flow visualization (x-y plane), the vertical contours of streamwise velocity were used for flow visualization in this experimental study. In this way, the vertical scale variations and streamwise motions of the large-scale turbulence structure were revealed in a more straightforward manner (x-z plane). The temporal scale of the flow was converted to the streamwise length according to Taylor's frozen turbulence hypothesis. Figure 5 shows the streamwise velocity contours obtained from experiment of s1-2, where the blue areas indicate velocity losses. From the velocity losses shown in Figure 5, there existed turbulent motions with a large streamwise length (approximately 0.23 m) in the flow field. The scale reached three times the thickness of the boundary layer (approximately 0.07 m, just as show in Table 1) and exhibited a trend of increasing with the height, which is consistent with previous studies.

From the streamwise velocity contours in Figure 5, we have confirmed the existence of large-scale turbulence structure in our experiment. We will analyse whether the impact force is directly correlated with the coherent turbulent structure. To clarify that the time scales and energy fractions between the streamwise velocity and the impart force, we obtained their normalized energy spectra using the wavelet transform method (Baas, 2006; Tang et al., 2013; Zheng et al., 2013; Gu et al., 2019). We used the basis functions of the Daubechies wavelet in this study. In order to reveal the relation between the flow filed and the impart force, the normalized energy spectra of the streamwise velocity *u* and the impart force *p* measured at 0.45 cm of s1-2 are compared in Figure 6A. Figure 6A clearly shows that the energy-containing turbulence structure in the flow field obtained from this experiment had a frequency of 10 Hz. As the mean flow velocity was 4.7 m/s for experiment of s1-2, the spatial scale of the large-scale structure was 0.47 m based on Taylor's frozen turbulence hypothesis, which was equal to six times the boundary layer thickness (approximately 0.07 m). In addition, the impact pressure spectrum not only exhibited a distribution pattern similar to that of the flow velocity spectrum but also peaked at 10 Hz, indicating that the impact force fluctuation is actually a manifestation of and is highly consistent with the flow field fluctuation.

To identify the frequency (scale) at which the flow field fluctuation is more significantly correlated with the impact pressure, a cross-spectral analysis of the flow velocity and impact pressure was performed (Figure 6B). As discussed above, the recurrent large-scale structure have a character frequency of 1–10 Hz and have a substantial contribution to the impart force as shown in Figure 6B. This also indicates that the large-scale coherent structure dominated the impact process.

The quantitative effects of the turbulence characteristics on the impact force

The addition of a grille (with a perforation ratio of 30% or 50%) can change the turbulence intensity in the flow field, but not change the mean velocity at the same experiment condition. Figure 7A shows the variations in the impact pressure (maximum and mean impact pressures) with the flow velocity obtained from the experiments. The mean flow velocities under several sets of experimental conditions were all approximately 4.6 m/s, and the correlation between the impact pressure (maximum and mean impact pressures) and the mean flow velocity was nonsignificant.

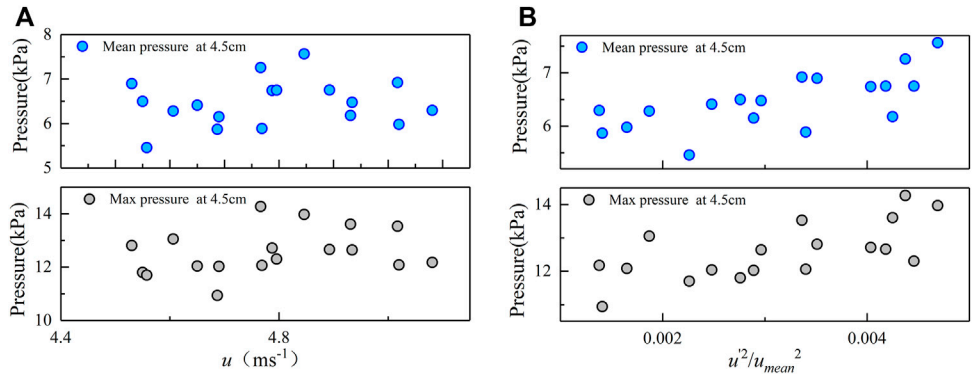

FIGURE 7
(A) Variations in the mean impact pressure and max impact pressure with the streamwise velocity; **(B)** Variations in the mean impact pressure and max impact pressure with the normalized turbulent intensity.

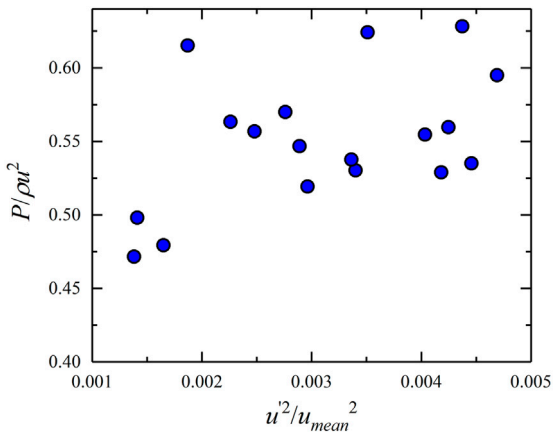

FIGURE 8
Variations in the $P/\rho u^2$ with the normalized turbulent kinetic energy (TKE).

Figure 7B shows the variations in the impact pressure (maximum and mean impact pressures) with the normalized turbulence intensity. Both the maximum and mean impact pressures increased with the turbulence intensity. Therefore, turbulence intensity-induced impact pressure variations are nonnegligible to the investigation of impact pressure.

For the impact process of flash flood, the impact pressure of the liquid-phase slurry can be calculated using Eq. 1:

$$P = \alpha\rho u^2 \tag{1}$$

The coefficient α can be approximated to be 0.5 according to the equation for the dynamic pressure of fluids given in fluid mechanics: $P = 1/2\rho u^2$. As shown by the variations in $P/\rho u^2$ with the normalized turbulent kinetic energy (TKE) in Figure 8, coefficient α of the impact force characterization equation obtained from the experimental measurements was approximately 0.5 at low turbulence intensities but increased to approximately 0.6 at high turbulence intensities. Thus, the impact force characterization equation that considers turbulence fluctuation can be expressed as: $P = \alpha\rho(\bar{u} + u')^2$, which can be simplified as:

$$P = \alpha\rho\left(\bar{u}^2 + u'^2\right) = \alpha\rho\bar{u}^2\left(1 + \frac{u'^2}{\bar{u}^2}\right) \tag{2}$$

The coefficient α can be improved as $\alpha^* = \alpha(1 + u'^2/\bar{u}^2)$. Considering that the normalized turbulence intensity obtained from the experiments in the range of 0.001–0.004, α* is almost not affected by turbulence fluctuation. However, coefficient α* obtained from the experiments reached a maximum of 0.6, representing an increase of approximately 20%.

Based on the spectral and cross-spectral analyses of the large-scale turbulence structure and impact pressure in the flow field, the cause of this phenomenon possibly lies in the large-scale structure. The meandering large-scale structure controlled the transport of kinetic energy and momentum. On the other hand, the inclination angle of the large-scale turbulence structure, which is believed to be a pathway for mass and momentum transport (Cheng et al., 2011; Dupont et al., 2013). The phenomenon of large-scale structures inclined at a shallow angle away from the wall is originally studied by Kovasznay et al. (1970). Studies also have found that the inclination angle decreases near linearly with the streamwise velocity gradient (Liu et al., 2017). Thus, the inclination angle of the large-scale turbulence structure is smaller at high turbulence intensities than low turbulence intensities in our experiment. This possibly resulted in the local maximum impact pressure being larger than the dynamic pressure of the fluid, thereby causing the phenomenon found in this experimental study.

Conclusion

This study conducts the synchronous measurements on the impact pressure and flow velocity in the flow field, aims to reveal the relation between the flow filed and the impart force of flash floods. Analysis on the measured data show that:

1) The existence of large-scale turbulence structure in flash flood from the streamwise velocity contours and the large-scale coherent structure in the flow field can reach up to six times the boundary layer thickness. Moreover, the turbulence and impact force energy spectra were very similar, indicating that the large-scale turbulence structure dominated the impact process.
2) The correlation between the impact pressure (maximum and mean impact pressures) and the mean flow velocity was nonsignificant. But the mean and maximum impact pressures increased with the turbulence kinetic energy. The cause of this phenomenon possibly lies in the large-scale structure. Therefore, the turbulence effect must be considered when assessing the vulnerability of a group of buildings. An equation for impact force characterization that considers the effects of turbulence and thus was more accurate was also given, providing a theoretical basis for the protection of engineering structures from the damage by flash floods.

Data availability statement

The original contributions presented in the study are included in the article/Supplementary Material, further inquiries can be directed to the corresponding author.

Author contributions

HG carried out the experimental investigation, data analysis, and manuscript writing. YL was involved in writing reviewing, manuscript editing, and supervision. All the authors participated and contributed to the final manuscript.

Funding

This work was supported by the Second Tibetan Plateau Scientific Expedition and Research Program (STEP) (Grant No.2019QZKK0903); The National Natural Science Foundation of China (Grant No. 41790433); The Sichuan Science and Technology Program (2021YFH0009) and the Chinese Academy of Sciences President's International Fellowship Initiative (2020FYC0004).

Conflict of interest

The authors declare that the research was conducted in the absence of any commercial or financial relationships that could be construed as a potential conflict of interest.

Publisher's note

All claims expressed in this article are solely those of the authors and do not necessarily represent those of their affiliated organizations, or those of the publisher, the editors and the reviewers. Any product that may be evaluated in this article, or claim that may be made by its manufacturer, is not guaranteed or endorsed by the publisher.

References

Baas, A. C. W., and Sherman, D. J. (2005). Formation and behavior of aeolian streamers. *J. Geophys. Res.* 110 (F3), F03011. doi:10.1029/2004jf000270

Baas, A. C. (2006). Wavelet power spectra of aeolian sand transport by boundary layer turbulence. *Geophys. Res. Lett.* 33 (5), L05403. doi:10.1029/2005gl025547

Balakumar, B. J., and Adrian, R. J. (2007). Large-and very-large-scale motions in channel and boundary-layer flows. *Phil. Trans. R. Soc. A* 365 (1852), 665–681. doi:10.1098/rsta.2006.1940

Bazai, N. A., Cui, P., Zhou, K. J., Abdul, S., Cui, K. F., Wang, H., et al. (2022). Application of the soil conservation service model in small and medium basins of the mountainous region of Heilongjiang, China. *Int. J. Environ. Sci. Technol. (Tehran).* 19 (1), 433–448. doi:10.1007/s13762-021-03136-1

Cheng, X., Zeng, Q. C., and Hu, F. (2011). Characteristics of gusty wind disturbances and turbulent fluctuations in windy atmospheric boundary layer behind cold fronts. *J. Geophys. Res.* 116 (D6), D06101. doi:10.1029/2010jd015081

Cui, P., Zeng, C., and Lei, Y. (2015). Experimental analysis on the impact force of viscous debris flow. *Earth Surf. Process. Landf.* 40 (12), 1644–1655. doi:10.1002/esp.3744

Cui, P. (1999). Impact of debris flow on river cannel in the upper reaches of the yangtse river. *Intern. J. Sediment Res.* 14, 201–203.

Dupont, S., Bergametti, G., Marticorena, B., and Simoëns, S. (2013). Modeling saltation intermittency. *J. Geophys. Res. Atmos.* 118 (13), 7109–7128. doi:10.1002/jgrd.50528

Gu, H., Wang, G., Zhu, W., and Zheng, X. (2019). Gusty wind disturbances and large-scale turbulent structures in the neutral atmospheric surface layer. *Sci. China Phys. Mech. Astron.* 62 (11), 114711–114717. doi:10.1007/s11433-019-9398-5

Hu, K., Wei, F., and Li, Y. (2011). Real-time measurement and preliminary analysis of debris-flow impact force at Jiangjia Ravine, China. *Earth Surf. Process. Landf.* 36 (9), 1268–1278. doi:10.1002/esp.2155

Hutchins, N., and Marusic, I. (2007). Large-scale influences in near-wall turbulence. *Phil. Trans. R. Soc. A* 365 (1852), 647–664. doi:10.1098/rsta.2006.1942

Kim, K. C., and Adrian, R. J. (1999). Very large-scale motion in the outer layer. *Phys. Fluids* 11 (2), 417–422. doi:10.1063/1.869889

Kline, S. J., Reynolds, W. C., Schraub, F. A., and Runstadler, P. W. (1967). The structure of turbulent boundary layers. *J. Fluid Mech.* 30 (4), 741–773. doi:10.1017/s0022112067001740

Kobayashi, H., Masutani, S. M., Azuhata, S., Arashi, N., and Nishinuma, Y. (1988). Dispersed phase transport in a plane mixing layer. *Transp. Phenom. Turbul. Flows Theory, Exp. Numer. Simul.* 34, 433–446.

Kolmogorov, A. N. (1941). Dissipation of energy in locally isotropic turbulence in an incompressible viscous liquid. *Dokl. Akad. Nauk. SSSR* 30, 299–303.

Kovasznay, L. S., Kibens, V., and Blackwelder, R. F. (1970). Large-scale motion in the intermittent region of a turbulent boundary layer. *J. Fluid Mech.* 41 (2), 283–325. doi:10.1017/s0022112070000629

Lei, Y., Cui, P., Zeng, C., and Guo, Y. (2018). An empirical mode decomposition-based signal process method for two-phase debris flow impact. *Landslides* 15 (2), 297–307. doi:10.1007/s10346-017-0864-1

Liu, H. Y., Bo, T. L., and Liang, Y. R. (2017). The variation of large-scale structure inclination angles in high Reynolds number atmospheric surface layers. *Phys. Fluids* 29 (3), 035104. doi:10.1063/1.4978803

Liu, Z., Qiu, H., Zhu, Y., Liu, Y., Yang, D., Ma, S., et al. (2022). Efficient identification and monitoring of landslides by time-series InSAR combining single-and multi-look phases. *Remote Sens.* 14 (4), 1026. doi:10.3390/rs14041026

Qiu, H., Zhu, Y., Zhou, W., Sun, H., He, J., and Liu, Z. (2022). Influence of DEM resolution on landslide simulation performance based on the Scoops3D model. *Geomatics. Nat. Hazards Risk* 13 (1), 1663–1681. doi:10.1080/19475705.2022.2097451

Reynolds, O. (1883). XXIX. An experimental investigation of the circumstances which determine whether the motion of water shall be direct or sinuous, and of the law of resistance in parallel channels. *Philos. Trans. R. Soc. Lond.* 174, 935–982.

Richardson, L. F. (1922). *Weather prediction by numerical process*. Cambridge, UK: University Press.

Smits, A. J., McKeon, B. J., and Marusic, I. (2011). High–Reynolds number wall turbulence. *Annu. Rev. Fluid Mech.* 43, 353–375. doi:10.1146/annurev-fluid-122109-160753

Tang, J. B., Hu, K. H., Zhou, G. D., Chen, H. Y., Zhu, X. H., and Ma, C. (2013). Debris flow impact pressure signal processing by Wavelet Analysis. *J. Sichuan Univ. Eng. Sci. Ed.* 45 (1), 8–13. (in Chinese).

Theodorsen, T. (1952). "Mechanism of turbulence," in Proceedings of the Second Midwestern Conference on Fluid Mechanics, 1952, Columbus, Ohio, March 17-19, 1952, 1–19.

Townsend, A. A. (1976). *The structure of turbulent shear flow*. Cambridge, UK: Cambridge Univ. Press.

Veerappadevaru, G., Gangadharaiah, T., and Jagadeesh, T. R. (2012). Temporal variation of vortex scour process around caisson piers. *J. Hydraul. Res.* 50 (2), 200–207. doi:10.1080/00221686.2012.666832

Wang, G., and Zheng, X. (2016). Very large scale motions in the atmospheric surface layer: A field investigation. *J. Fluid Mech.* 802, 464–489. doi:10.1017/jfm.2016.439

Wang, G., Zheng, X., and Tao, J. (2017). Very large scale motions and PM10 concentration in a high-Re boundary layer. *Phys. Fluids* 29 (6), 061701. doi:10.1063/1.4990087

Wang, G., Gu, H., and Zheng, X. (2020). Large scale structures of turbulent flows in the atmospheric surface layer with and without sand. *Phys. Fluids* 32 (10), 106604. doi:10.1063/5.0023126

Wang, L., Qiu, H., Zhou, W., Zhu, Y., Liu, Z., Ma, S., et al. (2022). The post-failure spatiotemporal deformation of certain translational landslides may follow the pre-failure pattern. *Remote Sens.* 14 (10), 2333. doi:10.3390/rs14102333

Yang, Y. C. E., Ray, P. A., Brown, C. M., Khalil, A. F., and Yu, W. H. (2015). Estimation of flood damage functions for river basin planning: A case study in Bangladesh. *Nat. Hazards (Dordr).* 75 (3), 2773–2791. doi:10.1007/s11069-014-1459-y

Yanmaz, A. M., and Altinbilek, H. D. G. A. (1991). Study of time-depenbent local scour around bridge piers. *J. Hydraul. Eng.* 117 (10), 1247–1268. doi:10.1061/(asce)0733-9429(1991)117:10(1247)

Zanuttigh, B., and Lamberti, A. (2006). Experimental analysis of the impact of dry avalanches on structures and implication for debris flows. *J. Hydraulic Res.* 44 (4), 522–534. doi:10.1080/00221686.2006.9521703

Zhang, G., Cui, P., Yin, Y., Liu, D., Jin, W., Wang, H., et al. (2019). Real-time monitoring and estimation of the discharge of flash floods in a steep mountain catchment. *Hydrol. Process.* 33 (25), 3195–3212. doi:10.1002/hyp.13551

Zheng, X., Zhang, J., Wang, G., Liu, H., and Zhu, W. (2013). Investigation on very large scale motions (VLSMs) and their influence in a dust storm. *Sci. China Phys. Mech. Astron.* 56 (2), 306–314. doi:10.1007/s11433-012-4985-1

frontiers | Frontiers in Earth Science

TYPE Original Research
PUBLISHED 13 January 2023
DOI 10.3389/feart.2022.1043403

OPEN ACCESS

EDITED BY
Wen Nie,
Jiangxi University of Science and Technology, China

REVIEWED BY
Jie Wang,
Anhui University, China
Guanghui Jiang,
Beijing Normal University, China

*CORRESPONDENCE
Lihong Meng,
mlh8158@163.com

SPECIALTY SECTION
This article was submitted to Geohazards and Georisks, a section of the journal Frontiers in Earth Science

RECEIVED 13 September 2022
ACCEPTED 31 October 2022
PUBLISHED 13 January 2023

CITATION
Liu Y, Huang H, Meng L, Liu M, Wu Z, Liu T and Labat D (2023), Spatial-temporal evolution of vegetation coverage and its relationship with terrain and human factors in the upper reaches of Ganjiang River Basin, China. *Front. Earth Sci.* 10:1043403. doi: 10.3389/feart.2022.1043403

Spatial-temporal evolution of vegetation coverage and its relationship with terrain and human factors in the upper reaches of Ganjiang River Basin, China

Youcun Liu[1], Haohong Huang[1], Lihong Meng[2]*, Mingxia Liu[3], Zidan Wu[1], Tao Liu[1] and David Labat[4]

[1]School of Geography and Tourism and Guangdong Provincial Key Laboratory of Conservation and Precision Utilization of Characteristic Agricultural Resources in Mountainous Areas, Jiaying University, Meizhou, Guangdong, China, [2]School of Geography and Environmental Engineering, Gannan Normal University, Ganzhou, Jiangxi, China, [3]School of Artificial Intelligence, Jiangxi University of Applied Science, Nanchang, Jiangxi, China, [4]Géosciences Environnement Toulouse, UMR 5563 UPS-CNRS-IRD-CNES, 14 Avenue Edouard Belin, 31400 Toulouse, France

Vegetation coverage is an important indicator for evaluating regional environmental quality. Based on MODIS NDVI and DEM data collected for the upper reaches of the Ganjiang River Basin, China, this study used trend analysis, coefficient of variation, Hurst index, and linear regression to analyze the temporal and spatial evolution of vegetation coverage and its relationship with terrain factors in the basin during the years 2000–2020. The vegetation coverage in the study area showed a fluctuating increasing trend at a rate of 5%/10y, and an increasing trend with increasing elevation. The maximum vegetation coverage was identified in the elevation zone of 750–1,000 m, with an average of 83.54%. Vegetation coverage also showed an increasing trend with increasing slope. The maximum vegetation coverage was up to 82.22% in the slope zone of ≥25°. There were no significant differences among the distributions of vegetation coverage in different aspects because the terrain in the study area is not rugged enough to form barriers against sunlight. The vegetation coverage was relatively stable in the study area, with an average coefficient of variation of 14.8%. Hurst analysis showed that the anti-sustainability effect of vegetation change was stronger than that of sustainability, and weak anti-sustainability was dominant. The effects of human activities mainly concentrated in the areas of low elevation and small slopes less than 2°where cities and towns are located. The findings can provide a scientific basis for the management of regional ecosystems in the future.

KEYWORDS

vegetation coverage, spatial-temporal variation, terrain factor, correlation, Ganjiang River basin

1 Introduction

RESPONSE of terrestrial ecosystems to global climate change is a core research subject raised in the International Geosphere-Biosphere Program (IGBP) (Deng et al., 2021; Bejagam et al., 2022; Wei et al., 2022), which has received great attention from the international scientific community. As an essential component of terrestrial ecosystems, vegetation significantly impacts the global flow of material and energy, biological diversity, and climate stability. It is the most sensitive indicator of global climate change (Shobairi et al., 2018; Zhan et al., 2021; Geng et al., 2022). Vegetation coverage is also influenced by terrain factors, for example, altitude affects vegetation growth due to changes in the effective accumulated temperature and soil moisture (Lamchin et al., 2018; Kalisa et al., 2019; Wang et al., 2020). Therefore, analysis of the influence of terrain factors on the spatial-temporal evolution of vegetation coverage is of great significance for evaluating regional environmental quality and maintaining balance in regional ecosystems (Przeździecki et al., 2017; Ranjbar et al., 2020).

To reflect the growth status of vegetation, fractional vegetation coverage (FVC) is an important parameter for describing terrestrial ecosystems. FVC is defined as the ratio of the vertical projection area of above ground vegetation organs (including leaves, stems, and branches) to the total vegetation area (Hilker et al., 2014; Sarfo et al., 2022). The measurement methods for FVC include ground surveys and remote sensing estimation. The latter is suitable for large-scale and long-term FVC assessments and has been widely used (Dardel et al., 2014; Chybicki and Łubniewski, 2017; Ranjan and Gorai, 2022). Vegetation indexes, such as normalized difference vegetation index ((NDVI) (Ivanov et al., 2008; Zhan et al., 2021) and enhanced vegetation index (EVI) (Zeng et al., 2022), are measure of surface reflectance that provides a quantitative estimation of vegetation growth. The NDVI has a good correlation with FVC and has been widely used for the assessment of vegetation dynamics at both regional and global scales (Huete, 2016; Liu et al., 2016; Xiong et al., 2021).

The Ganjiang River is one of the main tributaries of the Yangtze River. The upper reaches of the Ganjiang River Basin are water conservation areas and its ecological environment directly affects the economic development in the lower reaches of the Yangtze River Basin (Liu et al., 2021). Rare earth elements (REEs) are necessary components of many modern devices, such as electric vehicles, wind turbines, and intelligent electronic devices. As the soil in the upper reaches of the Ganjiang River Basin is highly rich in rare-earth resources, it has been exploited for REEs, leading to ecological and environmental problems, such as vegetation destruction, soil erosion, debris flow, and water pollution (Liu et al., 2020). Given the fragile ecosystem and climatic conditions, the ecosystem of the region is bound to be affected by terrain and human factors. The FVC can objectively reflect the overall condition of the regional ecological environment. Previous studies have analyzed the change in vegetation coverage and its correlation with geomorphological factors in the southern Jiangxi region (Li et al., 2014). However, existing research has not explored the influence of terrain factors on the spatial-temporal evolution of vegetation coverage.

Therefore, the present study was designed with the following objectives: 1) to qualitatively evaluate the spatiotemporal evolution of vegetation coverage in the upper reaches of the Ganjiang River Basin, China, and 2) to identify its relationship with terrain factors. The Terra Moderate Resolution Imaging Spectroradiometer (MODIS) Normalized Difference Vegetation Index (NDVI) data collected over the years 2000–2020 were used to calculate the FVC in different time periods, and future changes were predicted using the Hurst exponent. The relationship with terrain factors was examined using data on elevation slope and aspect with partial correlation analysis. As the complete exclusion of the effects of human activities is impossible, a partial discussion of this aspect was also included. This study will facilitate a deeper understanding of the interactions between the ecosystem and terrain in the Ganjiang River Basin.

2 Study area and data source

The upper reaches of the Ganjiang River Basin are located in the south of Jiangxi Province, China, which span across 24°29′–27°09′N and 113°54′–116°38′E with an area of 30,277 km^2 (Figure 1) (Liu et al., 2020). Several administrative districts, including the prefecture-level city of Ganzhou, are located in this basin. Several tributaries, including the Zhangjiang, Gongjiang, Meijiang, Pingjiang, Taojiang, and Shangyoujiang Rivers are present in this basin. The basin has a subtropical monsoonal climate, with a mean annual precipitation of 1,600 mm. Its topography is characterized by mountains and hills, with a gradual increase in elevation from the center to the perimeter. The soil types within the basin include red, yellow, and purple soils. The vegetation types are diverse as the basin is located on the southern edge of the mid-subtropical zone.

The MODIS vegetation index Version 6 data, MOD13Q1 product, is provided every 16 days at a 250 m spatial resolution as a gridded level-3 product in the sinusoidal projection. The data over the years 2000–2020 (totally 480 scenes) were downloaded from the website run by the NASA's Goddard Space Flight Center (https://ladsweb.modaps.eosdis.nasa.gov/). MODIS NDVI products are computed from atmospherically corrected bidirectional surface reflectance that is masked for water, clouds, heavy aerosols, and cloud shadows (García et al., 2014). Consequently, they have been widely used in studies to assess changes in regional vegetation coverage. In addition, the data of digital elevation

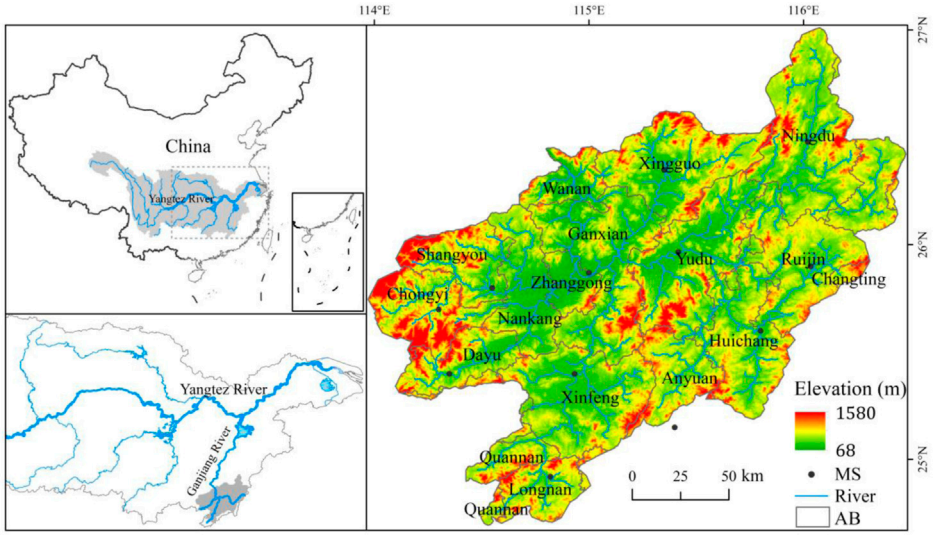

FIGURE 1
Location of the study area; MS and AB denote meteorological station and administrative boundary, respectively.

model (DEM), including the V3 version of the Advanced Spaceborne Thermal Emission and Reflection Radiometer (ASTER) Global Digital Elevation Model (GDEM), were obtained from the Geospatial Data Cloud run by the Computer Network Information Center of the Chinese Academy of Sciences (http://www.gscloud.cn/) with a spatial resolution of 30 m.

3 Methods

3.1 Data pre-processing

Data pre-processing mainly included the following steps: 1) the MODIS Reprojection Tool (MRT) was used to convert the format and projection of the downloaded MODIS NDVI data; 2) the Savitzky-Golay (S-G) filter was used to smooth MODIS NDVI data and eliminate the influence of noise (Savitzky and Golay, 1964); and 3) maximum value composite (MVC) was used to synthesize the maximum NDVI in an annual time series. As the annual maximum NDVI can reflect the vegetation coverage during the best vegetation growth period of a year and eliminate the influence of atmosphere, clouds, and solar altitude angle on remote sensing images, it was used to analyze the temporal and spatial variation in vegetation coverage in the current study.

In addition, the DEM data for the study area were obtained in the following procedures: first, the DEM data were mosaiced using ArcGIS; second, the mosaiced DEM data were resampled with a resolution of 250 m; finally, the DEM data for the study area were cut out along its boundary.

3.2 Estimation of vegetation coverage and its variation

The dimidiate pixel model is a simple and widely used one for the estimation of FVC using remote sensing data (Zhang et al., 2017). The model assumes that a pixel is composed of vegetation and non-vegetation components, and the FVC can be calculated using the following equation:

$$FVC = \frac{S - S_s}{S_V - S_S} \quad (1)$$

Where S is the spectral response of the remote sensing data, S*v* and S*s* are the spectral responses for pure vegetation and pure soil within the pixel, respectively.

There is a strong correlation between FVC and NDVI. Based on previous studies (Carlson and Ripley, 1997; Jing et al., 2011), an NDVI-based vegetation coverage estimation model was established. The calculation formula is as follows (Gutman and Ignatov, 1998):

$$FVC = \frac{NDVI - NDVI_{\min}}{NDVI_{\max} - NDVI_{\min}} \quad (2)$$

Where NDVI represents the value of a mixed pixel, NDVI*max* represents the maximum NDVI value of a pure vegetation pixel, which is close to 1 in theory, and NDVI*min* represents the minimum NDVI value of pure non-vegetation pixels, which is close to 0 in theory.

Affected by meteorological factors, vegetation types, seasonal changes, and other factors, the NDVI*max* and NDVI*min* of different remote sensing images are different to some extent. The maximum and minimum values of NDVI within a certain

TABLE 1 Classification of vegetation coverage grade in the study area.

Scope (FVC)	Grade
FVC<10%	Extremely low vegetation coverage
10%≤FVC<30%	Low vegetation coverage
30%≤FVC<50%	Medium vegetation coverage
50%≤FVC <70%	Medium-high vegetation coverage
FVC≥70%	High vegetation coverage

TABLE 2 Classification of grade for the evolution trend of vegetation coverage in the study area.

Scope (slope)	Grade
−1≤Slope<-0.1	Extremely significant decrease (ESD)
−0.1≤Slope<-0.02	Significant decrease (SD)
−0.02≤Slope<0.02	Not significant change (NSC)
0.02≤Slope<0.1	Significant increase (SI)
0.1≤Slope<1	Extremely significant increase (ESI)

confidence interval are generally used. Most researchers set the confidence interval to be 1–99% or 5–95% (Duo et al., 2016; Wei et al., 2017). Considering the actual situation in the study area, we chose a confidence interval of 1–99%. In addition, we divided FVC into five levels with reference to several previous studies, as shown in Table 1 (Li et al., 2014; Hao et al., 2020; Sun et al., 2020).

The coefficient of variation (CV) represents the ratio of standard deviation to mean. It is a useful parameter for comparing the degree of variation from one data series to another, even if the means are significantly different among different data series. This index was used to assess FVC stability in the current study.

3.3 Trend analysis

Univariate linear regression analysis was adopted for the trend analysis to linearly fit the temporal variation trend of vegetation coverage in the upper reaches of the Ganjiang River Basin from 2000 to 2020. The calculation formula is as follows:

$$\text{Slope} = \frac{\text{n} \times \sum_{i=1}^{n} (i \times FVC_i) - \sum_{i=1}^{n} i \sum_{i=1}^{n} FVC_i}{\text{n} \times \sum_{i=1}^{n} i^2 - \left(\sum_{i=1}^{n} i\right)^2} \quad (3)$$

Where Slope is the slope of the univariate linear regression equation, indicating the trend in FVC evolution in the research time series; n is the total number of monitoring years; i is the serial number of monitoring years; and FVC_i indicates the vegetation coverage of the ith year. Slope>0 indicates that the vegetation coverage in the study area shows an increasing trend; slope<0 indicates that the vegetation coverage shows a decreasing trend; and the slope around zero indicates that the changes in vegetation coverage are not obvious. In this study, trend in FVC evolution was divided into five grades (Huo and Sun, 2021; Fu et al., 2022), as shown in Table 2.

3.4 CV exponent and hurst exponent analyses

The CV index can be used to reveal relative fluctuations in grid pixel values (Rey et al., 2016; Kalisa et al., 2019). If the CV index value is larger, the fluctuation in the vegetation coverage FVC pixel is greater and the FVC value is more unstable. In contrast, if the CV index value is smaller, the distribution of the time series data is more homogeneous, and the FVC is more stable. The calculation formula is as follows:

$$CV = \frac{1}{\overline{FVC}} \sqrt{\frac{1}{n-1} \sum_{i=1}^{n} \left(FVC_i - \overline{FVC}\right)^2} \quad (4)$$

Where CV is the coefficient of variation of the grid pixel value, FVC_i represents the maximum vegetation coverage in the ith year, and $\overline{FVC}$ is the average vegetation coverage of each grid unit in the study area from 2000 to 2020. The Hurst exponent is an effective measure for quantitatively describing the long-term memory of a time series (Zhang et al., 2019a). It was proposed by British hydrologist Harold Edwin Hurst (Hurst, 1951) and can be used to predict future changes in vegetation coverage. In this study, rescaled range (R/S) analysis, a method that can provide information on the maximum fluctuation of statistical parameters, was used to calculate the Hurst exponent of vegetation coverage changes. The basic principle is as follows (Caccia et al., 1997): The calculation of the mean of time series:

$$\overline{FVC}_{(\tau)} = \frac{1}{\tau} \sum_{t=1}^{\tau} FVC_t \quad (5)$$

Calculation of the cumulative deviation:

$$X(t, \tau) = \sum_{t=1}^{\tau} \left(FVC_{(t)} - \overline{FVC}_{(\tau)}\right) \quad (6)$$

Calculation of the range sequence:

$$R_{(\tau)} = \max X(t, \tau) - \min X(t, \tau) \quad (7)$$

Calculation of the standard deviation sequence:

$$S_{(\tau)} = \left[\frac{1}{\tau} \sum_{t=1}^{\tau} \left(FVC_{(t)} - \overline{FVC}_{(\tau)}\right)^2\right]^{\frac{1}{2}} \quad (8)$$

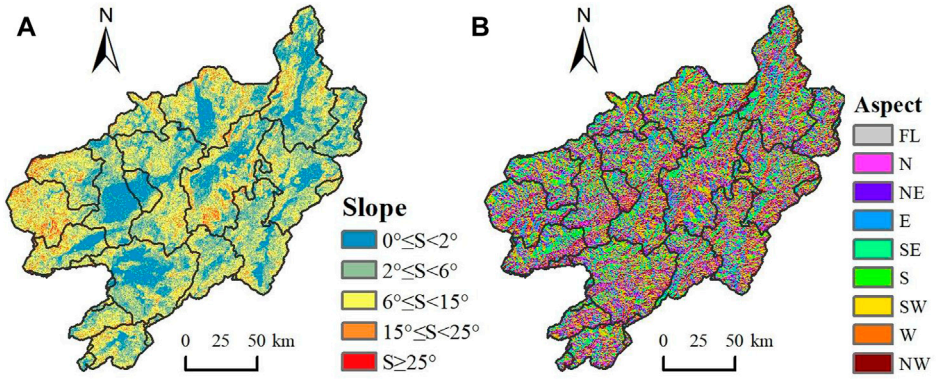

FIGURE 2
Spatial distribution characteristics of slope and aspect in the upper reaches of Ganjiang River Basin. FL, N, NE, E, SE, S, SW, W, and NW denote flat land, north slope, northeast slope, east slope, southeast slope, south slope, southwest slope, west slope, and northwest slope, respectively. **(A)** Distribution of slope **(B)** Distribution of aspect.

Calculation of the Hurst exponent:

$$\frac{R_{(\tau)}}{S_{(\tau)}} = (\alpha\tau)^H \tag{9}$$

Where H is the Hurst exponent; $FVC_{(t)}$ is the time series, $1 \leq t \leq \tau$, and τ is the length of the time series, $\tau = 1, 2, \ldots, n$; a is a constant.

The Hurst exponent varies between 0 and 1. It can be categorized into three types: 1) $0.5 < H < 1$, indicating that the sequence is persistent, and the future change trend is consistent with the past change trend. The closer the value of H is to 1, the stronger the persistence; 2) $H = 0.5$, indicating that the sequence is a random sequence, and the future change trend is independent of the past change trend; 3) $0 < H < 0.5$, indicating that the sequence is an anti-persistent sequence, and the future change trend is opposite to the past change trend. The closer the value of H is to 0, the stronger the anti-persistence. H was used to assess the sustainability of FVC in this study.

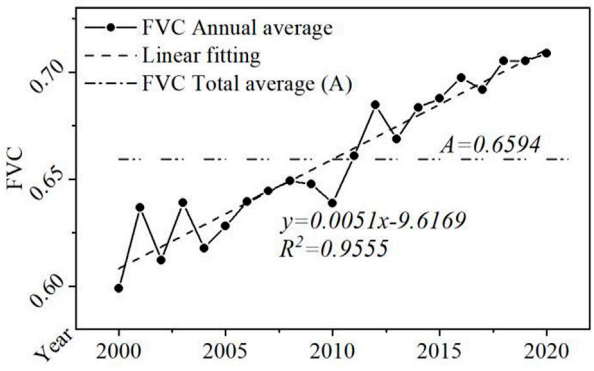

FIGURE 3
Interannual variation of FVC in the upper reaches of Ganjiang River Basin, China during the years 2000–2020.

3.5 Analysis of terrain factors

Based on the above calculations, the annual average spatial distribution and annual variation in vegetation coverage in the upper reaches of the Ganjiang River Basin can be obtained. In view of the altitude distribution in the upper reaches of the Ganjiang River Basin, the elevation of GDEM data was divided into five intervals: 68–250 m, 250–500 m, 500–750 m, 750–1,000 m, and 1,000–1,580 m. In addition, slopes of mountains and hills in the study area were analyzed using ArcGIS software based on the results of the second national land survey, and reclassified into five intervals: 0°–2°, 2°–6°, 6°–15°, 15°–25°, and ≥25° (Liu et al., 2018). According to the aspect model in DEM data, the aspects were also analyzed using ArcGIS software, and reclassified into nine types: flat land (FL), north slope (337.5°–22.5°), northeast slope (22.5°–67.5°), east slope (67.5°–112.5°), southeast slope (112.5°–157.5°), south slope (157.5°–202.5°), southwest slope (202.5°–247.5°), west slope (247.5°–292.5°), and northwest slope (29.5°–337.5°). The spatial distribution characteristics of elevation, slope, and aspect (Figure 2) in the upper reaches of the Ganjiang River Basin were obtained.

4 Results and discussion

4.1 Spatiotemporal variation of FVC

1) Temporal variation of FVC

The interannual variation in FVC in the upper reaches of the Ganjiang River Basin, China, over the years 2000–2020 is shown in Figure 3. The average annual FVC in the study area showed a

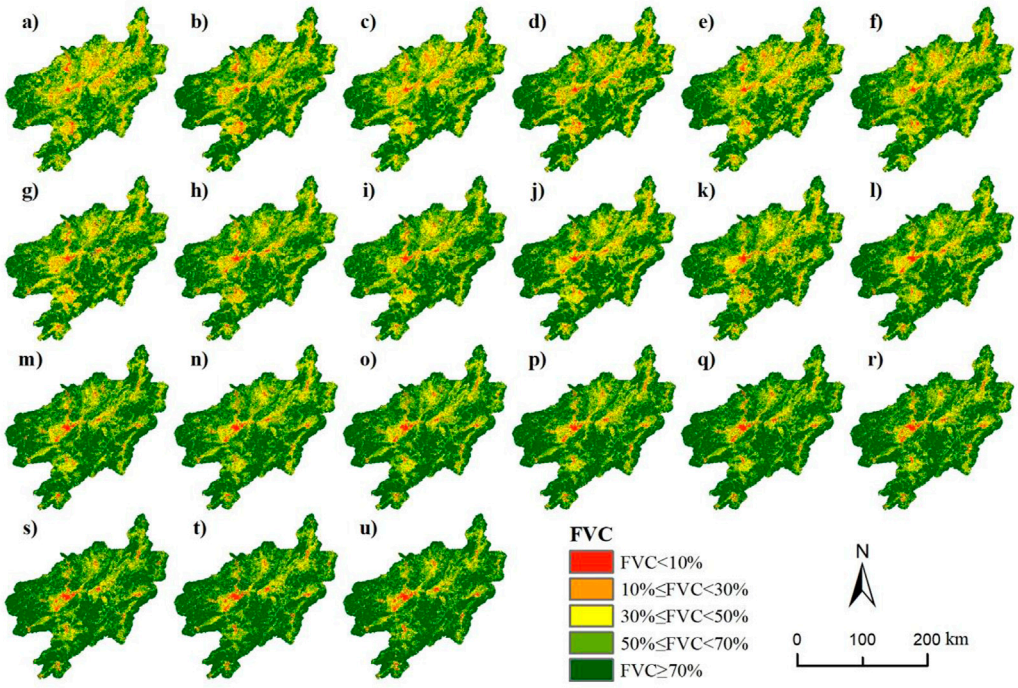

FIGURE 4
Spatial distribution of annual vegetation coverage in the upper reaches of Ganjiang River Basin from 2000 to 2020. **(A–U)** are the annual vegetation coverage for the years from 2000 to 2020, respectively.

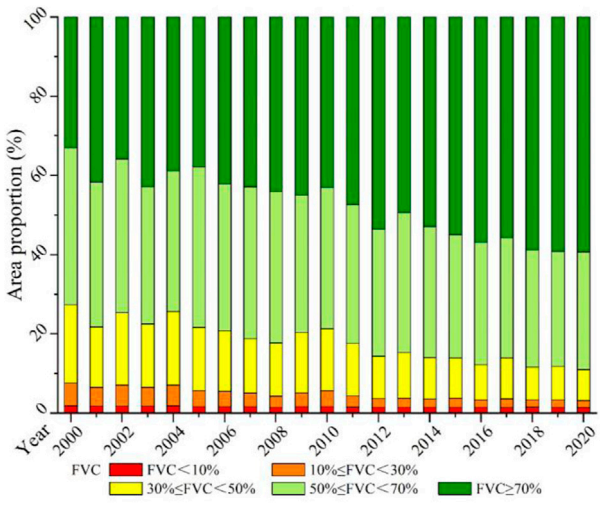

FIGURE 5
Evolution of the proportion of each vegetation coverage in the upper reaches of Ganjiang River Basin from 2000 to 2020.

fluctuating increasing trend (p <0.001), with a growth rate of 5%/10y. The lowest value of average annual FVC was 59.9% (i.e., 0.59) in 2000, and the highest value of average annual FVC was 70.9% in 2020. This is mainly due to the fact that Ganzhou City has implemented measures conducive for ecological improvement since 2000, such as restriction of mineral exploitation, afforestation, and reclamation of mined areas. The upper reaches of Ganjiang River Basin are 80% mountains, 10% water, and 5% fields, and the area of farmland is small. Owing to the undeveloped economy, most of the working population work away from home. The phenomenon of farmland abandonment was serious, which induced an increase in vegetation coverage.

2) Spatial distribution of FVC

Figure 4 and Figure 5 show the spatial distribution and proportion of each vegetation coverage grade in the upper reaches of the Ganjiang River Basin from 2000 to 2020, respectively. The overall situation of vegetation coverage was good, mainly with high and higher vegetation coverage (FVC≥50%). The annual average vegetation coverage was 65.94% (Figure 3), with the proportion of low, lower, medium, higher, and high vegetation coverage of 0.9%, 2.5%, 12.3%, 38%, and 46.3%, respectively (Figure 5). The sum of the latter two grades of vegetation coverage was greater than 50%. This is because the upper reaches of the Ganjiang River Basin have a warm climate, abundant rainfall, and are rich in forest

resources. In addition, the topographical characteristics of the study area are "high around, low in the middle with the west side higher than the east side". Terrain characteristics limit the range of human activity. Areas with low vegetation coverage are mainly cities and towns where human activities are intensive, such as Zhanggong District, Ganxian District, Nankang District, Yudu County, Ningdu County, Xinfeng County, Xingguo County, Huichang County, Ruijin City, and Longnan County. The areas with high vegetation coverage are mainly located in the middle and low mountain areas where human activities are less, such as west of Chongyi County, west of Dayu County, northwest of Shangyou County, and Quannan County. The proportion of high vegetation coverage (FVC≥70%) in the upper reaches of Ganjiang River Basin showed a fluctuating increasing trend with time, with the lowest proportion of 35.9% in 2002 and the highest proportion of 59.3% in 2020. A detailed examination of Figure 4 and Figure 5 found that the growth of plants in the transition zone between high and higher vegetation coverages (68%≤FVC≤72%) varied in different years. This was due to the difference in weather and water conditions in different years, which resulted in the mutual conversion between the two grades of vegetation coverage, such as 2000 to 2003 in the northwest areas (Figures 4A–D) and 2012 to 2014 in the northeast areas (Figures 4M–4O). Consequently, this was also the reason for the observed fluctuations in the proportion of areas with high vegetation coverage. The high vegetation areas also extend to a certain degree in their surroundings. This was because of afforestation with the enforcement of environmental and ecological policies. In addition, the proportion of high vegetation coverage increased, reflecting the growth of afforested trees, such as in the central area, from 2013 to 2016 (Figures 4N–4Q). Since 2012, the proportion of the areas with high vegetation coverage turned to be more than 50%. In contrast, the proportion of areas with higher vegetation coverage, moderate vegetation coverage, and lower vegetation coverage showed a fluctuating decreasing trend. The decreasing degree were as follows: moderate vegetation coverage (from 19.8% in 2000 to 7.8% in 2020), higher vegetation cover (from 39.6% in 2000 to 29.1% in 2019), and lower vegetation cover (from 5.7% in 2000 to 1.8% in 2020). Owing to the undeveloped economy, the abandonment of farmland accelerated, and agricultural production activities decreased, which resulted in the transfer of some moderate vegetation coverage areas to higher or high vegetation coverage areas, such as in the central and southern parts of the basin from 2017 to 2020 (Figures 4R–4U). In contrast, the areas with low vegetation coverage showed a slight down trend, but the proportion was relatively stable, accounting for between 1.4% and 1.85%. Areas with low vegetation coverage mainly concentrate in places where human activities are intensive, and the land is mainly constructed land. It is not easy to change construction land to other land use types.

3) Trend in FVC evolution

To better analyze the spatiotemporal evolution characteristics of vegetation coverage in the upper reaches of the Ganjiang River Basin, the period from 2000 to 2020 was further divided into seven sub-periods: 2000–2002, 2003–2005, 2006–2008, 2009–2011, 2012–2014, 2015–2017, and 2018–2020, respectively. Figure 6 and Figure 7 show the spatial distribution and proportion of vegetation coverage change in the upper reaches of the Ganjiang River Basin from 2000 to 2020, respectively. Because of the need for urban construction in some counties and districts during 2000–2002 and 2003–2005, parts of the land with vegetation coverage were transformed into construction land, resulting in a decrease in vegetation coverage in different areas, especially during 2000–2002 (Figure 6). In the northeast of Yudu, vegetation coverage decreased from 2006 to 2008, started to increase from 2009 to 2011, and remained stable after 2011. This area is mainly a transitional zone between high and higher vegetation coverages, as shown in Figures 4G,I. Influenced by climatic conditions, this transition zone changed from high vegetation coverage to higher vegetation coverage during 2006–2008, but gradually changed back to high vegetation coverage after 2009. During 2009 to 2020, different areas showed different degrees of increase or decrease in different time periods. Overall, the changes remained stable, and there was a significant increase in vegetation coverage. The increase in vegetation coverage was mainly due to the return of farmland to forests and afforestation enforced by the environmental protection policies. The central and eastern parts of Zhanggong District were the most stable areas during 2009–2020 because urban construction had been done earlier. The construction land in the west part of the district had been gradually expanded since 2008. Consequently, the vegetation coverage first decreased and then stabilized at middle and low levels (Figure 4I, Figure 6C, Figure 7). The changes in vegetation coverage in the seven sub-periods between 2000 and 2020 were mainly insignificant, significant increase, and significant decrease, while those with extremely significant increases and decreases were relatively fewer (Figure 7). The changes in proportions at different time periods were different. The reasons were that the meteorological conditions, human activities, and related policies varied in different time periods, such as the construction of towns and central urban areas in the upper reaches of the Ganjiang River Basin from 2003 to 2005, accompanied by the transformation of part of the vegetation land to construction land. Vegetation coverage decreased, resulting in an increase in the proportion of significant decreases. Affected by the so-called "Lucid waters and lush mountains are invaluable assets" national movement for the promotion of ecological protection during 2015–2017, more attention was paid to the protection of ecological environment

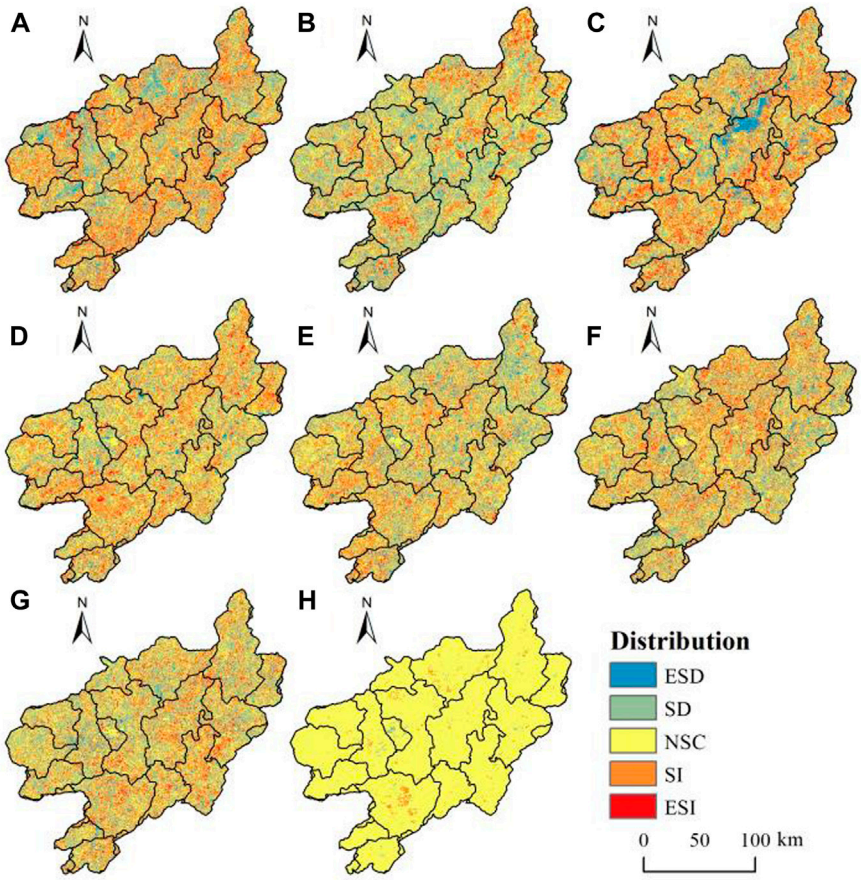

FIGURE 6
Evolution trend of changes in vegetation coverage in the upper reaches of Ganjiang River Basin from 2000 to 2020. **(A–H)** are for the sub-periods of 2000–2002, 2003–2003, 2006–2008, 2009–2011, 2012–2014, 2015–2017, 2018–2020, and 2000–2020, respectively. ESD, SD, NSC, SI, and ESI denote extremely significant decrease, significant decrease, non-significant change, significant increase, and extremely significant increase, respectively.

than before. The vegetation coverage increased, and the proportion of significant increase improved. From 2000 to 2020, the vegetation coverage in 98% of the total area of the upper reaches of Ganjiang River Basin did not change significantly. The proportion of significant increase only accounted for 1.52% (Figure 6), and was mainly distributed in the middle of Xinfeng County, the north of Gan County, the south of Xingguo County, and the west of Nankang District. Other counties and districts showed a sporadic distribution.

In recent years, the coordinated development of the navel orange industry and ecological environment in Xinfeng County, restriction on exploitation of mineral resources, afforestation, and the implementation of land reclamation policies in mining areas in the northern part of Gan County, southern part of Xingguo County, and western part of Nankang County have contributed a lot to the protection of the ecological environment in these areas. The areas with significant decrease only accounted for 0.48%, which were mainly distributed in the eastern part of Nankang District, the central part of Zhanggong District, the central part of Ruijin City, and the periphery of each city. The transformation of vegetated land into construction land was the reason for the decrease in vegetation coverage.

Overall, the areas without significant changes accounted for more than 95% (Figure 6 and Figure 7). Areas with increased and decreased vegetation coverage occurred at different locations during different periods. The increase and decrease cancelled each other out on the long time scale. This was also verified by the area changes reflected by the Hurst index, as shown later, indicating consistency with this conclusion.

4) Stability and sustainability of FVC

The spatial distribution of the coefficient of variation (CV) of FVC in the upper reaches of the Ganjiang River Basin during the time period between 2000 and 2020 is shown in Figure 8A. CV represents the dispersion and fluctuation of the data distribution.

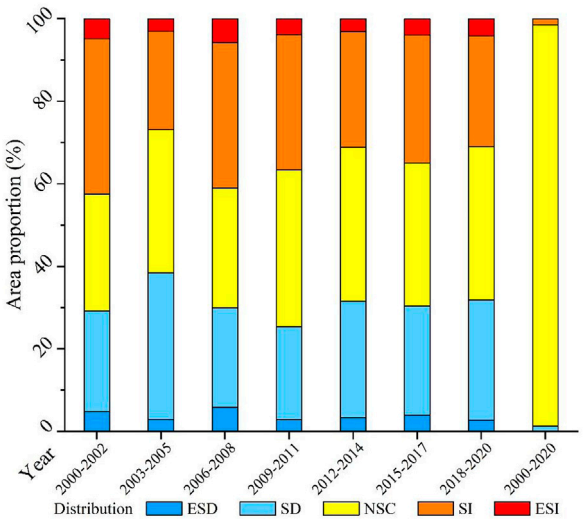

FIGURE 7
Proportion of vegetation coverage change in the upper reaches of Ganjiang River Basin in different time periods. ESD, SD, NSC, SI, and ESI denote extremely significant decrease, significant decrease, non-significant change, significant increase, and extremely significant increase, respectively.

TABLE 3 Stability associated with changes in vegetation coverage in the upper reaches of ganjiang river basin during 2000–2020.

Scope (CV)	Grade	Area (km^2)	Proportion (%)
0≤CV<0.15	Stability	267.3081	63.5
0.15≤CV<0.4	Instability	145.3239	34.5
CV≥0.4	Extreme instability	8.505	2.0

The larger the CV, the more dispersed is the data distribution. The greater the fluctuation, the greater is the variation, and *vice versa*. In this study, the CV of FVC was divided into three grades (Li et al., 2021; Liu et al., 2022), as shown in Table 3. Vegetation coverage in the study area was relatively stable. The CV of FVC ranged from 2.56% to 98.83%, with an average of 14.8%. The areas with stable FVC (CV less than 15%) accounted for 63.47% of the total area of the study, mainly distributed in the surrounding mountains. Fewer human activities in mountainous areas were conducive to vegetation growth; thus, the change in FVC in mountainous areas was small. The areas with unstable FVC (CV between 15% and 40%) accounted for 34.51%, mainly including the south of Nankang District, the middle of Xinfeng County, the north of Yudu County, and the south of Xingguo County. The areas with extremely unstable FVC (CV higher than 40%) accounted for 2.02%, including the middle of Xinfeng County, the middle of Nankang District, the middle of Yudu County, the south of Xingguo County, and the middle of Ruijin City. In recent years, Xinfeng County has focused on the coordinated development of the navel orange industry and strengthened the protection of the ecological environment, so the changes in FVC in this area were dramatic. The drastic changes in FVC in the middle of the Nankang District and Ruijin City were due to urban expansion. Drastic changes in FVC in the middle of Yudu County and south of Xingguo County were induced by the implementation of afforestation and land reclamation in mined areas.

The spatial distribution of the Hurst exponent of FVC in the upper reaches of the Ganjiang River Basin from 2000 to 2020 is shown in Figure 8B. The average Hurst exponent of FVC in the study area was 0.46. The pixels with Hurst exponents less than 0.5 accounted for 66.38% and those with Hurst exponents greater

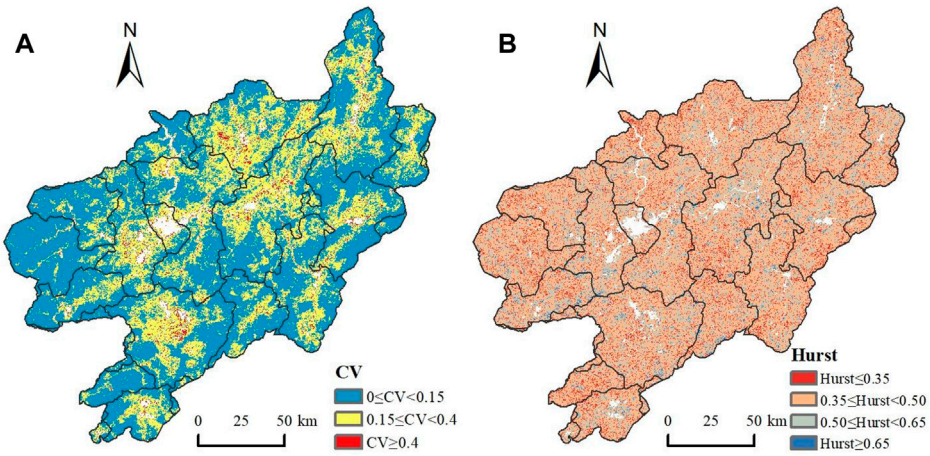

FIGURE 8
Spatial distribution of coefficient of variation (CV) and Hurst exponent of FVC in the upper reaches of Ganjiang River Basin during 2000–2020. **(A)** Distribution of CV **(B)** Distribution of Hurst exponent.

TABLE 4 Sustainability associated with changes in vegetation coverage in the upper reaches of ganjiang river basin during 2000–2020.

Scope (Hurst)	Grade	Area (km^2)	Proportion (%)
Hurst<0.35	Strong anti-sustainability	46.7460	11.1
0.35≤Hurst<0.50	Weak anti-sustainability	232.8228	55.3
0.50≤Hurst<0.65	Weak sustainability	129.6	30.8
Hurst≥0.65	Strong sustainability	11.9682	2.8

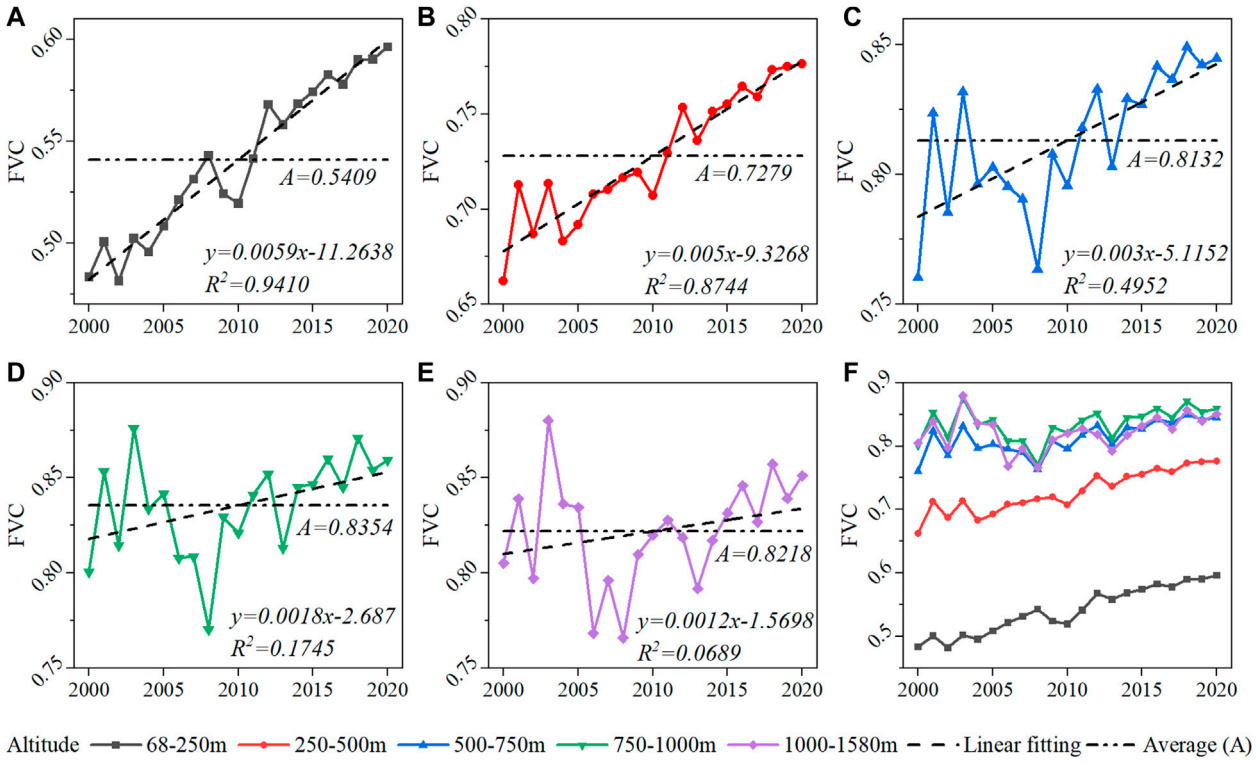

FIGURE 9
Evolution characteristics of vegetation coverage with increase in altitude in the upper reaches of Ganjiang River Basin from 2000 to 2020.

than 0.5 accounted for 33.62%. The anti-sustainability of vegetation coverage change in the study area was stronger than that of sustainability, indicating that the FVC in the upper reaches of the Ganjiang River Basin would decrease in the future. The pixels showing strong anti-sustainability accounted for 11.1% of the study area and those with weak anti-sustainability accounted for 55.28%. The pixels showing strong sustainability accounted for 30.78% of the study area and those with weak sustainability accounted for 2.84% (Table 4). The vegetation coverage change in the study area was dominated by weak anti-sustainability, indicating that the FVC in the upper reaches of the Ganjiang River Basin will decrease slightly in the future. This was consistent with the results reported (Liu et al., 2021).

4.2 Response of FVC to terrain

1) Distribution of vegetation coverage with altitude

The vegetation coverage in the upper reaches of the Ganjiang River Basin increased continuously with increasing altitude (Figure 9). The vegetation coverage in the elevation zone of 68–250 m was the lowest, with an average of 54.09%. The zone with highest vegetation coverage was 750–1,000 m, with an average of 83.54%. In addition, the annual average vegetation coverage in different elevation zones showed a fluctuating increase; the elevation zones with obvious fluctuating growth were 68–250 m and 250–500 m. However, there was a trough in

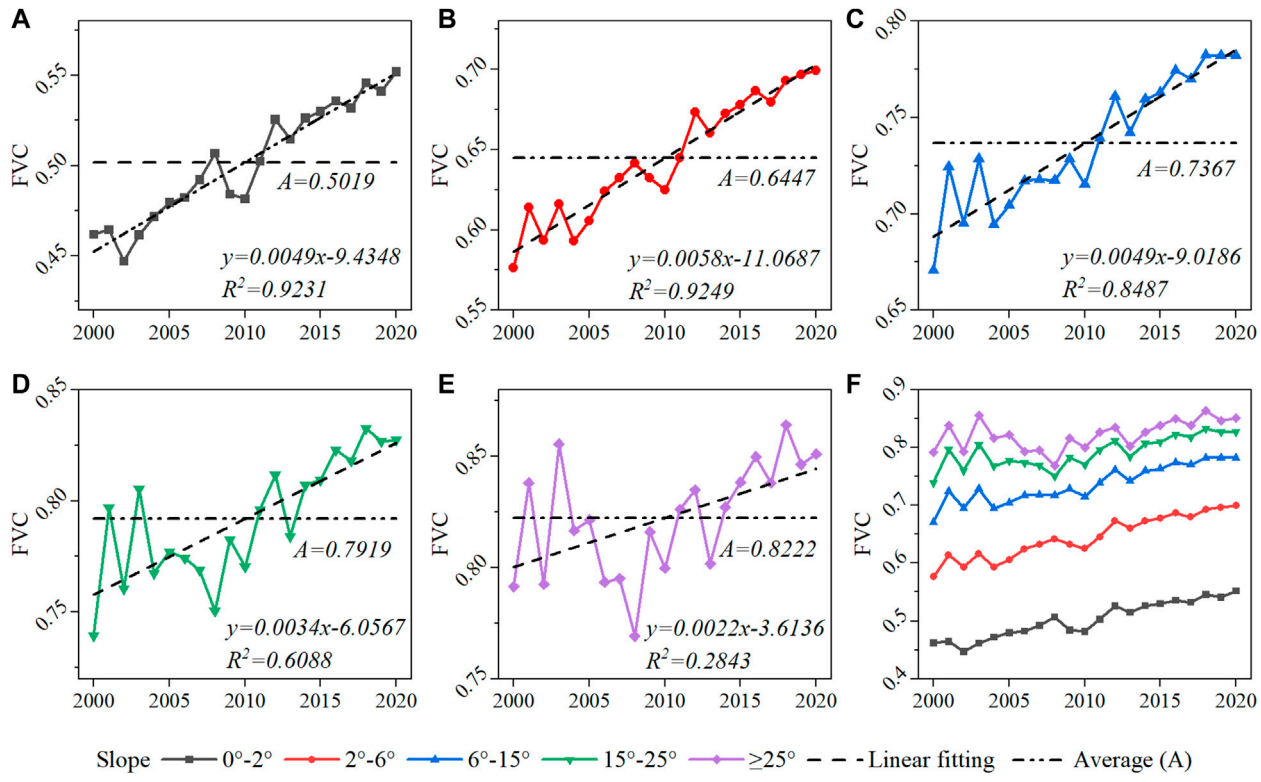

FIGURE 10
Variation characteristics of vegetation coverage with increase in slope degree in the upper reaches of Ganjiang River Basin from 2000 to 2020.

the average vegetation coverage in the 500–1,580 m elevation zone from 2006 to 2008, which was less disturbed by human beings. Meteorological factors, such as increase in air temperature, decrease in precipitation, and enhanced evaporation, were thought to be the reasons that led to less water for plants, and were not conducive to the improvement of vegetation coverage. The increase in vegetation coverage above 250 m indicated that human activities mainly concentrated in the areas below 250 m. Both vegetation coverage and rate of increase of vegetation increased without human disturbance.

In general, altitude affects local weather and water conditions, which consequently affect vegetation growth. Weather and water conditions in low-altitude areas are better and more suitable for plant growth, and therefore, the vegetation coverage should be relatively higher in low-altitude than in high-altitude areas. However, disturbance from human activities in low-altitude areas leads to a sharp decrease in vegetation coverage, mainly due to the transformation of vegetated land to construction land. The average vegetation coverage of the elevation zones: 500–750 m, 750–1,000 m, and 1,000–1,580 m was more than 80%, and the degree of variation becomes smaller with the increase in altitude. The highest altitude in the upper reaches of the Ganjiang River Basin is 1,580 m. A height greater than 1,000 m restricts plant growth, and the vegetation coverage above that tends to remain unchanged. The weather and water conditions in the elevation zone of 1,000–1,580 m were not favorable for vegetation growth compared to those in the elevation zone of 750–1,000 m. Therefore, the vegetation coverage in the elevation zone of 1,000–1,580 m was lower than that in the elevation zone of 750–1,000 m. With increasing altitude, vegetation coverage tends to remain stable. This phenomenon is similar to that reported for the Hanjiang River Basin (Liu et al., 2018).

2) Distribution of vegetation coverage with slope

Vegetation coverage in the upper reaches of the Ganjiang River Basin increased as the slope increased (Figure 10). The lowest vegetation coverage was located in the slope zone of 0°–2°, with an average of 50.19%. The highest vegetation coverage was located in a slope zone greater than 25°. This is because a gentle slope zone is suitable and convenient for human activities such as industrial and agricultural production. Most people in the Ganjiang River Basin live in a slope zone of 0°–2°, where cities and towns are located. Less natural vegetation is distributed in this slope zone, resulting in lower vegetation coverage. The slope zone of 2°–6° is a transition zone between the industrial and agricultural production lands, resulting in relatively higher

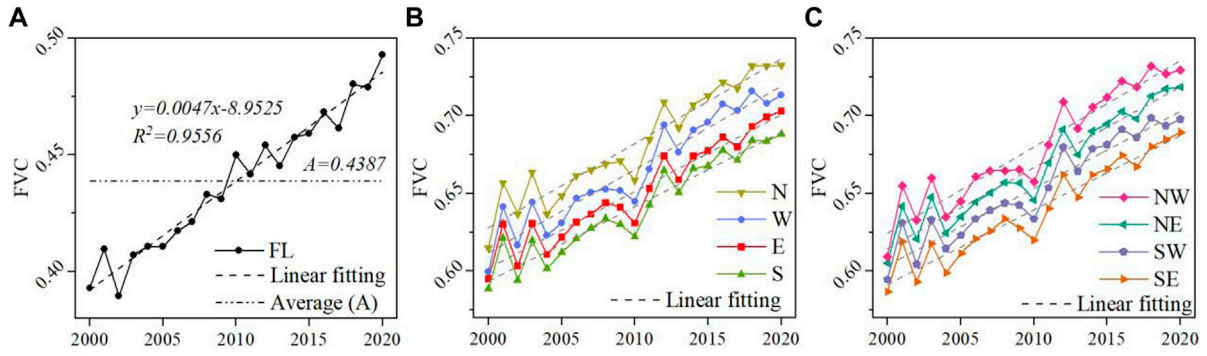

FIGURE 11
Distribution characteristics of vegetation coverage with aspect in the upper reaches of Ganjiang River Basin from 2000 to 2020. FL, N, NE, E, SE, S, SW, W, and NW denote flat land, north slope, northeast slope, east slope, southeast slope, south slope, southwest slope, west slope, and northwest slope, respectively.

vegetation coverage compared with that in the slope zone of 0°–2°. The vegetation coverage in the slope zone of 6°–15° was higher than that in the slope zone of 2°–6°, because the original woodlands in this slope zone were easier to be reclaimed as terraced fields for agricultural production.

In general, the steeper the slope, the lower the accumulated temperature and precipitation, the worse the water retention capacity of the soil, and the worse the weather and water conditions for vegetation growth. Vegetation coverage should decrease with an increase in the slope degree. However, the areas with highest vegetation coverage in this study were identified in the areas with slopes greater than 25°. This is because local human production activities were greatly reduced owing to topographical and traffic restrictions with the increase in slope degree. Vegetation growth in areas with steeper slopes was mainly affected by natural conditions, with less interference from human activities. The changed trend of vegetation coverage returned to normal and showed an increasing trend. This finding is similar to that of a study on the upper Minjiang River Basin (Zhang et al., 2018). The difference was that the maximum slope in the study area was only 40°, and that in the upper Minjiang River Basin was more than 55°. The areas with the maximum vegetation coverage were in the zones with slope degrees between 25° and 45°. A similar phenomenon was also found in other basins, such as the Guandu River basin reported (Chen et al., 2019). Both the elevation and slopes in this study area are relatively small compared with those in the other basins.

3) Distribution of vegetation coverage with aspect

Overall, there was no significant difference among the distributions of average vegetation coverage in the different aspects in the upper reaches of the Ganjiang River Basin (Figure 11). This is because the terrain in the study area is not rugged enough to form barriers against hydrothermal cycle. The average vegetation coverage in the upper reaches of the Ganjiang River Basin was in the following order: vegetation coverage of north slope > northwest slope > northeast slope > west slope > southwest slope > east slope > south slope > southeast slope > flat land (Table 5 and Table 6). Aspects with higher average vegetation coverage, such as the north and northwest slopes, are shady slopes, while the aspects with low average vegetation coverage, such as the east, south, and southeast slopes, are commonly known as sunny slopes. Although the upper reaches of the Ganjiang River Basin have a subtropical monsoon climate with abundant precipitation, long-term solar radiation leads to excessive water evaporation from plants and soils, resulting in fewer water conditions and growth retardation. The plants on shady slopes received less solar radiation than those on sunny slopes leading to low evaporation, retaining a certain amount of water for plant growth. Therefore, the plant growth conditions on shady slopes were slightly better than those on sunny slopes in the study area. It also reported that evaporation in the hilly regions of South China was negatively correlated with relative humidity and positively correlated with temperature and percentage of sunshine (Liu et al., 2019). Receiving too much solar radiation not only inhibits the photosynthetic efficiency of plants but also accelerates the evaporation of surface water. In contrast, the average vegetation coverage of flat land was significantly smaller than that of mountains and hills, mainly due to interference from human activities.

Human activities play an important role in vegetation growth, which can have positive or negative impacts on surface vegetation coverage through indirect impact or direct transformation. For example, afforestation, deforestation, urbanization development, engineering construction and ecological recovery will inhibit or promote the growth of vegetation, cause dramatic changes in surface vegetation in a short period of time, and play a key role in ecosystem restoration and healthy development (Zhang et al.,

TABLE 5 Linear regression between the vegetation coverage and aspect in the upper reaches of ganjiang river basin from 2000 to 2020.

Aspect	Trend	R^2	Aspect	Trend	R^2
N	Y = 0.0054X–10.2152	0.907	NW	Y = 0.0056X–10.484	0.9017
W	Y = 0.0053X–10.0954	0.9048	NE	Y = 0.0052X–9.7893	0.9184
E	Y = 0.0049X–9.2799	0.9136	SW	Y = 0.005X–9.2863	0.9081
S	Y = 0.0048X–9.0027	0.9124	SE	Y = 0.0048X–8.9705	0.9136

TABLE 6 Average vegetation coverage in each aspect in the upper reaches of ganjiang river basin from 2000 to 2020.

Aspect	FVC average	Aspect	FVC average
N	0.6821	NW	0.6799
W	0.6654	NE	0.6666
E	0.6512	SW	0.6533
S	0.6414	SE	0.6394

2019b). In the past 20 years, the accumulated afforestation area in the upper reaches of Ganjiang River is about 0.5 million hectares, which has improved the vegetation coverage to a certain degree; On the other hand, with the continual expansion of the economic specification, the urbanization rate of the upper reaches of the Ganjiang River has increased from 37.53% in 2010 to 55.31% in 2020, the growth rate has reached 47.37% (Liu, 2021). At the same time, the decline of forest ecological function, the intensification of water and soil loss, the general increase of population density and the mining of rare earth minerals have led to the degeneration of the surface vegetation in some areas in varying degrees. In recent years, in order to improve the living quality of residents, the local government has carried out greening construction and ecological livelihood projects actively, the surface vegetation coverage has improved greatly. Therefore, the concept of "green" and "coordination" in high-quality development is vital to the protection of the ecological environment.

4.3 Discussion

This study analyzed the spatiotemporal evolution of vegetation coverage and its relationships with terrain and human factors in the upper reaches of the Ganjiang River Basin, China. The FVC showed a fluctuating increasing trend, and also human activities have different impacts on vegetation coverage under different terrain conditions. Consistent with the achievements of previous studies (Liu et al., 2021; Fu et al., 2022; Tian and Wang, 2022), the ecological environment of the Ganjiang River basin is generally showing a good trend, and at the same time, the basin is subject to some human impact.

However, there are still other factors, such as climate factors, which influence vegetation dynamics that have not been considered. Therefore, quantifying the contributions of various factors and determining the main influencing factors should be the focus of future research. In addition, this study did not use multisource NDVI data for mutual verification. The resolution and quality of the different NDVI data varied. This also affected the results associated with the estimation of vegetation coverage. Further studies considering such factors are ongoing for a deeper understanding of the interrelationships among the ecological environment, climate factors, terrain factors, and human activities in the study area.

Taking the upper reaches of Ganjiang River of long-term sequence research, this study not only enriches the research content of dynamic and rapid monitoring of the change process of ecological environment quality, but also provides reference for rapid assessment of ecological environment quality and construction of ecological environment quality model to analyze the main driving forces. The methods and models adopted in this paper are also applicable in the Yellow River Basin, the Manas River Basin and other watersheds (Liu et al., 2018; Zhang et al., 2019b). Considering the time step of research and analysis is relatively long, the subtle changes among years being ignored, future study will integrating other higher resolution data sources to optimize the evaluation index of ecological environment quality in order to analyze the evolution characteristics of ecological environment quality accurately.

5 Conclusion

Based on MODIS NDVI and DEM data collected for the upper reaches of the Ganjiang River Basin, this study used trend analysis, coefficient of variation, Hurst index, and linear regression to analyze the temporal and spatial evolution of vegetation coverage and its relationships with terrain factors in the upper reaches of the Ganjiang River Basin, China during the years 2000–2020. The major conclusions drawn from this study are as follows.

1) The FVC showed a fluctuating increasing trend ($P<0.001$), with an increase rate of 5%/10y. Spatially, the vegetation coverage was dominated by high vegetation coverage in the study area, showing a low-value distribution in the middle and high-value distribution in the surroundings.

Themultiyear average FVC was 65.94%. The areas with significant increase and significant decrease accounted for 1.52% and 0.48% respectively, while those with insignificant changes accounted for 98%.

2) The vegetation coverage was relatively stable in the study area, with an average CV of 14.8%. The FVC showed large changes in the middle of Xinfeng County, middle of Nankang District, middle of Yudu County, south of Xingguo County, and middle of Ruijin City, followed by that in the south of Nankang District, middle of Xinfeng County, north of Yudu County, and south of Xingguo County. The surrounding mountains with high altitudes exhibited the smallest changes in the FVC. Hurst analysis showed that the anti-sustainability effect of vegetation change was stronger than that of sustainability, and weak anti-sustainability was dominant. The average Hurst exponent was 0.46.
3) Vegetation coverage in the upper reaches of the Ganjiang River Basin showed an increasing trend with increasing elevation. The maximum vegetation coverage was identified in the elevation zone of 750–1,000 m, with an average of 83.54%. Vegetation coverage also showed an increasing trend with increasing slope. The maximum vegetation coverage was up to 82.22% in the slope zone of ≥25°. There were no significant differences among the distributions of vegetation coverage in different aspects. Overall, the vegetation coverage of flat land was the lowest with a percentage of 43.87, and the maximum was that of the north slope (68.21%). The vegetation coverage on shady slopes was better than that on sunny slopes.

Therefore, under good terrain conditions such as low altitude, gentle slope and aspect with sufficient water and heat conditions, the vegetation coverage is higher. And the differences in topographic factors in the background of the watershed lead to both common and unique characteristics of vegetation differentiation. In addition, terrain conditions affect the range and intensity of human activities, which in turn affects the long-term evolution trend of vegetation cover.

In the context of the background of carbon peaking and carbon neutrality goals, the upper reaches of the Ganjiang River should maintain a good ecosystem, continue to protect the ecological environment of the basin, and build a watershed ecological security pattern. And it is necessary to balance resource development and ecological protection, develop in protection, and protect in development, so as to realize the coordination of economic development and ecological protection in the basin.

Data availability statement

The datasets presented in this study can be found in online repositories. The names of the repository/repositories and accession number(s) can be found below https://ladsweb.modaps.eosdis.nasa.gov/.

Author contributions

All authors listed have made a substantial, direct, and intellectual contribution to the work and approved it for publication. YL: Conceptualization, Writing-original draft, Visualization, Funding acquisition. HH: Methodology. LM: Resources, Project administration. ML: Investigation, Data curation. ZW: Formal analysis. TL: Writing-review. DL: Editing, Supervision.

Funding

This work was supported in part by the National Natural Science Foundation of China (41861002), the Natural Science Foundation of Guangdong Province of China (2022A1515012010), the Natural Science Foundation of Jiangxi Province of China (20202BABL203031), the Foundation of Education Department of Jiangxi Province of China (GJJ202015), the Key Research Foundation of Education Department of Guangdong Province of China (2021ZDZX4046).

Acknowledgments

Sincere thanks to Prof Ming Zhang, who was from the Geological Survey of Japan, National Institute of Advanced Industrial Science and Technology for his assistance in completing the paper when he was alive, we also thank the reviewers and the editor for their advice on this manuscript.

Conflict of interest

The authors declare that the research was conducted in the absence of any commercial or financial relationships that could be construed as a potential conflict of interest.

Publisher's note

References

Bejagam, V., Keesara, V. R., and Sridhar, V. (2022). Impacts of climate change on water provisional services in Tungabhadra basin using InVEST Model. *River Res. Appl.* 38 (1), 94–106. doi:10.1002/rra.3891

Caccia, D. C., Percival, D., Cannon, M. J., Raymond, G., and Bassingthwaighte, J. B. (1997). Analyzing exact fractal time series: evaluating dispersional analysis and rescaled range methods. *Phys. A Stat. Mech. its Appl.* 246 (3-4), 609–632. doi:10.1016/s0378-4371(97)00363-4

Carlson, T. N., and Ripley, D. A. (1997). On the relation between NDVI, fractional vegetation cover, and leaf area index. *Remote Sens. Environ.* 62, 241–252. doi:10.1016/s0034-4257(97)00104-1

Chen, H., Ouyang, W., and Liu, F. (2019). Variation of vegetation cover and its correlation of topographic factors in Guandu River Basin. *Soil Water Conserv.* 26, 135–147.

Chybicki, A., and Łubniewski, Z. (2017). Optimized AVHRR land surface temperature downscaling method for local scale observations: case study for the coastal area of the gulf of gdańsk. *Open Geosci.* 9 (1), 419–435. doi:10.1515/geo-2017-0032

Dardel, C., Kergoat, L., Hiernaux, P., Mougin, E., Grippa, M., and Tucker, C. (2014). Re-greening sahel: 30 years of remote sensing data and field observations (Mali, Niger). *Remote Sens. Environ.* 140, 350–364. doi:10.1016/j.rse.2013.09.011

Deng, Z., Lu, Z., Wang, G., Wang, D., Ding, Z., Zhao, H., et al. (2021). Extraction of fractional vegetation cover in arid desert area based on Chinese Gf-6 satellite. *Open Geosci.* 13 (1), 416–430. doi:10.1515/geo-2020-0241

Duo, A., Zhao, W., Qu, X., Jing, R., and Xiong, K. (2016). Spatio-temporal variation of vegetation coverage and its response to climate change in north China plain in the last 33 years. *Int. J. Appl. Earth Observation Geoinformation* 53, 103–117. doi:10.1016/j.jag.2016.08.008

Fu, B., Yang, W., Yao, H., He, H., Lan, G., Gao, E., et al. (2022). Evaluation of spatio-temporal variations of FVC and its relationship with climate change using GEE and Landsat images in Ganjiang River Basin. *Geocarto Int.*, 1–31. doi:10.1080/10106049.2022.2082551

García, M., Alloza, J., Mayor, Á., Bautista, S., and Rodriguez, F. (2014). Detection and mapping of burnt areas from time series of MODIS-derived NDVI data in a Mediterranean region. *Open Geosci.* 6 (1), 112–120. doi:10.2478/s13533-012-0167-y

Geng, W. L., Li, Y. Y., Sun, D. Q., Li, B., Zhang, P., Chang, H., et al. (2022). Prediction of the potential geographical distribution of Betula platyphylla Suk. in China under climate change scenarios. *Plos one* 17 (3), e0262540. doi:10.1371/journal.pone.0262540

Gutman, G., and Ignatov, A. (1998). The derivation of the green vegetation fraction from NOAA/AVHRR data for use in numerical weather prediction models. *Int. J. Remote Sens.* 19 (8), 1533–1543. doi:10.1080/014311698215333

Hao, J., Xu, G., Luo, L., Zhang, Z., Yang, H., and Li, H. (2020). Quantifying the relative contribution of natural and human factors to vegetation coverage variation in coastal wetlands in China. *Catena* 188, 104429–104514. doi:10.1016/j.catena.2019.104429

Hilker, T., Lyapustin, A. I., Tucker, C. J., Hall, F. G., Myneni, R. B., Wang, Y., et al. (2014). Vegetation dynamics and rainfall sensitivity of the Amazon. *Proc. Natl. Acad. Sci. U. S. A.* 111, 16041–16046. doi:10.1073/pnas.1404870111

Huete, A. (2016). Vegetation's responses to climate variability. *Nature* 531, 181–182. doi:10.1038/nature17301

Huo, H., and Sun, C. (2021). Spatiotemporal variation and influencing factors of vegetation dynamics based on geodetector: A case study of the northwestern yunnan plateau, China. *Ecol. Indic.* 130, 108005. doi:10.1016/j.ecolind.2021.108005

Hurst, H. (1951). Long term storage capacity of reservoirs. *T. Am. Soc. Civ. Eng.* 116, 770–799. doi:10.1061/taceat.0006518

Ivanov, V. Y., Bras, R. L., and Vivoni, E. R. (2008). Vegetation-hydrology dynamics in complex terrain of semiarid areas: 2. Energy-water controls of vegetation spatiotemporal dynamics and topographic niches of favorability. *Water Resour. Res.* 44 (3). doi:10.1029/2006wr005595

Jing, X., Yao, W., Wang, J., and Song, X. Y. (2011). A study on the relationship between dynamic change of vegetation coverage and precipitation in Beijing's mountainous areas during the last 20 years. *Math. Comput. Model.* 54, 1079–1085. doi:10.1016/j.mcm.2010.11.038

Kalisa, W., Igbawua, T., Henchiri, M., Zhang, S., and Bai, Y. (2019). Assessment of climate impact on vegetation dynamics over East Africa from 1982 to 2015. *Sci. Rep.* 9 (1), 16865–16920. doi:10.1038/s41598-019-53150-0

Lamchin, M., Lee, W. K., Jeon, S. W., Wang, S. W., and Song, C. (2018). Long-term trend and correlation between vegetation greenness and climate variables in Asia based on satellite data. *Sci. total Environ.* 618, 1089–1095. doi:10.1016/j.scitotenv.2017.09.145

Li, H., Liu, X., and Li, B. (2014). Vegetation coverage variations and correlation with geomorphologic factors in red soil region: a case in south Jiangxi Province. *Sci. Geogr. Sin.* 34 (1), 103–109.

Li, Y., Zhao, Z., Wang, L., Li, G., and Chang, L. (2021). Vegetation changes in response to climatic factors and human activities in Jilin Province, China, 2000–2019. *Sustainability* 13 (16), 8956. doi:10.3390/su13168956

Liu, C., Zhang, X., Wang, T., Chen, G., Zhu, K., Wang, Q., et al. (2022). Detection of vegetation coverage changes in the Yellow River basin from 2003 to 2020. *Ecol. Indic.* 138, 108818. doi:10.1016/j.ecolind.2022.108818

Liu, G., Wang, X., Wang, X., Wang, B. X., and Xiao, S. M. (2021). Spatial heterogeneity and driving factors of land use change in the middle and upper reaches of Ganjiang River, southern China. *Chin. J. Appl. Ecol.* 32 (7), 2545–2554. doi:10.13287/j.1001-9332.202107.016

Liu, H., Zheng, L., and Yin, S. (2018). Multi-perspective analysis of vegetation cover changes and driving factors of long time series based on climate and terrain data in Hanjiang River Basin, China. *Arab. J. Geosci.* 11 (17), 509–516. doi:10.1007/s12517-018-3756-3

Liu, M. (2021). Study on the change of vegetation coverage and its driving factors in the upper reaches of Ganjiang River basin. MA thesis. China: Jiangxi University of Science and Technology.

Liu, X., Zhou, W., and Bai, Z. (2016). Vegetation coverage change and stability in large open-pit coal mine dumps in China during 1990–2015. *Ecol. Eng.* 95, 447–451. doi:10.1016/j.ecoleng.2016.06.051

Liu, Y., Ding, Q., Chen, M., Zhong, L., Labat, D., Zhang, M., et al. (2020). Analyses of runoff and sediment transport and their drivers in a rare Earth mine drainage basin of the Yangtze River, China. *Water* 12 (8), 2283. doi:10.3390/w12082283

Liu, Y., Liu, Y., Chen, M., Labat, D., Li, Z., and Bian, Z. (2019). Characteristics and drivers of reference evapotranspiration in hilly regions in southern China. *Water* 11 (9), 1914. doi:10.3390/w11091914

Przeździecki, K., Zawadzki, J., Cieszewski, C., and Bettinger, P. (2017). Estimation of soil moisture across broad landscapes of Georgia and South Carolina using the triangle method applied to MODIS satellite imagery. *Silva Fenn. Hels.* 51 (4), 1683. doi:10.14214/sf.1683

Ranjan, A. K., and Gorai, A. K. (2022). Evaluating phenological trends of different vegetation types in response to climate change over the Rajmahal Hills in India during 2001-2019. *Remote Sens. Lett.* 13, 898–911. doi:10.1080/2150704x.2022.2106455

Ranjbar, A., Vali, A., Mokarram, M., and Taripanah, F. (2020). Investigating variations of vegetation: climatic, geological substrate, and topographic factors—a case study of kharestan area, fars Province, Iran. *Arab. J. Geosci.* 13 (14), 597. doi:10.1007/s12517-020-05615-0

Rey, D., Holman, I. P., Daccache, A., Morris, J., Weatherhead, E., and Knox, J. (2016). Modelling and mapping the economic value of supplemental irrigation in a humid climate. *Agric. water Manag.* 173, 13–22. doi:10.1016/j.agwat.2016.04.017

Sarfo, I., Shuoben, B., and Otchwemah, H. B. (2022). Validating local drivers influencing landuse cover change in southwestern Ghana: a mixed-method approach[J]. *Environ. Earth Sci.* 81 (14), 1–34.

Savitzky, A., and Golay, M. J. E. (1964). Smoothing and differentiation of data by simplified least squares procedures. *Anal. Chem.* 36 (8), 1627–1639. doi:10.1021/ac60214a047

Shobairi, S. O. R., Usoltsev, V. A., and Chasovskikh, V. P. (2018). Dynamic estimation model of vegetation fractional coverage and drivers. *Int. J. Adv. Appl. Sci.* 5 (3), 60–66. doi:10.21833/ijaas.2018.03.009

Sun, Y., Shan, M., Pei, X., Zhang, X. K., and Yang, Y. L. (2020). Assessment of the impacts of climate change and human activities on vegetation cover change in the Haihe River basin, China. *Phys. Chem. Earth Parts A/B/C* 115, 102834. doi:10.1016/j.pce.2019.102834

Tian, J., and Wang, Y. (2022). A study on the temporal and spatial changes of vegetation primary productivity in Ganjiang River basin based on the background of urbanization. *Territ. Nat. Resour. Study* 01, 83–87.

Wang, B., Xu, G., Li, P., Li, Z., Zhang, Y., Cheng, Y., et al. (2020). Vegetation dynamics and their relationships with climatic factors in the Qinling Mountains of China. *Ecol. Indic.* 108, 105719. doi:10.1016/j.ecolind.2019.105719

Wei, X., Wang, S., and Wang, Y. (2017). Spatial and temporal change of fractional vegetation cover in north-western China from 2000 to 2010. *Geol. J.* 53, 427–434. doi:10.1002/gj.3030

Wei, Z., Zhen, Y., Zhang, R., Du, L., Huang, Q., and Yang, S. (2022). Trends of vegetation dynamics and its response to climate change in Pearl River Basin of southwestern China. *Arab. J. Geosci.* 15 (5), 454–513. doi:10.1007/s12517-022-09556-8

Xiong, Y., Li, Y., Xiong, S., Wu, G., and Deng, O. (2021). Multi-scale spatial correlation between vegetation index and terrain attributes in a small watershed of the upper Minjiang River. *Ecol. Indic.* 126, 107610. doi:10.1016/j.ecolind.2021.107610

Zeng, Y., Hao, D., Huete, A., Dechant, B., Berry, J., Chen, J. M., et al. (2022). Optical vegetation indices for monitoring terrestrial ecosystems globally. *Nat. Rev. Earth Environ.* 3, 477–493. doi:10.1038/s43017-022-00298-5

Zhan, Y., Fan, J., Meng, T., Li, Z., Yan, Y., Huang, J., et al. (2021). Analysis on vegetation cover changes and the driving factors in the mid-lower reaches of Hanjiang River Basin between 2001 and 2015. *Open Geosci.* 13 (1), 675–689. doi:10.1515/geo-2020-0259

Zhang, B., Cui, L., Shi, J., and Wei, P. (2017). Vegetation dynamics and their response to climatic variability in China. *Adv. Meteorology* 2017, 1–10. doi:10.1155/2017/8282353

Zhang, M., Luo, G., Cao, X., Hamdi, R., Li, T., Cai, P., et al. (2019). Numerical simulation of the irrigation effects on surface fluxes and local climate in typical mountain-oasis-desert systems in the central asia arid area. *JGR. Atmos.* 124 (23), 12485–12506. doi:10.1029/2019jd030507

Zhang, M., Wang, J., and Li, S. (2019). Tempo-spatial changes and main anthropogenic influence factors of vegetation fractional coverage in a large-scale opencast coal mine area from 1992 to 2015. *J. Clean. Prod.* 232, 940–952. doi:10.1016/j.jclepro.2019.05.334

Zhang, S., Zhang, Y., and Wang, C. (2018). Vegetation coverage and its correlation with topographic factors in upstream watershed of Minjiang River. *Bull. Soil Water Conservation* 38 (1), 69–75.

frontiers | Frontiers in Earth Science

TYPE Original Research
PUBLISHED 13 January 2023
DOI 10.3389/feart.2022.1054394

OPEN ACCESS

EDITED BY
Haijun Qiu,
Northwest University, China

REVIEWED BY
Li Jun,
Chengdu University of Technology, China
Hui Wang,
China University of Mining and Technology, China

*CORRESPONDENCE
Gang Zhang,
zg@swust.edu.cn
Xingchang Chen,
mygeotech@126.com

SPECIALTY SECTION
This article was submitted to Geohazards and Georisks, a section of the journal Frontiers in Earth Science

RECEIVED 26 September 2022
ACCEPTED 31 October 2022
PUBLISHED 13 January 2023

CITATION
Zhang G, Tu F, Tang Y, Chen X, Xie K and Dai S (2023), Application of geophysical prospecting methods ERT and MASW in the landslide of Daofu County, China. *Front. Earth Sci.* 10:1054394. doi: 10.3389/feart.2022.1054394

Application of geophysical prospecting methods ERT and MASW in the landslide of Daofu County, China

Gang Zhang[1,2,3]*, Fangzhou Tu[1], Yushu Tang[1], Xingchang Chen[1,2,3]*, Kuilin Xie[1] and Sen Dai[1]

[1]School of Environment and Resource, Southwest University of Science and Technology, Mianyang, Sichuan, China, [2]Tianfu Institute of Research and Innovation, Southwest University of Science and Technology, Mianyang, Sichuan, China, [3]Mianyang S&T City Division, the National Remote Sensing Center of China, Mianyang, Sichuan, China

Natural disasters such as debris flow caused by earthquakes seriously threaten the local infrastructure and economy, as well as the lives of people in the area. As the material source of debris flow, it has significance to accurately and effectively study the underground structure of the landslide to prevent debris flow disasters. A landslide has a complex structural system, and its underground characteristics play an important role in its stability. The early identification of fracture surfaces and unstable bodies, and assessment of potential hazards are essential for prevention and protection. The research object of this paper is a landslide that occurred in Yige Village, Xianshui Town, Daofu County, which is on the Xianshui River Earthquake Zone, an area subject to frequent earthquakes. In western Sichuan, the frequent occurrence of landslides has caused considerable economic losses. Developing methods for efficient and accurate risk assessment is a top priority. The Daofu landslide is a typical example of a landslide directly threatening the road below and forming a debris flow channel. The lithology is composed of Jurassic sedimentary rocks, such as marl and clay, covered by limestone. In this study, we combined traditional methods (drilling and field investigation) with two geophysical techniques, multichannel analysis of surface waves (MASW) and electrical resistivity tomography (ERT) to effectively determine the electrical characteristics, velocity characteristics and spatial structure of the landslide. It is found that the buried depth of the sliding surface of the landslide is about 16–20 m. The sliding body above the sliding surface forms a low velocity and low resistivity Quaternary cover. The rock mass below the sliding surface is Triassic Zhuwo Formation sandstone and slate with high velocity and high resistivity. According to comprehensive analysis, the landslide lacks sufficient stability under rainstorm. Our study shows that the use of MASW and ERT can quickly and effectively characterize the subsurface of landslides to assess landslide risk and prevent debris flow hazards.

KEYWORDS

ERT, MASW, landslide, subsurface structure, integrated geophysics

1 Introduction

Daofu county, where this study was conducted, is located in the western of Sichuan Province and lies on the Xianshui River Earthquake Zone (Allen et al., 1991). Historically, this seismic zone has been characterized by frequent seismic activity, large magnitude and strong intensity of damage, which is the highest in Sichuan (Papadimitriou et al., 2004).

Landslide is one of the most common geological disasters in nature, and it is also one of the most dangerous natural phenomena (Petley and D., 2012). In a landslide, the soil or rock mass on a slope slides down as a whole or in a way along a certain weak surface or zone, affected by river scouring, rainwater soaking, groundwater movement, earthquake, or artificial slope cutting (Mekonnen et al.; Allen, 2017; Wang et al., 2022). Debris flow caused by landslide remains one of the greatest threats to the lives, properties, and infrastructure of residents during or following an earthquake. Landslides occur frequently in western Sichuan, examples include the Jiagu landslide in 2006 (Yin et al., 2010), the No. 2 landslide of the Sichuan Tibet Highway 102 landslide group in 2002 (Li et al., 2003), and the Qingning landslide in 2008 (Hu et al., 2008). It is a time and resource consuming task to thoroughly investigate them and fully prevent debris flow disasters before they occur. The estimation of landslide stability must consider the three-dimensional shape of the unstable body, especially the possible location of the slip surface associated with it (Yueping et al., 2013). Consequently, it is necessary and urgent to formulate and implement actions to accurately and quickly identify the underground characteristics of natural slopes.

When investigate landslide hazards, the distribution characteristics of the sliding surface, landslide zone, and geological stratification must be determined (Liu et al., 2022). The means of landslide identification and monitoring are extremely rich. In terms of exploration methods in geological engineering and geological disaster prevention, traditional geophysical prospecting methods, such as drilling and geological survey, have some shortcomings, such as high cost, insufficient information acquisition, and low efficiency (McCann and Forster, 1990). Geophysical exploration is an indirect observation method that uses the properties for known ore rock specimens, according to an established relationship (mathematical, physical model) and the principle of the corresponding method, to explain the parameter values observed in the field, and then the final results (physical parameters information of the corresponding profiles after inversion) are sufficient to illustrate the information on the subsurface structure of the exploration site. In recent years, the application of geophysics for landslide studies has widely increased, especially for near-surface exploration of landslide areas marked by a complex geological setting (Popescu et al., 2016).

Due to complex and changeable ground conditions and the influence of the working climate, the efficiency and results of different geophysical methods may significantly vary (Hussain et al., 2019; Qiu et al., 2022). A single geophysical exploration method usually only analyzes one kind of physical characteristic of the target medium, and the results of interpretation often have many solutions and other limitations (Cardarelli et al., 2013). Therefore, we use two geophysical methods to fully obtain the subsurface information of the landslide, and also to overcome the limitation of single method results interpretation, which can improve the efficiency of the work and the accuracy of the results (Schrott and Sass, 2008; Cardarelli et al., 2013).

In recent years, using comprehensive exploration geophysical methods to carry out geological exploration has gradually become the norm (Bedair et al., 2021). The two geophysical methods used in this paper are multichannel analysis of surface waves (MASW) and electrical resistivity tomography (ERT), both have proved to be the efficient methods for landslide research among all geophysical methods, (Loke et al., 2015; Khalil et al., 2017; Marciniak et al., 2021). We use a combination of these two methods because a single geophysical method is non-unique in the interpretation of the results, which limit us to make accurate judgments about the subsurface structural information obtained from the inversion, MASW is a good match for ERT in terms of detection depth, and the combination of their inversion results can provide more complete information to the subsurface structural of the landslide. To some extent, this can eliminate the impact of multiple solutions of a single geophysical method.

Many seismic methods have been proposed for near-surface characterization and measurement of shear wave velocity, using various test configurations, processing techniques, and inversion algorithms. The most widely used technologies are spectral analysis of surface waves (SASW) and multichannel analysis of surface waves (MASW). The MASW used in this paper is widely used due to its easy generation, detection (recording), and processing, as well as its effectiveness and reliability. This technology uses the propagation of surface waves (mainly Rayleigh) and is, therefore, based on the Rayleigh wave dispersion principle.

ERT has been widely used in various landslide studies under different geological environments (Dahlin, 2001; Jongmans and Garambois, 2007), it responds to changes in resistivity and is used to determine the distribution of resistivity of subsurface media. The resistivity of the subsurface medium varies over a wide range and the electrical conductivity of the medium is influenced by various factors such as mineral composition, soil porosity and water content, etc. ERT has the ability to efficiently respond to differences in the electrical conductivity of the medium (Colangelo et al., 2008; Falae et al., 2019; Wang et al., 2021).

The advantages of geophysical methods can almost entirely compensate for the disadvantages of conventional geotechnical engineering (Al-Heety et al., 2021). The joint application of MASW and ERT can solve the problems encountered in most

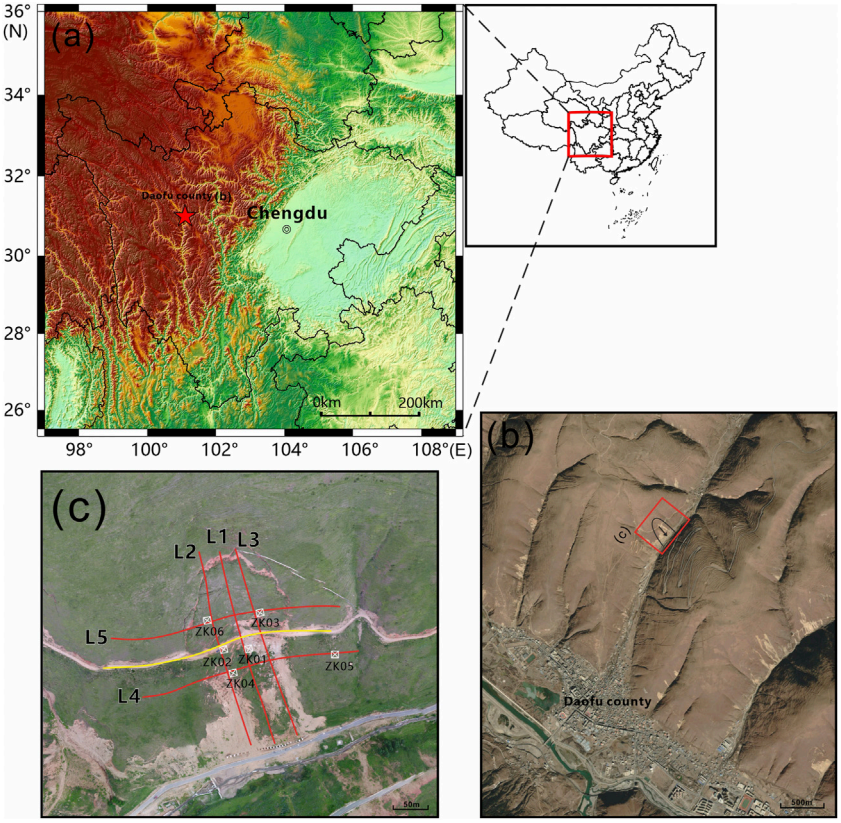

FIGURE 1
(A) Map of China, Location of Sichuan Province**(B)**Elevation topographic map of Sichuan Province and location of study area, the red five pointed star is the location of the study area**(C)**Aerial photo of the study area, survey line layout and borehole location.

shallow geophysical explorations. Specifically, MASW provides more useful shallow layer information, while ERT is more suitable for medium-thick layers (Rahimi et al., 2018). Therefore, the combination of the two methods is considered to be a valuable tool for pre-evaluating high-risk slip areas. However, more verification of the accuracy and applicability of this combined approach is required when detecting landslides. Therefore, in this study, based on using a combination of MASW and ERT to distinguish the underground structure of a clay slope, geological drilling was also conducted on five survey lines at the same time. Through the verification and calibration of borehole data and on-site observation, unstable bodies and potential slip surfaces can be fully inferred, which ensures the scientific basis and accuracy of the exploration results of the two geophysical methods.

The aim of this paper is to demonstrate the utility of the combination of geophysical methods (MASW and ERT) to characterize the subsoil media and potential risk areas for landslides in Daofu County. By analyzing the media and geophysical inversion below the surface and investigating the bedrock structures near the surface, such as cavities, soft soil, and weak zones, we can infer the possible location of the sliding surface, which can then make preparations for the prevention and control of debris flow disasters.

2 Research background

2.1 Study area

The landslide under study is in Yige village, Xianshui Town, Daofu county (Figure 1B). The geographical coordinates of the landslide are 101° 07′ 52″–101° 08′10″E and 31° 00′ 00”–31° 01′ 10″ N (Figure 1A). The landslide location is in the north of Daofu County, about 5 km away from city proper, it is an accumulation slope with a gradient of 40–60°, an elevation of 3,110–4000 m, and a relative elevation difference of about 900 m. At the foot of the slope is County Road 179 (Daofu county to Malkang, Figure 1C), which is also the direct threat of the landslide. The exploration area is located at the foot of the middle and low mountain formed due to tectonic erosion, with convenient transportation. A

total of five ERT survey lines, one MASW survey lines, and six geological boreholes were made (Figure 1C).

Daofu County belongs to the subtropical humid climate zone of the Qinghai Tibet Plateau, with a plateau valley cold temperate climate. Winters are cold, summers are mild, sunshine is sufficient, the frost-free period is short, the temperature difference between day and night is large, and the dry and wet seasons are distinct. According to the statistical data from Daofu County Meteorological Station from 1957 to 2007, the rainy season in Daofu County generally lasts from the first 10 days of June to the last 10 days of September, with an average annual precipitation of 458.6 mm, accounting for 74.2% of the annual total. The highest precipitation occurs in July, followed by August and October. The dry season generally lasts from the last 10 days of October to the last 10 days of March of the following year, with precipitation of only 21.3 mm, accounting for only 3.4% of the annual total. The maximum rainfall in 24 h is 49.7 mm,14.00 mm in 1 h, and 11.9 mm in 10 min. All these values exceed the critical rainfall values for forming debris flow and causing landslides.

Affected by the relative position relationship between landslide and Daofu County. When landslide occurs, it will directly threaten County Road 179 below the toe of the slope, and the landslide will wash into the ditch under the action of rain, causing the blockage of the debris flow ditch in the Daofu Valley, which can lead to the formation of a barrier lake that will seriously threaten the safety of the lives and property of the residents of Daofu County and various government agencies based at the gully mouth.

2.2 Stratum lithology in the study area

In order to better have the geological information of the study area, we made a detailed geological survey and six geological boreholes. According to geological drilling and geological survey results, the exposed strata in the survey area are mainly the Quaternary Holocene colluvium and slope deposit (Q_4^{cl+dl}), landslide accumulation (Q_4^{del}), alluvial proluvial (Q_3^{apl})strata of the Cenozoic, and the upper triassic Zhuwo formation (T_3zh), as follows:

2.2.1 Quaternary system (Q_4)

1) Holocene landslide deposit (Q_4^{del}): mainly distributed on the landslide mass. It is mostly composed of angular rock fragments in clay and loam, with a loose structure.
2) Holocene colluvium and diluvium (Q_4^{cl+dl}): mainly distributed on the hillsides on both sides of the valley. It is mostly composed of angular rock fragments contained in clay and loam, generally loose ~ slightly dense, and the accumulation thickness is large around Daofu county.
3) Pleistocene alluvium (Q_3^{apl}): distributed on the high-level platform on both sides of the river, it is composed of yellowish-gray clay, loam, coarse sand, gravelly sand, gravelly soil, pebble soil, and boulder soil, containing calcareous nodules and calcareous semi cementation. It has an obvious binary structure. The lithology is generally miscellaneous, with good compactness, and is generally slightly dense to medium dense.

2.2.2 Upper Triassic Zhuwo Formation (T_3zh)

It is gray to dark gray, thin, medium to thick, with a few massive fine-grained meta feldspathic quartz sandstones, meta lithic sandstones, meta fine sandstones, siltstones, locally meta tuffaceous sandstones, tuffs of this layer, and dark gray silty slate, spotted sericite slate, phyllite slate (or phyllite), dark gray to black-gray carbonaceous phyllite (or slate) are produced in an unequal thickness distribution. Sandstone and slate are interbedded, the attitude of the rock stratum is 55°∠ 45°, and the thickness ratio of the upper sandstone and slate is about 5:3; the middle part is of rhythmic interbedding with unequal thickness, which is often mixed with 1–2 layers of thick massive metasandstone with a thickness of tens of meters. The thickness ratio of sandstone to slate is about 1:1; there are more sandstones in the lower part, and sandstone and slate are produced in unequal thickness interbedding, with a thickness ratio of sandstone to slate of about 4:1.

2.3 Sample soil parameters

During the drilling activity, soil and rock samples from six boreholes were carefully collected and transported to the laboratory for measurement of their basic physical properties and mechanical parameters. According to this survey, six undisturbed samples (undisturbed soil samples) were collected by the static pressing method using a thin-walled soil sampler in the borehole. All samples were sealed with wax on-site, packed in special shockproof wooden boxes, and sent immediately to the Geotechnical Test Center. The accuracy of the test data met the requirements of this study. The specific parameters were comprehensively determined by laboratory tests of the rock and soil samples taken from the boreholes, empirical analogy, and the parameter inversion method, Table 1 and Table 2 show the physical and mechanical properties of soil samples obtained in the experiment.

As the original crushed stone composition in the soil mass is removed before the mechanical properties of the sliding zone soil are measured, the experimental data is different from the local empirical data and only serves as a reference in terms of a comprehensive value. Based on the geological drilling data, the mechanical parameters of the soil in the landslide area are calculated, and the corresponding geotechnical engineering soil mechanical information is obtained. The data in Table 1 can help us calculate the shear strength of the soil (Sharma and Bora, 2003; Tang et al., 2010), the data in Table 2 directly provides three

TABLE 1 Statistical table of soil mechanical parameters in landslide area.

Statistical table of mechanical performance parameters test results in landslide area (undisturbed soil)

Test number	Sampling depth(m)	Natural		Saturated	
		Cohesion	Internal friction angle	Cohesion	Internal friction angle
		c	φ	c	φ
		kPa	°	kPa	°
ZK01	0–14.0	14.60	24.60	10.80	19.10
ZK02	0–29.0	12.00	25.50	10.50	19.30
ZK03	0–17.0	14.00	24.90	9.80	18.60
ZK04	0–28.0	12.10	25.20	11.10	19.60
ZK05	0–14.0	12.60	25.40	9.30	20.70
ZK06	0–17.0	13.20	25.60	9.10	19.90
Number of statistical samples		6	6	6	6
Maximum		14.60	25.60	11.10	20.70
Minimum		12.00	24.60	9.10	18.60
Average value		13.08	25.20	10.10	19.53
Standard deviation		1.05	0.38	0.82	0.72
Coefficient of variation		0.08	0.02	0.08	0.04
Calculation process		2.45	2.45	2.45	2.45
		36.00	36.00	36.00	36.00
		0.70	0.70	0.70	0.70
		0.13	0.13	0.13	0.13
		0.07	0.01	0.07	0.03
Statistical correction coefficient		0.93	0.99	0.93	0.97
Standard value		12.22	24.88	9.42	18.94

proportional indicators of the sample soil (Jabro, 1992). Finally, combined with soil sample data,CD-test (consolidation drained test) is conducted, and the results provide strong material support for geophysical inversion interpretation. The above materials and experimental results were combined to conclude that the specimen soil is susceptible to shear failure under saturated conditions. This conclusion indicates that the landslide body in the study area has low shear strength and poor stability under heavy rainfall conditions.

3 Methodology and data

3.1 Methodology

Combining MASW and ERT surveys with geological drilling samples, we identified and studied the underground characteristics of landslides, especially the profiles of potentially unstable bodies and potential sliding surfaces, which are initially assumed to be fault or joint planes, and the interfaces between highly fractured rocks of topsoil or complete bedrock (Duc, 2013).

MASW method is a geophysical method to derive the velocity profile of underground shear wave based on the dispersion characteristics of Rayleigh wave in layered media. Rayleigh waves are surface waves that propagate along a free surface, such as a solid-air or solid-water interface. Relatively low velocity, low frequency and high amplitude are the characteristics of Rayleigh wave (Largo et al., 2021). It is the result of interference P-wave and SV-wave, corresponding to the vertical component and radial component of surface wave respectively. The amplitude of this wave motion decreases exponentially with depth and is confined to a vertical plane consistent with the wave propagation direction (Xia et al., 2004). The propagation velocity of surface wave is related to frequency, which is called dispersion (Park et al., 1999). Put it another way: assuming that the vertical velocity changes, surface wave has a different propagation velocity on each unique frequency component (Foti, 2005). The principle states that if there is a low-velocity capping layer or a layered medium on the surface,

TABLE 2 Statistical table of physical and mechanical parameters of landslide area.

Test type	Sample number	Natural		Saturated		Density		Proportion	Void ratio
Indoor test		Water content W (%)	Severe (KN/m3)	Water content W (%)	Severe (KN/m3)	Natural density (g/cm3)	Saturation density (g/cm3)	Gs	e0
	ZK01	21.70	18.84	25.05	20.40	1.82	1.98	1.98	0.68
	ZK02	23.60	19.23	25.52	20.31	1.86	1.97	1.97	0.69
	ZK03	20.30	18.74	21.36	20.70	1.81	2.01	2.01	0.58
	ZK04	21.00	18.13	22.55	20.40	1.85	1.98	1.98	0.61
	ZK05	23.80	19.54	25.49	20.31	1.79	1.97	1.97	0.69
	ZK06	18.70	19.52	20.58	20.89	1.89	2.03	2.03	0.56
Number of statistical samples	6.00	6.00	6.00	6.00	6.00	6.00	6.00	6.00	6.00
Maximum		23.80	19.52	25.52	20.89	1.89	2.03	2.03	0.69
Minimum		18.70	18.54	20.58	20.31	1.79	1.97	1.97	0.56
Average value		21.52	19.00	23.43	20.50	1.84	1.99	1.99	0.63
Standard deviation		1.96	0.36	2.21	0.24	0.04	0.02	0.02	0.06
Coefficient of variation		0.09	0.02	0.09	0.01	0.02	0.01	0.01	0.09
Calculation process		2.45	2.45	2.45	2.45	2.45	2.45	2.45	2.45
		36.00	36.00	36.00	36.00	36.00	36.00	36.00	36.00
		0.70	0.70	0.70	0.70	0.70	0.70	0.70	0.70
		0.13	0.13	0.13	0.13	0.13	0.13	0.13	0.13
		0.08	0.02	0.08	0.01	0.02	0.01	0.01	0.08
Statistical correction coefficient		0.92	0.98	0.92	0.99	0.98	0.99	0.99	0.92
Standard value		19.90	18.70	21.60	20.30	1.81	1.97	1.97	0.59

the Rayleigh wave will have a distinct "dispersion" characteristic, i.e., the different frequency harmonic components of the Rayleigh wave will propagate at different speeds. Through an effective inversion process, the dispersion curve can be inverted to obtain the one-dimensional (depth) shear wave velocity (Vs.) profile of the surveyed site and the final pseudo-two-dimensional section can then be obtained by combining multiple one-dimensional profiles (Zhang et al., 2004; Bensen et al., 2007; Ritzwoller et al., 2008). Compared to other geophysical methods, MASW has been proved to be a more effective method to reveal the nature of shallow underground (Anbazhagan and Sitharam, 2008).

ERT method is to use conventional resistivity measurement methods and high and new technologies such as resistivity imaging (C-T) to conduct high resolution and high efficiency electrical exploration (Huntley et al., 2019). It is performed by applying a constant current to the ground through two current electrodes and measuring the voltage difference generated across the two electrodes. From the current and voltage values, an apparent resistivity value is calculated. The basic principle is to study the distribution law of conductive current of geological body in underground half space under the action of external electric field based on the difference of conductivity of underground medium (Auken et al., 2006; Tsai et al., 2021). The features are high horizontal resolution and vertical resolution. The electrodes are laid at one time, reducing the faults and interference caused by electrode setting; At the same time, more abundant geological information about geoelectric section can be obtained (Abdullah et al., 2018). The main drawback of the ERT method is the extensive overlap of the subsurface resistivity ranges of different geological units. For example, the resistivity of chalk loam is 30–100 Ω, mudstone is 105 Ω, and limestone is 100–105 Ω. The resistivity depends to a large extent on the porosity and water content (Sass et al., 2008).

3.2 Data acquisition

To investigate the underground structure and obtain the input data of the Daofu landslide, we completed a total five ERT (L1 to L5) and one MASW survey lines of measurement in June 2022. As seismic methods use the same lens collection method, multiple geophysical methods aimed at collecting datasets are cost-effective. These survey lines cover the landslide area so that the landslide mass is in the middle of them. MASW survey line is located in the middle of landslide (Figure 1C, yellow line).

The technical parameters adopted for ERT method detection are as follows: the electrodes are arranged in a Wenner device, the electrode spacing is 5m, the minimum isolation coefficient

Nmin=1, the maximum isolation coefficient Nmax=19, the power supply time is 2s, the number of electrodes is 60, and the maximum detection depth is about 40 m. In this structure, the divergence between current electrode pairs (AB) is the same as that between potential electrode pairs (MN), and is usually an integral multiple. Wenner structure is very sensitive to the horizontal changes and resistivity changes between each dipole and electrode, so it can well plot vertical structures such as cavities. To obtain a dense dataset, so the geophone and electrode spacing was set to 5 m. This electrode spacing is ideal because it allows the use of gradient arrays for surveys up to 40 m deep. In the Daofu country landslide, the two-dimensional mapping of the multi-electrode resistivity method was carried out by applying a constant current to the ground through two current electrodes and measuring the voltage difference between the two electrodes.

The device used in the MASW study was an SWS-5 multi-wave train digital image engineering exploration and engineering detection device. This is a high-performance and multi-functional geotechnical engineering investigation and detection device. An active artificial source multichannel transient surface wave survey was adopted for this study, with an offset and track spacing of 5 m. It is symmetrically arranged with the test point as the center, and 24 channel geophone receiving mode is selected. The frequency of the detector is 40Hz, the sampling interval time is 0.5 ms, and the recording length is 1.5s.

3.3 Data processing

Code and algorithms within the RES2DINV software package developed by Aarhus GeoSoftware (Denmark) were used to invert the resistivity datasets on all profiles collected. By eliminating bad data points, terrain positioning, root mean square convergence constraints, least squares inversion, and robust smoothing constraints, two-dimensional resistivity images were obtained (Loke, 1996). The inherent error (RMS) of the two-dimensional inversion model ranged from 4.3% to 8.3%, and the results were good and reliable. However, it was found that as the surface soil of the landslide at the research site is dry and loose, this led to poor contact of some electrodes, resulting in noisy data in some areas and high error, but this did not seriously affect the data interpretation.

MASW data processing uses the frequency velocity (F-P) method was used to calculate the anti-dispersion curve to determine the variation of shear wave velocity profile with depth (Grandjean et al., 2011; Lima Júnior et al., 2012). After assembling multiple 1D pseudo-profiles, the final shear wave velocity-depth two-dimensional pseudo-profile is obtained.

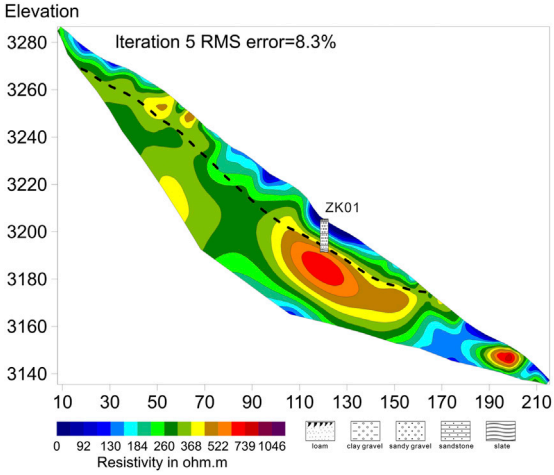

FIGURE 2
Inversion results of L1 survey line.

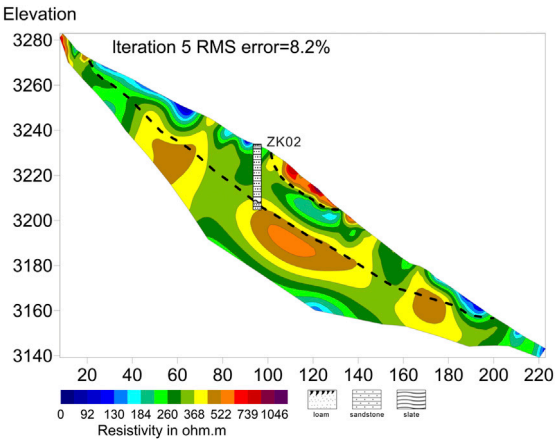

FIGURE 3
Inversion results of L2 survey line.

4 Results and discussion

4.1 Interpretation of ERT inversion results

Figures 2–6 show the underground information obtained from the ERT profiles, corresponding to the five measuring lines L1, L2, L3, L4, and L5, respectively. Besides, the location, depth and lithology information of borehole ZK01-06 are also marked in the figure. The deepest measurement depth of the borehole is about 30 m underground.

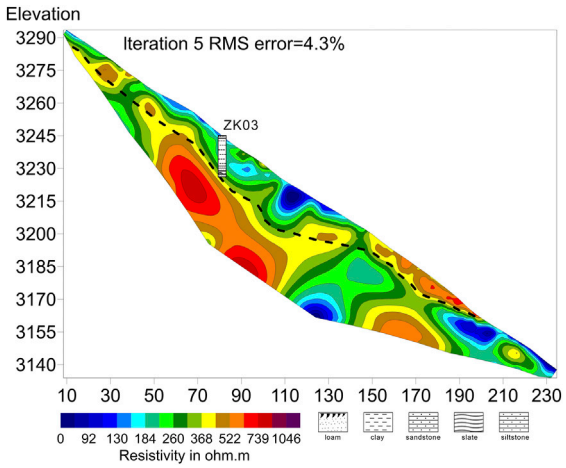

FIGURE 4
Inversion results of L3 survey line.

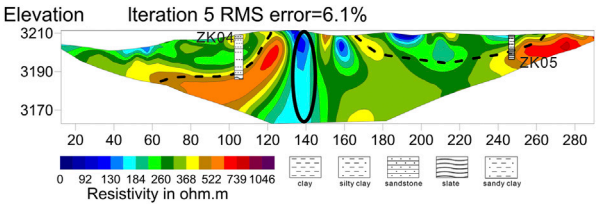

FIGURE 5
Inversion results of L4 survey line.

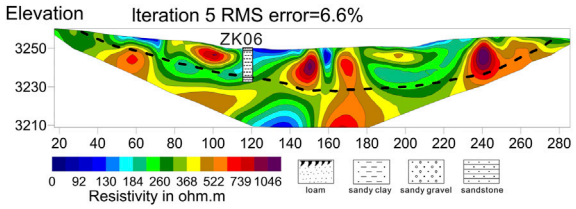

FIGURE 6
Inversion results of L5 survey line.

The electrical structure model of each section obtained in this study can provide the corresponding formation lithology information, and also reveal the morphological characteristics of geoelectric section or stratum to a certain extent, which provides an effective basis for the structure and stability evaluation of landslide.

From the inversion electrical structure model (Figures 2–6), it can be seen that the study area has an overall low resistivity-high resistivity electrical characteristic from shallow to deep. The electrical properties of shallow layers are generally characterized by low resistivity, mainly concentrated in the landslide surface depth of about 5 m–30 m; the middle and deep electrical properties are mainly characterized by medium and high resistivity, while there are banded or massive abnormal bodies with low resistivity locally in the section. Combined with the information from the borehole, the lithology from the surface to the depth is mainly sandy clay layer of the Quaternary—sand and gravel layer—bedrock (sandstone and slate) of the Upper Triassic Zhuwo Formation. The location where there is obvious difference or change in electrical properties is usually the place that reflects the boundary of electrical media. Obviously, as shown in the figure, there is a significant interface of electrical properties difference between shallow low resistivity and deep high resistivity. Combined with the borehole data, it can be known that this interface is the stratum contact surface of the Quaternary system and Triassic system. Therefore, we infer this stratigraphic interface as the main sliding surface of the landslide (as shown by the dotted line in the figure), and consider this landslide as a bedding landslide.

The low resistivity anomaly in the profile is divided into two parts by taking the sliding surface as the boundary, the low-resistivity anomalies above the sliding surface are mainly caused by the water-bearing clay and conglomerate debris with loose structure of the Quaternary System, while the low-resistivity anomalies below the sliding surface are presumed to be caused by the water-filled cracks formed by a series of tensile shear damage to the underlying bedrock during the landslide deformation. In addition, the section shows a typical electrical gradient zone between the high resistivity layer and the overlying rock and soil mass, and the high resistivity part of the gradient zone is sandstone and slate of the Upper Triassic Zhuwo Formation according to the borehole information.

By analyzing the inversion results of L1 survey line (Figure 2), The surface shallow layer generally presents low resistivity characteristics (<368 Ω·m), which is related to the overburden bond layer composed of silty clay and granular gravel. The high resistivity zone is located directly below well ZK01 and is approximately 18–28 m thick, and the borehole data indicate that the high resistivity anomaly in this block is derived from the metamorphic rocks of the Upper Triassic Zhuwo Formation. Moreover, There is a low resistivity abnormal zone at the lower edge of the section, which divides two high resistivity abnormal bodies. It is speculated that the abnormal zone is caused by the shear failure of the underlying rock strata caused by the landslide deformation and the water filling in the cracks. Similar situations can be seen in the inversion results of L3 lines (Figure 4). On the other hand, in Figures 2, 3, it can be seen that the local high resistivity anomaly occurs on the shallow surface of the landslide. It is presumed to be the residue formed after denudation of high resistivity rock mass which was transported to here.

FIGURE 7
Geological drilling sample (ZK05,ZK06).

The inversion result of L4 (Figure 5) shows that in the middle section (horizontal distance 120–140 m), there is a longitudinal low-resistivity abnormal zone running up and down the section. We speculate that the cause is surface water infiltration in the cracks caused by the compression deformation of the landslide front.

Figure 6 shows the inversion results of L5. There are many areas with high resistivity anomalies near the shallow surface. There are some abnormal areas of high resistivity in the shallow part of the landslide, and the electrical transition between these high-resistance blocks and the deep high-resistance bodies is natural and interconnected. From the surface geological survey, it is known that there is a reverse fault near the landslide. Therefore, we speculate that this phenomenon is caused by the fact that under the control of the fault structure in this area, the original underlying bedrock invades the landslide accumulation body under the action of compressive stress and shear stress. This interpretation is also applicable to the interpretation of high resistivity areas in the landslide body of Line L2-4 in Figures 3–5.

After obtaining all the results, by comparing the ERT electrical results with the borehole data (Figure 7, representative geological borehole sampling images, ZK05 and ZK06), we concluded that the electrical structure was in good agreement with the borehole data. The inversion structure of three longitudinal and two transverse survey lines at the same place of coincidence also shows the accuracy of the underground electrical structure obtained from the study. In order to further verify the validity of the above results and conduct a more comprehensive landslide risk assessment, we conducted a MASW survey.

4.2 Interpretation of MASW inversion results

Figure 8 shows the MASW inversion results, the Vs. model inversion results of the MASW transverse section along the survey line. The shear wave velocity ranges from 309 m/s to 809 m/s. From shallow layer to deep layer, the shear wave velocity generally presents the characteristics of low-velocity, medium-velocity and high-velocity structure, which reflects the changes of the composition, structure and rock strength of the underground media of the landslide to a certain extent.

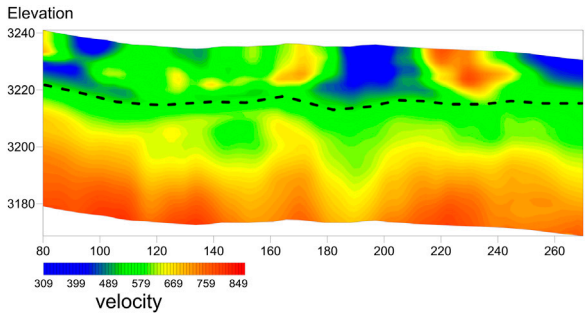

FIGURE 8
Inversion results of MASW survey line.

As can be seen from the figure, there are three low-velocity abnormal areas (<400 m/s) above the elevation of 3220 m, corresponding to the low-resistivity abnormal areas shown in the ERT section and the landslide deposits with low strength in the borehole data. Besides, there are two high-velocity abnormal areas (>669 m/s) on the surface at the distance of 170 m and 230 m. Similarly, we believe that this is related to the upward invasion of the underlying bedrock to the landslide under the action of tectonic stress, which is mainly caused by metamorphic rocks with high strength. In addition, part of the 486–669 m/s wave velocity at the surface may be related to less weathering/fracture of the surface bedrock and the crystalline gypsum in the mudstone interbedding. The dotted line in the figure shows the boundary position between the shallow high-speed layer

and the low-speed layer on the surface, and the interface is presumed to be a landslide surface. On the other hand, we can see from the diagram, below the sliding surface of high velocity layer exist evident in the interface, we believe that in the process of landslide movement under the cover of the bedrock under stress produced in the bedrock fissure deformation or damage, caused the top velocity is relatively low, bedrock lower due to relatively intact rock mass, the strength is larger, Therefore, the shear wave velocity is higher.

5 Conclusion

In this study, a total of 5 ERT survey lines and 1 MASW survey line were completed to completely cover the target landslide area. The electrical structure of the five profiles was studied by inversion calculations using the least squares method, and the results showed that the overall electrical characteristics of the study area ranged from low resistivity to high resistivity from shallow to deep. The sliding surface is roughly located on the interface between the high resistivity and low resistivity areas. The shallow low-resistivity area above the slip surface is composed of the Quaternary accumulation; the deeper high-resistivity area below the slip surface is composed of the Upper Triassic Zhuwo Formation. Through velocity structure model obtained by inversion of MASW data, the results show that the study area has a low-moderate-high velocity structure from shallow to deep. The shallow low-velocity area is composed of loose overburden, and the medium-velocity zone is composed of cracked bedrock, while the high-speed area is composed of more complete bedrock and slate. Furthermore, the structural characteristics of the landslide in the study area are determined by combining the borehole data and the structural characteristics of the two models. The main sliding surface of the landslide is the interface between the Quaternary overburden layer and the sandstone/slab layer of the Triassic Zhuwo Formation, which belongs to the bedding landslide. The average buried depth of the sliding surface is about 16–20 m. The area above the sliding surface has the characteristics of low speed and low resistance. The sliding surface is characterized by high speed and high resistance, and the sliding surface is located at the interface between the low speed zone and the high speed zone.

Based on the study results, we believe that combining MASW and ERT for landslide exploration to obtain subsurface information is an effective method. This is also a more efficient and economical solution for debris flow prevention and management than traditional exploration methods such as geological boreholes.

Data availability statement

The original contributions presented in the study are included in the article/Supplementary Material, further inquiries can be directed to the corresponding author.

Author contributions

GZ contributed to the conception of the study. GZ performed the experiment. FT contributed significantly to analysis and manuscript preparation. FT performed the data analyses and wrote the manuscript. YT helped modify the pictures. YT improved the paper contents. XC helped perform the analysis with constructive discussions. KX provided the soil sample experimental data. SD revised paper contents.

Funding

This paper was supported by The Second Tibetan Plateau Scientific Expedition and Research (STEP) program (Grant No. 2019QZKK0902).

Conflict of interest

The authors declare that the research was conducted in the absence of any commercial or financial relationships that could be construed as a potential conflict of interest.

Publisher's note

References

Abdullah, F. M., Loke, M. H., Nawawi, M., and Abdullah, K. (2018). Assessing the reliability and performance of optimized and conventional resistivity arrays for shallow subsurface investigations. *J. Appl. Geophys.* 155, 155237–155245. doi:10.1016/j.jappgeo.2018.06.018

AL-Heety, A. J., Hassouneh, M., and Abdullah, F. M. (2021). Application of MASW and ERT methods for geotechnical site characterization: A case study for roads construction and infrastructure assessment in abu dhabi, uae. *J. Appl. Geophys.* 193104408, 104408. doi:10.1016/j.jappgeo.2021.104408

Allen, C. R., Zhuoli, L., Hong, Q., Xueze, W., Huawei, Z., and Weishi, H. (1991). Field study of a highly active fault zone: The Xianshuihe fault of southwestern China. *Geol. Soc. Am. Bull.* 103 (9), 1178–1199. doi:10.1130/0016-7606(1991)103<1178:fsoaha>2.3.co;2

Allen, P. A. (2017).Cambridge, UK *Sediment routing systems: The fate of sediment from source to sink*. Cambridge University Press.

Anbazhagan, P., and Sitharam, T. G. (2008). Mapping of average shear wave velocity for Bangalore region: A case study. *J. Environ. Eng. Geophys.* 13 (2), 69–84. doi:10.2113/jeeg13.2.69

Auken, E., Pellerin, L., Christensen, N. B., and Sørensen, K. (2006). A survey of current trends in near-surface electrical and electromagnetic methods. *Geophysics* 71, G249–G260. doi:10.1190/1.2335575

Bedair, S., Abdel-Raouf, O., and Meneisy, A. M. (2021). Combined GPR, DC resistivity, and hydrogeochemical data for hydrogeological exploration: A case study at the red sea coast. *Arab. J. Geosci.* 14 (8), 727–815. doi:10.1007/s12517-021-07039-w

Bensen, G. D., Ritzwoller, M. H., Barmin, M. P., Levshin, A. L., Lin, F., Moschetti, M. P., et al. (2007). Processing seismic ambient noise data to obtain reliable broad-band surface wave dispersion measurements. *Geophys. J. Int.* 169 (3), 1239–1260. doi:10.1111/j.1365-246x.2007.03374.x

Cardarelli, E., Cercato, M., De Donno, G., and Di Filippo, G. (2013). Detection and imaging of piping sinkholes by integrated geophysical methods. *Near Surf. Geophys.* 12 (3), 439–450. doi:10.3997/1873-0604.2013051

Colangelo, G., Lapenna, V., Loperte, A., Perrone, A., and Telesca, L. (2008). 2D electrical resistivity tomographies for investigating recent activation landslides in Basilicata Region (Southern Italy). *Ann. Geophys.* 51 (1), 275–285.

Dahlin, T. (2001). The development of DC resistivity imaging techniques. *Comput. Geosciences* 27 (9), 1019–1029. doi:10.1016/s0098-3004(00)00160-6

Duc, D. M. (2013). Rainfall-triggered large landslides on 15 december 2005 in van canh district, binh dinh province, vietnam. *Landslides* 10 (2), 219–230. doi:10.1007/s10346-012-0362-4

Falae, P. O., Kanungo, D. P., Chauhan, P. K. S., and Dash, R. K. (2019). Electrical resistivity tomography (ERT) based subsurface characterisation of Pakhi Landslide, Garhwal Himalayas, India. *Environ. Earth Sci.* 78 (14), 430–518. doi:10.1007/s12665-019-8430-x

Foti, S. (2005).Vienna, Austria. Springer, 47–71.Surface wave testing for geotechnical characterization", *Surface waves in geomechanics, direct inverse Model. soils rocks*

Grandjean, G., Gourry, J., Sanchez, O., Bitri, A., and Garambois, S. (2011). Structural study of the Ballandaz landslide (French Alps) using geophysical imagery. *J. Appl. Geophys.* 75 (3), 531–542. doi:10.1016/j.jappgeo.2011.07.008

Hu, R., Ming, Z., and Cui, F. (2008). Analysis of basic characteristics and forming mechanism of Qingning landslide, Daxian, Sichuan Province, China. *Earth Sci. Front.* 15 (4), 250–257. doi:10.3321/j.issn:1005-2321.2008.04.030

Huntley, D., Bobrowsky, P., Hendry, M., Macciotta, R., Elwood, D., Sattler, K., et al. (2019). Application of multi-dimensional electrical resistivity tomography datasets to investigate a very slow-moving landslide near Ashcroft, British Columbia, Canada. *Landslides* 16 (5), 1033–1042. doi:10.1007/s10346-019-01147-1

Hussain, Y., Hussain, S. M., Martino, S., Cardenas-Soto, M., Hamza, O., Rodriguez-Rebolledo, J. F., et al. (2019). Typological analysis of slidequakes emitted from landslides: Experiments on an expander body pile and sobradinho landslide (brasilia, Brazil). *Rem. Int. Eng. J.* 72, 72453–72460. doi:10.1590/0370-44672018720110

Jabro, J. D. (1992). Estimation of saturated hydraulic conductivity of soils from particle size distribution and bulk density data. *Trans. ASAE* 35 (2), 557–560. doi:10.13031/2013.28633

Jongmans, D., and Garambois, S. (2007). Geophysical investigation of landslides: A review. *Bull. Société géologique Fr.* 178 (2), 101–112. doi:10.2113/gssgfbull.178.2.101

Khalil, A. E., Nawawi, M., Arifin, M. H., Abdullah, F. M., Kayode, J. S., Usman, N., et al. (2017). Soil investigation at wet world hot spring complex for future development using active multichannel analysis of surface waves. *Sains Malays.* 46 (4), 537–543. doi:10.17576/jsm-2017-4604-04

Largo, D., Hidalgo, C., and Olarte, J. (2021). Bristol, UK"Comparison of invasive and non-invasive methods in site response, case study: Soil deposits of La estrella, *IOP conference series: Earth and environmental science* (IOP Publishing), 012119.

Li, T. L., Zhao, J. L., and Li, P. (2003). Analysis on the characteristics and stability of the No. 2 landslide of 102 landslide group on Sichuan-Tibet Highway. *J. Catastrophol* 18 (4), 40–45.

Lima Júnior, S. B., Prado, R. L., and Mendes, R. M. (2012). Brazil.*Application of multichannel analysis of surface waves method (MASW) in an area susceptible to landslide at Ubatuba City*, Revista Brasileira de Geografia.

Liu, Z., Qiu, H., Zhu, Y., Liu, Y., Yang, D., Ma, S., et al. (2022). Efficient identification and monitoring of landslides by time-series InSAR combining single-and multi-look phases. *Remote Sens.* 14 (4), 1026. doi:10.3390/rs14041026

Loke, M. H. (1996).TheNetherlands "Least-squares inversion of large 3D resistivity data sets using auxiliary storage," in *58th EAGE conference and exhibition* (European Association of Geoscientists & Engineers), 48–00591.

Loke, M. H., Wilkinson, P. B., and Chambers, J. E. (2015).TheNetherlands "Rapid inversion of data from 2-D and from 3-D resistivity surveys with shifted electrodes, *Near surface geoscience 2015-21st European meeting of environmental and engineering geophysics* (European Association of Geoscientists & Engineers), 1–5.

Marciniak, A., Kowalczyk, S., Gontar, T., Owoc, B., Nawrot, A., Luks, B., et al. (2021). Integrated geophysical imaging of a mountain landslide–a case study from the Outer Carpathians, Poland. *J. Appl. Geophys.* 191104364, 104364. doi:10.1016/j.jappgeo.2021.104364

Mccann, D. M., and Forster, A. (1990). Reconnaissance geophysical methods in landslide investigations. *Eng. Geol.* 29 (1), 59–78. doi:10.1016/0013-7952(90)90082-c

Mekonnen, A. A., Raghuvanshi, T. K., Suryabhagavan, K. V., and Kassawmar, T.Gis-based landslide susceptibility zonation and risk assessment in complex landscape, *A Case Beshilo Watershed, North. Ethiop.*, 100586, 8,2022

Papadimitriou, E., Wen, X., Karakostas, V., and Jin, X. (2004). Earthquake triggering along the Xianshuihe fault zone of Western Sichuan, China. *Pure Appl. Geophys.* 161 (8), 1683–1707. doi:10.1007/s00024-003-2471-4

Park, C. B., Miller, R. D., and Xia, J. (1999). Multichannel analysis of surface waves. *Geophysics* 64 (3), 800–808. doi:10.1190/1.1444590

Petley &, D. (2012). Global patterns of loss of life from landslides. *Geology* 40 (10), 927–930. doi:10.1130/g33217.1

Popescu, M., Serban, R., Urdea, P., and Onaca, A. L. (2016). Conventional geophysical surveys for landslide investigations: Two case studies from Romania. *Carpathian J. earth Environ. Sci.* 11 (1), 281–292.

Qiu, H., Zhu, Y., Zhou, W., Sun, H., He, J., and Liu, Z. (2022). Influence of DEM resolution on landslide simulation performance based on the Scoops3D model. *Geomatics, Nat. Hazards Risk* 13 (1), 1663–1681. doi:10.1080/19475705.2022.2097451

Rahimi, S., Wood, C. M., Coker, F., Moody, T., Bernhardt-Barry, M., and Kouchaki, B. M. (2018). The combined use of MASW and resistivity surveys for levee assessment: A case study of the melvin price reach of the wood river levee. *Eng. Geol.* 241, 24111–24124. doi:10.1016/j.enggeo.2018.05.009

Ritzwoller, M. H., Yang, Y., and Pasyanos, M. E. (2008).Boulder, CO, USA *Short-period surface-wave dispersion from ambient noise tomography in western China*. Colorado univ at boulder.

Sass, O., Bell, R., and Glade, T. (2008). Comparison of GPR, 2D-resistivity and traditional techniques for the subsurface exploration of the Öschingen landslide, Swabian Alb (Germany). *Geomorphology* 93 (1-2), 89–103. doi:10.1016/j.geomorph.2006.12.019

Schrott, L., and Sass, O. (2008). Application of field geophysics in geomorphology: Advances and limitations exemplified by case studies. *Geomorphology* 93 (1-2), 55–73. doi:10.1016/j.geomorph.2006.12.024

Sharma, B., and Bora, P. K. (2003). Plastic limit, liquid limit and undrained shear strength of soil-reappraisal. *J. Geotech. Geoenviron. Eng.* 129 (8), 774–777. doi:10.1061/(asce)1090-0241(2003)129:8(774)

Tang, C., Shi, B., and Zhao, L. (2010). Interfacial shear strength of fiber reinforced soil. *Geotext. Geomembranes* 28 (1), 54–62. doi:10.1016/j.geotexmem.2009.10.001

Tsai, W., Chen, C., Chiang, C., Chen, P., Kuo, C., Wang, K., et al. (2021). Electrical resistivity tomography (ERT) monitoring for landslides: Case study in the lantai area, yilan taiping mountain, northeast taiwan. *Front. Earth Sci. (Lausanne).* 929. doi:10.3389/feart.2021.737271

Wang, B., Wang, J., Tian, G., Shi, Z., and Zhao, W. (2021). Three-dimensional high-density resistivity measurement method based on electrode random distribution and exploration system.WO/2019/200905.

Wang, L., Qiu, H., Zhou, W., Zhu, Y., Liu, Z., Ma, S., et al. (2022). The post-failure spatiotemporal deformation of certain translational landslides may follow the pre-failure pattern. *Remote Sens.* 14 (10), 2333. doi:10.3390/rs14102333

Xia, J., Miller, R. D., Park, C. B., Ivanov, J., Tian, G., and Chen, C. (2004). Utilization of high-frequency Rayleigh waves in near-surface geophysics. *Lead. Edge* 23 (8), 753–759. doi:10.1190/1.1786895

Yin, Y., Zheng, W., Liu, Y., Zhang, J., and Li, X. (2010). Integration of GPS with InSAR to monitoring of the jiaju landslide in sichuan, China. *Landslides* 7 (3), 359–365. doi:10.1007/s10346-010-0225-9

Yueping, Y., Chuanzheng, L., Hongqi, C., Jian, R., and Chuanbing, Z. (2013). Investigation on catastrophic landslide of january 11, 2013 at zhaojiagou, zhenxiong county, yunnan province. *J. Eng. Mater.* 21 (1), 6–15.

Zhang, S. X., Chan, L. S., and Xia, J. (2004). The selection of field acquisition parameters for dispersion images from multichannel surface wave data. *Pure Appl. Geophys.* 161 (1), 185–201. doi:10.1007/s00024-003-2428-7

frontiers | Frontiers in Earth Science

TYPE Original Research
PUBLISHED 16 January 2023
DOI 10.3389/feart.2023.1122562

OPEN ACCESS

EDITED BY
Haijun Qiu,
Northwest University, China

REVIEWED BY
Linwei Li,
Guizhou University, China
Jie Dou,
China University of Geosciences Wuhan, China

*CORRESPONDENCE
Anle Zhang,
1548104595@qq.com
Shufeng Wang,
422530802@qq.com

SPECIALTY SECTION
This article was submitted to Geohazards and Georisks, a section of the journal Frontiers in Earth Science

RECEIVED 13 December 2022
ACCEPTED 04 January 2023
PUBLISHED 16 January 2023

CITATION
Dai Z, Zhang A, Wang S, Fu X, Yang L, Jiang X and Wang H (2023), The development characteristics and mechanisms of the Xigou debris flow in the Three Gorges Reservoir Region. *Front. Earth Sci.* 11:1122562. doi: 10.3389/feart.2023.1122562

The development characteristics and mechanisms of the Xigou debris flow in the Three Gorges Reservoir Region

Zhenwei Dai [1], Anle Zhang [2]*, Shufeng Wang [1]*, Xiaolin Fu [1], Longwei Yang [3], Xiannian Jiang [4] and Heng Wang [4]

[1]Wuhan Center, China Geological Survey, (Central South China Innovation Center for Geosciences), Wuhan, Hubei, China, [2]College of Civil Engineering and Architecture, China Three Gorges University, Yichang, Hubei, China, [3]Wuhan Design and Research Institute Co., Ltd., of China Coal Technology and Engineering Group, Wuhan, Hubei, China, [4]No. 208 Hydrogeology and Engineering Geology Team of Chongqing Bureau of Geology and Minerals Exploration, Chongqing, China

Debris flow is a common geological hazard in mountainous areas of China, often causing secondary disasters and seriously threatening residents and infrastructure. This paper uses the Xigou debris flow in the Three Gorges Reservoir Region (TGRR) as an example case study, the development characteristics and initiation pattern of which were analyzed based on field investigation. The disaster dynamics software DAN-W was then used to simulate the entire initiation-movement-accumulation process of the debris flow and conduct the debris flow dynamics analysis. The paper also simulated and predicted the movements of landslides in the formation area of a debris flow after its initiation. The results show that the movement duration of the Xigou debris flow was approximately 40 s, the maximum velocity was 37.1 m/s, the maximum thickness of the accumulation was 18.7 m, and the farthest movement distance was 930 m, which are consistent with the field investigation. When the volumes of landslide transformed into a new source material of debris flow are 5×10^4, 10×10^4, 15×10^4, 20×10^4, and 26×10^4 m^3, the movement distances of the debris flows are 250, 280, 300, 340, and 375 m, respectively. When the volume of the source material exceeds 20×10^4 m^3, debris flow movement can seriously impact the residential houses at the entrance of the gully. This paper can provide a scientific basis for the prevention and mitigation of the Xigou debris flow.

KEYWORDS

DAN-W, debris flow, development characteristics, disaster mechanism, the three gorges reservoir region

1 Introduction

A debris flow is an extremely fast torrent (solid-liquid two-phase flow) that forms in deep gullies or ravines (Hungr et al., 2001). The Three Gorges Reservoir Region (TGRR) is an area that witnesses frequent debris flow of multiple source types, large material volumes, severe climatic conditions, and intense human engineering activities and therefore possesses the conditions for macro and giant debris flow outbreaks (Zhang et al., 2021; Tang et al., 2015). The TGRR has a relatively more concentrated population following the resettlement project, which will lead to substantial losses, in both lives and property, in the event of a debris flow outbreak in the settlement areas.

As debris flow disasters continue to occur, methods to prevent or mitigate these disasters have become an urgent issue. Therefore, some experts and scholars have sought to better understand debris flows and reduce the damage they cause (Cui et al., 2011; Dowling and Santi, 2014;

Nocentini et al., 2015; Zhang and Matsushima, 2018; Hu et al., 2019; Lee et al., 2020; Wang et al., 2022). In these studies, the reliability of numerical simulation methods has been demonstrated through back analyses of landslide and debris flow cases. Non-etheless, the selection of suitable rheological models and parameters is still the main challenge for the predictive analysis of debris flow movement characteristics. To this end, back analysis of historical hazard cases with similar damage types is crucial, as successful back analysis can be used to correct models and improve prediction accuracy, and provide rheological models and parameters that are suitable for potential landslide and debris flow predictive analysis (Xing et al., 2014). Thus, more accurate prediction and assessment of landslide and debris flow can be carried out (Chang et al., 2019; Dou et al., 2019; Dou et al., 2020; Zhao et al., 2021; Liu et al., 2022; Yin et al., 2022).

With the difficulties inherent in model experiments and field observation, numerical simulation is gradually becoming an important approach to studying debris flows. Advances in numerical computation of debris flows have provided a number of different models to describe debris flow movements, including continuum medium method, discrete medium method, and mixed medium method based on the descriptions of the constituent materials and movements (Hu et al., 2012). The continuum medium model assumes a continuous and void-free distribution of the debris flow body in space and can be primarily classified into one-fluid and multifluid models. The discrete medium model reduces the debris flow into a system consisting of a large number of material particles of a certain size, and the simplest discrete medium model is the discrete element method (DEM) model. The mixed media model describes the movements of the liquid and solid phases of a debris flow in a continuum and a discrete media model, respectively, and is the model that can best reflect the physical nature of a debris flow. The main numerical methods commonly used in debris flow numerical calculations are the finite element method (FEM), finite volume method (FVM), finite difference method (FDM), Boltzmann method (LBM), and smoothed particle hydrodynamics (SPH) method (Wang and yao, 2007; Hu et al., 2014; Qiu et al., 2022). Hungr and Evans (2004) developed the dynamic simulation software DAN-W based on the Lagrangian analytic solution of the Saint-Venant equations and used different rheological models to perform back analysis of the debris flow movement and accumulation process; the results showed that the frictional and Voellmy rheological models are more applicable for debris flow simulation and analysis.

On 18 June 2018, the Xigou debris flow occurred in Wushan County, Chongqing (located at 31°09′16″N, 109°58′34″E), burying the buildings at the entrance of gully and damaging the road, directly threatening 195 households and 773 people living. The analysis of the mechanism and development characteristics of the debris flow is of great significance to the follow-up preventing work. In this paper, the development characteristics of the Xigou debris flow were studied through detailed field investigation. The geological dynamics model DAN-W was used to simulate the initiation-movement-accumulation process of the debris flow and to analyze the mechanism and kinematic characteristics of the debris flow. The best combination of rheological models and parameters was obtained through the trial-error method to improve the accuracy of debris flow dynamics analysis, providing a reliable reference for disaster prevention and mitigation of the same debris flow type. The paper also adopted the DAN-W model to analyze and predict the landslide state in the landslide area and obtained the movement characteristics, such as the distance, accumulation thickness, and slip velocity, of the debris flow under different conditions. Then, the impact force of the Xigou debris flow on residential buildings and other buildings at the gully entrance was calculated when the material source value totaled 20×10^4 m^3 and 26×10^4 m^3 to provide a reference for disaster prevention and mitigation in the study area.

2 Geological background of the study area

The Xigou debris flow is located in Wushan County, Chongqing (Figure 1). The study area is generally at a lower elevation in the south and higher in the north, ranging from 265 to 1890 m, with steep slopes of 30°–50° in the upper part of the gully and gentle slopes of 10°–20° in the lower part. The Xigou debris flow basin contains three debris flow gullies—#1, #2, and #3—all of which are rectangular in shape, with an overall basin area of approximately 1.28 km^2.

The strata in the study area are Quaternary artificial fill (Q_4^{ml}), Quaternary Holocene landslide accumulation (Q_4^{del}), Quaternary colluvium (Q_4^{col+dl}), and Quaternary Pleistocene alluvium (Q_4^{al+pl}), and the exposed bedrock primarily consists of Triassic Patung Schichten (T_2b) mudstone, fractured marl, and Lower Triassic Jialingjiang Formation (T_1j^4) limestone. The study area is located on the southeastern flank of the Qiyao Mountain anticline, with a monoclinal output and a rock formation yield of 160°–180°∠45°–58°, and does not exhibit any fault development.

The study area features a humid subtropical monsoon climate with an average annual temperature of 18.4°C, an average annual precipitation of 1066.2 mm, a maximum annual rainfall of 1,509.9 mm, a maximum monthly rainfall of 445.9 mm (September), and a maximum daily rainfall of 384.6 mm (31 August 2014), with 68.8% of the rainfall occurring during the rainy season (May-September). The cumulative rainfall between January and August of the year when the debris flows occurred was 824.8 mm, with the cumulative rainfall in June reaching 194.2 mm, much larger than the historical average for June (Figure 2). On 18 June 2018, Wushan County witnessed continuous heavy rainfall, with a cumulative rainfall of 174.3 mm.

3 Description of the xigou debris flow

The overall shape of the Xigou debris flow basin is rectangular, with a valley orientation of 10° ESE, a slope of nearly 25°, and a ditch length of 1.82 km, which is located in the elevation range of 282–1,424 m. When experiencing heavy rainfall, the side slopes produce strong runoff, which scours and coats the loose accumulation material sources in the gully, gradually accumulating and expanding to form debris flows. As they move, these debris flows collide with the slopes and scrape and excavate the substrate, causing some of the side slopes to collapse and, eventually, gradually accumulate at the entrance of the gully as the speed decreases. In terms of dynamics, the Xigou debris flow can be divided into four areas: a catchment area, formation area, movement area, and accumulation area (Figure 3). The catchment area is located in the upper part of the debris flow gully and has the largest area that easily catches water. The formation and movement areas are located in the middle of the gully. The formation area is large, and the debris flow forms in the formation area and flows toward the movement area. The

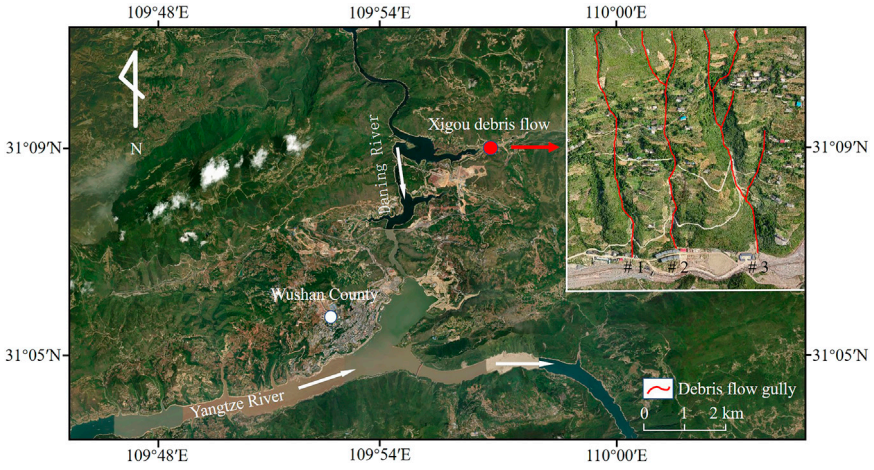

FIGURE 1
Geographical location map of the Xigou debris flow.

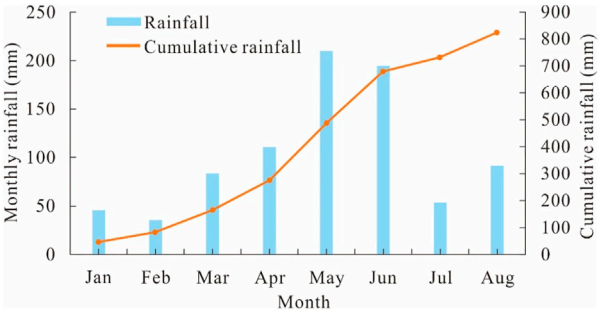

FIGURE 2
Monthly and cumulative rainfall in the study area in 2018 c.

accumulation area is located at the gully entrance at the foot of the slope, and the debris flow flows from the upper part to this area, where accumulation occurs.

3.1 Catchment area

The catchment area is a roughly rectangular shape that is distributed within the elevation range of 530–1,462 m. The terrain is steep, with a relative height difference of 864–922 m. The vegetation cover is over 85%, primarily consisting of shrubs. The cover layer is thin, with local outcrops of fractured marl and mudstone, experiencing few avalanches and landslides and other unfavorable geological conditions in addition to minimal soil erosion. The ditches in the catchment area are well developed, providing the necessary dynamic conditions for forming debris flows.

3.2 Formation area

The formation area is primarily located within the elevation range of 310–560 m, with a steep topography and slope of approximately 30°

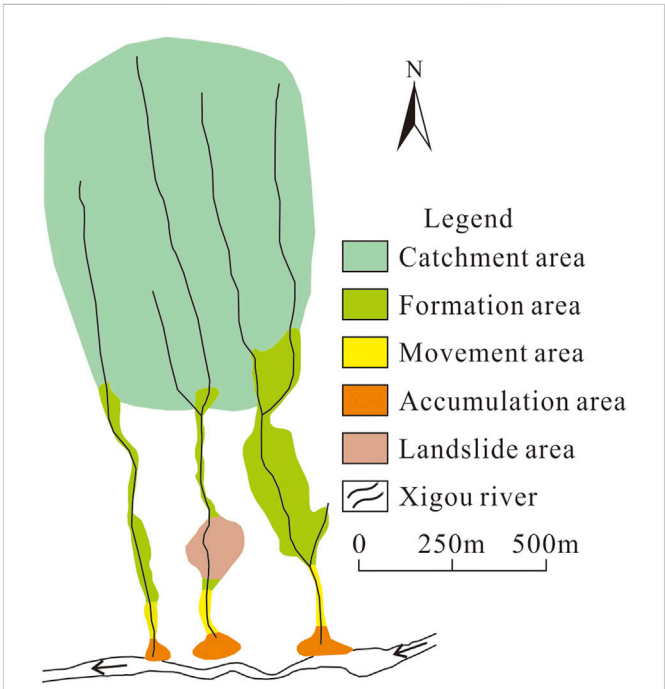

FIGURE 3
Xigou debris flow partition.

and an overall area of approximately .448 km^2 (Figure 4A). The surface layer of the formation area is mostly Quaternary Holocene colluvial soil, with a thickness of approximately 20 m, and most of the debris flow material sources are concentrated in this area. The catchment area is located in the upper part of the formation area. When it rains, rainwater collects in the catchment area and flows toward the formation area, and the debris flow forms in the formation area and flows downstream. The landslide area is located in the formation area of Xigou #2, which is approximately 100 m long and 80 m wide, with a volume of approximately 26.0 × 10^4 m^3. The

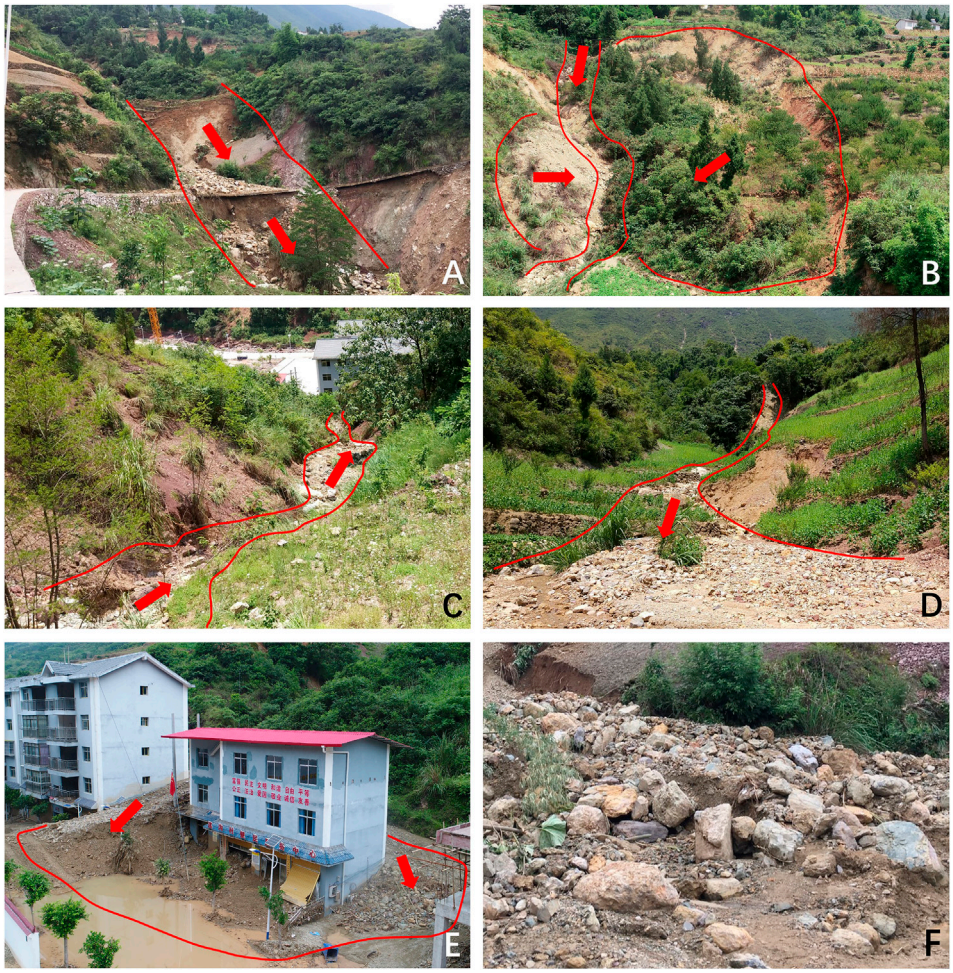

FIGURE 4
Features of Xigou debris flow partitions. **(A)** Formation area **(B)** Landslide area **(C,D)** Movement area **(E)** Accumulation area **(F)** Accumulation distribution.

large amount of accumulation in this area provides a rich material source for debris flow movement (Figure 4B).

3.3 Movement area

The movement area is primarily distributed from the elevation of 310 m to the entrance of the gully. The length of the movement area for gully #1, #2, and #3 is 90, 135, and 220 m, respectively. The slope in this area is approximately 25°, and the channel is generally narrow and straight, which is conducive to the rapid flow of debris. During high-speed movement, the debris flow collides, scrapes, and entrains a large volume of loose accumulation on the gully surface (Figures 4C,D).

3.4 Accumulation area

The accumulation area is located below 300 m in elevation, with an open space and fan-shaped area (Figure 4E). The accumulation areas of gully #1, #2, and #3 are approximately 3,065, 6,643, and 6,886 m^2, respectively. According to site investigations, the accumulation is primarily composed of gravelly soil and clay, with a grain size of 5–30 cm and a maximum grain size of 1.5 m (Figure 4F).

Due to the relatively large slope drop in the upper part of each branch gully in the basin, the debris flow is fast, and the loose accumulation is relatively small, while the middle and lower parts of the main gully are relatively gentle, and the debris flow produces a large amount of material accumulation in the accumulation area due to the reduced kinetic energy. This area is where human construction activity is concentrated, including houses and roads in Xigou Village.

4 Formation mechanism of the xigou debris flow

In the study area, the Xigou debris flow occur due to heavy rainfall. During debris flow movement, they continuously scour and erode the bank slopes on both sides of the gully, leading to landslides within the landslide area, further increasing the volume of the material source of debris flows, and a large amount of debris flow material accumulates at the gully entrance. Heavy rainfall is the main cause for debris flow formation. The Xigou debris flow disaster formation process is divided into three main phases: initiation phase, amplification phase, and siltation phase (Figure 5).

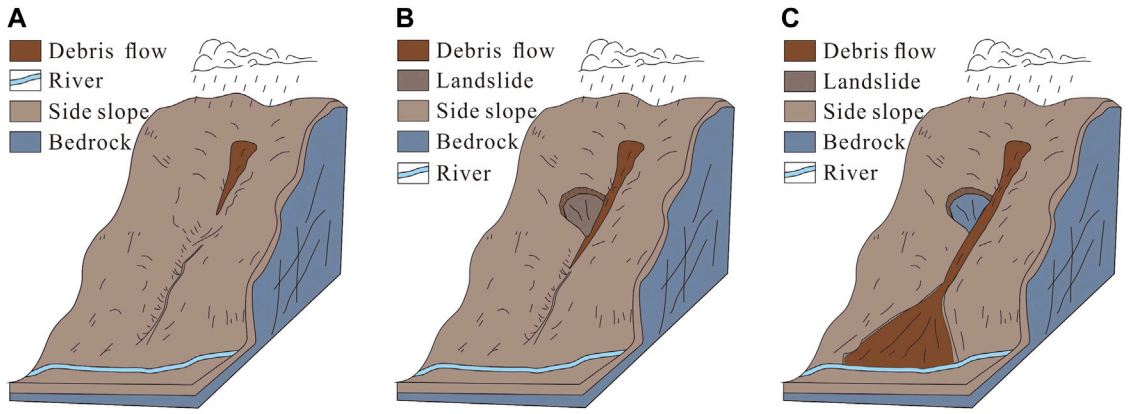

FIGURE 5
Formation mechanism of the Xigou debris flow. **(A)** Initiation phase **(B)** Amplification phase **(C)** Siltation phase.

Initiation phase: Heavy rainfall on 18 June 2018 caused a number of small landslides on the rear edge of the slope, a large number of avalanches and rock slides gathered in the gully, and the amount of loose solid material sources increased greatly. The catchment area was large, the terrain was steep, and the gully easily caught water. A large amount of rainwater quickly gathered in the narrow gully channel and quickly formed into a flood. Then, the floodwater mixed with the loose solid material sources in the formation area to form a debris flow, scouring and mobilizing the loose accumulation of material sources in the gully channel and moving downstream.

Amplification phase: As the runoff increased, the debris flow generated greater kinetic energy in the narrow gully, and the erosion capacity gradually increased. Both sides of the gully were steep, and the loosely accumulated soil on both slopes was mainly fragmented rocky soils. As the debris flow moved, it continuously scraped and scoured the bank slopes on both sides of the gully, which intensified the lateral erosion effect on the front edge of the landslide area, resulting in slope slip damage. The landslide provided favorable conditions for the solid material source of debris flow movement.

Siltation phase: The debris flow movement induced the landslide, and the loose landslide mass moved downstream with the debris flow. The entrainment and dynamic erosion of the debris flow in the transportation process led to a gradual reduction in the kinetic energy of the debris flow. The debris flow eventually accumulated at the gully entrance with a relatively gentle slope.

5 Numerical simulation of debris flow

5.1 Introduction to DAN

DAN-W is a numerical simulation software developed by Hungr to simulate the debris flow movement process and its dynamics. DAN-W uses the Lagrangian analytic solution of the Saint-Venant equations to decompose the landslide into a number of blocks and assumes that these blocks will not undergo internal deformation during movement. After establishing the balance equations and kinetic equations and then solving the equations *via* the Lagrangian finite difference method, data on the movement velocity, movement distance, and accumulation thickness were obtained (Hungr, 1995).

The DAN model treats landslides as equivalent fluids and further back analyzes landslide movement by setting the paths and directions of movement and selecting different rheological models to calculate the movement distance, velocity, and accumulation thickness of landslides.

Hungr (2009) and Sosio (2008) showed that the frictional and Voellmy rheological models can reflect the movement and accumulation characteristics of landslides more accurately. The rheological relationships are specified as follows:

The expressions for the resistance of the frictional model are as follows:

$$\tau = \sigma\left(1 - \gamma_{\mu}\right) tan\,\varphi \tag{1}$$

where τ is the resistance at the bottom of the slide (N); σ is the total stress perpendicular to the direction of the sliding path (Pa); γ_{μ} is the pore pressure coefficient, i.e., the ratio of pore pressure to total stress; and φ is the internal friction angle (°).

The expression for the resistance of the Voellmy model is as follows:

$$\tau = f\sigma + \gamma\frac{v^2}{\xi} \tag{2}$$

where τ is the resistance at the bottom of the slide (N), f is the slip friction coefficient , σ is the total stress perpendicular to the direction of the sliding path (Pa); γ is the material volumetric weight (N/m^3); v is the transportation velocity of the slide (m/s); and ξ is the turbulent diffusion coefficient (m/s^2).

5.2 Model establishment and parameter selection

As a result of the heavy rainfall on 18 June 2018, debris flow hazards broke out in gullies #1, #2, and #3 in the study area, of which the most threatening was the debris flow in gully #2. Therefore, gully #2 was chosen for modeling and calculation. Through field geological investigation, the profile of gully #2 before and after the debris flow occurred was determined (Figure 6). In this paper, two rheological models, the frictional model and the Voellmy model, were used to simulate the

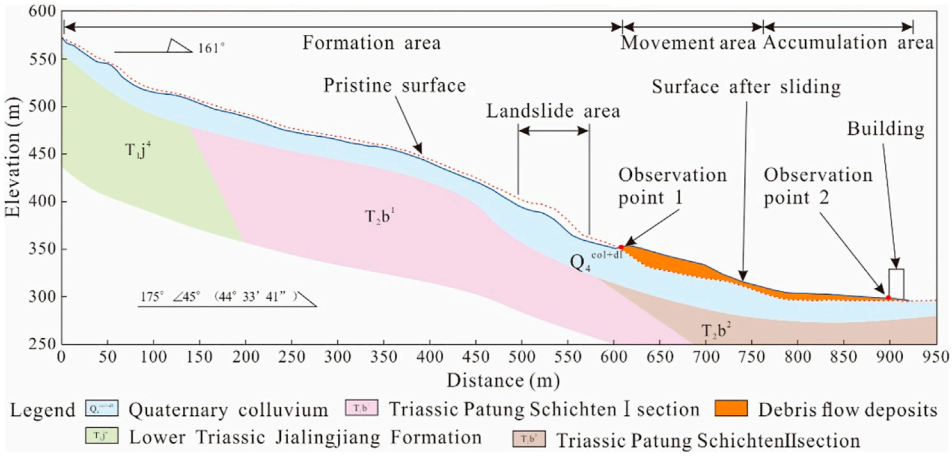

FIGURE 6
Geological profile of gully #2 of the Xigou debris flow.

TABLE 1 Model combinations for xigou debris flow.

Model	Debris flow partition			Movement distance (m)	Actual distance (m)
	Formation area	Movement area	Accumulation area		
F-F-F	Frictional	Frictional	Frictional	1,100	950
F-V-V	Frictional	Voellmy	Voellmy	820	
F-V-F	Frictional	Voellmy	Frictional	930	
F-F-V	Frictional	Frictional	Voellmy	820	

TABLE 2 Parameters for the F-V-F model.

Model	Friction coefficient	Internal friction angle (°)	Turbulent diffusion coefficient (m/s)	Volumetric weight (kN/m^3)	Scraping depth (m)
F		20		20	
V	0.4		300	20	3
F		20		20	

movement characteristics of the debris flow in different areas according to the gully characteristics and debris flow movement characteristics in the formation, movement, and accumulation areas. Research results have shown that the frictional model is suitable for application in the formation area (Yang et al., 2020). The frictional model and the Voellmy model were applied to the movement area and the accumulation area, respectively, and four model combinations of F-F-F, F-V-V, F-V-F, and F-F-V were obtained, which corresponded to debris flow movement distances of 1,100, 820, 930, and 820 m, respectively (Table 1). A comparison of the four models by the trial-error method revealed that the simulation results of the F-V-F model were closer to the actual movement distance of 950 m of the Xigou debris flow; therefore, the F-V-F rheological model was used for simulation calculation (Table 2 shows the parameters of the F-V-F model).

5.3 Results

5.3.1 Movement characteristics of the debris flow

The movement characteristics of the Xigou debris flow are shown in Figures 7, 8. Figure 7 indicates that the debris flow movement lasted approximately 40 s, with the head and tail starting almost simultaneously. During the initiation phase, a large amount of rainwater collected in the gully, which mixed with the loose accumulation on the surface and flowed downstream, causing the velocity of the debris flow head to gradually increase during 0–8 s. At 8 s, the velocity reached a maximum of 18.7 m/s until approximately 14 s, when the head entered the accumulation area. As the gully in the accumulation area was gentler, the velocity started to decrease. The head was blocked by the building at the foot of the slope where the velocity dropped to 0 m/s and then flowed out on a side of the building before finally stopping its movement at a horizontal

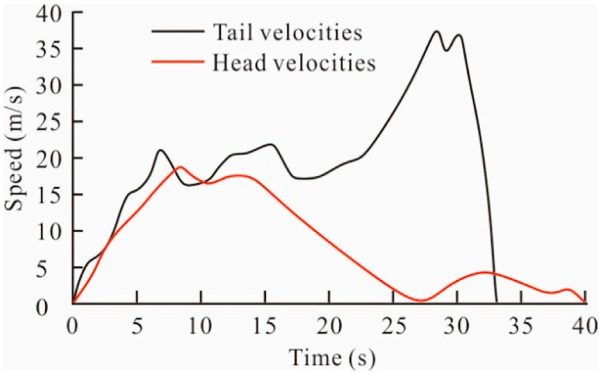

FIGURE 7
Velocities of the debris flow head and tail over time.

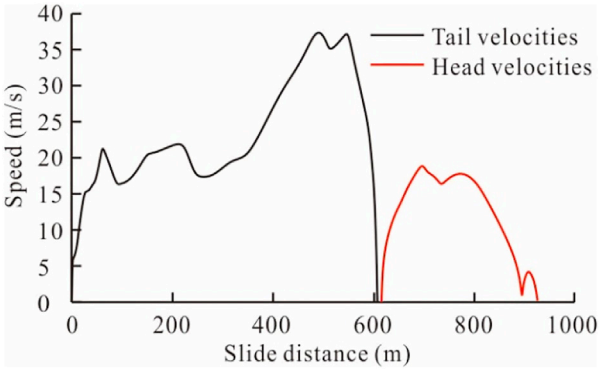

FIGURE 8
Velocities of the debris flow head and tail over slide distance.

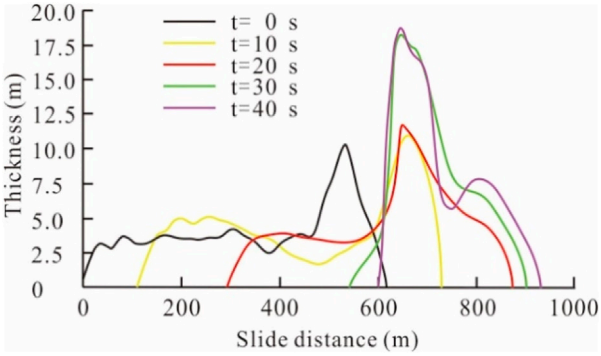

FIGURE 9
Debris flow thickness variation.

distance of 930 m. The steeper slope of the rear edge of the slope and the large amount of rainwater flowing into the formation area caused the velocity of the debris flow tail to increase sharply at 0–7 s, after which the movement path was relatively gentle, and the velocity remained at 15–20 m/s until approximately 22 s, when the tail entered the steep slope, and the velocity increased, reaching a maximum of 37.1 m/s at 27 s. Thereafter, the tail was blocked by the accumulation in the movement area, and the velocity decreased linearly until the tail accumulated in the movement area and stopped.

5.3.2 Morphological characteristics of debris flow movement

The changes in the accumulation thickness and morphology of the debris flow at 10 s intervals from start to stop are shown in Figures 9, 10. At 0 s, the debris flow head was located at a horizontal distance of 610 m, and the tail was located at a horizontal distance of 0 m. The average thickness of the debris flow accumulation ranged from 2.5 to 17.5 m, with the maximum accumulation thickness of 18.7 m located at a horizontal distance of 620 m. The head of the debris flow began to decrease in velocity at 15 s, while the tail remained at a higher velocity moving downstream, resulting in the gradual accumulation of the debris flow in the movement area, reaching a maximum accumulation thickness of 18.7 m at a horizontal distance of 620 m. At 40 s, the tail was located at a horizontal distance of 600 m, the accumulation thickness in the movement area was 7–18 m, and the debris flow movement stopped at a horizontal distance of 930 m.

During the 20 s after the initiation of the debris flow, the head exhibited a high velocity and moved a distance of approximately 260 m. Within 20–40 s, the debris flow moved to the accumulation area, where the terrain was flat, and gradually decelerated, moving only 60 m during this period. Therefore, after t=20 s, the debris flow thickness in the accumulation area did not change notably. The horizontal distance of approximately 620 m is typical of negative terrain, so the debris flow accumulated much more at this distance, leading to a peak in debris flow thickness at this location.

5.3.3 Movement characteristics of the debris flow at the observation point

According to the field investigation, observation point one and observation point 2 were set at horizontal distances of 600 m and 900 m, respectively, for analysis (Figure 6), and the variation in debris flow velocities and thicknesses at the observation points with times were obtained (Figures 11, 12). Observation point one is located at the intersection of the formation area and the movement area, and the movement characteristics at observation point one were selected for the analysis. In terms of velocity, the debris flow arrived at observation point one within 2 s of startup with a velocity of 5 m/s. As the debris flow was in the initiation phase, the velocity of the debris flow through observation point one increased and reached a maximum velocity of 19 m/s at approximately 8 s. At approximately 10 s, the debris flow started to accumulate in the movement area, and the velocity of the debris flow at observation point one gradually decreased. Between 20 and 25 s, the debris flow velocity picked up at observation point one due to the faster tail movement. The large accumulation of debris flow in the narrow movement area impeded the flow of the tail downstream, causing the tail velocity to gradually decrease as it flowed through observation point one until it stopped moving. In terms of thickness, within 0–15 s, the debris flow thickness past observation point one was approximately the same as the thickness of the initial debris flow, indicating that the overall flow downstream after the initiation of the debris flow remained essentially unchanged. Between 15 and 30 s, the debris flow gradually piled up in the movement area, and the debris flow thickness gradually increased at observation point 1. After 30 s, the accumulation in the movement area extended to

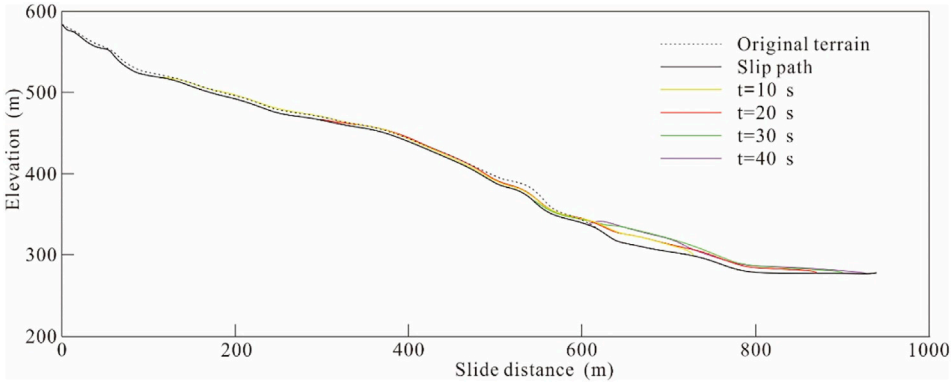

FIGURE 10
Debris flow morphology variation.

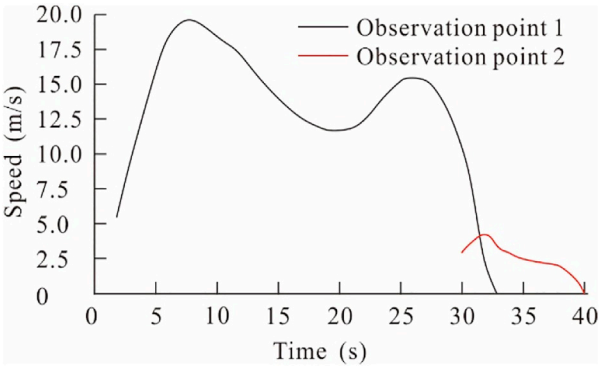

FIGURE 11
Velocity versus time as the debris flow passed through the observation point.

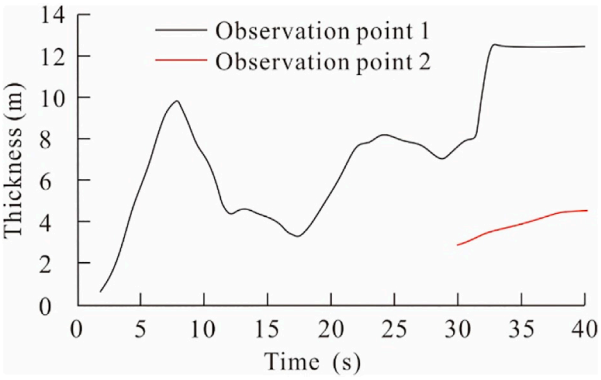

FIGURE 12
Velocity versus thickness as the debris flow passed through the observation point.

observation point one, where the debris flow tail continued to accumulate until the tail stopped moving and the thickness of the accumulation reached a maximum of 12.5 m and remained constant.

Observation point 2 was located at a building in the accumulation area, where the Xigou debris flow posed a threat to residential houses and other buildings at the foot of the slope; therefore, the movement characteristics at observation point 2 were chosen for the analysis. Figure 11 indicates that the debris flow passed through this point at approximately 30 s, at which point the velocity was 3.25 m/s, exhibiting an overall slowing velocity until the debris flow ultimately stopped moving. After the debris flow passed through observation point 2, the accumulation thickness at this point increased until the movement ended when the accumulation thickness was approximately 4.5 m. Thus, the debris flow did not stop moving when it reached observation point 2 and had a certain impact on the buildings.

6 Discussion

6.1 Simulation analysis of the transformation from landslide to debris flow

Based on the field investigation and unmanned aerial vehicle (UAV) images, a landslide was identified within the central formation area of the debris flow gully (Figure 4B). The landslide area is located within the elevation range of 350–410 m, with the front edge of the landslide body at an elevation of 350 m and the back edge at an elevation of 407 m. The landslide area had a relative height difference of 57 m, a length of approximately 100 m, a width of approximately 80 m, and a material source volume of approximately 26.0×10^4 m^3. The slide body is dominated by rubble, and the main slide direction is 211°; boundary conditions have formed, the frontal slide has blocked the debris flow gully, and the entire landslide area is unstable.

On 18 June 2018, the study area was subjected to persistent heavy rainfall, and large amounts of rainwater rapidly collected upstream of the debris flow gully and surged into the narrow gully channel, rapidly forming a flood, which mixed with loose solid material sources on the gully surface to form a debris flow that continued to scour the loose accumulation sources in the gully and moved downstream. After the debris flow moved to the landslide area, it continuously scraped and scoured the bank slopes on both sides of the gully channel. The scraping and lateral erosion of the

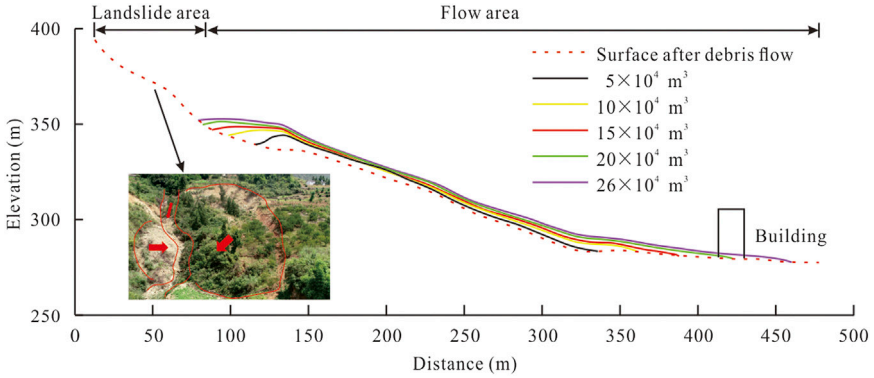

FIGURE 13
Morphology of accumulation formed by different landslide volumes.

slope of the landslide area by the debris flow destroyed the stability of the original slope body, resulting in a landslide on the slope of the landslide area. Some of the landslide bodies continued to move downstream after being transformed into debris flow and eventually accumulated at the gully entrance. The remaining landslides and slope accumulations became new sources of debris flow, and under heavy rainfall conditions, they are prone to destabilize and form debris flows again.

In this section, the DAN-W model was used to simulate the movement state of debris flow when it breaks out again under heavy rainfall conditions. Assuming that the volume of landslide volumes that transform into new sources of debris flow are 5×10^4, 10×10^4, 15×10^4, 20×10^4, and 26×10^4 m^3, these source volumes are used as five sets of working conditions to simulate and predict the movement states of debris flow with different source volumes and obtain the movement characteristics, such as distance, accumulation thickness, and slide velocity, of debris flow under various conditions.

Figures 13–15 present the accumulation morphology, movement velocity, and accumulation thickness of debris flows at different source volumes. When the volume of the material source was 5×10^4 m^3, due to the small volume of the material source, the accumulation thickness was small, and the movement distance was limited. The thickness of the accumulation body reached its maximum value of 11 m at the horizontal distance of 130 m, with a movement distance of the debris flow of approximately 250 m and a maximum speed of 16 m/s, located at the horizontal distance of 130 m. Subsequently, the speed gradually decreased until it slid to the horizontal distance of 340 m and stopped, not impacting any buildings, such as residential buildings. When the volume of the source was 10×10^4 m^3 and 15×10^4 m^3, the distance of the debris flow was 280 m and 300 m, respectively, and the maximum velocity was 17.5 m/s and 19.0 m/s, respectively. The debris flow did not reach the house at the gully entrance, so it did not affect the house and other buildings. When the volume of the material source was 20×10^4 m^3, the debris flow moved approximately 340 m and reached a maximum velocity of 20.5 m/s at a horizontal distance of 150 m. The debris flow collided with buildings, such as houses at the gully entrance, at a lower velocity with a horizontal distance of 415 m and stopped after it reached a horizontal distance of 425 m. When the volume of the material source was 26×10^4 m^3, due to its larger volume, the movement distance of the debris flow was greater, along with the accumulation thickness. The movement distance of the debris flow was approximately 375 m. The terrain at the horizontal distances of 130 m and 335 m was relatively flat, which is conducive to the accumulation of mudslide materials, and the accumulation thickness at these two places was relatively large, at 12.5 and 7.5 m, respectively.

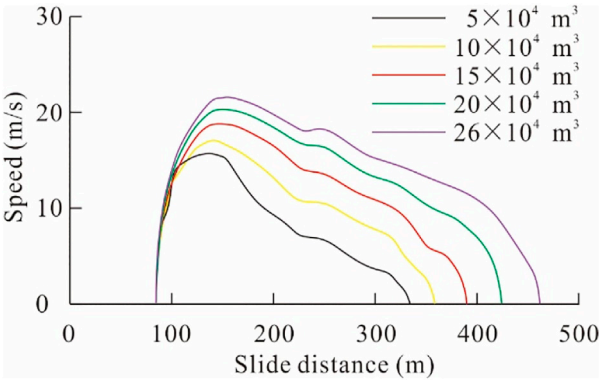

FIGURE 14
Velocity versus slide distance for different landslide volumes.

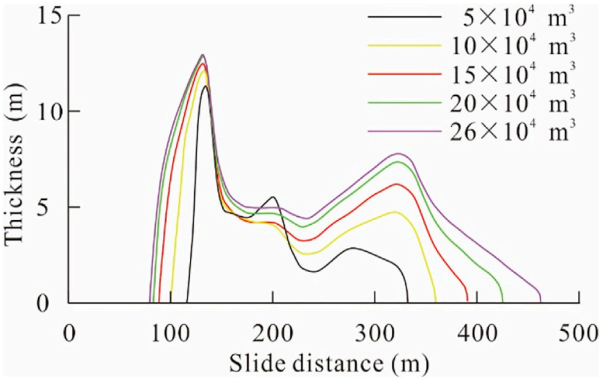

FIGURE 15
Thickness versus slide distance for different landslide volumes.

TABLE 3 Calculation results of the impact forces of debris flow on the residential houses at the gully entrance.

Working conditions	λ	γ_c (kN/m^3)	V_c (m/s)	α (°)	g (m/s^2)	δ (kPa)
Xigou Debris Flow	1.33	20.00	3.25	90	9.8	28.67
Working conditions for 20×10^4 m^3	1.33	20.00	3.80	90	9.8	39.19
Working conditions for 26×10^4 m^3	1.33	20.00	9.43	90	9.8	241.37

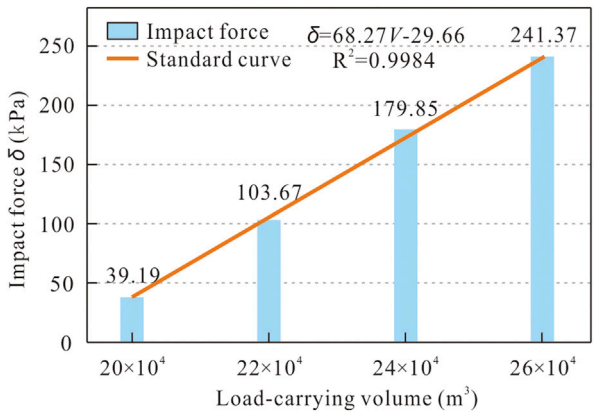

FIGURE 16
Association between debris flow material source volume and its impact force.

The maximum velocity of the debris flow was 21.5 m/s at a horizontal distance of 150 m, and buildings, such as residential houses, were located in the path of the debris flow movement and would suffer from debris flow impacts and siltation, threatening the safety of the residents on both sides of gully entrance #2.

The movement distances, velocities, thicknesses, and morphologies of debris flows under different working conditions were calculated for debris flows with different source volumes to provide a basis for future disaster prevention and mitigation of the Xigou debris flow.

6.2 Impact of debris flow on buildings

The debris flow impact force is the most important indicator for assessing building resistance to debris flow damage (Hu et al., 2012), and its magnitude is related to the debris flow velocity, volumetric weight, etc. Determining the impact force of debris flows on buildings is the most important step when designing debris flow control projects.

The impact force of debris flow on residential houses in the accumulation area can be calculated by the following equation (T/CAGHP 006–2018, 2018):

$$\delta = \lambda \frac{\gamma_c}{g} V_c^2 \sin\alpha \tag{3}$$

where δ is the overall impact pressure of the debris flow (kPa); γ_c is the volumetric weight of the debris flow (kN/m^3); V_c is the flow velocity of the debris flow (m/s); g is the acceleration of gravity (m/s^2); α is the angle between the force surface of the building and the impact force direction of the debris flow (°); and λ is the building shape coefficient, which is 1.0 for circular buildings, 1.33 for rectangular buildings, and 1.47 for square buildings.

On 18 June 2018, a debris flow disaster occurred in the study area, resulting in two residential houses and the ground floor of a residential building at the gully entrance being buried, and Eq. 3 was used to calculate the impact force of this debris flow on the residential houses and other buildings. Figure 13 shows that the debris flow movement affects the residential houses and other buildings at the gully entrance under the working conditions of the debris flow source volume of 20 × 10^4 m^3 and 26 × 10^4 m^3 in the landslide area. Therefore, the impact forces of the debris flow on the residential houses and other buildings under these two working conditions were also calculated to predict the degree of damage caused by the debris flow to the residential houses.

The impact force of Xigou debris flow at the entrance of the gully was calculated to be 28.67 kPa, and the impact force of the debris flow on the houses was 39.19 and 241.37 kPa for the source volumes 20 × 10^4 m^3 and 26 × 10^4 m^3, respectively (Table 3). Zanchetta (2004) analyzed the relationship between the debris flow impact force and the damage to buildings and proposed a damage rating for buildings under debris flow impact. When the impact force of the debris flow is stronger than 90 kPa, the building is completely destroyed; when the impact force is less than 90 kPa but greater than 35 kPa, most of the building is severely damaged; and when it is less than 35 kPa, the building is slightly damaged. Figure 4C shows the damage to two residential buildings at the gully entrance, which suffered frontal impacts from the debris flow, with severe damage to doors, windows, and walls, including partially broken walls, and the ground floor was covered in silt but suffered no structural damage. According to the damage levels of buildings under the debris flow impact proposed by Zanchetta et al. (2004), it is presumed that when the material source volume is 20 × 10^4 m^3, buildings, such as residential houses, at the entrance of the gully will suffer more serious debris flow impacts, and some walls will be punched through and some floors will be covered in silt. When the material source volume is 26 × 10^4 m^3, residential houses at the gully entrance will be completely demolished.

Further calculations of the impact forces generated by the debris flow with material source volumes of 20 × 10^4 m^3, 22 × 10^4 m^3, 24 × 10^4 m^3, and 26 × 10^4 m^3 led to the following equation for the relationship between the material source volume and impact force under general conditions:

$$\delta = 68.27V - 29.66 \tag{4}$$

where δ is the overall impact force of the debris flow (kPa) and V is the volume of the debris flow source (m^3).

As the debris flow material source volume increases, the impact force generated by the debris flow increases linearly (Figure 16). Thus, the magnitude of the impact force that will be generated by the debris flow can be further predicted by measuring the material source volume of the debris flow.

Several suggestions have been proposed to avoid damage to buildings from debris flows: (1) Construct interceptor gullies and diversion channels upstream of the debris flow formation area to intercept some of the flood

water and reduce the flood peak. (2) Set up tailing dams in the gullies to stop the mud and sand and reduce the size of debris flows. (3) Reinforce debris flow retaining walls behind residential houses to prevent water flow and debris flow from directly washing over the foot of the slope.

7 Conclusion

Taking the Xigou debris flow as an example, this paper summarizes and analyzes the development characteristics of the debris flow and its destabilization mode based on field investigation. The process of initiation-movement-accumulation was simulated, and the debris flow dynamics analysis was conducted using the dynamics software DAN-W with the rheological model and parameters of the back analysis of the Xigou debris flow. The main conclusions are as following.

(1) Heavy rainfall is the main trigger for Xigou debris flows. Their formation process is divided into three main phases: initiation, amplification, and siltation.
(2) The F-V-F rheological model well simulated the movement distance and accumulation morphology of the debris flow *via* the DAN-W software. The duration of Xigou debris flow movement is approximately 40 s, the maximum velocity is 37.1 m/s, the maximum thickness of the accumulation is 18.7 m, and the farthest movement distance is 930 m.
(3) After the debris flow moved to the landslide area, it continuously scraped and scoured the bank slopes on both sides of the gully channel, resulting in failure of the landslide. The loose landslide mass moved downstream with the debris flow, and provide the new material source of the debris flow. For the remaining landslides, the numerical simulation predicts the movements of landslides with different volumes after transformation into debris flows. It is presumed that after the volume of material source exceeds 20×10^4 m^3, the movement of debris flows will affect the safety of buildings such as residential houses at the gully entrance.

Data availability statement

The original contributions presented in the study are included in the article/supplementary material, further inquiries can be directed to the corresponding authors.

Author contributions

ZD: conceptualization, methodology, funding acquisition, and writing-original draft. AZ: investigation, supervision, writing-review, and editing. SW: writing-review and editing. XF: formal analysis. LY: data curation, numerical simulation method. XJ: investigation. HW: investigation.

Funding

This research was funded by the follow-up of the Geological Disaster Prevention and Control Project in the Three Gorges area (Grant Nos. 000121 2019C C C60 001 & 000121 2021C C C60 001), the Hubei Provincial Natural Science Foundation of China (Grant Nos. 2020CFB352) and the Qianlong Plan Top Talent Project of Wuhan Center of China Geological Survey (Grant Nos. QL 2022-06). Special thanks are given to Prof. Yueping YIN, China Institute of Geo-Environment Monitoring. We are also grateful to Prof. O. Hungr for supplying a copy of the DAN-W software.

Conflict of interest

Author LY was employed by the company Wuhan Design and Research Institute Co., Ltd. of China Coal Technology and Engineering Group.

The remaining authors declare that the research was conducted in the absence of any commercial or financial relationships that could be construed as a potential conflict of interest.

Publisher's note

References

Chang, K. T, Merghadi, A., Yunus, A. P., Pham, B. T., and Dou, J. (2019). Evaluating scale effects of topographic variables in landslide susceptibility models using GIS-based machine learning techniques. *Sci. Rep.* 9 (12296), 1603–1604. doi:10.1038/s41598-019-48773-2

Cui, P., Chen, X. Q., Zhu, Y. Y., Su, F. H., Wei, F. Q., Han, Y. S., et al. (2011). The wenchuan earthquake (may 12, 2008), sichuan province, China, and resulting geohazards. *Nat. Hazards* 56 (1), 19–36. doi:10.1007/s11069-009-9392-1

Dou, J., Yunus, A. P., Bui, D. T., Sahana, M., and Pham, B. T. (2019). Evaluating GIS-based multiple statistical models and data mining for Earthquake and Rainfall-induced landslide susceptibility using the LiDAR DEM. *Remote Sens.* 11 (6), 638. doi:10.3390/rs11060638

Dou, J., Yunus, A. P., Bui, D. T., Merghadi, A., and Sahana, M. (2020). Improved landslide assessment using support vector machine with bagging, boosting, and stacking ensemble machine learning framework in a mountainous watershed, Japan. *Landslides* 17, 641–658. doi:10.1007/s10346-019-01286-5

Dowling, C. A., and Santi, P. M. (2014). Debris flows and their toll on human life: A global analysis of debris-flow fatalities from 1950 to 2011. *Nat. Hazards* 71 (1), 203–227. doi:10.1007/s11069-013-0907-4

Hu, K., Cui, P., and Ge, Y. G. (2012). Building destruction patterns by August 8,2010 debris flow in zhouqu,Western China. *J. Mt. Sci.* 30 (4), 484–490. (in Chinese). doi:10.3969/j.issn.1008-2786.2012.04.015

Hu, K., Cui, P., and Li, P. (2014). Debris flow dynamic models and numerical computation. *Chin. J. Nat.* 36 (5), 313–318. (in Chinese). doi:10.3969/j.issn.0253-9608.2014.05.001

Hu, X. D., Hu, K. H., Tang, J. B., You, Y., and Wu, C. (2019). Assessment of debris-flow potential dangers in the Jiuzhaigou Valley following the August 8, 2017, jiuzhaigou earthquake, Western China. *Eng. Geol.* 256, 57–66. doi:10.1016/j.enggeo.2019.05.004

Hungr, O. (1995). A model for the runout analysis of rapid flow slides, debris flows, and avalanches. *Can. Geotechnical J.* 32 (4), 610–623. doi:10.1139/t95-063

Hungr, O., Evans, S. G., Bovis, M. J., and Hutchinson, J. N. (2001). A review of the classification of landslides of the flow type. *Environ. Eng. Geosci.* 7 (3), 221–238. doi:10.2113/gseegeosci.7.3.221

Hungr, O., and Evans, S. G. (2004). Entrainment of debris in rock avalanches: An analysis of a long run-out mechanism. *Geol. Soc. Am. Bull.* 116 (9-10), 1240–1252. doi:10.1130/b25362.1

Hungr Oand McDougall, S. (2009). Two numerical models for landslide dynamic analysis. *Comput. Geosciences* 35, 978–992. doi:10.1016/j.cageo.2007.12.003

T/CAGHP 006-2018 (2018). *Specification of geological investigation for debris flow stabilization*. Beijing, China: China Geological Disaster Prevention and Engineering Industry Association.

Liu, G. N., Wu, Y., Wang, S. C., Liao, J., and Yu, S. W. (2022). The Main Water Environmental Issues and Assessment-zonation of Eco-environmental Geology Risks for Typical River-lake-wetland Systems in the Central Yangtze River. *South China Geology* 38 (2), 226–239. (in Chinese).

Lee, D. H., Cheon, E., Lim, H. H., Choi, S. K., Kim, Y. T., and Lee, S. R. (2020). An artificial neural network model to predict debris-flow volumes caused by extreme rainfall in the central region of South Korea. *Eng. Geol.* 281 (4), 105979. doi:10.1016/j.enggeo.2020.105979

Qiu, H. J., Zhu, Y. R., Zhou, W. Q., Sun, H. S., and He, J. Y. (2022). Influence of DEM resolution on landslide simulation performance based on the Scoops3D model. *Geomatics, Natural Hazards and Risk* 13 (1), 1663–1681. doi:10.1080/19475705.2022.2097451

Nocentini, M., Tofani, V., Gigli, G., Fidolini, F., and Casagli, N. (2015). Modeling debris flows in volcanic terrains for hazard mapping: The case study of ischia island (Italy). *Landslides* 12 (5), 831–846. doi:10.1007/s10346-014-0524-7

Sosio, R., Crosta, G. B., and Hungr, O. (2008). Complete dynamic modeling calibration for the Thurwieser rock avalanche (Italian Central Alps). *Eng. Geol.* 100 (1-2), 11–26. doi:10.1016/j.enggeo.2008.02.012

Tang, H. M., Li, C. D., Hu, X. L., Su, A. J., Wang, L. Q., Wu, Y. P., et al. (2015). Evolution characteristics of the Huangtupo landslide based on in situ tunneling and monitoring. *Landslides* 11, 511–521. doi:10.1007/s10346-014-0500-2

Wang, L. Y., Qiu, H. J., Zhou, W. Q., Zhu, Y. R., and Liu, Z. J. (2022). The post-failure spatiotemporal deformation of certain translational landslides may follow the pre-failure pattern. *Remote Sens.* 14, 2333. doi:10.3390/rs14102333

Wang, Q., and yao, L. K. (2007). Lattice Boltzmann method and its application in the study on deposition of debris flow. *J. Catastrophology* 22 (3), 1–5. (in Chinese). doi:10.7666/d.y1131768

Xing, A. G., Wang, G., Yin, Y. P., Jiang, Y., Wang, G. Z., Yang, S., et al. (2014). Dynamic analysis and field investigation of a fluidized landslide in Guanling, Guizhou, China. *Eng. Geol.* 181 (7), 1–14. doi:10.1016/j.enggeo.2014.07.022

Yang, L. W., Wei, Y. J., Peng, L., Wang, W., Zhu, S., Wang, J., et al. (2020). Kinematical characteristics of collapse in red beds in kangsu town, wuqia county, xinjiang. *J. Eng. Geol.* 28 (3), 520–529. (in Chinese). doi:10.13544/j.cnki.jeg.2019-109

Yin, Z. M., Zhao, B. Q., and Ye, R. Q. (2022). Identification of potential landslides in the head area of the three Gorges reservoir based on time series InSAR. *South China Geology* 38 (2), 273–280 (in Chinese).

Zanchetta, G., Sulpizio, R., Pareschi, M. T., Leoni, F., and Santacroce, R. (2004). Characteristics of may 5-6, 1998 volcaniclastic debris flows in the sarno area (campania, southern Italy): Relationships to structural damage and hazard zonation. *J. Volcanol. Geotherm. Research133* 133 (1-4), 377–393. doi:10.1016/s0377-0273(03)00409-8

Zhang, C., Yin, Y., Yan, H., Li, H., Dai, Z., and Zhang, N. (2021). Reactivation characteristics and hydrological inducing factors of a massive ancient landslide in the three Gorges Reservoir, China. *Eng. Geol.* 292, 106273. doi:10.1016/j.enggeo.2021.106273

Zhang, N., and Matsushima, T. (2018). Numerical investigation of debris materials prior to debris flow hazards using satellite images. *Geomorphology* 308, 54–63. doi:10.1016/j.geomorph.2018.02.008

Zhao, Q. R., Cao, S. H., Wen, W. F., and Zhou, L. Y. (2021). Landslide susceptibility evaluation based on weights of evidence method for the Zaoshi reservoir in Shimen county, Hunan province. *South China Geology* 37 (2), 216–225. (in Chinese).

frontiers | Frontiers in Earth Science

TYPE Original Research
PUBLISHED 16 January 2023
DOI 10.3389/feart.2022.1054027

OPEN ACCESS

EDITED BY
Haijun Qiu,
Northwest University, China

REVIEWED BY
Yingjun Sun,
Shandong Jianzhu University, China
Qi Wen,
Technology and Engineering Center for Space Utilization (CAS), Beijing, China

*CORRESPONDENCE
Rong Tang,
trr_trr@163.com

SPECIALTY SECTION
This article was submitted to Geohazards and Georisks, a section of the journal Frontiers in Earth Science

RECEIVED 26 September 2022
ACCEPTED 21 October 2022
PUBLISHED 16 January 2023

CITATION
Ye C, Tang R, Wei R, Guo Z and Zhang H (2023), Generating accurate negative samples for landslide susceptibility mapping: A combined self-organizing-map and one-class SVM method. *Front. Earth Sci.* 10:1054027. doi: 10.3389/feart.2022.1054027

Generating accurate negative samples for landslide susceptibility mapping: A combined self-organizing-map and one-class SVM method

Chengming Ye, Rong Tang*, Ruilong Wei, Zixuan Guo and Huajun Zhang

Key Laboratory of Earth Exploration and Information Technology of Ministry of Education, Chengdu University of Technology, Chengdu, China

The accuracy of data-driven landslide susceptibility mapping (LSM) is closely affected by the quality of non-landslide samples. This research proposes a method combining a self-organizing-map (SOM) and a one-class SVM (SOM-OCSVM) to generate more reasonable non-landslide samples. We designed two steps: first, a random selection, a SOM network, a one class SVM model, and a SOM-OCSVM model were used to generate non-landslide sample datasets. Second, four machine learning models (MLs)—namely logistic regression (LRG), multilayer perceptron (MLP), support vector machine (SVM), and random forest (RF)—were used to verify the effects of four non-landslide sample datasets on LSM. From the region along the Sichuan-Tibet Highway, we selected 11 conditioning factors and 1186 investigated landslides to perform the aforementioned experiments. The results show that the SOM-OCSVM method achieves the highest AUC (>0.94) and minimum standard deviation (<0.081) compared with other methods. Moreover, RF achieves the best performance in different datasets compared with other ML models. The aforementioned results prove that the proposed method can enhance the performance of ML models to produce more reliable LSM.

KEYWORDS

landslide susceptibility mapping, self-organizing map, one-class SVM, the Sichuan-Tibet highway, machine learning

1 Introduction

The fragile geological environment of the Sichuan-Tibet highway, with its complex geotechnical and climatic conditions, has created suitable conditions for mountain disasters such as landslides, debris flows, and flash floods (Chen et al., 2019; Wang et al., 2020a; Liu et al., 2022; Wang et al., 2022). The area is frequently exposed to the risk of slope instability and landslides, which seriously affect sustainable socio-economic development and pose a major security risk for national defense construction and national

communication. It is therefore of great practical significance to complete landslide susceptibility mapping (LSM) along the highway, and hence improve decision-making aimed at reducing highway disasters.

LSM has developed rapidly over the past two decades and is considered an effective measure for mitigating landslide effects (Wang et al., 2020b). LSM focuses on the quantitative analysis of landslide spatial distribution, using a set of region-specific conditioning factors (Hess et al., 2017). Recently, machine learning (ML) algorithms have shown promising and effective ways of solving non-linear real-world problems with high accuracy and are widely used in LSM, including random forest (RF), support vector machine (SVM), multilayer perceptron (MLP), logistic regression (LGR), decision tree, and artificial neural network (ANN) models (Aditian et al., 2018; Ye et al., 2022). These methods have essential similarities in the way they select critical condition factors, which reduce the impact of highly correlated factors on the generalization ability of the model. However, when assessing landslide susceptibility based on machine learning—which is data-driven—accuracy depends on the selection of landslide (positive) and non-landslide (negative) samples.

Landslide samples can be produced by field surveys, remote sensing interpretation of landslides, and historical landslide cataloging data. By contrast, non-landslide samples are less certain. In the past, researchers mainly used the following methods to obtain non-landslide samples: 1) random selection (Felicísimo et al., 2013); 2) the creation of landslide buffers (Pham et al., 2016); and 3) collection from low-slope streams and topographic areas (Kavzoglu et al., 2014). These methods depend on subjective speculation or random selection, however, and cannot make good use of existing landslide contributing factors. The spatial distribution relationship between landslides and contributing factors is ignored, yet this needs to be rationally considered when designing a method to optimize the samples.

To solve the aforementioned problems, we propose a method based on the spatial distribution relationship between landslides and contributing factors to obtain the frequency ratio of non-landslide samples. This is achieved, first, by randomly selecting non-landslide samples beyond a certain distance from the landslides; second, by combining the frequency ratio information on the factors and the landslides and using the SOM unsupervised learning method to obtain the low frequency ratio partition; third, by combining the contributing factors and landslide data to train the OC-SVM and screen out the non-landslide samples with low similarity; and finally, by combining the two methods to screen out the non-landslide samples with low similarity by the trained OC-SVM in the low frequency ratio partition, using the SOM. To assess its effectiveness, we applied our SOM-OCSVM method to the area along the Sichuan-Tibet Highway.

2 Materials

2.1 Study area

The Sichuan-Tibet Highway starts at Chengdu in the east and ends at Lhasa in the west, includes the G318 and G317 national roads, and is 2142 km in length (Figure 1). The highway is located in the collision zone between the Indian and Eurasian plates, which is a zone of strong geological and tectonic activity (Ma et al., 2020). The Sichuan-Tibet Highway crosses a large area from the basin to the plateau, spanning three major geomorphological types: the Chengdu Plain, the Hengduan Mountains, and the Tibetan Plateau. The stratigraphy along the highway is geologically complex, ranging from the Upper Paleozoic Aurignacian to the Cenozoic Quaternary. The G318 passes through a region with terrain that is high in the west and low in the east and that crosses three major mountain systems: the Hengduan, the Nyingchi Tanggula, and the Himalayas; and four major water systems: the Yangtze, Lancang, Nujiang, and Yarlung Tsangpo rivers.

2.2 Data

2.2.1 Landslide inventory

In this study, we collected data from 1186 landslides. The spatial distribution of the landslide inventory within the study area is shown in Figure 1. The landslide inventory was obtained from remote sensing interpretations, field surveys, and historical records.

2.2.2 Landslide conditioning factors

Landslide occurrence is controlled by a variety of conditioning factors, and therefore, reasonable selection of such factors is essential for improving LSM reliability. Drawing on extensive research in the study area (Ma et al., 2020; Wei et al., 2022; Ye et al., 2022), 11 factors were chosen for LSM (Figure 2), i.e., slope, aspect, plan curvature, profile curvature, relief amplitude, annual rainfall, distance to fault, land use, geomorphology, lithology, and distance to river. We divided the original ongoing factors into several subclasses according to their variable impact on landslide occurrence, as shown in Figure 5.

Slope is considered a key topographical factor directly affecting slope body stability (Keles and Nefeslioglu, 2021). Generally, slopes between 20° and 40° are considered prone to causing landslides. Aspect was chosen because it affects erosion. The non-continuous direction of wind and sunlight, which regulates soil moisture and vegetation growth, in turn affects the stability of soil (Bordoni et al., 2020). Relief amplitude describes the variation in terrain associated with landslide occurrence (Qiu et al., 2022), with landslides more likely in areas with greater relief amplitude.

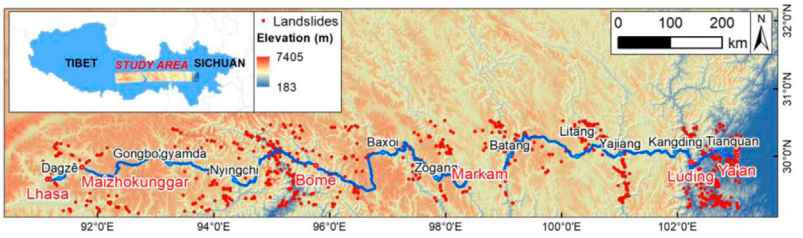

FIGURE 1
Historical landslide inventory and the Sichuan-Tibet Highway location.

Landslide occurrence is also closely related to geomorphology. Land-use type is one of the most sensitive factors, with slope body stability vulnerable to a constantly changing environment due to human activities. Lithology is often considered one of the more important factors in LSM because it directly affects rock strength and the soil permeability (Kavzoglu et al., 2014). In this study, the geomorphology, land use, and lithology are classified into seven, eight, and five categories, respectively, and the detailed information is shown in Figure 5.

There is a strong correlation between distance to a river and landslide susceptibility, as rivers are associated with slope toe erosion (Erener and Düzgün, 2010). The area near the fault is also more favorable to landslide occurrence (Yalcin et al., 2011); hence, the distance to fault was taken into account in this study. The buffer map along faults and rivers was constructed and reclassified into five groups.

Plan curvature describes the terrain's horizontal characteristics and expresses the change rate. Profile curvature reflects the slope change rate and the flatness of the flow line slope. Rainfall is one of the key contributing factors here. Landslides induced by heavy and extreme rainfall in steep mountainous regions occur frequently (Zhou et al., 2022).

3 Methods

A detailed flowchart of the present study is given in Figure 3, and the process contains the following specific steps. First, we prepared a positive sample dataset of 1186 landslides with a label value of 1. Next, four non-landslide sample datasets, as negative samples with a label value of 0, were constructed using four methods. The number of samples in each negative sample dataset was consistent with the positive samples (Petschko et al., 2014). Third, we combined the positive samples, negative samples, and the 11 conditioning factors to generate four sample datasets, which were divided for training and validation at 70% and 30%, respectively. Finally, the performance of the ML models was assessed and the final LSM obtained by comparison.

3.1 Non-landslide data generation

Traditionally, non-landslide samples are randomly selected from areas outside the area of recorded landslides. However, these areas usually include a large number of unstable slopes and many unidentified landslides, and hence cannot be used as negative samples. To overcome these drawbacks, this study presents a negative sample generation method based on a self-organizing-map and a one-class SVM model. The flowchart is given in Figure 4.

3.1.1 Self-organizing map

A self-organizing map (SOM) (Ritter and Kohonen, 1989) is an unsupervised learning algorithm and a special artificial neural network (ANN). The SOM can map high dimensional data with complex and nonlinear relationships onto a low-dimensional space with simple geometrical structures and relationships. It can perform cluster analysis and divide the entire input space into several disjointed regions. The SOM network has an input layer and a competitive layer.

If we assume that $\mathbf{X} = [x_1, x_2, ..., x_n]^T$ is the input variable, and $\mathbf{W}_j = [w_{j1}, w_{j2}, ..., w_{jn}]^T$, $j = 1, 2, ..., M$ is the weight coefficient of neurons, where M is the number of neurons in the competitive layer. In the competitive layer, neighboring neurons are connected to each other through certain relationships. The SOM employs a competitive learning algorithm in training (Huang et al., 2017). The learning rule is to calculate the distance between the $\mathbf{W}$ and $\mathbf{X}$, and the neuron with the smallest distance is considered the winner. In this study, the distance is calculated using the Euclidean distance formula:

$$dist(\mathbf{X}, \mathbf{W}_j) = \sqrt{(\sum_{i=1}^{N} (x_i - w_{ji})^2)}. \quad (1)$$

3.1.2 One-class SVM

The one-class SVM (OC-SVM) (Schölkopf et al., 1999) is the more classical single classification algorithm and

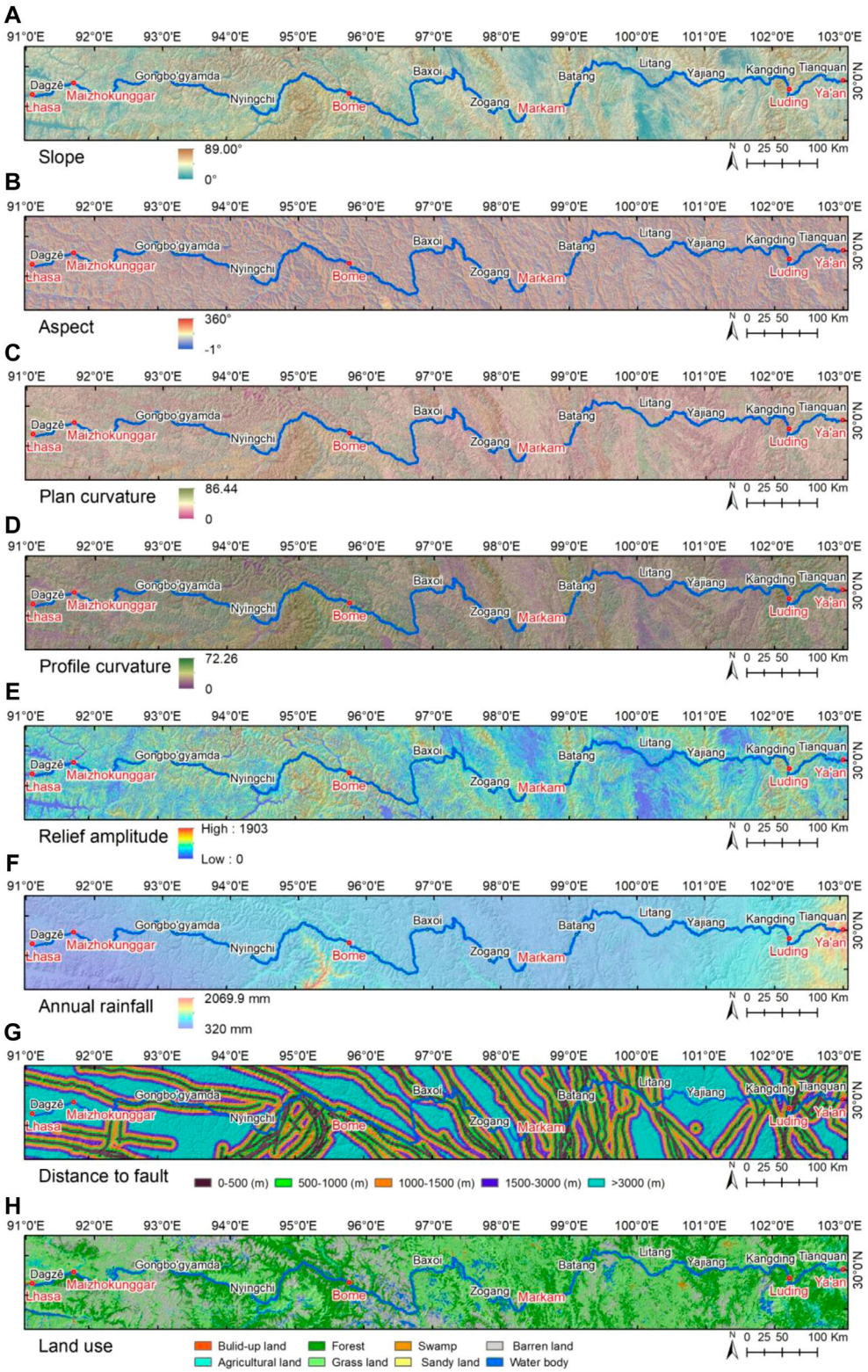

FIGURE 2
(Continued).

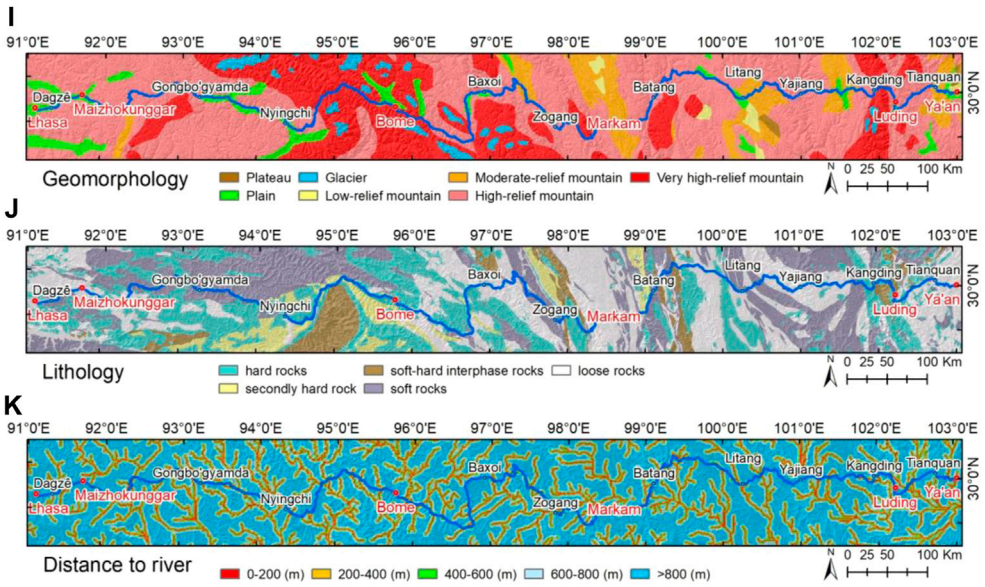

FIGURE 2
(Continued). Landslide conditioning factor along the Sichuan-Tibet Highway: **(A)** slope, **(B)** aspect, **(C)** plan curvature, **(D)** profile curvature, **(E)** relief amplitude, **(F)** annual rainfall, **(G)** distance to fault, **(H)** land use, **(I)** geomorphology, **(G)** lithology, **(K)** distance to river.

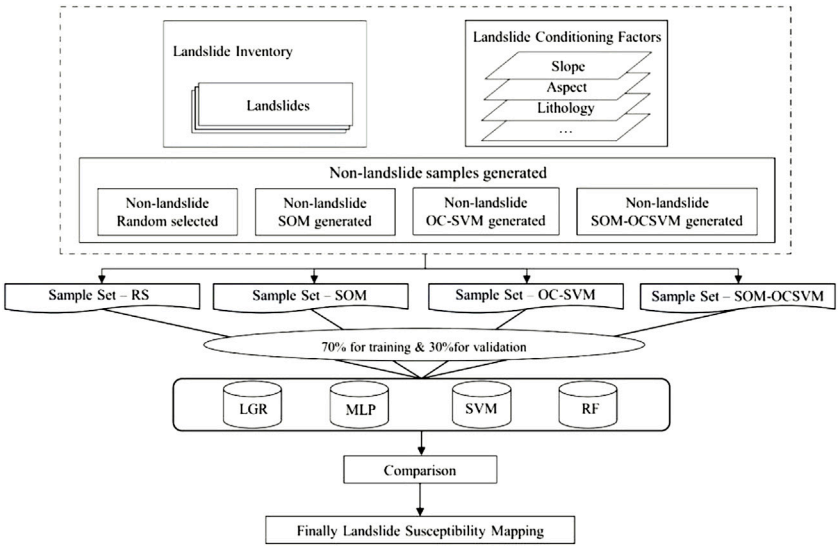

FIGURE 3
Flowchart of this study.

unsupervised classification method. Assuming that Φ is the nonlinear mapping kernel function defined in the n-dimensional data space, the samples are $\{x_i, i = 1, 2, \ldots, M\}, x_i \in R^n$. The OC-SVM maps the samples from low-dimensional to high-dimensional space through the Φ, establishing an optimal hyperplane between the zero point and the high-dimensional space (Chen et al., 2021). This hyperplane can be described by the n-dimensional vector $W = [w_1, w_2, \ldots, w_n]$ and a constant b. The determination function is defined as the following:

$$f(x) = \begin{cases} +1, & \boldsymbol{Wx} + b > 1 \\ -1, & \boldsymbol{Wx} + b < -1 \end{cases} \quad (2)$$

To ensure that the hyperplane clusters the samples with the optimal bounds, the quadratic programming problem needs to be optimized:

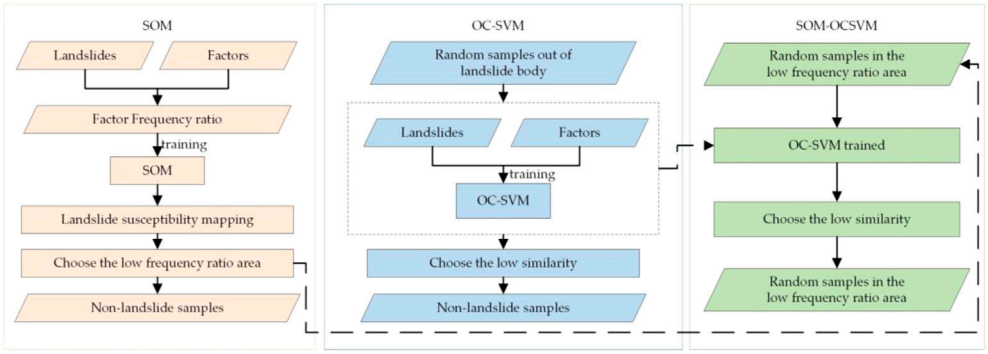

FIGURE 4
Flowchart of non-landslide dataset generation.

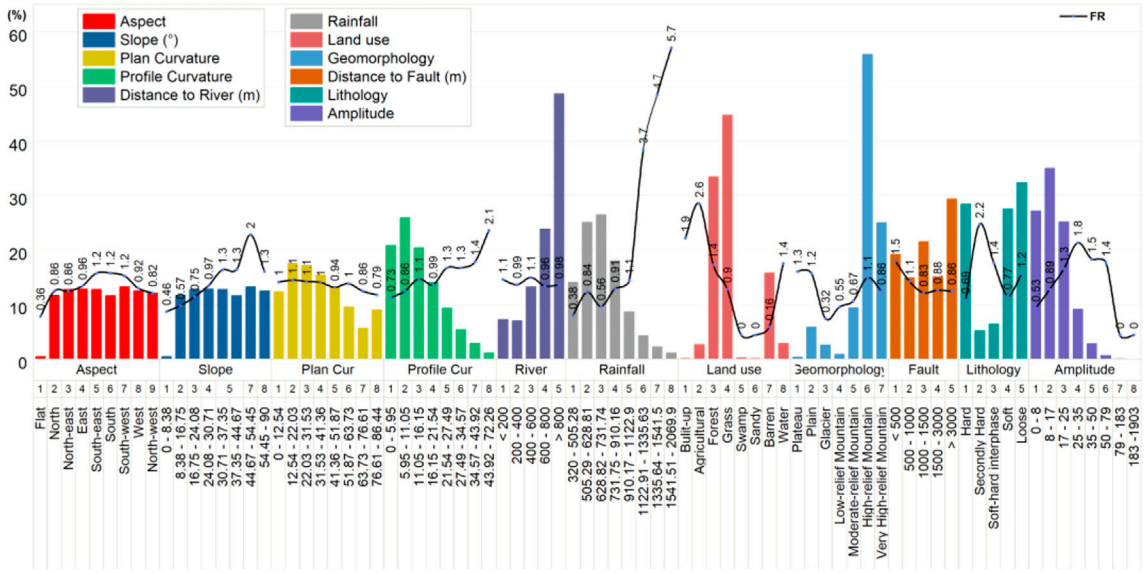

FIGURE 5
Statistical distribution and frequency ratio (FR) values of conditioning factors.

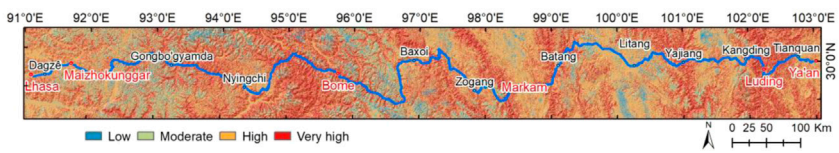

FIGURE 6
Landslide susceptibility map generated by SOM.

TABLE 1 Frequency ratios of the four susceptibility levels of SOM network.

	Classification	Pixels	Percentage of pixels (%)	Number of landslides	Percentage of landslides (%)	Frequency ratio
SOM	Very low	23863	3.64	4	0.34	0.09
	Low	84268	12.84	25	2.11	0.16
	Moderate	325473	49.60	485	40.89	0.82
	High	222531	33.92	672	56.66	1.67

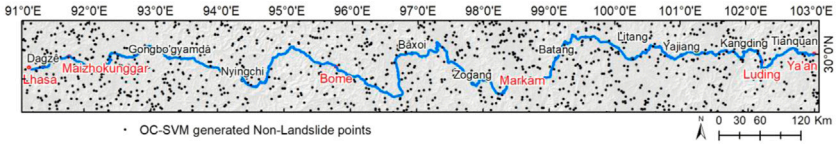

FIGURE 7
OC-SVM generated distribution map of non-landslide samples.

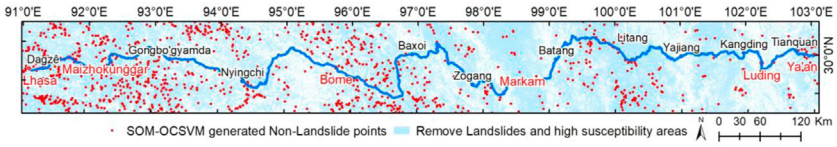

FIGURE 8
SOM-OCSVM generated distribution map of non-landslide samples.

$$min_{\omega,\xi_i,\rho}\frac{1}{2}\|\omega\|^2+\frac{1}{vN}\sum_{i=1}^{N}\xi_i-\rho, \tag{3}$$

$$s.t.(\omega,\Phi(x_i))>\rho-\xi_i,\ i=1,2,\ldots,n,\ \xi_i\geq 0, \tag{4}$$

where ω,ρ is the weight and threshold of the support vector, ρ, ξ_i is the relaxation variable, $\Phi(x_i)$ is the mapping function that maps x_i to a higher dimensional space, and $v\in(0,1)$. This method creates a hyperplane with parameters w,ρ that maximizes the hyperplane distance from the zero point in the feature space and separates the zero point from all data.

3.2 Machine learning

In this study, four machine learning (ML) models, which are currently widely used, were selected to verify the effects of non-landslide samples on LSM, i.e., the logistic regression (LGR) (Aslam et al., 2022), multilayer perceptron (MLP) (Li et al., 2019), support vector machine (SVM) (Cortes and Vapnik, 1995), and random forest (RF) models (Breiman, 2001).

3.3 Model evaluation

The standard deviation (Std) effectively reflects the stability of the model. The smaller the value of the Std, the more stable the model. Receiver operating characteristics (ROCs) are important tools for model evaluation (Swets, 1988). Formula 5 calculates the true positive rate (TPR) and the false positive rate (FPR) and plots a curve with both the TPR and FPR. The area under the curve (AUC) is used to reflect the model performance and is usually between 0.5 and 1.

$$TPR=\frac{TP}{TP+FN},\ FPR=\frac{FP}{FP+TN}. \tag{5}$$

4 Experimental results

4.1 Factor analysis

Frequency ratios (FRs) are often used to reflect the effects of factors on landslide occurrence. Figure 5 shows the FR value of all

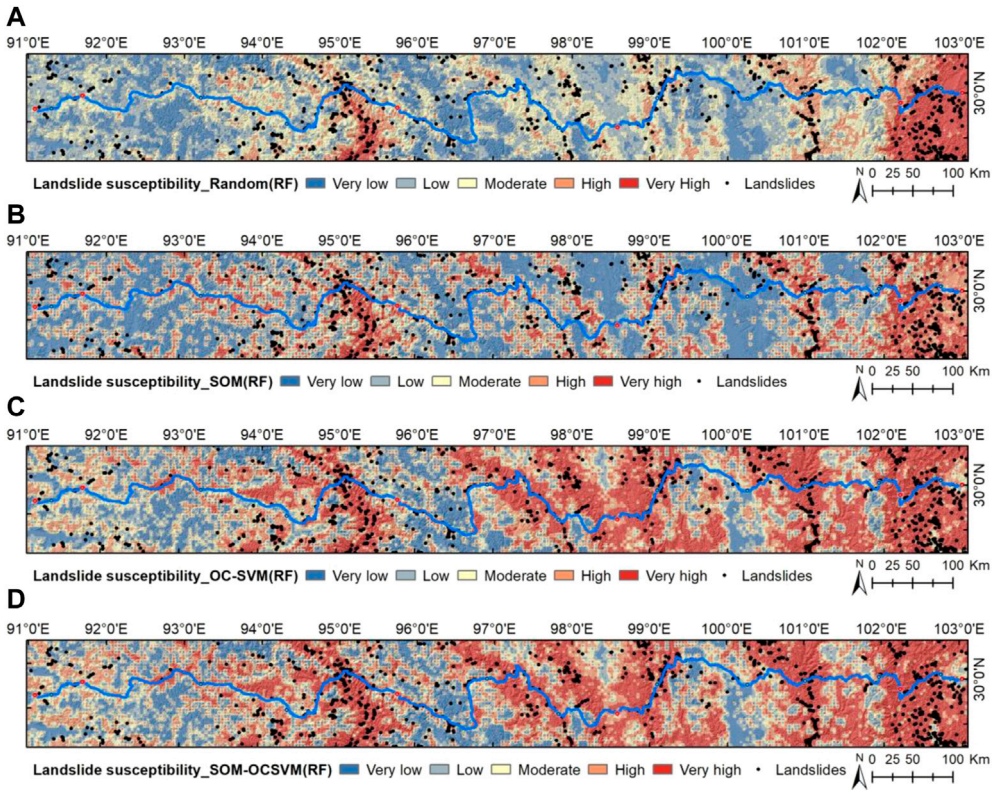

FIGURE 9
Landslide susceptibility map based on the RF with different negative data: **(A)** random, **(B)** SOM, **(C)** OC-SVM, and **(D)** SOM-OCSVM.

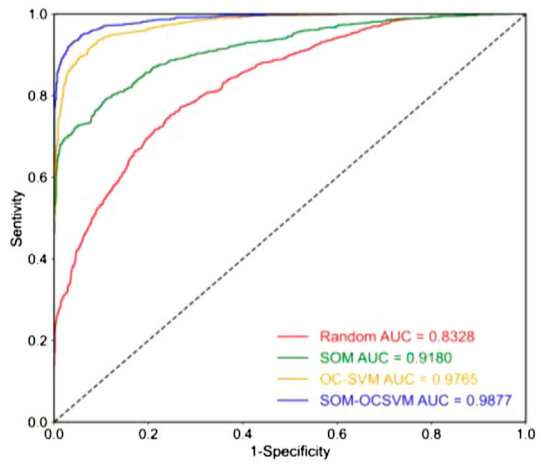

FIGURE 10
ROC curves of four non-landslide data generation strategies.

factors and their subclass percentages. It reveals that the probability of a landslide increases as the slope, the profile curvature, and the annual rainfall rise, and decreases as the distance to fault and to river rise. For aspect, the flat class had a lower FR value, indicating less probability of landslide in flat areas. The majority of landslides occur on built-up and agricultural land. In terms of geomorphology, there are small landslides in the glaciers, low-relief mountains, and moderate-relief mountains. Concerning relief amplitude, the range of 25–79 m is generally prone to landslides, while in terms of lithology, second-hand rocks and soft-hard interphase rocks are more prone to landslides.

4.2 Non-landslide sample generation

4.2.1 Non-landslide sample generation based on the SOM network

The SOM network was used to generate reasonable non-landslide samples. We used the normalized frequency ratios of the factors as the input variables, which consider about the distribution relationship between landslides and factors. The output variables are the four levels of landslide susceptibility. Therefore, the input layer has eleven neurons representing the frequency ratio of the conditioning factors, and the output layer has four neurons representing four different susceptibility levels. For the training process, the learning

TABLE 2 Landslide susceptibility levels and percentage of landslides in the study area.

Susceptibility level	Pixels	Percentage of pixels (%)	Number of landslides	Percentage of landslides (%)
Random				
Very low	112787	17.20	23	1.94
Low	204504	31.18	141	11.89
Moderate	199040	30.35	288	24.28
High	89736	13.68	378	31.87
Very high	49787	7.60	356	30.02
SOM				
Very low	172593	26.32	74	6.24
Low	158675	24.19	161	13.58
Moderate	111092	16.93	182	15.35
High	110798	16.89	317	26.73
Very high	102696	15.66	452	38.11
OC-SVM				
Very low	79357	12.10	25	2.11
Low	96733	14.75	51	4.30
Moderate	116826	17.81	100	8.43
High	150057	22.88	272	22.93
Very high	212881	32.46	738	62.23
SOM-OCSVM				
Very low	76198	11.62	19	1.60
Low	93700	14.29	49	4.13
Moderate	113573	17.32	111	9.36
High	155069	23.64	250	21.08
Very high	217314	33.13	757	63.83

TABLE 3 AUC and Std of four machine learning models with different non-landslide datasets.

Sample method	LGR		MLP		SVM		RF	
	AUC	Std	AUC	Std	AUC	Std	AUC	Std
Random	0.7194	0.1947	0.7048	0.1754	0.7206	0.1963	0.8328	0.1703
SOM	0.8420	0.1160	0.7810	0.1576	0.8467	0.1207	0.9180	0.1025
OC-SVM	0.9073	0.0856	0.9360	0.0864	0.9485	0.0601	0.9765	0.0519
SOM-OCSVM	0.9480	0.0517	0.9562	0.0803	0.9689	0.0445	0.9877	0.0354

rate is initialized to a value of 0.5 and reduced linearly to 0.01 during the training process. The maximum number of iterations is set at 1000. When it is reached, the training process is finished.

As shown in Figure 6, the landslide susceptibility map produced using the SOM network is classified into four levels: very low (3.64%), low (12.84%), medium (49.60%), and high (33.92%). Table 1 shows the frequency ratio of each level. The levels of very low, low, and medium susceptibility have low frequency ratios. It is therefore reasonable that non-landslide samples were randomly selected from them.

4.2.2 Non-landslide sample generation based on a one-class SVM method

The OC-SVM only needs to input landslide samples to the network for training since it only focuses on learning the features of the landslides. The specific process is as follows:

First, we inputted the landslide samples to train the OC-SVM model. Second, we randomly selected five times the number of landslides as the prediction data in the areas outside the landslides, and inputted them into the model. These were assigned a value of 1 or −1, according to their similarity with the features of the landslides learned by the model. The value of low similarity was −1. We selected the data with low similarity as the non-landslide samples, and the spatial distribution is shown in Figure 7.

4.2.3 Non-landslide sample generation based on the SOM-OCSVM method

In order to further optimize the selection of non-landslide samples and enhance the performance of data-driven models, this study combined the SOM network with the OC-SVM network to determine the non-landslide samples participating in ML-based LSM. The specific process was as follows: First, we randomly selected the prediction data in the susceptible area with the low frequency ratios generated by the SOM network. Next, we inputted the prediction data into the OC-SVM model trained by the landslides and screened out the data with low similarity. The spatial distribution is shown in Figure 8. The final non-landslide samples were all outside the landslide and high susceptibility area generated by the SOM, which can better ensure the separation of the positive and negative samples inputted to the ML model and generate more accurate LSM.

4.3 Effects of non-landslide sample selection

Figure 9 shows the LSMs generated by the RF model based on different non-landslide sample datasets. The natural break classification was applied to divide landslide susceptibility into five levels: very high, high, moderate, low, and very low. The LSMs show significant differences in the spatial distribution of the susceptibility area. As the ML algorithm and the landslide samples are consistent, this difference comes from the different non-landslide sample datasets. This result suggests a close relationship between the quality of non-landslide samples and the performance of LSM. To quantitatively evaluate the performance of the model, Figure 10 shows the ROC curves for the four non-landslide sample datasets. The AUC values are 0.8328, 0.9180, 0.9765, and 0.9877, respectively. Among the four datasets, the RF based on the SOM-OCSVM reached the highest AUC value (0.9877). The AUC value of the SOM-OCSVM had the most significant improvement (0.1549), confirming that the non-landslide sample generation method proposed in this study results in a remarkable improvement in the performance of RF-based LSM.

In order to quantitatively describe the differences brought by different non-landslide sample datasets to LSM, we computed the proportion of areas from each susceptibility level and the proportion of the landslides by overlaying the landslide distribution, as shown in Table 2. The evaluation results reflect a great difference. The levels of moderate, high, and very high are the landslide hazard areas. From the randomly generated non-landslide sample dataset, 86.17% of the landslides exist in 51.63% of the hazard area of LSM. For SOM, 80.19% of the landslides exist in 49.66% of the hazard area. For OC-SVM, 93.59% of the landslides exist in 73.15% of the hazard area. For SOM-OCSVM, however, 94.27% of landslides exist in 74.09% of the hazard area, with only 5.73% of landslides in the very low and low susceptibility areas. This confirms that the SOM-OCSVM can effectively obtain the areas with a small probability of landslide occurrence in the study area and hence better eliminate the influence of unstable slopes and unidentified landslides on LSM.

To further validate the impact of non-landslide samples on ML-based landslide susceptibility evaluation (LSE), we compared four ML models: MLP, SVM, LGR, and RF. Table 3 shows in detail the AUC and Std of the four ML models for different non-landslide sample datasets. It can be seen that for the randomly generated non-landslide sample dataset, the AUC values are the lowest and the Std values are the highest. The non-landslide sample dataset, generated based on the SOM-OCSVM model, has the most elevated AUC values and the most reduced Std values of the four machine learning models. That is, the accuracy and stability of all four models increased sequentially as the non-landslide sample dataset changed. The result confirms that the non-landslide samples can affect the accuracy of the models driven by data, and that the non-landslide samples generated by the SOM-OCSVM method proposed in this study are reasonable and accurate.

5 Discussion

As stated in the introduction, most data-driven methods for predicting the distribution of areas of landslide susceptibility depend on data sets with both positive (landslide) and negative (non-landslide) data. However, the list of landslides obtained by remote sensing interpretations, field surveys, and historical records is incomplete. Therefore, unidentified landslides and unstable slopes may be mistakenly selected as non-landslides when the non-landslide samples are considered, which can affect the reliability of LSM. Based on results, the method proposed in this study can improve the reliability of the data-driven model-based LSM by providing reliable non-landslide samples.

There are differences in the performance of the four machine-learning algorithms (MLP, SVM, LGR, and RF) utilized in this work to estimate landslide susceptibility in the same study area. The RF

outperformed the other models. It is impossible to find a general approach that applies to all regions. It is therefore necessary to evaluate and compare multiple methods and models in an integrated manner (Lv et al., 2022), or to integrate different algorithmic models (Dou et al., 2020). This will ensure the most suitable method for obtaining reliable LSMs and predicting the location of future landslides more accurately is found, thereby mitigating the damage and loss caused by such disasters.

6 Conclusion

In this study, we proposed a method combining SOM and OC-SVM (SOM-OCSVM) models to generate more reasonable non-landslide samples. Based on four ML models (LGR, MLP, SVM, and RF) established by the generated negative datasets (random, SOM, OC-SVM, and SOM-OCSVM), we performed LSM for the landslides of the Sichuan-Tibet Highway (G318). Model performance was compared using the ROC curve, AUC, and Std. The results show that the selection of non-landslide samples has great influence on the ML model performance in LSM studies, and the method presented in this study can effectively reduce the uncertainty surrounding negative data and significantly improve the performance of the landslide susceptibility model. This method of landslide susceptibility mapping may also be extended to regions with different geological conditions, which may in turn be helpful for further landslide prevention and mitigation.

Data availability statement

The raw data supporting the conclusion of this article will be made available by the authors, without undue reservation.

Author contributions

CY: model design, formal analysis, conceptualization and writing—review; RT: formal analysis, conceptualization, writing—review and editing; RW, ZG, and HZ: visualization, writing—review and editing, software, and methodology.

Funding

This work was supported in part by the Second Tibetan Plateau Scientific Expedition and Research Program (2019QZKK0902), the National Natural Science Foundation of China (42071411), and the key research and development program of Sichuan Province (2022YFG0200).

Conflict of interest

The authors declare that the research was conducted in the absence of any commercial or financial relationships that could be construed as a potential conflict of interest.

Publisher's note

All claims expressed in this article are solely those of the authors and do not necessarily represent those of their affiliated organizations, or those of the publisher, the editors, and the reviewers. Any product that may be evaluated in this article, or claim that may be made by its manufacturer, is not guaranteed or endorsed by the publisher.

References

Aditian, A., Kubota, T., and Shinohara, Y. (2018). Comparison of GIS-based landslide susceptibility models using frequency ratio, logistic regression, and artificial neural network in a tertiary region of Ambon, Indonesia. *Geomorphology* 318, 101–111. doi:10.1016/j.geomorph.2018.06.006

Aslam, B., Maqsoom, A., Khalil, U., Ghorbanzadeh, O., Blaschke, T., Farooq, D., et al. (2022). Evaluation of different landslide susceptibility models for a local scale in the chitral district, northern Pakistan. *Sensors* 22, 3107. doi:10.3390/s22093107

Bordoni, M., Galanti, Y., Bartelletti, C., Persichillo, M. G., Barsanti, M., Giannecchini, R., et al. (2020). The influence of the inventory on the determination of the rainfall-induced shallow landslides susceptibility using generalized additive models. *CATENA* 193, 104630. doi:10.1016/j.catena.2020.104630

Breiman, L. (2001). Random forests. *Mach. Learn.* 45, 5–32. doi:10.1023/A:1010933404324

Chen, F., Chen, J., Huang, W., Chen, S., Huang, X., Jin, L., et al. (2019). Westerlies Asia and monsoonal Asia: Spatiotemporal differences in climate change and possible mechanisms on decadal to sub-orbital timescales. *Earth. Sci. Rev.* 192, 337–354. doi:10.1016/j.earscirev.2019.03.005

Chen, S., Miao, Z., Wu, L., Zhang, A., Li, Q., and He, Y. (2021). A one-class-classifier-based negative data generation method for rapid earthquake-induced landslide susceptibility mapping. *Front. Earth Sci.* 9. doi:10.3389/feart.2021.609896

Cortes, C., and Vapnik, V. (1995). Support-vector networks. *Mach. Learn.* 20, 273–297. doi:10.1023/A:1022627411411

Dou, J., Yunus, A. P., Bui, D. T., Merghadi, A., Sahana, M., Zhu, Z., et al. (2020). Improved landslide assessment using support vector machine with bagging, boosting, and stacking ensemble machine learning framework in a mountainous watershed, Japan. *Landslides* 17, 641–658. doi:10.1007/s10346-019-01286-5

Erener, A., and Düzgün, H. S. B. (2010). Improvement of statistical landslide susceptibility mapping by using spatial and global regression methods in the case of More and Romsdal (Norway). *Landslides* 7, 55–68. doi:10.1007/s10346-009-0188-x

Felicísimo, Á. M., Cuartero, A., Remondo, J., and Quirós, E. (2013). Mapping landslide susceptibility with logistic regression, multiple adaptive regression splines, classification and regression trees, and maximum entropy methods: A comparative study. *Landslides* 10, 175–189. doi:10.1007/s10346-012-0320-1

Hess, D. M., Leshchinsky, B. A., Bunn, M., Benjamin Mason, H., and Olsen, M. J. (2017). A simplified three-dimensional shallow landslide susceptibility framework considering topography and seismicity. *Landslides* 14, 1677–1697. doi:10.1007/s10346-017-0810-2

Huang, F., Yin, K., Huang, J., Gui, L., and Wang, P. (2017). Landslide susceptibility mapping based on self-organizing-map network and extreme learning machine. *Eng. Geol.* 223, 11–22. doi:10.1016/j.enggeo.2017.04.013

Kavzoglu, T., Sahin, E. K., and Colkesen, I. (2014). Landslide susceptibility mapping using GIS-based multi-criteria decision analysis, support vector machines, and logistic regression. *Landslides* 11, 425–439. doi:10.1007/s10346-013-0391-7

Keles, F., and Nefeslioglu, H. A. (2021). Infinite slope stability model and steady-state hydrology-based shallow landslide susceptibility evaluations: The Guneysu catchment area (Rize, Turkey). *CATENA* 200, 105161. doi:10.1016/j.catena.2021.105161

Li, D., Huang, F., Yan, L., Cao, Z., Chen, J., and Ye, Z. (2019). Landslide susceptibility prediction using particle-swarm-optimized multilayer perceptron: Comparisons with multilayer-perceptron-only, BP neural network, and information value models. *Appl. Sci. (Basel).* 9, 3664. doi:10.3390/app9183664

Liu, Z., Qiu, H., Zhu, Y., Liu, Y., Yang, D., Ma, S., et al. (2022). Efficient identification and monitoring of landslides by time-series InSAR combining single- and multi-look phases. *Remote Sens. (Basel).* 14, 1026. doi:10.3390/rs14041026

Lv, L., Chen, T., Dou, J., and Plaza, A. (2022). A hybrid ensemble-based deep-learning framework for landslide susceptibility mapping. *Int. J. Appl. Earth Obs. Geoinf.* 108, 102713. doi:10.1016/j.jag.2022.102713

Ma, S., Xu, C., and Shao, X. (2020). Spatial prediction strategy for landslides triggered by large earthquakes oriented to emergency response, mid-term resettlement and later reconstruction. *Int. J. Disaster Risk Reduct.* 43, 101362. doi:10.1016/j.ijdrr.2019.101362

Petschko, H., Brenning, A., Bell, R., Goetz, J., and Glade, T. (2014). Assessing the quality of landslide susceptibility maps – case study Lower Austria. *Nat. Hazards Earth Syst. Sci.* 14, 95–118. doi:10.5194/nhess-14-95-2014

Pham, B. T., Pradhan, B., Tien Bui, D., Prakash, I., and Dholakia, M. B. (2016). A comparative study of different machine learning methods for landslide susceptibility assessment: A case study of uttarakhand area (India). *Environ. Model. Softw.* 84, 240–250. doi:10.1016/j.envsoft.2016.07.005

Qiu, H., Zhu, Y., Zhou, W., Sun, H., He, J., and Liu, Z. (2022). Influence of DEM resolution on landslide simulation performance based on the Scoops3D model. *Geomat. Nat. Hazards Risk* 13, 1663–1681. doi:10.1080/19475705.2022.2097451

Ritter, H., and Kohonen, T. (1989). Self-organizing semantic maps. *Biol. Cybern.* 61, 241–254. doi:10.1007/BF00203171

Schölkopf, B., Williamson, R. C., Smola, A., Shawe-Taylor, J., and Platt, J. (1999). "Support vector method for novelty detection," in *Advances in neural information processing systems* (MIT Press).

Swets, J. A. (1988). Measuring the accuracy of diagnostic systems. *Science* 240, 1285–1293. doi:10.1126/science.3287615

Wang, L., Qiu, H., Zhou, W., Zhu, Y., Liu, Z., Ma, S., et al. (2022). The post-failure spatiotemporal deformation of certain translational landslides may follow the pre-failure pattern. *Remote Sens. (Basel).* 14, 2333. doi:10.3390/rs14102333

Wang, W., He, Z., Han, Z., Li, Y., Dou, J., and Huang, J. (2020a). Mapping the susceptibility to landslides based on the deep belief network: A case study in sichuan Province, China. *Nat. Hazards* 103, 3239–3261. doi:10.1007/s11069-020-04128-z

Wang, Y., Feng, L., Li, S., Ren, F., and Du, Q. (2020b). A hybrid model considering spatial heterogeneity for landslide susceptibility mapping in Zhejiang Province, China. *CATENA* 188, 104425. doi:10.1016/j.catena.2019.104425

Wei, R., Ye, C., Sui, T., Ge, Y., Li, Y., and Li, J. (2022). Combining spatial response features and machine learning classifiers for landslide susceptibility mapping. *Int. J. Appl. Earth Obs. Geoinf.* 107, 102681. doi:10.1016/j.jag.2022.102681

Yalcin, A., Reis, S., Aydinoglu, A. C., and Yomralioglu, T. (2011). A GIS-based comparative study of frequency ratio, analytical hierarchy process, bivariate statistics and logistics regression methods for landslide susceptibility mapping in Trabzon, NE Turkey. *CATENA* 85, 274–287. doi:10.1016/j.catena.2011.01.014

Ye, C., Wei, R., Ge, Y., Li, Y., Junior, J. M., and Li, J. (2022). GIS-based spatial prediction of landslide using road factors and random forest for Sichuan-Tibet Highway. *J. Mt. Sci.* 19, 461–476. doi:10.1007/s11629-021-6848-6

Zhou, W., Qiu, H., Wang, L., Pei, Y., Tang, B., Ma, S., et al. (2022). Combining rainfall-induced shallow landslides and subsequent debris flows for hazard chain prediction. *CATENA* 213, 106199. doi:10.1016/j.catena.2022.106199

frontiers | Frontiers in Earth Science

TYPE Original Research
PUBLISHED 18 January 2023
DOI 10.3389/feart.2022.1053327

OPEN ACCESS

EDITED BY
Haijun Qiu,
Northwest University, China

REVIEWED BY
Li Shen,
Southwest Jiaotong University, China
Lei He,
Chengdu University of Information Technology, China
Wenting Zhang,
Huazhong Agricultural University, China

*CORRESPONDENCE
Chang Liu,
1004526632@qq.com

SPECIALTY SECTION
This article was submitted to Geohazards and Georisks, a section of the journal Frontiers in Earth Science

RECEIVED 25 September 2022
ACCEPTED 02 November 2022
PUBLISHED 18 January 2023

CITATION
Sui H, Liu C, Ye C, Xu X and Sui T (2023), Analysis of ecosystem resilience in Jiuzhaigou Valley Scenic Area under the effect of geohazards.
Front. Earth Sci. 10:1053327.
doi: 10.3389/feart.2022.1053327

Analysis of ecosystem resilience in Jiuzhaigou Valley Scenic Area under the effect of geohazards

Haixia Sui[1], Chang Liu[2]*, Chengming Ye[2], Xiaolong Xu[2] and Tianbo Sui[2]

[1]School of Tourism and Culture Industry, Chengdu University, Chengdu, China, [2]College of Geophysics, Chengdu University of Technology, Chengdu, China

The effects of geohazards on the ecological environment and ecological spatial pattern have received wide attention from scholars. However, the positive role played by ecological restoration projects on the environment and in the reduction of geohazards has usually been neglected. Jiuzhaigou Valley Scenic Area is a world natural heritage area, has a high incidence of geohazards, and is a demonstration area for ecological restoration projects. Based on remote sensing technology, this paper adopted an InVEST model (Integrated Valuation of Ecosystem Services and Tradeoffs) and ecological landscape index to extract information about spatio-temporal changes in Jiuzhaigou from 2013 to 2020. This study utilized a quantitative analysis of the ecological recoverability of Jiuzhaigou in cases of artificial restoration and spontaneous restoration under different types of geohazards. Results showed that forests play a vital role in maintaining and controlling habitat quality; artificial restoration can significantly ameliorate the impact of geohazards on the scenic area. As of 2020, the forested scenic area recovered 3.868 km^2, and the habitat quality index rebounded to 98.88% of the historical high. The ecological restoration project significantly shortened the scenic area recover time of its ecosystem service capability.

KEYWORDS

Jiuzhaigou tourist scenic, ecosystem services, ecological restoration project, InVEST model, geohazards

Introduction

The evaluation of ecosystem services has guiding significance in promoting the coordinated development of regional construction and ecological environmental protection. Nature reserves are effective in maintaining biodiversity, improving the ecological environment and enhancing ecosystem service function (Maes et al., 2012; Van Vooren et al., 2018; Melzer and Bellingrath-Kimura, 2021). But natural reserves are vulnerable to human factors and geohazards. Among them, human impacts include the deterioration of the ecological environment caused by human disturbance; however, there is a benefit of human scientific management in ecological restoration. Therefore, analyzing the spatial and temporal evolution of regional ecosystem service functions

not only helps to quantitatively assess the role of anthropogenic management after geohazards, which relates to the natural evolution of the gain, but also clarifies the value and significance of the scientific management system for ecosystem service functions.

Habitat quality is an essential condition in measuring ecosystem service functions within the environment. The InVEST model is widely used in the quantitative assessment of ecosystem services such as habitat quality, carbon storage, soil conservation, and water supply. Scholars have completed many regional habitat quality assessments based on the InVEST model. For example, Li Mengyao used the habitat quality module of the InVEST model and a GIS spatial analysis method to assess the spatial and temporal differences in habitat quality in Shiyan City to provide a theoretical basis for ecological restoration in earthquake-damaged areas (Li et al., 2021). Based on the InVEST HQ model, Wu Linlin estimated the spatial and temporal variation of GBA habitat quality from 1995 to 2015 and analyzed the potential factors that affected habitat quality (Wu et al., 2021). Aneseyee analyzed the spatial and temporal variability of habitat quality in different land-use types for the southern Ethiopian watershed (Aneseyee et al., 2020). Ding used FLUS (Future Land Use Simulation) and the InVEST model to establish a modeling framework to analyze the spatial characteristics and multiple scenarios of habitat quality in Dongying City (Ding et al., 2021). In conclusion, the InVEST model incorporates a relatively complete system in terms of habitat quality, and it helps to develop regional ecological planning and management strategies through a comprehensive assessment to deal with the damage of geohazards.

The spatial changes of ecological landscape patterns are closely related to the material and energy cycles among habitat patches, and the changes of their spatial patterns significantly affect the ecosystem service functions of the whole region (Sowinska-Swierkosz, 2017). It is clear that remote sensing technology has advantages of a wide range and high efficiency in analyzing ecological landscape pattern changes. Scholars mostly used remote sensing images to extract corresponding information and explore spatial pattern changes. For example, Maingi used Landsat MSS and other imagery data to obtain information on the dynamic change of the wetland area of the Tana River in Kenya. Then, he analyzed the link between human activities and wetland landscape changes and clearly indicated that human activities would cause changes in wetland landscape patterns (Maingi and Marsh, 2001). In combination with the ecological landscape index method and GIS technology, Liu Gui analyzed the ecological landscape changes in Poyang Lake Ecological Economic Zone from 1990 to 2005. He concluded that the degree of ecological landscape fragmentation in the study area increased and the overall degree of aggregation showed an upward trend (Liu et al., 2013). In a study of the landscape pattern, the calculated results of the landscape pattern index are mostly used for quantitative and qualitative analysis of the regional landscape pattern.

Using anthropogenic factors as the driving force, the process of interaction between human activities and nature reserves exacerbates changes in ecosystem service functions. Scholars mainly focus on anthropogenic disturbances to quantify and clarify the negative effects of anthropogenic disturbances on ecological service functions. They focused less attention on the accelerated restoration and gain effect of the ecological environment, which were generated by anthropogenic management. For example, Wenmin Hu used the water yield module of the InVEST model to explore the impact of a poplar ecological conversion (PER) project, and the results provided an important reference for the national government to formulate sustainable wetland ecological policies (Hu et al., 2020). Recently, human activities have overexploited natural resources. Coupled with the impact of geohazards (Liu et al., 2022; Qiu et al., 2022; Wang et al., 2022), the ecological environment has suffered serious damage. These conditions have had an irreversible impact on regional ecosystems and led to ecological and environmental problems such as land degradation, vegetation destruction and a loss of biodiversity. Human scientific management can not only rationally utilize natural resources, but also reduce the destructive power of geohazards.

In this paper, we used remote sensing technology to obtain information on land cover changes in Jiuzhaigou Nature Reserve

TABLE 1 Tourism economic statistics of Jiuzhaigou Scenic Area from 2013 to 2020.

Time	Total number of visitors	Year-on-year	Total tourism revenue	Year-on-year
2013	3.71 million	27.20%	¥4.62 billion	21.22%
2014	4.63 million	24.80%	¥5.57 billion	20.56%
2015	4.82 million	4.10%	¥5.93 billion	6.46%
2016	5.07 million	5.19%	¥6.25 billion	5.40%
2017	3.12 million	−38.46%	¥6.07 billion	−2.88%
2018	0.15 million	−95.19%	¥0.17 billion	−97.20%
2019	1.21 million	706.67%	¥1.76 billion	935.29%
2020	2.20 million	81.82%	¥4.98 billion	182.95%

TABLE 2 Data and parameters.

Data type	Parameter	Definition and description
Landsat-7 image	B1 to B7	Band reflectance
	NDWI	(B3-B5)/(B3+B5)
	NDVI	(B5-B4)/(B5+B4)
Spectral indices	RVI	(B5/B4)
	NDBI	(B6-B5)/(B6+B5)
	NDSI	(B3-B6)/(B3+B6)
Terrain features	Elevation	DEM
	Slope	DEM grad

TABLE 3 Date of remote sensing images.

Year of remote sensing images	Date of remote sensing images
2013	6 April, 16 July, 1 August, 17 August, 4 October, 7 December
2014	8 January, 25 February, 1 June, 17 June, 23 October
2015	11 January, 12 February, 6 July, 23 August, 27 November
2016	14 January, 15 February, 2 March, 18 March, 3 April, 13 November
2017	17 February, 6 April, 11 June, 18 December
2018	19 January, 9 April, 19 November, 5 December
2019	22 January, 7 February, 11 March, 1 July, 22 November, 24 December
2020	10 February, 26 February, 14 April, 19 July, 20 August, 24 November

and Scenic Area from 2013 to 2020. Specifically, we used the InVEST model to quantitatively estimate habitat quality and analyze its spatial and temporal evolution characteristics. Using the "7.26 mudslide" and the "8.8" Jiuzhaigou earthquake (Zhang et al., 2021) as a starting point, we focused on the comprehensive assessment of recovery of the native environment under anthropogenic management and natural recovery. Finally, we explored the impact of the ecological restoration project on the restoration of ecosystem services.

Study area and data

Study area

Jiuzhaigou Valley Scenic Area is located in Jiuzhaigou County, Sichuan Province. It belongs to the Yangtze River system and its main ditch is more than 30 km long with a total area of 65,074.7 ha. Jiuzhaigou Valley Scenic Area includes a human-managed scenic area and a natural reserve without disturbance, as shown in Figure 1.

The study area is the core site and corridor zone of the Minshan population of giant pandas and is a typical natural ecosystem. Because of the abundant animal and plant resources in the study area, species scarcity is outstanding and there is a high value of ecological protection, scientific research and esthetic tourism. However, Jiuzhaigou Scenic Area is located in an active crustal zone. Geohazards such as earthquakes, landslides and mudslides are frequent in Jiuzhaigou (Wang and Mao, 2022), which poses a great threat to the sustainable development of its ecosystem service functions.

The "7.26 mudslide" in 2016 and the "8.8 Jiuzhaigou earthquake" in 2017 both caused great damage to Jiuzhaigou's infrastructure and ecological environment, and Jiuzhaigou's tourism economy suffered a major blow as shown in Table 1. The data in Table 1 were derived from the national economic and social development statistical bulletin and statistical yearbook of Jiuzhaigou County. Because the earthquake epicenter was located at the core of the scenic area, the surrounding area of the scenic highway was seriously damaged by geohazards. According to statistics, 153 geohazards, including avalanches, mudslides, landslides, and unstable slopes, were developed in Jiuzhaigou Scenic Area because of the "8.8 Jiuzhaigou earthquake."

After the "8.8 Jiuzhaigou earthquake," the provincial government officially issued "the Overall Plan for the Recovery and Reconstruction of Jiuzhaigou" on November 4. Then, the Jiuzhaigou Administration invested 11.4 billion yuan and implemented a number of ecological restoration projects. The ecological restoration projects adopted the most advanced and environment-friendly technologies to repair 80% of the damaged area.

First, vibrofotation stone columns were used to reinforce the dam body and enhance the stability and bearing capacity of the dam. Second, the Jiuzhaigou administration used a Rock-Soil Anchoring Technique to reinforce the unstable part of the rock and soil. Third, Protophyta and sticky rice lime mortar were used to fill the dam body and restore its original plant ecological environment. Finally, the Jiuzhaigou administration adopted landscape design technology to restore the original landscape before the earthquake.

Data and data processing

The study dataset mainly contains satellite images, topographic data, spectral index data and the resulting extracted land cover dataset. All spatial data were uniformly converted to the WGS_1984_UTM_48N coordinate system and the specific methodological data information is shown in Table 2.

The Landsat-7 images for the study period were obtained from the USGS and covered the period from 2013 to 2020. Referring to Global Land 30, Jiuzhaigou was divided into ten land cover types including agricultural land, forest, grass land, shrub,

TABLE 4 Stress factors and their stress intensity.

Stress factors	Weight coefficient	Maximum impact distance (km)	Attenuation type
Agricultural land	0.5	4.0	Linear
Construction land	1.0	5.0	Linear
Barren land	0.9	5.0	Exponent

TABLE 5 Sensitivity of land-use types to habitat stress factors.

Types of land cover	Suitability of habitat	Agricultural land	Construction land	Barren land
Agricultural land	0.5	0.3	0.8	0.4
Forest	1.0	0.5	0.9	0.5
Grass land	0.7	0.5	0.6	0.4
Shrub	0.8	0.5	0.8	0.3
Wetland	0.7	0.6	0.5	0.4
Water body	0.9	0.7	0.7	0.6
Construction land	0.0	0.0	0.0	0.4
Barren land	0.1	0.1	0.2	0.0
Snow and ice	0.0	0.0	0.0	0.1

TABLE 6 Ecological landscape index and significance.

Landscape index	Formula	Significance
Number Of Patches (NP)	$NP = \sum_{i=1}^{n} N_i$	The number of patches in a landscape type
Patch Density (PD)	$PD = \frac{\sum_{i=1}^{n} S_i}{A} * 100\%$	The degree to which landscape matrix is segmented by landscape type patches
Edge Density (ED)	$ED = \frac{\sum_{i=1}^{m}\sum_{j=1}^{n} e_{ij}}{A}$	The degree of isolation between habitat patches
Largest Patch Index (LPI)	$LPI = \frac{max_{j=1}(a_{ij})}{A} * 100\%$	The proportion of the total landscape area occupied by the largest patch in a patch type
Mean Area Of Patch (AREA_MN)	$AREA\_MN = \frac{\sum_{i=1}^{1} S_i}{NP}$	The scale of a certain type of patch in the landscape
Contagion Index (CONTAG)	$CONTAG = [1 + \frac{\sum_{i=1}^{m}\sum_{j=1}^{n}[P_i * \frac{g_{ij}}{\sum_{j=1}^{m} g_{ij}}] * [\ln (P_i * \frac{g_{ij}}{\sum_{j=1}^{m} g_{ij}})]}{2\ln(m)}]$	The degree of aggregation among different patch types in the landscape
Shannon's Diversity Index (SHDI)	$SHDI = -\sum_{i=1}^{m} P_i * \ln (P_i)$	The non-uniform distribution of patch types in the landscape
Aggregation Index (AI)	$AI = [\sum_{i=1}^{m} (\frac{g_{ii}}{max - g_{ii}}) P_i] * 100\%$	The connectivity between patches of each landscape type

wetland, water body, construction land, barren land, snow, and ice (Newbold et al., 2015; Camara, 2020).

We obtained samples from high-definition images using manual annotation and used a random forest algorithm to automatically extract land cover information in Jiuzhaigou (Svoboda et al., 2022). Two hundred samples were divided into two groups with a ratio of 7:3 for training and validation of the random forest model. The input features of the samples included band reflectance, a spectral index, and topographic features, and the specific feature information is shown in Table 2. The spectral features were calculated from annual synthetic cloud-free images, and DEM data were obtained from SRTM with a spatial resolution of 30 m. We selected images whose cloud cover fraction was lower than 20% in the study area from 2013 to 2020. We made the median mosaic synthesis of the images year by year to obtain the annual cloud-free images of Jiuzhaigou from 2013 to 2020. A total of 42 images (Table 3) were used in this paper, and the average cloud cover fraction was 13.72. The random forest classifier was used in this paper and achieved an overall accuracy of 81% and a Kappa coefficient of 0.77.

Research methodology

Habitat quality model

We used the raster of land cover types in the study area, the distance and weight between habitats and stressors, and the relative sensitivity of habitat types to stressors as input data (Terrado et al., 2016). We used the Habitat Quality module in the InVEST model to assess the quality of habitats in the study area.

The calculation formula is shown in Eq. 1:

$$Q_{xj} = H_j\left(1 - \frac{D_{xj}^z}{D_{xj}^z + k^z}\right) \quad (1)$$

In Eq. 1, Q_{xj} is the habitat quality index of the land cover type j and the raster x; H_j is the habitat suitability of the land cover type j and the raster x; k is the half-saturation constant; and z is the normalization factor and usually set to 2.5.

D_{xj} is the degree of habitat degradation, which is exhibited by stressors and is calculated as Eq. 2.

$$D_{xj} = \sum_{r=1}^{R}\sum_{y=1}^{Y_r}\left(\frac{W_r}{\sum_{r=1}^{R} W_r}\right) r_y i_{rxy} \beta_x S_{jr} \quad (2)$$

$$i_{rxy} = 1 - \left(\frac{d_{xy}}{d_{r\,max}}\right)(Linear\ recession) \quad (3)$$

$$i_{rxy} = exp\left(-\left(\frac{2.99}{d_{r\,max}}\right)d_{xy}\right)(Exponent\ recession) \quad (4)$$

In Eqs 2–4, D_{xj} is the habitat degradation of the land cover type j and the raster x; R is the number of stressors; W_r is the weight of the stressor; Y_r is the number of grids of the stressor; r_y is the intensity of the stressor; i_{rxy} is the level of stress of the stressor on the grid y for x; β_x is the level of habitat disturbance resistance (1 is full accessibility); S_{jr} is the sensitivity of stress factor r for the land type j; d_{xy} is the linear distance between x and y; and $d_{r\,max}$ is the maximum action distance of the stress factor r.

Selecting specific land cover types as stressors that destroy habitat quality, we established a link between stressors and land cover types, and we evaluated the effects of land cover type change patterns on habitat quality in the study area under multiple time phases. The parameters mainly included the influence distance and weight of the stressors (Table 4) and habitat suitability and sensitivity of land cover types to the stressors (Table 5).

Ecological landscape index

In this paper, we selected eight landscape indicators (Table 6) to quantitatively analyze the landscape pattern of Jiuzhaigou Scenic Area and the nature reserve ecosystem from 2013 to 2020. All

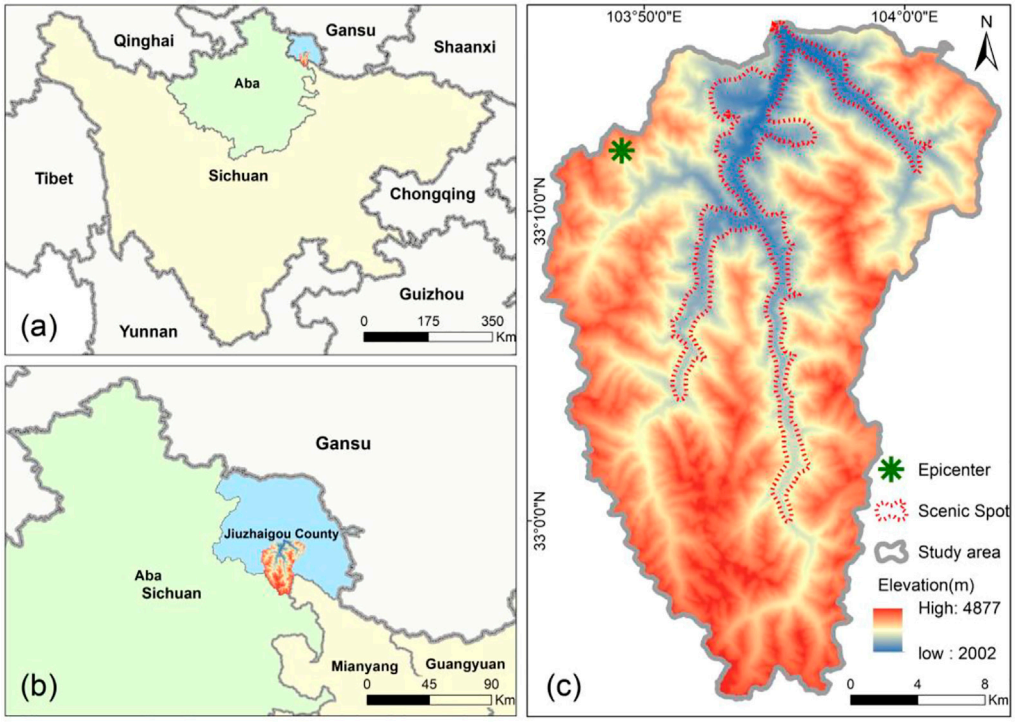

FIGURE 1
Geographical location of the study area. **(A)** Location of Jiuzhaigou in Sichuan Province. **(B)** Location of Jiuzhaigou in Jiuzhaigou County. **(C)** The study area in Jiuzhaigou.

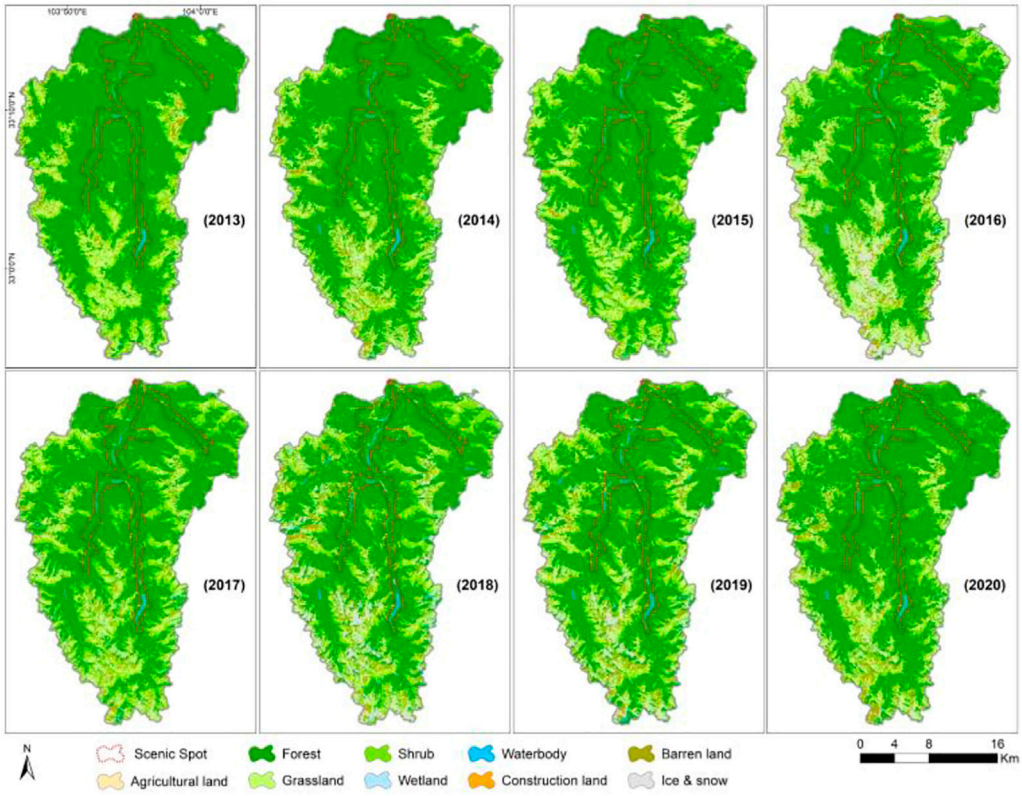

FIGURE 2
Spatio-temporal presentation of land cover in Jiuzhaigou.

indicators reflected the spatial characteristics of the Jiuzhaigou landscape pattern including area, shape, degree of heterogeneity, and fragmentation of the landscape (Berglund et al., 2012; Haddad et al., 2015; Schroter and Remme, 2016).

In Table 6, N_i is the number of patches of landscape i; A is the total area of all landscape areas of patches i; S_i is the total area of the landscape i; e_{ij} is the length of the boundary of landscape i and j; P_i is the ratio of landscape i; g_{ij} is the number of adjacent patches of landscape i and landscape j; and g_{ii} is the number of similar and adjacent patches of landscape type i.

Results and discussion

Spatial and temporal changes in land cover

The combination of Figure 2 and Table 7 shows that the land cover in Jiuzhaigou was mainly forest, grassland and shrub. The land cover also contains a variety of cover types such as wetland, water body, agricultural land, barren land, and snow and ice. The spatial distribution characteristics of Jiuzhaigou are related to the topography and altitude of the area. Overall, the scenic area had fewer land cover types, mainly forest and water body, which have slowly changed. The nature reserve had a full range of cover types that are under the pressure of geohazards, and its land cover interchanged among forest, grassland, shrub, and barren land.

Figures 3 and 4 represent the main land cover changes in Jiuzhaigou Nature Reserve and Scenic Area during the study period. With the continuous development of tourism in Jiuzhaigou and a breakthrough in the number of tourists year after year (Table 1), the forest area continuously declined from 2013 to 2018. As of 2016, the forest area in the scenic area decreased 3.705 km^2 and 5.96%, which was still smaller than the 14.95% of the nature reserve. As of 2018, the forest area in the scenic decreased by 6.109 km^2 and 9.82%, which was still smaller than the 20.21% that occurred in the nature reserve. Due to the implementation of standardized management and ecological restoration projects, the forest area of Jiuzhaigou grew rapidly from 2019 to 2020. The area of the forest in the scenic area increased by 3.868 km^2 and 6.9%, and the nature reserve increased by 71.5 km^2 and 21.48%. The forest restoration status achieved the highest level in 2013, which indicates that rational development and ecological protection projects played a leading role in the change of forest cover.

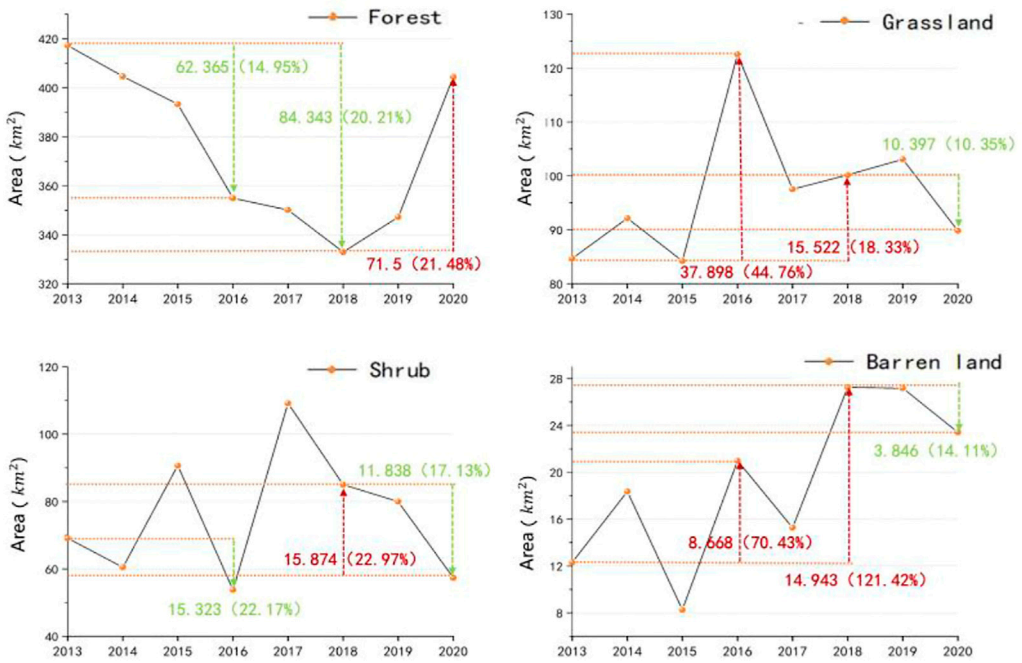

FIGURE 3
Main land cover changes in the Jiuzhaigou Nature Reserve.

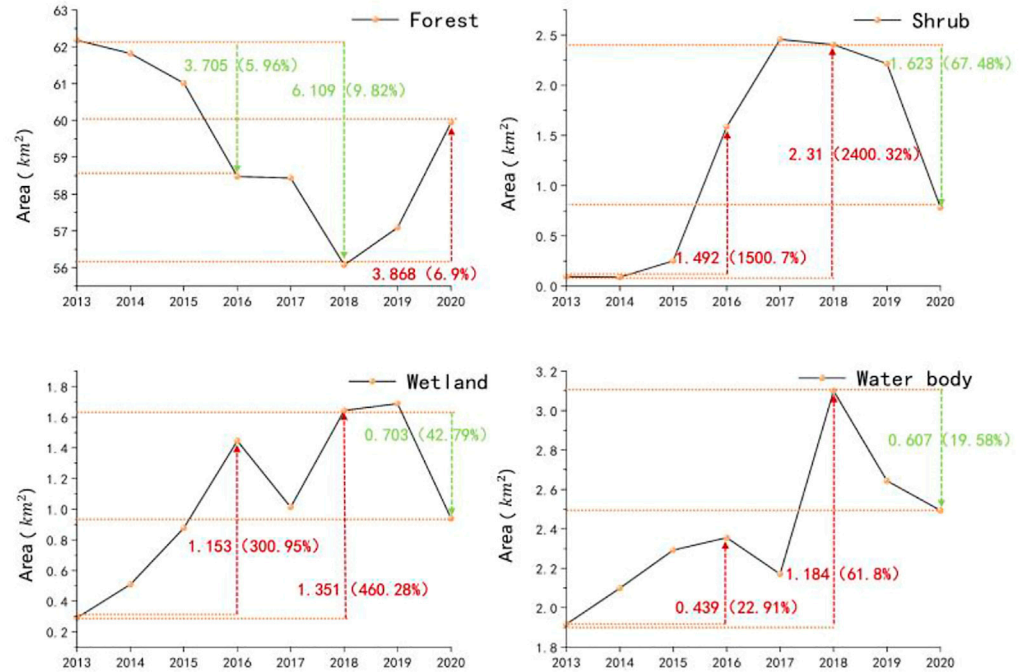

FIGURE 4
Main land cover changes in Jiuzhaigou Scenic Area.

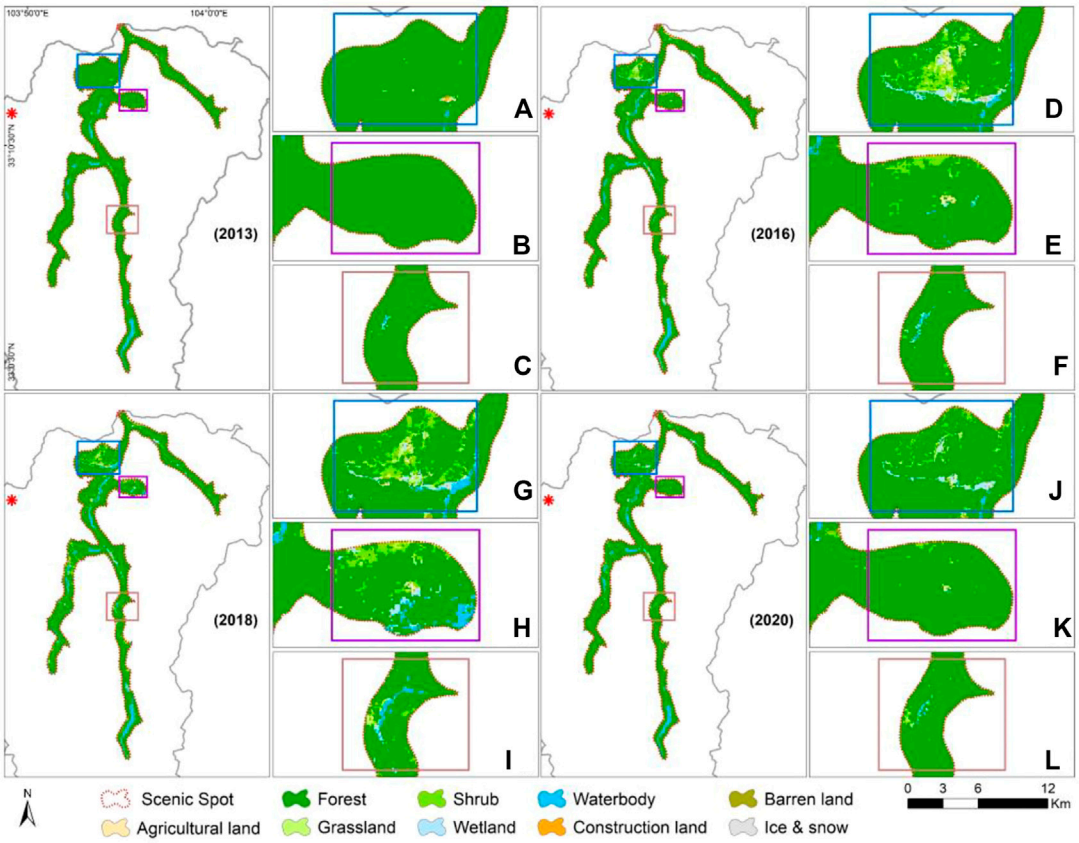

FIGURE 5
Spatial and temporal variation of main cover types in Jiuzhaigou Scenic Area: change in **(A,D,G,J)** shrub area, **(B,E,H,K)** wetland area, and **(C,F,I,L)** waterbody area.

TABLE 7 Change of land cover area in Jiuzhaigou (km^2).

Time	2013	2014	2015	2016	2017	2018	2019	2020
Agricultural land	0.07	0.05	0.04	0.22	0.05	0.21	0.03	0.09
Forest	479.45	466.43	454.28	413.38	408.56	388.99	404.30	464.36
Grass land	84.70	92.23	84.32	123.04	97.93	101.18	103.88	90.08
Shrub	69.21	60.59	90.92	55.38	111.59	87.40	82.19	58.06
Wetland	2.98	6.85	6.61	5.83	8.43	10.75	7.51	5.48
Water body	2.93	4.12	7.22	5.21	7.00	11.21	11.68	5.07
Construction land	0.24	0.24	0.25	0.10	0.25	0.23	0.21	0.19
Barren land	12.31	18.36	8.25	20.98	15.28	27.25	27.18	23.40
Snow and ice	0.14	3.14	0.13	27.9	2.93	24.80	15.04	5.28

In Figure 5, the forest in the scenic area landscape was converted to shrub, wetland, and water body during the study period due to geohazard stresses. As of 2016, shrub increased by 1.492 km^2, wetland increased by 1.153 km^2, and water body increased by 0.439 km^2. As of 2018, shrub increased by 2.31 km^2, wetland increased by 1.351 km^2, and water body increased by 1.184 km^2. Between 2018 and 2020, under the guidance of human management, the ecological environment of the scenic area gradually recovered. Areas such as shrub, wetland, and water body converted to forest, and they decreased by 1.623, 0.703, and 0.607 km^2, respectively.

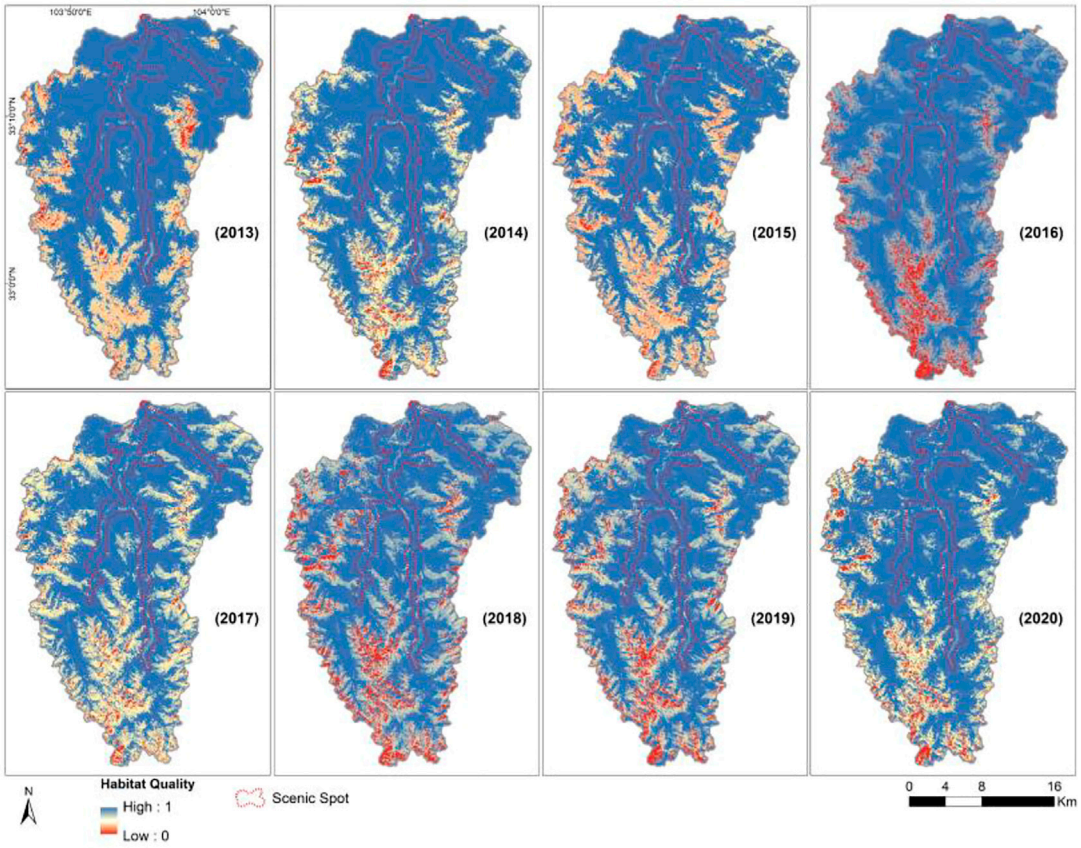

FIGURE 6
Spatio-temporal changes of habitat quality in Jiuzhaigou.

The nature reserve is a vast area with a wide variety of cover, and damaged forest was converted to shrub, grassland, and barren land, while other cover types did not significantly change. Compared with the change of cover types in the scenic area, the increase of barren land in the nature reserve was most noteworthy. Up to 2016 and 2018, the area of barren land increased by 8.668 and 14.943 km^2, respectively, with an increase of 70.43% and 121.42%, which indicated that there was a significant difference in the level of resistance between the scenic area and nature reserve in the same state of geohazards. The reasons for changes of the land cover species were closely related to the ecological suitability, pressure of geohazards and anthropogenic management.

Spatial and temporal changes in habitat quality

In Figure 6, the habitat quality service function in Jiuzhaigou from 2013 to 2020 showed obvious spatial differentiation characteristics. The high value areas of habitat quality service were mainly distributed along tourist attractions and surrounding areas, which had a vast area of forest (Table 2), perfect ecological protection measures and few habitat threat factors. The low value of habitat quality service was concentrated in the south of Jiuzhaigou, which had sparse vegetation cover and frequent geohazards. It was difficult to achieve systematic human management due to the high altitude, which has maintained the original ecology for a long time.

The habitat quality service function of Jiuzhaigou during the study period was divided into a declining period (2013–2018) and a recovery period (2019–2020). Both the "7.26 mudslide" in 2016 and the "8.8 Jiuzhaigou earthquake" in 2018 caused serious damage to the habitat quality service function of Jiuzhaigou, and its habitat quality index decreased significantly in 2016 and 2018. The "8.8 Jiuzhaigou earthquake" extensively affected the whole area of Jiuzhaigou, and the "7.26 mudslide" mainly affected the southern high-altitude area of the Jiuzhaigou Nature Reserve. This showed that habitat quality responded differently to different geohazard types and intensities. Different measures should be implemented for different types of geohazards.

Figure 7 and Table 8 show that between 2013 and 2020, the nature reserve and overall regional habitat quality index changed in a similar trend. Influenced by geohazards and compared with

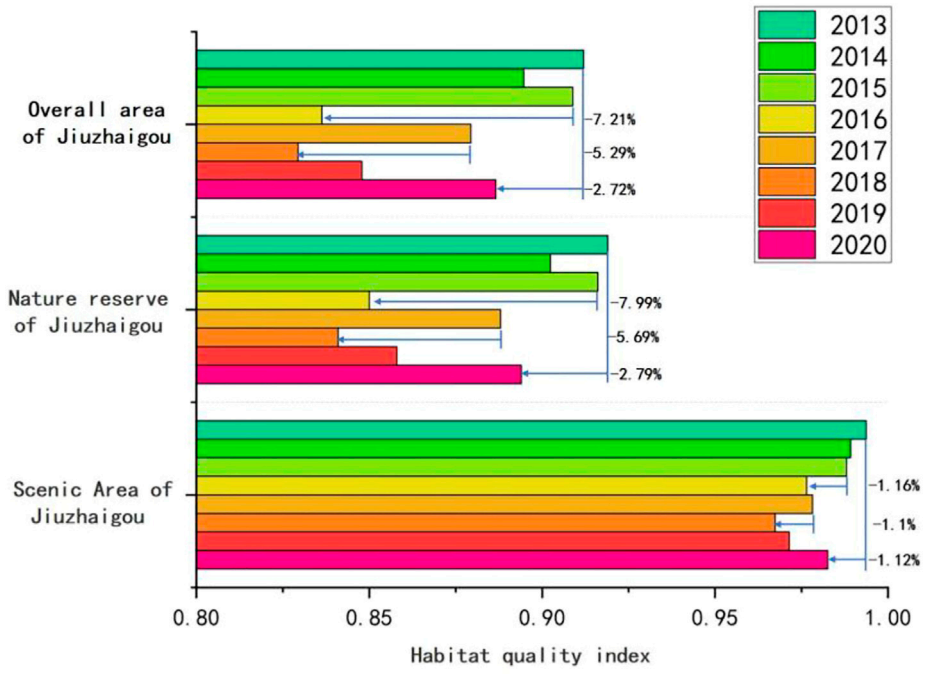

FIGURE 7
Temporal variation of the Habitat Quality Index in Jiuzhaigou.

TABLE 8 The change of the Habitat Quality Index in Jiuzhaigou from 2013 to 2020.

Time	Jiuzhaigou Scenic Area	Jiuzhaigou Nature Reserve	Jiuzhaigou overall area
2013	0.9937	0.9120	0.9190
2014	0.9892	0.8947	0.9024
2015	0.9880	0.9089	0.9161
2016	0.9765	0.8363	0.8500
2017	0.9782	0.8794	0.8880
2018	0.9674	0.8294	0.8410
2019	0.9715	0.8479	0.8580
2020	0.9826	0.8866	0.8940
Change from 2013 to 2018	−0.0263 (−2.6467%)	−0.0826 (−9.0570%)	−0.078 (−8.4875%)
Change from 2018 to 2020	0.0152 (1.5712%)	0.0572 (6.8966%)	0.053 (6.3020%)
Change from 2013 to 2020	−0.0111 (−1.1170%)	−0.0254 (−2.7851%)	−0.025 (−2.7203%)

the previous year, the habitat quality index of the nature reserve decreased by 7.99% in 2016 and by 5.69% in 2018. Therefore, the frequency of geohazards was the main factor that limited the habitat stability of Jiuzhaigou.

Under a guarantee of ecological restoration projects and the geohazards warning system, the impact of geohazards on the habitat quality of Jiuzhaigou Scenic Area was limited. Compared with the previous year, the habitat quality index of Jiuzhaigou Scenic Area decreased by 1.16% in 2016 and by 1.1% in 2018. Compared with the highest value of habitat quality in 2013, the nature reserve decreased 2.79% and the scenic area decreased 1.12% during the study period, which indicated that standardized management played a positive role in the recovery of ecological functions after geohazards. In a similar study, Mengist Wondimagegn used the InVEST model to assess habitat quality in the Kaffa biosphere reserve (Mengist et al., 2021). According to the comparison, the habitat quality index of the

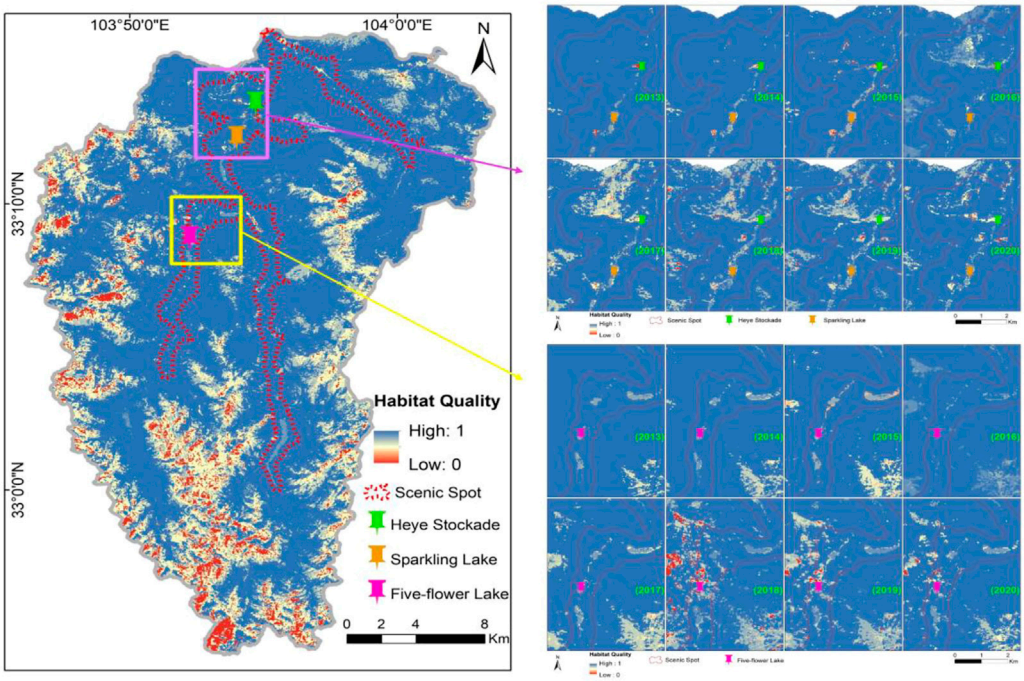

FIGURE 8
Change of the Habitat Quality Index of the area of ecological restoration projects.

FIGURE 9
Change of Five-Flower Lake: **(A)** before the earthquake, **(B)** after the earthquake, and **(C)** after the ecological restoration projects.

TABLE 9 Ecological Landscape Index of Jiuzhaigou Nature Reserve from 2013 to 2020.

Time	NP	PD	LPI	ED	AREA_MN	CONTAG	SHDI	AI
2013	12,829	21.90	35.80	83.50	4.60	70.00	0.89	87.20
2014	19,653	33.50	66.20	106.30	3.00	63.20	0.99	83.80
2015	17,307	29.50	33.20	104.40	3.40	65.60	0.98	84.10
2016	23,443	39.90	30.00	125.00	2.50	56.40	1.18	81.00
2017	22,773	38.80	28.30	130.00	2.60	57.20	1.14	80.20
2018	29,816	50.80	22.10	148.30	2.00	53.20	1.30	77.50
2019	25,200	42.90	28.90	134.80	2.30	56.50	1.23	79.50
2020	21,310	36.30	34.20	112.80	2.80	64.30	1.00	82.80

TABLE 10 Ecological Landscape Index of Jiuzhaigou Scenic Area from 2013 to 2020.

Time	NP	PD	LPI	ED	AREA_MN	CONTAG	SHDI	AI
2013	308	4.76	96.17	13.63	20.99	93.19	0.19	96.42
2014	461	7.13	95.60	18.25	14.02	91.93	0.22	95.73
2015	634	9.80	94.36	25.37	10.20	89.69	0.28	94.67
2016	1,084	16.77	90.30	44.80	5.96	83.76	0.45	91.79
2017	1,011	15.64	90.00	43.26	6.40	83.37	0.44	92.01
2018	1,670	25.83	74.46	65.76	3.87	77.05	0.59	88.66
2019	1,474	22.80	75.63	57.39	4.39	80.74	0.53	89.90
2020	902	13.95	92.70	35.17	7.17	86.44	0.36	93.22

unmanaged biosphere reserve in the natural state decreased by 3% from 2009 to 2019, which was also much higher than the 1.12% decline of Jiuzhaigou Scenic Area in this paper.

Figure 8 shows that Heye Stockade, Sparking Lake, and Five-Flower Lake are the most famous attractions in Jiuzhaigou Scenic Area, and they are typical areas for human-managed ecological restoration. Comparing the overall area map and local map in Figure 7, we can see that many low habitat quality areas occurred in scenic areas in 2018 and they slowly disappeared until 2020. Therefore, to maintain the ecological service function of Jiuzhaigou, it is necessary to scientifically and legally manage the ecological environment of the scenic area, strengthen the construction and protection of the woodland, improve the overall quality of the ecological land, and thus improve the overall quality of habitat in the watershed.

Figure 9 shows that the "8.8 Jiuzhaigou earthquake" in 2018 caused serious damage to Five-Flower Lake. From this, we can clearly see the huge destructive power of geohazards and the positive effect of ecological restoration projects.

Ecological landscape pattern index changes

According to Tables 9 and 10, the number and density of patches in both the scenic area and nature reserve increased significantly during 2013–2018, while they decreased in 2019–2020. Similarly, the mean area of the patch and the largest patch index also showed a similar trend. However, the decrease of the mean area of the patch also led to an increase in the patch edge density. The degree of isolation between the plaques significantly increased. As a whole, the change of the ecological landscape pattern fragmentation degree took a turning point in 2018. The landscape fragmentation of the scenic area was more serious compared with the nature reserve and its landscape fragmentation phenomenon was alleviated in 2019–2020. Therefore, the internal connectivity and stability of the landscape of the scenic area was improved by implementation of standardized management and ecological restoration projects.

In the above tables, the aggregation index and contagion index of the scenic area showed a decreasing and then increasing trend, and the values were higher than the nature reserve. Under the effect of standardized management, the scenic area had a faster recovery ability of fragmented landscape, which facilitated the formation of highly connected dominant patches. In addition, the Shannon's diversity index directly represented landscape heterogeneity, and the diversity index of Jiuzhaigou Nature Reserve was relatively stable, while the landscape diversity index of scenic area showed an obvious trend of first increasing and then decreasing.

Conclusions

The evaluation results based on the InVEST model in this study directly and accurately revealed the Spatio-temporal evolution of habitat quality in Jiuzhaigou from 2013 to 2020.

1) The overall habitat quality index of the study area decreased significantly from 2013 to 2018 and recovered from 2019 to 2020. As of 2020, the nature reserve habitat quality index recovered to 97.21% of its highest value (2013), and the scenic habitat quality index recovered to 98.88% of its highest value (2013). Therefore, the ecological restoration projects effectively contributed to the restoration of habitat quality after geohazards.
2) The maximum decrease in scenic habitat quality compared to the early stage of the study (2013) was 2.65%, while the maximum decrease in nature reserve habitat quality compared to the early stage of the study (2013) was 9.06%. Thus, the ecological restoration projects effectively suppressed the damage of geohazards to the ecological environment of the scenic area.
3) Jiuzhaigou Scenic Area is mainly involved in tourism and cultural dissemination activities. The land cover type in the area was relatively homogeneous and mainly forest and water body. Therefore, the habitat quality in the scenic area was superior and stable. The landscape of scenic area is more likely to break but it had a stronger recovery ability than the nature reserve. The main

way to improve the habitat quality and optimize the spatial pattern of the landscape was to restore the forest cover type.

Data availability statement

The raw data supporting the conclusion of this article will be made available by the authors without undue reservation.

Author contributions

HS: methodology, writing—original draft, and writing—review and editing. CL: conceptualization, writing—review and editing, supervision, and funding acquisition. CY: writing—review and editing. XX and TS: investigation and visualization.

Funding

This work was supported in part by the Second Tibetan Plateau Scientific Expedition and Research Program (2019QZKK0902), the National Natural Science Foundation of China (42071411), the key research and development program of Sichuan Province (2022YFG0200), the project "Research on the Integrated Development of Sports City and Agriculture, Commerce, Culture, and Tourism in Chengdu (CDMC 2021B05)," which is from the Research Center for Philosophy and Social Sciences of Chengdu (Chengdu Research Center for World Championship City), and the project "Research on Rural Ecological Cultural Landscape in the View of Rural Revitalization (JGYQ2022008)," which is from the Sichuan Landscape and Recreation Research Center (Research Base of Humanities and Social Sciences of Sichuan Provincial Department of Education).

Conflicts of interest

The authors declare that the research was conducted in the absence of any commercial or financial relationships that could be construed as a potential conflict of interest.

Publisher's note

References

Aneseyee, A. B., Soromessa, T., and Elias, E. (2020). The effect of land use/land cover changes on ecosystem services valuation of Winike watershed, Omo Gibe basin, Ethiopia. *Hum. Ecol. Risk Assess. Int. J.* 26, 2608–2627. doi:10.1080/10807039.2019.1675139

Berglund, M., Jacobi, M. N., and Jonsson, P. R. (2012). Optimal selection of marine protected areas based on connectivity and habitat quality. *Ecol. Modell.* 240, 105–112. doi:10.1016/j.ecolmodel.2012.04.011

Camara, G. (2020). On the semantics of big Earth observation data for land classification. *J. Spat. Inf. Sci.*, 21–34. doi:10.5311/JOSIS.2020.20.645

Ding, Q., Chen, Y., Bu, L., and Ye, Y. (2021). Multi-scenario analysis of habitat quality in the yellow river delta by coupling FLUS with InVEST model. *Int. J. Environ. Res. Public Health* 18, 2389. doi:10.3390/ijerph18052389

Haddad, N. M., Brudvig, L. A., Clobert, J., Davies, K. F., Gonzalez, A., Holt, R. D., et al. (2015). Habitat fragmentation and its lasting impact on Earth's ecosystems. *Sci. Adv.* 1, e1500052. doi:10.1126/sciadv.1500052

Hu, W., Li, G., Gao, Z., Jia, G., Wang, Z., and Li, Y. (2020). Assessment of the impact of the Poplar Ecological Retreat Project on water conservation in the Dongting Lake wetland region using the InVEST model. *Sci. Total Environ.* 733, 139423. doi:10.1016/j.scitotenv.2020.139423

Li, M., Zhou, Y., Xiao, P., Tian, Y., Huang, H., and Xiao, L. (2021). Evolution of habitat quality and its topographic gradient effect in northwest hubei province from 2000 to 2020 based on the InVEST model. *Land* 10, 857. doi:10.3390/land10080857

Liu, G. Y., Wang, P., and Xie, H. L. (2013). Analysis of ecological landscape pattern change in the Poyang Lake eco-economic zone of China. *Adv. Mat. Res.* 864–867, 2639–2644. doi:10.4028/www.scientific.net/AMR.864-867.2639

Liu, Z., Qiu, H., Zhu, Y., Liu, Y., Yang, D., Ma, S., et al. (2022). Efficient identification and monitoring of landslides by time-series InSAR combining single- and multi-look phases. *Remote Sens. (Basel).* 14, 1026. doi:10.3390/rs14041026

Maes, J., Paracchini, M. L., Zulian, G., Dunbar, M. B., and Alkemade, R. (2012). Synergies and trade-offs between ecosystem service supply, biodiversity, and habitat conservation status in Europe. *Biol. Conserv.* 155, 1–12. doi:10.1016/j.biocon.2012.06.016

Maingi, J. K., and Marsh, S. E. (2001). Assessment of environmental impacts of river basin development on the riverine forests of eastern Kenya using multi-temporal satellite data. *Int. J. Remote Sens.* 22, 2701–2729. doi:10.1080/01431160010031298

Melzer, M., and Bellingrath-Kimura, S. (2021). GIS-based modeling of ecosystem services - status quo, potentials and trade-offs [GIS-gestützte Modellierung von ökosystemleistungen – status quo, Potenziale und Trade-offs] [WWW Document]. Available at https://schlr.cnki.net/en/Detail/index/GARJ2021_2/XQSP2171699C460C6EA617478B242A25D769 (accessed 22 10, 22).

Mengist, W., Soromessa, T., and Feyisa, G. L. (2021). Landscape change effects on habitat quality in a forest biosphere reserve: Implications for the conservation of native habitats. *J. Clean. Prod.* 329, 129778. doi:10.1016/j.jclepro.2021.129778

Newbold, T., Hudson, L. N., Hill, S. L. L., Contu, S., Lysenko, I., Senior, R. A., et al. (2015). Global effects of land use on local terrestrial biodiversity. *Nature* 520, 45–50. doi:10.1038/nature14324

Qiu, H., Zhu, Y., Zhou, W., Sun, H., He, J., and Liu, Z. (2022). Influence of DEM resolution on landslide simulation performance based on the Scoops3D model. *Geomat. Nat. Hazards Risk* 13, 1663–1681. doi:10.1080/19475705.2022.2097451

Schroter, M., and Remme, R. P. (2016). Spatial prioritisation for conserving ecosystem services: Comparing hotspots with heuristic optimisation. *Landsc. Ecol.* 31, 431–450. doi:10.1007/s10980-015-0258-5

Sowinska-Swierkosz, B. (2017). Application of surrogate measures of ecological quality assessment: The introduction of the Indicator of Ecological Landscape Quality (IELQ). *Ecol. Indic.* 73, 224–234. doi:10.1016/j.ecolind.2016.09.019

Svoboda, J., Stych, P., Lastovicka, J., Paluba, D., and Kobliuk, N. (2022). Random forest classification of land use, land-use change and forestry (LULUCF) using sentinel-2 data-A case study of Czechia. *Remote Sens. (Basel).* 14, 1189. doi:10.3390/rs14051189

Terrado, M., Sabater, S., Chaplin-Kramer, B., Mandle, L., Ziv, G., and Acuna, V. (2016). Model development for the assessment of terrestrial and aquatic habitat quality in conservation planning. *Sci. Total Environ.* 540, 63–70. doi:10.1016/j.scitotenv.2015.03.064

Van Vooren, L., Reubens, B., Broekx, S., Reheul, D., and Verheyen, K. (2018). Assessing the impact of grassland management extensification in temperate areas on multiple ecosystem services and biodiversity. *Agric. Ecosyst. Environ.* 267, 201–212. doi:10.1016/j.agee.2018.08.016

Wang, L., Qiu, H., Zhou, W., Zhu, Y., Liu, Z., Ma, S., et al. (2022). The post-failure spatiotemporal deformation of certain translational landslides may follow the pre-failure pattern. *Remote Sens. (Basel).* 14, 2333. doi:10.3390/rs14102333

Wang, X., and Mao, H. (2022). Spatio-temporal evolution of post-seismic landslides and debris flows: 2017 M-S 7.0 Jiuzhaigou earthquake. *Environ. Sci. Pollut. Res.* 29, 15681–15702. doi:10.1007/s11356-021-16789-9

Wu, L., Sun, C., and Fan, F. (2021). Estimating the characteristic spatiotemporal variation in habitat quality using the InVEST model-A case study from guangdong-Hong Kong-Macao greater bay area. *Remote Sens. (Basel).* 13, 1008. doi:10.3390/rs13051008

Zhang, M., Seyler, B. C., Di, B., Wang, Y., and Tang, Y. (2021). Impact of earthquakes on natural area-driven tourism: Case study of China's Jiuzhaigou National Scenic Spot. *Int. J. Disaster Risk Reduct.* 58, 102216. doi:10.1016/j.ijdrr.2021.102216

frontiers | Frontiers in Earth Science

TYPE Original Research
PUBLISHED 26 January 2023
DOI 10.3389/feart.2022.1107094

OPEN ACCESS

EDITED BY
Haijun Qiu,
Northwest University, China

REVIEWED BY
Suli Cui,
Northwest University, China
Peifen Xu,
Institute of Geology and Geophysics (CAS), China

*CORRESPONDENCE
Weimin Liu,
xaliuweiming1971@126.com

SPECIALTY SECTION
This article was submitted to Geohazards and Georisks,
a section of the journal
Frontiers in Earth Science

RECEIVED 24 November 2022
ACCEPTED 28 December 2022
PUBLISHED 26 January 2023

CITATION
Liu W, Xu C and Huang X (2023), Brief analysis of the development characteristics and deformation mechanism of ground fissures on the MH Highway in the Ethiopian Rift Valley.
Front. Earth Sci. 10:1107094.
doi: 10.3389/feart.2022.1107094

Brief analysis of the development characteristics and deformation mechanism of ground fissures on the MH Highway in the Ethiopian Rift Valley

Weimin Liu[1]*, Cheng Xu[2] and Xiaonian Huang[2]

[1]CCCC First Highway Consultants Co., Ltd., Xi'an, China, [2]Xi'an China Highway Geotechnical Engineering Co., Ltd., Xi'an, China

Ground fissures are widely developed in the Ethiopian Rift Valley, posing a major threat to the construction of the proposed Modjo–Hawassa (MH) Highway. The development characteristics, distribution, and communication law of ground fissures along the highway are studied using the comprehensive investigation method and technology. On this basis, the deformation mechanism and evolution of ground fissures are analyzed, which can provide geological support for the prevention and control of highway cracks in the area where ground fissures are developed.

KEYWORDS

Ethiopian Rift Valley, ground fissure, highway, developmental characteristics, deformation mechanism

1 Introduction

The Ethiopian Rift Zone—the world's largest East African Great Rift Valley fault collapse zone—is a roughly NW-SE depressed rift valley, with about 40–60 km width and 1 km depth, formed by crustal extensions resulting from the uplift of the mantle plume. Satellite monitoring data indicate that the Rift Valley nowadays undergoes expansion at a rate of 2.5–5 cm/y (Williams et al., 2004; Hoffman et al., 1997; Ebinger, 1989; Chorowicz et al., 1998; Ebinger et al., 2000; Wilson, 2000). In the context of active deep tectonic movements, the high and frequent occurrences of ground fissures have become a serious geological disaster and problem in the area, wreaking havoc on local transportation facilities, populated areas, and cultivated land.

In this paper, the distribution area of ground fissures at the fourth section of the Modjo–Hawassa (MH) Highway in Ethiopia is regarded as the research object. The distribution and development characteristics of typical ground fissures in this area are summarized, and preliminary analysis of the cause mechanism and evolution process of ground fissures is carried out through field investigation, remote sensing interpretation, engineering exploration, and laboratory tests. It can provide a reference for road engineering countermeasures in the area where ground fissures are developed.

2 Overview of the research area

As shown in the geological map of Ethiopia in Figure 1 (Geological Survey of Ethiopia) (Ministry of Mines, 1976), the formation of the area is a binary structure: the upper part is covered by the Quaternary Holocene overburden of alluvial–proluvial powdery clay and silt, which is about 5–20 m thick, and the underlying stratum is

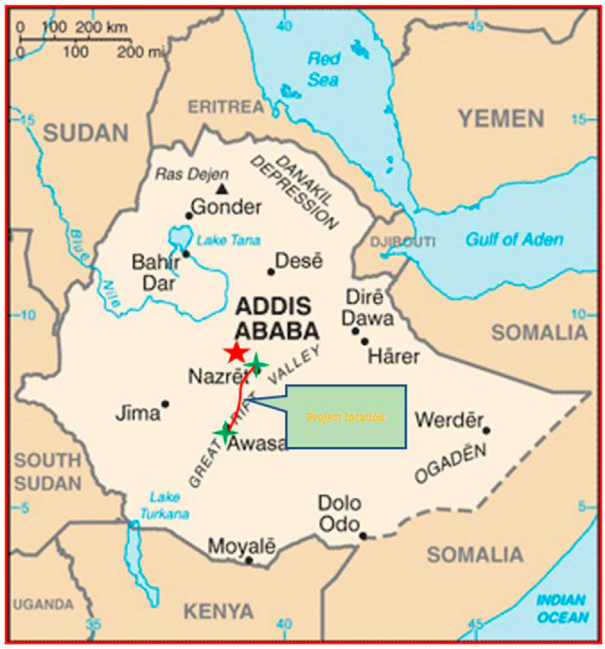

FIGURE 1
Geological map along the MH Highway.

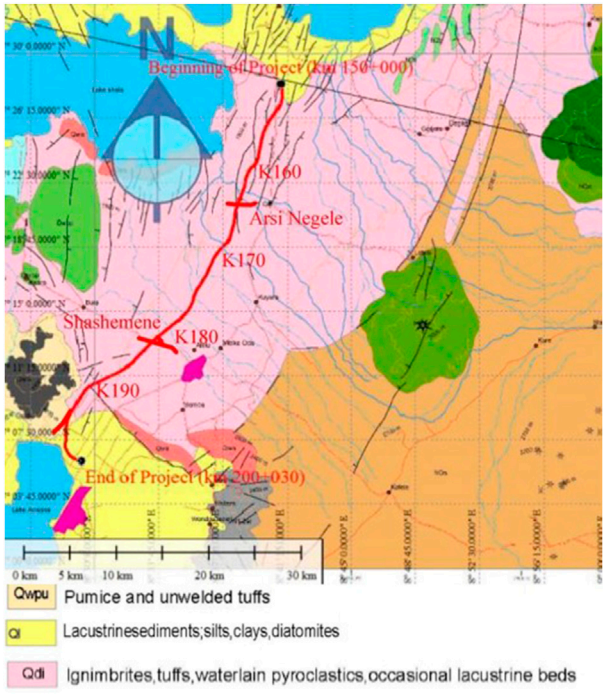

FIGURE 2
Geographical location map of the MH Highway.

the Magdala Group tufa of the Miocene series, where the rock mass is broken, unevenly weathered, soft, and full of visible air holes.

There are many ground fissures along the MH Highway on the floor of the Ethiopian Rift Valley, most of which are secondary faults of the rift. These fractures are relatively short in extension and small in scale. Ground fissures were developed at 600 m to the right of main K169+600, the Arsi Negele connecting line, and the Shashemene connecting line. Basically, these upright fractures, with about 60–200 m length, 5–8 m width or so, and visibly 8–10 m depth, are the culprit of country road cracks. Moreover, a series of depressions and collapse pits are distributed like a string of beads in the K180 interchange area of the MH Highway.

3 Characteristics of ground fissures

3.1 Distribution and morphological characteristics of ground fissures

Ground fissures are widespread within the research area, most of which are secondary faults of the rift. These fractures are relatively short in extension and small in scale. The main locations and characteristics of 11 ground fissures discovered through investigation are listed in Table 1.

From the surface manifestation of fractures as a whole, it can be seen that the ground fissures in the research area can be divided into two types: exposed fissures and concealed fissures, which have the following characteristics.

3.1.1 Exposed fissures

Exposed ground fissures are divided into two types. As shown in Figure 2, the first type is the surface crack of linear extension, mostly horizontally ripped, and the stratigraphic dislocation on both sides is not obvious. It is generally 5.0–10.0 m wide, and the wall on each side is usually upright and takes on a wedge-shaped pattern of being wide at the top and narrow at the bottom in the profile. Generally, the depth from the surface to the fracture closure can reach a maximum of 20.0 m or so, and the fracture has a noticeable stretching direction. Figure 3 shows that the exposed fissure of the Arsi Negele connecting line linearly spreads from NW to SE in the same direction of the main Rift Valley's tectonic line, indicating that the main Rift Valley structure has a significant controlling effect on the development of fractures.

The second type, as illustrated in Figure 4, presents a stripped collapse zone, and the strip extends in the direction of the main Rift Valley's tectonic line, mostly represented by vertical subsidence. Such zones vary in widths and have a certain height difference with the original surface. The investigation reveals that this zone is covered with a sedimentary formation of certain thickness, suggesting that it is formed by the collapse of the stratum on both sides of the first type, namely, exposed fissure, after it becomes relatively stable in the later stage. The collapse zone of the outcrop-type ground fissure at the Shashemene connecting line shown in Figure 2 is about 100 m long, 20–40 m wide, and 10–15 m deep. According to local people, the pit began to appear in June 2017. The depth of the pit is about 15 m, indicating that the sinkhole zone has been reactivated.

3.1.2 Concealed fissures

Concealed fissures are manifested as collapsed depressions in the plane modality. In a plane, it takes on the shape of an ellipse. The middle of the depression is wide and gentle, and the height difference with the periphery of the depression is normally 1.0–3.0 m. In the

TABLE 1 Location and morphological characteristics of ground fissures in the research area.

Item	Development segment	Morphological characteristic
1	Collapsed depression on the right side of K165+730–165+900	At a distance of 100 m to the right side of K165+875, there is a collapse pit of about 17 m long, 10 m wide, and visibly 12–15 m deep and is devoid of fillers
2	Collapsed depression on the right side of K166+100	Two collapse pits are observed at a distance of 65 m to the right side of K166+100. 1# pit is about 9.7 m long and 4.7 m wide with a visible depth of 13 m or so, and 2# pit is about 18.9 m long and 14.7 m wide with a visible depth of probably 15 m. Both have no fillers
3	Collapsed depression on the right of K166+300–400	It is situated on the right side of K166+300–400, partially extending to the roadbed area. There are three collapse pits developed in this area. 1# pit is approximately 11.5 m long, 5 m wide, and 6.2 m deep; 2# pit is around 7.1 m long, 6.2 m wide, and 2.5 m deep; and 3# pit is about 7 m long, 7.8 m wide, and 2 m deep. None of them have fillers
4	Collapsed depression on the left side of the K167+400 ~ K167+600 section	Left edge of this section of route K167+400~K167+600 is a collapse depression about 200 m long and 150 m wide, with a height difference of 5–6 m or so. The roadbed partially traverses the edge of the depression
5	Ground fissure on the right side of K169+900	Ground fissures in this section are developed on unsurfaced country roads by a length of about 60 m, a width of 5–7 m, and a depth of 7 m. These fractures have upright walls and are 700 m from the project. There are two obviously parallel fractures beside the small stake mark of the main line, and the ground between them has 20–30 cm subsidence; the cleft near the large stake mark toward the main line is about 15–20 m wide and 5 m deep. Collapse pits emerge again though local people have planted crops in the low-lying zone between these fractures
6	Collapsed depression along K172+350 ~ K172+700	It is a 350-m-long and 150-m-wide ground subsidence with a height difference of 2–2.5 m or so. The highway passes through the middle of the depression, which has certain impact on the roadbed
7	Ground fissure on the left side of K173+000~K173+200	This segment of ground fissures is about 40 m in length, 2–3 m wide, 4–5 m in depth, and 60–100 m away from the expressway. In addition, five collapse pits with a diameter of 3–5 m appear along the direction of the ground fissure
8	Collapsed depression on the left side of K173+900~K174+200	Located on the left side of the expressway, this depression is about 300 m long, 100 m wide, and 2–3 m in height difference. The roadbed is partially laid near the fringe of the depression
9	Collapsed depression in the K179+400~K181+466 interchange area	The segment is located in an interchange area and is composed of totally eight collapsed depressions, one of which is within the ramp and the rest are on the periphery of the ramp, which has certain impact on the interchange area and ramp
10	Arsi Negele connecting line	Ground fissures are at K1+800 of the Arsi Negele connecting line, which is 1.6 km to the left of the main line, basically parallel to the highway, and intersects perpendicularly with Arsi Negele. The cracks are about 100 m long, 5–8 m wide, 8–10 m deep, and vertical on the whole. At the already chapped end, the ground fissures bifurcate, forming two 100-m-long and 10-cm-wide crannies, and the land in between is 3–5 m wide and has a 10–20 cm settlement. Furthermore, there is a collapse pit—approximately 7 m in diameter—about 600 from the large stake mark of the main line—but its depth is unknown. According to local residents, the sound of flowing water was heard at the mouth of this deep hole during the rainy season
11	Shashemene connecting line	Located 100 m away from the end point of the Shashemene connecting line and 300 m on the right side of the main line, the ground fissure intersects with the Shashemene connecting line and is basically parallel to the main line. Damage is caused by the fissure to the existing bituminous concrete pavement. On the east side of the current asphalt road, the crack is about 200 m long, 20–25 m wide, and 15–20 m deep and vertical. This segment of fractures appeared two years ago in the rainy season, according to local people. There is another 100-m-long gap to the west of the present asphalt road, which is 20–40 m wide and 10–15 m deep. There is a sinkhole of 20 m from the end of this ground crack. According to local people, this sinkhole occurred in June 2017, and it is still collapsing

depressions, there often exist string-bead-like ground collapse pits, rounded on the surface and varying in diameters, and the maximum depth measures up to 10.0 m. As shown in Figure 5, the depression on the right side of the roadbed of the K165+700~K166+450 section is about 500 m long, 50–80 m wide, and 6–8 m in height difference. Three collapse pits are observed on the right side of K166+300-400, which have a diameter of 3–5 m and a depth of about 4–5 m, and are only 10 m from the side boundary of the roadbed.

The collapsed depressions are elliptically distributed in the plane, and their long-axis direction coincides with the structural trend of the

FIGURE 3
Arsi Negele exposed fissures.

FIGURE 4
Shashemene exposed fissures.

main Rift Valley. There are eight collapsed depressions in the interchange area of K179+400~K181+466, as shown in Figure 6. A geophysical survey reveals that the depressions are interconnected by several parallel fissures, and the overall direction of the ground fissures is N45°E, which is consistent with the direction of the main Rift Valley structure, except for partial intersections.

The ground cracks are currently exposed and concealed. The causes are the same. They are caused by the geological structure, but they are different in the form of expression.

3.2 Characteristics of ground fissure activity

3.2.1 Characteristics of ground fissure activity

Figure 7 illustrates the multi-year development characteristics of ground fissures in the vicinity of the Arsi Negele connecting line for the period 2004–2020. From the pictures, it can be seen that in 2004, there was a band-shaped collapse zone in the area, and distinct collapse and ground fissures had not appeared yet; in 2013, small-scale collapse pits and ground fissures appeared on both sides of the road; in 2017, these cracks kept developing, extending, and widening to the degree that existing roads were cut off and greatly damaged; and in 2020, the roads cracked again under the action of ground fissures despite being repaired and backfilled. Overall, the ground fissures remain in a state of developmental activity at the macro level. Therefore, from the changes in the cracks on the surface, it can be seen that the cracks on the ground are gradually developing and changing over time.

3.2.2 Seasonal characteristics of ground fissure activity

It can be inferred from the investigation and exploration results that the ground fissure activity has seasonal characteristics in the time series. To be more specific, their development is not obvious in the dry season, but they often showcase the features of sudden destruction or intensified development in the rainy season (National meteorological Agency of Ethiopia, 2001). In addition, short-term heavy rainfall will often lead to the reopening of concealed fissures or the formation of collapse pits, such as the Shashemene connecting line ground fissure. The ground fissure of the Arsi Negele connecting line developed at a faster pace and damaged the road after a strong rainfall in June 2017; the ground fissure at 700 m on the right of the main line K169+900 had not taken shape before May 2016, but a new ground fissure with a width of 5.0 m and a depth of 7.0 m formed at this location after a continuous heavy rainfall.

3.3 Geophysical characteristics of the ground fissure zone

The bedrock in the research area is dominated by tuffs, and the surface is mostly covered by the loose Quaternary overburden. The binary stratigraphic texture is simple, and the stratigraphic physical parameters are relatively stable and continuous. While in the locations where ground fissures and crevices are developed, the ground fissures cause discontinuities in the original stratigraphy or affect the geophysical characteristics of the rock and soil bodies situated in a certain range around them, such as forming geophysical anomalies, a condition good for geophysical prospecting (Wang and Liu, 2003a; Wang and Liu, 2003b; Wang and Liu, 2004). In this study, electrical prospecting and radon gas testing were carried out in the ground fissure area.

3.3.1 Electrical characteristics

The electrical prospecting results report that in the area without fracture distribution, the apparent resistivity value generally follows the rule of low to high from shallow to deep stratum, which is basically identical with the binary structure characteristics of the stratum, while the apparent resistivity of the area with developed fractures is notably different from the background field of the resistivity of surrounding strata. For exposed fissures, the apparent resistivity anomalies are generally high in the upper unfilled depth range at the center of the fracture, and the concealed fractures on the other hand present a remarkable zone of low-resistance anomalies.

Figure 8 shows the vertical electrical prospecting rate profile along the concealed fissure in the interchange area from K179+400 to

FIGURE 5
String-bead-shaped collapse pits on the right side of K166+300-400.

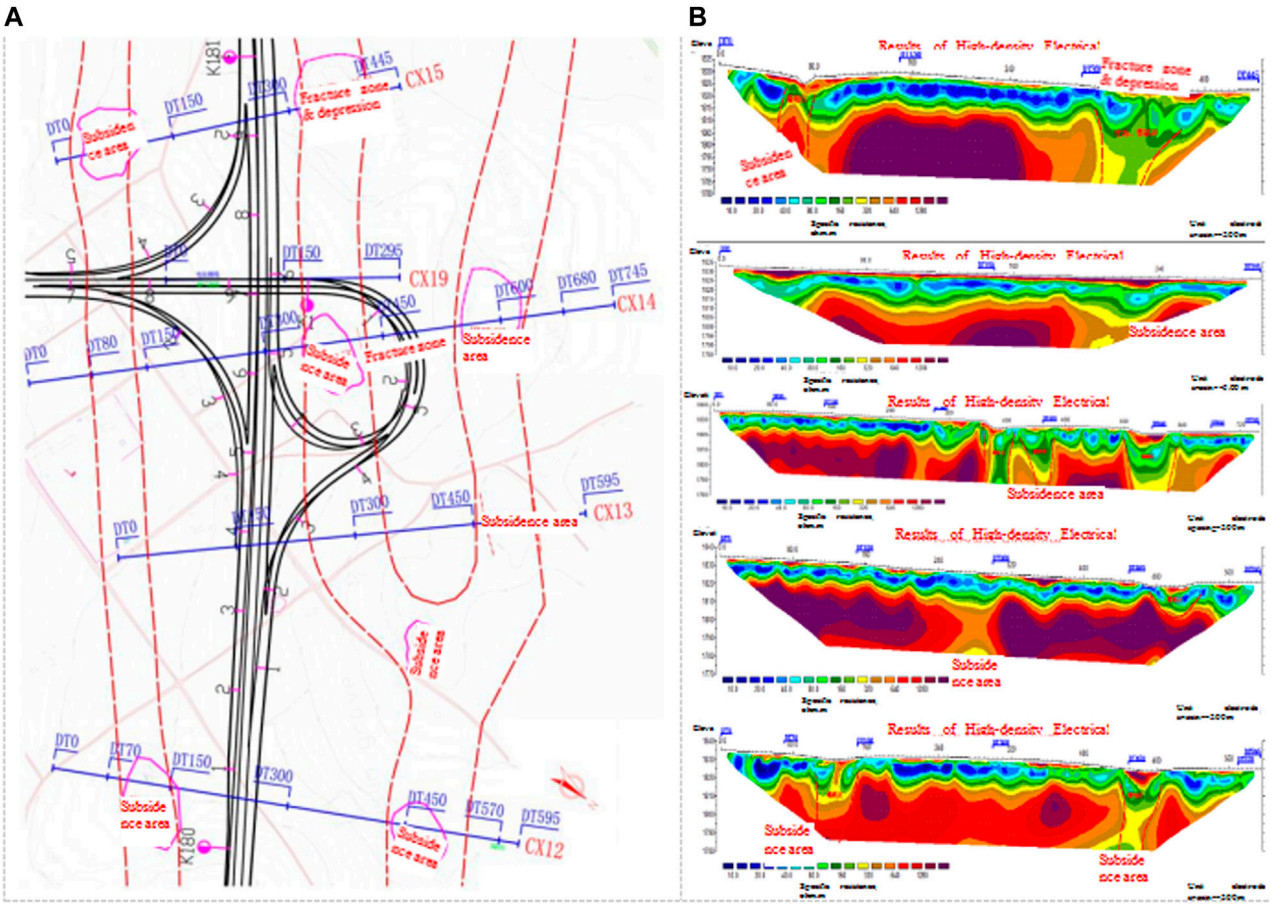

FIGURE 6
Comprehensive geophysical prospecting result map of the K179+400~K181+466 interchange area.

FIGURE 7
Ground fissure development of the Arsi Negele connecting line: **(A)** remote sensing images, October 2004; **(B)** satellite remote sensing images, November; **(C)** remote sensing images, December 2017; and **(D)** remote sensing images, October.

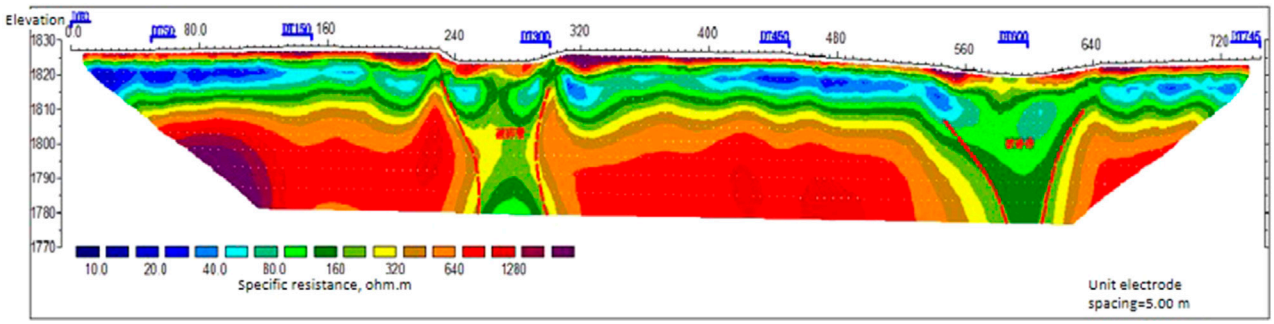

FIGURE 8
Typical profile of high-density electrical method in the K179+400~K181+466 interchange area.

K181+466. According to the exploration results, there are low-resistance anomalies in the DT230–DT310 and DT550–DT640 sections, both low-lying and having obvious collapse pits, which are thus deciphered as ground fissure development zones.

3.3.2 Radon gas characteristics

The fracture zone in the research area is a good migration channel for groundwater and gas, and the stratum contains thick, porous, and broken tuff. As a result, radon gas can easily leak out from depths to the surface, providing favorable geophysical conditions for inferring the development and distribution of ground fissures through radon gas concentration. The radon gas test carried out in the ground fissure development area demonstrates that the background value of the radon gas concentration in the research area is generally high, that is, 103–104 Bq·m^{-3} in the order of magnitude, but there are massive radon gas concentration anomalies in the vicinity of the fractures.

Figure 9 shows the radon gas test profile of the K179+400~K181+466 interchange area arranged perpendicular to ground fissures. The test results show that the radon gas concentration is not highly abnormal near the development position of exposed ground fissures or collapse pits. This is mainly

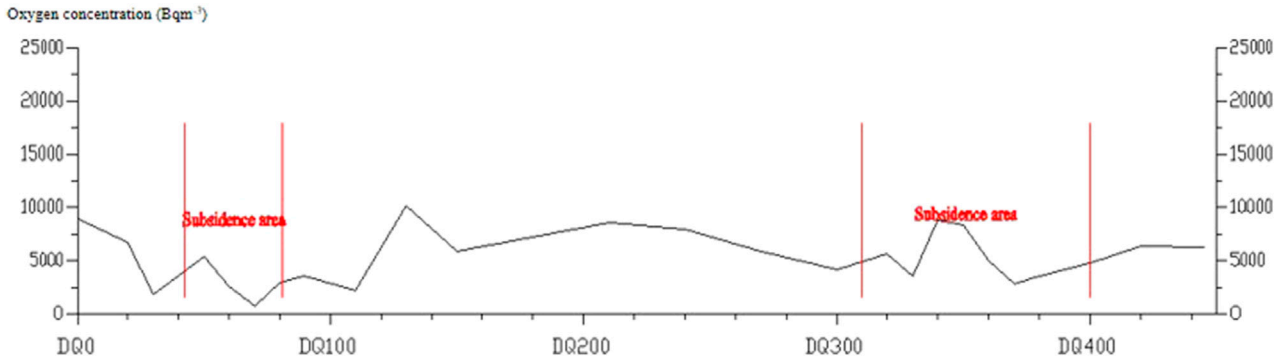

FIGURE 9
Typical profile of the radon gas test in the K179+400~K181+466 interchange area.

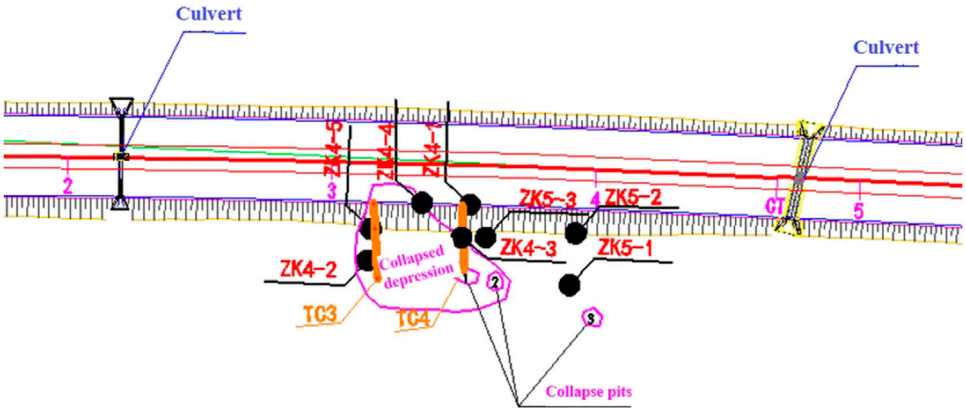

FIGURE 10
Exploration layout of the collapsed depression on the right side of the K165+700~K166+450 section.

because the ground fissures are underground radon gas escape channels, but as the ground fissures have developed to the surface, radon gas in the soil leaks to the air, causing the radon gas value at the place directly above the fissures to be slightly lower than that of surrounding areas. So, the radon concentration curve at the location of the fissure is "M"-shaped. Around the fracture zone, the radon concentration will rise steeply, generally more than twice the background value, forming an anomaly zone of high radon concentration. The radon concentration profile fairly reflects the location of ground fissures. In this profile, two radon gas concentration anomalies exist within survey lines DQ40–DQ80 and DQ310–DQ400, wherein DQ40–DQ80 is the location of the collapse pit and DQ310–DQ400 is the location of the fracture zone where the rock masses are shattered and prone to collapse.

3.4 Stratigraphic texture characteristics of the ground fissure area

Drilling and trenching the collapsed depression on the right of the section K165+700~K166+450 in the research area are implemented, as shown in Figure 10. The typical drilling results show that the overlying soil is mainly loose, powdery clay and silt, and the core of the lower bedrock, namely, tuff, is basically fragmented, cracked, and porous. Among them, there is a loose layer emerging 9–19 m of the ZK4-1 borehole, and the drilling speed is fast. Other boreholes on the external side of the roadbed do not show any abnormality, which is judged to be the result of filling the main fracture with clay.

Trenching was carried out in the middle of the concealed fissure in section K166+300–k166+400. From the T3 trench in Figure 11, it can be seen that there are traces of developed fractures, mostly filled with gray clay. The engineering geological profile of the trench in Figure 12 reveals that the surface layer of the ground is covered with powdery clay, which is about 1–2 m thick at both ends, gradually deepening from the middle part until a maximum of 4 m. At the same time, there is a silt layer deposited at the lower part of the thickest part of the silty clay, as thick as 2 m in the middle, disappearing gradually on both sides. It can be seen that there are signs of later deposition in the stratum exposed in the middle of the trench.

FIGURE 11
TC3 trench.

The photograph of the TC4 trench in Figure 13 reveals that there are two collapse pits. During the wet season, the surface water converges into No. 1 collapse pit and flows away from its bottom, but the sound of the water flow can be heard in No. 2 collapse pit, implying that the bottoms of the two pits are unblocked. In addition, near No. 1 collapse pit, a small hollow with a depth of about 4 m and a fissure penetrating the ground are found in trench TC4. The engineering geological profile of the TC4 trench shows that the surface overburden is 1–2 m and composed of thick powdery clay, as shown in Figure 14. On the left side of the trench is a stratum consisting of only powdery clay and completely weathered tuff; in the transition to No. 1 collapse pit, a silt layer with a maximum thickness of about 2.5 m gradually appears. This is also caused by later collapse deposition.

4 Exploration on the causes of ground fissures and deformation mechanism

The formation and deformation processes of ground fissures in the Ethiopian Rift Valley are closely related to the strong tectonic activity of the basement, the stratigraphic texture, and the infiltration of precipitation. In general, the violent tensile and tectonic movement of the basement is the main controlling factor in the formation of ground fissures; unfavorable stratigraphic textures provide conditions for the formation of ground fissures; and heavy rainfall infiltration intensifies the formation process of ground fissures and exhibits different development patterns (Ayalew et al., 2004; Roberts et al., 2012).

4.1 Geological structure action

Ground fissures can be divided into tectonic fractures and non-tectonic fractures in terms of formation conditions. The Ethiopian Rift Valley area has a high incidence of ground fissures, which is bound up with the distribution of widely developed fractures in the valley (China Water&Power Press, 1980; Zhang, 1980). It is a typical area of tectonic fractures. Laike Mariana Asfaw (1982) investigated the distribution, generation, and development of ground fissures in Ethiopia from geological, geophysical, and tectonic aspects, compared and analyzed the ground fissures in the area with the seismic data of the same period, and concluded that the generation of ground fissures is influenced by the geological structure. Williams (2020) studied the scale and age of the tensional fracture swarm in the north of the Ethiopian Grand Canyon and arrived at the conclusion that the ground fissures are associated with the expansion of the East African Great Rift Valley.

The consistency of the planar distribution pattern and spreading direction of the ground fissures in the research area with the fault structure of the basement indicates that the basement structure appreciably controls the evolution of the ground fissures. It is the

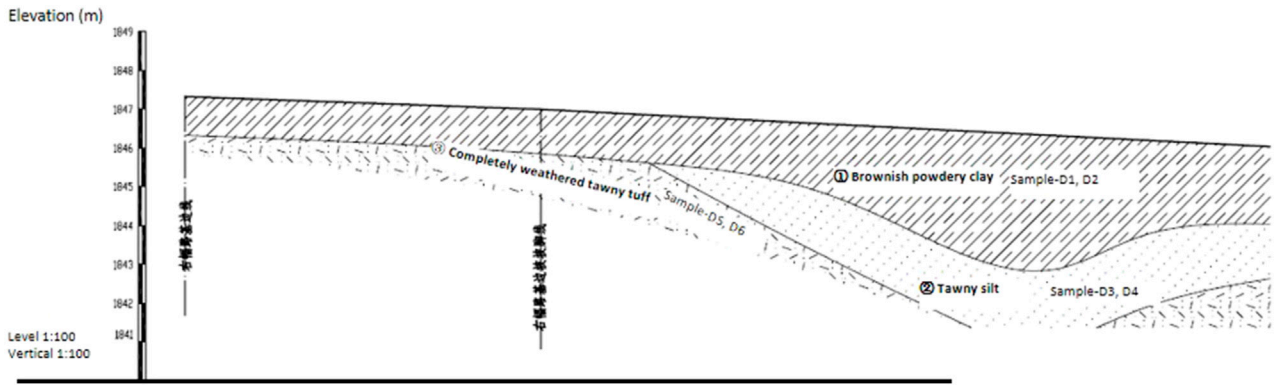

FIGURE 12
Engineering geological profile of the TC3 trench.

FIGURE 13
TC4 trench.

ferocious tensioning and priming of the basal geological structure that forms the basis for ground fissures, and the slow creeping expansion of the basement structure that leads to the tensional cracking of the overlying stratum is the main controlling factor of the occurrence of ground fissures in the research area.

4.2 Effects of stratigraphic texture

The surface overburden in the research area is dominated by silt, sandy soil, and breccia, which has the characteristics of a thin soil body, a large pore ratio, poor grading, a loose structure, and high permeability; the central rock mass is mostly composed of soft ignimbrite but with hidden tectonic fractures; the lower rock mass, being low in diagenetic grade, is where tensional fractures, cracks, and cavities are scattered and groundwater runoff channels are formed. According to the investigation, there are dense bedrock fractures in the research area, with an aperture varying from 3 mm to 200 mm (Cao and Li, 1986; Wang et al., 1986). The monotonous stratigraphic texture and the fractures and cavities in the underlying stratum provide an environment for water infiltration and creep, creating conditions for surface fissures and collapses.

On the right collapse depression of K165+700~K166+450, 11 holes were drilled in the section of the highway. The drilling results revealed that a hole of 30 cm was found in the lower part of the collapse depression during drilling, with water leakage and no filling. Other boreholes in the vicinity were in a normal state, indicating that the cavities exist only in low-lying areas and have no impact on the roadbed and its vicinity.

Figure 15 shows an isobath map of the clay blanket in the collapsed depression, where the thickness of clay in the collapsed depression takes on a pot-bottom shape, indicating that it was formed due to the sedimentation of clay at a later stage.

4.3 Effects of precipitation and water infiltration

The results of investigation in the research area suggest that the average annual rainfall in the ground fissure zones in the research area exceeds 400 mm (Geological Survey of Ethiopia). Meanwhile, the development of ground fissures is closely related to the process of short-term heavy rainfall, which may lead to the reopening of hidden fractures or the formation of collapse pits, indicating that rainfall constitutes an important causative factor of ground fissure development and deformation.

According to the surveys and visits paid to local residents, copious ground fissures in the research area are generated after acute heavy rainfall, such as the cracks at 700 m on the right side of the main line K169+900, of the Shashemene connecting line, and on the east side of the existing asphalt road. Moreover, at the investigation site, during the trenching near the concealed fissures of the K166+300 section, no obvious cavity was observed at the beginning of excavation. After the strong rainfall in this area, the soil about 2 m deep below the ground appeared to have collapsed into a hollow under the action of hydrodynamic force, and the hole became larger with the increase in rainwash time; at the same time, the sound of water flow was heard in the void, indicating that there was an unimpeded runoff channel beneath it.

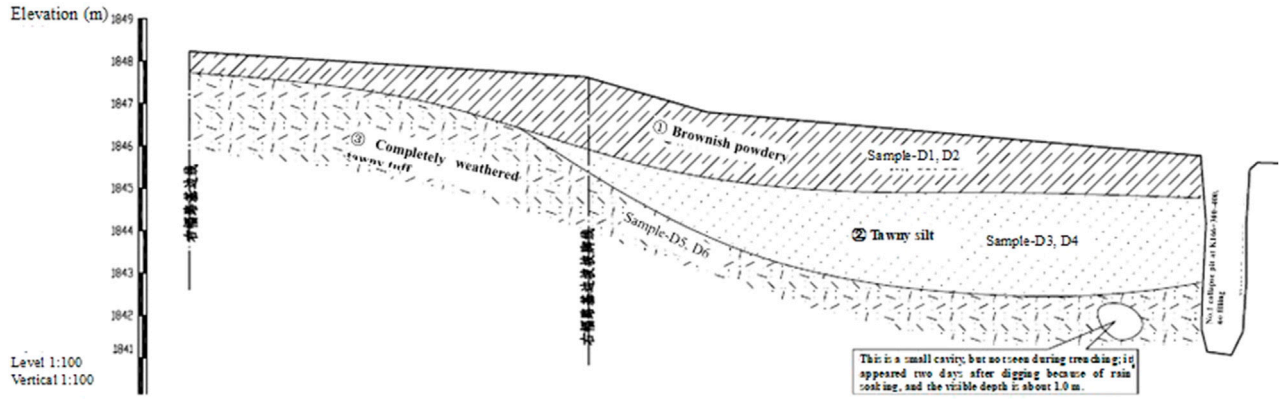

FIGURE 14
Engineering geological profile of the TC4 trench.

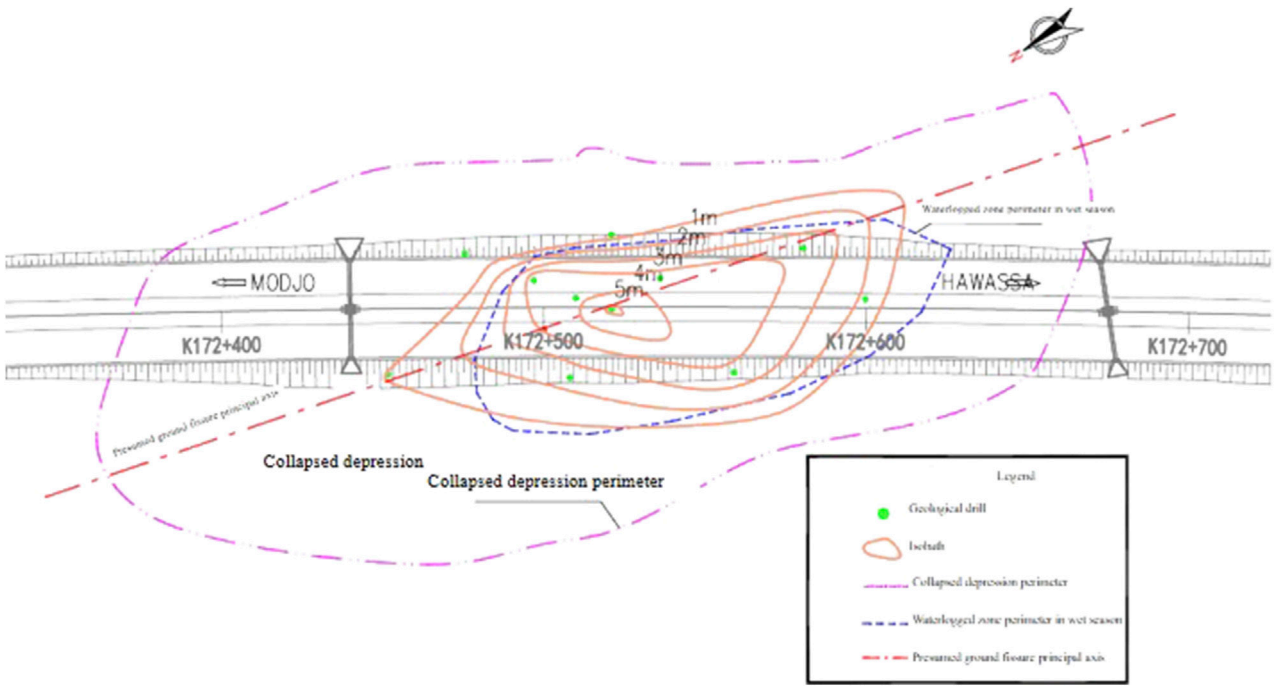

FIGURE 15
Isobath map of the upper clay layer of the collapsed depression in the K165+700~K166+450 section.

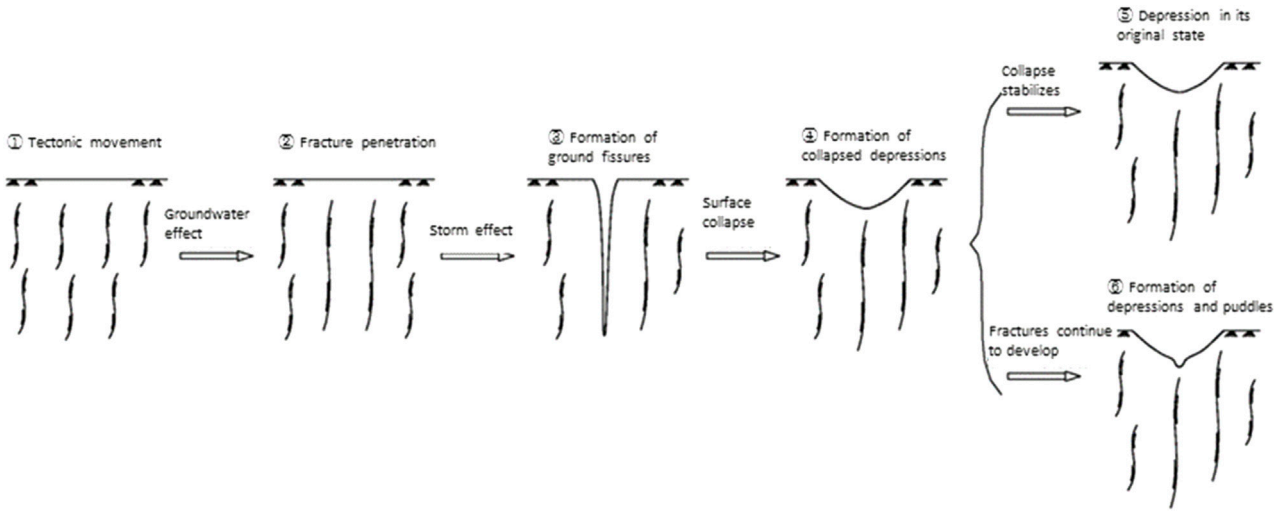

FIGURE 16
Diagram of ground fissure evolution.

As it can be inferred from the phenomenon of rain water converging into overland runoff, the surface water in the research area is mainly recharged by atmospheric precipitation. Due to the special stratigraphic texture of the project area, the surface water permeates rapidly through the loose sedimentary mantle and a great many bedrock fissures and quickly infiltrates and disappears even within a short period of time after heavy rainfall. In the process of infiltration along the cracks, the soil on both sides is scoured and eroded, and the fine particles are migrated through the underlying bedrock crevices, which damages the structure of the soil, loosens or destroys the soil, leads to the formation of cracks or pits, and gradually enlarges the opening of the cracks.

From the stratigraphic conditions revealed by drilling and trenching, it can be seen that underground erosion also occurred in the area of ground fissures. Wang Xiuyan and Liu Changli considered that if the soil inhomogeneity coefficient is greater than 10, the ratio of permeability coefficients of the upper and lower contact soils is higher than 2, and the seepage hydraulic gradient is larger than the critical

hydraulic gradient of underground erosion (the hydraulic gradient is usually considered >5). It is susceptible to leakage and water creep (2003–2004). The stratigraphic conditions in the research area are basically same as the conditions for the occurrence of underground erosion, and the cavities exposed by trenching also prove the existence of underground erosion in the lower part.

4.4 Evolutionary characteristics of ground fissures

According to the stratigraphic texture revealed by trenching, the formation process of ground fissures can be analyzed as follows: first, under the action of tectonic movement and heavy rainfall, outcrop-type cracks are generated. Then, the loose soil begins to subside from the edges of the crack, and the topsoil on both sides will migrate and deposit to the fracture zone. As the composition of the clay granules is carried away by water, a sedimentary silty layer that is thin on the periphery and thick in the middle forms in the center of the fracture. Meanwhile, under relatively stable fracture activities, the fracture zone gradually develops into a collapsed depression, the middle part of which is easily accumulated with water that seeps into the openings of the ground fissures to generate a passage, causing the soil at the upper part of the fracture to subside. This is how collapse pits are formed. As a result, the surrounding soil is further and repeatedly accumulated and carried to the middle low-lying area to expand the collapse pits gradually. Figure 16 shows the ground fissure evolution. Moreover, the development and evolution of ground fissures in the research area are recurrent in nature.

5 Conclusion

The main conclusions drawn by studying the ground fissures on the MH Highway in the Ethiopian Rift Valley are as follows:

1) The ground fissures are divided into two types: exposed fissures and concealed fissures, whose distribution and direction are closely related to the distribution of geological structures. The exposed fissures are crevasses or stripped collapse zones, and the concealed fissures are collapsed depressions and string-bead-like collapse pits.
2) The ground fissures are highly active, and their development process presents strong seasonal characteristics, that is, emerging or developing in the rainy season.
3) The ground fissures have significant geophysical anomalies, which are mainly manifested as low-resistance anomalies and radon gas anomalies through field exploration.
4) The violent tectonic activity of the basement (expansion of the East African Rift Valley) plays a controlling role in the generation of ground fissures. Meanwhile, adverse stratigraphic textures provide basic conditions for the development of ground fissures, and the infiltration and underground erosion resulting from heavy precipitation are important factors to aggravate the development of ground fissures.
5) In the ground cracks and collapse areas, the route should be taken as far as possible. For areas that cannot be avoided, try to adopt the form of roadbeds. Reinforcement should be performed during the process of road processing. If the bridge is needed, appropriate reinforcement and preventive measures should be taken to regularly monitor and adjust in time. The influence and erosion of groundwater are important causes of the induction of ground crack development and collapse. It is recommended to note ground drainage and flow measures in the cracks and collapse areas to limit the mining of groundwater.

Data availability statement

The original contributions presented in the study are included in the article/Supplementary Material; further inquiries can be directed to the corresponding author.

Author contributions

WL contributed to the preparation of the article through on-site investigation and data analysis, CX contributed to the preparation of the article, and XH modified the content of the article. All the authors discussed the results and edited the manuscript.

Conflict of interest

Xi'an China Highway Geotechnical Engineering CO., LTD is a wholly-owned subsidiary of CCCC First Highway Consultants CO., LTD. Authors XU Cheng and HUANG Xiaonian are/were employed by Xi'an China Highway Geotechnical Engineering CO., LTD.

The remaining authors declare that the research was conducted in the absence of any commercial or financial relationships that could be construed as a potential conflict of interest.

Publisher's note

All claims expressed in this article are solely those of the authors and do not necessarily represent those of their affiliated organizations, or those of the publisher, the editors, and the reviewers. Any product that may be evaluated in this article, or claim that may be made by its manufacturer, is not guaranteed or endorsed by the publisher.

References

Asfaw, L. (1982). Development of earthquake-induced fissures in the main Ethiopian rift. *Nature* 297, 393–395. doi:10.1038/297393a0

Ayalew, L., Yamagishi, H., and Reik, G. (2004). Ground cracks in Ethiopian Rift Valley: Facts and uncertainties. *Eng. Geol.* 75, 309–324. doi:10.1016/j.enggeo.2004.06.018

Cao, W., and Li, K. (1986). An indoor research method for the process of water release, absorption and transfluence in clayey soil layers due to water level rise and fall. *Site Investigation Sci. Technol.* (4), 22–28.

China Water&Power Press (1980)., 1. Nanjing, Jiangsu: China Water&Power Press, 118–136.Soil mechanics teaching and research office of east China technical university of water resources, *Geotechnical Principles and Calculations*.

Chorowicz, J., Collet, B., Bonavia, F., Mohr, P., Parrot, J. F., and Korme, T. (1998). The Tana basin, Ethiopia: Intra-plateau uplift, rifting and subsidence. *Tectonophysics* 295, 351–367. doi:10.1016/s0040-1951(98)00128-0

Chorowicz, J. (2005). The East African rift system. *J. Afr. Earth Sci.* 43, 379–410. doi:10.1016/j.jafrearsci.2005.07.019

Ebinger, C. J. (1989). Tectonic development of the Western branch of the East African rift system. *Geol. Soc. Am. Bull.* 101, 885–903. doi:10.1130/0016-7606(1989)101<0885:tdotwb>2.3.co;2

Ebinger, C. J., Yemane, T., Harding, D. J., Tesfaye, S., Kelley, S., and Rex, D. C. (2000). Rift deflection, migration, and propagation: Linkage of the Ethiopian and Eastern rifts, Africa. *Afr. Geol. Soc. Am. Bull.* 112, 163–176. doi:10.1130/0016-7606(2000)112<163:rdmapl>2.0.co;2

Hoffman, C., Courtillot, V., Feraud, G., Rochette, P., Yirgu, G., Ketefo, E., et al. (1997). Timing of the Ethiopian flood basalt event: Implications for plume birth and global change. *Nature* 389, 838–841. doi:10.1038/39853

Ministry of Mines (1976). *Regional geoloSSSgical map of Ethiopia (1:250,000)*. Addis Ababa, Ethiopia: Geological Survery of Ethiopia.

National meteorological Agency of Ethiopia (2001). *Rainfall data for langona and Arsi Negele meteorological stations*. Addis Ababa, Ethiopia: National meteorological Agency of Ethiopia.

Roberts, E. M., Stevens, N. J., O'Connor, P. M., Disks, P. H. G. M., Gottfried, M. D., Clyde, W. C., et al. (2012). Initiation of the Western branch of the East African Rift coeval with the eastern branch. *Nat. Geosci.* 5, 289–294. doi:10.1038/ngeo1432

Wang, X., and Liu, C. (2003a). A new understanding of the pore water infiltration law of cohesive soil. *Acta Geosci. Sin.* 1, 91–95.

Wang, X., and Liu, C. (2003b). Exploration on the law of water permeation and release of deep cohesive soil. *Chin. J. Geotechnical Eng.* (3), 308–312.

Wang, X., and Liu, C. (2004). Seepage law of pore water in low permeability media. *J. Eng. Geol.* 1004.

Wang, Z., Sun, G., Liu, S., Zhu, X., Tang, G., and Huang, S. (1986). *Geotechnical testing techniques*. Beijing, China: China Architecture & Building Press, 61–78.

Williams, F. M. (2020). Safeguarding geoheritage in Ethiopia: Challenges faced and the role of geotourism. *Geoheritage* 12, 31. doi:10.1007/s12371-020-00436-9

Williams, F. M., Williams, M. A. J., and Aumento, F. (2004). Tensional fissures and crustal extension rates in the northern part of the Main Ethiopian Rift. *J. Afr. Earth Sci.* 38, 183–197. doi:10.1016/j.jafrearsci.2003.10.007

Wilson, M., and Nyambok, I. O. (2000). Ground subsidence and its socio-economic implications on the population: A case study of the nakuru area in central Rift Valley, Kenya. *Environ. Geol.* 39 (6), 567–574. doi:10.1007/s002540050468

Zhang, Zhongyin (1980). *On combination of hydraulics and soil Mechanics*. Missoula, MT, USA: Geology Press, 40–100.

frontiers | Frontiers in Earth Science

TYPE Original Research
PUBLISHED 22 March 2023
DOI 10.3389/feart.2023.1051913

OPEN ACCESS

EDITED BY
Wen Nie,
Jiangxi University of Science and Technology, China

REVIEWED BY
Chaoying Zhao,
Chang'an University, China
Kun He,
Southwest Jiaotong University, China
Bouhadad Youcef,
National Earthquake Engineering Center (CGS), Algeria

*CORRESPONDENCE
Hongyan Deng,
annedeng@swjtu.edu.cn

SPECIALTY SECTION
This article was submitted to Geohazards and Georisks, a section of the journal Frontiers in Earth Science

RECEIVED 23 September 2022
ACCEPTED 01 March 2023
PUBLISHED 22 March 2023

CITATION
Song Y, Deng H, Tang C and Li B (2023), Critical area identification and dynamic process simulation for landslide hazard chain formation in the upstream Jinsha River.
Front. Earth Sci. 11:1051913.
doi: 10.3389/feart.2023.1051913

Critical area identification and dynamic process simulation for landslide hazard chain formation in the upstream Jinsha River

Yixian Song[1], Hongyan Deng[1]*, Chenxiao Tang[2] and Bokai Li[1]

[1]School of Civil Engineering, Southwest Jiaotong University, Chengdu, China, [2]Institute of Mountain Hazard and Environment, Chinese Academy of Sciences, Chengdu, China

The upper reaches of the Jinsha River, with their complex terrain and active tectonic movements, are vulnerable to landslide-induced hazard chain events, which endanger the safety of residents and infrastructure construction. Based on the analysis of the development background of the hazard chain in the upstream area of the Jinsha River, five factors, including the lithology, distance to faults, distance to rivers, peak ground acceleration, and slope degree, were selected to identify the critical landslide-prone areas. Principal component and grey correlation analyses were then conducted to determine the contributions of these different factors. Based on ArcGIS, the study zone was categorized into five classes of landslide susceptibility: very high, high, moderate, low, and very low. The identification of the critical target areas for landslide hazard chain formation showed satisfactory accuracy. The very high- and high-susceptibility areas are concentrated along the Jinsha River. The dynamic process of a typical landslide in a very high-susceptibility area was numerically simulated using OpenLISEM. The high-precision Baige landslide data of the study area were used to calibrate the practicality of the input mass parameters, including cohesion, internal friction angle, D50, and D90. The movement and accumulation processes of a typical landslide were then numerically simulated with the verified data. The entire landslide accumulation covers an area of 0.45 km^2, with a length of 1,600 m and a width of 270 m. Thus, the OpenLISEM model, which combines mass, topography, and landcover parameters, is feasible for the numerical simulation of landslide dynamic processes. The prediction of the dynamic processes and accumulation morphology of landslides can provide a reference for the formation processes and mechanisms of the landslide-induced hazard chain in the upper Jinsha River.

KEYWORDS

landslide, susceptibility assessment, OpenLISEM, numerical simulation, Jinsha River

1 Introduction

Due to the compressed active fault zone and severe erosion of the valley shear, the Jinsha River basin exhibits unique fold mountains and deep valley geomorphology (Xu et al., 2018; Zhu et al., 2021). With the complicated lithology and steep slope degree, the upper reaches of the Jinsha River are vulnerable to landslide–dam breach–flood hazard chain events, e.g., the Baige (Fan et al., 2020), Sela (Zhu et al., 2021), Temi (Chen et al., 2021), and Guili (Xu et al., 2022) landslides, which threaten the safety of people and property upstream and

downstream (Wei and Siming, 2020; Jin, 2021; Li et al., 2021). Therefore, the identification of critical areas and simulation of the dynamic processes of landslide hazard chain formation is critical in the upstream Jinsha River basin.

Field surveys are exceedingly difficult to perform in this region because the landslide disaster site is in a remote alpine canyon area with a harsh environment and limited access. Thus, high-precision ground observation technologies, including remote sensing, interferometric synthetic aperture radar (InSAR), and light laser detection and ranging (LiDAR), are used to identify landslide hazards (Lu et al., 2019). Moreover, Landsat, ALOS, Quick Bird, and other satellites with high-resolution images have been widely used for landslide identification; however, they only identify landslide hazards with clear deformation (McDonald and Grubbs, 1975; Sato and Harp, 2009; Youssef et al., 2009; García-Davalillo et al., 2014). InSAR with centimeter-high precision and all-weather surface observation technology can perform large-scale landslide identification and monitoring to build a landslide hazard inventory (Woods et al., 2020; Urgilez Vinueza et al., 2022; Zhang et al., 2022). Because of the satellite lateral imaging mode, the terrain may cause geometric distortion of SAR images, including perspective shortening, overlap, and shadow (Jie et al., 2018). LiDAR can not only directly obtain three-dimensional terrain coordinates to provide high-accuracy topographic images but also remove the effective influence of vegetation to obtain true ground elevation data (Gorsevski et al., 2016; Abdulwahid and Pradhan, 2017; Xu et al., 2019). However, LiDAR is not suitable for large-scale disaster identification due to its harsh operating conditions and high costs (Lu et al., 2019). Thus, while high-accuracy remote sensing technology has become an important means to obtain landslide hazard information, the reliability of remote sensing data interpretation and the accessibility and costs of high-precision image data remain issues in landslide risk assessment. In addition to satellite sensing technology, scholars have proposed statistical models for landslide susceptibility assessment, with remarkable results (Song et al., 2012; Xu et al., 2013; Khan et al., 2019; Liu D et al., 2021; Yong et al., 2022). Models such as the information quantity model (Yang et al., 2018), the weight-of-evidence model (Wang et al., 2016), the logistic regression model (Xing et al., 2021), the analytical hierarchic process (Yoshimatsu and Abe, 2006), and the principal component analysis (Chang et al., 2014) have demonstrated excellent accuracy. Based on the rich results in the selection of evaluation factors, the weight of the factor determination, and the construction of the evaluation model, the present study applied mathematical statistics to identify the key target areas of landslide hazards to not only objectively analyze the assessment of regional landslide disaster susceptibility but also the relationships and impact degrees of slope failure factors.

Many numerical simulation tools for the simulation of landslide dynamic processes are effective for the analysis of landslide hazards. Pastor et al. (2021) and Ouyang et al. (2019) used the depth-integrated continuum method for the dynamic simulation of debris and landslides. Based on the discrete element method An et al. (2021) established an adapted Hertz–Mindlin contact model between particles and the ground surface to accurately simulate the landslide dynamic process. Zhang et al. (2012) simulated the entire process of failure and instability of the Jiweishan high-speed remote landslide in Chongqing *via* PFC 3D software. Smoothed particle hydrodynamics (SPH) based on Lagrangian particle-based meshless methods have been widely employed in applications in geotechnical engineering (Peng et al., 2019; Zhu et al., 2020). The depth-integrated continuum and discrete element methods consider the landslide body as a fluid and can efficiently simulate the landslide motion and accumulation processes. However, they cannot easily simulate the initial failure mechanism and triggering factors such as the erosion and volume expansion processes due to the disaggregation and fragmentation of the rock mass (Wen-Jie et al., 2021). The landslide movement process is affected by many factors, including mass composition, trigger mechanism, and vegetation environment. The above numerical simulation methods do not consider the interaction between the material source and the environment during the movement process. Aiming to precisely assess the landslide dynamic process, the present study used OpenLISEM to perform the numerical simulations. OpenLISEM divides the research area into several grids of equal size; inputs corresponding terrain, vegetation, and material source parameters into different grids; couples the distributed basin hydrological and two-phase flow models; compares the slope, ground roughness, and other parameters of adjacent grids; and simulates disaster processes such as landslides, debris, and flash floods (OpenLISEM manual 2017, https://lisemmodel.com).

The complete geohazard chain includes potential hazards, primary hazards, secondary hazards (series), and hazard-bearing

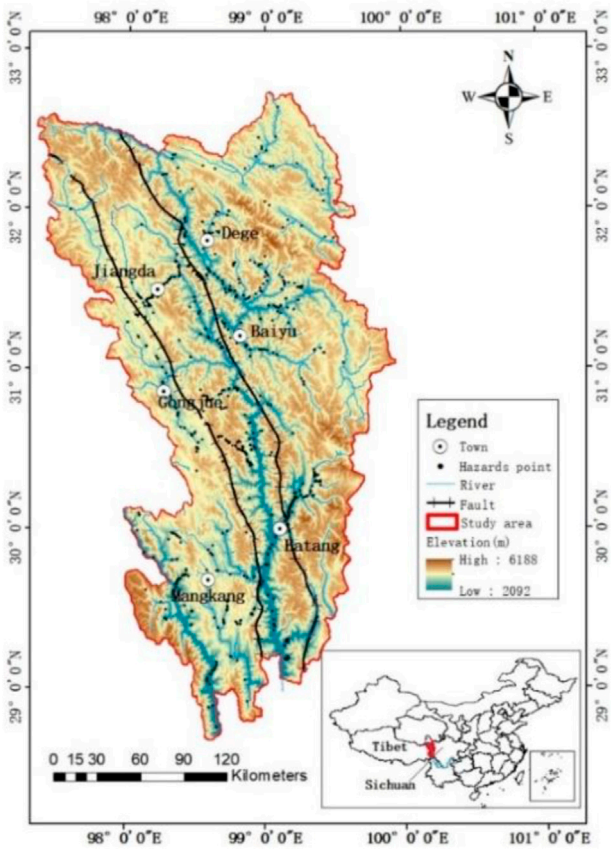

FIGURE 1
Location of the study area.

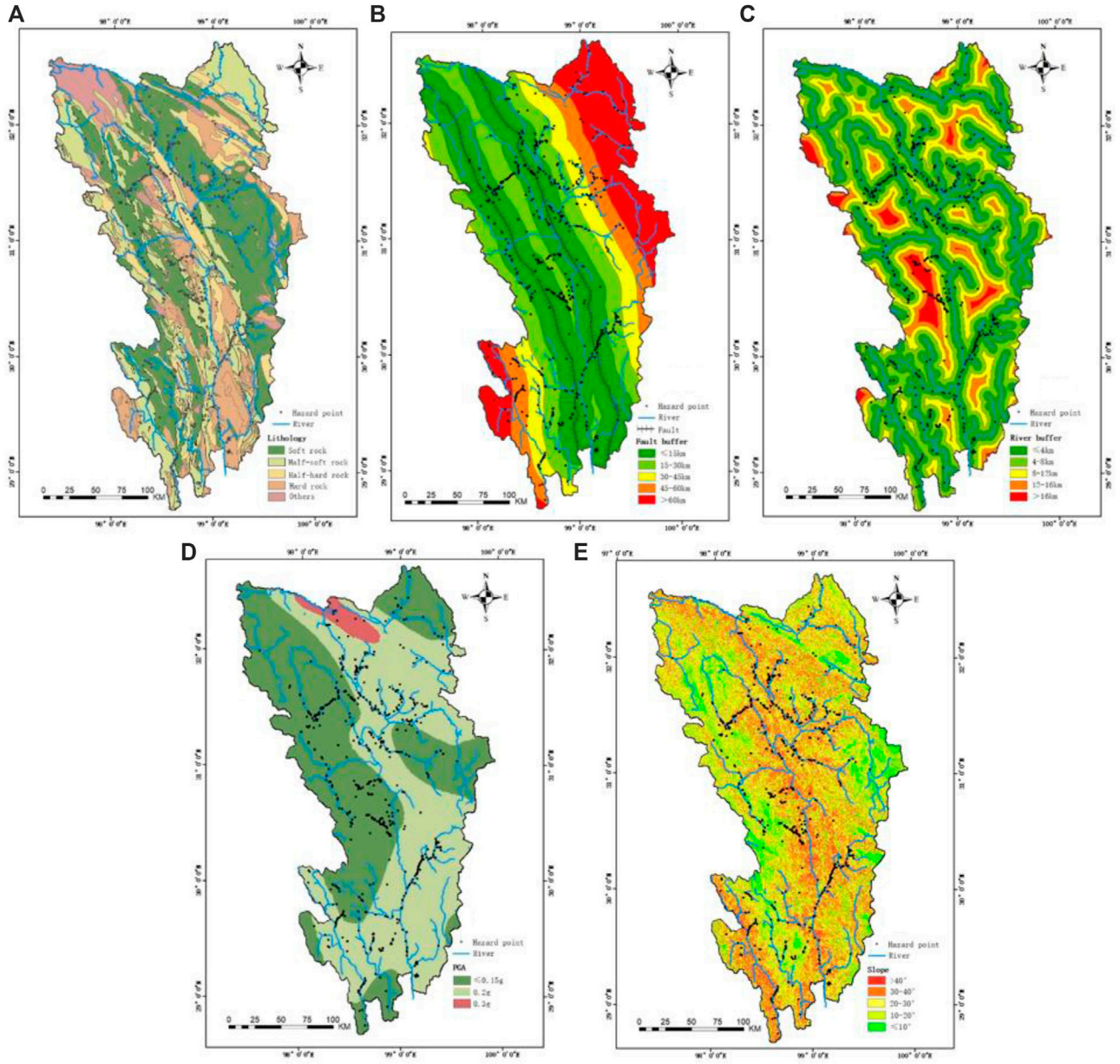

FIGURE 2
Factor distribution in the study area: **(A)** lithology, **(B)** fault, **(C)** river, **(D)** PGA, and **(E)** slope.

bodies (Peng and Jian, 2021). This study identified potential geatators by hazard susceptibility assessment and researched the dynamic process of the primary hazard by numerical simulation. Based on remote sensing and field investigation data, the weights of the landslide factors were determined *via* principal component analysis and the grey correlation degree method. A landslide susceptibility evaluation model was then constructed to identify high-susceptibility landslide areas. Based on the vulnerability assessment, the key target areas of landslide hazards were numerically simulated in OpenLISEM to obtain the movement process and accumulation form of landslides, and to provide a reference for a landslide–dam breach–flood disaster chain prevention in the upstream area of the Jinsha River.

2 Study area

The study area is situated in the upper Jinsha River valley, at the intersection of Tibet and Sichuan, and covers an area of 60,352 km^2. The geographic coordinates are 97.33°E–99.94°E and 28.68°N–32.73°N (Figure 1). The terrain is characterized by "V"-shaped gullies in the high-mountain region, which is severely affected by river erosion. The elevation of the study area ranges from 2092 to 6,088 m. Based on the genesis, the geomorphic types in the study area can be divided into five types: erosion accumulation, structural erosion, structural denudation, structural dissolution, and glacier geomorphology (Bai et al., 2014). The main fault strikes have a northwest-southeast orientation. The lithology of the study area is

TABLE 1 Data sources.

Data type	Data source
Lithology	RESDC of the Chinese Academy of Science: https://www.resdc.cn
Fault	RESDC of the Chinese Academy of Science: https://www.resdc.cn
River	Open Street Map: https://www.openstreetmap.org
PGA	China's seismic ground motion parameter zonation map
DEM	ALOS ASF Data Search (alaska.edu)
Hazard Inventory	RESDC of the Chinese Academy of Science: https://www.resdc.cn

complicated, including marine Upper Triassic system, Ordovician granite, Cretaceous granite, Quaternary sandstone, Permian, Triassic, Paleogene, and Jurassic systems.

The study area has highland climates with an average temperature of -4.9°C–7.8°C. Furthermore, due to the high terrain and strong solar radiation, the area is cold and dry with 53–67% relative humidity, an annual average rainfall of 387.0–657.6 m, and an average of 100.3–169.8 days of precipitation. The rainy season is from May to October, accounting for more than 90% of the annual rainfall. Snow is the main form of precipitation in the region, and the daily rainfall in most areas is 50 mm. Additionally, the vegetation is mainly grassland and swamp meadows (Wu, 2007).

3 Database and method

3.1 Susceptibility assessment

3.1.1 Factor sources

Landslide susceptibility mapping is essential for identifying areas with high landslide risk. In this study, the landslide inventory with a total of 635 hazard points was extracted from the Resource and Environment Science and Data Center (RESDC) of the Chinese Academy of Science. Based on previous research, the specific characteristics of the study region, including lithology, distance to the fault, distance to the river, and peak ground

TABLE 2 Numbers and densities of landslides in the study area.

Factors	Classes	Area (km^2)	Landslide number	Landslide density (landslide number/km^2)	Scores
Lithology	I	22,645.627	321	0.014174922	5
	II	15,837.825	156	0.009849837	3
	III	6,609.371	66	0.009985822	4
	IV	11,455.568	71	0.006197859	2
	V	3,804.447	21	0.005519856	1
Fault	≤15 km	23,923.96017	330	0.0137937	5
	15–30 km	13,892.70801	159	0.01144485	4
	30–45 km	6,872.80138	50	0.00727505	2
	45–60 km	5,460.90858	58	0.01062094	3
	>60 km	10,202.46206	38	0.00372459	1
River	≤4 km	25,597.48631	460	0.01797051	5
	4–8 km	18,554.48587	89	0.00479668	3
	8–12 km	10,368.69513	42	0.00405065	2
	12–16 km	4,112.58464	16	0.0038905	1
	>16 km	1,718.46238	28	0.01629364	4
PGA	≤0.15 g	28,855.31	300	0.0103967	1
	0.2 g	30,189.11	329	0.01089797	3
	0.3 g	1,308.466	6	0.00458552	5
Slope	≤10°	7,277.5427	103	0.014153	5
	10°–20°	14,813.384460	164	0.011071	4
	20°–30°	18,561.758800	173	0.009320	2
	30°–40°	13,660.906230	142	0.010395	3
	>40°	6,015.9348	53	0.00880994	1

TABLE 3 Discriminant coefficient matrix of landslides in the study area.

Landslide code	Lithology	Fault	River	PGA	Slope
L-001	5	5	3	1	2
L-002	5	5	5	1	4
L-003	5	5	5	1	3
.....	.....	.....	.....	.....	.....
L-633	4	5	5	3	2
L-634	5	4	5	3	4
L-635	3	5	5	3	4

TABLE 4 Composition matrix table of landslide factors in the study area.

Factors	Composition matrix			
Lithology	0.346	0.508	−0.187	0.622
Fault	−0.412	−0.24	0.587	0.438
River	0.426	−0.202	0.577	0.391
PGA	0.44	−0.207	0.311	−0.56
Slope	−0.133	0.732	0.569	−0.338
Eigenvalue	1.467	1.069	0.882	0.863
Contribution rate (%)	29.35%	21.38%	17.65%	17.26%
Cumulative contribution rate (%)	29.35%	50.73%	68.37%	85.63%

acceleration (PGA), were selected to assess the landslide susceptibility (Table 1). The lithology and fault were obtained from the RESDC of the Chinese Academy of Science, while the river data were obtained from the Open Street Map. The fault and river buffer distances were calculated using the surface analysis tools in ArcGIS. The slope data were extracted from the digital elevation model (DEM) downloaded from the advanced land observation satellite (ALOS) with a resolution of 12.5 m × 12.5 m. The influence degree of seismic intensity was reflected by PGA extracted using the seismic ground motion parameter zonation map of China (GB18306 2015).

3.1.2 Factor classification

The geographic information system (GIS) was used to show the terrain features of the lithology and other factors. The hazard inventory, combined with the five evaluation factors, was digitized and stored in the GIS. The classification of the five factors in this study is shown in Figure 2. The lithology composition in the study area is sophisticated. Herein, it is divided into five categories: soft rock (I), half-soft rock (II), half-hard rock (III), hard rock (IV), and others (V), which include loose deposits, complex structural surfaces, and unknown rock. Landslides are mainly located in soft rock composed of siltstone, sandstone, etc. because these rocks are vulnerable to external forces (Figure 2A). The faults are densely distributed in the study area. This study selected the Jinsha-Honghe fault as the main research target. The rock near the fault zone is relatively broken and has poor stability. The landslide activity intensity decreases with increasing

TABLE 5 Related coefficients and weights of landslide factors in the study area.

Factors	Degree	Scores	Weights
Lithology	1	5	0.33
Fault	0.73	3	0.2
River	0.69	4	0.27
PGA	0.685	1	0.07
Slope	0.160	2	0.13

distance from the fault (Figure 2B). The surface stream deepens in the valley in the study area through erosion and transportation, producing favorable conditions for hazards. More than 50% of the hazards are located within 4 km of the river (Figure 2C). PGA was used to represent the magnitude of the earthquake intensity and was divided into <0.15, 0.2, and 0.3 g. According to the seismic intensity map in the spatial distribution, most landslides are mainly concentrated in areas of high earthquake intensity (Figure 2D). The slope gradient was obtained using the 3D-analysis slope tool in ArcGIS. The landslides are concentrated in regions ranging from 10° to 40° (Figure 2E).

3.1.3 Factor weight calculations

According to the landslide intensities for the selected factors, a score was given to the different intervals of each evaluation factor (Table 2). The discriminant coefficient matrix of the landslide inventory in the study area and factors is shown in Table 3.

The contribution degrees of the five factors were obtained *via* principal component analysis (Chang and Tang et al., 2014). The discriminant coefficient matrix (Table 3) was imported into SPSS software for principal component analysis to obtain the contributions of the factors. The first four factors, i.e., lithology, faults, rivers, and PGA, contributed to >80%. Lithology was the most influential factor and was, therefore, selected to determine the contribution of the other factors (Table 4).

The grey correlation analysis (Wei et al., 1998) mainly determines the correlation between the dominant factor and the other four factors. When the variable was transformed into dimensionless data, the outcome was a coefficient matrix of factors and initialized data. From this, the absolute D-value Eq. 1was calculated:

$$x_i(k) = \begin{pmatrix} x_0(1) & x_0(2) & x_0(n) \\ x_1(1) & x_1(2) & x_1(n) \\ x_i(1) & x_i(2) & x_i(n) \end{pmatrix}$$
$$\Delta_i(k) = |x_i(k) - x_i(0)| \quad (1)$$

where i=1,2. . . . .m; k=1,2,. . . . .n; $x_i(k)$ =coefficient matrix of factor lithology; and $\Delta_i(k)$ =absolute value. The extreme of the matrix (Δ_{min} *and* Δ_{max}) was obtained *via* Eq. 2

$$\Delta_{min} = minmin\Delta_i(k), \Delta_{max} = maxmax\Delta_i(k) \quad (2)$$

The correlation coefficient of the evaluation factors was calculated using Eq. 3:

$$\xi_i(k) = \frac{\Delta_{min} + \rho\Delta_{max}}{\Delta_i(k) + \rho\Delta_{max}} \quad (3)$$

where $\xi_i(k)$ is the correlation coefficient and ρ is the distinguishing coefficient, which takes 0.5 as the value. The size of the value can control the data transformation and significant differences in the correlation coefficients. The greater the correlation between other factors and the dominant factor, the greater the impact on geological disasters. The weights of the evaluation factors are shown in Table 5.

3.1.4 Model generation

Five-factor raster maps with 12.5 m resolution were constructed using GIS. The values of the factor raster were calculated using the Raster Computing Tool. The final model was established using these factors.

$$\mathbf{R} = \sum_{i=1}^{n} x_i(k)\omega_i \tag{4}$$

where i = 1, 2. . . . .5, R is the value of landslide susceptibility evaluation, $x_i(k)$ is the value of the landslide in Table 2, and ω_i is the weight of the landslide in Table 5.

According to the value of R, the susceptibility degree of the study area can be divided into three categories: very low (R ≤ 2), low (2<R ≤ 2.5), moderate (2.5 < R ≤ 3.5), high = (3.5 < R ≤ 4), and very high (R >4) susceptibility.

3.2 Landslide numerical simulation

3.2.1 Theory

To better simulate the dynamic process of critical landslide hazards, a discrete numerical modeling method was applied using the open-source software OpenLISEM, which requires the subdivision of both space and time into a discrete set of locations (https://lisemmodel.com). Originally, OpenLISEM was a physically based numerical model designed to simulate event-based runoff, flooding, and erosion on a catchment scale. By combining solid and water runout flow equations, OpenLISEM includes a series of dynamic hydrological processes, such as precipitation, interception, surface flow, splash detachment, erosion, and sediment transportation. Many revisions and additions have subsequently been incorporated into the OpenLISEM application. OpenLISEM was further developed as a multi-hazard model, including groundwater flow, slope stability, slope failure, mass movements, deposition, entrainment, and earthquake effects (Pudasaini, 2012; Bout et al., 2018; Scaringi et al., 2018). Furthermore, the model incorporates the iterative slope failure method based on a modified infinite slope mode. The conventional infinite slope model predefines the bottom of the soil layer as the potential slip surface, while the iterative method iteratively searches the potential slip surface. The equation for determining the factor of safety (FOS) is

$$\mathbf{FOS} = \frac{c + c' + [(\gamma - m\gamma_\omega)z + m\gamma_\omega z]cos^2\beta \tan\varphi'}{[(\gamma - m\gamma_\omega)z]\sin\beta\cos\beta} \tag{5}$$

where c and c' (kpa) are the effective soil cohesion and root cohesion, respectively; γ and γ_ω (kg/m^3) are the soil and water densities, respectively; m is the effective saturation level of the soil; z (m) is the soil depth; β (°) is the slope angle; and φ' (°) is the effective internal friction.

The two-phase runout flow within OpenLISEM is a combination of water and solid dynamics (Pudasaini, 2012). Using it, landslides, water flow, and debris flow can be simulated, including their interactions. The full momentum source terms for both the fluid and solid phases are as follows:

$$\begin{aligned} S_{x,s} = \alpha_s\Bigg(& g\left(\frac{\partial b}{\partial x}\right) - \frac{u_s}{|\vec{u}_s|}\tan(\partial P_{b_s}) - \varepsilon P_{b_s}\left(\frac{\partial b}{\partial x}\right)\Bigg) \\ & -\varepsilon\alpha_s\gamma P_{b_f}\left(\frac{\partial h}{\partial x} + \frac{\partial b}{\partial x}\right) \\ & +C_{DG}(u_f - u_s)|\vec{u}_f - \vec{u}_s|^{j-1} \end{aligned} \tag{6}$$

$$\begin{aligned} S_{y,s} = \alpha_s\Bigg(& g\left(\frac{\partial b}{\partial y}\right) - \frac{v_s}{|\vec{u}_s|}\tan(\partial P_{b_s}) - \varepsilon P_{b_s}\left(\frac{\partial b}{\partial y}\right)\Bigg) \\ & -\varepsilon\alpha_s\gamma P_{b_f}\left(\frac{\partial h}{\partial y} + \frac{\partial b}{\partial y}\right) \\ & +C_{DG}(v_f - v_s)|\vec{u}_f - \overrightarrow{vu}_s|^{j-1} \end{aligned} \tag{7}$$

$$\begin{aligned} S_{x,f} = \alpha_f\Bigg\{& g\left(\frac{\partial b}{\partial x}\right) - \varepsilon\Bigg[\frac{1}{h}\frac{\partial}{\partial x}\left(\frac{h^2}{2}P_{b_f}\right) + P_{b_f}\frac{\partial b}{\partial x} \\ & -\frac{1}{\alpha_f N_R}\left(2\frac{\partial^2 u_f}{\partial x^2} + \frac{\partial^2 v_f}{\partial x\partial y} + \frac{\partial^2 u_f}{\partial y^2} - \frac{\chi v_f}{\varepsilon^2 h^2}\right) \\ & +\frac{1}{\alpha_f N_R}\left(2\frac{\partial}{\partial x}\left(\frac{\partial\alpha_s}{\partial x}(u_f - u_s)\right) + \frac{\partial}{\partial y}\left(\frac{\partial\alpha_s}{\partial x}(v_f - v_s) + \frac{\partial\alpha_s}{\partial y}(u_f - u_s)\right)\right) \\ & -\frac{\xi\alpha_s(v_f - v_s)}{\varepsilon^2\alpha_f N_{RA} h^2}\Bigg]\Bigg\} - \frac{1}{\gamma}C_{DG}(u_f - u_s)|\vec{u}_f - \vec{u}_s|^{j-1} \end{aligned} \tag{8}$$

$$\begin{aligned} S_{y,f} = \alpha_f\Bigg\{& g\left(\frac{\partial b}{\partial y}\right) - \varepsilon\Bigg[\frac{1}{h}\frac{\partial}{\partial y}\left(\frac{h^2}{2}P_{b_f}\right) \\ & +P_{b_f}\frac{\partial b}{\partial y} - \frac{1}{\alpha_f N_R}\left(2\frac{\partial^2 v_f}{\partial y^2} + \frac{\partial^2 u_f}{\partial x\partial y} + \frac{\partial^2 v_f}{\partial y^2} - \frac{\chi v_f}{\varepsilon^2 h^2}\right) \\ & +\frac{1}{\alpha_f N_R}\left(2\frac{\partial}{\partial y}\left(\frac{\partial\alpha_s}{\partial y}(v_f - v_s)\right)\right. \\ & \left.+\frac{\partial}{\partial y}\left(\frac{\partial\alpha_s}{\partial y}(u_f - u_s) + \frac{\partial\alpha_s}{\partial y}(v_f - v_s)\right)\right) - \frac{\xi\alpha_s(u_f - u_s)}{\varepsilon^2\alpha_f N_{RA} h^2}\Bigg]\Bigg\} \\ & -\frac{1}{\gamma}C_{DG}(u_f - u_s)|\vec{u}_f - \vec{u}_s|^{j-1} \end{aligned} \tag{9}$$

where S_s and S_f (m/s^2) are the momentum source terms for the solid and fluid phases, respectively; α_s and α_f are the volume fractions for the solid and fluid phases, respectively; P_b (kg/ms^2) is the pressure at the base surface; b (m) is the basal surface of the flow; N_R is the Reynolds number; N_{RA} is the quasi-Reynolds number; C_{DG} is the drag coefficient; γ is the density ratio between the fluid and solid phase; χ (m/s) is the vertical shearing of fluid velocity; ε is the aspect ratio of the model; and ξ (1/m) is the vertical distribution of α_s.

3.2.2 Data input and calibration

This study ignores the interception model. Therefore, the input data of the OpenLISEM model can be divided into three categories: landcover, mass, and topography parameters.

The landcover parameters include land-use type, vegetation cover (vegc), vegetation height (ch; m), and leaf area index of the plant cover in a grid cell (lai; m^2/m^2). Land-use type and ch were obtained from Wang et al. (2012). The upper reaches of the Jinsha River are mainly grassland and farmland. Based on ArcGIS software, vegc was obtained from the linear range of NDVI (normalized difference vegetation index) from Landsat remote images (http://

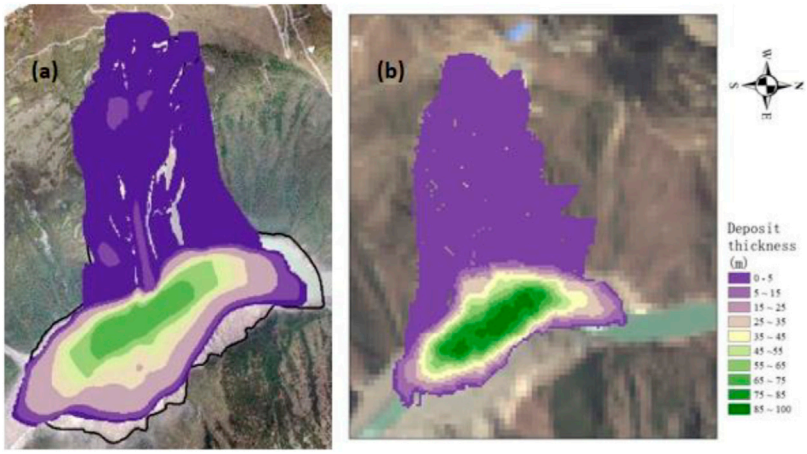

FIGURE 3
Deposit thickness of the first Baige landslide: **(A)** actual result and **(B)** numerical simulation.

TABLE 6 Calibrated landslide mass parameters in the study area.

Cohesion (kpa)	Internal friction angle (radians)	Initial moisture (%)	Porosity (%)	Density (kg/m^3)	D50 (cm)	D90 (cm)
30	0.54	13.9	21.93	2000	60	480

www.gscloud.cn/search). Finally, lai was derived as follows (Choudhury, 1987; Choudhury et al., 1994):

$$\mathbf{lai} = \frac{\mathbf{ln}\ (\mathbf{1} - \boldsymbol{vegc})}{\mathbf{-0.4}} \tag{10}$$

Topography parameters such as the slope, sine of slope gradient in the direction of the flow (Gradient), random roughness (RR), local surface drainage direction network (LDD), and main catchment outlet corresponding to LDD (Outlet) can be derived from the DEM using the PCRaster program. Manning's index, another topography parameter, was obtained using the OpenLISEM Manual (2017), according to land use (Wang, 2018).

The mass parameters numerically used in the simulation include mass depth (mm), initial moisture (-), cohesion (kpa), internal friction angle (radians), porosity (-), density (kg/m^3), and D50 and D90 (cm). The mass depth is calculated based on the empirical formula reported by Tang et al., 2012:

$$\mathbf{T} = \mathbf{1.432}\,\mathbf{ln}\,(\boldsymbol{s_l}) - \mathbf{4.895} \tag{11}$$

where T is the average soil depth (m) and s_l is the landslide area (m^2).

It is difficult to directly obtain accurate values for the other mass parameters due to the limitations of field testing technology. On October 10 and November 3, 2018, two large landslides near Baige village occurred in the same location on the right bank of the Jinsha River (Figure 5). Many scholars performed field investigations, and research on the slope failure mechanisms and parameters showed inversion in the Baige landslide, which provided a valuable opportunity to adjust parameters (Ouyang et al., 2019; Chen et al., 2021; Xu et al., 2021; Zhou et al., 2020; Zhao et al., 2020; Zhang et al., 2020; Zhou et al., 2022; Liu X et al., 2021; Sun, 2021; Wang et al., 2019). The first Baige landslide was successfully simulated using the OpenLISEM program. The results were consistent with the modeling performed by Ouyang et al., 2019 (Figure 3). The appropriate parameters were obtained by numerically simulating the first Baige landslide event, as shown in Table 6.

4 Results

4.1 Critical landslide identification

To identify the critical areas for landslide hazard chains, factors such as lithology, fault, river, PGA, and slope were selected for the landslide susceptibility analyses. The five landslide factors were weighed *via* principal component and grey correlation analyses. Table 5 shows that lithology has the greatest impact on the landslide hazard chain, with a weight value of 0.33, while PGA has the least impact, with a weight value of 0.07. Fault, river, and slope have weights of 0.2, 0.27, and 0.13, respectively. Consequently, the R-value reflecting the landslide susceptibility ranges from 1.33 to 5, which is classified into five groups (Table 7). Very high and high susceptibility areas account for 45.42% of the total area. However, the area accounts for 75.28% of the landslides. To verify the reliability and applicability of the model for the vulnerability evaluation of landslide hazard points in the study area, ROC (receiver operating characteristic) curve and AUC (area under the curve) values were selected for testing. The ROC curve is an effective method to evaluate the performance of the classification algorithm; that is, the relationship between the simulated and sampled values. The horizontal axis is the cumulative value of the false positive rate (FPR), which indicates the proportion of susceptible areas, and the vertical axis is the true positive rate (TPR), which

TABLE 7 Statistics of landslide susceptibility in the study area.

Susceptibility class	Area covered (%)	Number of landslides (%)
Very low	1.78	0.47
Low	8.17	2.52
Moderate	44.63	21.73
High	28.41	29.61
Very high	17.01	45.67

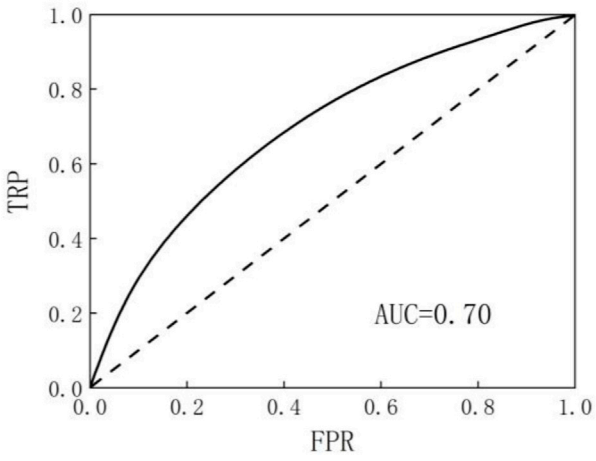

FIGURE 4
ROC curve.

indicates the cumulative value of the proportion of disaster points. The AUC value represents the area between the ROC curve and the abscissa axis and, with values in the range of [0.5,1], it indicates the good fitting effect of the model on the processed data. Figure 4 shows that the AUC value of this model is 0.70.

These results demonstrated the high evaluation accuracy of the susceptibility assessment model. The landslide susceptibility distribution map in the Jinsha river upstream is shown in Figure 5. The very low and low susceptibility areas are mainly located in the northeast and southwest of the study area, mainly covering the Dege and Mangkang counties. The moderate susceptibility area is very dispersed and primarily located in central Batang county and the western area of Dege county. The very high and high susceptibility areas with the largest floor areas are located near the main stream and tributaries of the Jinsha River.

Based on the susceptibility assessment results, the Litang landslide area with very high susceptibility was selected as a critical hazard for the numerical prediction simulation (Figure 6). The landslide shape was obtained from Cui et al. (2020).

4.2 Dynamic numerical simulation

The Litang landslide, with an area of 1.32 km^2, is located near the Baige landslide. Based on Eq. 7, the mass average soil depth is

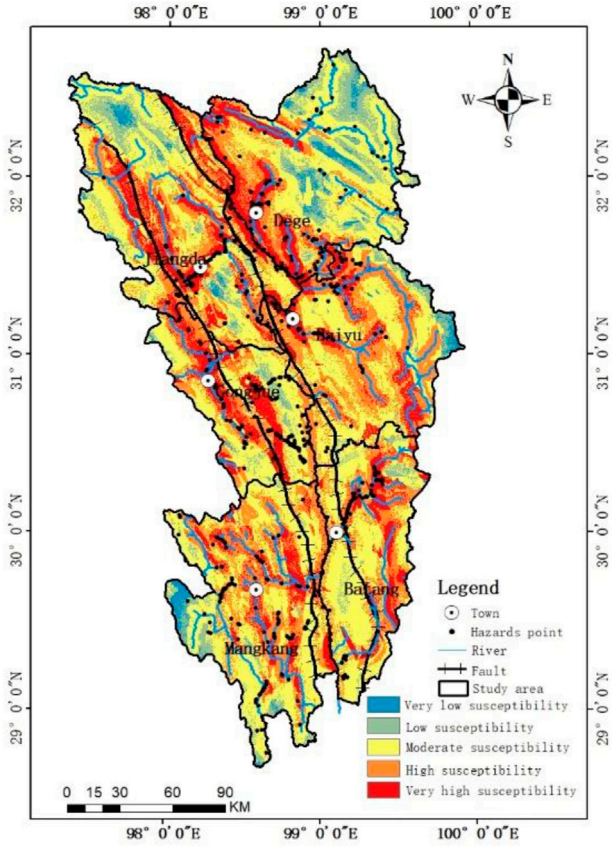

FIGURE 5
Landslide susceptibility map in the study area.

15.2 m. Based on the GIS platform, the mass, topography, and landcover parameters were converted into a "map" file by QGIS and PCRaster. These map data were then input into OpenLISEM for numerical simulation.

According to the simulation results, Figure 7, which is plotted at 20s intervals, displays the entire dynamic process of the landslide from startup to relative stability, which occurs in approximately 100 s. At the initial stage of the landslide dynamic process, the rock mass encounters stability failure and begins to slide along the bedrock surface. From time t = 0–20 s, the landslide body slides downstream in the northwest direction with an average velocity of about 12 m/s (Figure 7A).

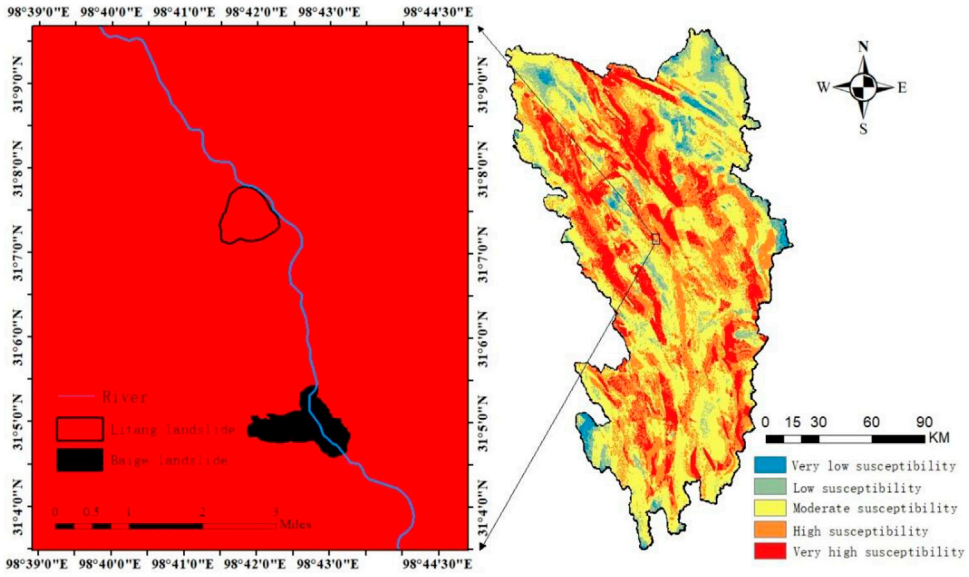

FIGURE 6
Critical landslide location in the study area.

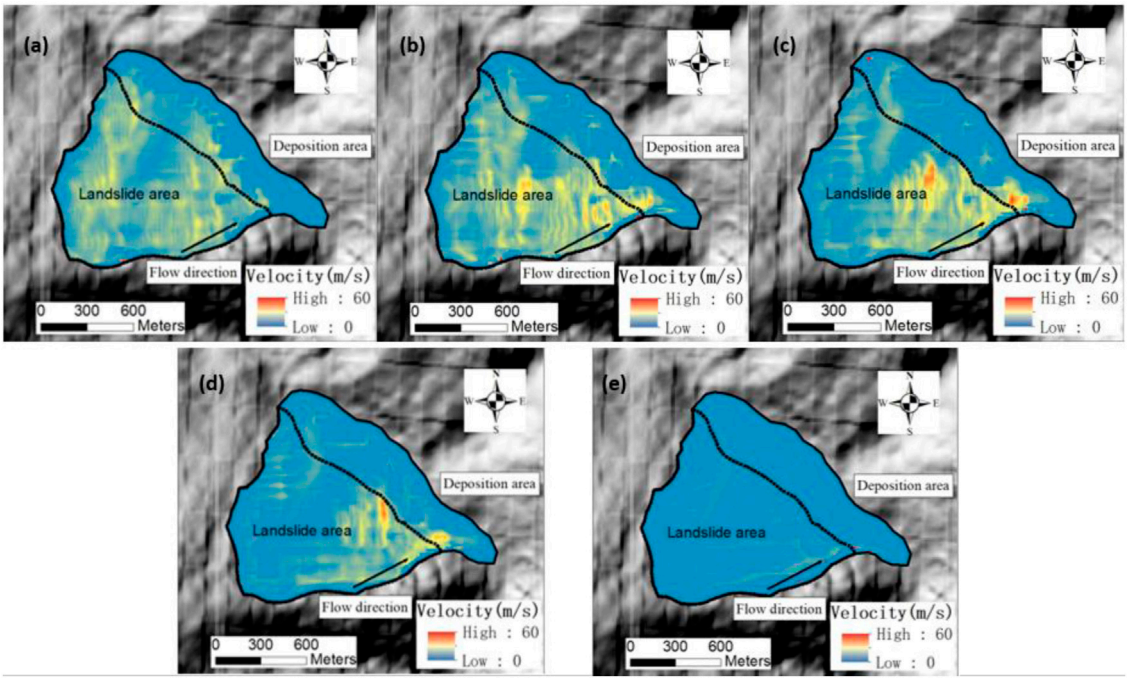

FIGURE 7
Velocity of the landslide movement: **(A)** t = 20 s, **(B)** t = 40 s, **(C)** t = 60 s, **(D)** t = 80 s, and **(E)** t = 100 s.

From t = 20–40 s, the landslide movement is uniform with an average velocity of 15 m/s (Figure 7B). The mass at the front edge of the landslide reaches the Jinsha River at t = 40 s. The main acceleration stage refers to the period from t = 40–80 s, and the peak value of the velocity reaches approximately 59 m/s (Figure 7C). During this period, the rock mass is divided into two parts,i.e., upstream and downstream, due to the influence of the watershed in the central section of the landslide. The deceleration stage refers to the period between t = 80–100 s Figure 7D). During this stage, the average velocity of the rock mass near the upstream part approaches zero, while the average velocity of the rock mass near the downstream part is <10 m/s.

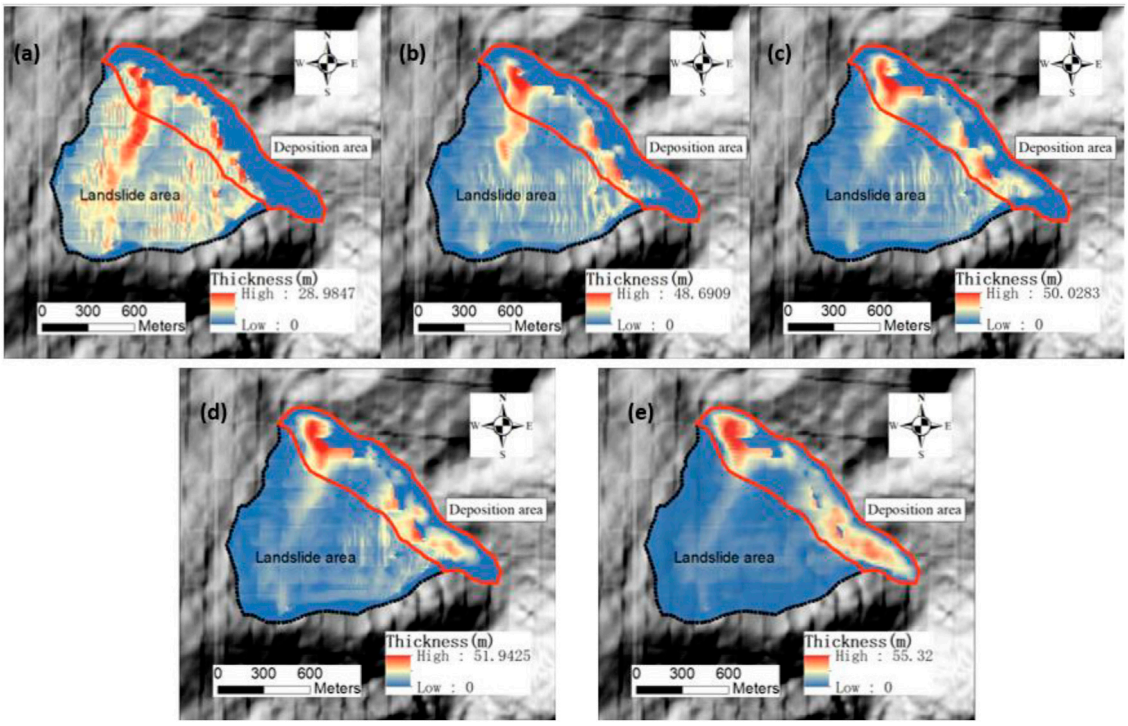

FIGURE 8
Thickness of the landslide movement: **(A)** t = 20 s, **(B)** t = 40 s, **(C)** t = 60 s, **(D)** t = 80 s, and **(E)** t = 100 s.

Simultaneously, some of the mass materials reach the Jinsha River, and the upstream part of the mass begins to form a barrier dam. When t = 100 s, the accumulation stage is complete, and the landslide nearly stops. A large volume of the mass is deposited in the valley within this period (Figure 7E).

As shown in Figure 8, the entire landslide dam covers an area of 0.45 km^2, with a length of 1,600 m and a width of 270 m. Due to the terrain, the final accumulation of the landslide includes two barrier dams with an average thickness of 17 m, which are thin on the sides and thick in the middle. The maximum accumulation thickness is higher on the upstream side relative to the downstream side of the dam (upstream, 55.32 m; downstream, 44.33 m).

5 Discussion and conclusion

This study used susceptibility assessment to identify an area with high susceptibility for a landslide, which was numerically simulated using an OpenLISEM model, to provide a reference for geological hazard prevention in the upper reaches of the Jinsha River.

For susceptibility assessment, the landslide inventory and five hazard factors, including lithology, fault, river, PGA, and slope data, were digitalized and categorized in the ArcGIS model. Based on the landslide intensity in the classification of the five factors, the discriminant coefficient matrix of landslides in the study area was constructed. Principal component and grey correlation analyses were performed to calculate the weights of the factors, which indicated that lithology had the largest impact on landslides. Furthermore, an assessment model was established. The susceptibility results indicated that the high-susceptibility zone accounts for 45.42% of the total area but comprises 75.28% of the landslide numbers, which are located near the main stream and tributaries of the Jinsha River. Therefore, the susceptibility map not only can be used as a basic tool for critical landslide identification but also helps in land use planning. A lack of accurate factor measurements may affect the precision of the factor data. Despite the limitations mentioned above, the ROC curve results showed that the proposed method has the potential for risk reduction in the study area. Moreover, we performed susceptibility analysis for one model. Quantitative and qualitative models are increasingly applied to research on landslide susceptibility, with continued improvements. Landslide hazard data provide important information for susceptibility assessment. However, due to technical limitations, additional research is needed on hazard risk evaluation in areas lacking landslide hazard data.

According to the susceptibility assessment results, the Litang landslide from the high-susceptibility area was selected as a typical hazard for simulation by OpenLISEM. Using the landslide that occurred in Baige on October 10, 2018, as an example, the mass parameters were calibrated to be inconsistent with the movement of the Baige landslide. Then, the mass, topography, and landcover parameters were input into OpenLISEM. The landslide dynamic process simulation was completed in approximately 100 s and comprised four stages: initial start-up, acceleration, deceleration, and accumulation. In the acceleration period, the landslide body was divided into two parts due to the terrain. The entire deposition covered an area of 0.45 km^2, with a maximum thickness of 55.32 m. The numerical simulation analysis of the Baige and Litang landslides showed that OpenLISEM can be applied to the research and analysis

of landslide movement. Using the PCRaster platform, OpenLISEM has good compatibility with the GIS platform, which can provide a reference for further analysis of secondary disaster evolution research (based on the GIS platform). OpenLISEM model simulation requires a large amount of accurate data, and some areas cannot be used for simulation studies of landslide dynamic processes without good simulation data.

Data availability statement

The original contributions presented in the study are included in the article/supplementary material. Further inquiries can be directed to the corresponding author.

Author contributions

YS performed the landslide identification and landslide numerical simulation, analyzed the results, and wrote the manuscript. HD designed the research study and acquired funding. CT provided and updated the data used in this study. BL guided the landslide parameter calibration. All authors contributed to the article and approved the submitted version.

Funding

This research was supported by the Second Tibetan Plateau Scientific Expedition and Research Program (STEP) (grant no. 2019QZKK0906).

Conflict of interest

The authors declare that the research was conducted in the absence of any commercial or financial relationships that could be construed as a potential conflict of interest.

The reviewer KH declared a shared affiliation with authors YS, HD, and BL to the handling editor at the time of review.

Publisher's note

All claims expressed in this article are solely those of the authors and do not necessarily represent those of their affiliated organizations, or those of the publisher, the editors, and the reviewers. Any product that may be evaluated in this article, or claim that may be made by its manufacturer, is not guaranteed or endorsed by the publisher.

References

Abdulwahid, W. M., and Pradhan, B. (2017). Landslide vulnerability and risk assessment for multi-hazard scenarios using airborne laser scanning data (LiDAR). *Landslides* 14, 1057–1076. doi:10.1007/s10346-016-0744-0

An, H., Ouyang, C., and Zhou, S. (2021). Dynamic process analysis of the Baige landslide by the combination of DEM and long-period seismic waves. *Landslides* 18, 1625–1639. doi:10.1007/s10346-020-01595-0

Bai, Y.-J., Li, M.-H., Wang, D.-H., and Gao, Y.-C. (2014). Characteristics and disastrous rule research of geohazards in batang county, the middle reaches of Jinsha river. *Chin. J. Geol. Hazard Control* 25 (2), 103–109. doi:10.16031/j.cnki.issn.1003-8035.2014.02.018

Bout, B., Lombardo, L., van Westen, C. J., and Jetten, V. G. (2018). Integration of two-phase solid fluid equations in a catchment model for flashfloods, debris flows and shallow slope failures. *Environ. Model. Softw.* 105, 1–16. doi:10.1016/j.envsoft.2018.03.017

Chang, M., Tang, C., Zhang, D. D., and Ma, G. c. (2014). Debris flow susceptibility assessment using a probabilistic approach: Acase study in the longchi area, sichuan province, China. *J. Mt. Sci.* 11, 1001–1014. doi:10.1007/s11629-013-2747-9

Chen, J., Cui, Z., Chen, R., and Zheng, X. (2021). The origin and evolution the Temi paleolandslide-dammed lake in the upper Jinsha River. *Earth Sci. Front.* 28 (2), 85–93.

Chen, Z., Zhou, H., Ye, F., Liu, B., and Fu, W. (2021). The characteristics, induced factors, and formation mechanism of the 2018 Baige landslide in Jinsha River, Southwest China. *Catena* 203, 105337. doi:10.1016/j.catena.2021.105337

Choudhury, B. J., Ahmed, N. U., Idso, S. B., Reginato, R. J., and Daughtry, C. S. (1994). Relations between evaporation coefficients and vegetation indices studied by model simulations. *Remote Sens. Environ.* 50 (1), 1–17. doi:10.1016/0034-4257(94)90090-6

Choudhury, B. J. (1987). Relationships between vegetation indices, radiation absorption, and net photosynthesis evaluated by a sensitivity analysis. *Remote Sens. Environ.* 22 (2), 209–233. doi:10.1016/0034-4257(87)90059-9

Cui, Y., Bao, P., Xu, C., Fu, G., Jiao, Q., Luo, Y., et al. (2020). A big landslide on the Jinsha River, Tibet, China: Geometric characteristics, causes, and future stability. *Nat. Hazards* 104, 2051–2070. doi:10.1007/s11069-020-04261-9

Cui, P., and Guo, J. (2021). Evolution models, risk prevention and control countermeasures of the valley disaster chain. *Adv. Eng. Sci.* 53 (3), 5–18.

Fan, X., Yang, F., Siva Subramanian, S., Xu, Q., Feng, Z., Mavrouli, O., et al. (2020). Prediction of a multi-hazard chain by an integrated numerical simulation approach: The baige landslide, Jinsha River, China. *Landslides* 17, 147–164. doi:10.1007/s10346-019-01313-5

García-Davalillo, J. C., Herrera, G., Notti, D., Strozzi, T., and Alvarez-Fernandez, I. (2014). DInSAR analysis of ALOS PALSAR images for the assessment of very slow landslides: The tena valley case study. *Landslides* 11, 225–246. doi:10.1007/s10346-012-0379-8

Gorsevski, P. V., Brown, M. K., Panter, K., Onasch, C. M., Simic, A., and Snyder, J. (2016). Landslide detection and susceptibility mapping using LiDAR and an artificial neural network approach: A case study in the cuyahoga valley national park, Ohio. *Landslides* 13, 467–484. doi:10.1007/s10346-015-0587-0

Jie, D., Liao, M., Qiang, X., Zhang, L., Tang, M., and Gong, J. (2018). Detection and displacement characterization of landslides using multi-temporal satellite SAR interferometry: A case study of danba county in the dadu River basin. *Eng. Geol.* 240 (5), 94–109.

Jin, J,J. (2021). *Study on the development characteristics and stability of the Xiongba giant ancient landslide in the Jinshajiang Fault Zone. A dissertation for maser degree*. Beijing: Chinese academy of geological sciences.

Khan, H., Shafique, M., Khan, M. A., Bacha, M. A., Shah, S. U., and Calligaris, C. (2019). Landslide susceptibility assessment using Frequency Ratio, a case study of northern Pakistan. *Egypt. J. Remote Sens. Space Sci.* 22 (1), 11–24. doi:10.1016/j.ejrs.2018.03.004

Li, X., Guo, C., Yang, Z., Wei, L., Ruian, W., Jijun, J., et al. (2021). Development characteristics and formation mechanism of the xiongba giant ancient landslide in the jinshajiang tectonic zone. *Geoscience* 35 (01), 47.

Liu, D., Cui, Y., Wang, H., Jin, W., Wu, C., Bazai, N. A., et al. (2021). Assessment of local outburst flood risk from successive landslides: Case study of Baige landslide-dammed lake, upper Jinsha river, eastern Tibet. *J. Hydrology* 599, 126294. doi:10.1016/j.jhydrol.2021.126294

Liu, X., Su, P., Li, Y., Zhang, J., and Yang, T. (2021). Susceptibility assessment of small, shallow and clustered landslide. *Earth Sci. Inf.* 14, 2347–2356. doi:10.1007/s12145-021-00687-2

Lu, H., Li, W., Xu, Q., Dong, X., Dai, C., and Wang, D. (2019). Early detection of landslides in the upstream and downstream areas of the baige landslide, the Jinsha River based on optical remote sensing and InSAR technologies. *Geomatics Inf. Sci. Wuhan Univ.* 44 (09), 1342–1354. doi:10.13203/j.whugis20190086

McDonald, H. C., and Grubbs, R. S. (1975). *Landsat imagery analysis: An aid for predicting landslide prone areas for highway construction*. Houston, Texas, USA: NASA Earth Resource Symposium.

Ouyang, C., An, H., Zhou, S., Wang, Z., Su, P., Wang, D., et al. (2019). Insights from the failure and dynamic characteristics of two sequential landslides at Baige village along the Jinsha River, China. *Landslides* 16, 1397–1414. doi:10.1007/s10346-019-01177-9

Pastor, M., Tayyebi, S. M., Stickle, M. M., Yague, A., Molinos, M., Navas, P., et al. (2021). A depth integrated, coupled, two-phase model for debris flow propagation. *Acta Geotech.* 16, 2409–2433. doi:10.1007/s11440-020-01114-4

Peng, C., Wang, S., Wu, W., Yu, H. s., and Chen, J. (2019). Loquat: An open-source GPU-accelerated SPH solver for geotechnical modeling. *Acta Geotech.* 14, 1269–1287. doi:10.1007/s11440-019-00839-1

Pudasaini, S. (2012). A general two-phase debris flow model. *J. Geophys. Research-Solid Earth* 117 (3). doi:10.1029/2011JF002186

Sato, H. P., and Harp, E. L. (2009). Interpretation of earthquake-induced landslides triggered by the 12 May 2008, M7.9 Wenchuan earthquake in the Beichuan area, Sichuan Province, China using satellite imagery and Google Earth. *Landslides* 6, 153–159. doi:10.1007/s10346-009-0147-6

Scaringi, G., Fan, X., Xu, Q., Liu, C., Ouyang, C., Domenech, G., et al. (2018). Some considerations on the use of numerical methods to simulate past landslides and possible new failures: The case of the recent xinmo landslide (sichuan, China). *Landslides* 15, 1359–1375. doi:10.1007/s10346-018-0953-9

Song, Y., Gong, J., Gao, S., Wang, D., Cui, T., Li, Y., et al. (2012). Susceptibility assessment of earthquake-induced landslides using bayesian network: A case study in beichuan, China. *Comput. Geosciences* 42, 189–199. doi:10.1016/j.cageo.2011.09.011

Sun, L. (2021). "Rapid information perception and calculation method of landslide barrier body in alpine and gorge region," in 2021 2nd International Conference on Artificial Intelligence and Information Systems, 1–7.

Tang, C., Zhu, J., Chang, M., Ding, J., and Qi, X. (2012). An empirical–statistical model for predicting debris-flow runout zones in the Wenchuan earthquake area. *Quat. Int.* 250, 63–73. doi:10.1016/j.quaint.2010.11.020

Urgilez Vinueza, A., Handwerger, A. L., Bakker, M., and Bogaard, T. (2022). A new method to detect changes in displacement rates of slow-moving landslides using InSAR time series. *Landslides* 19, 2233–2247. doi:10.1007/s10346-022-01913-8

Wang, F. (2018). *The research of numerical simulation on the initiation and run-out scale of post-earthquake debris flow based on OpenLISEM*. Chengdu: Chengdu University of Technology.

Wang, G., Han, L., Tang, X., and Jin, Z. (2012). Temporal and spatial variation of vegetation in the jinsha river basin. *Resour. Environ. Yangtze Basin* 21 (10), 1191–1196.

Wang, K., Guo, C., Ma, S., Liu, X., and Niu, R. (2016). Landslide susceptibility evaluation based on weight-of-evidence modeling in the xianshuihe fault zone, east Tibetan plateau. *Geoscience* 30 (03), 705–715.

Wang, L., Wen, M., Feng, Z., Sun, W., Wei, Y., Li, J., et al. (2019). Researches on the baige landslide at jinshajiang river, Tibet, China. *Chin. J. Geol. Hazard Control* 30 (01), 1–9. doi:10.16031/j.cnki.issn.1003-8035.2019.01.01

Wei, L. I. U., and Siming, H. E. (2020). Numerical simulation of the evolution process of disaster chain induced by potential landslide in Woda of Jinsha River basin[J]. *Adv. Eng. Sci.* 52 (2), 38–46.

Wei, Y., Xie, Y., and Wu, Y. (1998). Applications of relativity analysis method and fuzzy synthetical assessment method in classification of dangerous degree of debris flow. *J. Nat. Disasters* 7 (2), 112–120.

Woods, A., Hendry, M. T., Macciotta, R., Stewart, T., and Marsh, J. (2020). GB-InSAR monitoring of vegetated and snow-covered slopes in remote mountainous environments. *Landslides* 17, 1713–1726. doi:10.1007/s10346-020-01408-4

Wu, L. (2007). *Research and detect on geological disasters the upriver of Jin sha jiang by remote sensing and GIS*. Hongshan: China University of Geosciences.

Xing, X., Wu, C., Li, J., Li, X., Zhang, L., and He, R. (2021). Susceptibility assessment for rainfall-induced landslides using a revised logistic regression method. *Nat. Hazards* 106, 97–117. doi:10.1007/s11069-020-04452-4

Xu, L., Chang, M., Wu, B., Liu, P., and Zhou, C. (2022). Development characteristics and movement process of Guili landslide in Jinsha River. *J. Disaster Prev. Mitig. Eng.* 2022, 1–9. doi:10.13409/j.cnki.jdpme.20210816001

Xu, Q., Dong, X., and Li, W. (2019). Integrated space-air-ground early detection, monitoring and warning system for potential catastrophic geohazards. *Geomatics Inf. Sci. Wuhan Univ.* 44 (7), 957–966.

Xu, Q., Zheng, G., Li, W., He, C., Dong, X., Guo, C., et al. (2018). Study on successive landslide damming events of Jinsha River in baige village on october 11 and november 3. *J. Eng. Geol.* 26 (6), 1534–1551. doi:10.13544/j.cnki.jeg.2018-406

Xu, W., Yu, W., Jing, S., Zhang, G., and Huang, J. (2013). Debris flow susceptibility assessment by GIS and information value model in a large-scale region, Sichuan Province (China). *Nat. Hazards* 65 (3), 1379–1392. doi:10.1007/s11069-012-0414-z

Xu, W. J., Xu, Q., Liu, G. Y., and Xu, H. Y (2021). A novel parameter inversion method for an improved DEM simulation of a river damming process by a large-scale landslide. *Eng. Geol.* 293, 106282. doi:10.1016/j.enggeo.2021.106282

Yang, G. Y., Zhou, W., and Fang, J. Y. (2018). Assessment of landslide susceptibility based on information quantity model and data normalization. *J. Geoinformation Sci.* 20 (5), 674–683. doi:10.12082/dqxxkx.2018.170535

Yong, C., Jinlong, D., Fei, G., Bin, T., Tao, Z., Hao, F., et al. (2022). Review of landslide susceptibility assessment based on knowledge mapping. *Stoch. Environ. Res. Risk Assess.* 36, 2399–2417. doi:10.1007/s00477-021-02165-z

Yoshimatsu, H., and Abe, S. (2006). A review of landslide hazards in Japan and assessment of their susceptibility using an analytical hierarchic process (AHP) method. *Landslides* 3, 149–158. doi:10.1007/s10346-005-0031-y

Youssef, A. M., Maerz, N. H., and Hassan, A. M. (2009). Remote sensing applications to geological problems in Egypt: Case study, slope instability investigation, sharm el-sheikh/ras-nasrani area, southern sinai. *Landslides* 6, 353–360. doi:10.1007/s10346-009-0158-3

Zhang, C., Li, Z., Yu, C., Chen, B., Ding, M., Zhu, W., et al. (2022). An integrated framework for wide-area active landslide detection with InSAR observations and SAR pixel offsets. *Landslides* 19, 2905–2923. doi:10.1007/s10346-022-01954-z

Zhang, L., Tang, H., and Xiong, C., (2012). Movement process simulation of high-speed long-distance Jiweishan landslide with PFC3D. *Chin. J. Rock Mech. Eng.* 31 (1), 2601–2611. (in Chinese).

Zhang, Y., Ba, R., Ren, S., and Li, Z. (2020). An analysis of geo-mechanism of the baige landslide in Jinsha River, Tibet. *Geol. China* 47 (6), 1637–1645. (in Chinese).

Zhao, C., Fan, X., Yang, F., Zhou, L., and Guo, C. (2020). Movement of baige landslide in Jinsha river and prediction of potential unstable rock mass. *Sci. Technol. Eng.* 20 (10), 3860–3867.

Zhou, S., Ouyang, C., and Huang, Y. (2022). An InSAR and depth-integrated coupled model for potential landslide hazard assessment. *Acta Geotech.* 17, 3613–3632. doi:10.1007/s11440-021-01429-w

Zhou, Y., Qi, S., Wang, L., Chen, M., Xie, C., and Zhou, J. (2020). Instability analysis of a quaternary deposition slope after two sudden events of river water fluctuations. *Eur. J. Environ. Civ. Eng.* 2020, 1–19. doi:10.1080/19648189.2020.1763849

Zhu, L., Liang, H., He, S. M., Liu, W., Zhang, Q., and Li, G. (2020). Failure mechanism and dynamic processes of rock avalanche occurrence in Chengkun railway, China, on August 14, 2019. *Landslides* 17, 943–957. doi:10.1007/s10346-019-01343-z

Zhu, S., Yin, Y., Wang, M., Zhu, M., Wang, C., Wang, W., et al. (2021). Instability mechanism and disaster mitigation measures of long-distance landslide at high location in Jinsha River junction zone: Case study of Sela landslide in Jinsha River, Tibet. *Chin. J. Geotechnical Eng.* 43 (4), 688–697.

Frontiers in Earth Science

Investigates the processes operating within the major spheres of our planet

Advances our understanding across the earth sciences, providing a theoretical background for better use of our planet's resources and equipping us to face major environmental challenges.

Discover the latest Research Topics

See more →

Frontiers

Avenue du Tribunal-Fédéral 34
1005 Lausanne, Switzerland
frontiersin.org

Contact us

+41 (0)21 510 17 00
frontiersin.org/about/contact